

THIS WEEK

EDITORIALS

EGYPT What now for science in the Arab world's most populous country? **p.306**

WORLD VIEW China's new water policy will need radical change to work **p.307**

TRUE BLUE Protein gives penguin feathers their hue **p.309**



Impossible arithmetic

As Congress tries to tackle the \$1.3-trillion US deficit by cutting the \$660-billion discretionary budget, scientists must unite with non-traditional allies to ensure that research doesn't suffer.

This week, as US presidents have done every year for decades, Barack Obama has sent a budget request to Congress that asks for strong support for research and education (see page 313). And, as usual, academic associations and scientific societies will now descend on Capitol Hill and urge Congress to give that support.

Given the financial mood in Washington DC, however, any community that pursues a slice of federal funding in isolation will probably fail. If scientists hope to maintain the kind of research budgets that they have enjoyed in the past, never mind see the increases that Obama hopes for, they will have to unite with groups that are not traditionally their allies, such as advocates for foreign aid and against poverty. And they will have to rally behind an issue that they have officially ignored in the past: serious federal-deficit reduction.

The election of a Republican majority to the House of Representatives last November made it clear that US voters are deeply disturbed by the deficit, which had not only risen to US\$1.3 trillion in the 2010 fiscal year, out of a total budget of \$3.5 trillion, but is projected to run to trillions of dollars more for the foreseeable future. Yet the election results also showed that voters are not convinced that deficit spending will do much to help the nation recover.

So far, neither the Republicans nor the Democrats in Congress have shown any appetite for cutting the 43% of the budget that goes to benefit entitlement programmes such as Social Security and health care for over-65s, which are hugely popular with voters. And the Republicans oppose raising taxes or cutting the 20% of the budget that goes to defence. So the determination of Congress to address the deficit comes up against impossible arithmetic. The \$1.3 trillion required to bring the budget into balance must somehow be cut from the only piece left: the \$660-billion 'discretionary' segment, which covers activities from air-traffic control and upkeep of national parks to education and research.

The House Republican majority has vowed to press ahead, and last week announced plans to trim the budget for 2011 by \$100 billion. Their list of cuts was overtly political, prominently targeting Obama's priorities in areas such as renewable energy and environmental protection. But these are also areas whose payoff, if there is to be any, lies well in the future. Once budget cuts start to reach deep enough to hurt constituents, risk-averse politicians find it easiest to target those parts of the discretionary budget in which the pain will not be felt immediately — that is, long-term investments such as research.

Obama has shown himself to be a strong supporter of science, education and infrastructure investments. In his State of the Union address on 25 January, he touted them as essential for what he called "winning the future" — a theme that he carried forward in this week's budget. Yet Obama, too, has shied away from tackling the deficit head on, either by cutting entitlements or by raising taxes.

To some extent, the duelling budget proposals can be seen as political theatre, in which the two sides publicly stake out their initial positions ahead of hard bargaining. But the proposals also represent very

different visions of government: when Obama says "win the future", activist Republicans tend to hear "another power grab by Washington DC". It seems all too conceivable that the bargaining will go nowhere, that the gridlock will continue indefinitely — and that science will be just one among many communities paying the price.

This explains why US researchers have to go beyond the usual lobbying. Individually, and through their professional societies, they must join their voices with others calling for a comprehensive solution to the deficit. Plausible blueprints based on the reform of taxes and entitlements were offered last December by several high-level, bipartisan deficit-reduction commissions, including one appointed by Obama. And in the Senate, a bipartisan group led by Democrat Mark Warner of Virginia and Republican Saxby Chambliss of Georgia is working to turn those blueprints into a plan that could be passed into law.

The research community should back these efforts as vocally and forcefully as they can, even if only as a matter of self-interest. The senators are trying to forge a rational solution to an issue fraught with political passion, and they need all the support they can get. ■

"Risk-averse politicians find it easiest to target long-term investments such as research."

Devil in the details

To ensure their results are reproducible, analysts should show their workings.

As analysis of huge data sets with computers becomes an integral tool of research, how should researchers document and report their use of software? This question was brought to the fore when the release of e-mails stolen from climate scientists at the University of East Anglia in Norwich, UK, generated a media fuss in 2009, and has been widely discussed, including in this journal. The issue lies at the heart of scientific endeavour: how detailed an information trail should researchers leave so that others can reproduce their findings?

The question is perhaps most pressing in the field of genomics and sequence analysis. As biologists process larger and more complex data sets and publish only the results, some argue that the reporting of how those data were analysed is often insufficient.

Take a recent survey by comparative genomist Anton Nekrutenko at Pennsylvania State University in University Park and computer scientist James Taylor of Emory University in Atlanta, Georgia. The

pair examined 14 sequencing papers published last year in *Science*, *Nature* and *Nature Genetics*, and found that the publications often lacked essential details needed to reproduce the analysis — the papers referenced merely bioinformatics software, for example, without noting the version used or the value of key parameters.

The two researchers presented their findings at the Advances in Genome Biology and Technology meeting in Marco Island, Florida, on 2 February. Although their account has not been published, it does not seem to have surprised anyone in the field. Indeed, it builds on a 2009 paper in *Nature Genetics* that found similar omissions in published accounts of microarray experiments. (J. P. A. Ioannidis *et al.* *Nature Genet.* **41**, 149–155; 2009). In this case, findings from 10 of the 18 studies analysed could not be reproduced, probably because of missing information.

If genomics were as politicized as climate science, the authors of studies in which the information trail is missing would probably face catcalls, conspiracy charges and demands for greater transparency and openness. Instead, many in the field merely shrug their shoulders and insist that is how things are done. Bioinformatics is a fast-paced science in which software and standards for data analysis change rapidly and with them, the protocols and workflows of users.

Nature does not require authors to make code available, but we do expect a description detailed enough to allow others to write their own code to do a similar analysis.

Some in the field say that it should be enough to publish only the original data and final results, without providing detailed accounts of the steps in between. Others argue that it is pointless to document the version of the software used, as new incarnations of programs differ little. But that is not always the case. Edward McCabe, then at the California NanoSystems Institute at the University of California, Los Angeles, was so perturbed when different versions of the

same bioinformatics software gave wildly different results that he published a paper on it (N. K. Henderson-MacLennan *et al.* *Mol. Genet. Metab.* **101**, 134–140; 2010). Reviewers resisted its publication, asking what was new about the findings, as it was already common knowledge that different software versions could dramatically affect analyses. There is a troubling undercurrent here: that the problem lies not with the lack of information, but rather with those who find the incomplete information a problem, such as researchers who are new to the field.

Transparency is a laudable goal, but given the complexity of the analyses, is it realistic? There are certainly examples of stellar documentation. The 1000 Genomes Project, for example, a project to

“Transparency is a laudable goal, but given the complexity of the analyses, is it realistic?”

sequence and analyse more than a thousand genomes, has carefully detailed its workflows, and makes both its data and its procedures available for the world to see. It is perhaps easier for members of that project — which is essentially repeating the same procedure more than a thousand times — to practise good experimental hygiene than it is for individual scientists, who have more flexible and varied research goals.

Nevertheless, tools are coming online to simplify documentation of the complex analyses required for genome analysis. These include freely available programs such as Taverna (www.taverna.org.uk) and Nekrutenko's more user-friendly Galaxy (<http://main.g2.bx.psu.edu>). Neither of these is perfect, but they illustrate the level of detail that could enrich published reports.

As genome sequencing spreads from the large, centralized sequencing centres that largely pioneered the technique into smaller labs and clinics, it is important that the community consider such solutions. ■

Line in the sand

In the wake of the revolution, Egypt should embrace a future based on scientific thinking.

On Saturday, Wael Ghonim, a Google executive who helped to instigate Egypt's revolution and has become its reluctant icon, tweeted, “Go back to your work on Sunday, work like never before and help Egypt become a developed country.”

More than two weeks of nationwide protests have finally toppled Hosni Mubarak, president of the country and leader of its repressive regime since 1981, who handing power to Egypt's Supreme Military Council in the early evening of 11 February. Considerable political uncertainty remains, but activists and intellectuals are vigilant, and insist that they will protect their revolution. This was a peaceful uprising, in which groups of educated youth attracted millions onto the streets to call for democracy, freedom and change: a movement with an uplifting sense of civic responsibility. For the first time, the faces of ordinary young Egyptians — and their aspirations for fundamental civil liberties and self-determination — could be seen internationally. So, what happens now, and what will it mean for science's role in the development of the Arab world's most populous nation?

Egypt's intellectuals and youth largely share Ghonim's instinct that their most urgent task is to begin a radical reconstruction of the country's society and economy. They know that an overhaul of the education and science systems will be crucial to this restructuring, unleashing the bottled-up energy and creativity of a youth that has been stifled for too long. Leading Egyptian researchers — including Ahmed Zewail, a chemist at the California Institute of Technology in Pasadena, who won the 1999 Nobel Prize in Chemistry and is

currently in Egypt to lend his hand to efforts to transition to democracy — are right to argue that education and research must be a top priority. They will be vital to taking the new Egypt and its young workforce into the twenty-first century, and to creating a more enlightened and productive society.

Research in Egypt, as in much of the Arab world, has long lagged behind that elsewhere, receiving only a paltry 0.2–0.3% of gross domestic product. Mubarak's regime was preoccupied instead with geopolitical security — an interest shared by the United States and other Western powers that propped it up — and neglected to invest in the infrastructure necessary for an educated and creative workforce. This contributed to the accumulation of social and economic woes that helped the revolution to win popular support.

As in Tunisia, the scene of an equally successful uprising this year, Egypt's repressive regime stifled research initiatives, and placed its cronies, rather than top scientists, in positions of academic power. Frustrated scientists left to seek opportunities abroad. Education in the country suffers similar problems: it is often based on rote learning, which smothers debate, creative thinking and entrepreneurship. As one Egyptian researcher told *Nature*, the universities “are simply assembly lines that produce thousands of unskilled graduates every year.”

With sufficient investment, realistic plans can be drawn up to reform and revamp Egypt's education and research systems. Vast expertise is available both inside and outside the country. But that alone will not be enough: democracy, freedom and a new culture that encourages criticism and creativity must underpin any reforms. As Ismail Serageldin, director of the Library of Alexandria, put it to

Nature on the eve of Mubarak's fall: “Building science is not just a question of money and projects, it is also about a whole climate of research, of freedom of enquiry, freedom of expression, education, the ability to question.” ■

➔ **NATURE.COM**
To comment online,
click on Editorials at:
go.nature.com/xhbnq

LI HUI



China's water crisis needs more than words

A new water strategy from the Chinese government is a step in the right direction, says Chaoqing Yu. But it will be difficult to put into practice.

Late last month, the Chinese government announced that it will invest four trillion renminbi (US\$600 billion) over the next ten years to protect and improve access to water. The policy was spelt out in this year's No 1 Document — the central government's first policy document of the year, setting the top priorities — released on 29 January, and comes as a severe and continuing drought in northern China threatens crops of winter wheat.

The Chinese government is right to highlight sustainable use of water resources as critical for China's food, economic, ecological and even national security. Among the measures it proposes are control of total water consumption, improved irrigation efficiency, restricted groundwater pumping, reduced water pollution and guaranteed funds for water-conservancy projects. Such a national policy could go a long way to help secure and protect China's water. How to put the policy into practice, however, remains challenging.

Since the 1950s, China has constructed 86,000 reservoirs, drilled more than four million wells, and developed 58 million hectares of irrigated land, which generates 70% of the country's total grain production. Efforts to conserve water have lagged far behind. The largest threat to sustainable water supplies in China is a growing geographical mismatch between agricultural development and water resources. The centre of grain production in China has moved from the humid south to the water-scarce north over the past 30 years, as southern cropland is built on and more land is irrigated further north. As the north has become drier, increased food production there has largely relied on unsustainable overuse of local water resources, especially groundwater. Wasteful irrigation infrastructure, poorly managed water use, as well as fast industrialization and urbanization, have led to serious depletion of groundwater aquifers, loss of natural habitats and water pollution.

To tackle water issues in China, one problem that must be addressed is the scattering of authority across different agencies. At present, major rivers are managed by the Ministry of Water Resources, whereas local governments control smaller water courses. Water supply, farmland irrigation, groundwater, water pollution and weather forecasting are separately administrated by, respectively, the Ministry of Housing and Urban-Rural Development, the Ministry of Agriculture, the Ministry of Land and Resources, the Ministry of Environmental Protection, and the State Meteorological Administration.

Data on precipitation, river runoff, groundwater, land use, pollution and water use are not shared between governmental agencies, or made accessible to the public. It will be difficult to implement the holistic policy laid out in the No 1 Document without breaking down these bureaucratic barriers.

As a starting point, China needs to build an integrated network to monitor surface and groundwater, and use it to assess and set water policies through an integrated water-resource management system. And for this to happen, China needs a law that sets out clear policies on data sharing, and penalties for those who do not comply.

Other legislation is needed too. A water law introduced in 1988, and amended in 2002, is too vague to apply in practice, and there remains confusion over water rights of individuals, such as whether to grant them based on land ownership or use.

As political attention to water increases, a new, fair water law, based on transparent decisions, is essential to protect citizens' rights and prevent corruption. Low-income farmers will suffer greatly if water prices rise. To protect them, and so food supplies, China must keep irrigation costs low. Clear measures will also be needed to better match food production with water availability. Without regulation to increase food production in the south, it will be difficult to maintain food security, even if water-use efficiency is improved in the north.

Some of the areas identified in the document need more attention. Despite increasing concern about the effects of climate change on the availability and suitability of water resources, the document does not specifically define adaption to climate impacts. It is also vague on how the departments of water resources and environment protection should cooperate on planned new limits on water pollutants. Ecological water use is mentioned, but the document does not outline the specific measures that will be needed to protect the water supply of ecosystems against conflicting demands of economic activity. The role of ecosystems in water availability must be explicitly accounted for.

How will the money be raised to deliver the government's promises on water? The document demands that local governments reserve 10% of the annual income (currently 70 billion renminbi) from land sales for real-estate development to be used for water projects. However, it is not clear whether this money would be better held by local governments or allocated by Beijing.

The current drought shows how urgent the problem of sustainable water use and supply is for China. Although many of the policies and measures in the No 1 Document are not new and still need more work, the high priority the government has placed on sustainable water use is extremely welcome. ■

**CHINA NEEDS
TO BUILD AN
INTEGRATED
NETWORK
TO MONITOR SURFACE
AND GROUNDWATER.**

➔ **NATURE.COM**
Discuss this article
online at:
go.nature.com/wxqs3y

Chaoqing Yu is associate professor in the Center for Earth System Science and the Institute for Global Change Studies, Tsinghua University, Beijing, China. Colleagues **Peng Gong** and **Yongyuan Yin** also contributed.
e-mail: chaoqingyu@gmail.com.

RESEARCH HIGHLIGHTS

Selections from the
scientific literature

ECOLOGY

Frogs at home with relatives

Charles Darwin proposed that competition would lower the success of species invasions if an ecosystem contained closely related species. But he may have been wrong, at least where amphibians are concerned. Members of this class are more likely to successfully establish themselves in new environments when they are related to species already resident there.

Reid Tingley and his colleagues at the University of Sydney, Australia, analysed data on 521 successful and failed introductions of 162 amphibian species. They found that the chances of successful invasion rose as the richness of related species grew.

The results could aid conservation efforts by helping to predict whether introduced species will be successful in establishing themselves.

Am. Nat. doi:10.1086/658342 (2011)

MATERIALS SCIENCE

Chemical scissors cut graphene

High-performance electronic devices made entirely of carbon could be created using low-cost, conventional microfabrication approaches to pattern one-atom-thick

layers of carbon called graphene.

Zhongfan Liu at Peking University in Beijing and his collaborators laid a titanium dioxide-based photomask — a small stencil — on a sheet of graphene. The photomask catalyses the formation of hydroxyl radicals when ultraviolet light is shone onto it. This highly reactive species oxidizes graphene only in the irradiated regions — essentially acting like scissors to break carbon bonds and produce patterns (**pictured**). Using this approach, the authors fabricated an all-carbon transistor that performed similarly to conventional ones. The method is solvent-free, so avoids possible contamination issues.

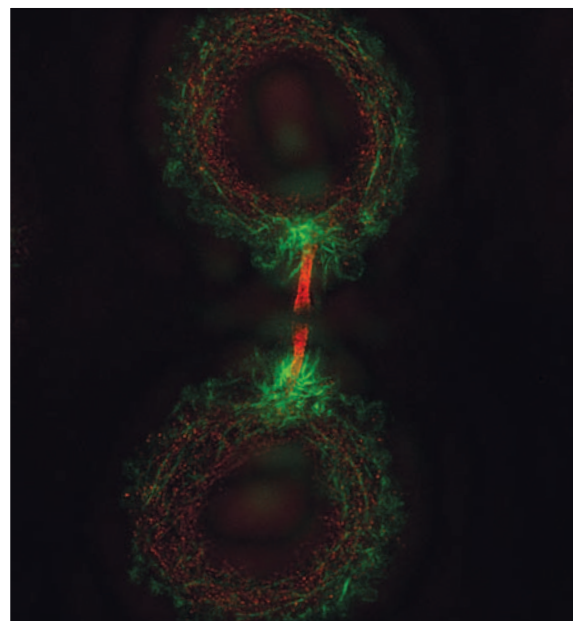
J. Am. Chem. Soc. doi:10.1021/ja109934b (2011)

INFECTIOUS DISEASES

Targeting typhoid fever

Many thousands of people around the world die of typhoid fever every year, but little is known about how the bacterium *Salmonella enterica* Typhi causes the disease. A protein identified on the microbe's outer surface seems to be key to *S. enterica* Typhi's virulence and could be a target for more effective vaccines.

Using bioinformatic techniques, Santasabuj Das and his colleagues at the National Institute of Cholera and Enteric Diseases in Kolkata, India, looked for *S. enterica* Typhi proteins that could bind to host receptors and homed in on one, called T2544. Bacteria in which the gene for this protein had been deleted showed reduced adhesion to human cells and, in particular, to laminin, a protein abundant in the matrix



CELL BIOLOGY

Cell division in a pinch

Time-lapse images have revealed the final steps of cell division, when a thin intercellular bridge connecting the two cells (**pictured**) splits.

Daniel Gerlich at the Swiss Federal Institute of Technology in Zurich and Thomas Müller-Reichert at Dresden University of Technology in Germany found that helical protein filaments wrap around and constrict this bridge, narrowing it to a single stalk just before the cells separate.

High-resolution imaging of a fluorescently tagged protein found in a complex called ESCRT-III revealed that the complex accumulates where the bridge tightens. In cells lacking the complex, the intercellular bridge did not constrict. The authors propose that ESCRT-III components join together to form the filament helices.

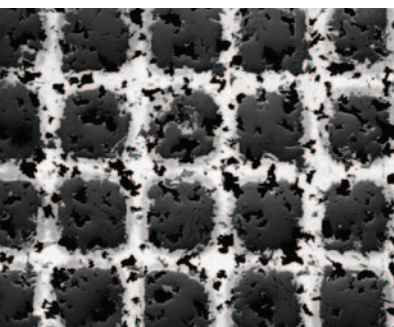
Science doi:10.1126/science.1201847 (2011)

between cells. When mice were infected with a specific dose of the normal bacteria, half died within a week, whereas animals infected with the same dose of the mutant strain all survived. Moreover, T2544 triggered a protective antibody response in the mice. *Proc. Natl Acad. Sci. USA* doi:10.1073/pnas.1016180108 (2011)

PALAEOCLIMATE

Ice-smothered British isles

Ice sheets repeatedly crept down to cover extensive areas of Britain and Ireland at the start of the Northern Hemisphere ice age — more than 1 million years earlier than previously thought.



Mieke Thierens of University College Cork in Ireland and her co-workers examined sediments deposited in coral carbonate mounds off Ireland's south-west Atlantic coast. Inspection of the grains and chemical analysis of their provenance suggested that the debris was deposited by icebergs calving off from an ice cap covering Britain and Ireland as long ago as 2.6 million years.

Scotland was previously the most southerly area assumed to be glaciated at the time, but it seems that colder climates — driven by changes in the tilt of Earth's axis — spurred ice sheets to encroach on even lower latitudes.

Quatern. Sci. Rev. doi:10.1016/j.quascirev.2010.12.020 (2011)

STEM CELLS

The way to a beating heart

Mouse skin cells have been directly reprogrammed to become beating heart cells. The method used could be safer and more efficient than previously developed techniques, which can take weeks, yield low numbers of cells and may generate stem cells with the potential to cause cancer.

Sheng Ding at the Scripps Research Institute in La Jolla, California, and his team found a short cut that bypasses the stem-cell stage. The researchers briefly exposed the skin cells to three genes often used in cellular reprogramming and grew the cells in a special medium to avoid the generation of stem cells. Then, treatment with a cocktail of cardiac growth factors coaxed the cells into becoming beating heart cells. The method took just 11–12 days to generate the first beating cells and yielded more cells than previous direct cardiac cell reprogramming techniques. *Nature Cell Biol.* doi:10.1038/ncb2164 (2011)



Bones made for walking

One of the earliest human ancestors had human-like foot arches that would have allowed it to walk effectively on two legs. The finding may help to resolve the debate about whether this species, *Australopithecus afarensis*, was completely adapted to terrestrial bipedalism or retained the ape-like ability to climb in the trees.

Carol Ward at the University of Missouri in Columbia and her team analysed a fossilized bone about 3.2 million years old from Ethiopia. The fossil, the fourth metatarsal, is one of the bones that makes up the mid-foot. In flat-footed, tree-climbing chimpanzees, the bone lies flat against the ground, whereas in humans it is twisted and angled — an indicator of stiff, arched feet well adapted for walking with a human-like stride. The *A. afarensis* bone was twisted and angled similarly to its modern human equivalent. *Science* 331, 750–753 (2011) For a longer story on this research, see go.nature.com/nxlyle

BIOMATERIALS

Nanofibre makes penguins blue

The colour that gives the blue penguin its name is produced by a protein nanostructure in the bird's feathers.

Matthew Shawkey at the University of Akron in Ohio, Vinodkumar Saranathan at Yale University in New Haven, Connecticut, and their colleagues analysed barbs on the feathers of blue penguins (*Eudyptula minor*; pictured). They found that a quasi-ordered structure made up of densely packed, parallel nanofibres of the protein β -keratin scatters light in a way that produces the blue tinge.

COMMUNITY CHOICE

The most viewed papers in science

NEUROSCIENCE

Shining a light on depression

HIGHLY READ
on www.
jneurosci.org in
Dec 2010

A reduction in the activity of neurons in the brain's prefrontal cortex is probably a cause, rather than a consequence, of depressive behaviours.

Eric Nestler at Mount Sinai School of Medicine in New York and his colleagues found, at post-mortem, unusually low expression of key genes in parts of the prefrontal cortex of people with depression. Mice displaying depressive behaviours after being repeatedly defeated by aggressive mice showed similar gene-expression changes in the same brain region. However, some resilient animals showed neither these behaviours nor reduced gene activity.

The researchers then used light to directly activate cortical neurons in the mice, which had been engineered to overexpress a light-sensitive protein in these cells. The depressive behaviour of susceptible mice was reversed — without affecting other behaviours such as movement or social memory.

J. Neurosci. 30, 16082–16090 (2010)

The structure is similar to ones made of collagen that are responsible for colours in the skin of some birds and mammals. Only two other non-iridescent colour-producing nanostructures have previously been reported in birds, the authors say, and both derive from β -keratin.

Biol. Lett. doi:10.1098/rsbl.2010.1163 (2011)



D. STAHL

PALAEOCLIMATE

Mexico's history in tree rings

An analysis of thousand-year-old trees has linked megadroughts to upheavals in ancient Mexican civilizations.

David Stahl at the University of Arkansas in Fayetteville and his colleagues measured tree rings from 30 Montezuma baldcypress trees (*Taxodium mucronatum*, pictured) growing in a central Mexican gorge. They used the measurements to reconstruct the region's climate between 771 and 2008.

A severe drought in Central America also reached into Mexico between 897 and 922,

and may have contributed to the fall of the Mayan empire. Another dry spell stretching between 1149 and 1167 overlapped with the decline of the region's Toltec culture and the abandonment of its capital in around 1150. And the Spanish conquest of the Aztecs in 1521 was preceded by an extended drought that may have exacerbated disease epidemics.

Geophys. Res. Lett. doi:10.1029/2010GL046472 (2011)

NATURE.COM

For the latest research published by Nature visit:

www.nature.com/latestresearch

SEVEN DAYS

The news in brief

POLICY

EU funding reform

The European Commission has launched a public consultation on the future of Europe's main research-funding mechanism. The current system, the 7-year, €50.5-billion (US\$68.3-billion) Seventh Framework Programme, will end in 2013. A green paper released on 9 February asks what the next programme might be called, and how it might be restructured to broaden participation, lower administrative burdens and mesh with national policies. Contributions are invited until 20 May. The Commission's top science advisory group, the European Research Area Board, has already recommended that there be less political interference in the framework programme (see *Nature* 470, 16; 2011).

US budget clash

Battle-lines have been drawn over the future of science funding in the United States, after US president Barack Obama released his 2012 budget request on 14 February. With increases sought for several science agencies, it sets Obama on a collision course with the Republican-controlled House of Representatives, which hopes to cut funding for many of the same organizations. See pages 313–315 for details.

Vaccine initiative

Kenya became the fifth country to roll out a new pneumococcal vaccine this week, under a plan to help developing countries adopt new vaccines as speedily as the developed world. Pharmaceutical companies usually have little incentive to research and produce affordable vaccines for poor nations. But the initiative, led by the GAVI Alliance, breaks

this impasse by guaranteeing firms a market for their products, and cuts vaccine prices further using public subsidies. If more money can be raised, more than 40 developing countries are expected to roll out the vaccine by 2015. See go.nature.com/hmkdyd for more.

Grants glitch

Computer glitches forced Australia's National Health and Medical Research Council to shut down its online system for accepting funding applications last week. The council's chief executive, Warwick Anderson, said that deadlines for some research

grants would be extended to April. As *Nature* went to press, the system was still down. The council awards AUS\$700 million (US\$700 million) in grants each year.

BUSINESS

Biofuel offering

Gevo, a company that genetically modifies microbes to produce chemicals from plant sugars, raised US\$107 million at \$15 a share in an initial public offering on 9 February. The company, headquartered in Englewood, Colorado, saw its shares rise about 10% on the opening day's trading.

Using technology in part licensed from metabolic engineer James Liao at the University of California, Los Angeles, Gevo plans to make and sell isobutanol, which could replace ethanol as a fuel additive, but which is also used to produce plastics and rubber.

Pollution fight

US oil giant Chevron of San Ramon, California, says that it will appeal a US\$8.6-billion fine imposed for environmental damages by an Ecuadorian court on 14 February, calling the judgment "illegitimate and unenforceable". The lawsuit was brought on behalf of thousands



AP PHOTO/K. HAMRA

Egypt's revolution offers hope to science

Elated scientists joined celebrations throughout Egypt following the resignation of Hosni Mubarak on 11 February, after 30 years of presidency. With the military in interim control, the country's future is unclear, but academics are already hoping to improve its moribund research system. Egyptian-born scientist Ahmed Zewail, winner of the 1999 Nobel Prize in Chemistry, told state television that he would present a plan to overhaul research

and education. Mohamed El Raey, a physicist at the University of Alexandria, told *Nature Middle East* that support for education, science and technology should be Egypt's "first line of defence" (see Editorial, page 306). Valuable treasures did not survive the revolution unscathed; it emerged on 12 February that eight objects were missing from Cairo's Museum of Egyptian Antiquities. For the latest news and interviews, see nature.com/arabawakening.

of Ecuadorians, who claim that the company should be held responsible for pollution stemming from drilling in the Amazon during the 1970s and 1980s. The drilling was carried out in part by the oil company Texaco, which Chevron later purchased.

RESEARCH

Comet flyby

NASA's Stardust spacecraft sped past comet Tempel 1 on 14 February. The probe, which had previously collected dust from the Wild 2 comet, snapped images of Tempel 1 five-and-a-half years after the agency's Deep Impact mission visited and shot a projectile into the same comet. Researchers hope to spot differences that will reveal how comets change with each orbit round the Sun, and will zero in on the Deep Impact crater to determine more about the strength and stability of Tempel 1's upper layers. See go.nature.com/fhikl9 for more.

Peruvian artefacts

Yale University in New Haven, Connecticut, is to establish a museum and joint research centre with the University of Cusco in Peru, to house a collection of tools, ceramics and bones from the Inca site Machu Picchu. The Peruvian government had long been demanding the return of

the objects, excavated by US archaeologist Hiram Bingham in the early 1900s; last November, Yale agreed to send them back to South America. Details of the formal accord, including plans for a laboratory for collaborative investigations, were unveiled on 11 February.



Trip to virtual Mars

Humans have walked on the surface of Mars — in a simulated expedition (pictured). For 520 days, the Mars500 mission is cooping up six men in three small rooms at the Institute of Biomedical Problems in Moscow, simulating the isolation of a journey to Mars and back. Eight months after 'launch', the expedition reached orbit and three crew members were selected to enter a lander on 8 February. Four days later, they walked on reddish sand resembling that of Mars's Gusev crater. After two more

sorties to the surface, the virtual journey back to Earth will start on 1 March.

Animal diseases

Livestock plagues are on the rise globally, owing to increasingly intensive farming practices and the world's growing taste for meat and other animal products. The warning came from scientists at the International Livestock Research Institute (ILRI), based in Nairobi, Kenya, at a conference in New Delhi on 10–12 February. Developing countries, including many in Africa and Asia, lag "dangerously behind" in controlling these diseases, says John McDermott, deputy director-general for research at the ILRI. See go.nature.com/bhbgby for more.

Forest rights

The intensifying hunt for land for agriculture and biofuels threatens the rights and livelihoods of millions of people who live in tropical forests, according to a report launched in London on 8 February. The Rights and Resources Initiative, a coalition of advocacy groups and non-governmental organizations based in Washington DC, found a "disturbing tendency of some governments to roll back hard-won local land rights" as forests become more valuable. The rights of local

COMING UP

22–23 FEBRUARY

In La Jolla, California, leading genetics researchers gather to discuss the promise of human genomics over the next decade.

go.nature.com/w8zzsx

23 FEBRUARY

NASA's Glory probe is scheduled to launch. It will monitor aerosols in the atmosphere and the Sun's radiation output.

go.nature.com/z3cke6

people in African countries have the least recognition, the report says. See go.nature.com/ayiyo3 for more.

PEOPLE

Stolen secrets

A former research chemist at the chemical giant Dow was last week found guilty of stealing trade secrets, and of perjury. Wen Chyu Liu, also known as David W. Liou, conspired with "at least four" current and former Dow employees to steal details on the industrial polymer chlorinated polyethylene. The information was then sold to companies in China, according to the US Department of Justice. Liu, who retired from Dow in 1992, faces a maximum of 15 years in prison on the charges; he has not yet been sentenced.

NAS president

Ralph Cicerone was re-elected president of the US National Academy of Sciences (NAS) on 10 February. Cicerone, an atmospheric scientist who was chancellor of the University of California, Irvine, before his NAS presidency began in 2005, will serve a second six-year term at the top, beginning on 1 July this year.

NATURE.COM

For daily news updates see:

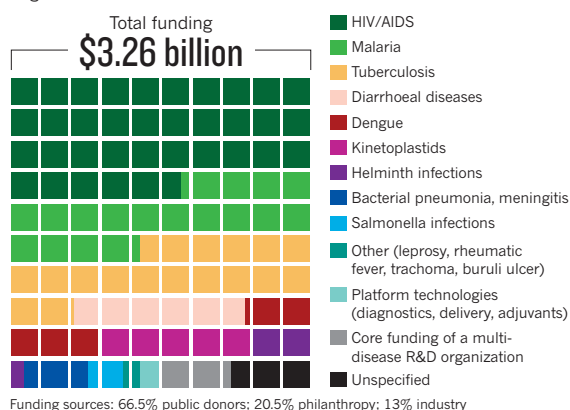
www.nature.com/news

TREND WATCH

Funding for work on neglected diseases totalled US\$3.26 billion in 2009 — an 8% rise in real terms over 2008, according to the third annual 'G-Finder' investment survey by Policy Cures, a health-policy analysis firm based in London and in Sydney, Australia. Funding for basic research jumped by 21%; but for product development, it rose only 5%. And funding for organizations that manage private-public partnerships to develop drugs dropped by 8.6%, which the report terms a "troubling trend".

FUNDING FOR NEGLECTED DISEASES

HIV, malaria and tuberculosis commanded 72% of funding for neglected diseases in 2009.



NEWS IN FOCUS

US BUDGET Republicans threaten deep cuts in 2011 science spending **p.314**

GULF SPILL After the gush of oil, a slow trickle of research funding **p.317**

EPIDEMIOLOGY Tracking every breath you take, every bite you eat **p.320**

SCIENCE AND RELIGION Does the Templeton Foundation blur the line? **p.323**

A. HARRER/BLOOMBERG/GETTY



How to innovate on US\$66.8 billion a year.

FUNDING

Obama resists research cuts

Increases for science and technology in the 2012 US budget prioritize innovation over reductions in the national deficit.

BY IVAN SEMENIUK, JEFF TOLLEFSON, MEREDITH WADMAN, ADAM MANN AND GWYNETH DICKEY ZAKAIB

On the morning his administration unveiled its budget request for the 2012 fiscal year, US President Barack Obama was addressing students at a school with a specialized science and technology programme in Baltimore, Maryland. The choice was deliberate. Obama has made numerous public appearances in recent weeks to push his strategy of “winning the future” for an embattled US economy by investing in research, innovation

and education. His latest budget, released on 14 February, puts numbers to the rhetoric, with a US\$66.8-billion request for federal science spending. The total represents a 6% increase over current funding, with some agencies (see table and graph) faring even better.

In a climate of fiscal restraint, the budget “contains more for science than many would have thought possible”, says John Holdren, Obama’s science adviser. But precisely what is possible is now the question. Obama’s budget portrays an alternative universe that stands in stark contrast to that of Republicans in the House of Representatives, who are calling for

huge cuts to all non-mandated government spending. Given the Republicans’ determination to rein in a record federal deficit (see ‘Budget battle heats up’), it is not at all clear that the president will be afforded the opportunity to play the innovation game that he hopes to win.

“It’s going to be bloody,” says Neal Lane of the political battle that is now set to unfold on Capitol Hill. A physicist at Rice University in Houston, Texas, Lane was director of the US National Science Foundation from 1993–98 — the last time a Democrat administration tangled with a Republican Congress over spending cuts — and later was President Bill Clinton’s science adviser. His concern, he says, is that acrimony over the budget will delay progress and leave researchers spinning their wheels. “People are really hungry for anyone [in Congress] showing any sign that they are willing to work together.”

For Patrick Clemons, a science-policy analyst and director of the research and development budget and policy programme at the American Association for the Advancement of Science in Washington DC, the differences between Obama and Republican leaders in the House are clear — but perhaps not as large as is sometimes assumed. “I think basic research is strongly supported by both sides,” he says. Where opinions diverge, he says, is on the extent to which government should be engaged in fostering innovation, with Republicans more inclined to let the private sector drive it forward.

Holdren disagrees with the premise that the budget’s theme represents an exclusively ‘top down’, government-driven model. “This is neither top down nor bottom up but both,” he says. “This is a matter of unleashing the innovation potential that is in our society by drawing on all levels and getting them to work together.”

Here is a closer look at what the budget will mean in key areas and agencies.

ENERGY

Energy is the domain in which Obama’s vision is most ambitious — and most at odds with that of Republicans. Under the proposed 2012 budget, funding for the Department of Energy would increase by almost 12% from 2010 levels to \$29.5 billion, while fulfilling the president’s pledge to bolster clean-energy research and development. The Office of Science would see its budget rise by 9.1% to \$5.4 billion, including \$2 billion for basic ▶

FOCUS ON 2011

Budget battle heats up

Even as Congress prepares to engage with US President Barack Obama's 2012 federal budget request, a clash of visions is continuing over the 2011 budget. Last year, the president's budget request included increases for most research-related functions in the government. That budget was never passed by the previous Congress and now, with a Republican majority in the House of Representatives, a very different scenario is emerging. In keeping with a campaign promise made during last autumn's midterm elections, this week House Republicans will introduce a bill that slashes US\$100 billion from Obama's 2011 request. The proposed cuts include reductions of 15% or more, relative to the 2010 budget, for several science agencies (see table).

One of the deepest cuts, an 18% reduction to the budget of the Office of Science at the US Department of Energy (DOE), reflects scepticism about Obama's energy agenda, says Barry Toiv, vice-president for public affairs at the Association of American Universities in Washington DC. If the cuts go through, he adds, some DOE labs may have to shut down for part of the fiscal year.

The House's vote will not be the final word on 2011 spending — the Democrat-controlled Senate and Obama will both need to agree to the budget.

The US government is still running at 2010 levels thanks to an interim bill — a continuing resolution — passed by Congress in December. That will expire on 4 March, adding urgency to this week's debate. Another continuing resolution could be required before the House and Senate agree. The delays prevent programme changes designated for 2011 (such as NASA's shift away from a mission to return to the Moon) from being enacted and reduce the window in which budget savings can be realized. If there is no agreement on either a budget or a continuing resolution, most government activities could be shut down, as occurred during the administration of then-president Bill Clinton in 1995–96.

"It's really disruptive," says Jennifer Zeitzer, the director of legislative relations for the Federation of American Societies for Experimental Biology in Washington DC. "Science benefits from advance planning. When budgets are frozen you can't plan," she says. **Eugenie Samuel Reich**

US BUDGET REQUESTS AND PROPOSED HOUSE CUTS (US\$ MILLION)

Agency	2010 enacted	2011 requested	2011 (after proposed cut)	2012 requested
National Institutes of Health (NIH)	31,089	32,089	30,519	31,829
NASA	18,724	19,000	18,421	18,724
Environmental Protection Agency (EPA)	10,298	10,020	7,283	8,973
National Science Foundation (NSF)	6,873	7,424	6,597	7,768
Centers for Disease Control and Prevention (CDC)	6,475	6,342	5,419	5,893
Department of Energy Office of Science (DOE OS)	4,895	5,121	4,010	5,416
National Oceanic and Atmospheric Administration (NOAA)	4,853	5,554	5,089	5,498
US Geological Survey (USGS)	1,112	1,133	1,105	1,118
National Institute of Standards and Technology (NIST)	862	922	700	1,004
Department of Homeland Security (science and technology) (DHS ST)	1,006	1,018	931	1,177

► energy sciences, an increase of 24.1%.

Funding for energy efficiency and renewable energy would increase by more than 44.4% to \$3.2 billion, and the Advanced Research Projects Agency–Energy would receive \$550 million, building on the \$400 million it received through the economic-stimulus bill in 2009. Cutting across programmes, the department is proposing to invest \$425 million in a new 'SunShot' project that is intended to reduce the cost of solar energy by 75% within a decade.

The budget also includes a request to fund three new Energy Innovation Hubs, which would focus on electricity storage, smart-grid technologies and critical energy materials such as rare metals used in solar panels. All told, six hubs would receive \$146 million. But Congress has so far limited that programme to the three existing hubs, and few expect that to change this year.

"This budget is going to run into significant headwinds in the Republican House," says Michael Lubell, director of public affairs for the American Physical Society, headquartered in College Park, Maryland. "There is going to be a big push back, and the administration is going to have to fight very hard to keep any of this."

To help offset the new costs, the Department of Energy will gain \$3.6 billion in revenue from fossil-fuel subsidies that the president is proposing to cancel — another idea that may encounter problems on Capitol Hill. The budget would also scale back fossil-fuel research by 44.5% to \$453 million, most of which would be focused on technologies for carbon capture and storage.

BIOMEDICAL

Under Obama's budget, the National Institutes of Health (NIH) in Bethesda, Maryland, would receive an increase of \$745 million (2.4%) over its 2010 budget, bringing its top line to \$31.8 billion in 2012.

The proposed increase is considered a win for the agency as other programmes throughout the

government face serious cuts. Still, it does not keep up with government projections of biomedical inflation, estimated at 3% in 2012. The agency thus projects a 2.4% drop in the number of new and competing research project grants it will award in 2012, a fall to 9,158. That, in turn, is expected to drive the success rate of grant applications down from 21% in 2010 to 19% in 2012.

Under Obama's proposal, most of the NIH's 27 institutes and centres would see their budgets grow by about 1.5–2%. The Office of the NIH Director would receive \$122 million in new money, a boost of 10.4%; of this, \$100 million would fund the Cures Acceleration Network (CAN), a new programme authorized in the 2010 health reform law that

aims to speed highly needed cures from lab to bedside.

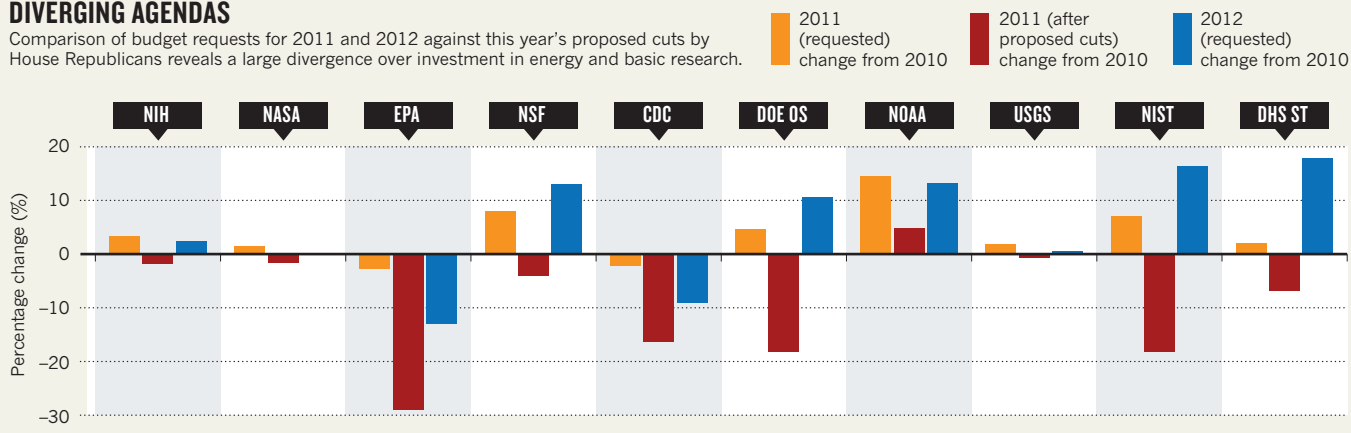
The CAN is slated to become part of the proposed National Center for Advancing Translational Sciences (NCATS),

which would be devoted to hastening the discovery of drugs and diagnostics. The NCATS featured prominently in the prose of the Obama budget, but was not funded as a discrete centre. Instead, the funding details for NCATS will be delivered to Congress in a budget amendment in the coming weeks, says NIH director Francis Collins. He adds that the agency has simply not had time to work out the detailed budget for the new centre, mainly because it has not determined the placement of the pieces of the National Center for Research Resources, which is to be broken up at the same time as the NCATS is constituted.

Constituents of the Centers for Disease Control and Prevention (CDC) in Atlanta, Georgia, were unsettled by Obama's proposal, which cuts the amount of agency funding that would flow through standard congressional

DIVERGING AGENDAS

Comparison of budget requests for 2011 and 2012 against this year's proposed cuts by House Republicans reveals a large divergence over investment in energy and basic research.



spending committees by \$588 million, to \$5.9 billion. At the same time, the Obama administration is proposing to pour \$753 million into the agency — money made available for disease prevention and public health by the 2010 health reform law.

Some adherents don't like the trade-off. "CDC does not fare well in this budget," says Georges Benjamin, executive director of the American Public Health Association in Washington DC. "Although it appears that they have gotten some overall increases, there were significant cuts and rearrangements in some vital programmes."

SPACE

In contrast to the increases at other agencies, NASA's overall proposed budget remained level at the \$18.7 billion it received in fiscal year 2010. Within that, however, the agency's science budget is slated to grow by roughly half a billion dollars, with \$360 million allocated to earth science and about \$175 million for planetary science. Astrophysics and heliophysics would also see modest increases of \$36 million and \$14 million, respectively.

"Science is moving gingerly forward amid greater uncertainty at the rest of NASA," says Matt Mountain, director of the Space Telescope Science Institute in Baltimore, Maryland.

One science project that exemplified the uncertainty is the James Webb Space Telescope (JWST), successor to the Hubble Space Telescope, which an independent review found would cost at least \$1.5 billion more than anticipated (see *Nature* 468, 353–354; 2010). The White House budget grants \$374 million to the JWST for 2012, although the review revealed that the telescope would need \$500 million

over the next two years to meet an expected launch date of September 2015.

With the 2011 budget still in limbo, a 2015

launch date is unrealistic and could even slip past 2016, said JWST programme manager Rick Howard in a press briefing. The delay could mean further cost overruns for the mission.

Most of NASA's 2012 reductions stem from the retirement of the space-shuttle fleet, which will see its final two budgeted flights, plus an additional flight that has been authorized by Congress but not yet funded in 2011. The new



A lesson in competitiveness: Barack Obama talks to students.

budget will usher in a post-shuttle future, albeit tentatively. It includes \$840.6 million to fund commercial companies to develop a vehicle that could ferry astronauts and cargo to the International Space Station, and \$2.8 billion towards a heavy-lift launch vehicle that would replace the now-defunct Constellation programme of the George W. Bush era. Neither decision will sit well with elected representatives who favour a more robust human programme. "This budget ignores the human space flight priorities outlined by Congress last year," congressman Peter Olson (Republican, Texas) posted on his web site after the budget's release. "We fought this battle last year and won, and I believe we will do so again."

COMPETITIVENESS

Under Obama's proposal, the National Science Foundation (NSF) would see a budget boost of 13% above 2010 enacted levels, with most of the nearly billion-dollar increase spread across the agency's core research-funding areas. The increase is "consistent" with the America COMPETES Act, says Amy Scott, associate vice-president for federal relations at

the Association of American Universities, referring to legislation that aims to double the money for key science-funding agencies, including the NSF, over 10 years. Similarly, Obama proposed that another agency under that Act, the National Institute of Standards and Technology, receive a 16.3% increase in funding for 2012.

The NSF increase includes funds to build major research facilities, including \$103 million for the Ocean Observatories Initiative, a project intended to provide continuous, interactive access to the ocean using a network of sensors. Another \$87.9 million would go to the construction of the National Ecological Observatory Network, a facility that will collect data on climate change, land-use change and US invasive species. Less fortunate is the Deep Underground Science and Engineering Laboratory in Lead, South Dakota, a joint project with the Department of Energy. As anticipated, it will receive no further NSF funding after this year (see *Nature* 468, 1013; 2010).

The increase at NSF would also extend to education and human resources; programmes aimed at providing better training for science teachers; and improvements to undergraduate instruction. This dovetails with the other education initiatives in the budget that Obama laid out in straightforward terms to the students he met this week.

"For us to be successful as a country, you're going to have to succeed. And for you to succeed, you're going to have to be able to possess the skills and knowledge of a twenty-first-century economy," Obama said. "That means math, and that means science." ■

NATURE.COM

For more on Congress and science funding, see: go.nature.com/nbapwi

Increased flood risk linked to global warming

Likelihood of extreme rainfall may have been doubled by rising greenhouse-gas levels.

BY QUIRIN SCHIERMEIER

Climate change may be hitting home. Rises in global average temperature are remote from most people's experience, but two studies in this week's *Nature*^{1,2} conclude that climate warming is already causing extreme weather events that affect the lives of millions. The research directly links rising greenhouse-gas levels with the growing intensity of rain and snow in the Northern Hemisphere, and the increased risk of flooding in the United Kingdom.

Insurers will take note, as will those developing policies for adapting to climate change. "This has immense importance not just as a further justification for emissions reduction, but also for adaptation planning," says Michael Oppenheimer, a climate-policy researcher at Princeton University in New Jersey, who was not involved in the studies.

There is no doubt that humans are altering the climate, but the implications for regional weather are less clear. No computer simulation can conclusively attribute a given snowstorm or flood to global warming. But with a combination of climate models, weather observations and a good dose of probability theory, scientists may be able to determine how climate warming changes the odds. An earlier study³, for example, found that global warming has at least doubled the likelihood of extreme events such as the 2003 European heatwave.

More-localized weather extremes have been harder to attribute to climate change until now.

"Climate models have improved a lot since ten years ago, when we basically couldn't say anything about rainfall," says Gabriele Hegerl, a climate researcher at the University of Edinburgh, UK. In the first of the latest studies¹, Hegerl and her colleagues compared data from

FATAL FLOODS

The most severe floods of the past 30 years cost thousands of lives and caused billions of dollars of damage.

Period	Region	Overall losses (US\$ billion)	Deaths
May–Sept. 1998	China	30.7	4,150
June–Aug. 1996	China	24	3,050
June–Aug. 1993	United States	21	50
Aug. 2002	Europe	16.5	40
July–Aug. 1995	North Korea	15	70

weather stations in the Northern Hemisphere with precipitation simulations from eight climate models (see page 378). "We can now say with some confidence that the increased rainfall intensity in the latter half of the twentieth century cannot be explained by our estimates of internal climate variability," she says.

The second study² links climate change to a specific event: damaging floods in 2000 in England and Wales. By running thousands of high-resolution seasonal forecast simulations with or without the effect of greenhouse gases, Myles Allen of the University of Oxford, UK, and his colleagues found that anthropogenic climate change may have almost doubled the risk of the extremely wet weather that caused

the floods (see page 382). The rise in extreme precipitation in some Northern Hemisphere areas has been recognized for more than a decade, but this is the first time that the anthropogenic contribution has been nailed down, says Oppenheimer. The findings mean that Northern Hemisphere countries need to prepare for more of these events in the future. "What has been considered a 1-in-100-years event in a stationary climate may actually occur twice as often in the future," says Allen.

But he cautions that climate change may not always raise the risk of weather-related damage. In Britain, for example, snow-melt floods may become less likely as the climate warms. And Allen's study leaves a 10% chance that global warming has not affected — or has even decreased — the country's flood risk.

Similar attribution studies are under way for flood and drought risk in Europe, melt-water availability in the western United States and drought in southern Africa, typical of the research needed to develop effective climate-adaptation policies. "Governments plan to spend some US\$100 billion on climate adaptation by 2020, although presently no one has an idea of what is an impact of climate change and what is just bad weather," says Allen.

Establishing the links between climate change and weather could also shape climate treaties, he says. "If rich countries are to financially compensate the losers of climate change, as some poorer countries would expect, you'd like to have an objective scientific basis for it."

The insurance industry has long worried about increased losses resulting from more extreme weather (see 'Fatal floods'), but conclusively pinning the blame on climate change will take more research, says Robert Muir-Wood, chief research officer with RMS, a company headquartered in Newark, California, that constructs risk models for the insurance industry. "This is a key part of our research agenda and insurance companies do accept the premise" that there could be a link, he says. "If there's evidence that risk is changing, then this is something we need to incorporate in our models." ■ [SEE NEWS AND VIEWS P.344](#)

1. Min, S.-K. *et al. Nature* **470**, 378–381 (2011).
2. Pall, P. *et al. Nature* **470**, 382–385 (2011).
3. Stott, P. A. *et al. Nature* **432**, 610–614 (2004).



The effects of severe weather — such as these floods in Albania — take a huge human and financial toll.



Efforts to understand the impacts of oil in the Gulf of Mexico are being delayed by funding uncertainties.

RESEARCH FUNDING

Gulf research cash still in limbo

Scientists are frustrated by slow progress in the roll-out of funds to investigate the aftermath of Deepwater Horizon.

BY MARK SCHROPE

A fund of half a billion dollars for research into the effects of last year's massive oil spill in the Gulf of Mexico has spent months mired in bureaucracy and political manoeuvring, leaving scientists uncertain about how or when the money will be awarded. Organizers, however, promise that relief is on the way.

On 24 May 2010, a month after the ruptured Deepwater Horizon wellhead began gushing, oil company BP announced that it was funding the Gulf of Mexico Research Initiative (GRI). The GRI will support a decade of independent research into five research themes, ranging from the physical and ecological fates of

oil and other spill contaminants to improved spill-mitigation technologies.

The prospect of US\$50 million in new annual funding had thrilled researchers and politicians in the region. With the exception of projects tied to fossil-fuel exploration and development, the federal government has provided only about \$4 million–\$6 million per year for research in the Gulf of Mexico in the past decade. By contrast, Chesapeake Bay, less than one-tenth the size of the Gulf but with some highly politicized ecological concerns, has received about \$20 million–\$50 million a year.

However, problems began soon after BP appointed an international advisory council of ten researchers to oversee the GRI grants.

Hoping to avoid conflicts of interest, BP says it did not include any scientists from the Gulf research institutions likely to be bidding for funds. But regional politicians felt that they had not been adequately consulted, and argued that without that representation, funds could largely end up going to higher-profile, non-Gulf institutions.

In response, BP said on 29 September that the Gulf of Mexico Alliance (GMA), a partnership of the states around the Gulf, would administer the grants. Awards would be made by an expanded advisory council of 20 members, with BP and the alliance each appointing half of the members. The original chair, Rita Colwell, an environmental microbiologist at Johns Hopkins University in Baltimore, Maryland, and a former director of the National Science Foundation, would remain in place.

Larry McKinney, executive director of Texas A&M Corpus Christi's Harte Research Institute for Gulf of Mexico Studies, who has consulted on the initiative's development, says that despite his initial scepticism, BP has worked hard to move the GRI forward. "I haven't found any indication that they were doing anything but trying to get the money out," he says.

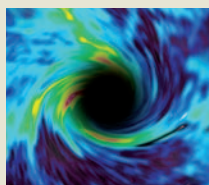
The initiative did give out \$40 million in fast-track funds last year, allowing some research to move forward. Most of this money was apportioned as lump sums to a few Gulf state research institutions, however, limiting the broader community's access to the funds. The bigger challenge has been to develop a request for proposals (RFP) acceptable to board members and stakeholders, a process that is now inching towards its conclusion. But many researchers are baffled and exasperated by the delay.

In November, at the GMA's request, McKinney recommended ways to shape the RFP, including mandating participation of a Gulf research institute in any consortium bidding for grants. He and others also suggested that the GRI purchase or lease a dedicated research vessel, in order to simplify logistics for offshore research and compensate for the scarcity of research vessels in the region (see M. Gaskill *Nature* doi:10.1038/news.2010.536; 2010).

But researchers say that it became impossible to get information from the council about when to expect the RFP and what it might require of grant applicants. "You would think they were negotiating a nuclear treaty," says McKinney, "but maybe the politics ▶



LATEST NEWS



How twisted light will help spot spinning black holes
go.nature.com/dsuclu

MORE NEWS

- Sex and violence linked in the brain go.nature.com/zadiyz
- Irish science funding hangs in electoral balance go.nature.com/o8samx
- Lucy was a walker go.nature.com/nxlyle
- Whooping cranes head back to Louisiana go.nature.com/hgzwor

SPECIAL



Scientists to the fore in the Arab awakening
go.nature.com/ox5oag

► around it makes that necessary.”

“We are waiting patiently and doing our best to plan,” adds Matthew Lee, interim associate vice-chancellor in Louisiana State University’s office of research and economic development in Baton Rouge, “but in the absence of an RFP we’re kind of constrained.”

Other researchers have all but given up on seeing the money. “It’s as far back on the stove as I can put it,” says Tracy Villareal, a marine scientist at the University of Texas at Austin in Port Aransas. “We’ve already had most of December and all of January wasted waiting on this. I just can’t afford to be sitting around and idly waiting for this thing to come out.”

Ralph Portier, an environmental scientist at Louisiana State University, fears that crucial research opportunities — such as gathering some key baseline data — have already been missed. He hopes, however, that there is still time to conduct work needed to understand Deepwater Horizon’s long-term legacy, and says that the delays may help to generate proposals that are informed by the latest information about the spill’s effects.

Like many researchers, *Nature* found it difficult to get information about the GRI’s progress. Council members and GMA leaders contacted by *Nature* said that Colwell was the only public spokesperson for the initiative; she in turn was unavailable for interview for several weeks.

Last week, however, Colwell said that an initial RFP, aimed at consortia addressing any of the five key themes, might be released as soon as next week. She expects that Gulf research institutions will be involved in these consortia, although there will be no requirement for such participation. A second RFP targeted at individual scientists and smaller groups will be released later this year. The proposal review process will be modelled on a well-established system used by the National Science Foundation.

But the council still needs to finalize protocols for data management, and how time on research vessels will be allocated, before the first RFP can be released. Colwell says that buying a dedicated ship is not an option, but that a long-term lease is possible. She declined to give specific details about the challenges of developing the RFP, but says that the delays were largely due to expanding the council’s membership and gathering everyone for a first meeting, which happened in December. Despite the slow progress, “I think that the outcome will be received with satisfaction by the scientists,” she says.

Others are not so sure. “Events to date raise serious questions about whether the proper structures and organizations are in place to manage this process,” says Villareal. “I am not optimistic about a speedy and forthright outcome.” ■

➔ **NATURE.COM**
For more on
Deepwater Horizon:
go.nature.com/oilspill

INTELLECTUAL PROPERTY

Licence rules hinder work on rare disease

Animal model off-limits to Rett-syndrome researchers.

BY ERIKA CHECK HAYDEN

Stashed away somewhere in a freezer in Cambridge, Massachusetts, is a mouse embryo that Etienne Joly would dearly like to get his hands on.

Joly is an immunologist based in Toulouse, France, with a keen interest in Rett syndrome, an incurable and debilitating disease that almost exclusively affects young girls. The mouse, developed by a team at the Novartis Institutes for Biomedical Research in Cambridge, carries a fluorescently tagged version of the gene that is mutated in the disease. It is the perfect tool, Joly says, for testing an idea he has about Rett syndrome. But a thicket of legal restrictions puts the mouse off-limits to anyone outside Novartis, even though scientists at the company are no longer using the model in their work on Rett syndrome.

“All scientists and families are asking for is the right to look into this disease and to try to understand it better,” says Joly, who has embarked on a letter-writing campaign against the restrictions. “And when you know that there is a tool, but you can’t use it because some lawyer says that you can’t have the materials, then you get angry.” Scientists and experts in intellectual-property issues say that the case shows how science can be impeded when onerous licensing rules govern the sharing of research materials.

Girls with Rett syndrome are healthy as

babies, then progressively lose the ability to speak, move, eat and breathe normally. Because the disease is rare, affecting just one in 10,000 to 20,000 girls, it is an unattractive target for drug companies. Academic researchers have picked up the slack, and the field has moved at breakneck speed in recent years, from the 1999 discovery that defects in the gene *MECP2* cause the disease, to clinical trials of possible treatments today.

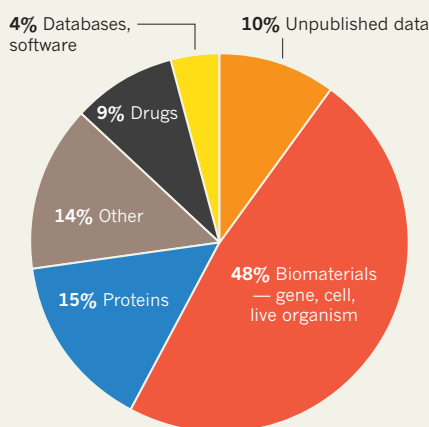
Yet no one knows how the mutation causes the disease. A few years ago, Joly, who works at the Institute of Pharmacology and Structural Biology, came up with what he calls a “slightly unconventional” idea that the Rett-syndrome gene might have a role in regulating immune responses in the central nervous system. To explore his hypothesis, Joly needed an animal model that would allow him to trace where the gene is expressed.

In 2008, Joly learned about the engineered mouse. Led by molecular biologist Cecile Blaustein, the Novartis team had joined a copy of the mouse *Mecp2* gene to a copy of the gene that makes enhanced green fluorescent protein (EGFP) to produce an animal in which the gene’s activity can be traced throughout the brain and body (R. S. Schmid *et al. Neuroreport* 19, 393–398; 2008).

But after three years of trying, neither Joly nor any other Rett-syndrome researcher has been able to gain access to the mouse. When researchers asked to share it, Blaustein and her

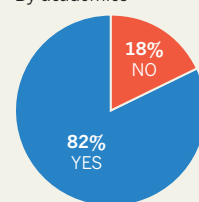
LIMITED ACCESS

A 2007 survey examined what materials researchers requested from other labs.

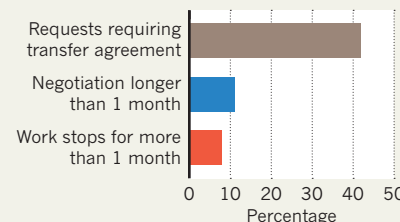
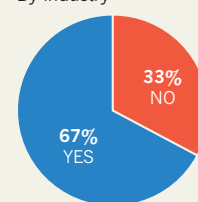


Were requests fulfilled?

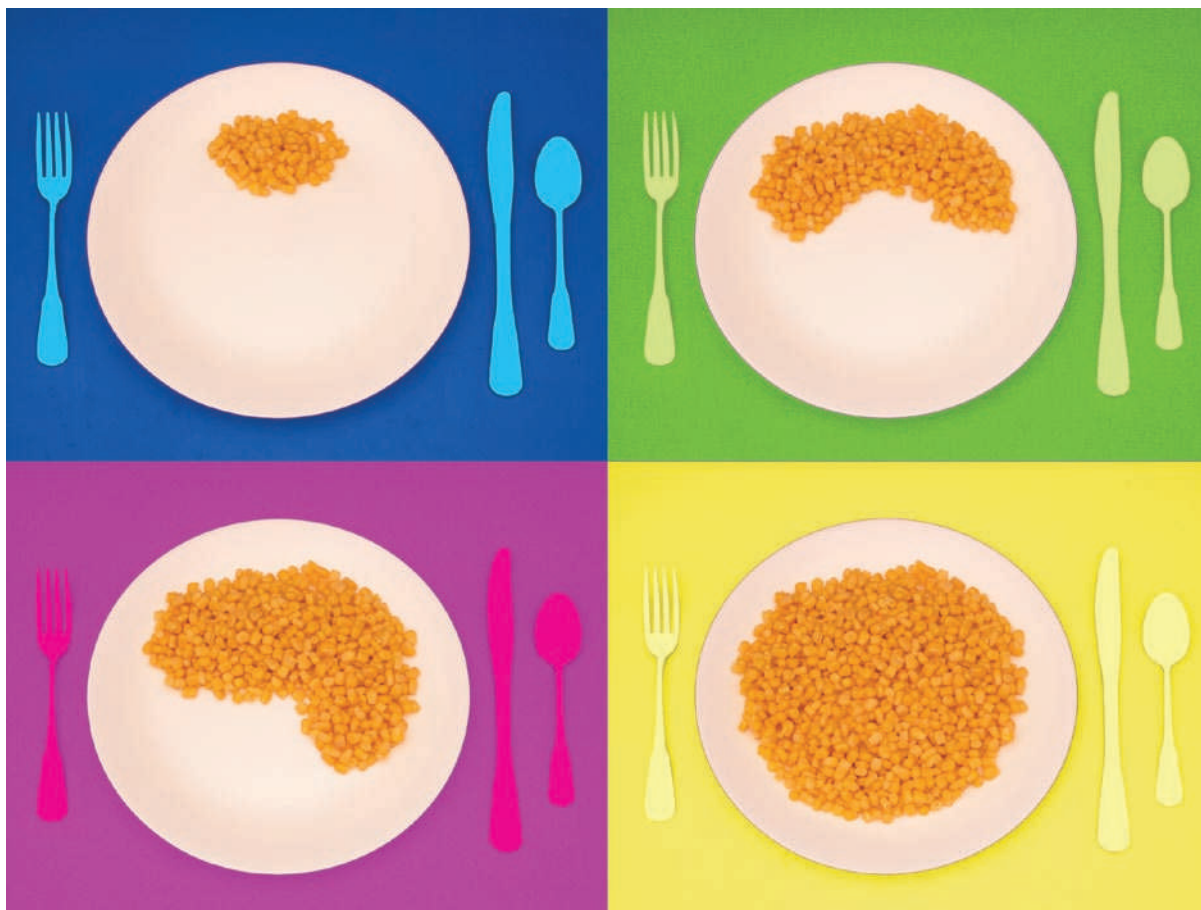
By academics



By industry



SOURCE: J. P. WALSH ET AL./ELSEVIER



EVERY BITE YOU TAKE

If a camera snaps everything you eat, you can't lie about it later. That's why scientists are building high-tech gadgets to measure the human 'exposome'.

BY BRENDAN BORRELL

A

decade ago, as part of a study on diet, psychologist Tom Baranowski was asked to recall everything he had eaten the previous day. A chicken dinner, he said confidently, remembering that he had prepared it for himself and his wife Janice. The thing was, he hadn't made chicken that night. It was only later that he realized he'd treated himself to a hamburger.

If Baranowski, who studies children's diets at Baylor College of Medicine in Houston, Texas, was an unlikely candidate for making such a mistake, consider how abysmal the dietary memories of everyone else must be. By observing his study subjects one day and following up the next, Baranowski has found that children routinely forget about 15% of the foods they have eaten, and more

than 30% of the foods they do recall turn out to be figments of their imagination. Adults show similar patterns. "The errors of dietary assessment are overwhelming," says Baranowski.

These mistakes are more than a reminder of the human memory's fallibility: they threaten to undermine the foundations of modern medical epidemiology. In this field, researchers make associations between past events and experiences, and later ones such as the emergence of cancer or other diseases. But if the initial records are inaccurate, these associations can be weak, misleading or plain wrong. Although the problem is most jarring in studies of diet, it also infects investigations of exercise, stress, pollution or smoking — basically, anything that relies on people reporting their own

Portion truths:
photos help
people recall
what they ate.

exposures through interviews or questionnaires. “This is the weak part of epidemiology,” says Paolo Vineis, an environmental epidemiologist at Imperial College London.

Baranowski and Vineis are at the forefront of a movement among health researchers to develop measurements of environmental exposures that are more precise and objective than questionnaires. Some are working to develop personalized exposure profiles using blood-based tests. Others want their study subjects to trot around town with sensors dangling off their bodies capturing their movements, snapping photos of their lunch and taking samples of the air they breathe. “We are getting to the point where you can conceive of doing a study with 500,000 people and giving them a cell-phone-sized device that they put in a charger every night,” says David Balshaw, the exposure-biology programme manager at the National Institute for Environmental Health Sciences in Research Triangle Park, North Carolina.

Some researchers foresee a day when they will keep track of the entire spectrum of environmental exposures for a single individual, dubbed the ‘exposome’ (see ‘How to measure everything’). That’s a long way off. In the meantime, *Nature* takes a look at efforts to measure three key elements of the exposome: air pollutants, physical activity and diet. Each of these is bringing the exposome one step closer to reality — and the questionnaire, with all its flaws, a step closer to extinction.

BREATH BY BREATH

The contraption fitted snugly inside a child’s backpack. The tangle of green plastic tubes, filters, pumps, circuit boards and a hefty battery weighed about 3 kilograms and made a low hum when it was switched on and began sucking in air. Tiny filters were designed to collect continuous records of all the grit and grime a child in the Bronx would be exposed to during their pilgrimage from their apartment, through the New York City subway system to school and back again.

For geochemist Steven Chillrud, whose team built the device in 2004, it represented the future of exposure biology. In the United States, environmental scientists have traditionally estimated human exposure to airborne pollutants by analysing data from building-mounted sensors. But the shortcomings of this approach became clear in a landmark study¹ published in 2005, in which researchers showed that levels of many hazardous compounds were higher inside homes than out. The findings made sense to Chillrud, who had already been thinking about the exposures of people living in New York City. “People do not live on buildings,” he says.

To the New York City Police Department (NYPD), though, Chillrud’s contraption was a potential terrorist threat. After four terrorists detonated bombs on London’s public transport

system on 7 July 2005, the NYPD had been conducting random searches on the subway system. When Chillrud stopped by the local police precinct to alert them to his planned study, officers were aghast, and even Chillrud admits his device looked intimidating. “We put a lot of effort into it,” Chillrud says now, as he hoists it onto his desk at Columbia University’s Lamont–Doherty Earth Observatory in Palisades, New York. “Then, the police shut us down.” But they also offered the team a way forward. “If we could shrink it to the size of a Walkman, we’d be back in business.”

Last November, after several iterations with his collaborators, the first of Chillrud’s Walkman-sized environmental sensors finally arrived. When participants in the study leave the vicinity of a ‘home’ beacon, the device switches between two filters, making it possible for Chillrud to distinguish between exposures at home and elsewhere; a Global Positioning System (GPS) device helps to differentiate exposures during the commute from those during the school or work day. After several days of use, the filters can be chemically analysed to identify different sources of black carbon and other chemicals. And the NYPD will be pleased: the pared-down version slips neatly into a special vest with an air inlet near the collar.

The first health studies with the contraption will be aimed at more accurately measuring passive contact with tobacco smoke. Chillrud will be studying 50 adults and a handful of children using portable sensors and a method developed by Avrum Spira, a pulmonary specialist at the Boston University School of Medicine in Massachusetts, which uses changes in gene expression in cells brushed from the nostril to assay smoke exposure². Spira believes that a more precise measure of cumulative smoke exposure can pin down the reasons why some smokers — but not all — develop lung cancer and conditions such as chronic obstructive pulmonary disease. “We are not measuring just exposure, but how you are responding to exposure,” Spira says.

STEP BY STEP

Another aspect of daily exposure is charted in Kevin Patrick’s maps of San Diego, California. They take a few minutes to understand. The blue Pacific lapping against the shore on the left is immediately recognizable, as is the city itself, a false-colour patchwork of highways, buildings and parkland. Finally, you begin to notice the green, yellow, orange and red dots, and it all starts to come together. The dots show an individual’s heart rate at different points in time: widely spaced green dots represent the sedentary drive to work; a day at the office generates green dots layered on top of each other; and finally, a jog or bike ride along the bluffs appears as a string of heart-thumping orange and red (see ‘Every step you make’).

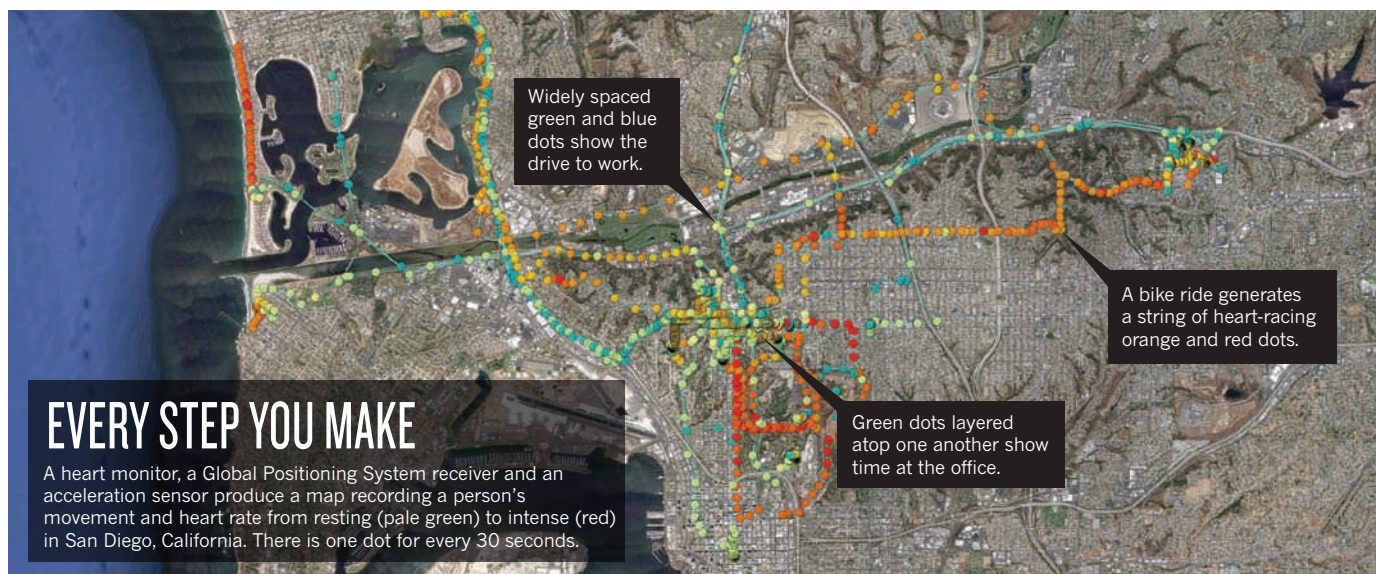
Patrick, a director of the Center for Wireless and Population Health Systems at the

In the 1998 film *The Truman Show*, the central character Truman Burbank gradually discovers that his entire life since conception has been broadcast through thousands of cameras hidden throughout a giant film set. Add to that surreal vision the chemical analyses of Burbank’s air, food and water, samples of his gut flora, and blood tests for endocrine-disrupting chemicals, heavy metals and metabolic products, and you have some idea of the overwhelming nature of the ‘exposome’ — the full catalogue of a person’s environmental exposures throughout their life.

The ability to draw up this catalogue could reveal which exposures contribute to developing disease in the future. But it is as technically difficult as it is conceptually overwhelming. “People may think it’s so complex that it’s not achievable,” says Christopher Wild, head of the International Agency for Research on Cancer in Paris, a branch of the World Health Organization, who coined the term exposome in 2005.

Sensors worn on the body can record some aspects of the ‘external’ exposome. But “those devices are not going to contribute more than a few per cent to our understanding”, says Stephen Rappaport, an environmental-health biologist at the University of California, Berkeley. That’s why he and others are working on ways to record the ‘internal’ exposome, profiles of biological molecules that reveal the effects of diet, toxins and other exposures. Metabolites from the pesticide DDT, for instance, can be detected in blood 20–30 years after exposure. But researchers are many years from a unified approach that could profile tens of thousands of compounds and extract from this a full history of life’s onslaughts. Part of the problem is that one person’s metabolic response to a change in diet, say, can be completely different from another’s.

For now, some investigators are combing existing exposure data for associations with specific diseases. Since 1999, for example, the Centers for Disease Control and Prevention in Atlanta, Georgia, has conducted the National Health and Nutrition Examination Survey, which includes interviews, medical examinations and biomonitoring of hundreds of chemicals in the blood. Last year, Atul Butte, a bioinformatician and paediatrician at the Stanford School of Medicine, California, used these data in an environment-wide association study to hunt for correlations between type 2 diabetes and 266 environmental factors. The biggest surprise came from the discovery that a form of vitamin E increased the risk of diabetes³. **B.B.**



SOURCE: PALMS PROJECT, UCSD/CALIT2

University of California, San Diego (UCSD), says that these maps measure physical activity more accurately than the pedometers and questionnaires he and other researchers used for years. “We realized we needed to know not only how active someone is, but where that activity occurs,” he says. Such monitoring can help the researchers understand how the layout of a city — with its parks, hills and smog traps — influences physical activity and, ultimately, public health.

Patrick launched the mapping project in 2007. Called the Physical Activity Location Measurement System, or PALMS, it combines heart-rate monitors, a GPS device and acceleration sensors to record body movements in detail. More than 1,500 people have already worn the US\$60 devices, after which they sit down to explain what they were doing at different points during the day. Working with computer scientists, Patrick hopes to develop a pattern recognition system to automatically distinguish different activities.

The first proposed health application of PALMS will measure physical activity among San Diego-based participants in the Hispanic Community Health Study/Study of Latinos, run by the US National Heart, Lung, and Blood Institute among other bodies. He also has plans to measure the effects of interventions, such as campaigns encouraging people to spend more time in parks than city streets.

Patrick works on another project, CitiSense, led by software engineer William Griswold, also at UCSD. This aims to measure physical activity and airborne pollutants with gadgets similar to Chillrud's. In one planned study, Patrick will give these devices to San Diego cyclists, providing them with real-time feedback on the quality of the air they breathe during bike rides. Patrick says he looks forward to the day when researchers can link up the data

that he is collecting with those on social networks, psychology and genetics to understand how these factors in combination contribute to disease. “I don't think it's going to be very long before that happens,” he says.

GULP BY GULP

No study of human exposure will be complete without examining food. That's why, on a rainy afternoon in December, Baranowski was looking closely at a dinner plate of maize (corn) on a flat-screen monitor. In fact, it was one of eight plates of maize, identically positioned on a blue table, differing only in their portion sizes from a few spoonfuls to a few cups. “The kids' job,” Baranowski says, “is to pick which size comes closest to the portion they consumed.”

Over the past few years, Tom and Janice Baranowski have taken serial pictures of foods prepared in the ‘metabolic’ kitchen on the third floor of the Children's Nutrition Research Center, ranging from breakfast cereal to chicken nuggets to grapes, amassing some 15,000 photographs altogether. The photos are part of an effort funded by the US National Cancer Institute to improve the Baranowskis' food intake recording software, called Automated Self-Administered 24-hour Dietary Recall (ASA24), and adapt it for use by children. During trials, the photo-prompts help children estimate portion sizes of meals they ate with about 60% accuracy, Baranowski says. The goal is to build a web-based tool that other researchers can use in place of food diaries to, for instance, link up dietary habits, genetic signatures and risk of disease.

Electrical engineer Mingui Sun of the University of Pittsburgh, Philadelphia, is trying to circumvent self-reporting entirely. He has built an all-purpose exposure-biology device that hangs around the neck and contains 5–8 sensors including a GPS device, an audio recorder, accelerometer and a digital camera programmed to take 2–5 pictures a second over the course of a

week³. Image-processing software can automatically recognize dinner plates or a glass of milk, segmenting the video stream so that meals and cooking procedures can later be reviewed by dietitians. Sun says the devices will soon be used in a pilot study estimating the caloric intake and physical activity levels of people who are obese.

Vineis, though, has taken a very different tack to measuring the dietary component of the exposome, as part of his work on the ten-country European Prospective Investigation into Cancer and Nutrition cohort. In November, his group published a proof-of-principle paper⁴, in which they compared blood-plasma analyses and dietary assessments of 24 people who went on to develop colon cancer over a seven-year period, compared with 23 healthy controls. They found one biomarker — a derivative of benzoic acid produced by fibre-digesting gut bacteria — that correlated with dietary fibre intake and a reduced colon cancer risk. Vineis calls this the “meet-in-the-middle approach” to discovering biomarkers that measure exposure at the same time as showing how the exposure might foreshadow disease.

But fibre is just one of the known and unknown environmental exposures to which a human body is subjected, and colon cancer just one of its many downfalls. A comprehensive exposome is many years off — so for now, Vineis is just hoping for a better way to measure one exposure at a time. “I don't think we'll completely give up on questionnaires,” he says. ■

Brendan Borrell is a freelance writer based in New York.

1. Weisel, C. P. *et al.* *J. Expos. Anal. Environ. Epidemiol.* **15**, 123–137 (2005).
2. Spira, A. *et al.* *Proc. Natl Acad. Sci. USA* **101**, 10143–10148 (2004).
3. Sun, M. *et al.* *J. Am. Diet. Assoc.* **110**, 45–47 (2010).
4. Chadeau-Hyam, M. *et al.* *Biomarkers* **16**, 83–88 (2010).
5. Patel, C. J., Bhattacharya, J. & Butte, A. J. *PLoS One* **5**, e10746 (2010).

► NATURE.COM

For more on detecting exposures see: go.nature.com/umxlhj

FAITH IN SCIENCE

The Templeton Foundation claims to be a friend of science. So why does it make so many researchers uneasy?

BY M. MITCHELL WALDROP

At the headquarters of the John Templeton Foundation, a dozen kilometres outside Philadelphia, Pennsylvania, the late billionaire seems to watch over everything. John Templeton's larger-than-life bust stands at one end of the main conference room. His life-sized portrait smiles down from a side wall. His face peers out of framed snapshots propped on bookshelves throughout the many offices.

It seems fitting that Templeton is keeping an eye on the foundation that he created in 1987, and that consumed so much of his time and energy. With a current endowment estimated at US\$2.1 billion, the organization continues to pursue Templeton's goal of building bridges between science and religion. Each year, it doles out some \$70 million in grants, more than \$40 million of which goes to research in fields such as cosmology, evolutionary biology and psychology.

As generous as the foundation's support is, however, many scientists find it troubling — and some see it as a threat. Jerry Coyne, an evolutionary biologist at the University of Chicago, Illinois, calls the foundation “sneakier than the creationists”. Through its grants to researchers, Coyne alleges, the foundation is trying to insinuate religious values into science. “It claims to be on the side of science, but wants to make faith a virtue,” he says.

But other researchers, both with and without Templeton grants, say that they find the foundation remarkably open and non-dogmatic. “The Templeton Foundation has never in my experience pressured, suggested or hinted at any kind of ideological slant,” says Michael Shermer, editor of *Skeptic*, a magazine that debunks pseudoscience, who was hired by the foundation to edit an essay series entitled ‘Does science make belief in God obsolete?’

The debate highlights some of the challenges facing the Templeton Foundation after the death of its founder in July 2008, at the age of 95. With the help of a \$528-million bequest from Templeton, the foundation has been radically reframing its research programme. As part of that effort, it is reducing its emphasis on religion to make its programmes more palatable to the broader scientific community. ►

Like many of his generation, Templeton was a great believer in progress, learning, initiative and the power of human imagination — not to mention the free-enterprise system that allowed him, a middle-class boy from Winchester, Tennessee, to earn billions of dollars on Wall Street. The foundation accordingly allocates 40% of its annual grants to programmes with names such as ‘character development’, ‘freedom and free enterprise’ and ‘exceptional cognitive talent and genius’.

Unlike most of his peers, however, Templeton thought that the principles of progress should also apply to religion. He described himself as “an enthusiastic Christian” — but was also open to learning from Hinduism, Islam and other religious traditions. Why, he wondered, couldn’t religious ideas be open to the type of constructive competition that had produced so many advances in science and the free market?

That question sparked Templeton's mission to make religion "just as progressive as medicine or astronomy". He started in 1972, by endowing the Templeton Prize for progress in religion. He stipulated that the cash value should always be higher than that of the Nobel Prizes; it currently stands at £1 million (US\$1.6 million). Early Templeton prizes had nothing to do with science: the first went to the Catholic missionary Mother Theresa of Calcutta in 1973.

By the 1980s, however, Templeton had begun to realize that fields such as neuroscience, psychology and physics could advance understanding of topics that are usually considered spiritual matters — among them forgiveness, morality and even the nature of reality. So he started to appoint scientists to the prize panel, and in 1985 the award went to a research scientist for the first time: Alister Hardy, a marine biologist who also investigated religious experience. Since then, scientists have won with increasing frequency. In 2010, the prize went to Francisco Ayala, a geneticist at the University of California, Irvine, and a former Dominican priest who has spent 30 years fighting the teaching of creationism and intelligent design in schools as alternatives to evolution.

The prize has come in for some academic scorn. “There’s a distinct feeling in the research community that Templeton just gives the award to the most senior scientist they can find who’s willing to say something nice about religion,” says Harold Kroto, a chemist at Florida State University in Tallahassee, who was co-recipient of the 1996 Nobel Prize in Chemistry and describes himself as a devout atheist.

SCIENTISTS AS ALLIES

Yet Templeton saw scientists as allies. They had what he called “the humble approach” to knowledge, as opposed to the dogmatic approach. “Almost every scientist will agree that they know so little and they need to learn,” he once said.

The scientific attitude informed the motto that Templeton crafted for his foundation: “How little we know, how eager to learn.”

The foundation began with just two employees in a room above the garage of his oldest son, Jack Templeton, in Bryn Mawr, Pennsylvania. The foundation's initial activities were also modest: administering the Templeton Prize, funding science and religion courses at universities and seminaries, and sponsoring essay contests.

“But the foundation was a research project in his mind,” says Jack Templeton, who retired from his career as a paediatric and trauma surgeon in 1995 to become the organization’s president. The slowly growing staff was bombarded with ideas and directives in a near-daily stream of faxes from Lyford Cay in the Bahamas, where the elder Templeton had lived since 1968.

Templeton's interests gave the resulting list of grants a certain New Age quality (See 'Top ten grants from the Templeton Foundation'). For example, in 1999 the foundation gave \$4.6 million for forgive-

ness research at the Virginia Commonwealth University in Richmond, and in 2001 it donated \$8.2 million to create an Institute for Research on Unlimited Love (that is, altruism and compassion) at Case Western Reserve University in Cleveland, Ohio.

"A lot of money wasted on nonsensical ideas," says Kroto. Worse, says Coyne, these projects are profoundly corrupting to science, because the money tempts researchers into wasting time and effort on topics that aren't worth it. If someone is willing to sell out for a million dollars, he says, "Templeton is there to oblige him".

But Templeton wasn't interested in funding mainstream research, says Barnaby Marsh, the foundation's executive vice-president. Templeton wanted to explore areas — such as kindness and hatred — that were not well known and did not attract major funding agencies. Marsh says Templeton wondered, “Why is it that some conflicts go on for centuries, yet some groups are able to move on?”

At the same time, says Marsh, the ‘dean of value investing’, as Templeton was known on Wall Street, had no intention of wasting his money on junk science or unanswerables such as whether God exists. So before pursuing a scientific topic he would ask his staff to get an assessment from appropriate scholars — a practice that soon evolved into a peer-review process drawing on experts from across the scientific community.

Because Templeton didn't like bureaucracy, adds Marsh, the foundation outsourced much of its peer review and grant giving. In 1996, for example, it gave \$5.3 million to the American Association for the Advancement of Science (AAAS) in Washington DC, to fund efforts that work with evangelical groups to find common ground on issues such as the environment, and to get more science into seminary curricula. In 2006, Templeton gave \$8.8 million towards the creation of the Foundational Questions Institute (FQXi), which funds research on the origins of the Universe and other fundamental issues in physics, under the leadership of

TEMPLETON PRIORITIES: Then and Now

In recent years, the Templeton Foundation has moved away from emphasizing religion in its grants, a trend that can be seen in word clouds created from its funding agendas in 1998 and 2011.



Anthony Aguirre, an astrophysicist at the University of California, Santa Cruz, and Max Tegmark, a cosmologist at the Massachusetts Institute of Technology in Cambridge.

THE DESIGN DEBATE

But external peer review hasn't always kept the foundation out of trouble. In the 1990s, for example, Templeton-funded organizations gave book-writing grants to Guillermo Gonzalez, an astrophysicist now at Grove City College in Pennsylvania, and William Dembski, a philosopher now at the Southwestern Baptist Theological Seminary in Fort Worth, Texas. After obtaining the grants, both later joined the Discovery Institute — a think-tank based in Seattle, Washington, that promotes intelligent design. Other Templeton grants supported a number of college courses in which intelligent design was discussed. Then, in 1999, the foundation funded a conference at Concordia University in Mequon, Wisconsin, in which intelligent-design proponents confronted critics.

Those awards became a major embarrassment in late 2005, during a highly publicized court fight over the teaching of intelligent design in schools in Dover, Pennsylvania. A number of media accounts of the intelligent design movement described the Templeton Foundation as a major supporter — a charge that Charles Harper, then senior vice-president, was at pains to deny.

Some foundation officials were initially intrigued by intelligent design, Harper told *The New York Times*. But disillusionment set in — and Templeton funding stopped — when it became clear that the theory was part of a political movement from the Christian right wing, not science. Today, the foundation website explicitly warns intelligent-design researchers not to bother submitting proposals: they will not be considered.

The foundation's critics are unimpressed. Avowedly antireligious scientists such as Coyne and Krotto see the intelligent-design imbroglio as a symptom of their fundamental complaint that religion and science should not mix at all.

"Religion is based on dogma and belief, whereas science is based on doubt and questioning," says Coyne, echoing an argument made by many others. "In religion, faith is a virtue. In science, faith is a vice." The purpose of the Templeton Foundation is to break down that wall, he says — to reconcile the irreconcilable and give religion scholarly legitimacy.

Foundation officials insist that this is backwards: questioning is their reason for being. Religious dogma is what they are fighting.

That does seem to be the experience of many scientists who have taken Templeton money. During the launch of FQXi, says Aguirre, "Max and I were very suspicious at first. So we said, 'We'll try this out, and the minute something smells, we'll cut and run.' It never happened. The grants we've given have not been connected with religion in any way, and they seem perfectly happy about that."

John Cacioppo, a psychologist at the University of Chicago, also had concerns when he started a Templeton-funded project in 2007. He had

just published a paper with survey data showing that religious affiliation had a negative correlation with health among African-Americans — the opposite of what he assumed the foundation wanted to hear. He was bracing for a protest when someone told him to look at the foundation's website. They had displayed his finding on the front page. "That made me relax a bit," says Cacioppo.

Yet, even scientists who give the foundation high marks for openness often find it hard to shake their unease. Sean Carroll, a physicist at the California Institute of Technology in Pasadena, is willing to participate in Templeton-funded events — but worries about the foundation's emphasis on research into 'spiritual' matters. "The act of doing science means that you accept a purely material explanation of the Universe, that no spiritual dimension is required," he says.

TEMPLETON WORRIED THAT THE WORD 'RELIGION' WAS ALIENATING TOO MANY GOOD SCIENTISTS.

It hasn't helped that Jack Templeton is much more politically and religiously conservative than his father was. The foundation shows no obvious rightwards trend in its grant-giving and other activities since John Templeton's death — and it is barred from supporting political activities by its legal status as a not-for-profit corporation. Still, many scientists

find it hard to trust an organization whose president has used his personal fortune to support right-leaning candidates and causes such as the 2008 ballot initiative that outlawed gay marriage in California.

Scientists' discomfort with the foundation is probably inevitable in the current political climate, says Scott Atran, an anthropologist at the University of Michigan in Ann Arbor. The past 30 years have seen the growing power of the Christian religious right in the United States, the rise of radical Islam around the world, and religiously motivated terrorist attacks such as those in the United States on 11 September 2001.

Given all that, says Atran, many scientists find it almost impossible to think of religion as anything but fundamentalism at war with reason. They have a reflexive reaction against the idea, espoused by Templeton, that progress in spirituality can help to solve the problems of the world.

THE BIG QUESTIONS

Towards the end of Templeton's life, says Marsh, he became increasingly concerned that this reaction was getting in the way of the foundation's mission: that the word 'religion' was alienating too many good scientists. This prompted a rethink of the foundation's research programme — a change most clearly seen in the organization's new website, launched last June. Gone were old programme names such as 'science and religion' — or almost any mention of religion at all (See 'Templeton priorities: then and now'). Instead, the foundation has embraced the theme of 'science and the big questions' — an open-ended list that includes topics such as 'Does the Universe have a purpose?'

Under this umbrella come new programmes in such areas as mathematical and physical sciences, life sciences, and philosophy and theology — each, for the first time, with its own team of programme officers. The peer-review and grant-making system has also been revamped: whereas in the past the foundation ran an informal mix of projects generated by Templeton and outside grant seekers, the system is now organized around an annual list of explicit funding priorities.

It remains to be seen how reassuring these changes will be for scientists still sceptical of the foundation — although Marsh notes that last year's inaugural announcement of 13 funding priorities drew some 2,500 submissions.

The foundation is still a work in progress, says Jack Templeton — and it always will be. "My father believed," he says, "we were all called to be part of an ongoing creative process. He was always trying to make people think differently."

"And he always said, 'If you're still doing today what you tried to do two years ago, then you're not making progress.'" ■

M. Mitchell Waldrop is an editor for *Nature* in Washington DC.

TOP TEN GRANTS FROM THE TEMPLETON FOUNDATION

Foundational Questions in Evolutionary Biology	\$10,500,000
Foundational Questions in Physics and Cosmology	\$8,812,078
The SEVEN Fund: Enterprise Based Solutions to Poverty	\$8,742,911
Establishing an Institute for Research on Unlimited Love	\$8,210,000
The Purpose Prize for Social Innovators Over the Age of 60	\$8,148,322
Templeton-Cambridge Journalism Fellowships and Seminars in Science and Religion	\$6,187,971
Accelerating Progress at the Interface of Positive Psychology and Neuroscience	\$5,816,793
AAAS Dialogue on Science, Ethics, and Religion	\$5,351,707
Promoting a Culture of Generosity, Part I: Feature Film	\$5,000,000
Promoting a Culture of Generosity, Part II: The Philanthropy Channel	\$5,000,000

COMMENT

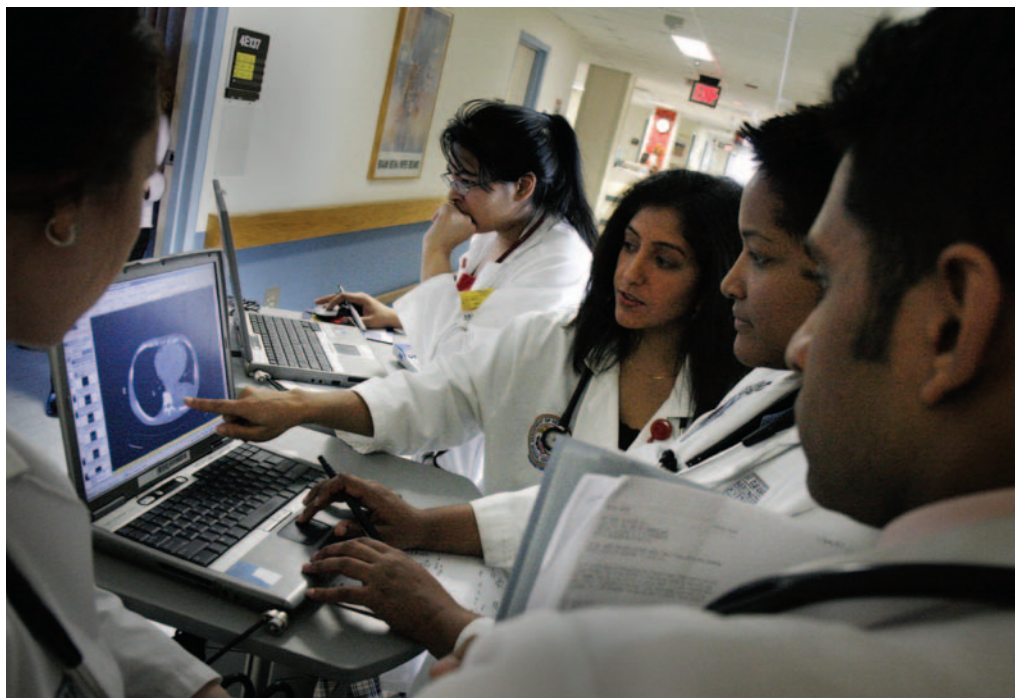
TECHNOLOGY Can online games save the world? **p.330**



NEUROSCIENCE Reviewed: two books debunking brain gender differences **p.332**

ASTRONOMY Atacama movie juxtaposes two very different desert searches **p.333**

ENVIRONMENT Chaotic land-use policies fingered for Brazil's landslides and floods **p.335**



Mobile access to electronic health records is expected to vastly improve health care, but the transition could be bumpy.

Health-care hit or miss?

Will the \$27-billion investment in electronic records in the United States revolutionize care and research, or will it be a missed opportunity for patients and science?

WILLIAM HERSH

Time to catch up with the pack

Professor and chair of medical informatics & clinical epidemiology, Oregon Health & Science University, Portland

When most people think about health-care reform in the United States, they think about President Barack Obama's Patient Protection and Affordable Care Act. But earlier legislation may prove more transformative: the Health Information Technology and

Economic and Clinical Health (HITECH) Act, which was part of the economic stimulus bill and is beginning to take effect.

The centrepiece of the act provides up to US\$27 billion in incentives for professionals and hospitals to achieve 'meaningful use' of electronic health records. That doesn't just mean putting computers into physician's offices and into hospital wards, but also using them to help to achieve five goals of the US health-care system: improve quality, safety and efficiency; engage patients in their care; increase coordination of care; improve the health of the population; and ensure privacy and security. Eligible professionals will receive \$44,000–\$66,000 and hospitals \$2 million–\$9 million, between 2011 and 2018. As in other areas of technology and

health care, the United States has been a laggard in the adoption of electronic health records. Less than 30% of US primary-care physicians use them, compared with near-universal adoption in developed countries, including the United Kingdom, Denmark and New Zealand. The HITECH Act is an opportunity for the United States to catch up.

The act also includes an additional \$2 billion for organizational infrastructure; \$677 million to establish 62 regional centres for technical support and general assistance; \$60 million for four collaborative research centres to develop best practice for gathering and using electronic health information; about \$250 million for 17 'beacon' projects that will demonstrate innovative technologies in communities; and \$118 million for ►

M. DU CILLE/THE WASHINGTON POST/GETTY IMAGES

► college- and university-level programmes to train the 50,000 or so biomedical informaticians and health-information managers needed to implement and support the systems. The likely result is a boost not just to general levels of health, but also in data available for research. It will help, for example, to compare the effectiveness of tests and treatments in real-world settings.

Such data should enable the health-care system to become more 'intelligent'. The act works in synergy with the Institute of Medicine's 'learning health care' initiative: a programme launched in 2007 that aims to take the growing volume of captured data to see which health-care strategies work and which don't. This programme has dovetailed with \$1.4 billion in funding for 'comparative effectiveness research' for those head-to-head health-care comparisons.

Collectively, these efforts provide a vision of a health-care system that learns from its successes and mistakes. Some elements of the HITECH Act experiment might fail, but in the end, the health-care system should benefit from this unprecedented investment by becoming more data-driven and adaptable.

JULIE A. JACKO

Narrow the gap in health literacy

Professor of public health and director of the University Partnership for Health Informatics, University of Minnesota, Minneapolis

The HITECH Act is intended to promote the meaningful use of electronic health data by health professionals, not meaningful use by patients. This is a missed opportunity.

Research shows that when people are empowered to access and interpret their own health information and data, and engage in shared decision-making with their physician, they make more meaningful and informed choices. Such consumer empowerment does not yet exist in the United States, despite years of talk about its importance.

Today, getting access to one's own health data in a format that is easy to understand is nearly impossible, even for those who have some knowledge about health matters, are well-educated and do not have physical or cognitive limitations. Although good health information is increasingly available online, it is difficult to access for those who don't speak English as a first language, or who face other barriers such as disabilities. As long as doctors remain the major decision-makers and sole source of information about healthy living and treatment options for patients, there will be people who do not take responsibility for their

own health. And as long as the technological tools needed to foster collaborative decision-making aren't available, the cost of transmitting information about healthy living will stay high, and doctors will continue to experience extreme pressures on their time.

The HITECH Act may actually widen the divide between those who manage their own health and those who cede all responsibility to doctors. There is an opportunity to do better. The act provides funding for research: some of this should be earmarked specifically for patient-accessible technology. More attention should be paid to the development of tools that are designed for use by patients, as opposed to electronic health records designed for practitioners. Above all, more research is needed on how people use health information, and how to deliver it for the best health outcomes.

ROBERT GREENES

Push for deeper innovation

Head of the Department of Biomedical Informatics, Arizona State University, Phoenix

The HITECH Act provides a once-in-a-generation opportunity. But there is a risk that it will lead to rapid, shallow change, missing the chance for deeper innovation.

The United States does not have a rational health information system. Rather, it has a collection of systems that have evolved since the first electronic medical records of the 1960s. Several reports have laid out aspects of what an ideal electronic health-care system would look like. In December 2010, the President's Council of Advisors on Science and Technology envisioned a system in which all data would be standardized and tagged with descriptors, to help protect privacy and to allow data reuse. The National Research Council in 2009 wrote of data visualization methods that would aid human decision-making, optimized workflows and better human-computer interaction. A good system for the future must take into account changing demographics, emphasize health maintenance and disease prevention, empower individuals to have control over their health, and harness data for research. It should make use of new technologies to capture data whenever possible, and utilize mobile devices, high-speed networks and large-scale computing to make it available anywhere.

The HITECH Act tries to make the best both of legacy systems and of new concepts. There is a danger, however, of just tinkering at the edges and preserving the status quo.

The bulk of the act's funding is going towards helping practitioners and hospitals to adopt electronic health records and improve the ability to share and exchange data. With loose coordination, individual states are devising and implementing their own plans for this. Vendors of electronic health record systems are largely unconstrained, other than with regard to how they interconnect and exchange data according to a set of meaningful-use criteria that are designed to ramp up over the next five years. Without a single guiding hand, multiple, suboptimal solutions are likely to be developed in different regions. Existing electronic-medical-record systems tend to bundle many functions into monolithic proprietary packages, preventing real competition or the evolution of optimal components and services.

Two smaller initiatives within the act are aimed at a grander vision: four strategic research projects to pursue more innovative health-care systems, and 17 'beacon' communities to showcase better systems.

The frenzied activity of hospital, practices, states and regions struggling to comply with the electronic-health-record rules is bound to collide with the grander vision of these more modestly funded but more-exciting projects. A danger of this imbalance is that the marketplace will consolidate around established vendors and their bundled products. It would be better to have time to evolve a market in which many vendors sell modular components and services that can be mixed and matched by users.

Developing and articulating the grand vision and a road map to get there must not be considered a sideline: it needs to be the main event. The model and the marketplace can evolve if given a solid direction in which to move, incentives to do so and time to adapt.

JOSEPH TAN

Standardize to avoid waste

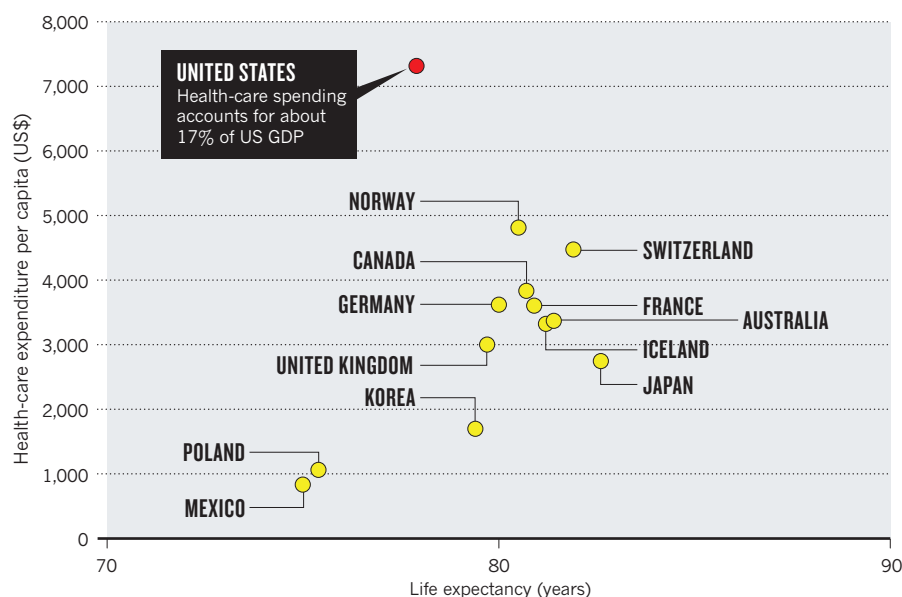
Professor at McMaster University in Hamilton, Canada, and editor-in-chief of the International Journal of Healthcare Information Systems & Informatics

Although I applaud the Obama administration for ushering in a reform strategy for health information technology (IT), I anticipate mass confusion and frustration, and roadblocks in trying to implement it equitably.

The most important element for a successful transition to electronic records is leadership, which is sadly missing in this case. Providers must show that they can make meaningful

MONEY WELL SPENT?

The United States has not seen an increase in life expectancy to match its huge outlay on health care.



use of their electronic records, but this definition keeps changing, causing confusion among health-care providers. Hundreds of consultants have sprung up to help advise hospitals and clinicians, all of them with slightly different interpretations of the rules because of the variety of electronic-records products being implemented. Everyone is pursuing their own solutions. Too many cooks have spoiled the broth.

In the midst of this confusion, smaller practices may be unwilling or unable to make the necessary technology investment, especially given the uncertainty that they will be able to meet the HITECH Act's requirements and recoup their money. Those who do invest but find that they are not eligible for the act's funds after all will be forced to pass on their costs to their patients. This could make health care even less affordable for poor people.

There are lessons that the United States could learn from other countries. Singapore, where I was born and raised, has for three decades steadily raised its standards of living and quality of health-care services while holding health-care expenditure at just above 3% of gross domestic product (GDP). Meanwhile, health-care expenditure in the United States has risen from about 9% of GDP in the 1970s to an unbelievable 17.3% in 2009, or almost one-fifth of the entire US economy (see graph). The key to Singapore's success partly lies in promoting individual responsibility to save for health care and individual choice in how to spend those savings, along with government subsidies to ensure a high standard of care. The country's strong government leadership has resulted in a sensible IT system, with two or three standardized regions, each large enough to

ensure a critical mass of patients and affordable and equitable uptake of the technology. Most, if not all, of the health-care facilities in Singapore are fully equipped with integrated IT systems, including the use of electronic tags to track the flow of patients, clinicians and even blood samples.

Singapore may be a small country, but even in Canada, where I now work, health care is standardized at the province level. Between 2002 and 2004, the government of British Columbia introduced health IT in the province through a programme that started small. This helped to overcome the natural resistance that physicians have to systems that might initially detract from the amount of time that they can spend with their patients. Doctors were first introduced to a web-based software kit for chronic-disease management, piloted for diabetic care, with financial incentives and reimbursements. This paved the way for early adopters and, five years later, 97% of physicians in British Columbia signed up to a broader programme that links them with patient information held by a central authority. This system enticed, rather than forced, practitioners into change.

Drawing lessons from both of these systems, the United States could, for example, subsidize the gradual adoption of new, standardized IT processes, perhaps at the state level.

In a true universally funded health-care system, such as those in the United Kingdom and Taiwan, it is easy to implement standardization and ensure affordability. The United States has a strong political devotion to the powers of a free-market economy. But in the case of electronic health records, this will create confusion, unequal opportunity and wasted funds.

**DANIEL JANIES,
PETER J. EMBI AND
PHILIP R. O. PAYNE**

Collect genetic data on pathogens

Ohio State University, Columbus

The HITECH Act's incentives for the meaningful use of electronic health records provide much-needed encouragement for the capture and exchange of data. But, by setting the bar too low, a great opportunity could be lost to science.

If a patient is diagnosed with an infectious disease such as influenza, the meaningful-use rules encourage physicians and hospitals to send data about the condition to a local public-health agency. This is a good first step, and this type of reporting is likely to be further encouraged by the HITECH Act in the coming years. But the current requirements focus on a perspective of disease surveillance that is quickly becoming outmoded: the counting of cases and symptoms. Comprehensive disease surveillance should focus on tracking the pathogens themselves, including their genetic evolution, zoonotic and geographic origins, and characteristics such as drug resistance.

Ideally, meaningful-use rules should give incentives to health-care providers to gather and transmit genetic data on pathogens. Electronic health records that include such details will improve personalized treatment, and enable the development of the science needed to understand, and one day predict, the spread of pathogens as they become epidemics. Such technologies are rapidly becoming more affordable: the cost of nucleotide sequencing has dropped more than 100,000-fold in the past decade.

National networks involving point-of-care testing for influenza already exist in Thailand, where they have been implemented at a relatively low cost and now help to inform rapid and appropriate use of antivirals. In the United States, point-of-care of testing for pathogens is done only sporadically under normal conditions, with just a fraction of the viral samples making their way to central facilities for genetic sequencing such as the Centers for Disease Control and Prevention or state health departments.

The meaningful-use rules are designed to change in stages over the coming years. This means there is still time to ensure that the country does not miss the great opportunity that the HITECH Act provides: advancing science as much as improving health care. ■



Computer games can have a serious purpose — *Evoke* promises a 'crash course in changing the world'.

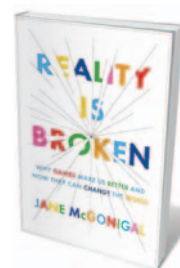
psychologist Mihaly Csikszentmihalyi — who has shown that happiness results from 'flow', a state of full, focused engagement with our activities — McGonigal argues that positive behaviours are mirrored in good game play. Positive emotions and social connectivity can be enhanced through good game design.

Her compelling argument combats the widespread prejudice she has observed against gaming. This bias has been stoked, she notes, by the many traditional psychologists who have found controversial links between violence and game play, just as other studies have associated violent behaviour with some types of film and television programme. Widely aired negative stories have amplified a one-sided understanding of game play as damaging. Similarly, derision of virtual worlds is rife in the media: inhabitants of *Second Life* are often generalized as geeky freaks and sad loners.

McGonigal argues that, in fact, many gamers are social, collaborative and involved in political issues. Through our greater understanding of this game culture, she says, altruistic and positive benefits can be gained for wider society. Gamers could show researchers and policy-makers new ways of modelling real-world scenarios, which might change standard work practices to make them more engaging; for example, motivating employees by creating collaborative team goals.

I have noticed in my own research that the tone of game playing has changed over the past decade. The growth of casual games on mobile devices — as well as multiplayer online games such as *World of Warcraft*, with 12 million subscribers — has broadened the number of players internationally and made inroads into traditionally non-gaming communities, such as women, and adults over 40 years old. For example, a 2010 survey of 73,000 people by the Interactive Software Foundation of Europe found that 25% of adults had played an electronic game in the past six months, which equates to 95 million adult gamers across 18 European Union countries. Twenty per cent of females and 31% of males are gamers, and almost 30% of those aged 30–49 play computer games. Gaming is no longer the preserve of young males, and this trend is growing.

Play is important in the development and maturation of humans and animals. A 1998 study by US psychiatrist Stuart Brown showed that "normal play behaviour was virtually



Reality is Broken:
Why Games Make Us Better and How They Can Change the World

JANE MCGONIGAL
Jonathan Cape/
Penguin: 2011.
320 pp./400 pp.
£12.99/\$26.95

J. GLASER/THE WORLD BANK

TECHNOLOGY

Game for change

Sara de Freitas applauds a bold argument that online gaming can save the planet.

After giving a presentation on the use of serious computer games for learning at the second World Innovation Summit in Education in Doha, Qatar, last December, I was asked a challenging question: what will happen to the real world if everyone spends much of their time in virtual worlds? As I gave my balanced response, it struck me that someone should write a book on the issue. Jane McGonigal, games developer and futurist, has penned that book.

Reality is Broken is brave and comprehensive. McGonigal declares controversially that the current state of our planet and society — damaged through widespread environmental destruction, social disintegration and conflict — can be repaired through games.

Challenges such as motivating individual action on climate change or improving poor health can be addressed through learning that is centred on play. McGonigal lists 14 fixes, including using games to raise work satisfaction, increase success and contribute to a sustainable economy. She explains how we can live less selfish and more rewarding lives through greater collaboration and better-designed games.

The author embraces the findings of positive psychology, a field that looks at human behaviour in terms of happiness and well-being. Pointing to the ideas of researchers such as Hungarian

NATURE.COM
For more on serious gaming:
go.nature.com/b3fttz

absent throughout the lives of highly violent, anti-social men regardless of demography". Games and play are thus powerful tools for socialization. They have potential for therapy, too: in children with attention deficit hyperactivity disorder, and in military personnel with post-traumatic stress disorder.

McGonigal gives vivid case studies of how games can be used for serious purposes, as well as for entertainment. She describes *World Without Oil*, a game she helped develop to encourage players of all ages to envisage possible scenarios for the world when oil has run out. *Quest to Learn* is a US school programme that uses role play and challenges to teach science to children aged 12–17 years. *Superbetter* is a superhero-themed, multiplayer game that aims to accelerate your recovery time after injury. Others include *Foldit*, a game in which players compete to discover how proteins fold; *Free Rice*, an educational game that helps fight real-world hunger; and *Lost Joules*, which investigates ways to save energy.

McGonigal is best known as a developer of alternate-reality games, which bring together real-world concerns and game-world experiences. She outlines, for example, *Chore Wars*, which introduces a competitive element into household tasks. Through a system of points and rewards, it can get people so motivated that they end up sneaking home to vacuum.

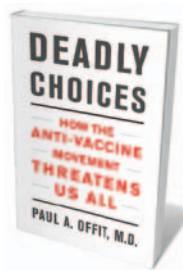
At the Serious Games Institute at Coventry University, UK, my colleagues and I are using games to foster learning about a diverse range of problems: for example, to train global emergency-response teams, to promote good hygiene in hospitals, to reduce misdiagnosis by physicians and to help children cross the road safely. Our research has shown that play can change behaviour among non-gamers and alter attitudes in those who play games regularly. But more investment and capacity-building are needed to reach out to wider sectors of the community.

As the cost of producing computer games drops, and as new devices become more mainstream — such as brain-computer interfaces and haptics that mimic the feel of objects in virtual environments — their appeal will continue to broaden and games will become more pervasive socially. In the future, the use of artificial intelligence will allow even more people to participate in immersive learning environments.

Games, McGonigal concludes, do more than engage, motivate and inspire. Increasingly part of our communities, online and offline, they support social interaction and are part of a collective intelligence. By playing together, she argues, we will be able to save the world and design a beautiful future. ■

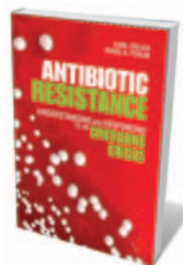
Sara de Freitas is director of research at the Serious Games Institute at Coventry University, UK.
e-mail: s.defreitas@coventry.ac.uk

Books in brief



Deadly Choices: How the Anti-Vaccine Movement Threatens Us All
Paul A. Offit BASIC BOOKS 288 pp. £18.99 (2011)

Following on from his widely praised book *Autism's False Prophets* (Columbia Univ. Press, 2008), vaccine researcher Paul Offit vigorously tackles claims that childhood inoculations cause autism, diabetes and cancer. He dismantles the reasoning of the anti-vaccine lobby and warns of the risks of the re-emergence of deadly childhood diseases owing to declining vaccination rates. With a greater focus on the underlying science, his book complements Seth Mnookin's recent work *The Panic Virus* (Simon & Schuster, 2011; reviewed in *Nature* **469**, 468–469; 2011).



Antibiotic Resistance: Understanding and Responding to an Emerging Crisis

Karl S. Drlica & David S. Perlin FT PRESS 288 pp. \$49.99 (2011)
The evolving resistance of bacteria to available antibiotics is of growing concern for public health and medicine. In their thorough primer, microbiologists Karl Drlica and David Perlin explain how such resistance arises and the array of difficulties it causes in the treatment of infectious diseases. They describe how drug resistance can be exacerbated by human activities such as the misuse of antibiotics, and set out strategies for minimizing resistance and extending the clinical life of these drugs.



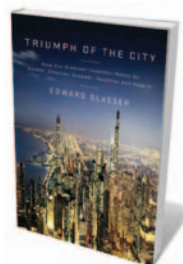
Quirk: Brain Science Makes Sense of Your Peculiar Personality
Hannah Holmes RANDOM HOUSE 288 pp. \$26 (2011)

Why are people so different? Science writer Hannah Holmes explains the brain science and human psychology behind our myriad personalities. She describes how we have evolved a range of character traits, such as extraversion, neuroticism or agreeableness, which allow us to navigate our social world. She details genetic clues behind mental disorders such as depression, schizophrenia and anxiety. And she explains how personality dictates other behaviours — from the political party you support to the type of car you drive.



The Quantum Story: A History in 40 Moments

Jim Baggott OXFORD UNIVERSITY PRESS 320 pp. \$29.95 (2011)
The story of twentieth-century physics is essentially a shift from our belief in certainty to our acceptance of uncertainty. The reason is the development of quantum theory, a set of counter-intuitive ideas about the atomic world that are hugely successful but still make physicists feel uncomfortable. Science writer Jim Baggott describes 40 major episodes in the growth of quantum ideas, from physicist Max Planck's musings on the energetics of black-body radiation to the latest aspects of particle physics being unearthed at CERN, Europe's high-energy physics lab near Geneva, Switzerland.



Triumph of the City: How Our Greatest Invention Makes Us Richer, Smarter, Greener, Healthier, and Happier

Edward Glaeser THE PENGUIN PRESS 352 pp. \$29.95 (2011)
Rather than being ridden with crime, filth and poverty, cities are healthy, green and rich, argues economist Edward Glaeser. Travelling to metropolitan areas around the globe, he reports that urbanites from New York to Kolkata have access to better health care and education and use less energy than those who live in the suburbs or in rural communities. We should feel more positively toward our cities, he feels, as they are great places to live and thrive.



PSYCHOLOGY

More alike than different

Two books debunk gender differences in the brain, discovers **Virginia Valian**.

Trying to distinguish the female from the male brain is a trap that many writers fall into. Two books provide a welcome corrective by reviewing scientific evidence showing that the sexes are more alike than different, and that small sex differences are not fixed but change with context and across generations.

Cordelia Fine's *Delusions of Gender* is aimed at a broad audience and debunks the egregious exaggerations common in popular books. Rebecca Jordan-Young's *Brain Storm* is directed at specialists who are interested in historical studies of the brain, sex hormones and gender differences. Fine, a psychologist at Macquarie University in Sydney, Australia, and Jordan-Young, a medical sociologist at Barnard College in New York, point out the methodological and theoretical limitations of such studies, and demonstrate the part that folk theories about gender differences have played in casting the sexes as inherently dichotomous.

Both books note that correlation and causation are often confused when looking at the results of brain or hormonal differences on behaviour — 'causing', for example, boys to be better than girls at mental rotation of three-dimensional objects. Too many studies ignore mediating variables and alternative explanations and exaggerate the extent of gender differences. Both accounts direct attention to the full range of results, including those that researchers might otherwise ignore.

Delusions of Gender: How Our Minds, Society, and Neurosexism Create Difference/The Real Science Behind Sex Differences

CORDELIA FINE

W. W. Norton/Icon Books: 2010. 338 pp./368 pp.
\$25.95/£14.99

Brain Storm: The Flaws in the Science of Sex Differences

REBECCA M. JORDAN-YOUNG

Harvard University Press: 2010. 408 pp. \$35

Although males and females differ in many ways, the authors note that the same could be said of any two groups — people with different hair colour or degrees of economic security, say. Because men and women have distinct reproductive functions, controlled in part by different hormones, we are prone to interpret their behavioural and psychological differences as not only biologically mediated but mandated. Putative brain differences are seized on as sex-based and other hypotheses can be overlooked.

To illustrate, Fine considers the corpus callosum linking the two brain hemispheres. The fact that it seems to be thicker in women than in men is sometimes associated with women's supposed greater verbal skill. According to

NATURE.COM
Neurobiologist Ben Barres on gender and science:
go.nature.com/pdo9ax

this 'just-so' reasoning, a thicker corpus callosum may allow easier integration of information from the two sides of the brain.

But, as both authors point out, the reported differences in corpus callosum size are unreliable between studies, and seem to be related to brain size. In both sexes, larger brains have a larger callosum, but in smaller brains they make up a greater percentage of brain volume. So if a sex difference in the corpus callosum exists, it is likely to be a by-product of the basic difference in average brain size — a fact that is missed by a focus on sex. Unless researchers conduct analyses that divide groups in ways other than gender, the real story might be missed.

The behaviours of both sexes are remarkably similar despite their presumed brain and hormonal differences. Although men's brains are roughly 10% larger than women's, the IQs of both genders are roughly equal, and most experiments in cognitive processing in children and adults reveal no sex differences.

In deflating spurious claims about the influences on sex differences, the books risk underestimating those effects. Consider congenital adrenal hyperplasia (CAH), a major topic in Jordan-Young's book, in which the fetus is exposed to higher levels of androgens than are unaffected children. This causes emotional and physical symptoms ranging in girls from early-onset puberty to infertility. Jordan-Young concludes that children with and without CAH are more alike than different. But in my view, she underestimates the differences between girls with CAH and their unaffected peers in two domains.

Although the data are mixed, girls with CAH seem to be better at mentally rotating shapes than are unaffected girls. The results are clearer for toy preferences: when asked to choose from various 'masculine', 'feminine' and 'neutral' toys, girls with CAH show more interest in masculine and less interest in feminine toys than girls who are unaffected. Boys with and without CAH are indistinguishable in their choices.

Whether a toy is perceived as masculine or feminine, however, depends on who plays with it; as Jordan-Young notes, children's play preferences have changed over time. Some activities once seen as masculine, such as playing with construction toys and balls, are now seen as neutral and on a par with books and puzzles. Dolls, by contrast, have remained feminine. Toy-preference studies show that girls divide their time equally among masculine, feminine and neutral toys, whereas boys tend to eschew feminine ones. So the girls with CAH are acting like control boys. But we cannot tell whether that is because they prefer masculine toys or are taking less interest in feminine ones. The way such questions are posed affects where one searches for answers.

So why do boys avoid dolls? They learn early that they will pay a social price for showing 'deviant' feminine interests. Girls can like the same toys as boys with little fear

of negative social consequences, as demonstrated by the different connotations of 'sissy' and 'tomboy'. For girls with CAH, there is another social issue: many undergo genital surgery in infancy and have impaired fertility. Girls' knowledge about their condition may trigger concerns about their femininity and lead to an avoidance of toys such as dolls.

To some extent, both books are brooms that sweep too clean. I contend that one cannot dismiss sex differences in mental rotation of three-dimensional objects as ill-documented or easily reversed, as both authors do. The difference is robust and difficult to neutralize; its precursors are seen in

infancy. Laying such distinctions only at the doorstep of social psychology — in different expectations of the two sexes, for example — closes off inquiry into underlying cognitive processes. Similarly, there is almost nothing about sex differences in mathematics and science in Jordan-Young's book, and only a cursory treatment in Fine's.

I share both authors' conclusions that the jury is still out over whether hormonal and neural sex differences are linked to behavioural divergence. I also agree that social context is often a more likely source of sex differences. Most behavioural sex differences are small, and there is no direct mapping

between a behaviour and a set of neural mechanisms. Different neural mechanisms can be responsible for the same behaviour.

It is no bad thing that there are many hypotheses still to test. Eventually, unsupported preconceptions about what counts as masculine and feminine will be discarded. Until then, people such as Fine and Jordan-Young are just who we need. ■

Virginia Valian is professor of psychology and co-director of the Gender Equity Project at Hunter College, City University of New York, New York 10065, USA.
e-mail: virginia.valian@hunter.cuny.edu

ASTRONOMY

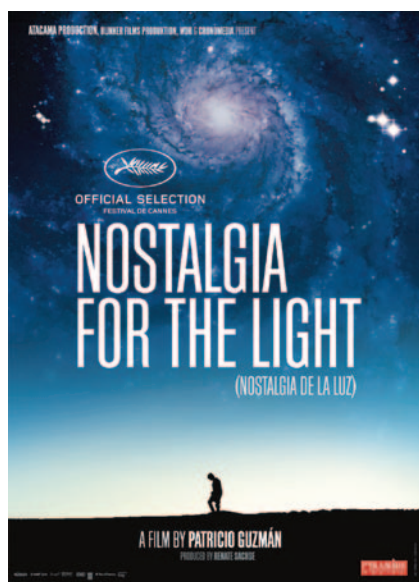
Answers from the Atacama

A Chilean film juxtaposes astronomy with the search for those killed under Augusto Pinochet, finds **Alison Abbott**.

The Atacama Desert in northern Chile is the driest place on Earth. Decades can pass with no rain. Patricio Guzmán tells the stories of the people who are searching in its arid expanse in his film *Nostalgia de la Luz* (Nostalgia for the Light) — winner of the 2010 European Film Academy award for best documentary and now showing in selected cinemas in Europe. On the desert's mountain tops, astronomers look skyward, hunting for cosmological truths. On its plains, others look towards the ground, hunting for political truths.

Astronomers love the Atacama. Its dryness and clear skies give them an unimpeded view of deep space. Since the mid-1960s, they have been building ever-more powerful telescopes there with which to gaze ever farther into the cosmos. Piecing together the history of the Universe from the ancient light of distant stars, they are largely unaware of the women below on the desert floor, digging — sometimes with their bare hands — for the remains of loved ones killed during the regime of dictator Augusto Pinochet in the 1970s.

Nostalgia de la Luz interweaves the stories of these two searches — one addressing modern history on a heartbreakingly human scale, the other deep history on a grandiose and edifying scale. Other scientific investigations also feature, including archaeology. It is a slow, poetic film that contemplates existential questions: where we



Nostalgia de la Luz
DIRECTED BY PATRICIO GUZMÁN
In some independent cinemas in Europe.

came from, where we are going and how we come to terms with the pain of the present. It is compelling, thanks to the characters that the director has found to explain their quests.

Gaspar is an articulate young Chilean astronomer working at the Cerro Tololo observatory, who can answer many questions about cosmic history but few about his country's recent past, when thousands disappeared or were killed and traces of their fate

covered up. Lautaro is an older archaeologist who followed the trails of ancient civilizations through the desert for decades, finding their mummified dead in the desiccating atmosphere. Now he teaches the searching women how to recognize from the surface grains whether a human body might lie below the sand.

Also featured is Luis. He spent years in one of Pinochet's concentration camps in the desert, where he learnt about astronomy from a fellow political prisoner. Stargazing helps him not to forget that time, he says. Miguel, an architect, survived five such camps. He committed their layouts to memory and drew them up precisely when he was freed, so that Chileans would never be able to deny their existence.

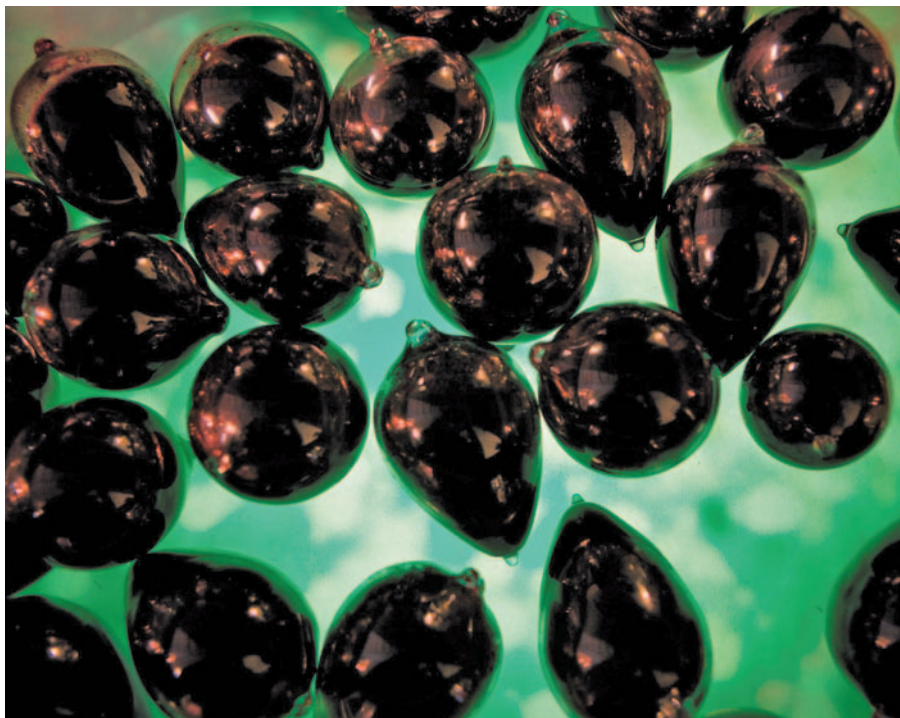
Towards the end of the dictatorship, Pinochet's soldiers dug up mass graves and dumped evidence of the massacres in the sea. The film follows Victoria and Violeta, who talk movingly about their continuing search for their loved ones. They have found fragments of their bones, smashed by the digging machinery, which has fed their determination to find out what happened.

And there is Valentina, whose mother and father were among those who disappeared, who became an astronomer after the grandparents who raised her taught her to observe the night sky. Understanding the infinite Universe, she says, has given her a comforting perspective on her loss.

Guzmán, the film's director, is himself a refugee from Pinochet's Chile, and now lives in France. Most of his films have been political, and this venture into science provides him with metaphors of immense power with which to explore this theme. *Nostalgia de la Luz* will also confront scientists with connections that they have not previously imagined. If only, the searching women say, the telescopes could instead point downwards to help them. ■

Alison Abbott is Nature's European correspondent.

NATURE.COM
For more on the spirit of observatories:
go.nature.com/ehdlon



Kathy High's *Blood Wars* uses donated blood to stage a Petri-dish contest between white blood cells.

CULTURE

Art that touches a nerve

Anthony King explores a Dublin exhibition that exposes the controversies of synthetic biology.

Do not expect an easy stroll through this exhibition. Visitors to *Visceral* at Dublin's Science Gallery may recoil at books made of human and pig skin or stand stupefied as hundreds of crickets watch a lecture on their own sex lives. On opening night, you could gaze at a film projected onto a living screen made of fish corneas and live human sperm, or listen to the Beach Boys' *Good Vibrations* mixed with farm sounds and pumped through a cow-bone audio speaker.

The works aim to twang a raw nerve rather than shock visitors, explains exhibition co-curator Oron Catts, who became interested in the life sciences as a design student in Perth, Australia, more than 15 years ago. He began the Tissue Culture and Art Project after visiting the lab of tissue researcher Miranda Grounds at the University of Western Australia, Perth. Early work on tissue engineering had disturbed and challenged him. "We are starting to treat biology and life as a raw material for us to engineer," he notes.

In 2000, with co-curator Ionat Zurr, Catts founded SymbioticA, an artistic research lab in the university's school of anatomy and human biology. The Dublin exhibition marks

**Visceral:
The Living Art
Experiment**
Science Gallery, Trinity
College Dublin.
Until 25 February
2011.

the lab's tenth anniversary. SymbioticA takes things that scientists view as mundane and repositions them so they seem strange, necessitating reassessment. Its visual art awakens views on the ethical and moral quandaries of biology.

Direct engagement with biotechnology is pivotal to SymbioticA's philosophy, so its artists wield the same tools as biologists. For example, Catts grew meat in the lab and ate it as a cultural comment in 2003. Artist Abhishek Hazra asks viewers of the exhibition to imagine a situation in which a rogue state must harness human biomaterials to create fertilizers and explosives. In a fully functioning lab within the gallery, his art experiment attempts to extract ammonia from breast milk. The political and scientific resonance is powerful.

During the exhibition, volunteers will donate blood for *Blood Wars*, a staged contest between individuals' white blood cells in a Petri-dish theatre. After a few hours, one set of cells will have destroyed the other. The artist, Kathy High, seeks to engage with debates

about blood traits and inherited diseases. She has Crohn's disease, and suggests that her cells are at an advantage in the contest because they are sensitive to foreign cells.

SymbioticA also explores how the language of engineering has filtered into biology. Catts cites unsettling precedents, such as the use of eugenics in the Nazi era, when a "mechanistic or engineering view of life was deployed". Synthetic biology is on his list of research topics owing to its pervasive engineering logic. In 2002, Catts's tissue-culture project lampooned "the hype" of the Human Genome Project by promising to grow pig wings.

An exhibit named *The Vision Splendid* displays living tissue from cells purchased

"What is happening in life sciences now is exciting, but we don't really have a cultural language to engage with it."

online, originally obtained in 1969 from a 13-year-old African-American girl. We are asked to ponder how many of her cells may now live beyond her original body. "What is happening in life

sciences now is exciting, but we don't really have a cultural language to engage with it. We can't articulate it outside of the science lab," says Catts.

This prodding of the public through disturbing visual-art installations has proved a success. The Tissue Culture and Art Project has an exhibit in the Museum of Modern Art, New York, and SymbioticA has a programme of residencies, research, academic courses, seminars and workshops. Catts notes that its work was mentioned in a paper for the US Congress on bioethics, and that the artists are often invited to comment about the impact of modern biology on culture. SymbioticA also set up the world's first master of biological arts degree programme.

Artists and scientists say that the frontier spirit of Perth — one of the world's most isolated cities — has had a big role in allowing SymbioticA to flourish. The lab does not have a display area for its works, and has had more impact beyond Australia. Its collaboration with Dublin's Science Gallery was born out of a common cause: a way to engage with science that is artistic and cultural rather than didactic.

Grounds, the researcher who first opened her lab to Catts, admits that this type of art can be challenging because you must "tune into it and learn the detail before you appreciate what it represents". But a gut response is hard to avoid. The last day of the exhibition will see a 'killing ritual' and funeral, devised with the help of the audience, to dispose of *Visceral's* living materials. ■

Anthony King is a writer based in Dublin.
e-mail: anthonyking@gmail.com

CORRESPONDENCE

Protect Brazil's land to avert disasters

The huge mudslides and flooding in Brazil that killed more than 890 people in Rio de Janeiro state have been blamed on heavy rains and soil features. We believe that the main culprits are the country's increasingly chaotic land-use policies.

The 1965 Brazilian Forest Act governs rural land use and guides it in urban areas so that all steep hills, hilltops and forests near water are permanently protected. These areas provide crucial ecosystem services, such as terrain stabilization, flood regulation and water supply.

But after decades of unplanned urban and agricultural expansion in contravention of the Act, natural calamities in Brazil are on the rise. In addition to the recent disaster, landslides and floods in other Brazilian states have killed hundreds of people during the past three years.

The Brazilian congress is now considering a draft bill that excludes hilltops from legal protection, reduces the width of protected areas adjoining small streams, and allows state governments to reduce such areas by up to 50% more than is permitted under federal rules. The draft bill also gives the municipalities more freedom to slacken land-use standards in urban areas.

Supporters of the new bill have failed to note the link between disregard of protected areas and the rise in natural catastrophes. Instead of enforcing the existing law, they propose to legitimize violations that are likely to contribute to more tragedies. Now, influential agribusiness lobbyists are trying to force a quick vote on this matter to reduce costly compliance pressures on

recalcitrant landowners.

As so often happens with environmental issues, the welfare of many is threatened by the interests of a few.

Carlos A. Zucco, Luiz Gustavo R. Oliveira-Santos, Fernando A. S. Fernandez *Federal University of Rio de Janeiro, Brazil.*

cazucco@hotmail.com

Balkan science: give support to Bulgaria

Policies restricting the future funding of Bulgarian science (*Nature* 469, 131–132 and 142–143; 2011) could have implications for the European Union's research landscape.

Take the contentious issue of genetically modified (GM) organisms. Attempts by the Bulgarian government to amend its laws on GM organisms to comply with EU regulations met with strong opposition in the media. However, the government was unable to garner support and advice from the scientific community, which had previously been alienated by government actions.

As a result, in March 2010, the Bulgarian parliament succumbed to media pressure and imposed severely restrictive amendments on its laws on GM organisms, banning all biotechnology research. It is now forbidden to grow GM plants for trials or commercial cultivation near nature reserves, apiaries or fields of organic produce, or to introduce genetic modifications into tobacco, vines, roses, wheat or any fruit or vegetable crops.

These bans are enforced by fines of between €250,000 (US\$340,000) and €500,000 for a first offence, and doubled thereafter. But they are not scientifically justifiable: there is no evidence that transgenic technology is inherently

riskier than any other, a matter investigated by the EU over 20 years at a cost of more than €300 million. The restrictions are apparently acceptable in Bulgaria, however, because science has been publicly discredited (seemingly for short-sighted political purposes).

I therefore appeal to the entire scientific community, not just Bulgaria's, to defend and promote the scientific arguments needed to guide important policy decisions and underpin research proposals.

Bojin Bojinov *Agricultural University of Plovdiv, Bulgaria.*
bojin.bojinov@gmail.com

Balkan science: how to halt the brain drain

Reforms to Romania's science education and research will provide a fresh start, but will not be easy to implement (*Nature* 469, 142–143; 2011). Crucial to progress will be more effective selection of high-ranking academics who can improve the quality of research output and serve as mentors for students and junior scientists.

Mentoring programmes in Romanian universities need to become common practice and be properly funded. Since Romania joined the European Union in 2007, grant competition has revitalized its research infrastructure. But intellectually energetic and highly innovative teams are needed to justify expenditure on hi-tech pieces of laboratory equipment.

Steps should be taken now to ensure that the most talented academics are hired. Their work environment must be financially secure to help alleviate the brain drain that still plagues the country's education and research system.

Tudor Luchian Alexandru Ioan *Cuza University, Iasi, Romania.*
luchian@uaic.ro

Forest loss began before bioethanol

The problem of bioethanol's 'dirty footprint' in Alagoas state in Brazil (*Nature* 469, 299; 2011) is real and deserves attention. But the historical background bears clarification.

The loss of Atlantic rainforest in Alagoas to sugar cane began well before the 35-year-old national sugar-cane ethanol programme was introduced. Sugar-cane plantations and mills were established in the state in the early seventeenth century, starting on the coastal plains and then moving inland (A. L. S. Santos *et al.* *Campo-Território* 2, 19–37; 2007). The state's forests have been logged for shipbuilding and other uses since the eighteenth century (W. Dean *With Broadax and Firebrand* Univ. California Press; 1995).

The authors' implication that Alagoas's forests are no longer a biodiversity hotspot is misleading. The entire Brazilian Atlantic Forest is listed as a hotspot precisely because of the huge areas that have been lost. Combined with the forest's richness of endemic plants, this fulfils the two criteria for a biodiversity hotspot (N. Myers *et al.* *Nature* 403, 853–858; 2000).

Thomas Michael Lewinsohn *State University of Campinas, Brazil.*
thomasl@unicamp.br

CONTRIBUTIONS

Correspondence may be sent to correspondence@nature.com after consulting the author guidelines at <http://go.nature.com/cmchno>. Readers are also welcome to comment online on anything published in *Nature*: www.nature.com/nature.

FORUM Genomics

Drugs, diabetes and cancer

Variation in a genomic region that contains the cancer-associated gene *ATM* affects a patient's response to the diabetes drug metformin. Two experts discuss the implications for understanding diabetes and the link to cancer.

THE PAPER IN BRIEF

- The authors¹ analyse genomic variation among a large group of patients who respond differently to metformin — the most commonly used drug for treating type 2 diabetes.
- This genome-wide association study (GWAS) involved 1,024 Scottish patients, as well as a further 2,896 patients to check for replication of the results.
- Treatment success was significantly linked to the presence of a single nucleotide-base

variation designated rs11212617.

- This variation occurs in a genomic region (locus) that also contains the gene *ATM*. *ATM* encodes a tumour-suppressor protein involved in DNA repair and cell-cycle control that is mutated in ataxia telangiectasia, a neurodegenerative disease associated with a predisposition to cancer.
- The authors further show, in a rat cancer cell line, that inhibition of *ATM* weakens metformin-mediated activation of a metabolic enzyme, AMPK.

interaction between *ATM* and the beneficial effects of metformin. Most crucial will be to find out whether there are other molecules, apart from AMPK, that both control metabolism and are influenced by *ATM*.

Morris J. Birnbaum is at the University of Pennsylvania Medical School, Philadelphia, Pennsylvania 19104-6148, USA.
e-mail: birnbaum@mail.med.upenn.edu

A clue to metformin action

MORRIS J. BIRNBAUM

Let me start on a positive note. The genetic association between *ATM* and metformin sensitivity¹ represents a triumph of modern pharmacogenetics, and it is reasonable to hope that it will lead to fundamental insights into metformin's mechanism of action and the regulation of carbohydrate metabolism.

You might ask how a rare variation linked to *ATM* could possibly be related to the treatment of a common disease such as diabetes. After all, given the prevalence of diabetes, it would be reasonable to assume that it takes only slight disruptions in nutritional intake or energy expenditure to shift the balance between health and metabolic disease.

This is in fact far from the truth. To contract an illness with the serious consequences of type 2 diabetes, not only must there be disturbances in energy balance, but the normal homeostatic mechanisms that regulate metabolism must also be impaired. In other words, if the regulatory system fails to respond to caloric overload, disease ensues. With the relative uniformity of the Western — and increasingly global — lifestyle, a major determinant of susceptibility to type 2 diabetes must therefore be an individual's genetic make-up, which dictates the response to nutritional overload or therapeutic intervention.

Metformin works mainly by reducing glucose production by the liver, but there is still uncertainty about its mechanism of action at a molecular level. The drug blocks a step in the aerobic production of the cellular energy molecule ATP, activating a signalling pathway in which the enzyme AMPK senses energetic stress within the cell. Nonetheless, despite activating AMPK, metformin actually works independently of the enzyme^{2,3}. The discovery of a role for *ATM* in modulating metformin responsiveness might provide a clue to the mechanism of action of this drug.

Unfortunately, however, it could equally well be a false lead. Classic genetic screens have taught us that some candidate genes can exert very indirect effects, providing little information about crucial signalling pathways. For example, variations in another gene also affect metformin responsiveness, but that gene's product, OCT1, influences the rate of uptake of metformin by cells, rather than any major signalling pathway⁴.

Another possibility is that *ATM* influences blood glucose levels through pathways parallel to — but not the same as — those modulated by metformin, and that its effects become apparent only with synergistic input from the drug. Indeed, 40 years ago, it was noted⁵ that patients with ataxia telangiectasia often display a type-2-diabetes-like syndrome characterized by an insulin resistance too severe to be caused just by changes in liver glucose production.

With the genetic clues now to hand, careful biochemical and cell-biological studies should be performed to figure out the nature of the

The cancer connection

REUBEN J. SHAW

A tumour-suppressor protein that mediates DNA repair and has ties with a metabolic disorder¹ — this might sound far-fetched. But in fact the reported link between responsiveness to metformin and a cancer gene is not without precedent.

Previous work has shown that activation of AMPK by metformin requires the activity of the kinase enzyme LKB1. The gene encoding LKB1 was originally identified for causing an inherited cancer disorder, and is one of the most commonly mutated genes in human lung cancer⁶. Animal studies also point to a role for this gene in a variety of spontaneously arising cancers. Notably, deletion of *Lkb1* in mouse liver leads to loss of AMPK activity in that organ and to the development of metabolic dysfunction, including hyperglycaemia and hepatic steatosis — symptoms resembling those of type 2 diabetes⁷. Furthermore, a genetic survey revealed that DNA-base variations in *LKB1* affect how women with polycystic ovary syndrome respond to treatment with metformin⁸.

The fact that the present study (the first GWAS to find a locus that 'dictates' metformin response) has identified a possible role for *ATM* — which is also a kinase enzyme — could fit in with several earlier observations. For instance, patients with ataxia telangiectasia show insulin resistance and are at a higher risk of developing diabetes, and mice with defective *ATM* activity

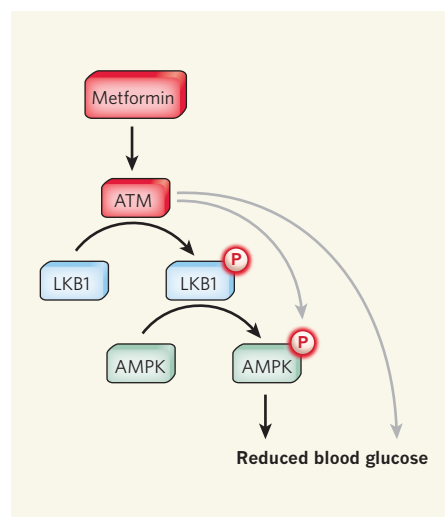


Figure 1 | Possible mechanisms of the anti-diabetic effects of ATM. In response to metformin, ATM could mediate the phosphorylation (P), and so the activation, of AMPK by phosphorylating LKB1. Alternatively, ATM might activate AMPK independently of LKB1, or reduce blood glucose levels through pathways entirely independent of AMPK.

show insulin resistance and abnormal glucose homeostasis⁹.

How might ATM be involved at a molecular level? The present work¹ hypothesizes that this enzyme modulates patients' responsiveness to metformin by affecting the drug's ability to activate AMPK. Indeed, ATM is known to phosphorylate LKB1 — AMPK's key activator^{10,11} — thereby affecting various cellular processes. ATM might also regulate AMPK independently of LKB1. Furthermore, it may affect metformin responsiveness by regulating other relevant targets that are independent of AMPK (Fig. 1). Indeed, ATM is known to phosphorylate other components of the insulin signalling pathway^{12,13}.

In light of these intriguing connections, it is essential to rigorously examine whether the rs11212617 variant serves to modulate ATM activity, towards AMPK activation or that of other downstream targets. From the present data, it is not clear whether ATM activity is even perturbed by this variant.

As for metformin's relevance to cancer therapy, patients with diabetes who take this drug have a lower risk of developing cancer than those on other anti-diabetes medications¹⁴. Whether metformin is a general activator of ATM and its targets in the DNA-damage-response pathway should therefore be thoroughly investigated. Although LKB1 and AMPK are good candidates for mediating some of the beneficial effects of metformin on cancer risk, the involvement of the broader tumour-suppressor pathways controlled by ATM is an intriguing possibility. Future studies dissecting the relationship between metformin action, ATM, LKB1 and AMPK should shed

light on the intersection between suppression of the risk of cancer and that of diabetes. ■

Reuben J. Shaw is at the Molecular and Cell Biology Laboratory, Howard Hughes Medical Institute, The Salk Institute for Biological Studies, La Jolla, California 92037, USA. e-mail: shaw@salk.edu

1. The GoDARTS and UKPDS Diabetes Pharmacogenetics Study Group & The Wellcome Trust Case Control Consortium *Nature Genet.* **43**, 117–120 (2011).
2. Foretz, M. *et al.* *J. Clin. Invest.* **120**, 2355–2369 (2010).
3. Miller, R. A. & Birnbaum, M. J. *J. Clin. Invest.* **120**, 2267–2270 (2010).

4. Shu, Y. *et al.* *Clin. Pharmacol. Ther.* **83**, 273–280 (2008).
5. Schallch, D. S., McFarlin, D. E. & Barlow, M. H. *N. Engl. J. Med.* **282**, 1396–1402 (1970).
6. Shackelford, D. B. & Shaw, R. J. *Nature Rev. Cancer* **9**, 563–575 (2009).
7. Shaw, R. J. *et al.* *Science* **310**, 1642–1646 (2005).
8. Legro, R. S. *et al.* *J. Clin. Endocrinol. Metab.* **93**, 792–800 (2008).
9. Schneider, J. G. *et al.* *Cell Metab.* **4**, 377–389 (2006).
10. Sapkota, G. P. *et al.* *Biochem. J.* **368**, 507–516 (2002).
11. Sherman, M. H. *et al.* *Mol. Cell* **39**, 873–885 (2010).
12. Yang, D.-Q. & Kastan, M. B. *Nature Cell Biol.* **2**, 893–898 (2000).
13. Matsuoka, S. *et al.* *Science* **316**, 1160–1166 (2007).
14. Pollak, M. *Cancer Prev. Res.* **3**, 1060–1065 (2010).

EVOLUTIONARY BIOLOGY

When life got big

Deposits in China dating to about 600 million years ago contain carbon compressions of algae and other organisms. The fossils provide a new window into the early evolution of complex multicellular life. SEE LETTER P.390

GUY M. NARBONNE

The Ediacaran period (635 million to 542 million years ago) represents a watershed in the history of life, when 'life got big' after nearly 3 billion years of microbial evolution¹. The early fossil record of large, architecturally complex, multicellular life has generally been regarded as starting with the Avalon assemblage of the Ediacara biota, known from Newfoundland, England and northwest Canada. The assemblage consists of centimetre- to metre-scale impressions of soft-bodied, fractal organisms (rangeomorphs) that first appeared 579 million years ago and dominated deep-water environments throughout the latter half of the Ediacaran². On page 390 of this issue, Yuan and colleagues³ describe centimetre-scale algal compressions and other fossils from the early Ediacaran. They provide both a different fossil search-image and a probable extension of the oldest record of macroscopic and morphologically complex life.

The fossils occur in huge numbers as carbon compressions on bedding surfaces in black shales in the Lantian Formation of southern China. Many of the fossils show branching patterns and other features typical of macroscopic fleshy algae, some of them comparable with modern kelp. Yuan *et al.* informally compare other examples of the fossils to cnidarians and bilaterian worms, but more work is needed before such connections can be established firmly.

The Lantian biota was discovered more than a decade ago, but in the absence of definitive age indicators it was originally regarded as correlating with the Miaohé biota of central

China (now dated at 551 million years old⁴). Revision of its age by Yuan and colleagues substantially increases its importance. The Lantian succession is highly condensed, with less than 150 metres of strata representing more than 90 million years, requiring great care in identifying subdivisions and correlations. Setting this caveat aside, new carbon-isotope data permit robust correlations that imply that the Lantian biota is much older than previously thought, probably between 577 million and 635 million years old.

The younger part of this range is indistinguishable from the 579-million-year date for the oldest occurrence of the Avalon assemblage of the Ediacara biota, and would suggest that complex macroscopic multicellularity occurred synchronously in both algae and rangeomorphs at the end of the Gaskiers glaciation 582 million years ago⁵. However, it is more likely that the Lantian algae are older than that, and that they appeared soon after the end of the Marinoan glaciation (635 million years ago⁴). If so, it implies a staggered acquisition of large, complex multicellularity by different groups of Ediacaran life in response to sequential global glaciations and changes in ocean chemistry⁶.

The Lantian biota offers a window into early complex multicellularity that superbly complements the view provided by the Avalon assemblage: there is little similarity between them other than their age. They have no taxa in common, possibly even at the kingdom level. Lantian fossils were preserved as carbon compressions that are broadly similar in preservational style to the Burgess Shale and other exceptional fossil deposits of Cambrian

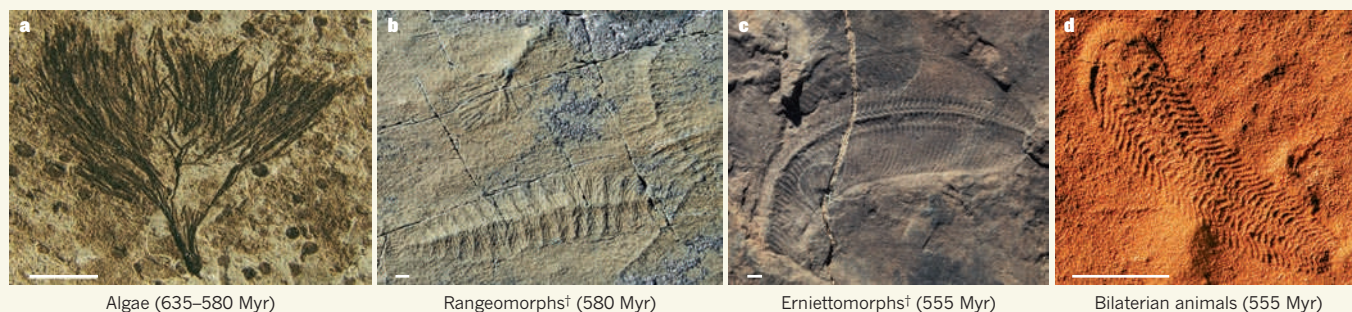


Figure 1 | Four biological groups that achieved macroscopic size and complex morphology during the Ediacaran. The numbers are the age of the oldest confirmed examples (Myr, millions of years). The scale bars represent 1 centimetre, and † denotes groups that have no extant descendants. The algal example (a) is a representative of the Lantian biota described by Yuan *et al.*³. It is reproduced from their paper, where other algae are depicted, as well as fossils of uncertain affinities. (Images b and c are field photographs by G. M. Narbonne; image d is from J. G. Gehling, SAM P40137.)

age (the geological period that follows the Ediacaran). Fossils of the Avalon assemblage were typically preserved as impressions beneath beds of volcanic ash or sandstone. Both sets of fossils are typically centimetre-scale in size, but the largest examples of the Avalon assemblage are one to two orders of magnitude bigger than the largest Lantian fossils.

The environmental contexts are also different. The Lantian algae inhabited quiet, shallow-water marine environments within the euphotic (sunlit) zone³, implying that they carried out photosynthesis. By contrast, the Avalon organisms lived in deeper water, up to abyssal depths, and probably acquired energy from the osmotic intake of dissolved organic compounds^{2,7}. Later, shallow-water assemblages of the Ediacara biota include other extinct groups such as the erniettomorphs, alongside probable ancestors of radial and bilaterian animals. But the differences in preservation between the carbon compressions of the Lantian/Miaohe biotas and the sandstone impressions of the Ediacara biota allow minimal taxonomic overlap in their resultant fossil assemblages⁸. These different preservational and ecological windows reveal different evolutionary pathways in the Ediacaran development of complex multicellularity among algae, animals and extinct groups such as rangeomorphs and erniettomorphs (Fig. 1).

With the exception of highly derived forms, large eukaryotes, including animals and even algae, strictly require oxygen for their metabolism, and numerous studies have shown a strong link⁶ between glaciation, oxidation and the development of complex life during the Neoproterozoic (the era between about 1,000 million and 542 million years ago). The Lantian biota probably predates the oxidation of the deep sea in the Avalon locations⁵ and northwest Canada⁹, which occurred 582 million years ago, but the Lantian deposits were laid down at much shallower (euphotic) depths that may well have been oxygenated by this time.

Geochemical studies have shown that

the Lantian⁹ and equivalent strata in central China¹⁰ were deposited under anoxic conditions. Yuan and colleagues³ regard the Lantian fossils as having been preserved in their original life positions on the sea floor, however, and thus that they are indicative of brief oxygenation events that may have gone unnoticed and unsampled in the geochemical studies^{9,10}. This hypothesis should be easy to test, and will help to elucidate the complex but crucial role of ocean oxidation in the Ediacaran emergence of complex multicellular life. ■

Guy M. Narbonne is in the Department of Geological Sciences and Geological Engineering, Queen's University, Kingston,

Ontario K7L 3N6, Canada.

e-mail: narbonne@geol.queensu.ca

1. Butterfield, N. J. *Palaeontology* **50**, 41–55 (2007).
2. Narbonne, G. M. *Annu. Rev. Earth Planet. Sci.* **33**, 421–442 (2005).
3. Yuan, X., Chen, Z., Xiao, S., Zhou, C. & Hua, H. *Nature* **470**, 390–393 (2011).
4. Condon, D. *et al. Science* **308**, 95–98 (2005).
5. Canfield, D. E., Poulton, S. W. & Narbonne, G. M. *Science* **315**, 92–95 (2007).
6. Narbonne, G. M. *Science* **328**, 53–54 (2010).
7. Sperling, E. A., Peterson, K. J. & Laflamme, M. *Geobiology* **9**, 24–33 (2011).
8. Zhu, M., Gehling, J. G., Xiao, S., Zhao, Y. & Droser, M. L. *Geology* **36**, 867–870 (2008).
9. Shen, Y., Zhang, T. & Hoffman, P. F. *Proc. Natl Acad. Sci. USA* **105**, 7376–7381 (2008).
10. Li, C. *et al. Science* **328**, 80–83 (2010).

BIOPHYSICS

Push it, pull it

During migration, cells interact with their environment by exerting mechanical forces on it. A combination of two techniques shows that they do so in all three dimensions by a push–pull mechanism.

PASCAL HERSEN & BENOÎT LADOUX

Mechanobiology is an emerging field that investigates how living cells sense and respond to the mechanical cues of their surroundings. In contrast to passive objects such as water droplets, living cells actively probe their environment by exerting forces on it as they migrate¹. Such forces not only drive mechanical events such as cell deformation but also trigger cellular processes such as cell–environment adhesion signalling and cytoskeletal reorganization. In this context, mechanical forces have been shown^{1–3} to have a key role in many biological functions, including cell migration, cancer progression and stem-cell differentiation. But the precise characterization of these forces in space and time has remained elusive. Writing in *Physical*

Review Letters, Delanoë-Ayari and colleagues⁴ describe a microscopic technique that does just that.

In the early 1980s, seminal work by Harris *et al.*⁵ demonstrated that cells can exert forces on and deform compliant two-dimensional (2D) substrates. Since then, various techniques have been developed to map the deformation induced by traction forces exerted by cells on elastic substrates¹. These traction-force microscopy techniques have led to a greater understanding^{6–8} of the processes that regulate cell–substrate interactions, from the molecular to the multicellular level. However, until recently, the techniques have been used only to compute in-plane (horizontal) forces, thus assuming that the cellular biomechanical components responsible for the establishment of forces within cells were mostly oriented parallel to the surface. In other

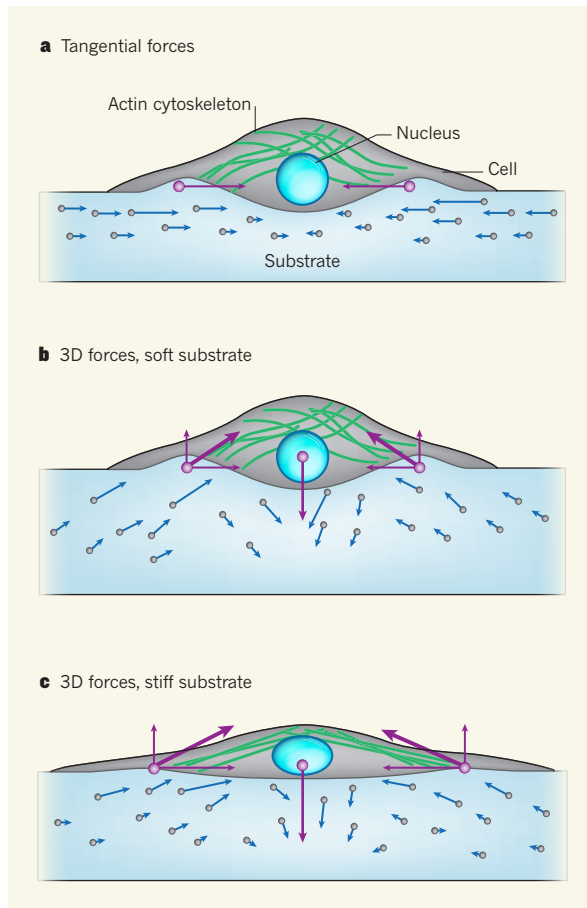


Figure 1 | Mechanical forces involved in cell adhesion.
a, Classic representation of the technique of traction-force microscopy, which involves measuring the tangential traction forces (purple arrows) exerted by a cell on a deformable substrate on the basis of the displacements (blue arrows) that the cell induces on fluorescent beads (grey dots) embedded in a substrate.
b, Delanoë-Ayari and colleagues⁴ extend the technique to allow the traction forces exerted by a cell on a soft substrate to be precisely determined in three dimensions. They find that cell–substrate interactions are regulated by a push–pull force mechanism: the substrate is pushed vertically in the region underneath the cell nucleus but pulled obliquely towards the cell centre at the cell's edges. Thin purple arrows represent the tangential and vertical components of the oblique forces.
c, On stiffer substrates, because cells are spread more thinly across the substrate surface, the nucleus may be subject to greater stress induced by tensions in the cell's actin cytoskeleton (green filaments).

of mechanobiology concerns understanding the interplay between gene expression and mechanical forces exerted by cells on the environment. The observed force pattern raises questions about the physical coupling between the nucleus and the elastic components of the cytoplasm¹⁵. The authors cultured cells on substrates that are softer than the cells' nuclei, so the implication is that, on contact with the substrate, the cells deformed the substrate more than their nuclei were deformed. The question of whether, on stiffer substrates, the pushing forces could lead to nuclear deformation and cell-fate reprogramming requires investigation.

It is well known that on stiffer substrates mammalian tissue cells exert larger forces and are more spread out across the substrate surface, thus leading to a higher nuclear compression (Fig. 1c). Increasing substrate rigidity may therefore result in an increase in the horizontal forces and a relative decrease in the vertical ones. To what extent the authors' technique can be applied over a broad range of substrate stiffness remains an open question.

Although we are still far from a complete understanding of the mutual interaction between cell function and mechanical cues, Delanoë-Ayari *et al.* have shown that cellular traction forces in all three dimensions matter, and should be taken into account to fully understand cell–substrate interactions. ■

Pascal Hersen and Benoît Ladoux are at the *Laboratoire Matière et Systèmes Complexes, Université Paris Diderot & CNRS UMR 7057, Paris 75013, France, and at the Mechanobiology Institute, National University of Singapore, Singapore 117411.*
e-mails: pascal.hersen@univ-paris-diderot.fr; benoit.ladoux@univ-paris-diderot.fr

- Discher, D. E., Janmey, P. & Wang, Y.-L. *Science* **310**, 1139–1143 (2005).
- Paszek, M. J. *et al. Cancer Cell* **8**, 241–254 (2005).
- Engler, A. J., Sen, S., Sweeney, H. L. & Discher, D. E. *Cell* **126**, 677–689 (2006).
- Delanoë-Ayari, H., Rieu, J. P. & Sano, M. *Phys. Rev. Lett.* **105**, 248103 (2010).
- Harris, A. K., Wild, P. & Stopak, D. *Science* **208**, 177–179 (1980).
- Beningo, K. A. & Wang, Y.-L. *Trends Cell Biol.* **12**, 79–84 (2002).
- Balaban, N. Q. *et al. Nature Cell Biol.* **3**, 466–472 (2001).
- Trepat, X. *et al. Nature Phys.* **5**, 426–430 (2009).
- Vogel, V. & Sheetz, M. *Nature Rev. Mol. Cell Biol.* **7**, 265–275 (2006).
- Ghibaudo, M. *et al. Biophys. J.* **97**, 357–368 (2009).
- Dembo, M. & Wang, Y.-L. *Biophys. J.* **76**, 2307–2316 (1999).
- Weeks, E. R., Crocker, J. C., Levitt, A. C., Schofield, A. & Weitz, D. A. *Science* **287**, 627–631 (2000).
- Hur, S. S., Zhao, Y., Li, Y. S., Botvinick, E. & Chien, S. *Cell. Mol. Bioeng.* **2**, 425–436 (2009).
- Maskarinec, S. A., Franck, C., Tirrell, D. A. & Ravichandran, G. *Proc. Natl Acad. Sci. USA* **106**, 22108–22113 (2009).
- Mazumder, A. & Shivashankar, G. V. *J. R. Soc. Interface* **7**, S321–S330 (2010).

words, they presumed that the component of the forces that is perpendicular to the substrate was negligible (Fig. 1a).

However, we have come to learn that cells act in all dimensions as they probe and respond to the three-dimensional (3D) geometry of their environment^{9,10}. In their study, Delanoë-Ayari *et al.*⁴ devise a method that can accurately map the 3D force pattern generated by adherent cells. The method is essentially an extension of the traction-force microscopy technique developed by Dembo and Wang¹¹. It consists of measuring a cell's traction forces, and so a substrate's deformation, on the basis of the substrate's elastic properties and the displacement that the cell induces on fluorescent beads embedded near the substrate's surface. Combined with a technique¹² that permits 3D tracking of the beads' dynamics, the method enables the spatial and temporal distributions of the cell's traction forces to be precisely determined in all directions.

The authors apply their method to cells of the soil-living amoeba *Dictyostelium discoideum* on a soft-gel substrate with easily controlled mechanical properties. Surprisingly, although the fluorescent beads are randomly distributed inside the gel, when focusing light on the gel's upper surface, the researchers observe a 'black hole' in the fluorescent signal just where the cell is located. This happens because the cell pushes the beads towards the gel's interior,

causing them to go out of focus. The fluorescent signal re-emerges when the cell is removed from the substrate, because the beads recover their equilibrium position. What's more, the observed 3D force pattern clearly indicates that *D. discoideum* cells regulate their interactions with the soft substrate through a push–pull force mechanism: the cells push the gel vertically in the region underneath the cell nucleus but pull it obliquely towards the cell centre at the cell's edges (Fig. 1b). Because the overall force has to be zero, the pulling forces in the vertical direction exactly balance the pushing forces.

Delanoë-Ayari *et al.*⁴ demonstrate not only that vertical forces exist, but also that they are of the same order of magnitude as horizontal forces, thus highlighting the need to consider vertical forces in studies that examine the role of cell–substrate interactions in biological functions. Taken together with previous studies^{13,14} on mammalian tissue cells that showed that they deform their environment in much the same way as *D. discoideum* does, the authors' findings not only highlight the importance of taking into account 3D forces for all adherent cell types, but also give a new and clear description of the mechanical balance between the pushing and pulling forces.

Because substrate elasticity can govern cell fate³, one of the main issues in the field

insulin resistance and neurodegenerative disorders. ■

Daniel P. Kelly is at the Sanford-Burnham Medical Research Institute, Lake Nona, Orlando, Florida 32827, USA.
e-mail: dkelly@sanfordburnham.org

1. Sahin, E. *et al. Nature* **470**, 359–365 (2011).
2. Hastie, N. D. *et al. Nature* **346**, 866–868 (1990).
3. Lee, H.-W. *et al. Nature* **392**, 569–574 (1998).

4. Balaban, R. S., Nemoto, S. & Finkel, T. *Cell* **120**, 483–495 (2005).
5. Wallace, D. C. *Annu. Rev. Genet.* **39**, 359–407 (2005).
6. Finley, L. W. S. & Haigis, M. C. *Ageing Res. Rev.* **8**, 173–188 (2009).
7. Wong, K.-K. *et al. Nature* **421**, 643–648 (2003).
8. Lin, J., Handschin, C. & Spiegelman, B. M. *Cell Metab.* **1**, 361–370 (2005).
9. Arnold, A.-S., Egger, A. & Handschin, C. *Gerontology* **57**, 37–43 (2011).
10. Chin, L. *et al. Cell* **97**, 527–538 (1999).
11. Matoba, S. *et al. Science* **312**, 1650–1653 (2006).

APPLIED PHYSICS

Extreme light-bending power

Metamaterials are best known for their ability to bend light in the opposite direction to that of all materials found in nature. A hidden ability of these man-made materials has now been discovered. [SEE LETTER P.369](#)

XIANG ZHANG

You've probably noticed that, if you look at it from the side, a straw in a glass of water seems to bend. This is because light bends and slows down when it travels from air into water or other substances. How much the light bends depends on the type of material through which it travels or, more specifically, on the material's refractive index. Ideally, with a view to applications, we would want unlimited power to control the refractive index. A computer-chip maker, for example, would be thrilled to have a lens of huge refractive index in their lithographic machine, because such a lens would allow chips to be made that are much smaller and perform better than those currently available. But nature cannot always supply our ideals: naturally occurring materials have only a limited range of optical refractive indices, typically between 1 and 3. However, on page 369 of this issue, Choi and colleagues¹ bring us good news: they have found a way to create metamaterials with an unnaturally high refractive index.

During the past decade, metamaterials² have generated great enthusiasm among scientists and engineers. These artificially engineered composite materials gain their unique properties, which are not attainable with naturally occurring materials, from their physical structure rather than their chemical composition. The very ability of metamaterials to reach beyond nature's limitations is not only scientifically exciting, but also technologically important: scientists have achieved intriguing physical phenomena and properties in these composite materials that their parent materials do not possess. For example, strong magnetic

responses in the terahertz frequency regime have been engineered³ with a composite material containing split-ring structures made of copper. Such strong magnetic responses do not occur in natural materials.

Metamaterials research has made it possible to create the negative-refractive-index materials first envisioned⁴ by the Russian scientist Victor Veselago in 1968. The negative electrical and magnetic responses of these materials cause them to bend light in the 'wrong' direction^{5,6}. Consider a fish in a tank of water. If water had a negative refractive index — which it doesn't — the fish would seem to an observer to be swimming upside down above the water. Naturally occurring materials have an index with a small positive value, which fundamentally limits the resolution of optical-imaging lens systems to about half the wavelength of the incident light, and so prevents the tiny details of an object from being imaged. Negative-index materials can overcome this limitation. The 'perfect imaging' capability of metamaterials would open the door to many exciting applications, including ultra-high-resolution medical imaging and data storage, and revolutionary miniaturization of computer chips⁷.

At the other end of the metamaterials spectrum would be materials with a very large positive index — beyond that of naturally occurring materials. A lens with such an index would allow more details to pass through an imaging system. Recently, an ultra-high-index metamaterial has been proposed theoretically⁸ that uses metallic (conducting) structures embedded in a dielectric (insulating) host. However, its experimental implementation has been impeded by its complicated three-dimensional geometry. Inspired by this idea, Choi *et al.*¹ stacked centimetre-

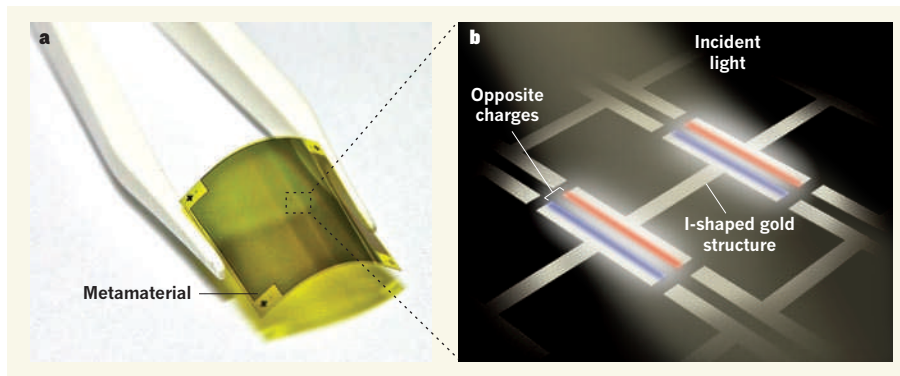


Figure 1 | Choi and colleagues' high-refractive-index metamaterial¹. **a**, Photograph of the centimetre-sized, free-standing and flexible metamaterial. **b**, The internal structure of the metamaterial consists of a lattice of I-shaped gold unit cells, each 60 micrometres in size. When light of terahertz frequency is shone onto the material, the small gap between the bars of two adjacent I cells produces an extremely strong electric dipole of equal but opposite oscillating charges, which confers a high refractive index on the material. (Modified from ref. 1.)

sized planar layers to create bulk-like metamaterials. They formed each layer by printing arrays of thin I-shaped gold building blocks, or 'meta-atoms', onto a polymer (polyimide) substrate using the conventional lithographic technique used for printing electronic circuits. The resulting metamaterials, which are free-standing and flexible (Fig. 1a), have a very high refractive index — more than 30 at the terahertz frequency regime.

The refractive index depends on the product of a material's electrical and magnetic responses to an electromagnetic field. The authors achieved a large electrical response by placing the I-shaped meta-atoms close to one another, leaving only a small gap. Upon irradiation with terahertz light, the small gap between the bars of two adjacent I meta-atoms produces an extremely strong electric dipole that significantly enhances the electrical response (Fig. 1b). However, at the same time, the incoming light has the detrimental effect of decreasing the material's magnetic response by inducing electric-current loops that prevent the light's magnetic field from penetrating the metallic structures. The authors came up with a creative approach to minimize this effect: they thinned the metallic structures such that the area subtended by the loop current was reduced, effectively minimizing the loss of the magnetic response. In this way, the overall refractive index, which arises primarily from huge electrical dipole moments, was kept at a high value.

To measure the refractive index, Choi *et al.*¹ used terahertz time-domain spectroscopy, in which terahertz pulses are sent through the sample and the time-dependent transmitted pulses are recorded and transformed into frequency-dependent values. The detailed features of these transmitted pulses are then used to deduce the sample's refractive index. The authors found that the metamaterial's observed high index occurs over a broad band of frequencies with low energy loss in the

metal. This is caused by strong interactions between the meta-atoms.

Choi *et al.*¹ estimate that a much higher refractive index — of a few hundred — could be obtained by further shrinking the gaps and embedding the layers of metamaterial in a substrate that has a higher refractive index than polyimide, for example strontium titanate. Such an index would be a remarkable amplification of the refractive indices of nature's materials. However, this requires a precision of 10–50 nanometres for the manufacture of the metallic

structures into a large (centimetre-scale) area of metamaterial, which can be challenging.

A shortcoming of Choi and colleagues' I-shaped metamaterials is the fact that they are sensitive to the polarization of incident light. Although the authors also designed isotropic two-dimensional metamaterials, which are insensitive to polarization, it will be a challenge to build truly isotropic three-dimensional metamaterials with a refractive index that is both high and does not depend on polarization. But for now, the unusually high index of Choi and colleagues' materials has demonstrated a hidden potential of metamaterials, which once again beats the limitations of naturally occurring materials and will greatly extend our ability to manipulate light. ■

Xiang Zhang is in the NSF Nanoscale Science and Engineering Center, University of California, Berkeley, California 94720–1740, USA.
e-mail: xiang@berkeley.edu

1. Choi, M. *et al. Nature* **470**, 369–373 (2011).
2. Pendry, J. B., Holden, A. J., Robbins, D. J. & Stewart, W. J. *IEEE Trans. Microw. Theory Techniques* **47**, 2075–2084 (1999).
3. Yen, T. J. *et al. Science* **303**, 1494–1496 (2004).
4. Veselago, V. G. *Sov. Phys. Uspekhi* **10**, 509–514 (1968).
5. Shelby, R. A., Smith, D. R. & Schultz, S. *Science* **292**, 77–79 (2001).
6. Valentine, J. *et al. Nature* **455**, 376–379 (2008).
7. Fang, N., Lee, H., Sun, C. & Zhang, X. *Science* **308**, 534–537 (2005).
8. Shin, J., Shen, J.-T. & Fan, S. *Phys. Rev. Lett.* **102**, 093903 (2009).

CLIMATE CHANGE

Human influence on rainfall

Rising concentrations of anthropogenic greenhouse gases in the atmosphere may already be influencing the intensity of rainfall and increasing the risk of substantial damage from the associated flooding. SEE LETTERS P.378 & P.382

RICHARD P. ALLAN

The varying distribution of fresh water across the globe, involving complex patterns of rainfall in space and time, crucially affects the ecosystems and infrastructure on which human societies depend. The recent severe floods in Australia, Sri Lanka and Brazil, which were partly associated with an episodic cooling in the equatorial Pacific Ocean (La Niña), highlight the effect of natural fluctuations in atmospheric circulation systems on rainfall distributions. However, global warming resulting from anthropogenic emissions of greenhouse gases may have compounded the effects of such fluctuations, a possibility that is considered in two papers in this issue^{1,2}.

Min *et al.* (page 378)¹ provide evidence that human-induced increases in greenhouse-gas concentrations led to the intensification of heavy precipitation events over large swathes of land in the Northern Hemisphere during the latter half of the twentieth century. They combined a rigorous 'detection and attribution' framework with extreme-value theory (a statistical technique designed for analysing rare events) to place daily rain-gauge data and climate-model simulations on a common scale. A tentative but intriguing finding by these authors is that climate models may underestimate the effects of anthropogenic global warming on rainfall intensification, a possibility that has implications for projections of future climate.

Climate models typically do not have sufficient resolution to satisfactorily represent processes at the level of cloud formation, and there is considerable variation in simulations of the relationship between rainfall extremes and warming in the tropics^{3,4}. Pall *et al.* (page 382)² get around this issue by considering an event relating to a large-scale weather pattern that can be represented by high-resolution versions of such models. They link human influence on global-warming patterns with an increased risk of severe flooding that is associated with a displacement in the North Atlantic jet stream (a fast, eastward-moving ribbon of air at around 8–12 kilometres altitude). The consequence of jet-stream displacement was recurrent, unusually prolonged periods of heavy rain over England and Wales in autumn (September–November) 2000 (Fig. 1).

The authors' approach involved conducting multiple climate simulations of this event, with realistic control runs and further scenarios in which the anthropogenic warming patterns were artificially removed. Building up convincing statistics required thousands of model simulations, which were made possible through the use of idle time on personal computers volunteered by members of the public.

Feeding the precipitation simulations into river-flow models allowed Pall *et al.* to gauge the influence of anthropogenic greenhouse-gas emissions on the risk of damaging floods occurring in England and Wales during autumn 2000. They conclude that flooding risk was indeed "substantially increased" by these emissions, although the exact scale of the effect is difficult to estimate. However, their results vary with the range of anthropogenic warming patterns estimated separately from four coupled ocean–atmosphere climate models. The set of different models used to simulate the relationships between temperature, precipitation and flooding also requires further evaluation. Nevertheless, applying their technique to further severe flooding events may prove valuable for informing policies aimed at improving adaptation to climate change.

More generally, in considering changes in the pattern and intensity of precipitation, the underlying physical and geographical context provides essential background. The root cause of the reported changes in rainfall with increasing atmospheric temperature is centred on atmospheric water vapour⁵. The convergence of moisture-laden air masses leads to air uplift, cloud formation and eventual precipitation (rain, snow or hail). A warming atmosphere can carry greater quantities of gaseous water (approximately 6–7% more is carried per °C of warming near Earth's surface, as determined by the Clausius–Clapeyron equation). It has long been thought that the intensity of the heaviest rainfall is modulated through this simple relationship, again increasing at around 6–7% per °C. However, water vapour also controls precipitation by influencing the radiative



Figure 1 | The floods of autumn 2000. Geese take to the inundated streets of York, northern England.

cooling of the atmosphere (through the absorption and emission of infrared radiation). The temperature dependence of radiatively induced increases in total global precipitation (around 2–3% per °C of warming^{5,6}) is substantially lower than the 6–7% per °C increase in intense rainfall implied from changes in atmospheric moisture.

Intense rainfall is inherently local, but is fuelled by a supply of atmospheric moisture from farther afield that may otherwise have contributed to more moderate rainfall elsewhere. So rapid increases in precipitation intensity in one region imply a decrease in intensity, duration and/or frequency in other regions⁷. Many climate models show this projection through an increasing intensity of rainfall in wet regions (above the 2–3% per °C rate of increase in global precipitation due to radiative cooling), together with a tendency towards diminished rainfall in the already dry subtropics^{5,6}. Because of the implications for future flooding and drought, it is vital to establish the physical basis for these changes⁵, and to verify theory with further observational evidence^{1,3,8}.

The detailed physical mechanisms determining changes in the distribution of extreme rainfall also require further investigation. Additional latent energy released within storms can invigorate vertical motion, increasing rainfall intensity to above 6–7% per °C (ref. 9). Alternatively, limitations on sources of moisture and counteracting dynamical feedbacks could explain increases in heavy-rain intensity of less than 6–7% per °C (ref. 8). One other possibility to explore is the role of atmospheric aerosols (especially those that absorb sunlight), which may influence global and regional precipitation by modulating the energy balance between the atmosphere and Earth's surface^{10,11}.

Predicting regional changes in the water cycle presents a considerable challenge, but that endeavour is essential in formulating strategies for adapting to and mitigating such changes. Subtle shifts in large-scale atmospheric circulation may affect local rainfall to a much greater extent than the thermodynamic processes relating to atmospheric water vapour content. Understanding the regional responses of rainfall patterns to global warming is therefore crucial. In the meantime, as these two papers^{1,2} demonstrate, robust physics, combined with carefully constructed observing systems and detailed modelling, indicate that the frequency of intense rainfall events is likely to increase with anthropogenic greenhouse-gas-induced warming. ■

Richard P. Allan is in the Department of Meteorology, University of Reading, Reading RG6 6BB, UK.
e-mail: r.p.allan@reading.ac.uk

1. Min, S.-K., Zhang, X., Zwiers, F. W. & Hegerl, G. C. *Nature* **470**, 378–381 (2011).
2. Pall, P. *et al.* *Nature* **370**, 382–385 (2011).
3. Allan, R. P., Soden, B. J., John, V. O., Ingram, W. & Good, P. *Environ. Res. Lett.* **5**, 025205 (2010).
4. O'Gorman, P. A. & Schneider, T. *Proc. Natl Acad. Sci. USA* **106**, 14773–14777 (2009).
5. Held, I. M. & Soden, B. J. *J. Clim.* **19**, 5686–5699 (2006).
6. Allen, M. R. & Ingram, W. J. *Nature* **419**, 224–232 (2002).
7. Trenberth, K. E., Dai, A., Rasmussen, R. M. & Parsons, D. B. *Bull. Am. Meteorol. Soc.* **84**, 1205–1217 (2003).
8. Haerter, J. O., Berg, P. & Hagemann, S. *Geophys. Res. Lett.* **115**, D17102, doi:10.1029/2009JD013384 (2010).
9. Lenderink, G. & van Meijgaard, E. *Environ. Res. Lett.* **5**, 025208 (2010).
10. Wild, M., Grieser, J. & Schär, C. *Geophys. Res. Lett.* **35**, L17706, doi:10.1029/2008GL034842 (2008).
11. Andrews, T. *et al.* *Geophys. Res. Lett.* **37**, L1470, doi:10.1029/2010GL043991 (2010).

The evolutionary context of the first hominins

Bernard Wood¹ & Terry Harrison²

The relationships among the living apes and modern humans have effectively been resolved, but it is much more difficult to locate fossil apes on the tree of life because shared skeletal morphology does not always mean shared recent evolutionary history. Sorting fossil taxa into those that belong on the branch of the tree of life that leads to modern humans from those that belong on other closely related branches is a considerable challenge.

The researchers who discovered and analysed the fossil evidence for *Ardipithecus ramidus*¹ are emphatic that it is an early member of the hominin clade, and comparable claims have been made by other research groups for earlier fossil evidence^{2–4}. This review examines the difficulties of substantiating these claims by exploring the evolutionary context of the earliest hominins. We offer alternative interpretations for where *Ardipithecus*, *Orrorin* and *Sahelanthropus* might be accommodated within the tree of life.

Relationships and ancestors

All the organisms alive today are the terminal twigs of the crown of the tree of life and all the organisms that have ever lived are on branches within the tree. Most branches end before they reach the crown and so, even though modern-day diversity is impressive, the animals alive today are only a tiny fraction of all the types of animals that have lived in the past. In the nineteenth century the only evidence that could be used to relate living taxa was the gross morphology of their hard and soft tissues. During the first half of the twentieth century new lines of molecular evidence began to emerge^{5–7}, followed most recently by genomic evidence^{8–10}. The conclusions from all of these lines of evidence are consistent with the results of a recent molecular supermatrix analysis based on both mitochondrial and nuclear genes¹¹ that supports a (((*Pan*, *Homo*) *Gorilla*) *Pongo*) pattern of relationships among humans and great apes. This all points to chimpanzees and bonobos (that is, *Pan*) and their extinct close relatives (called panins) being more closely related to modern humans and our extinct close relatives (called hominins) than to gorillas (Table 1); therefore, hominins and panins are referred to as sister taxa. Some of these data can be used to generate hypotheses about the timing of the splitting events that are implied by these relationships. Several lines of evidence^{9–11} suggest that the common ancestor of panins and hominins probably lived in the period between 8 and 4 million years ago, and most probably between 6 and 4 million years ago.

Despite being each other's closest living relatives, there are still substantial morphological, molecular and behavioural differences between living chimpanzees and bonobos on the one hand, and modern humans on the other. It is simplistic to assume that only hominins have undergone significant evolutionary change since the most recent common ancestor (MRCA) of panins and hominins: the African fossil record suggests that very few, if any, mammalian lineages have remained unchanged since the late Miocene (10 to 5 million years ago)¹². However, there are sound logical reasons based on the morphology of their nearest modern outgroups to support the inference that the skeleton of the panin/hominin

MRCA would have had more in common with chimpanzees and bonobos than with modern humans¹³.

Reconstructing ancestors

An important concept in phylogenetic reconstruction is the ancestral morphotype, a compilation of the derived features primitively shared by sister taxa such as *Pan* and *Homo*. The degree to which those taxa are more or less divergent from their last common ancestor affects the ease with which one can retrodict their shared ancestral morphology from the terminal states¹⁴. In cases where they are divergent, ancestral morphotypes can be imperfect or even misleading approximations with relatively low resolution, rather than precise and accurate formulations of the ancestral condition. Given that the extant apes and modern humans represent relict and probably highly specialized terminal members of what were once diverse radiations¹⁴, the accurate reconstruction of ancestral morphotypes among the hominoids has proved problematic.

Recent efforts to redefine the nested set of ancestral morphotypes of hominoids proceeding from the assumption that *Ar. ramidus* is a stem hominin¹ nicely illustrate the inherent problems. Should the discovery of a purported fossil hominin overturn predictions about an ancestral

Table 1 | Extant hominoids plus fossil hominines

Superfamily Hominoidea (hominoids)
Family Hylobatidae (hylobatids)
Genus <i>Hylobates</i>
Family Hominidae (hominids)
Subfamily Ponginae (pongines)
Genus <i>Pongo</i>
Subfamily Homininae (hominines)
Tribe Gorillini (gorillins)
Genus <i>Gorilla</i>
Tribe Panini (panins)
Genus <i>Pan</i>
Tribe Hominini (hominins)
Genus <i>Australopithecus</i>*
Genus <i>Kenyanthropus</i>*
Genus <i>Paranthropus</i>*
Genus <i>Homo</i>
Tribe incertae sedis
Genus <i>Ardipithecus</i>†
Genus <i>Orrorin</i>†
Genus <i>Sahelanthropus</i>†

Fossil hominines are shown in boldface.

* These are almost certainly early hominins.

† These are purported early hominins.

¹CASHP, The George Washington University, 2110 G Street, NW Washington, District of Columbia 20052, USA. ²Center for the Study of Human Origins, Department of Anthropology, New York University, 25 Waverly Place, New York, New York 10003, USA.

morphotype based on a wealth of comparative data from extant taxa, or should one defer to the hypothetical morphotypes that best fit the comparative evidence and critically reassess the phylogenetic placement of fossil taxa that contradicts such a hypothesis? If *Ardipithecus* is in fact not a hominin then it would require (as noted by its supporters¹⁵) the confluence of a number of shared specializations developed in parallel between *Ardipithecus* and later hominins, but the opposite scenario, in which *Ardipithecus* is assumed to be a hominin, requires remarkably high levels of homoplasy among extant great apes¹. These different appeals to Occam's razor are predicated on the scale of the phylogenetic perspective. The former is a taxonomically more inclusive and hominoid-centric perspective; the latter hominin-centric perspective is taxonomically more exclusive.

On a related theme, when assessing the phylogenetic relationships of extinct hominids, comparisons are often limited to modern humans or great apes, but this simple dichotomy can lead to incorrect assumptions about interpretations of morphocline polarities and the functional-behavioural associations of particular features. The temptation is to assume that features that distinguish modern humans from great apes are related to the unique behaviours of modern humans. However, the Miocene ape precursors of extant great apes and modern humans were anatomically, and presumably behaviourally, quite different from modern great apes, and many of the features often associated uniquely with modern humans are likely to be primitive retentions or specializations that have broader functional-behavioural relationships. For example, the position and orientation of the foramen magnum and aspects of the anatomy of the pelvis and proximal femur that distinguish modern humans from great apes, typically identified as being uniquely related to bipedalism, are, in fact, also found in non-hominoid primates associated with quite different locomotor behaviours. To resolve this problem a broader comparative context is needed to be able to delineate the universe of functional-behavioural possibilities, as well as a more critical appreciation that modern human-like features absent among extant great apes should not simply be presumed to be autapomorphies (that is, unique specializations) of the hominin lineage. A sideways look at closely related extant and extinct taxa should be an important component of any analysis of a purported early hominin.

The detailed justifications for including *Sahelanthropus*, *Orrorin* and *Ardipithecus* in the hominin clade vary according to what anatomical regions are represented^{1–4}, but three main threads run through the claims for hominin status. The first involves a reduction in size and a change in morphology of the canines accompanied by the partial or complete loss of upper canine/lower third premolar (P_3) honing and a reduction in the degree of canine sexual dimorphism, associated with inferences about social organization. The second involves the location and orientation of the foramen magnum and inferences about upright posture, and the third involves features of the pelvis and other preserved postcranial elements that imply a dependence on bipedalism. In each case the assumption is that these character complexes and their inferred behaviours are unique and thus confined to the hominin clade.

The canine morphology that *Ardipithecus* and *Sahelanthropus* share with later hominins is, perhaps, the most convincing evidence to support their hominin status, but it is important to recognize that during the late Miocene a number of Eurasian hominids (for example, *Oreopithecus*, *Ouranopithecus* and *Gigantopithecus*) also developed small canines in conjunction with reduced canine-premolar honing, presumably as a result of parallel shifts in dietary behaviour in response to changing ecological conditions. Thus, these changes are in fact not unique to hominins and it is conceivable that similar evolutionary responses could have occurred in contemporary African hominids, not just in the hominin lineage.

The more anteriorly positioned and horizontally oriented foramen magnum in modern humans compared to extant great apes has been assumed to relate to the more upright posture and bipedal locomotion in hominins^{16–18}. However, comparisons with other primates, especially gibbons and short-faced monkeys, suggest that this feature is more broadly associated with differences in head carriage and facial length,

rather than uniquely with bipedalism. The distinction between bonobos and chimpanzees in this respect, and the overlap between the morphology of bonobos and that of *Sahelanthropus* and *Ardipithecus* further support this contention.

The postcranial evidence for bipedalism in *Orrorin* and *Ardipithecus kadabba* mainly involves the dorsal canting of a proximal pedal phalanx (presumed to belong to *Ar. kadabba*, but from an older geological horizon and with no associated cranio-dental remains)¹⁹, and the morphology of the proximal femur in *Orrorin*^{20,21}. However, these hominin-like postcranial features are also as likely to be functionally and behaviourally associated with arboreal above-branch and terrestrial quadrupedalism as they are with bipedalism^{22,23}. Likewise, the claim that *Ardipithecus ramidus* was a facultative terrestrial biped is vitiated because it is based on highly speculative inferences about the presence of lumbar lordosis and on relatively few features of the pelvis and foot, many of which also occur in the arboreally adapted *Oreopithecus*.

Shared morphology need not mean shared history

For much of its history, systematics was predicated on the assumption that there is a direct relationship between morphological similarity and genetic relatedness: that is, the more skeletal morphology two taxa share, the closer their relationship. For extant taxa, this hypothesis can be tested against relationships on the basis of molecular evidence. Such data, either on their own, or in combination with morphological evidence, have been used in efforts to try to resolve relationships among taxa, including those within large clades of medium- to large-sized mammals (for example, refs 24 and 25). But even at this 'macro' scale it is apparent that a substantially similar skeletal phenotype does not always mean a shared recent evolutionary history. Long ago, Lankester²⁶ suggested that the term homoplasy be used for morphology that is seen in sister taxa, but not in their MRCA. Such morphology gives the impression the two taxa are more closely related than they really are and because homoplasy can be mistaken for shared derived similarity (or synapomorphy) it complicates attempts to reconstruct relationships.

One could cope with the confounding effects of homoplasy if the 'noise' generated by the latter was trivial compared to the strength of the phylogenetic 'signal.' But in some attempts to infer relationships among extant higher primates using skeletal data (in the form of either traditional non-metrical characters or characters generated from metrical data) the ratio between 'noise' and 'signal' was of the order of 1:2. The results of these analyses were not only frustratingly inconclusive, but also when they were compared with the pattern of relationships generated using molecular data, some were misleading^{27,28}. Other researchers suggested that this dismal performance was due to the exclusion of character state data from fossil taxa²⁹, but this argument is moot because soft-tissue characters (for which there are no fossil data) are capable of recovering a pattern of relationships among extant higher primates that is consistent with the molecular evidence^{30,31}. If it is not just the absence of fossils, it must be something about hard-tissue evidence. But thankfully, not all hard-tissue evidence is problematic; it can produce results congruent with the relationships generated from molecular data as long as the anatomical regions targeted have a high enough signal-to-noise ratio^{32,33}. This suggests that the basic problem is with either, or both, the nature of the data or the scale of the enquiry, and not with cladistic methodology. It is not good news for palaeoanthropologists that the type of data the fossil record provides (that is, mostly craniodental hard-tissue morphology) seems to be particularly prone to homoplasy when used at this relatively fine taxonomic level.

There is also comparative evidence for concluding that homoplasy needs to be taken into account when generating hypotheses about the relationships among the taxa in the higher primate part of the tree of life. Although there is overwhelming molecular and morphological evidence for a (((*Pan*, *Homo*) *Gorilla*) *Pongo*) pattern of relationships among the extant hominids, selected morphological character states can be used to infer a (((*Pongo*, *Homo*) *Pan*) *Gorilla*) pattern of relationships, but these are almost certainly homoplasies. Similarly, homoplasy complicates attempts to resolve the relationships of fossil apes such as *Sivapithecus*³⁴,

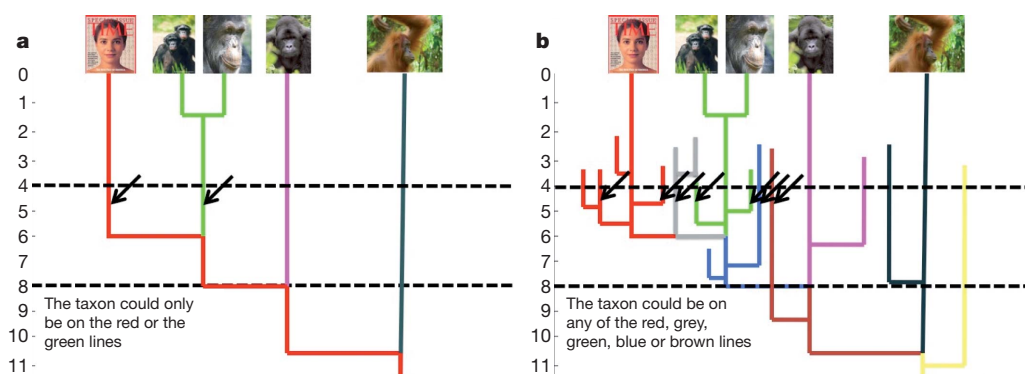


Figure 1 | Hypothetical trees. **a**, According to this hypothesis a 4.4-Myr-old hominid closely related to hominins and panins could only be a hominin ancestor or a panin ancestor. **b**, According to this hypothesis a 4.4-Myr-old

hominid closely related to hominins and panins could be a hominin or a panin ancestor, but is more probably a member of an extinct clade. This hypothesis more closely reflects the comparative evidence.

Morotopithecus^{35,36} and *Chororapithecus*³⁷. Moreover, studies of other mammalian clades evolving in Africa during the same time period as hominins and in similar palaeoenvironments (such as bovids³⁸, equids³⁹, elephantids⁴⁰, carnivores⁴¹ and Old World monkeys⁴²) point to substantial and recurrent homoplasy. There is no reason to assume that extinct sympatric and synchronic higher primate lineages were immune from the tendency to adapt in similar morphological and phylogenetically confounding ways to similar ecological challenges.

The important point is that shared similarities can only take one so far in determining phylogenetic relationships, because homoplasy, as well as uncertainties in determining the polarity of character transformation, have the potential to generate substantial noise that serves to confound attempts to generate reliable hypotheses about relationships. These considerations have clear implications for generating hypotheses about the phylogenetic position of *Ardipithecus*, *Sahelanthropus* and *Orrorin*. Even if these taxa share some derived features with later Pliocene hominins, it would be rash simply to assume that those features are immune from homoplasy, especially when other aspects of their respective phenotypes are consistent with a more distant relationship with the hominin clade.

Simplicity or complexity in phylogeny

There are two schools of thought about the reconstruction of human evolutionary history. One, which is rooted in the principle of parsimony and takes little or no account of homoplasy around and within the hominin clade, takes the view that the only thing that we 'know' is that the evolutionary history of each extant higher primate taxon comprises a series of ancestral–descendant species that can be traced back to the MRCA of all higher primates. While fossil evidence may suggest the presence of extinct clades, such clades are not necessary in the way that direct ancestors of extant taxa are necessary. Thus, the appropriate null hypothesis for such a world-view is that extinct taxa are ancestors of living descendants until proved otherwise. But given that the fossil records of other African mammalian groups document a diversity of extinct lineages with evidence for substantial amounts of homoplasy^{38–42}, an alternative and perhaps more prudent null hypothesis is that a fossil species should only be considered a potential ancestor of a descendant species if its morphology is concordant with the hypothesized ancestral morphotype and lacks any autapomorphies. These different approaches have led to debates in the palaeoanthropological community about whether the shape of human evolutionary history was ladder-like and anagenetic, involving a series of time-successive species⁴³, or more bushy and cladogenetic, with several extinct collateral lineages⁴⁴ (Fig. 1).

Comparative evidence points to cladogenesis being the null hypothesis. For example, although a single species of orang-utan, *Pongo pygmaeus*, occurs today on Borneo and Sumatra (some authorities recognize a second species, *Pongo abelii*), we know from the fossil record that this is a relict taxon belonging to a diverse radiation of pongins, originating

13 million years ago, that occurred during the Miocene and Pliocene^{45,46}. The Eurasian fossil record includes evidence of several extinct subspecies or species of *Pongo*, as well as a number of Miocene pongine genera (that is, *Lufengpithecus*, *Ankarapithecus*, *Sivapithecus*, *Khoratpithecus*, and probably *Gigantopithecus*)^{45–47} (Fig. 2). Climatic and ecological changes during the later Miocene, associated with cooler, more seasonal conditions, coincided with a sharp decline in the diversity of hominids, and by the close of the Miocene pongines had disappeared from much of their former geographical range, surviving only in the subtropical and tropical forests of southeastern Asia⁴⁶. During the Pliocene, the range of *Pongo* extended from southern China through to mainland and island Southeast Asia, but a combination of climatic fluctuations and the arrival of sophisticated human hunters forced a major reduction in the range of orang-utans, eventually leading to their current relictual distribution⁴⁸.

This context is critical to appreciating the apparent diversity of the early purported hominins. Currently, four species are recognized but some researchers have intimated that these taxa might best be subsumed into one or two species of *Ardipithecus*^{1,4,43}. Obviously, detailed comparisons are needed to resolve these taxonomic issues, but based on published accounts of the morphological differences between the species and what we already know about hominoid diversity during the late Miocene of Eurasia and Africa, it would not be unexpected or surprising to have multiple genera and lineages represented.

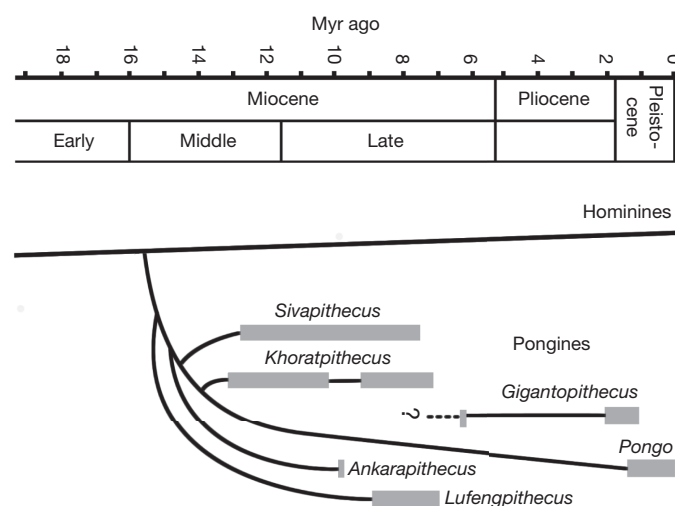


Figure 2 | Phylogenetic tree for extant orang-utans (*Pongo*) and fossil pongines. Grey bars show the time ranges and black lines indicate inferred relationships among the species.

Scale in phylogeny reconstruction

Primate systematists generally have no problem using hard-tissue evidence to establish relationships among taxa as disparate as lemurs, Old World monkeys and apes. However, in the case of closely related taxa or stem taxa, the combination of homoplasies, retained primitive features and uncertainties about the polarity of the character sequences used in cladistic analysis generates noise that can overwhelm the modest signal generated by the relatively small number of informative derived characters that separate such taxa from either the MRCA or from stem members of their sister lineage. The problem is one of taxonomic scale; methods that work well for larger taxonomic units may be ineffective or generate misleading results when applied to closely related taxa.

Two examples of uncertainties about the relationships among archaic hominin taxa illustrate the problem of scale. As presently defined, *Australopithecus* is almost certainly not a monophyletic group, or clade, but a paraphyletic cluster of stem species from which *Homo* and *Paranthropus* apparently derive their ancestry. Five species are currently recognized: *Au. anamensis*, *Au. afarensis* (including *Au. bahrelghazali*), *Au. africanus*, *Au. garhi* and the recently named *Au. sediba*⁴⁹. Of these, *Au. anamensis* and *Au. afarensis* are probable time-successive sister taxa^{50,51}, but the relationships of *Au. garhi* and *Au. sediba*, as well as the relationship of *Australopithecus* species to *Paranthropus* and *Homo*, are still unresolved. A second example concerns *Paranthropus*. The vast majority of cladistic analyses of early hominins conclude that the megadont archaic hominins from East and southern Africa (that is, *P. boisei* and *P. robustus*) are sister taxa, in which case there are grounds for recognizing that clade as a genus (that is, *Paranthropus*). However, several independent lines of evidence, both macrostructural (for example, facial and premolar root morphology)^{52–54} and microstructural (for example, enamel daily secretion rates)⁵⁵, are not consistent with their being sister taxa. In both of the examples given above the problem arises because the taxa concerned are closely related and adaptively similar. Each species manifests morphology that allows them to be diagnosed as separate taxa, but from a phylogenetic perspective the overlapping combinations of features result in high levels of homoplasy that confound phylogenetic analyses.

So why do researchers persist in trying to solve a phylogenetic problem that may well be at the limits of, or even beyond, the analytical capabilities of the data and the available methods? The reason is that our own ancestry matters to us. Most vertebrate palaeontologists would be content to accept that the ancestry of *Homo* resides in *Australopithecus*, without needing or expecting to unravel the topological complexity of the different species within the latter genus. We are not advocating that researchers abandon trying to draw inferences about the phylogenetic relationships of hominins at the finest scale possible. However, we do suggest that those who present and accept these hypotheses need to be aware that such inferences, especially ones about stem taxa, are likely to be inherently prone to refutation and subsequent revision.

Cautionary tales from South Asia and Tuscany

Logic dictates that the earliest hominin taxon should be distinguishable from the reconstructed ancestral morphotype of hominines by at least one derived feature, or synapomorphy, it shares with later hominins. The obvious candidate synapomorphies are those related to facial shortening, encephalization, smaller and more vertically implanted incisors, reduction in the overall size and degree of sexual dimorphism of the canines, modification of the P₃ associated with a reduced honing function of the upper canine, postcanine megadontia, as well as specialized features of the vertebral column, pelvis, hindlimb and foot associated with adaptations to upright posture and terrestrial bipedalism. Indeed, the evidence put forward to support the hypothesis that *Ar. ramidus* belongs to the hominin clade includes its relatively small incisors, small canines exhibiting slight sexual dimorphism, relatively small P₃ with a mesiodistally shortened crown, lack of upper canine honing, relatively short face, anteriorly placed foramen magnum and a pelvis with a mediolaterally broad ilium, abbreviated iliac isthmus, inferosuperiorly short pubic symphysis, prominent anterior inferior iliac spine and discrete greater

sciatic notch^{1,56,57}. It remains to be seen how many of these alleged hominin synapomorphies withstand close scrutiny, but they are at the crux of the argument in favour of *Ardipithecus* being a hominin.

Only a quarter of a century ago the palaeoanthropological community learned, or should have learned, a sobering lesson about how easily homoplasy can lead to misinterpretation. The lesson concerns *Ramapithecus punjabicus*, a late Miocene hominoid from south Asia. Its short face, robust jaws, small canines and thick-enamelled, bunodont molars, were widely interpreted to be evidence that it was an early hominin⁵⁸. However, the molecular clock implications of the DNA evidence^{8–10}, combined with additional fossil material recovered during the 1980s, made it abundantly clear that the fossil evidence for *Ramapithecus* comprised female specimens of *Sivapithecus*, a creature that is almost certainly a close relative of the orang-utan^{45,59}.

A further cautionary tale is provided by *Oreopithecus bambolii*, a late Miocene hominoid from Italy (Fig. 3). Its remains are known from fossil sites in Tuscany and Sardinia that, during the late Miocene (about 7 to 8 million years ago), were located on islands in the northern Mediterranean. *Oreopithecus* was first described in 1872, but it was not until the discoveries by the Swiss palaeontologist, Johannes Hürzeler, in the late 1950s that a clear appreciation of its anatomy was obtained^{60–62}. Although the teeth and skull of *Oreopithecus* are uniquely specialized, its postcranial skeleton confirms that it is a hominid (that is, a member of the clade that includes the great apes and modern humans)⁶³. Its precise relationships are still debated, but in a number of key features it is more primitive than all extant hominids and is best considered a stem hominid, possibly related to late Miocene hominids from mainland Europe^{63–65}.

What is instructive about *Oreopithecus* with respect to developing hypotheses about the relationships of *Ar. ramidus* is that it is a species of hominoid that is well-enough known anatomically (that is, almost every bone in the skeleton is represented) to be certain that it is not a member of the hominin clade, yet it shares many anatomical similarities with later hominins, including some that are generally considered to be uniquely associated with bipedal behaviour. The shared similarities include: small and vertically implanted incisors, relatively small canines, a small non-sectorial P₃ with a high incidence of a prominent metaconid, absence or small size of a diastema in the upper tooth row, a vertically oriented mandibular symphysis, a mental foramen situated high on the mandibular corpus, a short orthognathic face, an anteriorly placed zygomatic process of the maxilla, anterior projecting nasal apophyses and a deep pit on the palmar aspect of the terminal phalanx of the thumb for attachment of a well developed flexor pollicis longus tendon^{63,64}. Shared similarities associated with bipedal behaviour include an anteriorly situated foramen magnum, short and broad iliac blades, infero-superiorly short pubic symphysis, a well-developed anterior inferior iliac spine, a large ischial spine, medial and lateral condyles of the distal femur similar in size, possibly associated with a bicondylar angle. The impressive suite

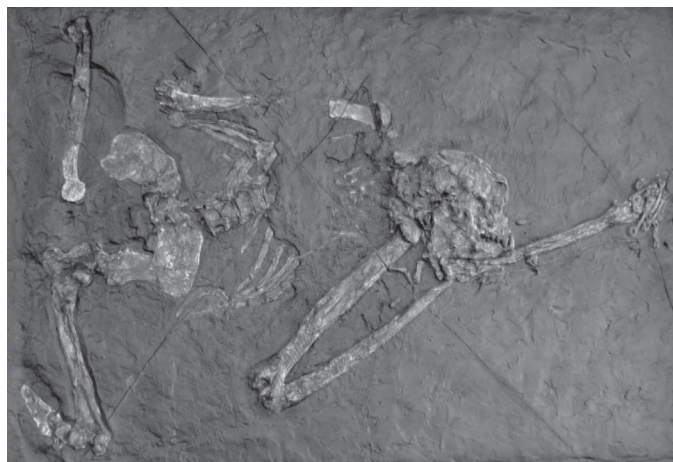


Figure 3 | Skeleton of *Oreopithecus bambolii* from Baccinello, Italy.

of shared features with fossil hominins led Hürzeler to deduce (not unreasonably) that *Oreopithecus* was a fossil hominin⁶², but these features are most parsimoniously interpreted as either homoplasies or retained primitive hominid features. *Oreopithecus* is a classic example of how a late Miocene hominid can independently acquire a suite of structural-functional complexes of the dentition, cranium, hand, hip and hindlimb that closely parallel the specialized features uniquely associated with the hominin lineage, and thereby encourage researchers to generate erroneous assumptions about evolutionary relationships. *Oreopithecus* highlights the dangers inherent in uncritically assuming that shared similarities are a secure indication of relationship or that extant primates are an adequate guide to the potential behavioural diversity of extinct taxa.

The object lesson that *Oreopithecus* provides is critical to the debate about interpreting the relationships of the earliest purported hominins. It demonstrates how features considered to be hominin specializations can be shown to have been acquired independently in a non-hominin lineage in association with inferred behaviours that are functionally related to, but not necessarily narrowly restricted to, terrestrial bipedalism.

Implications for palaeoanthropology

There are an impressive number of contrasts between the morphology of chimpanzees/bonobos and modern humans, but the differences between the earliest panins and the earliest hominins were fewer and almost certainly more subtle. The working hypothesis has been that whereas the early panins would have had, at some stage in their evolution, projecting faces that accommodated elongated jaws bearing relatively small chewing teeth and large, sexually dimorphic canine teeth, early hominins would have had a masticatory apparatus that combined relatively larger chewing teeth with more modestly sized and less sexually dimorphic canines. As for the locomotor system, it has been hypothesized that early panins were adapted for a combination of arboreal and terrestrial quadrupedalism, vertical climbing and forelimb suspensory behaviours and possibly knuckle-walking, whereas early hominins would show skeletal adaptations for a locomotor strategy that included long bouts of terrestrial bipedalism.

However, this scenario implies that the only option for a 7–4-million-year-old hominid that shares some features with later hominins is that it is a stem hominin. The lessons of *Ramapithecus* and *Oreopithecus* suggest that researchers should be skeptical about this assumption. Leaving aside the strong possibility that not all of the purported hominin-like features of *Ar. ramidus* will withstand critical scrutiny, many of them are also to be found in *Oreopithecus* and so the possibility that some, or all, of them are primitive hominid features or homoplasies should not be discounted. That *Ardipithecus* is from Africa (rather than an insular species from the northern Mediterranean), that it has a more conservative craniodental morphology (as opposed to the uniquely specialized skull and teeth of *Oreopithecus*) and that it chronologically precedes the earliest occurrence of indisputable hominins (*Au. anamensis* at 4.2 million years ago) does not diminish the likelihood of potential homoplasies. Indeed, one might argue that homoplasies would be more likely given the shared ecogeography and because *Ar. ramidus* probably has closer phylogenetic ties with early hominins than does *Oreopithecus*.

This review has dwelt on the probability that homoplasy will confound attempts to identify 7–4-million-year-old hominid taxa as unambiguous early hominins, but the same arguments apply to the evolutionary context of the two associated skeletons of unambiguous hominins recovered from the southern Africa cave site of Malapa and attributed to *Au. sediba*⁴⁹. In their case the discussion is complicated by the juvenile status of one of the associated skeletons and an inadequate consideration of intraspecific variation, but the debate is analogous. Instead of 'hominin versus hominid' the debate is about whether some features of the cranial (for example, the margins of the orbit) and the postcranial (for example, the ilium) skeleton of the two Malapa skeletons are sufficient evidence to interpret this material as belonging to *Homo* rather than to *Australopithecus*. The analogies go deeper, for just as the researchers involved in the analysis of *Ar. ramidus* make light of the many ways its morphology resembles

that of chimpanzees and bonobos (for example, much of the preserved hand and foot morphology of *Ar. ramidus* is African-ape-like) Berger and colleagues make light of the substantial amount of limb morphology shared between *Au. sediba* and other *Australopithecus* taxa.

We emphasize that we are not claiming that the presence of homoplasy in and around the hominin clade, and the other methodological and analytical limitations of phylogenetic analyses noted above, doom all efforts to recover evolutionary relationships to failure. Nor are we claiming that *Ar. ramidus*, *S. tchadensis* and *O. tugenensis* are definitely not hominins. We do, however, advocate that those palaeoanthropologists whose considerable and much valued efforts in the field are rewarded with fossils as significant as those from Aramis, Toros Menalla, Lukeino and Malapa acknowledge the potential shortcomings of their data when it comes to generating hypotheses about relationships. We urge researchers, teachers and students to consider the published phylogenetic interpretations of these taxa as among a number of possible interpretations of the evidence. In the meantime, the rest of us should concentrate on developing methods and approaches that help to discriminate between phylogenetically informative characters and homoplasies. For example, there are new imaging methods providing much better morphological detail⁶⁶, and some of these methods provide non-destructive access to the microstructure of fossils^{55,67}.

There is no reason why higher primate evolution in Africa in the past ten million years should not mirror the complexity observed in the evolutionary histories of other mammals during the same time period. Nor is there any reason, especially with the lessons from *Ramapithecus* and *Oreopithecus* fresh in the minds of researchers, to assume that hominins should not be prone to the same limitations and uncertainties of phylogenetic analysis as other fossil primates. By giving appropriate consideration to parsimony in reconstructing ancestral morphotypes, as well as to the confounding influences of homoplasy and the correct determination of character state polarities, the possibility that one or more of the purported earliest hominins represents a stem hominine or a stem hominid appears to be a plausible, perhaps even preferable, alternative hypothesis. Nevertheless, the fossil evidence from the Aramis, Toros Menalla, Lukeino and Malapa sites, whichever taxonomic and systematic hypotheses survive refutation over the next decade, will continue to provide critical evidence, comparative or otherwise, about the early stages of human evolution.

- White, T. D. *et al.* *Ardipithecus ramidus* and the paleobiology of early hominins. *Science* **326**, 75–86 (2009).
- Senut, B. *et al.* First hominid from the Miocene (Lukeino Formation, Kenya). *C. R. Acad. Sci.* **332**, 137–144 (2001).
- Brunet, M. *et al.* A new hominid from the Upper Miocene of Chad, Central Africa. *Nature* **418**, 145–151 (2002).
- Haile-Selassie, Y., Suwa, G. & White, T. D. Late Miocene teeth from Middle Awash, Ethiopia, and early hominid dental evolution. *Science* **303**, 1503–1505 (2004).
- Goodman, M. in *Classification and Human Evolution* (ed. Washburn, S. L.) 204–234 (Aldine, 1963).
- Zuckerkandl, E. in *Classification and Human Evolution* (ed. Washburn, S. L.) 243–272 (Aldine, 1963).
- King, M.-C. & Wilson, A. C. Evolution in two levels in humans and chimpanzees. *Science* **188**, 107–116 (1975).
- Ruvolo, M. Molecular phylogeny of the hominoids: inferences from multiple independent DNA sequence data sets. *Mol. Biol. Evol.* **14**, 248–265 (1997).
- Bradley, B. Reconstructing phylogenies and phenotypes: a molecular view of human evolution. *J. Anat.* **212**, 337–353 (2008).
- Patterson, N. *et al.* Genetic evidence for complex speciation of humans and chimpanzees. *Nature* **441**, 1103–1108 (2006).
- Fabre, P.-H., Rodrigues, A. & Douzery, E. J. P. Patterns of macroevolution among primates inferred from a supermatrix of mitochondrial and nuclear DNA. *Mol. Phylog. Evol.* **53**, 808–825 (2009).
- Werdelin, L. & Sanders, W. J. (eds) *Cenozoic Mammals of Africa* (University of California Press, 2010).
- Pilbeam, D. R. in *The Primate Fossil Record* (ed. Hartwig, W. C.) 303–310 (Cambridge University Press, 2002).
- Andrews, P. & Harrison, T. in *Interpreting the Past: Essays on Human, Primate, and Mammal Evolution in Honor of David Pilbeam* (eds Lieberman, D. E., Smith, R. J. & Kelley, J.) 103–121 (Brill, 2005).
- Shreeve, J. 4.4 Million years ago: the birth of bipedalism. *Nat. Geogr. Mag.* **218**, 63–66 (2010).
- White, T. D., Suwa, G. & Asfaw, B. *Australopithecus ramidus*, a new species of hominid from Aramis, Ethiopia. *Nature* **371**, 306–312 (1994).

17. Suwa, G. *et al.* The *Ardipithecus ramidus* skull and its implications for hominid origins. *Science* **326**, 68e1–68e7 (2009).
18. Zollikofer, C. P. E. *et al.* Virtual cranial reconstruction of *Sahelanthropus tchadensis*. *Nature* **434**, 755–759 (2005).
19. Haile-Selassie, Y. Late Miocene hominids from the Middle Awash, Ethiopia. *Nature* **412**, 178–181 (2001).
20. Galik, K. *et al.* External and internal morphology of the BAR 1002'00 *Orrorin tugenensis* femur. *Science* **305**, 1450–1453 (2004).
21. Richmond, B. G. & Jungers, W. L. *Orrorin tugenensis* femoral morphology and the evolution of hominin bipedalism. *Science* **319**, 1662–1665 (2008).
22. Rein, T. R. & Harrison, T. Quantifying the angle of orientation of the metatarsophalangeal joint surface of proximal phalanges in extant primates. *Am. J. Phys. Anthropol.* **132** (S44), 197 (2007).
23. Rafferty, K. L. Structural design of the femoral neck in primates. *J. Hum. Evol.* **34**, 361–383 (1998).
24. Fernández, M. H. & Vrba, E. S. A complete estimate of the phylogenetic relationships in Ruminantia: a dated species-level supertree of extant ruminants. *Biol. Rev. Camb. Philos. Soc.* **80**, 269–302 (2005).
25. Flynn, J. J. *et al.* Molecular phylogeny of the Carnivora (Mammalia): assessing the impact of increased sampling on resolving enigmatic relationships. *Syst. Biol.* **54**, 317–337 (2005).
26. Lankester, E. R. On the use of the term homology. *Ann. Mag. Nat. Hist. Zool. Botany Geol.* **6**, 34–43 (1870).
27. Collard, M. & Wood, B. Hominin homology: an assessment of the impact of phenotypic plasticity on phylogenetic analyses of humans and their fossil relatives. *J. Hum. Evol.* **52**, 573–584 (2007).
28. Collard, M. & Wood, B. How reliable are human phylogenetic hypotheses? *Proc. Natl Acad. Sci. USA* **97**, 5003–5006 (2000).
- This paper showed that when conventional metrical and non-metrical hard-tissue characters are used to generate hypotheses about the relationships among the great apes and the baboon/mangabey group the resulting cladograms are not consistent with the pattern of relationships supported by molecular evidence.**
29. Strait, D. S. & Grine, F. E. Inferring hominoid and early hominid phylogeny using craniodental characters: the role of fossil taxa. *J. Hum. Evol.* **47**, 399–452 (2004).
30. Gibbs, S., Collard, M. & Wood, B. Soft-tissue characters in higher primate phylogenetics. *Proc. Natl Acad. Sci. USA* **97**, 11130–11132 (2000).
- This paper showed that in contrast to the poor performance of hard-tissue characters when soft-tissue characters are used to generate hypotheses about the relationships among the great apes the resulting cladograms are consistent with the pattern of relationships supported by molecular evidence.**
31. Gibbs, S., Collard, M. & Wood, B. Soft-tissue anatomy of the extant hominoids: a review and phylogenetic analysis. *J. Anat.* **200**, 3–49 (2002).
32. Lockwood, C. A., Kimbel, W. H. & Lynch, J. M. Morphometrics and hominoid phylogeny: support for a chimpanzee-human clade and differentiation among great ape subspecies. *Proc. Natl Acad. Sci. USA* **101**, 4356–4360 (2004).
33. Harvati, K. & Weaver, T. D. In *Neanderthals Revisited: New Approaches and Perspectives* (eds Harvati, K. & Harrison, T.) 239–254 (Springer, 2006).
34. Young, N. M. A reassessment of living hominoid postcranial variability: implications for ape evolution. *J. Hum. Evol.* **45**, 441–464 (2003).
35. Harrison, T. In *Cenozoic Mammals of Africa* (eds Werdelin, L. & Sanders, W. J.) 429–469 (University of California Press, 2010).
36. Nakatsukasa, M. Comparative study of Moroto vertebral specimens. *J. Hum. Evol.* **55**, 581–588 (2008).
37. Suwa, G. *et al.* A new species of great ape from the late Miocene epoch in Ethiopia. *Nature* **448**, 921–924 (2007).
38. Gatesy, J. *et al.* A cladistic analysis of mitochondrial ribosomal DNA from the Bovidae. *Mol. Phyl. Evol.* **7**, 303–319 (1997).
39. Bernor, R. L. *et al.* In *Cenozoic Mammals of Africa* (eds Werdelin, L. & Sanders, W. J.) 685–721 (University of California Press, 2010).
40. Todd, N. E. New phylogenetic analysis of the family Elephantidae based on cranio-dental morphology. *Anat. Rec.* **293**, 74–90 (2010).
41. Van Valkenburgh, B. *Déjà vu*: the evolution of feeding morphologies in the Carnivora. *Integr. Comp. Biol.* **47**, 147–163 (2007).
42. Jablonski, N. G. & Leakey, M. G. (eds) *Koobi Fora Research Project Vol. 6 The Fossil Monkeys* (California Academy of Science, 2008).
43. White, T. D. In *The Paleobiological Revolution: Essays on the Growth of Modern Paleontology* (eds Sepkoski, D. & Ruse, M.) 122–148 (University of Chicago Press, 2009).
44. Wood, B. A. Reconstructing human evolution: achievements, challenges and opportunities. *Proc. Natl Acad. Sci. USA* **107** (Suppl. 2), 8902–8909 (2010).
45. Kelley, J. In *The Primate Fossil Record* (ed. Hartwig, W. C.) 369–384 (Cambridge University Press, 2002).
46. Harrison, T. Apes among the tangled branches of human origins. *Science* **327**, 532–534 (2010).
- This paper shows that there is a remarkable diversity of fossil apes from the Miocene that represents precursors of the hominins and highlights the uncertainties in interpreting the phylogenetic placement of the earliest purported hominins.**
47. Harrison, T., Ji, X. & Su, D. On the systematic status of the late Miocene and Pliocene hominoids from Yunnan Province, China. *J. Hum. Evol.* **43**, 207–227 (2002).
48. Harrison, T., Krigbaum, J. S. & Manser, J. In *Primate Biogeography* (eds Fleagle, J. G. & Lehman, S. M.) 323–364 (Springer, 2006).
49. Berger, L. R. *et al.* *Australopithecus sediba*: a new species of Homo-like australopithecine from South Africa. *Science* **328**, 195–204 (2010).
50. Lockwood, C. A., Kimbel, W. H. & Johanson, D. C. Temporal trends and metric variation in the mandibles and dentition of *Australopithecus afarensis*. *J. Hum. Evol.* **39**, 23–55 (2000).
51. Kimbel, W. H. & Deleuzene, L. K. “Lucy” redux: a review of research on *Australopithecus afarensis*. *Ybk Phys. Anthropol.* **140** (49), 2–48 (2009).
52. Rak, Y. *The Australopithecine Face* (Academic Press, 1983).
53. Wood, B. A. In *Evolutionary History of the “Robust” Australopithecines* (ed. Grine, F. E.) 269–284 (Aldine de Gruyter, 1988).
54. McCollum, M. The robust australopithecine face: a morphometric perspective. *Science* **284**, 301–305 (1999).
55. Lacruz, R. S., Dean, M. C., Ramirez-Rossi, F. & Bromage, T. G. Megadontia, striae periodicity and patterns of enamel secretion in Plio-Pleistocene fossil hominins. *J. Anat.* **213**, 148–158 (2008).
56. Lovejoy, C. O. *et al.* The pelvis and femur of *Ardipithecus ramidus*: the emergence of upright walking. *Science* **326**, 71e1–71e6 (2009).
57. Suwa, G. *et al.* Paleobiological implications of the *Ardipithecus ramidus* dentition. *Science* **326**, 94–99 (2009).
58. Simons, E. L. The phyletic position of *Ramapithecus*. *Postilla* **54**, 1–20 (1961).
59. Pilbeam, D. R. New hominoid skull material from the Miocene of Pakistan. *Nature* **295**, 232–234 (1982).
60. Hürzeler, J. Zur systematischen Stellung von *Oreopithecus*. *Verh. Naturf. Ges. Basel* **65**, 88–95 (1954).
61. Straus, W. L. In *Classification and Human Evolution* (ed. Washburn, S. L.) 146–177 (Aldine, 1963).
62. Hürzeler, J. *Oreopithecus bambolii* Gervais: a preliminary report. *Verh. Naturf. Ges. Basel* **69**, 1–48 (1958).
63. Harrison, T. & Rook, L. In *Function, Phylogeny and Fossils: Miocene Hominoid Evolution and Adaptation* (eds Begun, D. R., Ward, C. V. & Rose, M. D.) 327–362 (Plenum, 1997).
- This is a detailed study of the anatomy and phylogenetic relationships of *Oreopithecus bambolii*, demonstrating that it is a stem hominid with many postcranial features that parallel the specialized anatomy of modern humans.**
64. Moyà Solà, S. & Köhler, M. The phylogenetic relationships of *Oreopithecus bambolii* Gervais, 1872. *C. R. Acad. Sci. Paris* **324** (sér. IIa) 141–148 (1997).
65. Sarmiento, E. E. The phylogenetic position of *Oreopithecus* and its significance in the origin of the Hominoidea. *Am. Mus. Novit.* **2881**, 1–44 (1987).
66. Skinner, M., Wood, B. A. & Hublin, J.-J. Enamel-dentine junction (EDJ) morphology distinguishes the lower molars of *Australopithecus africanus* and *Paranthropus robustus*. *J. Hum. Evol.* **55**, 979–988 (2008).
67. Smith, T. & Tafforeau, P. New visions of dental tissue research: tooth development, chemistry, and structure. *Evol. Anthropol.* **17**, 213–226 (2008).

Acknowledgements Support was provided by the GW Vice-President for Academic Affairs and to the GW Selective Excellence Program (to Provost and B.W.) and the NSF (BCS-0309513) (to T.H.). We thank R. Bernstein, J. DeSilva, T. Kivell, D. Pilbeam and B. Richmond for their critical comments and suggestions.

Author Contributions The authors contributed equally to the research and writing.

Author Information Reprints and permissions information is available at www.nature.com/reprints. The authors declare no competing financial interests. Readers are welcome to comment on the online version of this article at www.nature.com/nature. Correspondence and requests for materials should be addressed to B.W. (bernardawood@gmail.com).

Asymmetric cell divisions promote Notch-dependent epidermal differentiation

Scott E. Williams¹, Slobodan Beronja¹, H. Amalia Pasolli¹ & Elaine Fuchs¹

Stem and progenitor cells use asymmetric cell divisions to balance proliferation and differentiation. Evidence from invertebrates shows that this process is regulated by proteins asymmetrically distributed at the cell cortex during mitosis: Par3–Par6–aPKC, which confer polarity, and $G\alpha_i$ –LGN/AGS3–NuMA–dynein/dynactin, which govern spindle positioning. Here we focus on developing mouse skin, where progenitor cells execute a switch from symmetric to predominantly asymmetric divisions concomitant with stratification. Using *in vivo* skin-specific lentiviral RNA interference, we investigate spindle orientation regulation and provide direct evidence that LGN (also called Gpsm2), NuMA and dynactin (Dctn1) are involved. In compromising asymmetric cell divisions, we uncover profound defects in stratification, differentiation and barrier formation, and implicate Notch signalling as an important effector. Our study demonstrates the efficacy of applying RNA interference *in vivo* to mammalian systems, and the ease of uncovering complex genetic interactions, here to gain insights into how changes in spindle orientation are coupled to establishing proper tissue architecture during skin development.

Asymmetric cell divisions are important regulators of stem cell and cancer biology¹. The genetic pathways underlying spindle orientation and asymmetric cell divisions have been best studied in *Caenorhabditis elegans* and *Drosophila*, where conserved sets of proteins are asymmetrically distributed at the cell cortex during mitosis: the Par complex (comprising Bazooka (Par3 in vertebrates), Par6 and atypical protein kinase C (aPKC)) functions as a master polarity determinant, whereas $G\alpha_i$, Pins (LGN and AGS3 in vertebrates), Mud (NuMA) and p150^{glued} (Dctn1) regulate spindle orientation^{2,3}. In *Drosophila* neuroblasts, Inscuteable (Insc, known as mInsc in mouse) links these complexes by binding to both Par3 and Pins^{4–6}. As neuroblasts progress through mitosis, Insc, Pins and Mud polarize and segregate into one daughter, retaining its progenitor status, whereas the other daughter inherits oppositely polarized proteins including the Notch inhibitor Numb, which promotes differentiation^{2,3}.

Asymmetric cell divisions have also been documented in vertebrates, including in mouse skin, where a shift from parallel/symmetric to predominantly perpendicular/asymmetric divisions occurs at embryonic day (E)14 coincident with stratification^{7–9}. Basal delamination has been implicated in the process, and although spindle orientation could be critical¹⁰, direct functional evidence is lacking to support or refute a role for asymmetric cell divisions in promoting tissue growth and architecture for this or any other mammalian system.

As in *Drosophila* neuroblasts, asymmetric cell division components polarize in mitotic basal keratinocytes, forming an apical crescent of LGN and an interacting partner, NuMA^{7,11–13}. NuMA in turn binds microtubules and interacts with the cytoplasmic Lis1/dynein/dynactin complex, partially co-localizing with the p150^{glued}/Dctn1 component in cultured keratinocytes⁷. LGN is thought to be recruited to the cell cortex through glycosyl-phosphatidylinositol-linked $G\alpha_i$ / $G\alpha_o$, which binds LGN's carboxy-terminal GoLoco motifs. Such interactions probably reorient the mitotic spindle through cortical capture of astral microtubules^{14–18}.

To explore the physiological relevance of the LGN–NuMA–Dctn1 pathway in mice, we devised a strategy to efficiently knock down its constituents at a time during skin development when divisions become primarily asymmetric. Our method uses ultrasound-mediated delivery of high-titre lentivirus into amniotic space¹⁹. Lentivirus selectively transduces the first cell layer it encounters, which shortly after gastrulation is single-layered epidermis. Avoiding tissue-specific promoters, we achieve efficient infection, stable integration and sustained epidermal expression of short hairpin RNAs (shRNAs) at the requisite early developmental stage that permits analysis of their consequences to asymmetric cell division.

LGN, NuMA and Dctn1 control spindle orientation

LGN regulates spindle orientation and promotes planar cell divisions in other systems^{20–22}, but is symmetrically inherited in each case. In developing skin, however, LGN remained apical even after cleavage furrow formation (Fig. 1a). LGN co-localized with NuMA and $G\alpha_{i3}$ in mitotic basal cells, whereas Dctn1 localized to centrosomes and cell cortex, where it frequently polarized with apical enrichment at mitosis (Fig. 1b and Supplementary Fig. 1). Thus, not only are these divisions operationally defined as asymmetric, but in addition, asymmetric cell division components appeared to partition selectively to the apical daughter cell.

To address whether *LGN*, *Numa1* (which encodes NuMA) and *Dctn1* function in spindle orientation and skin biology, we first identified shRNAs²³ that reduced (often >90%) target messenger RNA expression in cultured keratinocytes (Fig. 1c). To guard against potential off-target effects, and also generate allelic series, we selected multiple hairpins for each gene studied. To label transduced skin cells, we cloned shRNAs into lentiviral vectors harbouring a fluorescent reporter (mRFP1, YFP or CFP fused to histone H2B).

E9.5 embryos were transduced (70–95% efficiency) *in utero* with lentiviruses harbouring *LGN*, *Numa1*, *Dctn1* or control (non-targeting)

¹Howard Hughes Medical Institute, Laboratory of Mammalian Cell Biology and Development, The Rockefeller University, New York, New York 10065, USA.

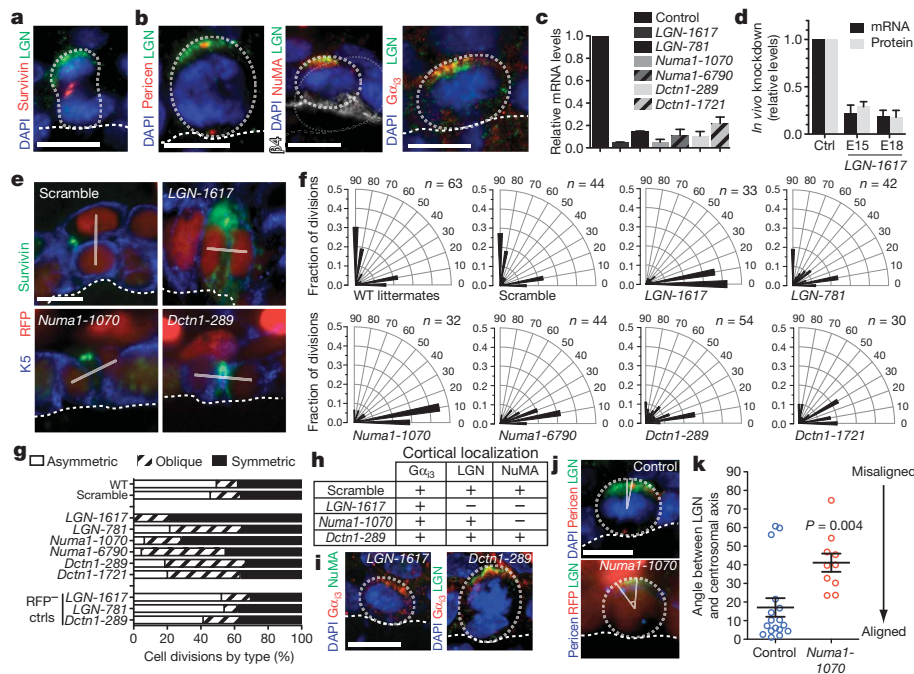


Figure 1 | Spindle orientation defects after *LGN*, *Numa1* and *Dctn1* depletion. **a**, Immunodetection of anaphase/telophase cells with the spindle mid-body marker survivin. **b**, Apical co-localization of asymmetric cell division components during mitosis. Pericen, pericentrin. **c**, **d**, shRNA knockdown efficiencies in keratinocytes and epidermis ($n = 3$ separate experiments). **e**, Representative axes of division (lines) in E16.5 transduced anaphase/telophase cells. **f**, Radial histogram quantification of division angles; n values scramble shRNAs (Supplementary Fig. 2). Expression was propagated stably, as evidenced by strong red fluorescent protein (RFP) levels in differentiated/suprabasal progeny of infected basal cells. Fluorescence-activated cell sorting (FACS) was used to quantify knockdown efficiencies and analyse cell cycle kinetics, mRNA and protein expression. As shown for *LGN*, and with similar results for *Numa1* and *Dctn1*, maximal *in vivo* knockdown ($\sim 80\%$ with *shLGN-1617*) was attained by stratification onset and maintained throughout development (Fig. 1d and Supplementary Fig. 1).

To explore whether *LGN*, *NuMA* and *Dctn1* orientate the spindle and promote asymmetric cell divisions, we knocked down each component and measured the division angle in late-stage mitotic H2B-RFP⁺ (transduced/knockdown) and H2B-RFP⁻ (non-transduced/control) basal cells. Quantifications were aided by co-labelling with the anaphase/telophase marker survivin (Fig. 1e–g). In E16.5 control shScramble basal cells, $\sim 36\%$ of divisions were symmetric (within 20° of horizontal), whereas most were asymmetric ($\sim 46\%$ perpendicular, $\sim 18\%$ oblique), a distribution identical to wild-type littermates. In contrast, basal cells transduced with *LGN*, *Numa1* or *Dctn1* shRNAs were biased towards symmetric divisions. Phenotypic severity correlated with hairpin strength, eliciting greatest effects with *shLGN-1617* and *shNuma1-1070*.

Because asymmetric cell division spindle rotations typically occur at metaphase^{9,24–26}, we analysed division planes in late mitosis after commitment to a division axis. To confirm that the apical daughter cell remains suprabasal and differentiates after an asymmetric cell division, we further monitored their progeny with a short 5-bromodeoxyuridine (BrdU) pulse protocol, detecting BrdU⁺/K5^{hi}/K5^{low} doublets in shScramble but not *LGN*-depleted epidermis. The predominantly parallel divisions observed in asymmetric cell division knockdowns did not seem to result from a developmental delay. Moreover, the effects of these knockdowns were cell-autonomous, as within mosaic tissue, RFP⁻ cells displayed the normal asymmetric cell division bias of wild-type cells. Chi-squared statistical analyses confirmed that patterns of asymmetric:symmetric:oblique divisions

are indicated. **g**, Cell-autonomous reduction of asymmetric cell divisions upon *LGN*, *Numa1* or *Dctn1* knockdown. **h**, **i**, Interdependence of $G\alpha_{13}$, *LGN* and *NuMA* cortical localization. **j**, **k**, Misalignment of angles between *LGN* crescent centre and centrosomal axis (spindle) upon *Numa1* knockdown (each dot indicates a single data point). All scale bars: 10 μ m. Error bars: s.d. (**c**, **d**); s.e.m. (**k**). Dotted lines denote basement membrane (bold) and cell boundaries (light).

achieved with each *LGN*, *Numa1* and *Dctn1* hairpin were significantly different ($P < 0.05$) than controls (Supplementary Fig. 3).

Given that *LGN*, $G\alpha_i$ and *NuMA* function together in other systems^{15–18}, we next sought to test the interdependence of their cortical localizations in developing epidermis. In wild-type mitotic basal cells, $G\alpha_{13}$ and *LGN* showed tight co-localization with a mean (\pm s.d.) radial difference in orientation angle of only $5.3 \pm 3.9^\circ$ ($n = 54$), and a statistically significant degree of correlation by paired *t*-test ($r = 0.9561$, $P < 0.0001$) (Fig. 1b and Supplementary Fig. 4). Both $G\alpha_{13}$ and *LGN* showed strong apical bias, with median orientation angles of 82° for $G\alpha_{13}$ and 80° for *LGN*. When either *Dctn1* or *Numa1* was depleted, *LGN* and $G\alpha_i$ remained cortically localized; however, cortical localization of *NuMA* required *LGN* (Fig. 1h, i), revealing a pathway hierarchy ($G\alpha_i > LGN > NuMA$). Notably, $G\alpha_{13}$ remained apical in *shLGN-1617* mitotic basal cells (median orientation angle = 80° , $n = 15$), and apical positioning of interphase centrosomes, Par3 and aPKC remained unchanged (Supplementary Fig. 4). Thus, apicobasal polarity was maintained after *LGN*, *Numa1* or *Dctn1* depletion.

Because *NuMA* is thought to link astral microtubules to cortical *LGN*²⁷, we tested whether $G\alpha_i$ or *LGN* would become mislocalized after *Numa1* knockdown. In wild-type basal keratinocytes, *LGN*'s cortical localization and (indirect) association with centrosomes commenced at early prophase. As one centrosome moved away in prometaphase⁹, *LGN* positioning varied, indicating that the spindle fluctuates at this time (Supplementary Fig. 4). Cell-cycle-dependent *LGN* localization and metaphase flux were also observed in *Numa1* knockdowns. However, in contrast to controls, centrosomes of *Numa1* knockdown cells often appeared misaligned with the *LGN* cortical domain (Fig. 1j, k). These data demonstrate that proper spindle orientation depends on coupling of *LGN* to *NuMA*.

Asymmetric cell divisions promote skin development

We next examined the consequences of impairing asymmetric cell divisions on epidermal differentiation. In low- Ca^{2+} (50 μ M) medium, cultured keratinocytes mimic 'symmetric division' mode, typified by

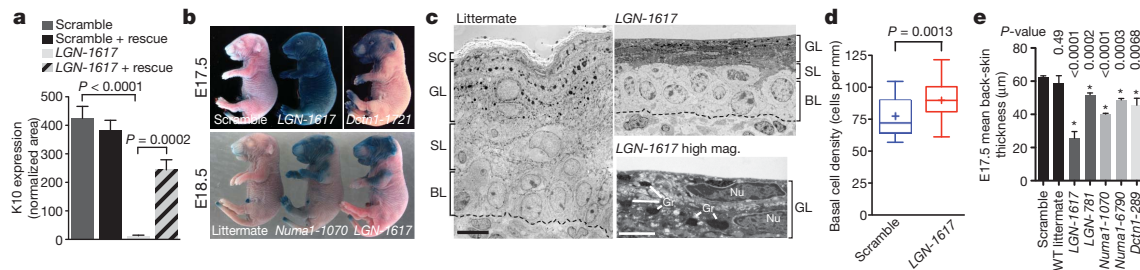


Figure 2 | Impaired stratification *in vitro* and *in vivo* when asymmetric cell divisions are impaired. **a**, Quantification of differentiation (K10) in *shLGN-1617*-transduced and rescued keratinocytes ($n = 8$ fields per condition). Error bars indicate s.e.m. **b**, Skin barrier defects in asymmetric cell division knockdown embryos. **c**, Epidermal ultrastructure. Layers: BL, basal; GL, granular; SC, stratum corneum; SL, spinous (scale bar, 10 μm). Late-stage differentiation defects in *LGN* knockdowns are shown at higher magnification

(scale bar, 2 μm; Gr, keratohyalin granules; Nu, nuclei). **d**, Quantifications revealing ~17% increase in basal nuclei density (~36% more basal cells per unit area) in E17.5 *shLGN-1617* epidermis. Whiskers indicate minimum and maximum values; boxes span 25–75 percentiles; centre bar denotes median value; + marks designate mean; $n > 20$ sections per condition. **e**, Measurements of epidermal thinning in knockdowns ($n > 3$ embryos per condition). Error bars represent s.d.

basal keratin expression and monolayer growth. Shifting to high- Ca^{2+} (1.5 mM) favours ‘asymmetric divisions’, characterized by epidermal sheet formation, stratification and induction of differentiation markers. Asymmetric *LGN* correlated with differentiation-promoting behaviour, as *LGN* was polarized in $>90\%$ of mitoses in high- Ca^{2+} (90% of those mitoses with detectable *LGN*), but much less so in low- Ca^{2+} (39%) ($n = 100$). After *LGN* depletion, calcium-shifted keratinocytes still organized into sheets, but failed to form *LGN* crescents, stratify or differentiate. This differentiation defect was rescued by a hairpin-resistant *LGN* (Fig. 2a and Supplementary Fig. 5).

To assess whether similar differentiation defects occur *in vivo*, we examined *LGN*, *Numa1* and *Dctn1* knockdown embryos at E17.5–E18.5, when epidermal maturation typically nears completion. Outside-in dye exclusion assays²⁸ revealed impaired barrier function, even with the hairpin (*shDctn1-1721*) displaying the weakest spindle orientation defect (Fig. 2b). These defects were most notable in head and extremities where transduction rates were highest¹⁹. Histological analyses revealed fewer suprabasal (differentiated) cells and ~36% more

basal cells per unit area, producing a significantly thinner epidermis (Fig. 2c–e). Morphological defects were paralleled by diminished immunostaining for early (K10), intermediate (involucrin) and late (loricrin) differentiation markers (Fig. 3a, b). Mosaic embryos provided built-in controls, revealing differentiation defects specifically in RFP⁺ epidermis irrespective of the asymmetric cell division gene targeted (Fig. 3b).

We next traced the temporal origins of these anomalies (Supplementary Fig. 6). At E15.5, both *shLGN-1617* and wild-type epithelium displayed a single K5/K14⁺ basal layer overlaid with sparse K10⁺ suprabasal cells. Nonetheless, even at this early age, a thinner epidermis was evident, and by E16.5, terminal differentiation was clearly suppressed. At birth, *shLGN-1617* pups displayed rough, shiny skin. As expected, the weaker hairpin *shLGN-781* caused milder abnormalities, and *shScramble* controls developed normally. Newborn *shLGN-1617* pups began losing weight and died soon afterwards. Such features reflected compromised barrier function, which results in dehydration.

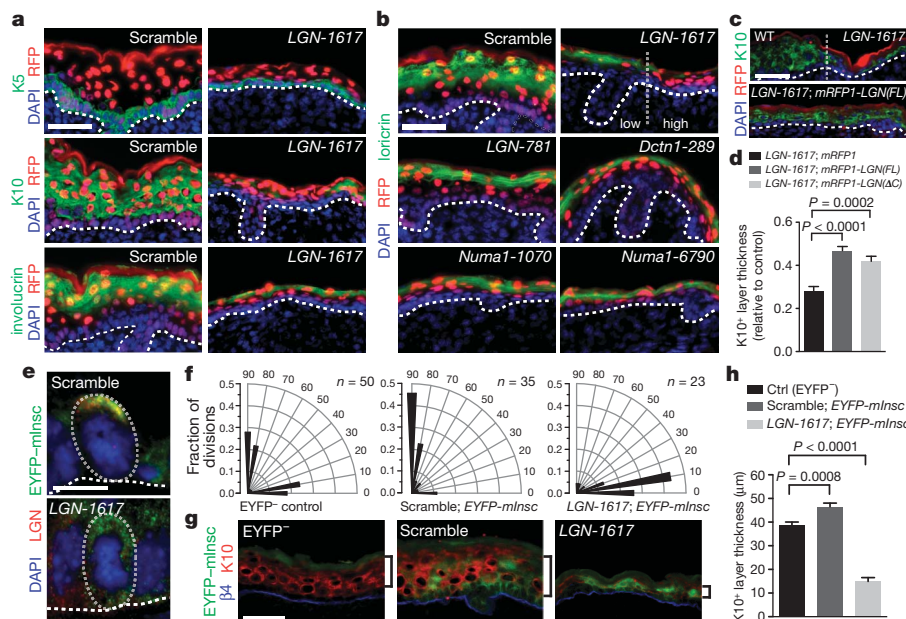


Figure 3 | Differentiation defects after *LGN*, *Numa1* and *Dctn1* depletion. **a**, **b**, Reduced terminal differentiation in E17.5 asymmetric cell division knockdowns. Basally transduced regions are identified by H2B-mRFP1, always most intense in suprabasal progeny. Note the correlation of repressed differentiation with transduction (RFP⁺; line demarcates low/high infection boundary). **c**, **d**, Partial restoration of *shLGN-1617* epidermal defects upon transducing full-length (FL) *LGN* or *LGN(ΔC)* ($n > 15$ fields; $n > 6$ embryos

per condition). **e**–**h**, EYFP-mInsc enhancement of *LGN*-dependent asymmetric cell divisions. **e**, EYFP-mInsc and *LGN* immunolocalization in mitotic cells of E17.5 *shScramble* or *shLGN-1617* epidermis after EYFP-mInsc co-transduction. **f**, Quantifications of division axes (n values indicated). **g**, **h**, *LGN*-dependent enhancement of spinous-layer thickness upon mInsc overexpression ($n > 10$ fields; $n > 3$ embryos per condition). Bracket indicates spinous layer. Scale bars: 50 μm (**a**–**c**, **g**); 10 μm (**e**). Error bars (**d**, **h**) indicate s.e.m.

These defects were directly attributable to *LGN* deficiency, and were largely rescued by resupplying a hairpin-resistant mRFP1-tagged full-length *LGN* on an *LGN*-knockdown background (Fig. 3c, d). However, the compromised skin phenotype of *shLGN-1617* pups was seemingly at odds with the viability of mice homozygous for an *LGN* mutation lacking the last three coding exons²¹. To address whether the resulting *LGN*(ΔC) protein might possess partial function, hence accounting for the difference, we engineered our *shLGN-1617* hairpin lentivirus to co-express a hairpin-resistant form of *mRFP1-LGN*(ΔC). When transduced into embryos, mRFP1-*LGN*(ΔC), but not mRFP1 alone, improved *shLGN-1617*-mediated defects in skin thickness and terminal differentiation. Although *LGN*(ΔC) was not as effective as full-length *LGN* in rescuing *shLGN-1617*-mediated defects, both appeared to be apically localized at mitosis (Supplementary Fig. 6). Taken together with the gross normality of newborn *shLGN-781* pups, these findings indicate that partial *LGN* loss of function can be tolerated, whereas severe loss of function results in dehydration and death.

Although *LGN*(ΔC) lacks a $G\alpha_i$ -interacting domain, its cortical association might still be mediated through mInsc⁴. Indeed, lentiviral EYFP-mInsc formed apically oriented cortical crescents with *LGN* and $G\alpha_{i3}$ in mitotic basal cells, and *LGN* co-localized with EYFP-mInsc with a mean (\pm s.d.) radial difference in orientation angle of $2.7 \pm 2.3^\circ$ ($r = 0.9828$, $P < 0.0001$ by paired t -test) (Fig. 3e and Supplementary Figs 6 and 7). Notably, whereas *LGN* was normally detected in only $\sim 75\%$ of mitotic cells ($n = 80$), EYFP-mInsc resulted in *LGN* co-localization in 100% of mitoses ($n = 36$).

If mInsc helps recruit *LGN* more efficiently to the apical cortex, then elevating mInsc in wild-type embryos should enhance asymmetric cell divisions²⁹. To test this, embryos were infected with *shScramble*;EYFP-mInsc, and the division axis was quantified for EYFP⁺ and EYFP⁻ mitotic cells. Like transgenic mInsc⁹, lentiviral EYFP-mInsc increased asymmetric cell divisions ($P = 0.0196$ by chi-squared test). Importantly, this shift required *LGN*, as predominantly symmetric divisions occurred in embryos infected with an *shLGN-1617*;EYFP-mInsc lentivirus (Fig. 3f and Supplementary Fig. 7).

EYFP-mInsc remained apical upon *LGN* depletion. However, $G\alpha_{i3}$ and EYFP-mInsc were often more diffusely localized in *shLGN-1617* mitotic cells, indicating that this complex is more stable when all three components are present^{4,17} (Fig. 3e and Supplementary Fig. 7). Interestingly, these spindle orientation alterations also caused differentiation perturbations, as *shLGN-1617*;EYFP-mInsc epidermis was thinner than littermate cohorts, whereas *shScramble*;EYFP-mInsc epidermis was thicker (Fig. 3g, h). Thus, suprabasal differentiation can be either promoted or impaired in an *LGN*-dependent manner, by a shift towards asymmetric or symmetric divisions, respectively.

In neural progenitors, the *LGN* homologue AGS3 (also called Gpsm1) regulates asymmetric cell divisions in a $G\alpha_i$ -dependent fashion³⁰. Although expressed in developing epidermis, AGS3 did not polarize at mitosis, and upon AGS3 knockdown, *LGN* still localized properly, asymmetric and symmetric divisions were balanced, and differentiation seemed normal. Moreover, co-depletion of AGS3 did not enhance the *LGN*-knockdown phenotype, and unlike *LGN*, AGS3 knockdown *in vitro* did not perturb calcium-induced differentiation (Supplementary Fig. 8). These results show that *LGN* is non-redundant in skin and further underscore the specificity of the *LGN*-NuMA-Dctn1 pathway in causing the defects we describe.

Asymmetric cell divisions promote Notch signalling

Knockdown of *LGN* and *Numa1* did not result in abnormalities in proliferation or apoptosis (Supplementary Fig. 9). In searching elsewhere for potential causes of differentiation defects, we investigated whether Notch signalling might be altered. In mammalian epidermis, Notch is an important effector of differentiation^{31–36}, and in *Drosophila* neuroblasts, it is activated in the daughter cell that displays localized Par3/Pins/Insc^{37–39}. Therefore, we tested the following: (1) whether components of the Notch pathway show abnormal expression patterns in asymmetric cell division knockdowns; (2) whether Notch activity is altered upon *LGN* or *Numa1* depletion; and (3) whether Notch acts genetically in a common pathway with, and downstream of, the asymmetric cell division machinery.

Microarray and quantitative polymerase chain reaction with reverse transcription (RT-qPCR) revealed the changes in Notch signalling that normally occur at the basal-suprabasal juncture (Fig. 4a). In agreement with and extending previous observations^{31,32,40}, Notch ligands *Dll1* and *Jag2* were enriched basally, whereas suprabasal cells expressed *Notch2* and *Notch3* receptors, along with *Jag1* ligand and *Hes1*, a well-known Notch target. The Notch inhibitor *Numb* has a role in asymmetric cell divisions in *Drosophila* neuroblasts, and in adult tail skin basal keratinocytes, *Numb* has been reported to be asymmetrically localized^{38,41–45}. However, although *Numb* overexpression generated a mild differentiation defect in embryonic epidermis, *Numb* was not consistently partitioned differentially in asymmetric cell divisions (Supplementary Fig. 10). That said, suprabasal *Hes1* was significantly reduced in asymmetric cell division knockdowns and restored by *mRFP1-LGN* rescue. Additionally, *Notch3* (and to a lesser extent *Notch1* and *Notch2*) was reduced after *LGN* knockdown (Fig. 4b–d and Supplementary Fig. 11). These data indicate that suprabasal Notch activity is diminished upon loss of *LGN*.

To measure this, we introduced a Notch reporter⁴⁶ into the lentiviral shRNA backbone (Fig. 4e). The reporter was designed so that

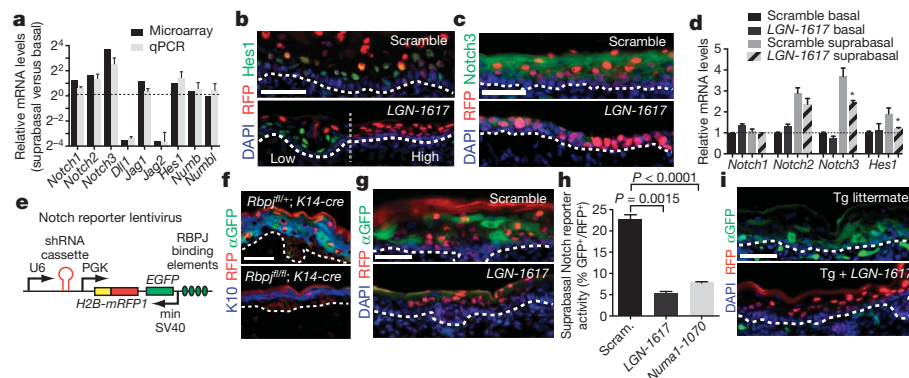


Figure 4 | Loss of *LGN* or *Numa1* impairs suprabasal Notch activation. **a**, qPCR and microarray comparisons of Notch pathway gene expression in E14–E15 wild-type epidermis. **b**, **c**, Diminished *Hes1* and full-length *Notch3* in *shLGN-1617*-transduced epidermis. The vertical line in **b** demarcates low/high infection boundary. **d**, Decreased *Notch3* ($P = 0.0133$) and *Hes1* ($P = 0.0169$) mRNAs in E18 *shLGN-1617* suprabasal cells. Note also dampened suprabasal/basal *Notch1* ($P = 0.20$) and *Notch2* ($P = 0.19$) gradients. **e**, Lentiviral Notch

reporter for coordinate shRNA knockdown. **f**, **g**, Abrogation of Notch reporter expression (EGFP⁺), concomitant with differentiation defects, in E17.5 *Rbpj* conditional knockout (**f**) and *shLGN-1617* (**g**) epidermis. **h**, Effects of *LGN* and *Numa1* knockdown on Notch reporter activity ($n > 24$ fields; > 3 embryos per condition). **i**, Reduced activity in P0 Notch reporter transgenics transduced with *shLGN-1617*;H2B-mRFP1. Error bars: s.d. (**a**, **d**), s.e.m. (**h**). All scale bars: 50 μ m. For qPCR (**a**, **d**), n values are triplicates from two separate experiments.

transduced cells are RFP⁺, and EGFP intensity reflects reporter activity. When tested *in vitro*, the reporter harbouring shScramble showed the anticipated minimal Notch activation under basal conditions, but strong elevation of EGFP after a switch to differentiation-promoting, high-Ca²⁺ medium. By contrast, *shLGN-1617*-transduced keratinocytes failed to induce robust reporter activity (Supplementary Fig. 11).

To test the physiological relevance of these findings, we first validated Notch reporter specificity in mouse embryos that were conditionally defective for *Rbpj*, the obligate DNA binding partner of Notch intracellular domains (NICDs). As expected, within suprabasal layers where *Hes1* and NICDs are active, transduced embryos (RFP⁺) showed EGFP induction only in control and not *Rbpj*-null epidermis (Fig. 4f). Similarly, the RFP⁺/EGFP⁺ co-labelled patches seen in shScramble;Notch reporter-transduced epidermis were markedly diminished upon *LGN* or *Numa1* knockdown (Fig. 4g, h). Analogous results were observed when Notch reporter transgenic mice⁴⁶ were transduced with *shLGN-1617*;H2B-mRFP1 lentivirus (Fig. 4i). As with *Hes1*, this decrease in reporter activity was partially restored by resupplying either *mRFP1-LGN* or *mRFP1-LGN(ΔC)* (Supplementary Fig. 11).

Genetic interaction between LGN and Notch

The poorly differentiated epidermis generated by knockdown of *LGN*, *Numa1* or *Dctn1* resembled *Rbpj* conditional ablation³². If RBPJ/Notch signalling lies downstream of the asymmetric cell division machinery in a common genetic pathway, then (1) asymmetric cell divisions should still occur in *Rbpj* mutants; (2) reducing *LGN* should not enhance *Rbpj*-mutant phenotypes; and (3) restoring active Notch signalling should partially rescue *LGN* knockdown phenotypes.

We addressed the first issue by quantifying division axis and LGN crescent orientation in mitotic cells in *Rbpj*^{fl/fl} (control) and *Rbpj*^{fl/fl};K14-cre (conditional knockout) embryos. To compromise Notch signalling even earlier in skin development, E9.5 *Rbpj*^{fl/fl} embryos were transduced with NLS-cre-mRFP1 lentivirus. In each case, asymmetric LGN segregation was maintained, and asymmetric/symmetric divisions were balanced. This placed asymmetric cell division upstream of, or parallel to, the Notch pathway (Fig. 5a–c and Supplementary Fig. 12).

To determine whether LGN and Notch act in common or independent pathways, we compared the phenotype of each single mutant to *shLGN-1617*;Rbpj double mutants. To this end, *Rbpj*^{fl/fl} embryos were co-infected with NLS-cre-mRFP1 and either shScramble or *shLGN-1617* lentiviruses. *shLGN-1617*;NLS-cre-mRFP1;*Rbpj*^{fl/fl} embryos showed similarly impaired differentiation to single *shLGN-1617* and shScramble;NLS-cre-mRFP1;*Rbpj*^{fl/fl} mutants, confirming that *LGN* is epistatic to the Notch pathway (Fig. 5d, e).

Finally, to address whether Notch signalling is the major downstream effector of the asymmetric cell division machinery, we tested whether the *shLGN-1617* loss-of-function phenotype could be rescued by restoring Notch signalling suprabasally. We used heterozygous *lox-stop-lox-Rosa-NICD-IRES-GFP* knock-in mice⁴⁷, which express active Notch (NICD) and nuclear GFP after Cre-mediated recombination. By infecting embryos with *shLGN-1617*;H2B-mRFP1 with or without NLS-cre, we generated clones of cells expressing *shLGN-1617*, NICD (GFP), or both. Consistent with our earlier observations, proper expression of differentiation markers K10/loricrin required LGN. However, NICD overexpression at this age (E16.5) revealed appreciable cell-autonomous rescue of *shLGN-1617* differentiation defects when suprabasal Notch signalling was restored (Fig. 5f–h). These data provide compelling evidence that asymmetric cell division and Notch signalling act in a common pathway promoting the basal to suprabasal switch in differentiation.

Discussion

We used a novel *in vivo* RNA-interference-based knockdown approach to systematically dissect a genetic pathway necessary to execute asymmetric cell divisions in developing epidermis—information that would

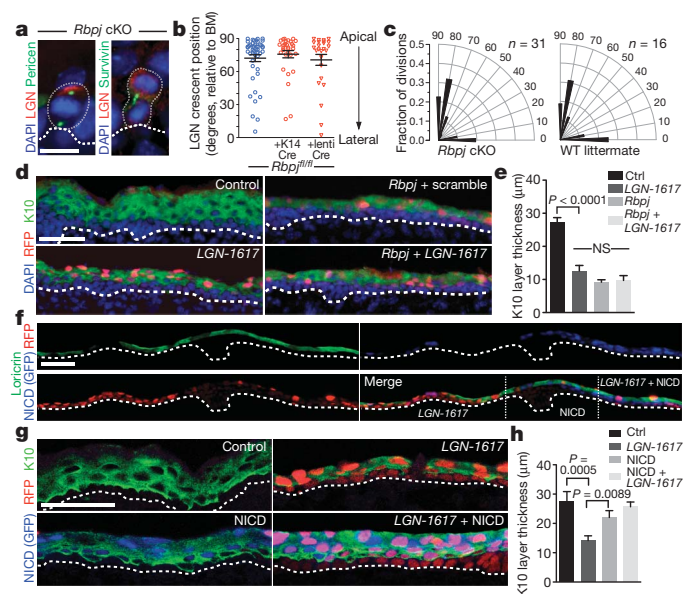


Figure 5 | Genetic interaction between asymmetric cell division and Notch pathways. **a–c**, Normal LGN localization and asymmetric cell divisions in *Rbpj* mutants (each dot represents one data point in **b**; *n* values are indicated in **c**). cKO, conditional knockout. **d, e**, Analyses of differentiation defects in E17.5 head skins from control (littermates) or *Rbpj*^{fl/fl} embryos transduced at E9.5 with *shLGN-1617*;H2B-mRFP1 (*LGN-1617*), shScramble;NLS-cre-mRFP1 (*Rbpj*+scramble), or *shLGN-1617*;NLS-cre-mRFP1 (*Rbpj*+*LGN-1617*). Comparable defects in double and single mutants/knockdowns indicate a common pathway for *Rbpj* and *LGN*. **f–h**, Restoring Notch signalling rescues *shLGN-1617* differentiation defects. Head skin, **f**; back skin, **g, h**. Combinations of single and double mutant clones (separated by vertical lines) expressing *shLGN-1617* (red) and active NICD (GFP, pseudocoloured in blue) were generated by co-infecting E9.5 *Rosa-lox-stop-lox-NICD-IRES-GFP* knock-in embryos with shScramble/*shLGN-1617*;H2B-mRFP1 and NLS-cre. Scale bars: 10 μm (**a**); 50 μm (**d, f, g**). Error bars represent s.d. (**b**) and s.e.m. (**e, h**). *P* values from two-tailed student's *t*-tests are indicated; NS, not statistically significant. For **e** and **h**, *n* > 10 fields; *n* > 3 embryos. Dotted lines in **a, d, f, g** denote basement membrane (BM).

have taken years of intensive labour to achieve by conventional mouse targeting. Moreover, our studies unveiled critical functions for *Numa1*, *Dctn1* and *LGN* in mammalian development. Specifically, they demonstrated that these asymmetric cell division components act by reorienting mitotic spindles to achieve perpendicular divisions, which in turn promote stratification and differentiation. Moreover, the resemblance between these knockdown phenotypes and *Rbpj* loss-of-function mutants provided important clues that suprabasal Notch signalling is impaired when asymmetric cell divisions do not occur. Our findings indicate that asymmetric cell divisions function not only to promote stratification but also to stimulate differentiation by enhancing compartmentalization of Notch signalling suprabasally. In the future, this methodology should unearth additional details underlying how asymmetric cell division regulates Notch signalling and orchestrates terminal differentiation. Overall, our data provide critical insights into how positional cues arising at the cell cortex regulate mitotic spindle orientation, and how coordinated actions of components of this pathway maintain the balance between stem-cell proliferation and differentiation.

METHODS SUMMARY

A detailed description of the ultrasound-guided lentiviral injection procedure and production of high-titre lentiviruses is described elsewhere¹⁹. For the present study, we used the following controls as comparisons to knockdown tissue: (1) age-matched embryos infected with a non-targeting scramble shRNA (shScramble) which activates the endogenous microRNA processing pathway, but is not predicted to target any known mouse gene; (2) uninjected littermates; and (3) RFP[−] (non-transduced) regions of mosaic injected embryos. All controls gave similar results, and thus they are used interchangeably in the text, although the nature of the specific control is always indicated.

RT-qPCR was performed using Absolutely RNA isolation kits (Stratagene), and Superscript VILO or III reverse transcriptase (Invitrogen) on a Roche LightCycler 480 using *Ppib* and *Hprt1* as reference genes. Immunohistochemistry was performed on fresh-frozen cryosections (8–10 µm) except in the case of the Notch reporter, where tissue was prefixed before embedding in OCT in order to preserve the GFP signal. Imaging was performed on a Zeiss Axioplan 2 epifluorescent or Zeiss LSM510 confocal microscope, with images acquired and analysed using MetaMorph. FACS isolation was performed on a BD Aria2 equipped with 355, 405, 488, 561 and 640-nm lasers, and analyses were performed on a BD LSRII. Sequences of all shRNAs used, qPCR oligonucleotides, antibodies, and mouse strains are provided in Methods.

Figures were prepared using Adobe Photoshop and Illustrator CS5. Graphing and statistical analyses were performed using Prism 5 (GraphPad Software) and Origin 8.1 (OriginLabs).

Full Methods and any associated references are available in the online version of the paper at www.nature.com/nature.

Received 27 May; accepted 22 December 2010.

- Neumuller, R. A. & Knoblich, J. A. Dividing cellular asymmetry: asymmetric cell division and its implications for stem cells and cancer. *Genes Dev.* **23**, 2675–2699 (2009).
- Knoblich, J. A. Mechanisms of asymmetric stem cell division. *Cell* **132**, 583–597 (2008).
- Siller, K. H. & Doe, C. Q. Spindle orientation during asymmetric cell division. *Nature Cell Biol.* **11**, 365–374 (2009).
- Yu, F., Morin, X., Cai, Y., Yang, X. & Chia, W. Analysis of partner of inscuteable, a novel player of *Drosophila* asymmetric divisions, reveals two distinct steps in inscuteable apical localization. *Cell* **100**, 399–409 (2000).
- Schober, M., Schaefer, M. & Knoblich, J. A. Bazooka recruits Inscuteable to orient asymmetric cell divisions in *Drosophila* neuroblasts. *Nature* **402**, 548–551 (1999).
- Wodarz, A., Ramrath, A., Kuchinke, U. & Knust, E. Bazooka provides an apical cue for Inscuteable localization in *Drosophila* neuroblasts. *Nature* **402**, 544–547 (1999).
- Lechler, T. & Fuchs, E. Asymmetric cell divisions promote stratification and differentiation of mammalian skin. *Nature* **437**, 275–280 (2005).
- Smart, I. H. Variation in the plane of cell cleavage during the process of stratification in the mouse epidermis. *Br. J. Dermatol.* **82**, 276–282 (1970).
- Poulson, N. D. & Lechler, T. Robust control of mitotic spindle orientation in the developing epidermis. *J. Cell Biol.* **191**, 915–922 (2010).
- Fuchs, E. Scratching the surface of skin development. *Nature* **445**, 834–842 (2007).
- Bowman, S. K., Neumuller, R. A., Novatchkova, M., Du, Q. & Knoblich, J. A. The *Drosophila* NuMA Homolog Mud regulates spindle orientation in asymmetric cell division. *Dev. Cell* **10**, 731–742 (2006).
- Izumi, Y., Ohta, N., Hisata, K., Raabe, T. & Matsuzaki, F. *Drosophila* Pins-binding protein Mud regulates spindle-polarity coupling and centrosome organization. *Nature Cell Biol.* **8**, 586–593 (2006).
- Siller, K. H., Cabernard, C. & Doe, C. Q. The NuMA-related Mud protein binds Pins and regulates spindle orientation in *Drosophila* neuroblasts. *Nature Cell Biol.* **8**, 594–600 (2006).
- Blumer, J. E., Kuriyama, R., Gettys, T. W. & Lanier, S. M. The G-protein regulatory (GPR) motif-containing Leu-Gly-Asn-enriched protein (LGN) and Gα3 influence cortical positioning of the mitotic spindle poles at metaphase in symmetrically dividing mammalian cells. *Eur. J. Cell Biol.* **85**, 1233–1240 (2006).
- Woodard, G. E. *et al.* Ric-8A and Gα3 recruit LGN, NuMA, and dynein to the cell cortex to help orient the mitotic spindle. *Mol. Cell Biol.* **30**, 3519–3530 (2010).
- Du, Q. & Macara, I. G. Mammalian Pins is a conformational switch that links NuMA to heterotrimeric G proteins. *Cell* **119**, 503–516 (2004).
- Johnston, C. A., Hirono, K., Prehoda, K. E. & Doe, C. Q. Identification of an Aurora-A/Pins^{LINKER}/Dlg spindle orientation pathway using induced cell polarity in S2 cells. *Cell* **138**, 1150–1163 (2009).
- Segalen, M. *et al.* The Fz-Dsh planar cell polarity pathway induces oriented cell division via Mud/NuMA in *Drosophila* and zebrafish. *Dev. Cell* **19**, 740–752 (2010).
- Beronja, S., Livshits, G., Williams, S. E. & Fuchs, E. Rapid functional dissection of genetic networks via tissue-specific transduction and RNAi in mouse embryos. *Nature Med.* **16**, 821–827 (2010); published online 6 June 2010.
- Morin, X., Jaouen, F. & Durbec, P. Control of planar divisions by the G-protein regulator LGN maintains progenitors in the chick neuroepithelium. *Nature Neurosci.* **10**, 1440–1448 (2007).
- Konno, D. *et al.* Neuroepithelial progenitors undergo LGN-dependent planar divisions to maintain self-renewability during mammalian neurogenesis. *Nature Cell Biol.* **10**, 93–101 (2008).
- Zheng, Z. *et al.* LGN regulates mitotic spindle orientation during epithelial morphogenesis. *J. Cell Biol.* **189**, 275–288 (2010).
- Moffat, J. *et al.* A lentiviral RNAi library for human and mouse genes applied to an arrayed viral high-content screen. *Cell* **124**, 1283–1298 (2006).
- Adams, R. J. Metaphase spindles rotate in the neuroepithelium of rat cerebral cortex. *J. Neurosci.* **16**, 7610–7618 (1996).
- Geldmacher-Voss, B., Reugels, A. M., Pauls, S. & Campos-Ortega, J. A. A 90-degree rotation of the mitotic spindle changes the orientation of mitoses of zebrafish neuroepithelial cells. *Development* **130**, 3767–3780 (2003).
- Kaltschmidt, J. A., Davidson, C. M., Brown, N. H. & Brand, A. H. Rotation and asymmetry of the mitotic spindle direct asymmetric cell division in the developing central nervous system. *Nature Cell Biol.* **2**, 7–12 (2000).
- Du, Q., Stukenberg, P. T. & Macara, I. G. A mammalian Partner of inscuteable binds NuMA and regulates mitotic spindle organization. *Nature Cell Biol.* **3**, 1069–1075 (2001).
- Hardman, M. J., Sisi, P., Banbury, D. N. & Byrne, C. Patterned acquisition of skin barrier function during development. *Development* **125**, 1541–1552 (1998).
- Kraut, R., Chia, W., Jan, L. Y., Jan, Y. N. & Knoblich, J. A. Role of inscuteable in orienting asymmetric cell divisions in *Drosophila*. *Nature* **383**, 50–55 (1996).
- Sanada, K. & Tsai, L. H. G protein βγ subunits and AGS3 control spindle orientation and asymmetric cell fate of cerebral cortical progenitors. *Cell* **122**, 119–131 (2005).
- Watt, F. M., Estrach, S. & Ambler, C. A. Epidermal Notch signalling: differentiation, cancer and adhesion. *Curr. Opin. Cell Biol.* **20**, 171–179 (2008).
- Blanpain, C., Lowry, W. E., Pasolli, H. A. & Fuchs, E. Canonical notch signaling functions as a commitment switch in the epidermal lineage. *Genes Dev.* **20**, 3022–3035 (2006).
- Moriyama, M. *et al.* Multiple roles of Notch signaling in the regulation of epidermal development. *Dev. Cell* **14**, 594–604 (2008).
- Demehri, S. *et al.* Notch-deficient skin induces a lethal systemic B-lymphoproliferative disorder by secreting TSLP, a sentinel for epidermal integrity. *PLoS Biol.* **6**, e123 (2008).
- Pan, Y. *et al.* γ-secretase functions through Notch signaling to maintain skin appendages but is not required for their patterning or initial morphogenesis. *Dev. Cell* **7**, 731–743 (2004).
- Rangarajan, A. *et al.* Notch signaling is a direct determinant of keratinocyte growth arrest and entry into differentiation. *EMBO J.* **20**, 3427–3436 (2001).
- Coumelleau, F., Furthauer, M., Knoblich, J. A. & Gonzalez-Gaitan, M. Directional Delta and Notch trafficking in Sara endosomes during asymmetric cell division. *Nature* **458**, 1051–1055 (2009).
- Emery, G. *et al.* Asymmetric Rab11 endosomes regulate delta recycling and specify cell fate in the *Drosophila* nervous system. *Cell* **122**, 763–773 (2005).
- Mummery-Widmer, J. L. *et al.* Genome-wide analysis of Notch signalling in *Drosophila* by transgenic RNAi. *Nature* **458**, 987–992 (2009).
- Nickoloff, B. J. *et al.* Jagged-1 mediated activation of notch signaling induces complete maturation of human keratinocytes through NF-κB and PPARγ. *Cell Death Differ.* **9**, 842–855 (2002).
- Knoblich, J. A., Jan, L. Y. & Jan, Y. N. Asymmetric segregation of Numb and Prospero during cell division. *Nature* **377**, 624–627 (1995).
- Wang, H., Ouyang, Y., Somers, W. G., Chia, W. & Lu, B. Polo inhibits progenitor self-renewal and regulates Numb asymmetry by phosphorylating Pon. *Nature* **449**, 96–100 (2007).
- Wirtz-Peitz, F., Nishimura, T. & Knoblich, J. A. Linking cell cycle to asymmetric division: Aurora-A phosphorylates the Par complex to regulate Numb localization. *Cell* **135**, 161–173 (2008).
- Rhyu, M. S., Jan, L. Y. & Jan, Y. N. Asymmetric distribution of numb protein during division of the sensory organ precursor cell confers distinct fates to daughter cells. *Cell* **76**, 477–491 (1994).
- Clayton, E. *et al.* A single type of progenitor cell maintains normal epidermis. *Nature* **446**, 185–189 (2007).
- Mizutani, K., Yoon, K., Dang, L., Tokunaga, A. & Gaiano, N. Differential Notch signalling distinguishes neural stem cells from intermediate progenitors. *Nature* **449**, 351–355 (2007).
- Murtaugh, L. C., Stanger, B. Z., Kwan, K. M. & Melton, D. A. Notch signaling controls multiple steps of pancreatic differentiation. *Proc. Natl Acad. Sci. USA* **100**, 14920–14925 (2003).

Supplementary Information is linked to the online version of the paper at www.nature.com/nature.

Acknowledgements We thank N. Stokes, L. Polak and D. Oristian for their assistance in the mouse facility; S. Lanier and T. Gettys for providing AGS3 and Gα3 antibodies; N. Gaiano and C. Cepko for constructs; D. Melton and T. Honjo for mice; S. Chai for Numb constructs; E. Ezhkova for sharing microarray data; and J. Knoblich for sharing unpublished results and reagents. We are grateful to M. Schober, D. Devenport, E. Ezratty, C. Luxenburg and members of the Fuchs laboratory for discussions and critical reading of the manuscript. We thank S. Mazel and the RU Flow Cytometry Resource Center for assistance with cell sorting; A. North and the RU Bioimaging Resource Center for assistance with image acquisition and the Comparative Biology Center (AAALAC accredited) for veterinary care of our mice. S.E.W. was supported by an American Cancer Society postdoctoral fellowship and S.B. was a Human Frontier Science Program postdoctoral fellow. E.F. is an investigator in the Howard Hughes Medical Institute. Work in the Fuchs laboratory was supported by a grant from the National Institutes of Health (E.F. R01AR27883).

Author Contributions S.E.W., E.F. and S.B. designed experiments. S.E.W. performed the experiments and analysed their raw data. H.A.P. conducted ultrastructural analyses. S.E.W. and S.B. performed lentiviral injections. S.E.W. and E.F. wrote the paper. All authors provided intellectual input, read and approved the manuscript.

Author Information Reprints and permissions information is available at www.nature.com/reprints. The authors declare no competing financial interests. Readers are welcome to comment on the online version of this article at www.nature.com/nature. Correspondence and requests for materials should be addressed to E.F. (fuchslb@rockefeller.edu).

METHODS

Mice. CD1 mice from Charles River laboratories were used for all experiments. Notch reporter transgenics⁴⁶ were obtained from Jackson laboratories (strain Tg(Cp-EGFP)25Gaia/J, stock no. 005854) and outbred over multiple generations to the CD1 background, where they were maintained as homozygotes. Homozygous *lox-stop-lox-Rosa^{NICD-IRES-GFP}* male breeder mice⁴⁷ were obtained from Jackson laboratories (strain Gt(Rosa)26Sortm1(Notch1)Dam/J, stock no. 008159) and crossed to CD1 females when used for lentiviral injections. *Rbpj^{fl/fl}* mice⁴⁸ were bred as homozygotes for lentiviral injections, or crossed to *K14-cre^{tg};Rbpj^{fl/+}* females for analyses of the conditional mutant phenotype. BrdU (50 µg g⁻¹) was injected intraperitoneally to pregnant females 4–6 h before killing by administration of CO₂. All animals were maintained in an AAALAC-approved animal facility and procedures were performed using IACUC-approved protocols.

Constructs and RNAs. All shRNAs except *shDctn1-1721* were obtained from The Broad Institute's Mission TRC-1 mouse library, and were present in the pLKO.1 lentiviral backbone, which harbours a puromycin-resistance cassette. shRNA sequences were cloned from the library vectors into our modified pLKO H2B-mRFP1, H2B-YFP, or H2B-CFP vectors¹⁹. The lentiviral Notch reporter was generated by cloning a KpnI–XbaI fragment containing the four CBF1 binding elements, SV40 minimal promoter, and EGFP from Addgene clone 17705 (ref. 46) into pLKO shScramble;H2B-mRFP1 or *shLGN-1617;H2B-mRFP1*. For expression of EYFP-mInsc, mRFP1-Numb and mRFP1-LGN (full length and ΔC), the pLKO backbone was modified to delete the puromycin-resistance gene following the PGK promoter, and replace it with a custom multiple cloning site (pLKO PGK MCS). This facilitated subsequent cloning and allowed the use of a single lentivirus that could both express a cDNA of interest and a shRNA. The 72-kDa Numb isoform was cloned from mouse cDNA by PCR and fused to mRFP1, whereas EYFP-mInsc was reported previously⁷. LGN(ΔC) was produced according to the published mutant²¹, which lacks exons 13, 14 and the coding region of the last exon 15. This truncates the protein at 474 amino acids, deleting the GoLoco motifs that mediate LGN's interaction with Gα_i/Gα_o. It was also empirically found to delete the epitope for our LGN antibody (see below), which was raised to the C terminus.

Viruses were produced as described¹⁹. The following shRNAs were used: *shLGN-1617* (TRCN0000028914), *shLGN-781* (TRCN0000028914), *shNuma1-1070* (TRCN0000037190), *shNuma1-6790* (TRCN0000072130), *shDctn1-289* (TRCN0000072128), *shAGS3-759* (TRCN0000037192), *shAGS3-1147* (TRCN0000037192), *shScramble* (Sigma SHC002). Detailed maps and constructs are available upon request. Full hairpin sequences (minus AgeI and EcoRI cloning sites) are as follows: *shScramble*, 5'-CAACAAGATGAAGAGCACCAACTCG AGTTGGTGCTCTTCATCTTGTG-3'; *shLGN-1617*, 5'-GCCGAATTGGA ACAGTGAAATCTCGAGATTTCACTGTTCCAATTCGGC-3'; *shLGN-781*, 5'-GCGCTCTACAATCTTGGAATCTCGAGATTTCCAAGATTGTAGAGC GC-3'; *shNuma1-1070*, 5'-GCCAGATGGATCGAAAGATTACTCGAGTAAT CTTTCGATCCATCTGGC-3'; *shNuma1-6790*, 5'-CCTTAGTCTCTGGACCT AGAAGCTCGAGTTCTAGGTCCAGAGACTAAGG-3'; *shDctn1-289*, 5'-CCA GTCCAGATCCAAGTATTCTCGAGAACTTGGATCTGGGACTGG-3'; *shDctn1-1721*, 5'-GCCATTGAGATGGAGTTGAGACTCGAGTCTCAACTCC ATCTCAATGGC-3'; *shAGS3-759*, 5'-CCACTACCTACTGGGAAGTCTCTC GAGAAGTTTCCAGTAGGTAGTG-3'; *shAGS3-1147*, 5'-GCCTTGACCT TTGCCAAGAACTCGAGTTTCTTGCCAAAGGTCAAGGC-3'.

Cell culture. Primary mouse keratinocytes were maintained in E medium with 15% FBS and 50 µM CaCl₂ (low Ca²⁺ medium). For viral infections, keratinocytes were plated in 6-well dishes at 100,000 cells per well and incubated with lentivirus in the presence of polybrene (100 µg ml⁻¹). After 2 days, we positively selected infected cells with puromycin (1–2 µg ml⁻¹) for 4–7 days, and processed them for mRNA and protein analyses. Calcium shift assays were performed as follows. Keratinocytes were seeded at a saturating density (200,000 cells/24-well) onto coverslips coated with collagen and fibronectin. Cells were switched to high Ca²⁺ (1.5 mM) medium 16–24 h later, and grown for the indicated period of time (24–72 h). Cells were fixed with 4% paraformaldehyde for 10 min at room temperature. Immunostaining was performed using the same protocol as for slides (below). As differentiation is sensitive to cell density, nuclei/field were quantified using Metamorph and only images with between 1,800–2,000 nuclei per ×10 field were quantified for K10 expression.

Antibodies, immunohistochemistry and imaging. Antisera against LGN were raised in guinea-pigs using the C terminus (amino acids 376–572) of LGN fused to GST, and were affinity purified using HiTrap NHS columns conjugated to purified immunogen protein (Pierce). Embryos were either embedded whole (<E16.5) or skinned and flat-mounted on paper towels. Both infected and littermate controls were embedded together in a single block to control for potential variability in immunostaining conditions. Embryos and skin were embedded unfixed in OCT (Tissue Tek), except for Notch reporter and Rosa^{YFP} sections, which were prefixed for 1 h in 4% paraformaldehyde to preserve the cytoplasmic GFP signal. To detect the reporter, antibodies against GFP were used, coupled to

either fluorescent secondary antibodies or POD-conjugated secondaries which were amplified using the TSA Plus fluorescein or Cy5 system (Perkin Elmer). For BrdU immunostaining, slides were treated with 1 N HCl for 1 h at 37 °C before adding the anti-BrdU antibody.

Frozen sections were cut at a thickness of 8–10 µm on a Leica cryostat and mounted on SuperFrost Plus slides (Fisher). Slides were air-dried for 30 min, then fixed for 10 min with 4% paraformaldehyde, rinsed with PBS, then blocked for 1 h in gelatin block (5% NDS, 1% BSA, 2% gelatin, 0.2% Triton X-100 in PBS) or BSA/NDS block (3% BSA, 5% NDS, 0.2% Triton X-100 in PBS) before incubating in primary antibody diluted in block at 4 °C overnight. After washing with PBS, secondary antibodies, conjugated to Alexa-488 (Molecular Probes), Cy3, RRX, DyLight 549, or Cy5 (Jackson Laboratories), were added for 1–2 h at room temperature. Slides were washed, counterstained with DAPI (0.5 µg ml⁻¹) and mounted in ProLong Gold (Invitrogen). Imaging was performed on a Zeiss Axioplan 2 using ×10/0.45 air, ×20/0.8 air, ×63/1.4 oil, or ×100/1.4 oil Plan-Apochromat objectives and the following Chroma filter sets: 49003 ET YFP (YFP), 49008 ET TR C94094 (mRFP1), 49004 ET dsR C94093 (Cy3, DyLight 549), 41008 Cy5 (Cy5), 41001 FITC (AlexaFluor 488/GFP); or a Zeiss LSM 510 Meta scanning confocal microscope with ×40/1.2 air or ×63/1.4 oil objective.

The following primary antibodies were used: mouse IgM anti-NuMA (BD Biosciences, 1:200), rabbit anti-pericentrin (Covance, 1:500), rabbit anti-Gα_i 977 (gift of T. Gettys, 1:400), rabbit anti-RFP (MBL, 1:4,000), rabbit mAb anti-survivin (Cell Signaling, 1:400), guinea-pig anti-K5 (Fuchs laboratory, 1:200), rat mAb anti-Ecad (Fuchs laboratory, 1:500), rabbit anti-K10 (Covance, 1:1,000), rabbit anti-K14 (Fuchs laboratory, 1:500), rat anti-CD104/β4 integrin (BD Pharmingen), rabbit anti-loricrin (Fuchs laboratory, 1:1,000), rabbit anti-involucrin (Covance, 1:1,000), rabbit anti-filaggrin (Covance, 1:1,000), rabbit anti-Hes1 (Fuchs laboratory, 1:500), chicken anti-GFP (Abcam, 1:5,000), rabbit anti-GFP (Invitrogen, 1:5,000), hamster mAb anti-Notch3 (Biolegend, 1:400), rabbit anti-Notch3/NICD3 (Abcam ab23426, 1:400), mouse mAb anti-acetylated tubulin (Sigma, 6-11B-1, 1:400), rabbit anti-γ-tubulin (Abcam, 1:500), mouse mAb anti-β-tubulin (Sigma, TUB 2.1, 1:500), rabbit anti-AGS3 pep32 (gift of S. Lanier, 1:500), rabbit anti-AGS3 pep22 (S. Lanier, 1:200), rabbit anti-aPKC (Santa Cruz, N-17, 1:200), rabbit anti-Par3 (Upstate/Millipore, 1:500), rat anti-HA (Roche, 1:200), rat anti-BrdU (Abcam, 1:200), rabbit anti-RFP-HRPDirect (MBL, 1:2,000), goat anti-Dctn1 (Abcam ab11806, 1:500).

RT-qPCR. mRNA was isolated using Absolutely RNA miniprep or microprep kits (Stratagene), and was quantified using a Nanodrop spectrophotometer. cDNA was synthesized from 2 to 500 ng of total RNA using either Superscript III with oligo-dT primers or Superscript VILO with random primers (Invitrogen). Real-time qPCR was performed on a LightCycler 480 (Roche), and relative quantification performed using Roche software, with data normalized relative to cyclophilin (*Ppip*) and *Hprt1* (using the geometric mean of the crossing point (Cp) values from both reference genes). To confirm the functionality of the primer sets used, multiple primer pairs were designed and tested for each gene; efficiencies of primer pairs were determined empirically (>1.8); specificity confirmed by the absence of product in samples prepared without reverse transcriptase (–RT controls); and product sizes calculated by melting curve analysis and confirmed by gel electrophoresis. The following primer sequences were used: *LGN* forward 5'-TCTGCTG CAAAGAGATCCAAACA-3' and 5'-TCCCCCAACACAGATGAGTTCTT-3', reverse 5'-TCATGGGCAGGTACAAAAAGTCC-3' and 5'-ATCTTGACCCCT GGCACITTTACA-3'; *Numa1* 5'-GTCAGGCCCTTGGAGACT-3' and 5'-CGG GAGCTGGAGGTGATGAC-3', reverse 5'-AGCGGGCCAGAGACTGAGTG-3' and 5'-TCAGACCCGAGCTCCTTGTTC-3'; *Dctn1* 5'-GTGCGGGAGTTACG GGAGACT-3' and 5'-CTCCAGCAGCCCTATGAGT-3', reverse 5'-GCCT GGGCAACTTCCATCTG-3' and 5'-CTCGTCCAGCCGTGTCTGAAC-3'; *AGS3* forward 5'-TTGGGGAGGCGAGAGCACT-3' and 5'-GAGCCGGGGGA TGAGTTTTT-3', reverse 5'-AGCGCCCCAAGAAGATGTGA-3' and 5'-ATCAT GGCCTTGGGAAGATTG-3'; *K14* forward 5'-CGCCGCCCTGGTGTGG-3'; reverse 5'-TCTGGCGGTTGGTGGAGTCA-3'; *K10* forward 5'-GGAGGGT AAAATCAAGGAGTGGA-3', reverse 5'-TCAATCTGCAGCAGCAGCTT-3'; *loricrin* forward 5'-GTAAGGTCACCGGGTTGCAA-3', reverse 5'-GCTTAAA ATGTGAAGGGTTTGAA-3'; *Notch1* forward 5'-CAAATGGCCCTGGGTGG GGACAT-3', reverse 5'-AAAAGCCAGAAAGAGCTGCCCTGAG-3'; *Notch2* forward 5'-GCAGCCGGAGCTCCCCAGACG-3', reverse 5'-GTCCCGCTGA CCGCTCCAC-3'; *Notch3* forward 5'-TGAGCTTGGGAAATCTGCCTTACA-3' and 5'-ACATGGCCAAAGGTGAGAGTCT-3', reverse 5'-CTTCTGCCCCG ACCACGAGTTCC-3' and 5'-GCTGGGCCCCCTTGACAGAT-3'; *Notch4* forward 5'-TGACACGGGCTCCTCTATTTT-3' and 5'-CGACGCTCGGGAG GTTTG-3', reverse 5'-CAGTAGAAGCGGTGGCTAAAGAGT-3' and 5'-AA GCGGCGTCTGTCTCCCTACT-3'; *Dll1* forward 5'-TGCGGCTCTTCCCTT GTT-3' and 5'-GAAGCCACGGTCAGGGATACA-3', reverse 5'-TGGCAGGT GGCCCCATTA-3' and 5'-GTCGGGCGCTCTGCTAA-3'; *Dlk1* forward 5'-CAGCGCAACGGAAGTCAC-3', reverse 5'-ACTGCCCTGGCTGTGT

CA-3'; *Dll3* forward 5'-ATGGGCGTGAGATGCGAGTT-3', reverse 5'-GGGGCTGGTATGACATAAATGGAT-3'; *Jag1* forward 5'-ACCCTGTCAAGGAAATTACCGATAA-3' and 5'-GTGGCTGGGAAGGAACAACCT-3', reverse 5'-CTTCCGCCGCTTCCTTACAC-3' and 5'-TGGCCCCAAGGCACAAG-3'; *Jag2* forward 5'-GAGGGCGCGGCACACGAC-3', reverse 5'-CCGGCCTGGCCGCTCAATGG-3'; *Hes1* forward 5'-AGAAGAGGCGAAGGGCAAGAA-3' and 5'-AGTGGTGCCGCTCTGA-3', reverse 5'-CATGGCGTTGATCTGGGTCAT-3' and 5'-TTCCGCCACGGTCTCCAC-3'; *Numb* forward 5'-AGTGCCCGAGGTGGAAGGA-3' and 5'-CTCGGCCACGTAGAAGTTGATG-3', reverse 5'-GCCCGCACACTCTTTGACACT-3' and 5'-CACTCCTTCTCCCGCTTCTGTT-3'; *Numb1* forward 5'-CACCAGTGGCAGGCAGATGA-3' and 5'-CGCAGCGACTTCCAGGTGA-3', reverse 5'-GTGCGGCATATGTAGGA GAAAG-3' and 5'-CGGCAGGAAACAGCCACTT-3'; *Ki67* forward 5'-CCCA GCTCGTCTCCACCACTAGAG-3' and 5'-GGCGTGAAACAAACACAAACG AAAG-3', reverse 5'-TCTGTGTGTTTCTGGTTGCCTTAC-3' and 5'-CTGT GGTGATGGGCTCAGGTATGTC-3'; *Ccna2* forward 5'-TGATGGCAGCGG TGCTATGC-3', reverse 5'-GTTGTGGCGCTTTGAGTAGG-3'; *Ccne2* forward 5'-CTGTGTCGCCCTTATGTCTATT-3' and 5'-AACTGTGCTCTAAA TGGGAGAACC-3', reverse 5'-CAGCTGCCCTCCTTTCTGTAGA-3' and 5'-ATATGGGGCTTAAAAATGGACCAC-3'; *Ccnb1* forward 5'-CCCCCAAG TCTCACTATCAACAGA-3', reverse 5'-GTGGCGCCTTGGTATGGT-3'; *Ccnd1* forward 5'-TGTGCGCCCTCCGTATCTTAC-3' and 5'-TCGTGCTAT TGGAGGGTCAG-3', reverse 5'-TTCTCGGCAGTCAAGGGAATG-3' and 5'-CACAACAGGCCGCTACAAGAAA-3'; *Bax* forward 5'-GACAGGGGCTTT TTTGCTACAG-3', reverse 5'-CTGATCAGCTCGGGCACTTTAGT-3'; *Bbc3* forward 5'-GAGCGGCGGAGACAAGAAGA-3' and 5'-CACCAGCCCCAG AGCACTTA-3', reverse 5'-CACCAGACGCTTCTCTGAGA-3' and 5'-TCGT ACTGCGCGTTGAGGTC-3'; *Noxa* forward 5'-CGCAGATGCCTGGGAAG TC-3', reverse 5'-CCAAAAGCAAGCGAGCGTTTCTCT-3'; *Hprt1* forward 5'-GATCAGTCAACGGGGGACATAAA-3', reverse 5'-CTTGCGCTCATCT TAGGCTTTGT-3'; *Pipb* forward 5'-GTGAGCGCTTCCCAGATGAGA-3', reverse 5'-TGCCGGAGTCGACAATGATG-3'.

Western blotting. Gel electrophoresis was performed using 4–12% NuPAGE Bis-Tris gradient gels (Invitrogen), transferred overnight at 100 mA to nitrocellulose membranes. Membranes were blocked for 1 h in Odyssey blocking buffer (LI-COR), then incubated with primary antibodies in Odyssey block + 0.1% Tween-20 overnight at 4 °C with gentle agitation. Membranes were rinsed several times in PBT (PBS + 0.1% Tween-20) before incubating in secondary antibodies diluted in Odyssey block for 30 min at room temperature in the dark. Membranes were washed in PBT, then in PBS before imaging on a LiCor infrared scanner. Quantification of band intensities was performed using Odyssey 3.0 software. Primary antibodies used were: guinea-pig anti-LGN (Fuchs lab, 1:2000), rabbit anti-LGN (S. Bahria, 1:2,000), mouse IgG anti- β -actin (Sigma, 1:5,000), rabbit anti-Hprt1 (Abcam, 1:2,000). Secondary antibodies were conjugated to IRDye680 or IRDye800CW (LiCor and Rockland), and were used at 1:15,000.

Flow cytometry. Embryos from K14H2B-GFP^{+/+} male \times CD1 female matings, injected with lentivirus at E9.5, were collected at either E15.5 or E18.5 and processed as follows. For E15.5 embryos, back and head skin were dissected, and digested in 0.25% collagenase (Sigma) in HBSS for 1 h at 37 °C with intermittent trituration and shaking. Epidermis was separated from dermal fibroblasts by filtering through a 70- μ m filter and collecting the retaining epidermis. For E18.5 embryos, back and head skin were dissected and treated with dispase for 1 h at 37 °C with shaking. The epidermis was peeled away from the underlying dermis using fine forceps. Isolated collagenase- or dispase-treated epidermis was then treated with 0.25% Trypsin-EDTA (Invitrogen) for 15 min at room temperature with shaking. Keratinocytes were isolated by filtering through a 70- μ m cell strainer, retaining the flow-through cell suspension. PBS + 1% FBS (treated with BioRad Chelex to remove calcium) was added to inactivate trypsin, and cells were collected by centrifugation for 5 min at 300g. Cell pellets were re-suspended in PBS + 1% FBS and stained with CD49f/ α 6 integrin-Alexa647 (AbD Serotec) diluted 1:50 for 30 min on ice. DAPI (20 ng ml⁻¹) was used for live/dead exclusion. FACS isolations were performed on a BD FACS Aria 2 equipped with 355, 405, 488, 561 and 640-nm lasers. Cells were gated as α 6^{hi} (basal) and α 6^{low} (suprabasal), and sorted for GFP⁺RFP⁺ (transduced, knockdown) and GFP⁺RFP⁻ (internal control) populations. GFP⁺RFP⁻ littermates were also sorted as controls (see Supplementary Fig. 2). Sorted cells were validated by post-sort analysis on a BD LSR II; and RFP, GFP and α 6 integrin expression assessed by RT-qPCR on RNA isolated from sorted populations. Sorted cells were divided for protein, RNA and cell cycle analyses.

For cell cycle analyses, ~200,000 cells were re-suspended in 150 μ l of PBS, then fixed by drop-wise addition of four volumes of ice-cold 100% EtOH while vortexing. Cells were fixed for 15 min on ice, and stored at 4 °C. After fixation, cells were centrifuged for 5 min at 1,000g, re-suspended in PBS, and centrifuged again. Cells

were re-suspended in propidium iodide solution (10 μ g ml⁻¹) with RNase A (250 μ g ml⁻¹), and stained for 15 min at 37 °C in the dark. Cell cycle analysis was performed on a BD LSR II, and data processed and graphed using FlowJo 8.8.4.

Histology and electron microscopy analysis. Skin samples were fixed in 2% glutaraldehyde, 4% PFA, and 2 mM CaCl₂ in 0.05 M sodium cacodylate buffer, pH 7.2, at room temperature for >1 h, post-fixed in 1% osmium tetroxide and processed for Epon embedding; semi-thin sections (1 μ m) were stained with toluidine blue and examined by light microscopy. For transmission electron microscopy, ultrathin sections (60–70 nm) were counterstained with uranyl acetate and lead citrate. EM images were taken with a transmission electron microscope (Tecnai G2-12; FEI) equipped with a digital camera (Model XR60; Advanced Microscopy Techniques, Corp.).

Barrier assay. Dye exclusion assays were performed as described²⁸. Essentially, unfixed embryos are immersed in a low-pH X-gal substrate solution (100 μ M NaPO₄, 1.3 mM MgCl₂, 3 mM K₃Fe(CN)₆, 3 mM K₄Fe(CN)₆, 1 mg ml⁻¹ X-gal, 0.01% sodium deoxycholate, 0.2% NP-40, pH 4.5) at 30–37 °C for several hours to overnight until colour develops. Tails were snipped to serve as a positive control for staining. The principle of the assay is that at low pH, skin contains abundant β -galactosidase activity, so when the epidermis has incomplete barrier function, X-gal is cleaved and the blue precipitate is deposited.

Measurements, quantification, graphing and statistics. Spindle orientation was determined by measuring the angle between the centrosomal axis and the basement membrane in late prophase and metaphase cells, when two centrosomes were observed at opposite sides of the cell (in early prophase, the centrosomal pair is localized apically). LGN orientation was determined by measuring the angle defined by a line transecting the middle of the LGN crescent through the cell centre, relative to the basement membrane. Stages of mitosis were defined as follows: early prophase cells had condensed chromatin lacking a clearly defined pair of centrosomes; late prophase cells had a pair of centrosomes positioned at opposing poles; metaphase cells resembled late prophase cells but displayed aligned chromosomes characteristic of the metaphase plate. All cells were positive for phospho-histone H3 and LGN.

Axis of division was determined in anaphase/telophase cells, as it became obvious from analyses of metaphase spindle orientation that cells at this stage were dynamic, and spindle orientation was not necessarily predictive of the ultimate plane of division. Because phospho-histone H3 staining is weak or undetectable at this stage of the cell cycle, we used a novel marker to identify anaphase/telophase cells. Survivin/Birc5 is a component of the chromosomal passenger complex (CPC), together with INCENP/Aurora B kinase and Borealin/Dasra B. At prometaphase/metaphase, the CPC localizes to the inner centromeres, but at anaphase it translocates to the central spindle, and then finally to the mid-body during cytokinesis. We therefore found this antibody to be an effective marker for anaphase/telophase cells, as survivin was present at the mid-zone between two daughter nuclei, allowing us to distinguish definitively between mitotic nuclei from a single cell and closely juxtaposed nuclei from neighbouring cells (this was confirmed secondarily by using the cell membrane marker E-cadherin). Angle of division was determined by measuring the angle defined by the plane transecting two daughter nuclei relative to the plane of the basement membrane.

Back-skin thickness was quantified by taking >40 measurements per embryo of RFP⁺ regions from five random \times 20 fields arrayed from anterior to posterior. Epidermal thickness was measured as the distance from the basement membrane (labelled with β 4 integrin) to the skin surface. Measurements of individual embryos are displayed as box and whisker plots (Fig. 2f), with the dimensions of the box encompassing the 25–75% percentile, the horizontal bar representing the mean, and the error bars representing the minimum and maximum values. These values were normalized to the mean thickness of uninfected embryos from the same litter to control for subtle differences in gestational age between litters. Spinous/granular layer thickness in analyses of *Rbpj* mutants and NICD rescue experiments was calculated using Metamorph. A common threshold intensity was set for K10 fluorescent intensity, creating a binary image, whose area was calculated, and divided by the length of the section to determine average thickness. Ten to forty sections of head and anterior back skin were quantified for each genotype, from $n > 3$ embryos. Data presented are the mean \pm s.e.m.

Data were analysed and statistics performed (unpaired two-tailed student's *t*-tests or chi-squared tests) in Prism 5 (GraphPad). For determination of axis of cell division, the number of cells analysed (n) is indicated in the radial histograms, and included cells from three or more embryos of the same age. Radial histograms of angle of division were plotted in Origin 8.1 (OriginLab) from raw data binned into 10° increments. All other graphs were prepared in Prism.

48. Tanigaki, K. *et al.* Notch-RBP-J signaling is involved in cell fate determination of marginal zone B cells. *Nature Immunol.* **3**, 443–450 (2002).
49. Vasioukhin, V., Degenstein, L., Wise, B. & Fuchs, E. The magical touch: genome targeting in epidermal stem cells induced by tamoxifen application to mouse skin. *Proc. Natl Acad. Sci. USA* **96**, 8551–8556 (1999).

Telomere dysfunction induces metabolic and mitochondrial compromise

Ergün Sahin^{1,2}, Simona Colla^{1,2*}, Marc Liesa^{3*}, Javid Moslehi^{2,4}, Florian L. Müller^{1,2}, Mira Guo⁵, Marcus Cooper⁶, Darrell Kotton³, Attila J. Fabian⁷, Carl Walkey⁸, Richard S. Maser^{1,2}, Giovanni Tonon^{1,2}, Friedrich Foerster^{1,2}, Robert Xiong¹, Y. Alan Wang¹, Sachet A. Shukla¹, Mariela Jaskelioff^{1,2}, Eric S. Martin^{1,2}, Timothy P. Heffernan¹, Alexei Protopopov¹, Elena Ivanova¹, John E. Mahoney¹, Maria Kost-Alimova¹, Samuel R. Perry¹, Roderick Bronson⁹, Rongli Liao⁴, Richard Mulligan⁷, Orian S. Shirihai³, Lynda Chin^{1,2} & Ronald A. DePinho^{1,2,4,7}

Telomere dysfunction activates p53-mediated cellular growth arrest, senescence and apoptosis to drive progressive atrophy and functional decline in high-turnover tissues. The broader adverse impact of telomere dysfunction across many tissues including more quiescent systems prompted transcriptomic network analyses to identify common mechanisms operative in haematopoietic stem cells, heart and liver. These unbiased studies revealed profound repression of peroxisome proliferator-activated receptor gamma, coactivator 1 alpha and beta (*PGC-1α* and *PGC-1β*, also known as *Ppargc1a* and *Ppargc1b*, respectively) and the downstream network in mice null for either telomerase reverse transcriptase (*Tert*) or telomerase RNA component (*Terc*) genes. Consistent with PGCs as master regulators of mitochondrial physiology and metabolism, telomere dysfunction is associated with impaired mitochondrial biogenesis and function, decreased gluconeogenesis, cardiomyopathy, and increased reactive oxygen species. In the setting of telomere dysfunction, enforced *Tert* or *PGC-1α* expression or germline deletion of *p53* (also known as *Trp53*) substantially restores PGC network expression, mitochondrial respiration, cardiac function and gluconeogenesis. We demonstrate that telomere dysfunction activates p53 which in turn binds and represses *PGC-1α* and *PGC-1β* promoters, thereby forging a direct link between telomere and mitochondrial biology. We propose that this telomere–p53–PGC axis contributes to organ and metabolic failure and to diminishing organismal fitness in the setting of telomere dysfunction.

Multiple biological processes driven by diverse molecular factors conspire progressively to diminish organ function with advancing age. Molecular and cellular analyses of age-related conditions such as muscle atrophy, diabetes and cardiomyopathy implicate diminished mitochondrial function and telomere dysfunction in driving pathogenesis^{1–3}. Aged tissues show accumulation of mitochondrial DNA (mtDNA) mutations causing respiratory chain deficiency and increased reactive oxygen species (ROS)^{2,4}, which may underlie declining mitochondrial energy production and progressive loss of vigour in the aged⁵. The importance of mitochondrial integrity for healthy ageing is reinforced by premature ageing in mitochondrial polymerase (PolgA) mutant mice, which sustain increased mtDNA mutations⁶. Whereas the instigating processes driving age-associated mitochondrial decline are not known, in the context of this study, it is notable that the activity of the master mitochondrial regulators *PGC-1α* and *PGC-1β* decreases across ageing tissues^{7,8}. The relevance of PGCs to age-related pathologies may stem from their regulation of mitochondrial biogenesis and control of metabolic processes (gluconeogenesis, fatty acid metabolism and β -oxidation), processes that relate to increased insulin resistance and diabetes in the aged⁹.

Increasing evidence also implicated telomeres in the pathogenesis of age-related disorders¹⁰. Telomeres are nucleoprotein complexes at chromosome ends that function to preserve chromosomal integrity and quell p53-dependent DNA damage and DNA repair activity at these free ends¹¹. In the absence of telomerase, continued cell division results in

telomere shortening, loss of ‘capping’ function, and p53 activation^{12–15}. The prevailing view of how uncapped telomeres compromise organ function posits that p53 mediates cellular checkpoints of growth arrest, senescence and apoptosis in stem/progenitor cells^{10,16}. Correspondingly, p53 deficiency ameliorates these phenotypes, particularly in organs with high proliferative demands supported by resident stem cells¹⁵. The relevance of p53 in ageing is evidenced by stem cell depletion and premature ageing in mice engineered with hyper-active p53 alleles^{17,18}.

Whereas stem/progenitor cell failure due to p53-mediated cellular checkpoints may underlie compromise of highly proliferative organs, this mechanism seems inadequate to explain the profound physiological decline in more quiescent tissues, for example, heart (cardiomyopathy) and liver (reduced detoxification capacity, glucose intolerance). These pathologies indicate that telomere dysfunction elicits a degenerative state via additional mechanisms beyond the classical senescence and apoptosis checkpoints.

Telomere dysfunction represses PGC network and mitochondrial biogenesis

Tert^{−/−} mice were intercrossed to produce successive generations of telomerase deficient mice with decreasing telomere reserves. The *Tert*^{+/+} controls, first generation (G1) *Tert*^{−/−} (telomerase deficient with largely intact telomeres), and fourth generation (G4) *Tert*^{−/−} (telomerase deficient with severe telomere dysfunction) are designated hereafter as ‘WT’, ‘G1’ and ‘G4’ mice. In this model, progressive

¹Belfer Institute for Applied Cancer Science, Dana-Farber Cancer Institute, Boston, Massachusetts 02115, USA. ²Department of Medical Oncology, Dana-Farber Cancer Institute, Harvard Medical School, Boston, Massachusetts 02115, USA. ³Department of Medicine, Boston University School of Medicine, Massachusetts 02118, USA. ⁴Department of Medicine, Brigham and Women's Hospital, Harvard Medical School, Boston, Massachusetts 02115, USA. ⁵School of Engineering and Applied Sciences, Harvard University, Cambridge, Massachusetts 02138, USA. ⁶Division of Cardiovascular Medicine, University of Massachusetts, Worcester, Massachusetts 01605, USA. ⁷Department of Genetics, Harvard Medical School, Boston, Massachusetts 02115, USA. ⁸St Vincent's Institute and Department of Medicine, St Vincent's Hospital, University of Melbourne, Victoria 3065, Australia. ⁹Rodent Histopathology Laboratory, Harvard Medical School, Boston, Massachusetts 02115, USA.

*These authors contributed equally to this work.

telomere shortening is associated with increasing atrophy and functional decline across proliferative organs (intestinal, haematopoietic) and equally profound impairment in relatively quiescent organs (liver and heart) that do not exhibit significant levels of apoptosis (Supplementary Fig. 1; not shown). Body composition analysis showed body weight reduction and striking decrease in fat mass with preserved lean mass, yet no differences in spontaneous activity or food intake were apparent, while running endurance capacity was significantly reduced in G4 mice (not shown). G4 mice also showed decreased blood triglyceride and cholesterol levels and increased free fatty acids (not shown). Thus, telomere dysfunction in the *Tert*^{-/-} model engenders a premature ageing condition with severe anatomic and functional compromise across diverse organ systems.

To illuminate mechanisms underlying the broad impact of telomeres, we profiled 'proliferative' (CD34low/- c-Kit+ Sca-1+ Lin-, hereafter haematopoietic stem cells, 'HSCs') and 'quiescent' (liver and heart) tissues from 12-16-week-old WT, G1 and G4 mice. Telomere dysfunction transcriptomes showed strong enrichment for networks regulated by PGC-1 α and PGC-1 β including oxidative phosphorylation (OXPHOS), mitochondrial function, oxidative stress and gluconeogenesis (Fig. 1; Supplementary Tables 1–3). G1 transcriptomes

showed modest downward trends consistent with less telomere dysfunction (Fig. 1). The most prominent network perturbations centred on repressed OXPHOS genes, among which are many PGC targets (Supplementary Fig. 2; Supplementary Tables 1–3), and on repression of key genes governing oxidative defence (*Sod1*, glutathione peroxidase), gluconeogenesis (*Pepck*, *Glc-6-P*), fatty acid and cholesterol synthesis (*Fasn*, *Dgat*, *Gpat*, *Hmgcs1*, *Hmgcr*) and β -oxidation (*Acadm*, *Acadl* and *Cpt1c*, respectively). Quantitative reverse transcriptase polymerase chain reaction analysis (RT-qPCR) and western blot analysis of G4 tissues confirmed decreased PGC-1 α and PGC-1 β expression (Fig. 1) and their critical targets such as NRF-1, ERR α (also known as ESRR α), PPAR α and TFAM (Fig. 1; Supplementary Fig. 3). G1 tissues showed marginal reductions in PGC-1 α , PGC-1 β and their target genes (Fig. 1). Thus, telomere dysfunction represses PGC-1 α/β and their downstream gene network, which controls many aspects of mitochondrial biology and cellular metabolism⁹.

Telomere dysfunction decreases mitochondrial mass and energy production

The above profiles prompted assessment of whether telomere dysfunction has an impact on mitochondrial biology. We documented reduced

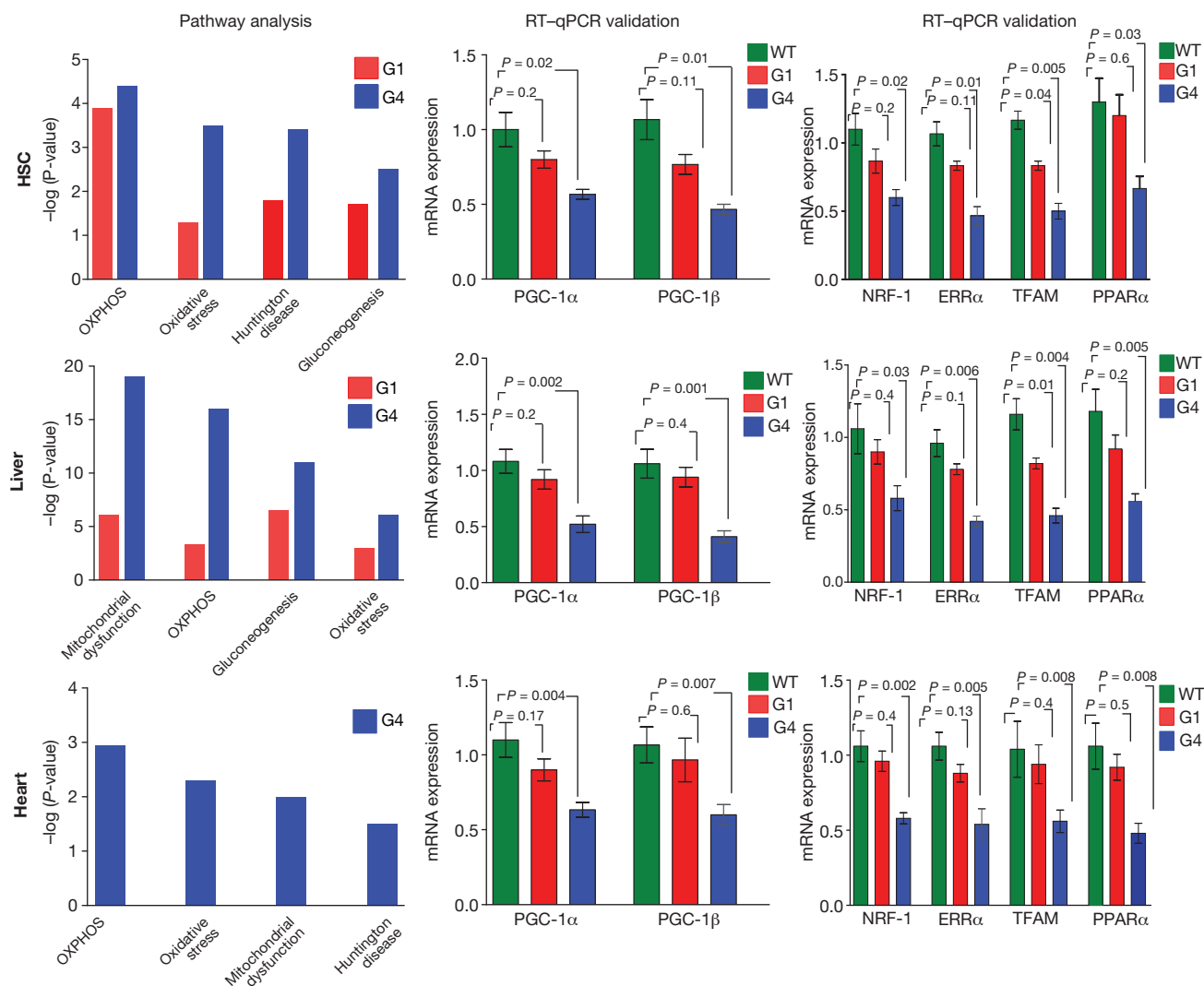


Figure 1 | PGC-regulated genes and networks are repressed in telomere dysfunctional tissues Microarray-based Ingenuity pathway analysis (IPA, left) and RT-qPCR validation of PGC-1 α , PGC-1 β (middle) and transcriptional targets NRF-1, ERR α , TFAM and PPAR α (right) in haematopoietic stem cells (HSC), liver and heart tissues show repression of genes in the PGC network

including oxidative phosphorylation (OXPHOS), mitochondrial dysfunction, gluconeogenesis, oxidative stress and Huntington Disease (HD). IPA results are expressed as $-\log(p\text{-value})$. $\Delta\Delta\text{Ct}$ method was used to analyse RT-qPCR data ($n = 5\text{--}8$ per group), t -test was used to calculate the statistical significance and error bars indicate s.e.m.

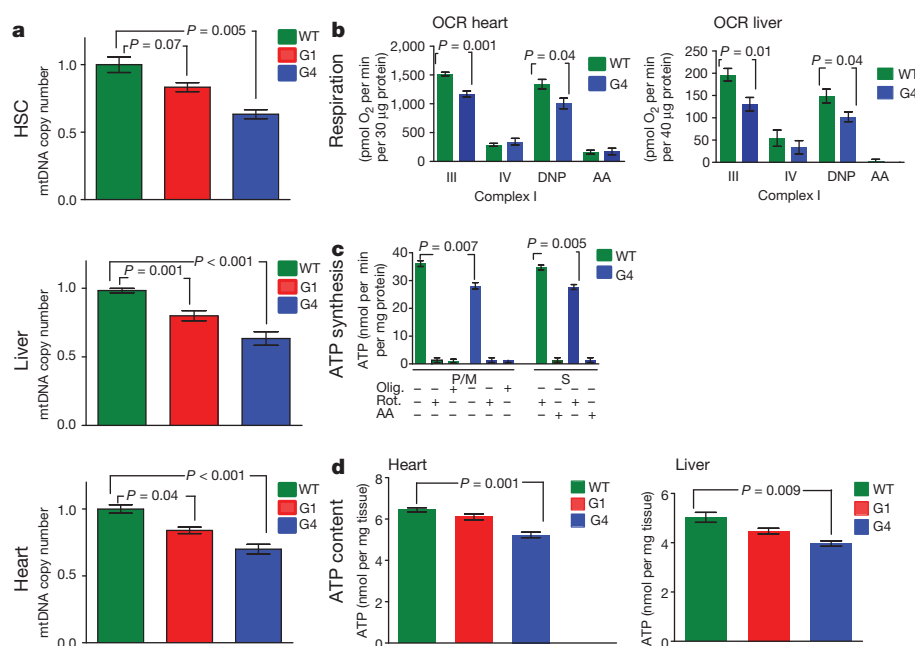


Figure 2 | Telomere dysfunction is associated with reduced mitochondrial DNA content in HSC, liver and heart and impaired mitochondrial function
a, Mitochondrial DNA copy number in HSC, liver and heart ($n = 5-8$).
b, Oxygen consumption rates (OCR) in heart and liver mitochondria in the presence of glutamate/malate (liver, $n = 3-5$) or pyruvate/malate (heart, $n = 3-5$). State III was induced by injection of ADP. State IV was induced by inhibition of the ATP synthase with oligomycin and uncoupled respiration rates were determined by injection of 2,4-dinitrophenol (DNP). Antimycin A (AA) was used to determine background, non-mitochondrial OXPHOS, OCR.

mitochondrial DNA content (Fig. 2a) and reduced mitochondrial density in G1 and G4 heart and liver (Supplementary Fig. 4a and b). Functionally, telomere dysfunction correlated with a marked decline in complex I and IV activity when assayed with either whole tissue lysates or isolated mitochondria from G1 and G4 heart and liver tissues (Supplementary Fig. 4c). The functional compromise of mitochondria was further substantiated by respiration studies of isolated liver and heart mitochondria from WT and G4 mice using the Seahorse XF24 (see Supplementary data online). State III (ADP-stimulated) respiration assay revealed a significant reduction in O_2 consumption in G4 heart and liver mitochondria (Fig. 2b; Supplementary Fig. 5a). Furthermore, respiration uncoupled from ATP synthesis (induced by 2,4-dinitrophenol, DNP) was also reduced in G4 liver and heart mitochondria (31% and 25%, respectively) (Fig. 2b). Additionally, complex II- and complex IV-dependent respiration was also decreased in G4 mitochondria (Supplementary Fig. 5a). Clark electrode-based studies in isolated liver mitochondria showed similar compromise in respiration (Supplementary Fig. 5b). Together, these results demonstrate defective electron transport chain activity in both G4 liver and heart mitochondria. In this regard, G4 heart mitochondria displayed significantly decreased ATP synthesis rates (Fig. 2c). This impaired mitochondrial ATP synthesis is associated with decreased total ATP content in G4 hearts and livers (Fig. 2d).

In addition, decreased expression of ROS detoxifying enzymes including known PGC-1 α targets was observed in G4 HSCs, liver and heart, which aligned with increased ROS levels by FACS in HSCs and increased carbonylated proteins in liver homogenates (Supplementary Fig. 6a-c). Further, complex I and complex II dependent H_2O_2 production rates were significantly increased in G4 mitochondria (Supplementary Fig. 6d). However, G1 or G4 mice treated from birth with *N*-acetylcysteine, a ROS scavenger, did not rescue defective HSC repopulation in competitive transplantations (Supplementary Fig. 6e), indicating that increased ROS is not mechanistically central to HSC failure.

c, ATP synthesis rates in isolated heart mitochondria driven by complex I (pyruvate /malate (P/M)) and complex II (succinate, S) respiration. The specificity of the measurements is verified by the effect of inhibitors (oligomycin (Olig.), rotenone (Rot.) and antimycin A (AA) ($n = 3$ per group, duplicate measurements per sample). Succinate-dependent ATP synthesis was determined in the presence of the complex I inhibitor rotenone. **d**, ATP content in liver and heart tissues was determined by HPLC ($n = 5$). *t*-test was used to calculate the statistical significance and error bars indicate s.e.m.

Taken together, these collective data establish that telomere-dysfunction-induced repression of the PGC network is associated with mitochondrial dysfunction as evidenced by compromised OXPHOS and respiration, decreased ATP generation capacity, and increased oxidative stress. Importantly, given evidence of non-telomere-related functions of *Tert*^{19,20}, we also demonstrated that, with onset of telomere dysfunction, *Terc*^{-/-} mice (normal *Tert* expression) experience degenerative phenotypes indistinguishable of those in the *Tert*^{-/-} model^{21,22}. Specifically, G2 *Terc*^{-/-} liver and hearts (exhibiting comparable telomere dysfunction as G4 *Tert*^{-/-} mice) exhibited the same canonical pathway alterations (Supplementary Fig. 7a; Supplementary Tables 4 and 5) as well as reductions in PGC and targets, mitochondrial DNA content, complex I and IV activity, and ATP levels (Supplementary Fig. 7b-e). The indistinguishable mitochondrial and energy profiles of *Tert* and *Terc* models indicate that telomere dysfunction *per se* is the principal factor driving these phenotypes.

Telomere dysfunction induces pathophysiologicals classical for impaired PGC function

Although these findings link dysfunctional telomeres to diminished PGC co-activator expression, we sought additional physiological evidence of such correlations *in vivo*. Previous work has established that repression of either or both co-activators (PGC-1 α or PGC-1 β) decreases mitochondrial biogenesis and function, elicits cardiomyopathy and impairs *de novo* glucose production²³⁻²⁵. G4 *Tert*^{-/-} mice exhibited these classical signs of impaired PGC function, including an age-progressive dilated cardiomyopathy with left ventricular wall thinning, increased left ventricular diameter, and reduced fractional shortening by 15 months of age (Fig. 3a), as reported previously in *Terc*^{-/-} mice²⁶. G4 mice also exhibited an inability to maintain plasma glucose levels under fasting conditions, experiencing a marked 30% drop at 12 h of fasting, yet maintained normal plasma glucose levels under fed conditions (Fig. 3b). This defect in gluconeogenesis

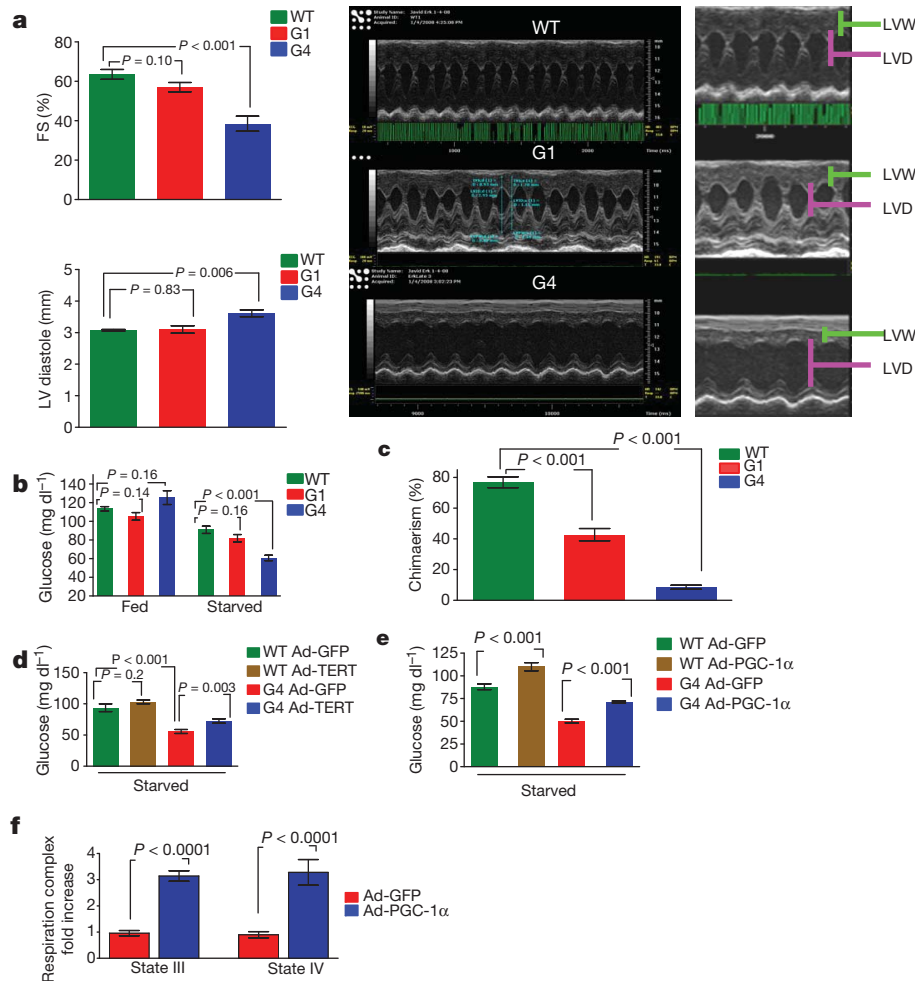


Figure 3 | Telomere dysfunction induces cardiomyopathy, defective gluconeogenesis and reduced HSC reconstitution capacity. Telomerase and PGC-1 α overexpression improves gluconeogenesis and mitochondrial respiration in G4 mice. **a**, Decreased fractional shortening (FS %) in 15-month-old G4 mice and signs of end-stage cardiomyopathy (left ventricular diameter (LVD) increase and thinning of left ventricular wall (LVW), $n = 5-8$ per genotype). **b**, Glucose levels in mice under fed and starved conditions ($n = 10$ per genotype). **c**, Long-term repopulation capacity in competitive transplants

was also evident in cultured hepatocytes from G4 mice (not shown), indicating a cell intrinsic defect. Finally, prompted by studies linking impaired mitochondrial function to defective HSC maintenance²⁷⁻²⁹, we showed that either enriched HSC or whole bone marrow derived from G4 mice show decreased capacity to reconstitute lethally irradiated recipients in competitive transplant experiments (Fig. 3c, not shown).

Additionally, to genetically strengthen the telomere–PGC–mitochondrial link *in vivo*, we reintroduced *Tert* in G4 livers via adenoviral delivery and monitored gene expression and gluconeogenic output under fasting conditions. Five days following Ad-Tert injection, partial rescue of PGC-1 α/β , Glc-6-P and Pepck expression (Supplementary Fig. 8a) was evident, accompanied by a 30% increase in glucose levels relative to Ad-GFP controls; Ad-Tert had no effect on gluconeogenesis in WT mice (Fig. 3d). We excluded multi-system causes affecting glucose control by documenting similar Ad-Tert responses in cultured G4 hepatocytes which show an 80% increase in glucose output relative to Ad-GFP controls (Supplementary Fig. 8b). Furthermore, this PGC-mitochondrial link is supported by Ad-PGC-1 α -induced rescue of gluconeogenesis *in vivo* and *in vitro* in G4 hepatocytes (Fig. 3e; Supplementary Fig. 8c). This Ad-PGC-1 α impact was markedly more pronounced in G4 mice than in WT mice or hepatocytes. Finally, to test whether PGC overexpression can also

reverse the mitochondrial respiration defect in telomere dysfunctional mice, we measured respiration in isolated liver mitochondria after adenoviral PGC delivery *in vivo*. One week after transduction, isolated liver mitochondria transduced with PGC-1 α showed an increase in state III (3.1-fold) and state IV (3.2-fold) respiration compared to GFP-transduced controls (Fig. 3f). WT mitochondria transduced with Ad-PGC showed increased respiration, albeit at lower levels (state III 1.8-fold; state IV 2.1-fold increase; not shown).

was determined using CD45.1- and CD45.2-specific antibodies. Shown is the percentage contribution of donors after 4 months. ($n = 8$ donors per group, three recipients per donor). **d**, Overexpression of *Tert* by adenovirus attenuates gluconeogenesis defect in G4 mice ($n = 8$ per group). **e**, Overexpression of PGC-1 α attenuates gluconeogenesis defect in G4 mice. ($n = 8-10$ per group). **f**, PGC-1 α overexpression rescues respiration defect (complex I) in G4 liver mitochondria ($n = 5$ per group). Student *t*-test was used to calculate the statistical differences in all assays described and error bars represent s.e.m.

p53 directly represses PGC-1 α and PGC-1 β

p53 deficiency markedly attenuates the degenerative phenotypes associated with telomere dysfunction, whereas constitutively activated p53 accelerates ageing phenotypes¹⁵⁻¹⁸. This role in ageing and p53's activation in telomere dysfunctional tissues of *Terc*^{-/-} mice and *Tert*^{-/-} mice (Supplementary Fig. 9a–d) prompted assessment of direct links between p53 activation and PGC-1 α/β regulation on multiple levels. First, relative to G2 *Terc*^{-/-} *p53*^{+/+} littermate controls, G2 *Terc*^{-/-} *p53*^{-/-} liver and hearts showed substantial or complete restoration of PGC-1 α and PGC-1 β expression (Fig. 4a) and downstream targets *ERR α* , *PPAR γ* and *TFAM* (not shown). Second, mitochondrial DNA copy number is significantly restored in G2 *Terc*^{-/-} *p53*^{-/-} livers and hearts relative to age- and gender-matched G2 *Terc*^{-/-} *p53*^{+/+} controls (Fig. 4b). Third, G2 *Terc*^{-/-} *p53*^{-/-} MEFs harbouring

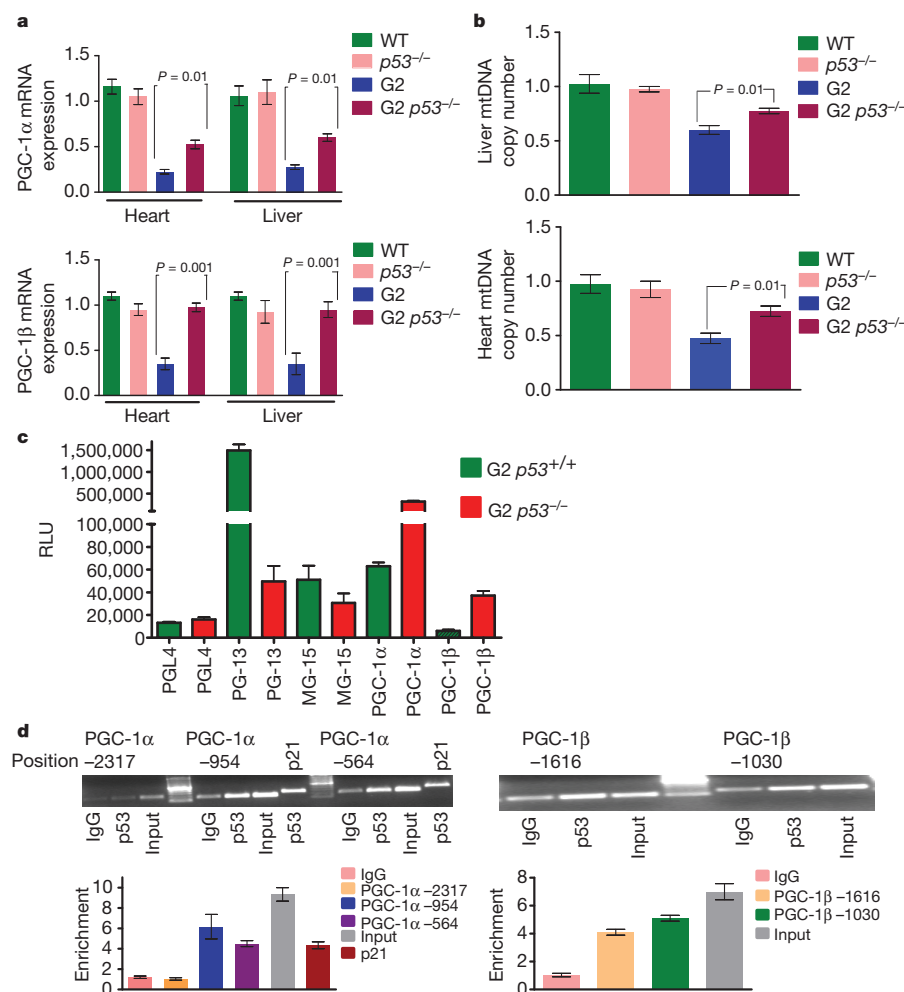


Figure 4 | p53 deficiency partially rescues the transcriptional regulation of PGC-1α/β and mitochondrial DNA copy number. **a**, PGC-1α and PGC-1β expression in liver and heart (*n* = 4). **b**, mtDNA quantification in liver and heart (*n* = 4). **c**, p53 represses PGC-1α and PGC-1β promoter reporters. G2 *Terc*^{+/+} and G2 *Terc*^{p53-/-} MEFs were transfected with empty reporter pGL4 or PGL4 containing various reporter fragments (-2.8 and -2.6 kb fragment of mouse PGC-1α and PGC-1β). Controls included the PG13-luc plasmid (containing 13 copies of a synthetic p53 DNA binding site) and MG15-luc (containing 15 copies of a mutated p53 DNA binding site). Shown is the average luciferase value (relative light units, RLU) of three different experiments. **d**, Chromatin immunoprecipitation (ChIP) showing p53 binding on the promoters of PGC-1α and PGC-1β at indicated sites and at p21 site (positive control). Graphs below show quantitative results in the proximal promoter regions by qPCR (three independent experiments). ΔΔCt method was used to analyse RT-qPCR data and *t*-test was used to calculate the statistical significance, error bars represent s.e.m.

a 4-hydroxytamoxifen (OHT)-induced p53-oestrogen receptor fusion construct (p53-ER) demonstrated potent OHT-dependent repression of PGC-1α, PGC-1β and downstream targets within 4 h of OHT treatment (Supplementary Fig. 10a; data not shown). Fourth, after 48 h of OHT treatment, G2 *Terc*^{-/-} *p53*^{-/-} p53-ER MEFs showed a 10–15% decrease in mitochondrial mass compared with no significant change in the OHT-treated G2 *Terc*^{-/-} *p53*^{-/-} controls (Supplementary Fig. 10b). Fifth, *in silico* promoter analysis (p53MH program) identified potential p53 binding elements in PGC-1α and PGC-1β promoters. These promoter regions were cloned into the PGL4 reporter and transfected into G2 *Terc*^{-/-} *p53*^{+/+} MEFs which showed fivefold repression of PGC-1α-PGL4 and PGC-1β-PGL4 reporter activity relative to G2 *Terc*^{-/-} *p53*^{-/-} MEFs (Fig. 4c). Positive (p21 responsive reporter, PG-13) and negative (empty vector PGL4; mutated p21 reporter 'MG') control reporters showed the expected reporter activity (Fig. 4c). Repressed reporter activity was also observed following transfection of a pCDNA-p53 expression vector into G2 *Terc*^{-/-} *p53*^{-/-} MEFs harbouring PGL4-PGC-1α and PGL4-PGC-1β reporters (not shown). Finally, anti-p53 chromatin-immunoprecipitation assays in G2 *Terc*^{-/-} *p53*^{+/+}, but not G2 *Terc*^{-/-} *p53*^{-/-}, MEFs demonstrated physical binding between p53 and (1) PGC-1α fragments containing p53 binding elements at -564 and -954, but not -2317, and (2) PGC-1β fragments containing p53 binding elements at -1616 and -1030 (Fig. 4d).

To test whether the herein and elsewhere documented³⁰ negative impact of p53 on mitochondrial function is context-specific, we over-expressed p53 at similar levels in *p53*^{-/-} and G2 *p53*^{-/-} MEFs by adenoviral delivery (Supplementary Fig. 11a). Increasing dosage of p53 in either *p53*^{-/-} or G2 *p53*^{-/-} MEFs showed repressed PGC-1α and PGC-1β levels and increasing occupancy of p53 binding

elements in PGC-1α and PGC-1β promoters (Supplementary Fig. 11b, c). Furthermore, WT MEF or heart tissues of mice treated with the DNA damage agent doxorubicin showed increased p53 levels after 24 h and coincident binding of p53 to PGC-1α promoter and repression of PGC-1α levels as documented before³¹ (not shown). This repression was significantly rescued by p53 deficiency in MEFs and in hearts treated with doxorubicin (not shown). Thus, increasing p53 levels can lead to PGC repression in these genetic contexts.

The functional relevance of p53-mediated repression of PGC-1α/β was examined by assessment of the impact of p53 status on liver and cardiac function. In liver, we observed higher gluconeogenic capacity upon fasting in G4 *p53*^{-/-} mice (Fig. 5a, top) and isolated hepatocytes relative to that of G4 *p53*^{+/+} controls (Fig. 5a). In heart, a protocol of low-dose doxorubicin-induced cardiomyopathy showed 30% improvement of fractional shortening in G4 *p53*^{-/-} mice relative to that of G4 *p53*^{+/+} controls (Fig. 5b). In mice with intact telomeres, p53 status had minimal impact on liver gluconeogenesis or cardiac function. In summary, combined biochemical, genetic and physiological results indicate that (1) activated p53 directly represses PGC-1α and PGC-1β, (2) p53 deficiency alleviates transcriptional repression and associated decline in mitochondrial DNA content in tissues and cells with telomere dysfunction, and (3) p53 deficiency partially rescues telomere dysfunction-induced heart and liver pathophysiology which have been classically associated with PGC deficiencies and mitochondrial dysfunction.

Discussion

Telomere dysfunction has been linked to many aspects of the ageing process. Genetic model systems have established the essentiality of preserved telomere function in the regenerative maintenance of highly

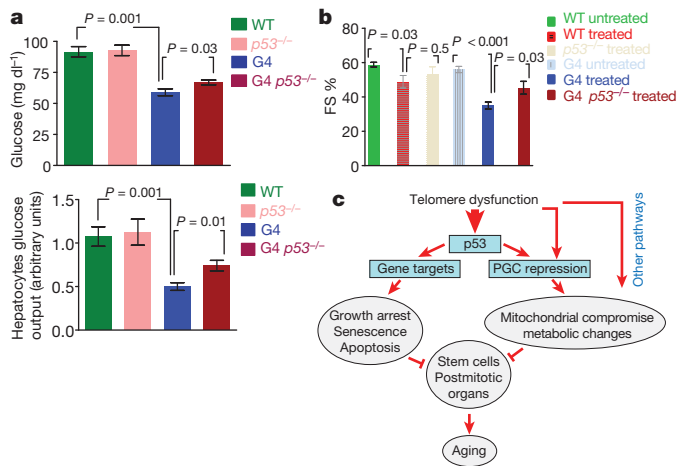


Figure 5 | p53 deficiency rescues gluconeogenesis and doxorubicin-induced cardiomyopathy. **a**, Glucose levels in mice (top) and in medium of hepatocytes (bottom, $n = 5-8$). **b**, Doxorubicin-induced cardiomyopathy (decreased fractional shortening, FS) in G4 mice can be partially rescued by p53 deficiency ($n = 3-5$, t -test, error bars represent s.e.m.). **c**, Proposed model: telomere-dysfunction-induced p53 represses PGCs and induces metabolic and mitochondrial compromise. Other pathways engaged by telomere dysfunction are also involved in mediating PGC repression and mitochondrial dysfunction. Together with classical cellular outcomes of p53 activation (senescence, apoptosis and growth arrest), metabolic and mitochondrial compromise might contribute to functional organ decline in the aged.

proliferative organs as well as in the preservation of physiological functions of more quiescent organs such as heart, brain and liver. Although classical p53-directed checkpoints of proliferative arrest and apoptosis have provided a strong basis for atrophy and functional impairment of high turnover tissues, the mechanistic basis for comparably severe compromise of less proliferative tissues has been an enigma. Here, combined transcriptomic, molecular, genetic and functional analyses on cellular and organismal levels established a direct molecular link between telomere dysfunction and repression of PGC-dependent processes of mitochondrial biogenesis/function, gluconeogenesis and oxidative defence. This combined repression of PGC-1 α and PGC-1 β and associated decline in mitochondrial biogenesis and function as well as metabolic changes aligns well with the phenotypes elicited by combined PGC-1 α and PGC-1 β knockdown *in vitro* or knockout *in vivo*^{25,32}. We propose that telomere dysfunction-induced repression of the PGC network and consequent mitochondriopathy and metabolic changes, along with telomere-induced apoptotic and proliferative checkpoints, contributes to functional multi-system decline in the setting of telomere dysfunction.

Given the diverse roles of PGC in multiple biological processes, the relative contribution of each of the dysregulated PGC arms to functional decline in the setting of telomere dysfunction may differ in various tissue types. For example, the PGC-directed mitochondrial dysfunction might be particularly critical in heart, whereas changes in metabolic gene expression may predominate in liver. Of potential clinical interest is the link of PGC to insulin resistance and diabetes in ageing, both of which are correlated with short telomeres^{33,34}. These mitochondrial and metabolic aspects of telomere-driven pathophysiology are not mutually exclusive with the well documented 'DNA damage' checkpoints associated with telomere dysfunction. These DNA damage checkpoints manifest primarily as cellular senescence and/or apoptosis which contribute to depletion and compromise of tissue stem cell reserves, particularly in highly proliferative organs such as intestine, skin and blood^{13,35,36}. Although the relative contributions of these checkpoints versus metabolic/mitochondrial dysfunction in a given degenerative phenotype will require further study, the latter mechanism may explain the profound physiological

impairment observed in the more static, post-mitotic tissues such as heart (cardiomyopathy) and liver (impaired gluconeogenesis), leading to feeble energy stress responses and overall frailty due to a fundamental inability to produce adequate cellular ATP. As with other mitochondriopathies, this mitochondrial defect in the setting of telomere dysfunction becomes increasingly apparent under conditions of physiological stress or advanced age². Whereas the instigator of decline in advanced age is not known, our findings raise the possibility that the well-known phenomenon of accelerating physiological decline in the aged could stem from a primary decline in PGC/mitochondrial function which in turn would lead to increased ROS, resulting from the diminished OXPHOS/complex activity and decreased expression of PGC-regulated oxidative defence genes. These increased ROS levels would set in motion a detrimental cycle of genotoxic damage with rapid erosion and damage of G-rich telomeres, sustained p53 activation, further repression of PGC, progressive mitochondrial decline, and so on^{37,38}. Under such circumstances, pharmacological correction of increased ROS would not be expected to substantially correct the primary mitochondrial defect and associated degenerative phenotypes, although such interventions may slow the rate of decline. Finally, beyond ROS accumulation, yeast genetic studies have shown that mitochondrial dysfunction results in a decline in iron-sulphur cluster biogenesis³⁹ which can cause nuclear genomic instability and thus would be expected to drive further decline in mitochondrial function via genotoxic activation of p53 and associated repression of PGC. It is also worth noting that p53-mediated repression of PGC is highly context dependent—shown here to occur in the setting of telomere dysfunction with increased p53 levels and activity—and that p53 can exert varied effects on mitochondrial biogenesis and function in other tissue and physiological settings depending on levels and kinetics of p53 activation, among other factors^{30,40}.

Mitochondria use oxidative phosphorylation to convert dietary intake into ATP, and in the process, generate ROS which can damage mitochondrial DNA, impair respiratory chain function, and cause nuclear DNA damage and cellular checkpoint activation. Given the central importance of mitochondria, one might anticipate that any genetic manipulation resulting in significantly decreased mitochondrial biogenesis/activity could accelerate the ageing process and cause age-related disorders such as diabetes, heart disease and neurological decline. From this perspective, it is worth noting that there are many molecules with important roles in organismal ageing or age-related disorders which interact directly with components of the telomere-mitochondrial axis. In particular, the increased lifespan associated with caloric restriction in model organisms is accompanied by increased mitochondrial density and respiration. Caloric restriction is associated with increased SIRT1 activity, which stabilizes PGC-1 α in turn increasing mitochondrial biogenesis and function⁴¹. Moreover, the beneficial impact of SIRT1 may also stem from its deacetylation and inactivation of p53, which may attenuate checkpoint responses and de-repress PGC-1 α expression; conversely, SIRT1 knockout mice show widespread p53 activation and shortened life expectancy^{42,43}.

In summary, multiple levels of evidence establish telomere dysfunction-induced p53 represses PGC-1 α and PGC-1 β , thereby linking telomeres to mitochondrial biology, oxidative defence, and metabolism. As illustrated in Fig. 5c, this telomere-p53-PGC pathway expands our understanding of how telomere dysfunction may compromise organ function and contribute to age-related disorders.

METHODS SUMMARY

Terc^{-/-} and *Tert*^{-/-}, *p53*^{-/-} mice have been described previously^{15,44}. Microarray analysis of HSCs, heart and liver tissues from WT, G1 and G4 *Terc*^{-/-} and G2 *Terc*^{-/-} mice was performed using either SAM (liver and heart) or fold change differences (HSCs) followed by Ingenuity pathway analysis (IPA). Quantitative RT-qPCR was analysed by $\Delta\Delta Ct$ method. qPCR-based mitochondrial quantification was performed with two different primer sets for genomic and mitochondrial loci. Shock-frozen heart and liver tissues were used for ATP determination by HPLC. Mitochondrial oxygen consumption studies were

performed in isolated heart and liver mitochondria using a XF24 extracellular flux analyser with substrates feeding electrons into complexes I, II and IV. Murine transthoracic echocardiography was conducted using a high-resolution micro ultrasound system as described previously⁴⁵. Competitive transplant experiments were performed following standard protocols. Fasting glucose concentrations were determined after 12–16 h of fasting. For *in vivo* Ad-Tert/PGC-1 α transduction studies, mice were transduced with 10⁹ virus particles per mouse and peripheral glucose levels determined 5–6 days post infection. Gluconeogenesis in isolated hepatocytes was determined following established protocols and glucose concentration is reported after protein standardization²⁴. For p53–ER activation studies in MEFs, control or experimental cells were either treated with ethanol vehicle or 4-OHT and mitochondrial mass was determined by MitoGreen and by qPCR. For promoter analysis, sequences of 2.8 kb (PGC-1 α) and 2.6 kb (PGC-1 β), upstream of the start sites, were amplified by PCR from genomic mouse heart DNA and cloned into a luciferase reporter vector. Upstream lengths were chosen based on potential p53 binding sites as identified by TRANSFAC. For chromatin immunoprecipitation, we followed the EZ-Chip protocol (Promega) using p53 specific antibody and control IgG. Doxorubicin was administered at 7.5 mg per kg body weight into 8-week-old mice and echocardiography was performed 7 days later. For full details, see Supplementary Methods.

Received 22 April; accepted 29 December 2010.

Published online 9 February 2011.

- Kirkwood, T. B. Understanding the odd science of aging. *Cell* **120**, 437–447 (2005).
- Wallace, D. C. A mitochondrial paradigm of metabolic and degenerative diseases, aging, and cancer: a dawn for evolutionary medicine. *Annu. Rev. Genet.* **39**, 359–407 (2005).
- Balaban, R. S., Nemoto, S. & Finkel, T. Mitochondria, oxidants, and aging. *Cell* **120**, 483–495 (2005).
- Guarente, L. Mitochondria—a nexus for aging, calorie restriction, and sirtuins? *Cell* **132**, 171–176 (2008).
- Conley, K. E., Marcinek, D. J. & Villarin, J. Mitochondrial dysfunction and age. *Curr. Opin. Clin. Nutr. Metab. Care* **10**, 688–692 (2007).
- Trifunovic, A. *et al.* Premature ageing in mice expressing defective mitochondrial DNA polymerase. *Nature* **429**, 417–423 (2004).
- Finley, L. W. & Haigis, M. C. The coordination of nuclear and mitochondrial communication during aging and calorie restriction. *Ageing Res. Rev.* **8**, 173–188 (2009).
- Arnold, A. S., Egger, A. & Handschin, C. PGC-1 α and myokines in the aging muscle—a mini-review. *Gerontology* **57**, 37–43 (2011).
- Lin, J., Handschin, C. & Spiegelman, B. M. Metabolic control through the PGC-1 family of transcription coactivators. *Cell Metab.* **1**, 361–370 (2005).
- Sahin, E. & Depinho, R. A. Linking functional decline of telomeres, mitochondria and stem cells during ageing. *Nature* **464**, 520–528 (2010).
- Maser, R. S. & DePinto, R. A. Connecting chromosomes, crisis, and cancer. *Science* **297**, 565–569 (2002).
- Hastie, N. D. *et al.* Telomere reduction in human colorectal carcinoma and with ageing. *Nature* **346**, 866–868 (1990).
- Lee, H.-W. *et al.* Essential role of mouse telomerase in highly proliferative organs. *Nature* **392**, 569–574 (1998).
- Blasco, M. A. *et al.* Telomere shortening and tumor formation by mouse cells lacking telomerase RNA. *Cell* **91**, 25–34 (1997).
- Chin, L. *et al.* p53 deficiency rescues the adverse effects of telomere loss and cooperates with telomere dysfunction to accelerate carcinogenesis. *Cell* **97**, 527–538 (1999).
- Wong, K. K. *et al.* Telomere dysfunction and Atm deficiency compromises organ homeostasis and accelerates ageing. *Nature* **421**, 643–648 (2003).
- Maier, B. *et al.* Modulation of mammalian life span by the short isoform of p53. *Genes Dev.* **18**, 306–319 (2004).
- Tyner, S. D. *et al.* p53 mutant mice that display early ageing-associated phenotypes. *Nature* **415**, 45–53 (2002).
- Maida, Y. *et al.* An RNA-dependent RNA polymerase formed by TERT and the RMRP RNA. *Nature* **461**, 230–235 (2009).
- Sarin, K. Y. *et al.* Conditional telomerase induction causes proliferation of hair follicle stem cells. *Nature* **436**, 1048–1052 (2005).
- Farazi, P. A., Glickman, J., Horner, J. & Depinho, R. A. Cooperative interactions of p53 mutation, telomere dysfunction, and chronic liver damage in hepatocellular carcinoma progression. *Cancer Res.* **66**, 4766–4773 (2006).
- Erdmann, N., Liu, Y. & Harrington, L. Distinct dosage requirements for the maintenance of long and short telomeres in *mTert* heterozygous mice. *Proc. Natl Acad. Sci. USA* **101**, 6080–6085 (2004).
- Arany, Z. *et al.* Transverse aortic constriction leads to accelerated heart failure in mice lacking PPAR- γ coactivator 1 α . *Proc. Natl Acad. Sci. USA* **103**, 10086–10091 (2006).
- Yoon, J. C. *et al.* Control of hepatic gluconeogenesis through the transcriptional coactivator PGC-1. *Nature* **413**, 131–138 (2001).
- Lai, L. *et al.* Transcriptional coactivators PGC-1 α and PGC-1 β control overlapping programs required for perinatal maturation of the heart. *Genes Dev.* **22**, 1948–1961 (2008).
- Leri, A. *et al.* Ablation of telomerase and telomere loss leads to cardiac dilatation and heart failure associated with p53 upregulation. *EMBO J.* **22**, 131–139 (2003).
- Pannicke, U. *et al.* Reticular dysgenesis (aleukocytosis) is caused by mutations in the gene encoding mitochondrial adenylate kinase 2. *Nature Genet.* **41**, 101–105 (2008).
- Sankaran, V. G., Orkin, S. H. & Walkley, C. R. *Rb* intrinsically promotes erythropoiesis by coupling cell cycle exit with mitochondrial biogenesis. *Genes Dev.* **22**, 463–475 (2008).
- Liu, J. *et al.* Bmi1 regulates mitochondrial function and the DNA damage response pathway. *Nature* **459**, 387–392 (2009).
- Bae, B. I. *et al.* p53 mediates cellular dysfunction and behavioral abnormalities in Huntington's disease. *Neuron* **47**, 29–41 (2005).
- Miyagawa, K. *et al.* Attenuation of doxorubicin-induced cardiomyopathy by endothelin-converting enzyme-1 ablation through prevention of mitochondrial biogenesis impairment. *Hypertension* **55**, 738–746 (2010).
- Uldry, M. *et al.* Complementary action of the PGC-1 coactivators in mitochondrial biogenesis and brown fat differentiation. *Cell Metab.* **3**, 333–341 (2006).
- Gardner, J. P. *et al.* Rise in insulin resistance is associated with escalated telomere attrition. *Circulation* **111**, 2171–2177 (2005).
- Salpea, K. D. & Humphries, S. E. Telomere length in atherosclerosis and diabetes. *Atherosclerosis* **209**, 35–38 (2010).
- Rudolph, K. L. *et al.* Longevity, stress response, and cancer in aging telomerase-deficient mice. *Cell* **96**, 701–712 (1999).
- Rossi, D. J. *et al.* Deficiencies in DNA damage repair limit the function of haematopoietic stem cells with age. *Nature* **447**, 725–729 (2007).
- Liu, L., Trimarchi, J. R., Smith, P. J. & Keefe, D. L. Mitochondrial dysfunction leads to telomere attrition and genomic instability. *Ageing Cell* **1**, 40–46 (2002).
- Passos, J. F. & von Zglinicki, T. Mitochondria, telomeres and cell senescence. *Exp. Gerontol.* **40**, 466–472 (2005).
- Veatch, J. R., McMurray, M. A., Nelson, Z. W. & Gottschling, D. E. Mitochondrial dysfunction leads to nuclear genome instability via an iron-sulfur cluster defect. *Cell* **137**, 1247–1258 (2009).
- Matoba, S. *et al.* p53 regulates mitochondrial respiration. *Science* **312**, 1650–1653 (2006).
- Rodgers, J. T. *et al.* Nutrient control of glucose homeostasis through a complex of PGC-1 α and SIRT1. *Nature* **434**, 113–118 (2005).
- Chen, W. Y. *et al.* Tumor suppressor HIC1 directly regulates SIRT1 to modulate p53-dependent DNA-damage responses. *Cell* **123**, 437–448 (2005).
- Cheng, H. L. *et al.* Developmental defects and p53 hyperacetylation in Sir2 homolog (SIRT1)-deficient mice. *Proc. Natl Acad. Sci. USA* **100**, 10794–10799 (2003).
- Farazi, P. A. *et al.* Differential impact of telomere dysfunction on initiation and progression of hepatocellular carcinoma. *Cancer Res.* **63**, 5021–5027 (2003).
- Minamishima, Y. A. *et al.* Somatic inactivation of the PHD2 prolyl hydroxylase causes polycythemia and congestive heart failure. *Blood* **111**, 3236–3244 (2008).

Supplementary Information is linked to the online version of the paper at www.nature.com/nature.

Acknowledgements We thank C. Bianchi, J. Moriarty, K. Marmon and E. Thompson for excellent mouse husbandry and care. We are grateful to B. Spiegelman, P. Puigserver, J. E. Dominy and J. L. Estall for providing Ad-PGC-1 α and Ad-GFP virus and helpful comments on the manuscript. We thank G. I. Evan for the p53–ER construct. We appreciate input, critical comments and helpful discussions from many Depinho/Chin lab members, in particular A.-J. Chen, C. Khoo, R. Carrasco, A. Kimmelman, S. Quayle, D. Liu and R. Wiedemeyer. We acknowledge the services of the Mouse Metabolism Cores at Yale (NIH/NIDDK U24 DK-59635) and at Baylor College of Medicine (BCM) and the BCM Diabetes & Endocrinology Research Center (DERC) grant (P30 DK079638). E.S. was supported by the Deutsche Forschungsgemeinschaft and this work and R.A.D. are supported by R01 and U01 grants from the NIH National Cancer Institute and the Robert A. and Renee E. Belfer Foundation. R.A.D. was supported by an Ellison Foundation for Medical Research Senior Scholar and an American Cancer Society Research Professor award. M.L. is a recipient of a postdoctoral fellowship from Fundación Ramón Areces.

Author Contributions E.S. performed all experiments and contributed to echocardiographies (J.M., R.L.), mitochondrial respiration studies (M.L., O.S.S., F.L.M., M.C.). S.C. was involved in microarray analysis and most of other experiments. G.T., R.X. and S.A.S. contributed to microarray analysis. D.K., A.J.F., C.W., M.J. and R.M. advised and helped with transplantation experiments. A.P., E.I., J.E.M., M.K.-A., S.R.P. helped with immunohistochemistry and peptide-nuclei-acid-probes-based fluorescence *in-situ* hybridization (PNA-FISH) studies. R.S.M. and F.F. provided MEFs and helped with MEF studies. R.B. assessed histological slides. E.S.M., T.P.H. and M.G. helped with ChIP experiments. M.G. helped with qPCR experiments. L.C. supervised bioinformatic analysis. L.C. and Y.A.W. helped with writing and contributed intellectually. E.S. and R.A.D. conceived the ideas, designed experiments and wrote the manuscript.

Author Information Reprints and permissions information is available at www.nature.com/reprints. The authors declare no competing financial interests. Readers are welcome to comment on the online version of this article at www.nature.com/nature. Correspondence and requests for materials should be addressed to R.A.D. (ron_depinho@dfci.harvard.edu).

Broad-line active galactic nuclei rotate faster than narrow-line ones

Wolfram Kollatschny¹ & Matthias Zetzl¹

The super-massive black holes of $10^6 M_\odot$ to $10^9 M_\odot$ that reside in the nuclei of active galaxies¹ (AGN) are surrounded by a region emitting broad lines, probably associated with an accretion disk. The diameters of the broad-line regions range from a few light-days to more than a hundred light-days¹, and cannot be resolved spatially. The relative significance of inflow, outflow, rotational or turbulent motions in the broad-line regions as well as their structure (spherical, thin or thick accretion disk) are unknown despite intensive studies over more than thirty years^{2,3}. Here we report a fundamental relation between the observed emission linewidth full-width at half-maximum (FWHM) and the emission line shape $\text{FWHM}/\sigma_{\text{line}}$ in AGN spectra. From this relation we infer that the predominant motion in the broad-line regions is Keplerian rotation in combination with turbulence. The geometry of the inner region varies systematically with the rotation velocity: it is flattest for the fast-rotating broad-line objects, whereas slow-rotating narrow-line AGN have a more spherical structure. Superimposed is the trend that the line-emitting region becomes geometrically thicker towards the centre within individual galaxies. Knowing the rotational velocities, we can derive the central black-hole masses more accurately; they are two to ten times smaller than has been estimated previously.

We investigated in detail the broad optical and ultraviolet emission line profiles of the largest homogeneous data set¹ of reverberation-mapped AGN to learn more about the kinematics and structure of the central broad-line-emitting regions in AGN. Usually the observed broad-line profiles are more or less contaminated by narrow emission lines. We therefore inspected the root-mean-square (r.m.s.) line profiles because they display clean profiles of the variable broad emission lines (the narrow-line profiles disappear in these spectra because they are constant over timescales of years). Broad-line profiles can be parameterized by the ratio of their FWHM to their line dispersion σ_{line} . The relationship between FWHM and σ_{line} gives us information about the shape of the profile. We used all optical and ultraviolet line profiles of the original AGN sample consisting of 37 objects (see Supplementary Table 1).

We generated separated diagrams of the r.m.s. linewidth ratios $\text{FWHM}/\sigma_{\text{line}}$ versus linewidth FWHM as well as $\text{FWHM}/\sigma_{\text{line}}$ versus σ_{line} for all emission lines (H β , H α , He II, C IV...) of the AGN sample. Figures 1 to 3 show the linewidth ratios $\text{FWHM}/\sigma_{\text{line}}$ versus linewidth FWHM for H β , He II $\lambda = 4,686 \text{ \AA}$ and C IV $\lambda = 1,550 \text{ \AA}$. The shape of the line profiles varies systematically with FWHM, but has a different gradient for different emission lines. In an earlier study⁴ the AGN sample¹ was divided into two populations on the basis of their H β line dispersion σ_{line} , with a division line at $\sigma_{\text{line}} = 2,000 \text{ km s}^{-1}$.

In a second step we determined the correlation coefficients between the observed linewidth ratios $\text{FWHM}/\sigma_{\text{line}}$ versus FWHM as well as between $\text{FWHM}/\sigma_{\text{line}}$ versus σ_{line} . Table 1 lists the correlation coefficients r (Pearson, Spearman and Kendall) and the probabilities P for random percentage correlations for H β , He II $\lambda = 4,686 \text{ \AA}$, and C IV $\lambda = 1,550 \text{ \AA}$. In all cases we obtained an even higher correlation coefficient for the linewidth ratio $\text{FWHM}/\sigma_{\text{line}}$ versus FWHM than for $\text{FWHM}/\sigma_{\text{line}}$ versus

σ_{line} . The shape of the line profiles varies systematically with the linewidth, as can be seen in Figs 1 to 3. The broader line profiles become more flat-topped. The relationship between FWHM and σ_{line} gives us information about the shape of the profile: a Gaussian profile has $\text{FWHM}/\sigma_{\text{line}} \approx 2.35$, a rectangular profile has $\text{FWHM}/\sigma_{\text{line}} \approx 3.46$, and the $\text{FWHM}/\sigma_{\text{line}}$ goes to zero for Lorentzian and logarithmic line profiles^{1,4}.

In a third step we tried to model all the observed line profile relations in a simple way using multiple combinations of Gaussian, double-Gaussian, Voigt, Lorentzian, logarithmic and rectangular profiles—but

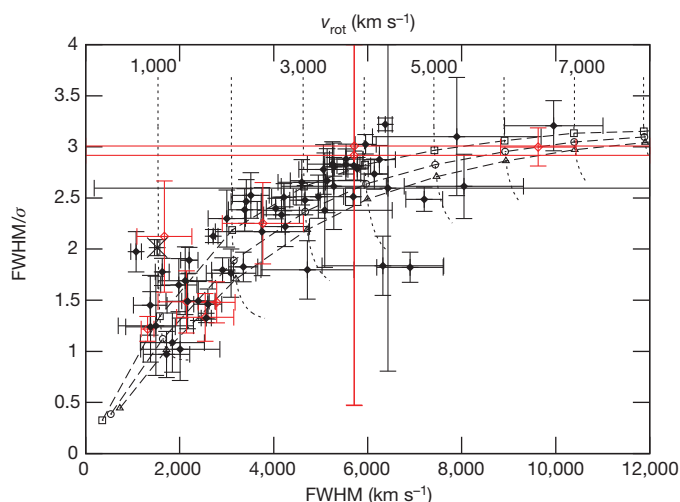


Figure 1 | Observed and modelled H β linewidth ratios $\text{FWHM}/\sigma_{\text{line}}$ versus linewidth FWHM. Observed H β r.m.s. linewidth ratios $\text{FWHM}/\sigma_{\text{line}}$ versus their linewidth FWHMs from our data set (Supplementary Table 1). Measurements that were regarded as being less reliable by the authors¹ (objects with a colon in Supplementary Table 1) are marked by open red diamonds. The linewidth uncertainties are 1σ errors derived from random subsets of N spectra. Details are extensively discussed in the presentation of the original data¹. The dashed curves show theoretical linewidth ratios of rotational line broadened Lorentzian profiles; the FWHMs are 300 km s^{-1} (squares), 500 km s^{-1} (circles) and 700 km s^{-1} (triangles). The associated rotation velocities range from $1,000$ to $8,000 \text{ km s}^{-1}$ (curved dotted lines, from left to right). A few galaxies show smaller linewidth FWHMs than expected for their $\text{FWHM}/\sigma_{\text{line}}$ ratio. Some of these deviations are explainable by orientation effects of the line-emitting accretion disk. It is in accordance with the unified model of AGN that an accretion disk is surrounding the central black hole^{17,18}. An inclined accretion disk leads to smaller linewidths owing to projection effects, while the FWHM/σ ratio remains constant. One of the galaxies showing smaller linewidths than expected is Mrk110 at $\text{FWHM} = 1,521 \text{ km s}^{-1}$ and $\text{FWHM}/\sigma_{\text{line}} = 2.01$ (marked by a cross in Fig. 1). Using independent methods, an inclination of $21 \pm 5^\circ$ has been derived for this galaxy¹⁹. Line-asymmetries also lead to slightly smaller $\text{FWHM}/\sigma_{\text{line}}$ ratios and slightly larger linewidth FWHMs compared to symmetric emission line-profiles. The three outliers showing broader FWHMs than expected (at $\text{FWHM}/\sigma_{\text{line}} \approx 1.8$) are not explainable in a simple way. The broader FWHMs might be caused by geometrical, nonspecific kinematical or optical thickness effects.

¹Institut für Astrophysik, Universität Göttingen, Friedrich-Hund-Platz 1, 37077 Göttingen, Germany.

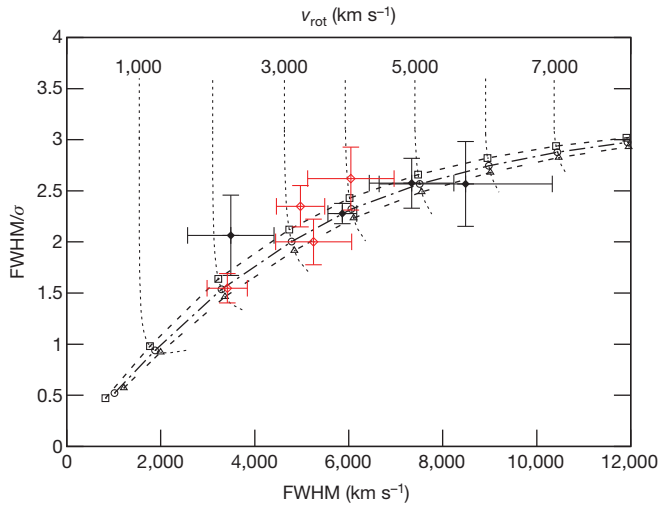


Figure 2 | Observed and modelled He II $\lambda = 4,686 \text{ \AA}$ linewidth ratios $\text{FWHM}/\sigma_{\text{line}}$ versus linewidth FWHM. The observed He II $\lambda = 4,686 \text{ \AA}$ r.m.s. linewidth ratios $\text{FWHM}/\sigma_{\text{line}}$ are shown versus their linewidth FWHMs from our data set. Measurements that were regarded as less reliable by the authors¹ (objects with colon in Supplementary Table 1) are marked by open red diamonds. The linewidth uncertainties are 1σ errors derived from random subsets of N spectra. Details are extensively discussed in the presentation of the original data¹. The dashed curves show theoretical linewidth ratios of rotational line-broadened Lorentzian profiles: the FWHMs are 800 km s^{-1} (squares), $1,000 \text{ km s}^{-1}$ (circles) and $1,200 \text{ km s}^{-1}$ (triangles). The associated rotation velocities range from $1,000$ to $7,000 \text{ km s}^{-1}$ (curved dotted lines, from left to right).

with little success. Supplementary Fig. 1 shows some test calculations. Finally, we made the assumption that all observed shapes of the different line profiles are caused by line broadening due to the rotation of only one intrinsic profile type. We computed the rotational convolution^{5,6} of the various (Gaussian, Lorentzian, Voigt and so on) profiles and

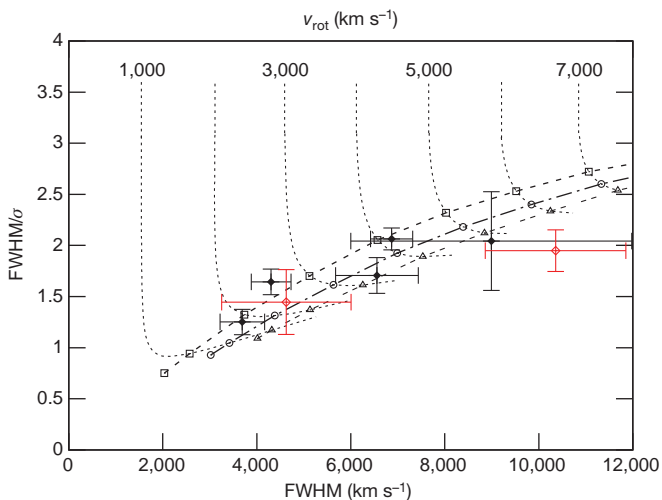


Figure 3 | Observed and modelled C IV $\lambda = 1,550 \text{ \AA}$ linewidth ratios $\text{FWHM}/\sigma_{\text{line}}$ versus linewidth FWHM. The observed C IV $\lambda = 1,550 \text{ \AA}$ r.m.s. linewidth ratios $\text{FWHM}/\sigma_{\text{line}}$ are shown versus their linewidth FWHMs from our data set. Measurements that were regarded as less reliable by the authors¹ (objects with colon in Supplementary Table 1) are marked by open red diamonds. The linewidths uncertainties are 1σ errors derived from random subsets of N spectra. Details are extensively discussed in the presentation of the original data¹. The dashed curves show theoretical linewidth ratios of rotational line-broadened Lorentzian profiles: the FWHMs are $2,000 \text{ km s}^{-1}$ (squares), $3,000 \text{ km s}^{-1}$ (circles) and $4,000 \text{ km s}^{-1}$ (triangles). The associated rotation velocities range from $1,000$ to $7,000 \text{ km s}^{-1}$ (curved dotted lines, from left to right).

Table 1 | Line profile versus linewidth correlations

	r_p	r_s	r_k	P_p	P_s	P_k
H β FWHM/ σ_{line} versus FWHM	0.792	0.823	0.649	6.4×10^{-15}	6.4×10^{-11}	3.5×10^{-14}
H β FWHM/ σ_{line} versus σ_{line}	0.364	0.513	0.350	0.003	4.7×10^{-5}	4.4×10^{-5}
He II FWHM/ σ_{line} versus FWHM	0.803	0.786	0.571	0.016	0.041	0.048
He II FWHM/ σ_{line} versus σ_{line}	0.464	0.357	0.214	0.247	0.361	0.458
C IV FWHM/ σ_{line} versus FWHM	0.821	0.821	0.619	0.023	0.049	0.051
C IV FWHM/ σ_{line} versus σ_{line}	0.599	0.643	0.429	0.155	0.126	0.176

Given are the Pearson correlation coefficient r_p , the Spearman's rank-correlation coefficient r_s , as well as the Kendall correlation coefficient r_k for H β , He II $\lambda = 4,686 \text{ \AA}$ and C IV $\lambda = 1,550 \text{ \AA}$ linewidth ratios $\text{FWHM}/\sigma_{\text{line}}$ versus FWHM as well as $\text{FWHM}/\sigma_{\text{line}}$ versus σ_{line} . P_p , P_s and P_k are the associated percentage probabilities for random correlations^{15,16}. The Pearson correlation coefficient tests a linear relation only, while the other correlation coefficients test for a general monotonic relation.

derived the FWHM and σ_{line} values of these new generated convolved profiles. We considered rotational velocities from 100 km s^{-1} to more than $10,000 \text{ km s}^{-1}$. To derive the σ_{line} values of the Lorentzian, logarithmic and Voigt profiles we integrated over linewidths of $\Delta\nu = \pm 12,335 \text{ km s}^{-1}$, corresponding to $\Delta\lambda = \pm 200 \text{ \AA}$ for H β . Then we derived the best fits for the observed $\text{FWHM}/\sigma_{\text{line}}$ -to-FWHM relations of the individual emission lines by line broadening of Lorentz profiles (see Figs 1 to 3) due to rotation. For the individual emission lines we had to consider different turbulent velocities: they range from $500 \pm 200 \text{ km s}^{-1}$ for H β , to $1,000 \pm 200 \text{ km s}^{-1}$ for He II $\lambda = 4,686 \text{ \AA}$, to $3,000 \pm 1,000 \text{ km s}^{-1}$ for C IV $\lambda = 1,550 \text{ \AA}$. The same turbulent velocity arises in the same individual emission line for all galaxies. The rotation velocities of our AGN broad-line-emitting regions vary from $1,000 \text{ km s}^{-1}$ to $7,000 \text{ km s}^{-1}$.

There are two dominant parameters controlling the line profiles: the rotation of the individual AGN and the turbulent velocity. It is known that the individual emission lines in AGN originate at different distances from the central black hole¹⁷. The typical distance of the H β line-emitting region is 20 light-days, that of the He II $\lambda = 4,686 \text{ \AA}$ line-emitting region is 8.5 light-days and that of the C IV $\lambda = 1,550 \text{ \AA}$ line-emitting region is 6.8–9.5 light-days in NGC5548 only (ref. 8). All these line-emitting regions at different distances from the centre are associated with distinct turbulent velocities.

The shape of line profiles (that is, their FWHM/σ ratio) varies systematically with the linewidth FWHM, as seen in Figs 1 to 3. There is no evidence for two separate existing H β -populations A ($\text{FWHM} \leq 4,000 \text{ km s}^{-1}$) and B ($\text{FWHM} \geq 4,000 \text{ km s}^{-1}$), as proposed earlier^{4,9}. Furthermore, we can assign a dedicated σ value to each FWHM value on the basis of Figs 1 to 3. A few galaxies do not exactly follow the general trend in Fig. 1: they show smaller linewidths FWHM than expected for their $\text{FWHM}/\sigma_{\text{line}}$ ratio. Some of these deviations are easily explained by orientation effects of the line emitting accretion disk. Line asymmetries also lead to slightly smaller $\text{FWHM}/\sigma_{\text{line}}$ ratios and slightly larger linewidth FWHMs compared to symmetric emission line-profiles. There are three outliers showing broader FWHMs than expected, which might be caused by geometrical, nonspecific kinematical or optical thickness effects.

The observed emission linewidths in AGN are the result of line-broadening of Lorentzian profiles due to rotation (Figs 1 to 3). We can allocate to each galaxy a rotational velocity for the individual emission lines based on our calculations. These rotational velocities should be used to calculate the central black-hole masses instead of the observed linewidth FWHM values or σ_{line} . The turbulent velocities and therefore the Lorentzian profiles are different for the different line-emitting regions. If we combined black-hole mass estimates based on the linewidths of different emission lines we would derive different black-hole masses. It has been discussed earlier^{10–12} that the FWHM of the C IV $\lambda = 1,550 \text{ \AA}$ line may not reflect the virial motion of the broad-line

region gas. Therefore, black-hole mass estimates based on the widths of the C IV $\lambda = 1,550 \text{ \AA}$ line might overestimate the black-hole masses. This is a particular problem for the high-redshift and more distant objects because in these galaxies only the redshifted C IV $\lambda = 1,550 \text{ \AA}$ line can be used to estimate the black-hole masses. Here we show that the C IV $\lambda = 1,550 \text{ \AA}$ line is broader in comparison to the H β line simply because of the convolution with a broader Lorentzian profile. By comparing the black-hole masses of the distant galaxies (based on the C IV line) with the black-hole masses of nearby AGN (based on the H β line) we overestimate the black-hole masses of high-redshift, high-luminosity AGNs. The black-hole masses have been overestimated by a factor of two to ten. This effect has to be considered in future investigations.

It has been shown in early studies of accretion disks¹³ that the ratio of their height H with respect to their radius R is proportional to their turbulence velocity v_{turb} with respect to their rotational velocity v_{rot} :

$$H/R = (1/\alpha)(v_{\text{turb}}/v_{\text{rot}}) \quad (1)$$

The parameter α is the unknown viscosity parameter. We assume that α is constant. The ratio of the turbulence velocity v_{turb} with respect to the rotational velocity v_{rot} is increasing with decreasing linewidth FWHM for the specific galaxies (Figs 1 to 3). This indicates that the geometrical thickness of the accretion disks is flattest for the broad-line objects, whereas the narrow-line objects have a more spherical structure. In this spirit, different geometries might be responsible for the Eigenvector 1 correlations¹⁴ between linewidth, strong Fe II emission and soft X-ray excess. It has been shown¹⁴ that the population B objects (FWHM $\geq 4,000 \text{ km s}^{-1}$) are more strongly correlated with radio-loud galaxies. This means that the radio-loudness is correlated with a higher rotation-velocity of the broad-line region. We simultaneously determined v_{turb} as well as the v_{rot} of the H β and C IV $\lambda = 1,550 \text{ \AA}$ lines for three galaxies in our sample (NGC5548, NGC7469, 3C390.9). The ratio of turbulent velocity with respect to rotational velocity is always higher for the C IV $\lambda = 1,550 \text{ \AA}$ line than for the H β line in these galaxies. This means that in individual galaxies the line-emitting region of the accretion disks becomes geometrically thicker towards the centre, under the realistic prerequisite that the C IV $\lambda = 1,550 \text{ \AA}$ line originates closer to the centre than does the H β line.

Received 26 August; accepted 17 December 2010.

1. Peterson, B. M. *et al.* Central masses and broad-line region sizes of active galactic nuclei. II: A homogeneous analysis of a large reverberation-mapping database. *Astrophys. J.* **613**, 682–699 (2004).

2. Blumenthal, G. R., & Mathews, W. G. Theoretical emission line profiles in QSOs and Seyfert galaxies. *Astrophys. J.* **198**, 517–526 (1975).
3. Sulentic, J. W., Marziani, P. & Dultzin-Hacyan, D. Phenomenology of broad emission lines in active galactic nuclei. *Annu. Rev. Astron. Astrophys.* **38**, 521–571 (2000).
4. Collin, S., Kawaguchi, T., Peterson, B. M. & Vestergaard, M. Systematic effects in measurement of black hole masses by emission-line reverberation of active galactic nuclei: Eddington ratio and inclination. *Astron. Astrophys.* **456**, 75–90 (2006).
5. Hubeny, I., Stefl, S. & Harmonec, P. How strong is the evidence of superionization and large mass outflows in B/Be stars? *Bull. Astron. Inst. Czech.* **36**, 214–230 (1985).
6. Hubeny, I., Lanz, T. & Jeffrey, C. S. in *Newsletter on Analysis of Astronomical Spectra No. 20* (ed. Jeffrey, C. S.) 30–42 (St Andrews University, 1994).
7. Kollatschny, W. Accretion disk wind in the AGN broad-line region: spectroscopically resolved line profile variations in Mrk 110. *Astron. Astrophys.* **407**, 461–472 (2003).
8. Peterson, B. M. & Wandel, A. Keplerian motion of broad-line region gas as evidence for supermassive black holes in active galactic nuclei. *Astrophys. J.* **521**, L95–L98 (1999).
9. Sulentic, J. W., Zwitter, T., Marziani, P. & Dultzin-Hacyan, D. Eigenvector 1: an optimal correlation space for active galactic nuclei. *Astrophys. J.* **536**, L5–L9 (2000).
10. Netzer, H. The largest black holes and the most luminous galaxies. *Astrophys. J.* **583**, L5–L8 (2003).
11. Netzer, H. *et al.* Black hole mass and growth rate at high redshift. *Astrophys. J.* **671**, 1256–1263 (2007).
12. Baskin, A. & Laor, A. What controls the CIV line profile in active galactic nuclei? *Mon. Not. R. Astron. Soc.* **356**, 1029–1044 (2005).
13. Pringle, J. E. Accretion discs in astrophysics. *Annu. Rev. Astron. Astrophys.* **19**, 137–160 (1981).
14. Zampieri, S., Sulentic, J. W., Marziani, P. & Dultzin, D. Detailed characterization of H β emission line profile in low- z SDSS quasars. *Mon. Not. R. Astron. Soc.* **403**, 1759–1786 (2010).
15. Bevington, P. R. & Robinson, D. K. *Data Reduction and Error Analysis* 2nd edn (McGraw-Hill, 1992).
16. Press, W. H., Teukolsky, S. A., Vetterling, W. T. & Flannery, B. P. *Numerical Recipes* 2nd edn (Cambridge University Press, 1992).
17. Blandford, R. D. Physical processes in active galactic nuclei. *Saas-Fee Adv. Courses* **20**, 161–275 (1990).
18. Elvis, M. A structure for quasars. *Astrophys. J.* **545**, 63–76 (2000).
19. Kollatschny, W. Spin orientation of supermassive black holes in active galaxies. *Astron. Astrophys.* **412**, L61–L64 (2003).

Supplementary Information is linked to the online version of the paper at www.nature.com/nature.

Acknowledgements We acknowledge discussions with W. Glatzel and S. Dreizler. This work has been supported by the Niedersachsen-Israel Research Cooperation Program ZN2318.

Author Contributions W.K. had the basic ideas. M.Z. made the detailed model calculations. Both authors discussed the results at length.

Author Information Reprints and permissions information is available at www.nature.com/reprints. The authors declare no competing financial interests. Readers are welcome to comment on the online version of this article at www.nature.com/nature. Correspondence and requests for materials should be addressed to W.K. (wkollat@astro.physik.uni-goettingen.de).

A terahertz metamaterial with unnaturally high refractive index

Muhan Choi^{1†*}, Seung Hoon Lee^{1*}, Yushin Kim¹, Seung Beom Kang², Jonghwa Shin³, Min Hwan Kwak², Kwang-Young Kang², Yong-Hee Lee³, Namkyoo Park⁴ & Bumki Min¹

Controlling the electromagnetic properties of materials, going beyond the limit that is attainable with naturally existing substances, has become a reality with the advent of metamaterials^{1–3}. The range of various structured artificial ‘atoms’ has promised a vast variety of otherwise unexpected physical phenomena^{3–17}, among which the experimental realization of a negative refractive index has been one of the main foci thus far. Expanding the refractive index into a high positive regime will complete the spectrum of achievable refractive index and provide more design flexibility for transformation optics^{9–14}. Naturally existing transparent materials possess small positive indices of refraction, except for a few semiconductors and insulators, such as lead sulphide or strontium titanate, that exhibit a rather high peak refractive index at mid- and far-infrared frequencies¹⁸. Previous approaches using metamaterials were not successful in realizing broadband high refractive indices^{19–21}. A broadband high-refractive-index metamaterial structure was theoretically investigated only recently²², but the proposed structure does not lend itself to easy implementation. Here we demonstrate that a broadband, extremely high index of refraction can be realized from large-area, free-standing, flexible terahertz metamaterials composed of strongly coupled unit cells. By drastically increasing the effective permittivity through strong capacitive coupling and decreasing the diamagnetic response with a thin metallic structure in the unit cell, a peak refractive index of 38.6 along with a low-frequency quasi-static value of over 20 were experimentally realized for a single-layer terahertz metamaterial, while maintaining low losses. As a natural extension of these single-layer metamaterials, we fabricated quasi-three-dimensional high-refractive-index metamaterials, and obtained a maximum bulk refractive index of 33.2 along with a value of around 8 at the quasi-static limit.

According to the Maxwellian macroscopic description, the effective relative permittivity of an artificial medium can be written as $\epsilon = 1 + (P/\epsilon_0 E)$ and the effective relative permeability can be defined by $\mu = 1 + (M/H)$, where E , H , P and M denote electric field, magnetizing field, polarization and magnetization, respectively. In order to tailor the value of the refractive index by controlling the degree of polarization and magnetization, we used a strongly coupled, thin ‘T’-shaped metallic patch to maximize the effective permittivity ϵ while suppressing the diamagnetic effect. A similar ‘T’-shaped patch structure in the weakly and moderately coupled regimes has been used to provide the index variations required for broadband ground-plane cloaking in the microwave frequency bands¹².

The basic building block (single-layer unit cell) of the proposed high-refractive-index terahertz metamaterial is shown in Fig. 1a, together with the polarization of an incident terahertz wave. (In Supplementary Information we describe the polarization dependence of this system. We note that two-dimensionally isotropic high-index

metamaterials can be designed; the results are given in Supplementary Information.) Here, the substrate is made from a dielectric material and the thin ‘T’-shaped metallic patch is embedded symmetrically in the substrate. Throughout this work, the substrate was implemented with polyimide (real part of the refractive index n , $\text{Re}(n)$, is 1.8) and the metals used to construct the metamaterials were gold (on chromium) or aluminium (see Methods Summary). Optical micrographs of the fabricated large-area (2×2 cm), free-standing, flexible metamaterials are shown in Fig. 1b. Precise alignment between stacked metamaterial layers has been achieved, as can be confirmed by the higher-magnification microscope images shown in the upper insets of Fig. 1b. As the substrate is made from flexible polyimide, the fabricated metamaterials are also extremely flexible, and the samples are perfectly free-standing (lower inset of Fig. 1b).

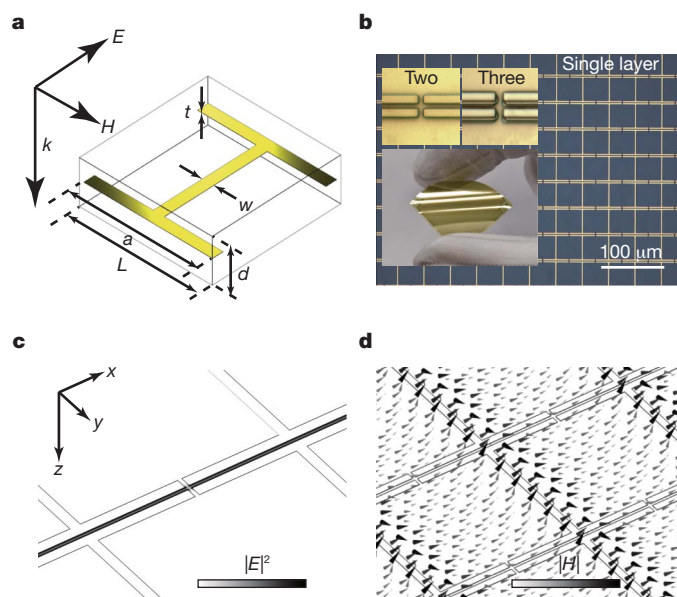


Figure 1 | Schematic view of the high-index metamaterials and images of the fabricated metamaterials. **a**, Unit cell structure of the high-index metamaterial, made of a thin ‘T’-shaped metallic patch symmetrically embedded in a dielectric material. The incident terahertz wave is directed downwards, with the polarization of the wave indicated by the arrows. **b**, Optical micrograph of fabricated single-layer metamaterial. Top insets, higher-magnification micrographs, showing the alignment of constituent metamaterial layers for double- and triple-layer metamaterials. Bottom inset, photograph of a flexibility test for the fabricated metamaterials. **c**, Saturated electric field (at 0.33 THz) for a single-layer metamaterial with a unit cell of $L = 60 \mu\text{m}$, $a = 58.8 \mu\text{m}$, $d = 2.45 \mu\text{m}$, and $w = 3 \mu\text{m}$. Shading indicates modulus of field to the power two. **d**, Vector plot of the magnetic field (at 0.33 THz) in the unit cells. Shading indicates modulus of field.

¹Department of Mechanical Engineering, Korea Advanced Institute of Science and Technology (KAIST), Daejeon 305-751, South Korea. ²Convergence Components and Materials Research Laboratory, Electronics and Telecommunications Research Institute (ETRI), Daejeon 305-700, South Korea. ³Department of Physics, Korea Advanced Institute of Science and Technology (KAIST), Daejeon 305-751, South Korea. ⁴School of Electrical Engineering and Computer Science, Seoul National University, Seoul 151-744, South Korea. [†]Present address: Convergence Components and Materials Research Laboratory, Electronics and Telecommunications Research Institute (ETRI), Daejeon 305-700, South Korea.

*These authors contributed equally to this work.

The gap width (defined by $g = L - a$; see Fig. 1a for details) plays a crucial role in raising the effective permittivity. For the thin 'T'-shaped metallic patch structure, the scaling of the charge accumulation and effective permittivity shows different asymptotic behaviours depending on the gap width, leading to weakly coupled ($g/L \lesssim 1$) and strongly coupled ($g/L \ll 1$) regimes. In the strongly coupled regime, a large amount of surface charge is accumulated on each arm of the metallic patch capacitor as the charges in each arm interact with opposite charges in close proximity across the gap. Charge accumulation on the edge of the metallic patch leads to an extremely large dipole moment in the unit cell, as the accumulated charge is inversely proportional to the gap width in the strongly coupled regime ($Q \propto L^3 g^{-1}$). This extreme charge accumulation contributes to a huge dipole moment inside the unit cell (or a large polarization density) and ultimately leads to a large effective permittivity. The behaviour of the charge accumulation differs significantly in the weakly coupled regime, in which the amount of charge increases quadratically with decreasing gap width ($Q \propto (L - g)^2$) in the quasi-static limit (Supplementary Information).

Although decreasing the gap width can enhance the effective permittivity, it is still necessary to suppress the diamagnetic effect to realize a high refractive index. A thin 'T'-shaped metallic structure can provide a pathway to effectively reduce the diamagnetic effect, as a thin 'T'-shaped patch has a small area subtended by the current loops²² (Supplementary Information). To put this theoretical argument into practice, all the metamaterial samples used in this work featured thin metallic structures, the thicknesses of which were of the order of a skin depth (less than 100 nm) in the terahertz frequency range. To confirm the physical origin of the high refractive index with the aforementioned approach, the electric and magnetic field around the metallic patch in the unit cells of a single-layer metamaterial were calculated for a frequency of 0.33 THz (Fig. 1c, d). As described above, the electric field was strongly concentrated in the gap and the magnetic field penetrated deeply into the unit cell because of the negligible metallic volume fraction (Supplementary Information).

In order to quantify the effect of extremely large dipole moments and weak diamagnetism associated with the proposed metamaterials, an effective parameter retrieving method was used to extract relevant material parameters, such as refractive index n and impedance z (or equivalently, the effective permittivity $\epsilon = nz_0/z$ and the permeability $\mu = nz/z_0$, where z_0 is the impedance of free space) from the scattering parameters²³ (S parameters). As can be confirmed from Fig. 2a, a strong electrical resonance was observed with a peak relative permittivity of 583 at a frequency of 0.504 THz and of 122 at the quasi-static limit; these values are remarkably higher than those of bare polyimide films²⁴ ($\text{Re}(\epsilon) \approx 3.24$). The magnetic permeability, however, remained near unity over the whole frequency domain, except near the frequency of the electric resonance, where a weak magnetic anti-resonance accompanying the strong electrical resonance was observed²⁵. By virtue of this extreme enhancement of permittivity along with the suppression of diamagnetism, a peak index of refraction of $n = 27.25$ at 0.516 THz was predicted, along with a value of $n = 11.1$ at the quasi-static limit. This unprecedented 'amplification' of refractive index relative to that of a host dielectric material shows the efficacy of employing strongly polarizable and weakly diamagnetic metallic patches. Considering the effective wavelength of a terahertz wave inside the metamaterial, the thickness ($d = 2.45 \mu\text{m}$) in the direction of propagation is much smaller than the effective wavelength ($d \leq 0.12\lambda/n$), which justifies the application of homogenization theory^{2,3} and the effective parameter descriptions. For the assignment of effective refractive indices to the single-layer metamaterial, we have used the physical thickness for consistent estimation of all effective parameters in the retrieval method. However, actual effective refractive index is slightly lower than the index acquired with physical thickness, as effective thickness should be introduced to account for the effect of mode decay in a single-layer metamaterial (Methods).

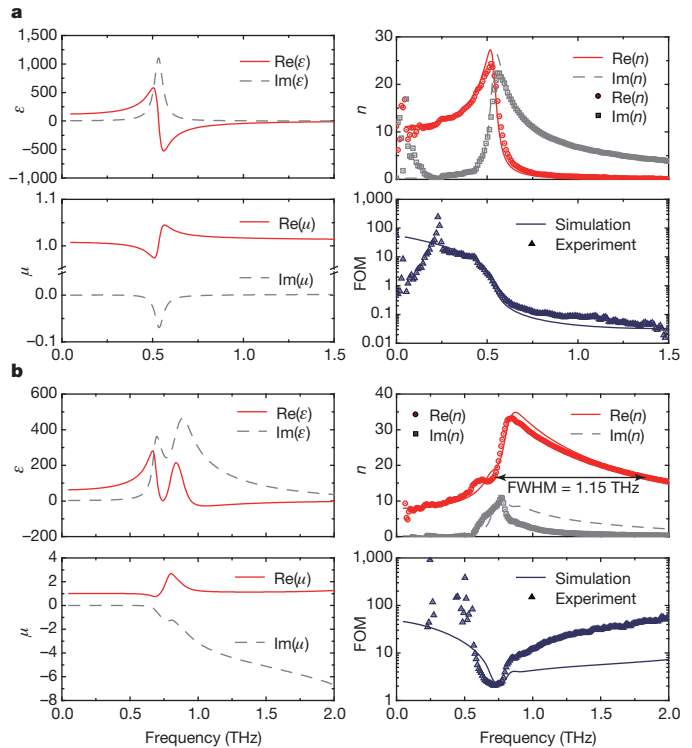


Figure 2 | Extracted effective permittivity, permeability, refractive index and figure of merit for high-index metamaterials. **a**, Effective permittivity (ϵ , top left) and permeability (μ , bottom left) extracted from the characterization of a single-layer metamaterial unit cell. Experimentally obtained complex refractive index (n) is shown top right, along with the corresponding numerically extracted values from the S-parameter retrieval method. Bottom right, the experimental figure of merit (FOM) together with the numerically obtained values. Geometrical parameters of the unit cell are the same as those used for the simulation performed for Fig. 1c and d. In the plots, data points and lines are used for the experimental and numerical data, respectively. **b**, As **a** but for a five-layer metamaterial. Here, the gap width g is set to $1.5 \mu\text{m}$, the length of a unit cell L is $40 \mu\text{m}$, the width of metallic structure w is $3 \mu\text{m}$, and the thickness d of the unit cell is $1.62 \mu\text{m}$ with an additional polyimide layer of $\sim 0.8 \mu\text{m}$ on both the top and bottom of the fabricated metamaterials.

To experimentally probe the enhancement of the effective refractive index, terahertz time-domain spectroscopy²⁶ (THz-TDS) was performed for a frequency range of 0.1–2 THz. All the samples were prepared with conventional micro/nano-fabrication processes (see Methods Summary). For reliable extraction of the complex refractive index from the THz-TDS experiments, an iterative algorithm considering multi-pass transmission through the sample was applied to the field transmission data (Methods)²⁷. Next, the complex refractive indices extracted from the THz-TDS measurements were compared with the numerically obtained refractive indices from the S-parameter extraction methods (Fig. 2a). Considering the uncertainties in the material parameters used for the simulation and the errors in the gap-width measurements, the experimentally acquired complex refractive index was in excellent agreement with the simulated refractive index. From the characterization of the single-layer metamaterial, a peak refractive index of $n = 24.34$ at 0.522 THz was observed, with a value of $n = 11.18$ at the quasi-static limit. The loss associated with the single-layer metamaterial is quantified by the figure of merit ($\text{FOM} = \text{Re}(n)/\text{Im}(n)$); experimental and numerical values of FOM are plotted in the bottom-right panel of Fig. 2a. For most frequency ranges, especially in the lower portion below the electric resonance, the FOM stays above 10, with a peak value exceeding 100.

Although the possibility of raising the refractive index has been experimentally demonstrated for single-layer metamaterials, further insights can be acquired with an investigation into three-dimensional

high-index metamaterials. In order to investigate the bulk properties, quasi-three-dimensional high-index metamaterials containing up to five layers were fabricated and tested. The measured complex refractive index and FOM are plotted in Fig. 2b, along with the corresponding numerically extracted parameters for this five-layer high-index metamaterial with small interlayer spacing ($d = 1.62 \mu\text{m}$). From the THz-TDS measurements and subsequent parameter extraction, the highest index of refraction of 33.22 is obtained at a frequency of 0.851 THz. Interestingly, the refractive index does not fall sharply at higher frequencies, and shows an extremely broadband high refractive index with a full-width at half-maximum (FWHM) of 1.15 THz. Although all of the effective refractive indices are given here for normal incidence, we have found that the high-index metamaterials are quite robust to incidence angle variations. This robustness has its origin in the weak dependence of effective permeability on the direction of incident magnetizing field (Supplementary Information).

The presence of coupling between layers of quasi-three-dimensional metamaterials leads to substantial differences in the refractive index and the transmission spectra when compared to single-layer metamaterials²⁸. To better understand the influence of the number of layers (N) on the optical characteristics, we analysed the band structure and plotted the dispersion relation (Fig. 3b). The thickness of the unit cell ($d = 12.2 \mu\text{m}$) was intentionally increased relative to those of the samples designed for high refractive index so that the interlayer coupling and the changes in the corresponding transmission spectra could be clearly investigated. The band structure is indicative of the limiting case of perfectly periodic metamaterials in the z -direction. In conjunction with the effective parameter description, the bandgap between 0.833 and 1.734 THz corresponds to the negative effective permittivity regime. As clearly shown in Fig. 3a, the transmission corresponding to these bandgap frequencies is gradually lowered as the number of layers is increased, which is indicative of a progressive bandgap formation. In addition to this bandgap formation, transmission peaks appear in the spectra, which can be interpreted several ways^{28,29}. From a homogeneous slab description, the metamaterial can be treated as a Fabry–Pérot etalon. The round trip phase delay should be a non-negative

integer multiple of 2π and the transmission of the slab is maximized under the condition $f_p = pc/2nNd$, where f_p denotes the frequency of the transmission peak, p is a non-negative integer and c is the speed of light. From a microscopic point of view, the transmission peaks originate from the Bloch-like modes that are phase-matched to the Fabry–Pérot resonance of the metamaterial slab. For example, the single transmission peak observed in the double-layer metamaterial corresponds to the Bloch mode that has a normalized wavenumber of $1/2 \times \pi/d$. Generalized to the samples with larger numbers of layers (Fig. 3a), the transmitting modes correspond to the Bloch modes having a wavenumber of $p/N \times \pi/d$, where $p = 0, \dots, N - 1$.

The value of the refractive index is a sensitive function of the gap width for the proposed high-index metamaterials. Bearing this in mind, the question of the positive limit of a physically achievable refractive index naturally arises. To experimentally approach this limit, we measured the refractive index of metamaterials having gap widths from 80 nm to 30 μm . Figure 4a shows the measured and numerically estimated indices of refraction as a function of the gap width (top panel, peak index and the index at the quasi-static limit; bottom panel, peak index frequency). Theoretical refractive indices obtained from an empirical asymptotic formula are also plotted for the quasi-static limit (see Supplementary Information for the asymptotic formula and its limitations). The numerically estimated index is 26.6 at the quasi-static limit and increases to 54.87 at 0.315 THz for the sample with 80 nm gap width (the experimentally measured value was greater than 20 at the quasi-static limit and 38.64 at its peak; Fig 4b and c). In the weakly coupled regime, the capacitive coupling between unit cells is negligible so that the refractive index can be approximated as

$$n \approx n_p \left\{ 1 + \frac{\pi\alpha L}{2\sqrt{2}d} \left(1 - \frac{g}{L} \right)^3 + \frac{\pi\alpha\beta L}{2\sqrt{2}d} \left(1 - \frac{g}{L} \right)^4 \right\}$$

where α and β are dimensionless fitting parameters. However, as the gap width decreases, the capacitive effect due to coupling between unit cells becomes dominant. As a result, the index of refraction is drastically increased, with a dominant term proportional to the inverse $(1 - \beta)/2$ -th power of the gap width, $n \propto n_p \alpha^{1/2} d^{-1/2} L^{(2-\beta)/2} g^{-(1-\beta)/2}$, to the

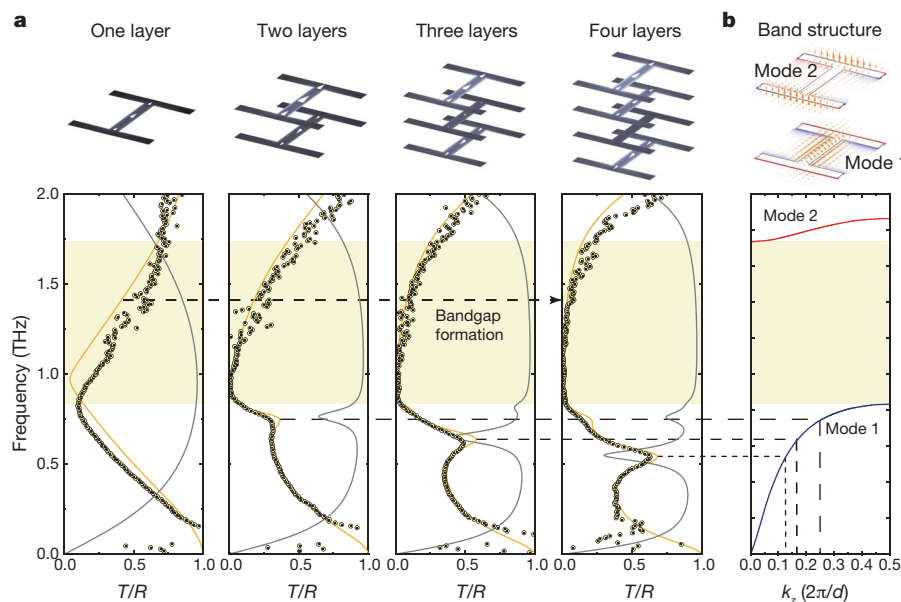


Figure 3 | Transmission/reflection spectra of multilayer metamaterials and the band structure. **a**, Main panels, transmission (T) and reflection (R) spectra for (left to right) single-, double-, triple- and quadruple-layer metamaterials. Here, the gap width g is set to $1.725 \mu\text{m}$, the length of unit cell L is $40 \mu\text{m}$, the width of the metallic structure w is $5 \mu\text{m}$, and the thickness d of the unit cell is $12.2 \mu\text{m}$ for the simulations. In the transmission spectra measured for these multilayer metamaterials, shading corresponding to the bandgap frequencies (in

Fig. 3b) is overlaid to show the progressive bandgap (rejection band) formation. Data points, experimental transmission; grey and orange lines, numerically calculated reflection and transmission, respectively. Top panels, the magnitude (colour map) and direction (arrow) of current density flowing in each layer for the corresponding metamaterial. **b**, Main panel, band structure calculated for the unit cell of the metamaterial. Top panel, corresponding electric (colour map) and magnetic field (arrow) profiles of band edge modes 1 and 2.

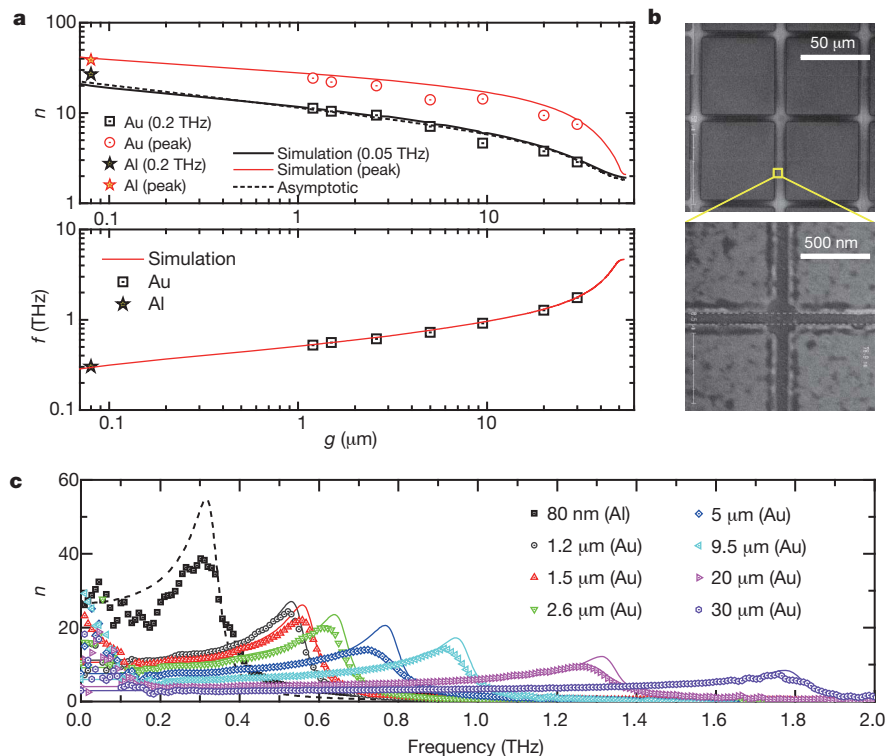


Figure 4 | Effective refractive index and peak index frequency as a function of the gap width for a single-layer metamaterial. **a**, Top, experimentally obtained refractive index n as a function of the gap width g . The quasi-static limits (near 0.2 THz) and the peak indices are plotted along with asymptotic and numerical values. Here, metamaterials are composed of a unit cell with $L = 60 \mu\text{m}$, $d = 2.45 \mu\text{m}$ and $w = 3 \mu\text{m}$. Data points and lines show

experimental and simulation data, respectively. Bottom, frequencies f of peak refractive index are plotted as a function of the gap width, along with simulated values. **b**, Scanning electron micrographs of a nanogap ($\sim 80 \text{ nm}$) high-index metamaterial ($d = 1.24 \mu\text{m}$). The metal used to define the metallic patch is aluminium (Al) for this specific sample. **c**, Frequency dependent effective refractive indices of single-layer metamaterials with varying gap widths.

first order (provided that the gap width is larger than the metal thickness). Furthermore, once the gap width becomes smaller than the thickness of the metallic patch, the effective refractive index will increase even faster as the parallel plate capacitor regime is reached ($n \propto n_p(t/g)^{1/2}$, see Supplementary Information). Therefore, it should be possible to achieve an even higher index of refraction by further reducing the gap width (g) or the spacing (d) between each metamaterial layer. As the gap closes, this increase is expected to continue until the gap width approaches the Thomas–Fermi length scale³⁰ or the quantum tunnelling scale of electrons. In addition to this gap width control, it is worth noting that the effective refractive index is proportional to the substrate index; thus, the introduction of a higher-index substrate (such as lead sulphide or strontium titanate) will lead to greater amplification of the refractive index and an unprecedentedly large effective refractive index.

The artificial high-refractive-index material demonstrated here can extend the spectrum of indices further into the positive regime and broaden the realm of metamaterials having the previously demonstrated negative index^{3–8}, although we note that enhancement of the value of the negative index is still much in demand. In particular, high-index metamaterials, owing to the rapid phase advance associated with them, could be an ideal starting point for development of subwavelength-scale functional devices; such devices include small-footprint cloaking devices, wide-angle metamaterial lenses, compact cavity resonators and broadband slow light devices. The operating principles of high-index metamaterials are universal and can be extended to even lower frequency ranges, such as microwaves and radio frequencies, as well as to near-infrared or visible frequencies once the difficulties in fabrication have been resolved.

METHODS SUMMARY

Fabrication processes for micrometre-gap metamaterials. Fabrication of multilayered flexible terahertz metamaterials started with a bare silicon substrate as a

sacrificial wafer. A polyimide solution (PI-2610, HD Microsystems) was spin-coated onto the substrate and baked at 180°C in a convection oven for 30 min as a flexible metamaterial substrate. The curing process of the polyimide layers was conducted at 350°C using an open-ended quartz tube furnace under an inert atmosphere to convert the polyamic acid into a fully aromatic and insoluble polyimide. A negative photoresist (AZnLOF2035, AZ Electronic Materials) was spin-coated and patterned using conventional photolithography. Au/Cr (90 nm/10 nm) was then evaporated and patterned as ‘T’-shaped array structures via the lift-off technique. Repeating the polyimide coating and curing processes, single-layered metamaterials were fabricated. Multilayered metamaterials on the silicon substrate were obtained by repeating the above single-layer processes until the desired number of metamaterial layers was stacked. Finally, the flexible terahertz metamaterials were fabricated by peeling off the metamaterial layers from the silicon substrate. The dimensions of the micrometre-gap metamaterials were estimated by optical microscopy, stylus profiler, and 3D profiler.

Fabrication processes for nano-gap metamaterial. Nano-gap flexible terahertz metamaterials were fabricated using the same process for the micrometre-gap metamaterials except for the nano-gap patterning process, which used electron beam lithography and consecutive metal etching. Thin aluminium film was evaporated onto the polyimide coated silicon substrate and patterned as a connected ‘T’-shaped patch structure using the lift-off technique. Etching windows for 80-nm gaps were opened using large area electron beam lithography. An ‘T’-shaped aluminium beam array was patterned by RIE (reactive ion etching) using an electron beam resist mask (ZEP520A, ZEON Corporation). After removing the residual resist and after the polyimide coating process, the nano-gap terahertz metamaterials were fabricated on the silicon sacrificial substrate.

Full Methods and any associated references are available in the online version of the paper at www.nature.com/nature.

Received 25 August; accepted 13 December 2010.

1. Veselago, V. G. The electrodynamics of substances with simultaneously negative values of ϵ and μ . *Sov. Phys. Usp.* **10**, 509–514 (1968).
2. Pendry, J. B., Holden, A. J., Robbins, D. J. & Stewart, W. J. Magnetism from conductors and enhanced nonlinear phenomena. *IEEE Trans. Microwave Theory Tech.* **47**, 2075–2084 (1999).

3. Smith, D. R., Padilla, J. W., Vier, D. C., Nemat-Nasser, S. C. & Schultz, S. Composite medium with simultaneously negative permeability and permittivity. *Phys. Rev. Lett.* **84**, 4184–4187 (2000).
4. Shelby, R. A., Smith, D. R. & Schultz, S. Experimental verification of a negative index of refraction. *Science* **292**, 77–79 (2001).
5. Eleftheriades, G. V., Iyer, A. K. & Kremer, P. C. Planar negative refractive index media using periodically L-C loaded transmission lines. *IEEE Trans. Microwave Theory Tech.* **50**, 2702–2712 (2002).
6. Xiao, S. *et al.* Loss-free and active optical negative-index metamaterials. *Nature* **466**, 735–738 (2010).
7. Valentine, J. *et al.* Three-dimensional optical metamaterial with a negative refractive index. *Nature* **455**, 376–379 (2008).
8. Zhang, S. *et al.* Negative refractive index in chiral metamaterials. *Phys. Rev. Lett.* **102**, 023901 (2009).
9. Pendry, J. B., Schurig, D. E. & Smith, D. R. Controlling electromagnetic fields. *Science* **312**, 1780–1782 (2006).
10. Schurig, D. *et al.* Metamaterial electromagnetic cloak at microwave frequencies. *Science* **314**, 977–980 (2006).
11. Cai, W. S., Chettiar, U. K., Kildishev, A. V. & Shalaev, V. M. Optical cloaking with metamaterials. *Nature Photon.* **1**, 224–227 (2007).
12. Liu, R. *et al.* Broadband ground-plane cloak. *Science* **323**, 366–369 (2009).
13. Valentine, J., Li, J. S., Zentgraf, T., Bartal, G. & Zhang, X. An optical cloak made of dielectrics. *Nature Mater.* **8**, 568–571 (2009).
14. Gabrielli, L. H., Cardenas, J., Poitras, C. B. & Lipson, M. Silicon nanostructure cloak operating at optical frequencies. *Nature Photon.* **3**, 461–463 (2009).
15. Pendry, J. B. Negative refraction makes a perfect lens. *Phys. Rev. Lett.* **85**, 3966–3969 (2000).
16. Liu, Z., Lee, H., Xiong, Y., Sun, C. & Zhang, X. Far-field optical hyperlens magnifying sub-diffraction-limited objects. *Science* **315**, 1686 (2007).
17. Smolyaninov, I. I., Hung, Y. J. & Davis, C. C. Magnifying superlens in the visible frequency range. *Science* **315**, 1699–1701 (2007).
18. Palik, E. D. *Handbook of Optical Constants of Solids* (Academic, 1998).
19. Enkrich, C. *et al.* Magnetic metamaterials at telecommunication and visible frequencies. *Phys. Rev. Lett.* **95**, 203901 (2005).
20. Sievenpiper, D. F. *et al.* 3D metallo-dielectric photonic crystals with strong capacitive coupling between metallic islands. *Phys. Rev. Lett.* **80**, 2829–2832 (1998).
21. Shen, J. T., Catrysse, P. B. & Fan, S. Mechanism for designing metallic metamaterials with a high index of refraction. *Phys. Rev. Lett.* **94**, 197401 (2005).
22. Shin, J., Shen, J. T. & Fan, S. Three-dimensional metamaterials with an ultrahigh effective refractive index over a broad bandwidth. *Phys. Rev. Lett.* **102**, 093903 (2009).
23. Smith, D. R., Vier, D. C., Koschny, Th & Soukoulis, C. M. Electromagnetic parameter retrieval from inhomogeneous metamaterials. *Phys. Rev. E* **71**, 036617 (2005).
24. Tao, H. *et al.* Terahertz metamaterials on free-standing highly-flexible polyimide substrates. *J. Phys. D Appl. Phys.* **41**, 232004 (2008).
25. Liu, R., Cui, T. J., Huang, D., Zhao, B. & Smith, D. R. Description and explanation of electromagnetic behaviors in artificial metamaterials based on effective medium theory. *Phys. Rev. E* **76**, 026606 (2007).
26. Ferguson, B. & Zhang, X. C. Materials for terahertz science and technology. *Nature Mater.* **1**, 26–33 (2002).
27. Duvillaret, L., Garet, F. & Coutaz, J. L. A reliable method for extraction of material parameters in terahertz time-domain spectroscopy. *IEEE J. Sel. Top. Quantum Electron.* **2**, 739–746 (1996).
28. Liu, N. & Giessen, H. Three-dimensional optical metamaterials as model systems for longitudinal and transverse magnetic coupling. *Opt. Express* **16**, 21233–21238 (2008).
29. Papasimakis, N. *et al.* Metamaterial analog of electromagnetically induced transparency. *Phys. Rev. Lett.* **101**, 253903 (2008).
30. Seo, M. A. *et al.* Terahertz field enhancement by a metallic nano slit operating beyond the skin-depth limit. *Nature Photon.* **3**, 152–156 (2009).

Supplementary Information is linked to the online version of the paper at www.nature.com/nature.

Acknowledgements We thank B. Kang for help in the fabrication of micrometre-gap metamaterials, J. S. Chang for proofreading the manuscript before submission, and D. S. Kim for discussions. This work was supported by National Research Foundation of Korea grants funded by the Korean government (numbers 2009-0069459, 2008-0062235 and 2010-0012058). K.-Y.K. acknowledges support by the IT Research and Development programme of MKE/KEIT (number 2006-S-005-04). Y.-H.L. acknowledges support from the National Research Foundation of Korea (number 2007-0093863) and N.P. acknowledges support from National Research Foundation (numbers GRL K20815000003 and 2010-0001859), funded by the Korean government.

Author Contributions M.C. and Y.K. performed the numerical simulations. S.H.L. fabricated micro/nano-gap metamaterial samples. S.B.K., M.H.K. and K.-Y.K. conducted THz-TDs experiments. M.C., S.H.L., Y.K., J.S. and B.M. analysed numerical and experimental data. M.C., S.H.L., Y.K., J.S., Y.-H.L., N.P. and B.M. discussed the results. M.C., J.S., Y.-H.L., N.P. and B.M. wrote the manuscript. B.M. led the overall direction of the project.

Author Information Reprints and permissions information is available at www.nature.com/reprints. The authors declare no competing financial interests. Readers are welcome to comment on the online version of this article at www.nature.com/nature. Correspondence and requests for materials should be addressed to B.M. (bmin@kaist.ac.kr).

METHODS

THz-TDS measurement. A conventional transmission-type THz-TDS system was used for the characterization of the fabricated metamaterials. A key component for generating and detecting the THz pulse is a photoconductive dipole antenna irradiated with femtosecond laser pulses (30–50 fs) from a Ti:sapphire laser with a repetition rate of 80 MHz. We used a dipole antenna fabricated on a low-temperature-grown GaAs (LT-GaAs) film with 5 μm gap and 30 μm length. The emitter antenna is d.c. biased from 10 V to 20 V and generates terahertz pulses with most of the spectral power density between 0.2 THz and 3 THz. The receiving antenna was fabricated on an LT-GaAs film and consisted of a coplanar transmission line structure with a 5 μm gap and 30 μm length. The metamaterial samples were attached to a sample holder that has an optical aperture 15 mm in diameter. An identical clear aperture was used as a free-space transmission reference. When the thickness of the samples is large enough, the first transmitted terahertz pulse and the following echoes caused by internal Fabry–Pérot reflection are temporally well separated. However, for the fabricated high-index metamaterials, the thickness was relatively small and the resulting transmitted pulse was the superposition of the components from multiple internal Fabry–Pérot reflections. Therefore, in order to reliably extract the effective parameters (complex refractive index), a numerical iterative method was used to minimize errors in the phase and magnitude.

Effective thickness estimation. Assignment of effective indices to a single-layer metamaterial must be made with extreme care, especially when there are no explicit physical boundaries (though this is not the case for the present work). Based on the criterion that the effective thickness should be defined as a distance between virtual boundaries, at which the reflected and transmitted wave behave like plane waves³¹ (this condition is equivalent to considering the decay length of the mode), we conducted additional simulations with increasing numbers of metamaterial layers and compared their effective refractive indices and the impedance at the quasi-static limit with that of a single-layer metamaterial. As the number of metamaterial layers increases, the effect of mode decay at the ends of the metamaterial becomes negligible; accordingly, the bulk refractive index can be defined as the converging value. As the effective refractive index (especially at the quasi-static limit) should be invariant with respect to the number of metamaterial layers, the effective thickness of a single-layer metamaterial can be defined as the thickness that renders the same bulk refractive index at the quasi-static limit. For example (corresponding to Fig. 2a), without the scaling, the refractive index at the quasi-static limit differ from the bulk value by $\sim 12\%$. Therefore, the refractive index (at the quasi-static limit) of the single-layer metamaterial decreases from 11.1 to 9.72 with an effective thickness of 2.79 μm (note that the physical thickness is 2.45 μm for this sample).

31. Chen, X., Grzegorzczak, T. M., Wu, B.-L., Pacheco, J. & Kong, J. A. Robust method to retrieve the constitutive effective parameters of metamaterials. *Phys. Rev. E* **70**, 016608 (2004).

Three-dimensional atomic imaging of crystalline nanoparticles

Sandra Van Aert¹, Kees J. Batenburg^{2,3}, Marta D. Rosell⁴, Rolf Erni⁵ & Gustaaf Van Tendeloo¹

Determining the three-dimensional (3D) arrangement of atoms in crystalline nanoparticles is important for nanometre-scale device engineering and also for applications involving nanoparticles, such as optoelectronics or catalysis. A nanoparticle's physical and chemical properties are controlled by its exact 3D morphology, structure and composition¹. Electron tomography enables the recovery of the shape of a nanoparticle from a series of projection images^{2–4}. Although atomic-resolution electron microscopy has been feasible for nearly four decades, neither electron tomography nor any other experimental technique has yet demonstrated atomic resolution in three dimensions. Here we report the 3D reconstruction of a complex crystalline nanoparticle at atomic resolution. To achieve this, we combined aberration-corrected scanning transmission electron microscopy^{5–7}, statistical parameter estimation theory^{8,9} and discrete tomography^{10,11}. Unlike conventional electron tomography, only two images of the target—a silver nanoparticle embedded in an aluminium matrix—are sufficient for the reconstruction when combined with available knowledge about the particle's crystallographic structure. Additional projections confirm the reliability of the result. The results we present help close the gap between the atomic resolution achievable in two-dimensional electron micrographs and the coarser resolution that has hitherto been obtained by conventional electron tomography.

High-angle annular dark field scanning transmission electron microscopy (HAADF STEM) is an imaging technique in which a focused electron probe is scanned across an electron-transparent sample¹². Using an annular-shaped high-angle detector behind the sample, the signal is dominated by Rutherford and thermal diffuse scattering. When applied to a nanocrystal in zone-axis orientation, the HAADF signal approximately scales with the square of the atomic number Z and with the thickness of the sample^{13–15}. By using aberration-corrected probe forming optics^{5–7}, a resolution of the order of 50 picometres can nowadays be demonstrated¹⁶. Therefore, it is generally believed that aberration-corrected HAADF STEM has the potential to achieve atomic resolution in three dimensions. Electron tomography is the most common approach used to reconstruct nanomaterials in three dimensions. The 3D reconstruction is computed from a tilt series of projection images acquired while rotating the sample. Spatial resolution for the reconstruction is around one cubic nanometre^{2–4}, limiting its use for attaining atomic resolution. Another potential technique with which to obtain 3D structure information is 'depth-sectioning', in which a sample is optically sliced by changing the objective lens focus¹⁷. Single atoms can be visualized using this technique¹⁸, yet 3D reconstructions at atomic resolution have not been demonstrated because the depth resolution is insufficient to resolve interatomic distances along the optical axis. Discrete tomography, a reconstruction approach that exploits prior knowledge about the discrete nature of atoms and their lattice structure, has been proposed as a promising technique for atomic resolution tomography^{10,11}, but only simulation results have been presented. Li *et al.*¹⁹ showed a 3D structure analysis

of a gold cluster from one single HAADF STEM image. However, this approach required strong a priori knowledge in combination with image simulations of regularly shaped models. Previous attempts have mostly focused on the technique and image acquisition, whereas the interpretation of the images was oversimplified, not taking into account the detailed probe characteristics^{20–22} and the statistical nature of the experimental data. Here, we combine aberration-corrected HAADF STEM carried out under low voltage conditions with model-based statistical parameter estimation^{8,9} and discrete tomography^{10,11} to obtain a full atomic-scale 3D reconstruction of an embedded nanoparticle.

A binary alloy consisting of Al with 3 at.% Ag was homogenized at 550 °C and quenched in ice-brine. During quenching, small Ag-rich clusters are formed which are fully coherent with the surrounding Al-rich matrix. This is clear from the electron diffraction patterns in Fig. 1a and d, from which it can not only be deduced that the structure of matrix and particle is face-centred cubic, but also that there is no lattice mismatch involved between matrix and particle (spot-splitting of the reflections, even far from the origin, is absent). The embedded clusters, with diameters slightly exceeding 2 nm, consist of nearly 100% Ag (refs 23 and 24). Electron-transparent foils with a measured thickness of about 12 nm were investigated in an electron microscope equipped with aberration correctors in the probe- and image-forming optical parts and operated at 80 kV (ref. 25). Although the resolution is better at higher acceleration voltages, operating the microscope at 80 kV guarantees the integrity of the nanoparticles during the acquisition of the data²⁶. Moreover, the particles, which are 2–3 nm in diameter, are fully contained in the depth of field of the electron probe, which is between 7 and 10 nm²⁷. High-resolution HAADF STEM images of nanosized Ag clusters embedded in the Al matrix viewed along the $[10\bar{1}]$ and $[100]$ zone-axes are shown in Fig. 1a and d, respectively. The white boxes enclose the same particle in both orientations.

A crucial step towards quantitative 3D structure determination of a nanoparticle at atomic resolution is the ability to count the number of atoms in each projected column. If one repeats this procedure reliably for several viewing directions, one will be able to reconstruct the 3D space using discrete tomography^{10,11}. We used a recent quantitative method to analyse HAADF STEM images, in which atomic columns with a difference in (average) atomic number of only three could be identified⁹. This model-based method accounts for the tails of the scanning probe^{20–22} (see Supplementary Information). Refined models, describing the contrast of the nanoparticle enclosed in the white boxes of Fig. 1a and d, are shown in Fig. 1b and e, respectively. The excellent agreement with the experimental contrast demonstrates the quality of the physics-based model used (see Supplementary Figs 1 and 2). Although dynamical scattering has not explicitly been taken into account, so-called cross-talk is shown to be negligible for the images in the $[10\bar{1}]$ and $[100]$ zone-axes (see Supplementary Information and Supplementary Fig. 3). (This effect, which seriously complicates the analysis, refers to transfer of probe intensity from one column to another column.)

¹Electron Microscopy for Materials Research (EMAT), University of Antwerp, Groenenborgerlaan 171, 2020 Antwerp, Belgium. ²Centrum Wiskunde & Informatica, Science Park 123, 1098XG Amsterdam, The Netherlands. ³IBBT-Vision Lab, University of Antwerp, Universiteitsplein 1, 2610 Wilrijk, Belgium. ⁴Department of Materials, ETH Zürich, Wolfgang-Pauli-Strasse 10, 8093 Zürich, Switzerland. ⁵Electron Microscopy Center, Empa, Swiss Federal Laboratories for Materials Science & Technology, 8600 Dübendorf, Switzerland.

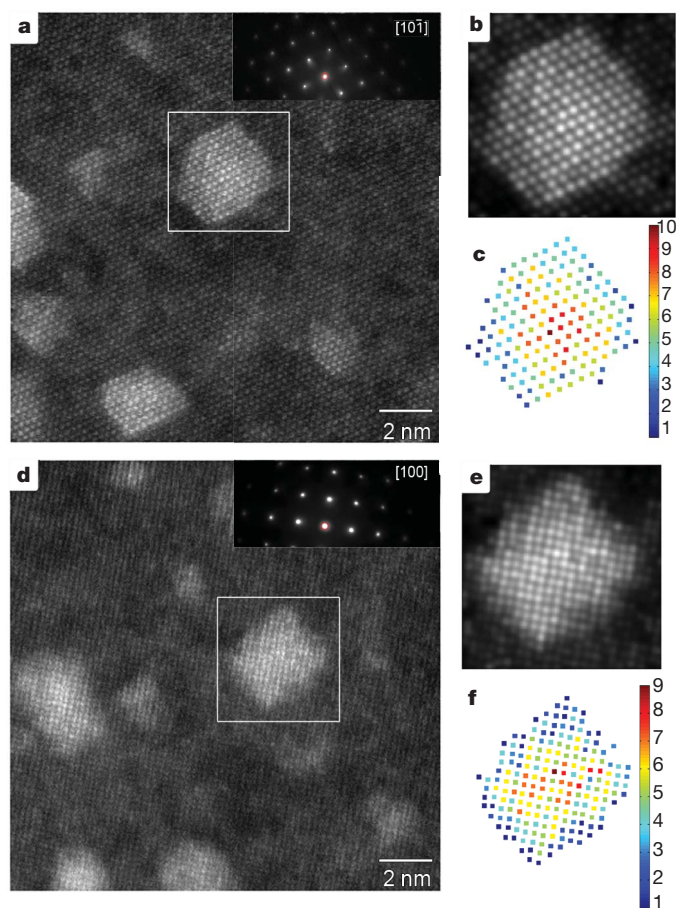


Figure 1 | Quantification of HAADF STEM images. **a**, Experimental HAADF STEM image of nanosized Ag clusters embedded in an Al matrix in $[10\bar{1}]$ zone-axis orientation, together with the corresponding electron diffraction pattern. **b**, Refined model of the boxed region in **a**. **c**, Number of Ag atoms per column. **d**, Experimental HAADF STEM image in $[100]$ zone-axis orientation, together with the corresponding electron diffraction pattern. **e**, Refined model of the boxed region in **d**. **f**, Number of Ag atoms per column.

Next, the scattered intensities can be computed⁹. These intensities scale with the average atomic number Z , allowing one to distinguish columns containing a certain amount of Ag ($Z = 47$) from pure Al ($Z = 13$) columns. For the nanoparticle viewed along the $[10\bar{1}]$ zone-axis, these columns are indicated by red markers in Fig. 2a. The corresponding scattered intensities are shown in the histogram in Fig. 2b. Because the thickness of the sample can be assumed to be constant over the particle area, substitution of an Al atom by an Ag atom leads to an

increase of the estimated intensity. An experimental histogram, however, shows broadened—rather than discrete—peaks owing to a combination of experimental detection noise, the surrounding aluminium matrix and residual instabilities. To determine the number of significant peaks and their positions, a statistics-based approach is proposed. The intensities are regarded as independent statistical draws from a so-called Gaussian mixture model²⁸. This model, defined as a superposition of Gaussians, describes the probability that a specific intensity value will be observed. To determine the number of significant peaks of this model, the Integrated Classification Likelihood criterion was used because it outperforms other order-selection criteria²⁸. In Fig. 2c, this criterion has been evaluated for an increasing number of peaks, clearly showing a minimum at ten. This indicates the presence of ten significant peaks in the histogram of Fig. 2b. Their positions, amplitudes and width have been estimated using the well-known expectation maximization algorithm²⁸. Its aim is to optimize the likelihood that the given intensities are generated by a mixture of Gaussians. The black solid curve in Fig. 2b shows the estimated mixture model; the individual Gaussian components are shown by means of dashed curves. Even though this has not been assumed a priori in the model, it is clear from Fig. 2b that the Gaussians are equidistantly separated. This means that the estimated mean intensity values, shown by black dots, linearly increase with the number of atoms in a column^{13,14} (see Supplementary Fig. 4). Next, the estimated mixture model can be used to identify the number of atoms in a particular column, as shown in Fig. 1c. The same counting procedure has been applied for the particle viewed along the $[100]$ zone-axis, resulting in Fig. 1f.

Using the atom counting results shown in Fig. 1c and f, discrete tomography was used to obtain a 3D reconstruction from these two projections. In general, two projections are insufficient to determine the 3D structure uniquely, because there may be many atom configurations leading to the same projections. We therefore incorporated here the following particle-specific knowledge, which is justified^{23,24,26} or could be verified: (1) the atoms are situated on a face-centred-cubic lattice, (2) the particle contains no holes, (3) each of the interior 2D slices (in the $x/y/z$ direction) that are at least two slices away from the particle boundary should be connected in 2D and contain no holes. We note that this a priori knowledge depends on the structure and configuration of interest. For a free-standing crystalline nanoparticle of any shape, even concave or containing holes, the same elegant procedure can still be applied to resolve the atoms in three dimensions.

Using a customized implementation of the simulated annealing algorithm for optimization²⁹, the reconstruction shown in Fig. 3a and in Supplementary Movie 1 was computed. Because the optimization algorithm is stochastic, it can be run repeatedly, each time yielding a reconstruction that may be different from the previous one. In 16 independent reconstruction runs, we observed a maximum difference

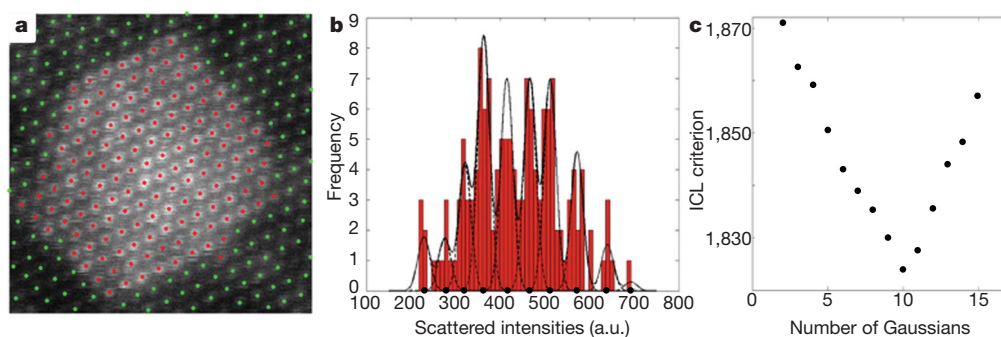


Figure 2 | Analysis of scattered intensities. **a**, Magnification of the boxed region in Fig. 1a. Columns containing Ag are indicated by red markers placed at the estimated positions. **b**, Histogram of scattered intensities of the Ag columns. The black solid curve shows the estimated mixture model; the individual

components are shown as dashed curves. **c**, The Integrated Classification Likelihood criterion evaluated as a function of the number of Gaussians in a mixture model.

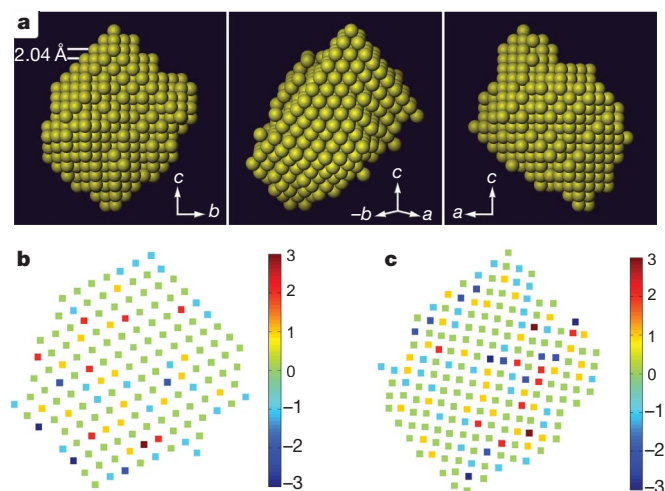


Figure 3 | Three-dimensional reconstruction. **a**, The computed 3D reconstruction of the Ag nanocluster viewed along three different directions. **b**, **c**, Difference between the computed atom counts for the reconstructed particle and the atom counts determined by the experiment in $[10\bar{1}]$ (**b**) and in $[100]$ (**c**) zone-axis orientation, respectively.

in the positioning of only 41 atoms on a total of 784 atoms. This indicates that the reconstruction is well determined by the projection data. Figure 3b and c shows the difference between the computed atom counts for the reconstructed crystal and the atom counts determined by the experiment. Although the match is not perfect owing to experimental errors, it is bounded by a maximum column difference of three, and far less on average.

The excellent match between the 3D reconstruction and the experimental data are illustrated in Fig. 4. Figure 4a–d shows micrographs of the particle along the $[10\bar{1}]$, $[100]$, $[4\bar{1}\bar{1}]$ and $[2\bar{1}\bar{1}]$ zone-axes, together with the corresponding snapshots (Fig. 4e–h) of Supplementary Movie 2. Owing to the limited resolution at 80 kV and cross-talk between closely spaced atomic columns, the micrographs in the $[2\bar{1}\bar{1}]$ and $[4\bar{1}\bar{1}]$ zone-axes could not be used in the atom count procedure. Nonetheless, the extra information from the $[2\bar{1}\bar{1}]$ and $[4\bar{1}\bar{1}]$ projections provides confidence about the validity of the reconstructed 3D particle's shape and the reliability of this new method. The validity of the reconstruction and the match with the underlying data are particularly convincing considering the potential experimental errors that could lead to errors in the count data for projected atom columns. To obtain a site-specific confidence estimate for each atom in the reconstruction, a second series of 20 independent reconstructions was computed in which the observed atom counts were perturbed, taking into

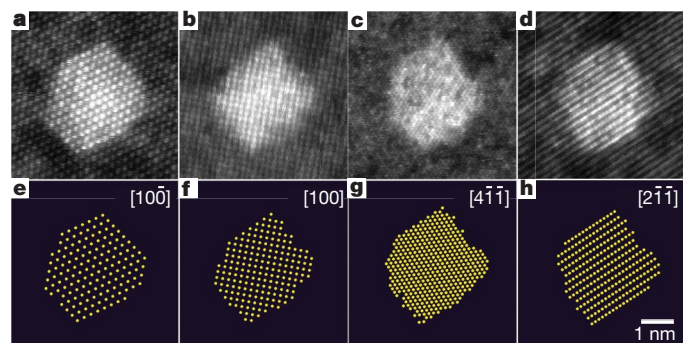


Figure 4 | Comparison of experimental images with projected 3D reconstructions. **a–d**, Images along $[10\bar{1}]$, $[100]$, $[4\bar{1}\bar{1}]$ and $[2\bar{1}\bar{1}]$. **e–h**, Projections of the 3D reconstruction along the same directions. The experimental images along the $[4\bar{1}\bar{1}]$ and $[2\bar{1}\bar{1}]$ directions, which were not used for the 3D reconstruction, confirm the shape of the reconstructed 3D model.

account that there is a probability of 5% of miscounting the total number of atoms in a column with one atom. This probability follows directly from the overlap of the Gaussian components shown in Fig. 2b. The probability of assigning a wrong number of atoms indeed increases with increasing overlap. By analysing the discrepancies between the 20 reconstructions thus obtained and the model in Fig. 3, a site-specific confidence map can be constructed (see the Supplementary Information, Supplementary Figs 5 and 6, and Supplementary Movie 3). The results indicate that over all atoms in our 3D reconstruction, the probability of wrongly assigning an atom at a specific site is only 3%, indicating a high level of confidence for the reconstruction.

In conclusion, we have demonstrated a comprehensive approach for three-dimensional atomic imaging: the combination of HAADF STEM, atom counting using a thorough model-based statistical analysis and 3D reconstruction by applying discrete tomography from only two projected images. The close match of the 3D reconstruction with the atom counts and particle shape information based on experimental data provides confidence that the proposed method represents a reliable routine for atomic resolution tomography of crystalline nanoparticles. Using nanosized Ag clusters embedded in an Al matrix we have demonstrated the strength of this method. Our results reveal the great potential of this new technique for various applications regarding the atomic characterization of all kinds of complex nanometre-scale structured materials, particularly nanoparticles and nanocavities.

METHODS SUMMARY

Specimen preparation. A binary alloy consisting of Al with 3 at.% Ag was prepared in an electric arc-furnace under an Ar atmosphere of 15 torr from pure Al (99.999%) and Ag_2Al ; it was homogenized for 3 h at 550 °C and quenched in ice-brine. During quenching small Ag-rich clusters are formed. Electron-transparent films were produced by mechanical polishing followed by electrolytic thinning. Using the EELS-based t/λ method³⁰, a specimen thickness of about 12 nm was measured.

STEM imaging. Electron microscopy was carried out using the TEAM0.5 microscope operated at 80 kV installed at the National Center for Electron Microscopy (NCEM) at the Lawrence Berkeley National Laboratory (LBNL). The images were recorded on a 3-mm-diameter specimen mounted to a double-tilt holder in a conventional compo-stage that enables a tilting range of ± 20 – 25° in combination with the ultrahigh-resolution pole-piece lens employed. A probe semi-convergence angle of 25.7 mrad was used. Hence, the (geometrical) depth of field is between 6 and 7 nm. The effects of chromatic defocus spread even enlarge the depth of field to about 10 nm (ref. 27). The HAADF detector was set to collect electrons scattered between 70 and 490 mrad. This detector setting guarantees that the collected signal results in an approximately incoherent atomic-number contrast STEM image.

Received 6 May; accepted 3 December 2010.

Published online 2 February 2011.

- Olson, G. B. Designing a new material world. *Science* **288**, 993–998 (2000).
- Arslan, I., Yates, T. J. V., Browning, N. D. & Midgley, P. A. Embedded nanostructures revealed in three dimensions. *Science* **309**, 2195–2198 (2005).
- Midgley, P. A. & Dunin-Borkowski, R. E. Electron tomography and holography in materials science. *Nature Mater.* **8**, 271–280 (2009).
- Batenburg, K. J. *et al.* 3D imaging of nanomaterials by discrete tomography. *Ultramicroscopy* **109**, 730–740 (2009).
- Haider, M. *et al.* Electron microscopy image enhanced. *Nature* **392**, 768–769 (1998).
- Batson, P. E., Dellby, N. & Krivanek, O. L. Sub-ångström resolution using aberration corrected electron optics. *Nature* **418**, 617–620 (2002).
- Müller, H., Uhlemann, S., Hartel, P. & Haider, M. Advancing the hexapole C_s -corrector for the scanning transmission electron microscope. *Microsc. Microanal.* **12**, 442–455 (2006).
- den Dekker, A. J., Van Aert, S., van den Bos, A. & Van Dyck, D. Maximum likelihood estimation of structure parameters from high resolution electron microscopy images. Part I: a theoretical framework. *Ultramicroscopy* **104**, 83–106 (2005).
- Van Aert, S. *et al.* Quantitative atomic resolution mapping using high-angle annular dark field scanning transmission electron microscopy. *Ultramicroscopy* **109**, 1236–1244 (2009).
- Batenburg, K. J. A network flow algorithm for reconstructing binary images from discrete x-rays. *J. Math. Imaging Vision* **27**, 175–191 (2007).
- Jinschek, J. R. *et al.* 3-D reconstruction of the atomic positions in a simulated gold nanocrystal based on discrete tomography: Prospects of atomic resolution electron tomography. *Ultramicroscopy* **108**, 589–604 (2008).

12. Crewe, A. V., Wall, J. & Welter, L. M. A high-resolution scanning transmission electron microscope. *J. Appl. Phys.* **39**, 5861–5868 (1968).
13. Hartel, P., Rose, H. & Dinges, C. Conditions and reasons for incoherent imaging in STEM. *Ultramicroscopy* **63**, 93–114 (1996).
14. Nellist, P. D. & Pennycook, S. J. The principles and interpretation of annular dark-field Z-contrast imaging. *Adv. Imaging Electron Phys.* **113**, 147–203 (2000).
15. Krivanek, O. L. *et al.* Atom-by-atom structural and chemical analysis by annular dark-field electron microscopy. *Nature* **464**, 571–574 (2010).
16. Erni, R., Rossell, M. D., Kisielowski, C. & Dahmen, U. Atomic-resolution imaging with a sub-50-pm electron probe. *Phys. Rev. Lett.* **102**, 096101 (2009).
17. Pennycook, S. J., Lupini, A. R., Borisevich, A. Y., Peng, Y. & Shibata, N. 3D atomic resolution imaging through aberration-corrected STEM. *Microsc. Microanal.* **10** (Suppl. 1.2), 1172–1173 (2004).
18. van Benthem, K. *et al.* Three-dimensional ADF imaging of individual atoms by through-focal series scanning transmission electron microscopy. *Ultramicroscopy* **106**, 1062–1068 (2006).
19. Li, Z. Y. *et al.* Three-dimensional atomic-scale structure of size-selected gold nanoclusters. *Nature* **451**, 46–48 (2008).
20. Hillyard, S. & Silcox, J. Detector geometry, thermal diffuse-scattering and strain effects in ADF STEM imaging. *Ultramicroscopy* **58**, 6–17 (1995).
21. Klenov, D. O., Zide, J. M., Zimmerman, J. D., Gossard, A. C. & Stemmer, S. Interface atomic structure of epitaxial ErAs layers on (001)In_{0.53}Ga_{0.47}As and GaAs. *Appl. Phys. Lett.* **86**, 241901 (2005).
22. Dwyer, C., Erni, R. & Etheridge, J. Measurement of effective source distribution and its importance for quantitative interpretation of STEM images. *Ultramicroscopy* **110**, 952–957 (2010).
23. Dubey, Ph. A., Schönfeld, B. & Kosterz, G. Shape and internal structure of Guinier-Preston zones in Al-Ag. *Acta Metall. Mater.* **39**, 1161–1170 (1991).
24. Malik, A., Schonfeld, B., Kosterz, G. & Pedersen, J. S. Microstructure of Guinier-Preston zones in Al-Ag. *Acta Mater.* **44**, 4845–4852 (1996).
25. Kisielowski, C. *et al.* Detection of single atoms and buried defects in three dimensions by aberration-corrected electron microscope with 0.5-angstrom information limit. *Microsc. Microanal.* **14**, 469–477 (2008).
26. Erni, R., Heinrich, H. & Kosterz, G. On the internal structure of Guinier-Preston zones in Al-3 at.% Ag. *Phil. Mag. Lett.* **83**, 599–609 (2003).
27. Xin, H. L. & Muller, D. A. Aberration-corrected ADF-STEM depth sectioning and prospects for reliable 3D imaging in S/TEM. *J. Electron Microsc.* **58**, 157–165 (2009).
28. McLachlan, G. & Peel, D. *Finite Mixture Models* (eds Shewhart, W. A. & Wilks, S. S.) (Wiley Series in Probability and Statistics, John Wiley & Sons, 2000).
29. Kirkpatrick, S., Gelatt, C. D. & Vecchi, M. P. Optimization by simulated annealing. *Science* **220**, 671–680 (1983).
30. Malis, T., Cheng, S. C. & Egerton, R. F. EELS log-ratio technique for specimen-thickness measurement in the TEM. *J. Electron Microsc. Tech.* **8**, 193–200 (1988).

Supplementary Information is linked to the online version of the paper at www.nature.com/nature.

Acknowledgements Part of this work was performed at the National Center for Electron Microscopy (LBNL) which is supported by the Office of Science, Office of Basic Energy Sciences of the US Department of Energy under contract number DE-AC02-05CH11231. Financial support from the European Union for the Framework 6 programme under a contract for an Integrated Infrastructure Initiative (reference 026019 ESTEEM) is acknowledged.

Author Contributions S.V.A. developed and applied a method of counting the number of atoms. K.J.B. reconstructed the nanoparticle in three dimensions. M.D.R. and R.E. prepared the sample and recorded the experimental images. G.V.T. advised on the methodology, the interpretation and on the paper. All the authors read and commented on the paper.

Author Information Reprints and permissions information is available at www.nature.com/reprints. The authors declare no competing financial interests. Readers are welcome to comment on the online version of this article at www.nature.com/nature. Correspondence and requests for materials should be addressed to S.V.A. (sandra.vanaert@ua.ac.be).

Human contribution to more-intense precipitation extremes

Seung-Ki Min¹, Xuebin Zhang¹, Francis W. Zwiers^{1†} & Gabriele C. Hegerl²

Extremes of weather and climate can have devastating effects on human society and the environment^{1,2}. Understanding past changes in the characteristics of such events, including recent increases in the intensity of heavy precipitation events over a large part of the Northern Hemisphere land area^{3–5}, is critical for reliable projections of future changes. Given that atmospheric water-holding capacity is expected to increase roughly exponentially with temperature—and that atmospheric water content is increasing in accord with this theoretical expectation^{6–11}—it has been suggested that human-influenced global warming may be partly responsible for increases in heavy precipitation^{3,5,7}. Because of the limited availability of daily observations, however, most previous studies have examined only the potential detectability of changes in extreme precipitation through model–model comparisons^{12–15}. Here we show that human-induced increases in greenhouse gases have contributed to the observed intensification of heavy precipitation events found over approximately two-thirds of data-covered parts of Northern Hemisphere land areas. These results are based on a comparison of observed and multi-model simulated changes in extreme precipitation over the latter half of the twentieth century analysed with an optimal fingerprinting technique. Changes in extreme precipitation projected by models, and thus the impacts of future changes in extreme precipitation, may be underestimated because models seem to underestimate the observed increase in heavy precipitation with warming¹⁶.

We compare observed and simulated changes in extreme precipitation based on the annual maxima of daily (RX1D) and five-day consecutive (RX5D) precipitation amounts for the second half of the twentieth century. We chose these indices because they characterize extreme events that often cause impacts on society^{1,2}, and because these annual extremes can be used to estimate the probability of rare events such as 100-year return values, which are used in the design of infrastructure. We use the Hadley Centre global land-based gridded climate extremes data set (HadEX)⁴, which is based on daily observations from 6,000 stations and covers the period 1951–2003. We restrict our analysis to the period 1951–99 for comparison with model simulations and because of loss of coverage at the end of the period of record (Supplementary Information). Multi-model simulations were obtained from the Coupled Model Intercomparison Project Phase 3 (CMIP3) archive and from individual modelling centres (Supplementary Table 1). The RX1D and RX5D indices were calculated from all available simulations from eight models. We used the 1951–99 segments of simulations of the twentieth century with either historical anthropogenic forcing (greenhouse gases and other anthropogenic factors including aerosols, ANT; 6 models, 19 runs) or a combination of historical natural (solar and volcanic) plus anthropogenic forcing (ALL; 5 models, 16 runs). Three models provided both ANT and ALL runs. We also used unforced control simulations (CTL; 106 non-overlapping 49-year segments).

Owing to the high spatial variability of precipitation and the sparseness of the observing network in many regions, estimates of area means

of extreme precipitation may be uncertain; for example, for regions where the distribution of individual stations does not adequately sample the spatial variability of extreme values across the region. In order to reduce the effects of this source of uncertainty on area means, and to improve representativeness and inter-comparability, we standardized values at each grid-point before estimating large area averages by mapping extreme precipitation amounts onto a zero-to-one scale¹⁵. The resulting ‘probability-based index’ (PI) equalizes the weighting given to grid-points in different locations and climatic regions in large area averages and facilitates comparison between observations and model simulations^{15,17,18}. Observed and simulated annual extremes are converted to PI by fitting a separate generalized extreme value (GEV) distribution^{15,19} to each 49-year time series of annual extremes and replacing values with their corresponding percentiles on the fitted distribution. Model PI values are interpolated onto the HadEX grid to facilitate comparison with observations (see Methods Summary and Supplementary Information for details).

Figure 1 shows the spatial patterns of the observed and multi-model mean trends in PI for RX1D and RX5D during 1951–99. Trends are shown only for grid-points with more than 40 years of observations. This confines the analysis to Northern Hemisphere land areas, including North America and Eurasia (including India). Spatial coverage for RX5D is somewhat greater than for RX1D due to broader spatial interpolation of the available station values⁴, possibly affecting reliability (Supplementary Information). We therefore also analyse RX5D only at locations where RX1D is available, and find that our main detection results are not affected (Supplementary Fig. 1). Observations show overall increasing trends in PI, with 65% and 61% of the total data-covered areas having positive trends for RX1D and RX5D, respectively. The multi-model mean from ANT simulations shows positive trends in both extreme indices almost everywhere, consistent with future projections^{17–20}, but with smaller amplitude than observed. Multi-model ALL simulations exhibit similar moderate increasing trends in RX1D, but show a mixed pattern of moistening and drying for RX5D (see below).

In order to consider long-term changes in extreme precipitation, we calculate non-overlapping five-year mean PI anomaly time series for 1955–99 and append a four-year mean for 1951–54. The time evolution of five-year mean PI anomalies averaged over Northern Hemisphere land (using the locations plotted in Fig. 1) is shown in Fig. 2. Observations exhibit increasing trends for both RX1D and RX5D, in accord with previous studies^{3–5}. The ANT simulations show also increasing trends, but with smaller amplitudes than observed, consistent with Fig. 1. No individual simulation has a trend as strong as observed (Supplementary Fig. 2). The ALL simulations exhibit weak positive trends globally in RX1D, and spatially variable weak positive and negative trends in both RX1D and RX5D. This seems to be partly due to the inclusion of natural forcing (NAT) in the ALL simulations, which on its own would have induced long-term overall cooling and drying trends for the analysis period^{13,15}, thus reducing the positive trends in intense precipitation due to ANT forcing (Supplementary Fig. 3). Considering that models underestimate the observed changes

¹Climate Research Division, Environment Canada, Toronto, Ontario M3H5T4, Canada. ²School of GeoSciences, University of Edinburgh, Edinburgh EH9 3JW, UK. [†]Present address: Pacific Climate Impacts Consortium, University of Victoria, Victoria, British Columbia V8W2Y2, Canada.

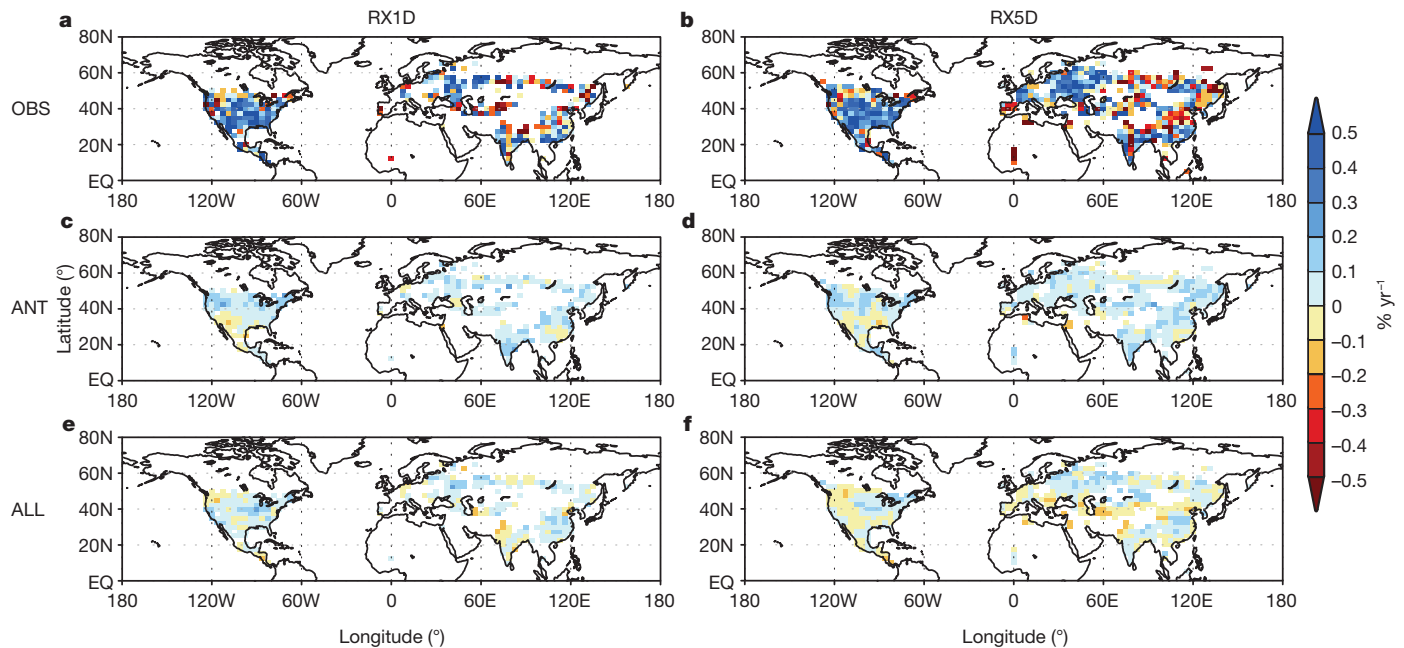


Figure 1 | Geographical distribution of trends of extreme precipitation indices (PI) during 1951–99. a, b, Observations (OBS); c, d, model simulations with anthropogenic (ANT) forcing; e, f, model simulations with anthropogenic plus natural (ALL) forcing. For each pair of panels, results are

shown for annual maximum daily (RX1D) and five-day (RX5D) precipitation amounts. For models, ensemble means of trends from individual simulations are displayed. Units: per cent probability per year.

in precipitation extremes¹⁶, and that smaller trends are more likely to be masked by noise, the ANT signal should be more detectable than the ALL signal in observations (see Supplementary Information for more discussion).

We use a rigorous optimal detection method²¹ to compare observed and simulated long-term variations in PI (see Methods Summary for details). In this method, observed patterns are regressed onto multi-model

simulated responses to external forcing (fingerprint patterns). The resulting best estimates and uncertainty ranges of the regression coefficients (or scaling factors) are analysed to determine whether the fingerprints are present in the observations. For detection, the estimated scaling factors should be positive and uncertainty ranges should exclude zero. If the uncertainty ranges also include unity, the model patterns are considered to be consistent with observations. Model performance in

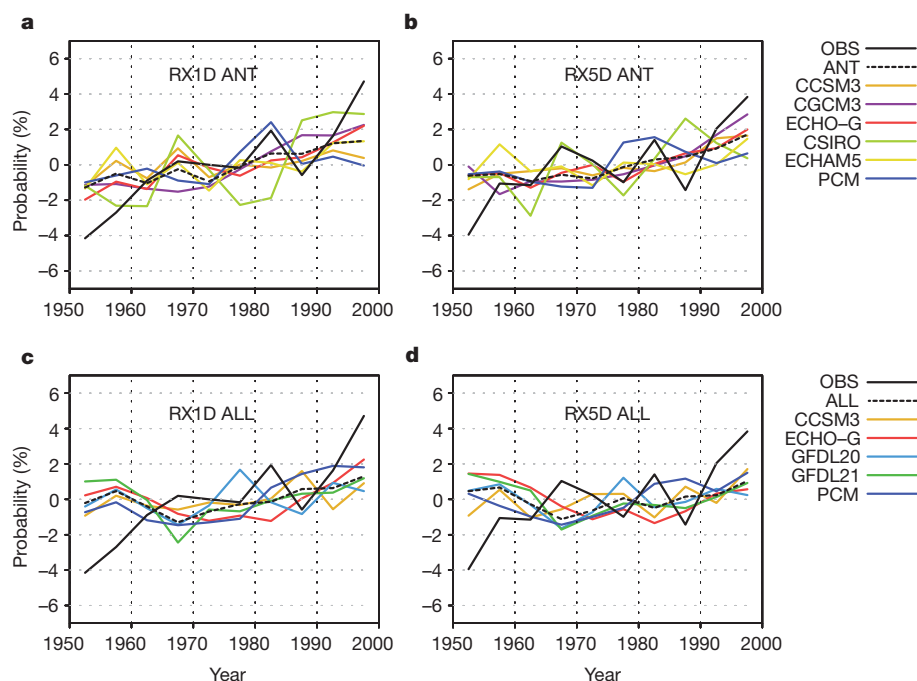


Figure 2 | Time series of five-year mean area-averaged PI anomalies over Northern Hemisphere land during 1951–99. a, b, Model simulations with anthropogenic (ANT) forcing; c, d, model simulations with anthropogenic plus natural (ALL) forcing. For each pair of panels, results are shown for RX1D and RX5D precipitation amounts. Black solid lines are observations and dashed

lines represent multi-model means. Coloured lines indicate results for individual model averages (see Supplementary Table 1 for the list of climate model simulations and Supplementary Fig. 2 for time series of individual simulations). Each time series is represented as anomalies with respect to its 1951–99 mean.

simulating internal variability must be considered carefully^{13,22} to avoid spurious detection. A standard residual consistency test²² is employed for this purpose and our detection analysis is confined to a reduced space in which the models used here simulate internal variability reasonably well (see Supplementary Information for more details).

The time evolution of five-year mean regionally averaged PI values was analysed using the optimal detection technique for both RX1D and RX5D. Given the limited data availability, we choose regions that would span either the meridional variation of changes in extremes (that is, the northern mid-latitudes and tropics), or the zonal variation in extremes (that is, Eurasia and the Americas), and repeated our detection analysis for both subdivisions. Figure 3 shows the results of four optimal detection analyses using the time evolution of extreme precipitation indices averaged over the Northern Hemisphere, over northern mid-latitudes and northern tropics individually, and over these two regions simultaneously for 1951–99. Regression coefficients obtained when using ANT fingerprints are significantly greater than zero for both RX1D and RX5D, indicating that anthropogenic influence is detectable in the observed temporal or spatiotemporal changes in extreme precipitation for this period. Results from a space-time analysis using the zonal decomposition also support our findings (Supplementary Fig. 4). The signals are detected only when PI is averaged

over hemispheric and continental scales, consistent with previous detectability studies¹⁵; detection fails when smaller sub-continental areas are considered (not shown). The ALL signal is detected in RX1D albeit less robustly, which reflects the lower signal-to-noise ratio due to the inclusion of NAT forcing (see also Supplementary Information).

Best estimates of the regression coefficients are larger than unity (Fig. 3), indicating that the extreme precipitation response to ANT forcing may be underestimated by models compared to observed changes, consistent with previous suggestions based on satellite observations over the tropical oceans¹⁶ and observed changes in annual precipitation amounts over the global and Arctic land areas^{23,24}. The residual consistency test²² as well as simple comparison of variances (Supplementary Table 2) show that the models simulate the internal variability of low-frequency hemispheric land mean PI reasonably well (Supplementary Information). Nevertheless, ANT detection generally continues to hold when our estimate of internal variability is doubled (dashed lines in Fig. 3).

Figure 3 also shows that ANT can be more robustly detected in RX1D than RX5D. The signal amplitude, as measured by the slope of the linear trend, is larger in model simulated RX1D (Supplementary Information). Observed trends are also larger in RX1D than in RX5D. This is consistent with previous findings^{6,9,16} that changes in more extreme precipitation follow the Clausius–Clapeyron relationship (which describes the rate of increase of atmospheric moisture with warming) more closely. Atmospheric circulation changes from global warming can also influence the pattern of extreme precipitation²⁵ but this is unlikely to substantially affect our findings because the Northern Hemisphere mid-latitude land region analysed here seems to be influenced predominantly by the Clausius–Clapeyron relationship^{9,25–27} (see Supplementary Information for more discussion concerning physical mechanisms). A series of sensitivity tests show that our detection results are robust to observational data coverage change, interpolation methods, influence of natural climate variability on observations, and different model sampling (see Supplementary Information).

Our results provide to our knowledge the first formal identification of a human contribution to the observed intensification of extreme precipitation. We used probability-based indices of precipitation extremes that facilitate the comparison of observations with models^{15,28}. Our results also show that the global climate models we used may have underestimated the observed trend, which implies that extreme precipitation events may strengthen more quickly in the future than projected and that they may have more severe impacts than estimated. There are, however, uncertainties related to observational limitations^{3,5}, missing or uncertain external forcings^{13,29} and model performance^{14,26–29}.

METHODS SUMMARY

Probability-based index. We use the GEV distribution¹⁹ to convert 49-year time series of the largest one-day and five-day precipitation accumulations annually, RX1D and RX5D, into corresponding time series of PI at each grid-point. A GEV distributed variable x has a cumulative distribution function that is characterized by location (μ), scale (σ) and shape (ξ) parameters as follows:

$$F(x; \mu, \sigma, \xi) = \begin{cases} \exp\left[-\exp\left\{-\frac{x-\mu}{\sigma}\right\}\right], & \xi = 0 \\ \exp\left[-\left\{1 + \xi \frac{x-\mu}{\sigma}\right\}^{-\frac{1}{\xi}}\right], & \xi \neq 0, \quad 1 + \xi \frac{x-\mu}{\sigma} > 0. \end{cases} \quad (1)$$

The parameters for a given grid-point are estimated by fitting the GEV distribution to individual 49-year (or shorter) time series of observed or model-simulated annual precipitation maxima by the method of maximum likelihood³⁰. We do not vary GEV parameters with time. Each annual maximum for a given grid-point and data set is converted to PI by evaluating the corresponding fitted cumulative distribution function at the value of that annual maximum. Stronger annual precipitation extremes will yield PI values closer to 1, while weaker extremes will yield PI values closer to 0. See the Supplementary Information for more details.

Detection and attribution. We use an optimal regression method²¹ in which observations (y) are expressed as a sum of scaled model-simulated fingerprint patterns (X) plus internal climate variability (ε) as $y = X\beta + \varepsilon$. The scaling factors

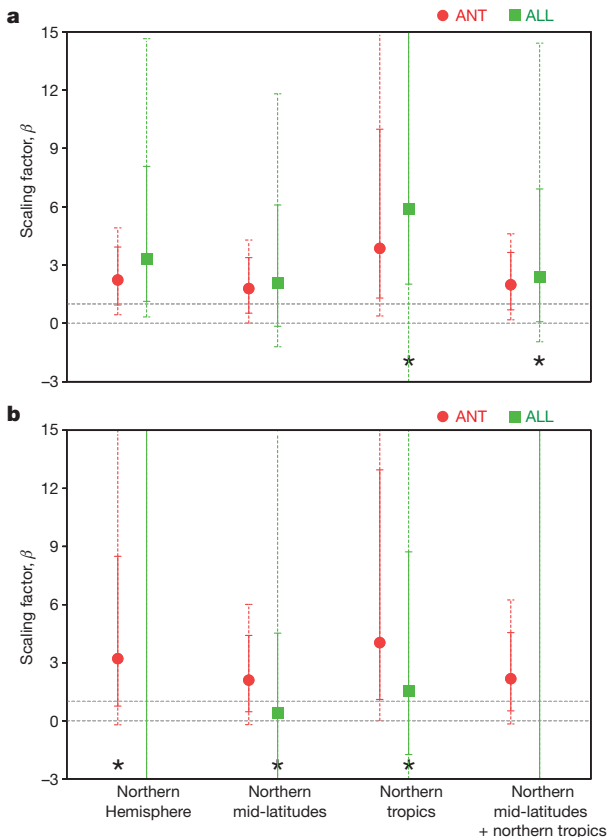


Figure 3 | Results from optimal detection analyses of extreme precipitation indices. **a**, PI for RX1D, **b**, PI for RX5D, both over the period 1951–99. Best estimates (data points) and 5–95% uncertainty ranges (error bars) of regression coefficients β are displayed for one-signal fingerprint detection analyses for ANT (red) and ALL (green), when using five-year mean PI averaged over the Northern Hemisphere, the northern mid-latitudes (30° N–65° N), the northern tropics (0°–30° N) (10-dimensional time vector in all three cases), and when using two regional averages combined (northern mid-latitudes + northern tropics; 20-dimensional space-time vector). Dashed error bars show β ranges when the internal variability is doubled. An error bar without a data point represents unbounded uncertainty in estimating β ranges. The two grey dashed horizontal lines represent zero and unity. An asterisk indicates passage of the residual consistency test²² only when the internal variability is doubled, suggesting insufficient model variability (see text for more details).

β adjust the magnitude of the fingerprints to best match the observations. Fingerprints are estimated from the means of forced (ANT or ALL) simulations and internal variability is estimated from CTL simulations (see Supplementary Information). The regression is fitted using the total least squares method²¹. Detection analyses are conducted in a reduced space in which observations and simulated patterns of change are represented by their projections onto the leading empirical orthogonal functions (EOFs) of internal variability. In the 1951–99 analysis (Fig. 3), the four leading EOFs are retained, which explain about 52–63% of the total variance.

Received 15 March; accepted 17 December 2010.

- Parry, M. L. Canziani, O. F., Palutikof, J. P., van der Linden, P. J. & Hanson, C. E. (eds) *Climate Change 2007: Impacts, Adaptation and Vulnerability* (Cambridge Univ. Press, 2007).
- Peterson, T. C. et al. in *Weather and Climate Extremes in a Changing Climate. Regions of Focus: North America, Hawaii, Caribbean, and U.S. Pacific Islands* (eds Karl, T. R. et al.) 11–34 (Synthesis and Assessment Product 3.3, US Climate Change Science Program, Washington DC, 2008).
- Groisman, P. & Ya. et al. Trends in intense precipitation in the climate record. *J. Clim.* **18**, 1326–1350 (2005).
- Alexander, L. V. et al. Global observed changes in daily climatic extremes of temperature and precipitation. *J. Geophys. Res.* **111**, D05109, doi:10.1029/2005JD006290 (2006).
- Trenberth, K. E. et al. in *Climate Change 2007: The Physical Science Basis* (eds Solomon, S. et al.) 235–336 (Cambridge Univ. Press, 2007).
- Allen, M. R. & Ingram, W. J. Constraints on future changes in climate and the hydrologic cycle. *Nature* **419**, 224–232 (2002).
- Trenberth, K. E., Dai, A., Rasmussen, R. M. & Parsons, D. B. The changing character of precipitation. *Bull. Am. Meteorol. Soc.* **84**, 1205–1217 (2003).
- Wentz, F. J. & Schabel, M. Precise climate monitoring using complementary satellite data sets. *Nature* **403**, 414–416 (2000).
- Pall, P., Allen, M. R. & Stone, D. A. Testing the Clausius-Clapeyron constraint on changes in extreme precipitation under CO₂ warming. *Clim. Dyn.* **28**, 351–363 (2007).
- Santer, B. D. et al. Identification of human-induced changes in atmospheric moisture content. *Proc. Natl Acad. Sci. USA* **104**, 15248–15253 (2007).
- Willett, K. M., Gillett, N. P., Jones, P. D. & Thorne, P. W. Attribution of observed surface humidity changes to human influence. *Nature* **449**, 710–712 (2007).
- Hegerl, G. C., Zwiers, F. W., Stott, P. A. & Kharin, V. V. Detectability of anthropogenic changes in annual temperature and precipitation extremes. *J. Clim.* **17**, 3683–3700 (2004).
- Hegerl, G. C. et al. in *Climate Change 2007: The Physical Science Basis* (eds Solomon, S. et al.) 663–745 (Cambridge Univ. Press, 2007).
- Kiktev, D., Caesar, J., Alexander, L. V., Shiogama, H. & Collier, M. Comparison of observed and multimodeled trends in annual extremes of temperature and precipitation. *Geophys. Res. Lett.* **34**, L10702, doi:10.1029/2007GL029539 (2007).
- Min, S.-K., Zhang, X. B., Zwiers, F. W., Friederichs, P. & Hense, A. Signal detectability in extreme precipitation changes assessed from twentieth century climate simulations. *Clim. Dyn.* **32**, 95–111 (2009).
- Allan, R. P. & Soden, B. J. Atmospheric warming and the amplification of precipitation extremes. *Science* **321**, 1481–1484 (2008).
- Tebaldi, C., Hayhoe, K., Arblaster, J. M. & Meehl, G. A. Going to the extremes: an intercomparison of model-simulated historical and future changes in extreme events. *Clim. Change* **79**, 185–211 (2006).
- Kharin, V. V., Zwiers, F. W., Zhang, X. & Hegerl, G. C. Changes in temperature and precipitation extremes in the IPCC ensemble of global coupled model simulations. *J. Clim.* **20**, 1419–1444 (2007).
- Zwiers, F. W. & Kharin, V. V. Changes in the extremes of the climate simulated by CCC GCM2 under CO₂ doubling. *J. Clim.* **11**, 2200–2222 (1998).
- Meehl, G. et al. in *Climate Change 2007: The Physical Science Basis* (eds Solomon, S. et al.) 747–845 (Cambridge Univ. Press, 2007).
- Allen, M. R. & Stott, P. A. Estimating signal amplitudes in optimal fingerprinting. Part I: theory. *Clim. Dyn.* **21**, 477–491 (2003).
- Allen, M. R. & Tett, S. F. B. Checking for model consistency in optimal fingerprinting. *Clim. Dyn.* **15**, 419–434 (1999).
- Zhang, X. et al. Detection of human influence on 20th century precipitation trends. *Nature* **448**, 461–465 (2007).
- Min, S.-K., Zhang, X. & Zwiers, F. Human-induced Arctic moistening. *Science* **320**, 518–520 (2008).
- Emori, S. & Brown, S. J. Dynamic and thermodynamic changes in mean and extreme precipitation under changed climate. *Geophys. Res. Lett.* **32**, L17706, doi:10.1029/2005GL023272 (2005).
- O’Gorman, P. A. & Schneider, T. The physical basis for increases in precipitation extremes in simulations of 21st-century climate change. *Proc. Natl Acad. Sci. USA* **106**, 14773–14777 (2009).
- Sugiama, M., Shiogama, H. & Emori, S. Precipitation extreme changes exceeding moisture content increases in MIROC and IPCC climate models. *Proc. Natl Acad. Sci. USA* **107**, 571–575 (2010).
- Durman, C. F., Gregory, J. M., Hassell, D. C., Jones, R. G. & Murphy, J. M. A comparison of extreme European daily precipitation simulated by a global and a regional climate model for present and future climates. *Q. J. R. Meteorol. Soc.* **127**, 1005–1015 (2001).
- Randall, D. A. et al. in *Climate Change 2007: The Physical Science Basis* (eds Solomon, S. et al.) 589–662 (Cambridge Univ. Press, 2007).
- Kharin, V. V. & Zwiers, F. W. Estimating extremes in transient climate change simulations. *J. Clim.* **18**, 1156–1173 (2005).

Supplementary Information is linked to the online version of the paper at www.nature.com/nature.

Acknowledgements We thank N. Gillett and B. Yu for comments, M. Wehner for provision of CCSM3 data, and J. Penner and M. Sugiama for discussion. We acknowledge the modelling groups, the Program for Climate Model Diagnosis and Intercomparison (PCMDI) and the World Climate Research Programme’s (WCRP’s) Working Group on Coupled Modelling (WGCM) for their roles in making available the WCRP CMIP3 multi-model data set. Support for this data set is provided by the Office of Science, US Department of Energy. We acknowledge the support of the International Detection and Attribution Group (IDAG) by the US Department of Energy’s Office of Science, Office of Biological and Environmental Research and the National Oceanic and Atmospheric Administration’s Climate Program Office. S.-K.M. was supported by the Canadian International Polar Year (IPY) programme. G.C.H. was supported by the NSF (grant ATM-0296007).

Author Contributions S.-K.M. carried out analysis. X.Z., F.W.Z. and G.C.H. contributed to the analysis. All authors discussed the results and contributed to writing the paper.

Author Information Reprints and permissions information is available at www.nature.com/reprints. The authors declare no competing financial interests. Readers are welcome to comment on the online version of this article at www.nature.com/nature. Correspondence and requests for materials should be addressed to S.-K.M. (seung-ki.min@ec.gc.ca) or F.W.Z. (fwzwiers@uvic.ca).

Anthropogenic greenhouse gas contribution to flood risk in England and Wales in autumn 2000

Pardeep Pall^{1,2†}, Tolu Aina³, Dáithí A. Stone^{1,4}, Peter A. Stott⁵, Toru Nozawa⁶, Arno G. J. Hilberts⁷, Dag Lohmann⁷ & Myles R. Allen^{1,4}

Interest in attributing the risk of damaging weather-related events to anthropogenic climate change is increasing¹. Yet climate models used to study the attribution problem typically do not resolve the weather systems associated with damaging events² such as the UK floods of October and November 2000. Occurring during the wettest autumn in England and Wales since records began in 1766^{3,4}, these floods damaged nearly 10,000 properties across that region, disrupted services severely, and caused insured losses estimated at £1.3 billion (refs 5, 6). Although the flooding was deemed a ‘wake-up call’ to the impacts of climate change at the time⁷, such claims are typically supported only by general thermodynamic arguments that suggest increased extreme precipitation under global warming, but fail^{8,9} to account fully for the complex hydrometeorology^{4,10} associated with flooding. Here we present a multi-step, physically based ‘probabilistic event attribution’ framework showing that it is very likely that global anthropogenic greenhouse gas emissions substantially increased the risk of flood occurrence in England and Wales in autumn 2000. Using publicly volunteered distributed computing^{11,12}, we generate several thousand seasonal-forecast-resolution climate model simulations of autumn 2000 weather, both under realistic conditions, and under conditions as they might have been had these greenhouse gas emissions and the resulting large-scale warming never occurred. Results are fed into a precipitation-runoff model that is used to simulate severe daily river runoff events in England and Wales (proxy indicators of flood events). The precise magnitude of the anthropogenic contribution remains uncertain, but in nine out of ten cases our model results indicate that twentieth-century anthropogenic greenhouse gas emissions increased the risk of floods occurring in England and Wales in autumn 2000 by more than 20%, and in two out of three cases by more than 90%.

Recent widespread UK floods—such as in spring 1998, autumn 2000, winter 2003 and summer 2007—have prompted debate as to whether these particular events are attributable to anthropogenic climate change^{6,7,13–15}. This is an ill-posed question, given uncertainty in the antecedent conditions; many untraceable factors, anthropogenic or natural, may have contributed to any individual event^{13,16}. Indeed, observed UK fluvial-flood and high-flow trends for recent decades suggest no clear evidence for any change above that of natural variability^{17,18}, mirroring the mixed picture in observed precipitation changes^{19,20}.

For this reason, only general explanations are usually offered for any expected increase in flooding¹⁵; these typically involve thermodynamic arguments for precipitation extremes increasing with atmospheric water vapour in a warming world. Although oversimplified^{8,9}, these arguments offer a physically plausible first guess. For example, following this simple thermodynamic framework, one may scale observed daily autumn precipitation extremes in England and Wales around the year 2000 by the reduction in atmospheric water vapour had estimated twentieth-century surface warming attributable to anthropogenic

greenhouse gas emissions^{21,22} not occurred. That suggests the probability of severe daily precipitation for these autumns is roughly 33% higher than had these emissions and resulting warming not occurred (Supplementary Figs 1, 2).

Scaling observed precipitation, however, cannot rigorously quantify the change in probability of a specific type of complex weather-related event. Only by explicitly modelling climates encompassing all possible weather states consistent with antecedent uncertainty for the period of interest, both with and without anthropogenic drivers, can one address a well-posed question: what fraction of the event probability is attributable to the anthropogenic drivers^{13,16}? If we can assume an unchanging relationship between hazard and resulting damage, then event probability becomes a proxy for risk.

Such an attribution framework was used to assess the contribution of anthropogenic drivers to European heatwave risk in summer 2003²³. However, that study used a relatively low-resolution climate model with a limited number of simulations, and assumed unchanging variability about an anthropogenic trend in mean summer temperatures. This is not appropriate for UK flooding, which is a smaller spatio-temporal-scale phenomenon subject to greater variability that may change under anthropogenic drivers^{2,15}.

Here we develop this attribution framework, and assess the contribution of twentieth-century anthropogenic greenhouse gas emissions to flood risk in England and Wales in autumn (September to November) 2000. We use a seasonal-forecast-resolution climate model, and account for any anthropogenic change in variability by generating ‘time-slice’ simulations under two driving scenarios constructed for autumn 2000: a realistic scenario representing the actual climatic conditions (A2000), and a hypothetical scenario representing the climatic conditions as they might have been had twentieth-century anthropogenic greenhouse gas emissions not occurred (A2000N).

The model is HadAM3-N144, with a global horizontal resolution of 1.25° longitude by 0.83° latitude, and 30 vertical hybrid-pressure levels²⁴. As atmosphere–ocean feedbacks were not believed to play a major role during autumn 2000^{10,25}, we use an atmosphere-only model, with sea surface temperatures (SSTs) and sea ice as bottom boundary conditions.

The A2000 scenario attempts to represent realistic autumn 2000 conditions in the model by prescribing greenhouse gas and other atmospheric pollutant (sulphate aerosol, ozone) concentrations for that time, as well as prescribing observed²⁶ SSTs and sea ice (see Methods). The A2000N scenario attempts to represent hypothetical autumn 2000 conditions in the model by altering the A2000 scenario as follows: greenhouse gas concentrations are reduced to year 1900 levels; SSTs are altered by subtracting estimated twentieth-century warming attributable to greenhouse gas emissions, accounting for uncertainty; and sea ice is altered correspondingly using a simple empirical SST–sea ice relationship determined from observed²⁶ SST and sea ice. The attributable SST warming is derived from estimates^{21,22} that used

¹Atmospheric, Oceanic and Planetary Physics, Department of Physics, University of Oxford, Oxford OX1 3PU, UK. ²Institute for Atmospheric and Climate Science, ETH Zurich, CH-8092 Zurich, Switzerland. ³Oxford e-Research Centre, University of Oxford, Oxford OX1 3QG, UK. ⁴Tyndall Centre Oxford, Oxford University Centre for the Environment, Oxford OX1 3QY, UK. ⁵Met Office Hadley Centre, Fitzroy Road, Exeter EX1 3PB, UK. ⁶National Institute for Environmental Studies, Tsukuba, Ibaraki 305-8506, Japan. ⁷Risk Management Solutions Ltd, London EC3R 8NB, UK. [†]Present address: Institute for Atmospheric and Climate Science, ETH Zurich, CH-8092 Zurich, Switzerland.

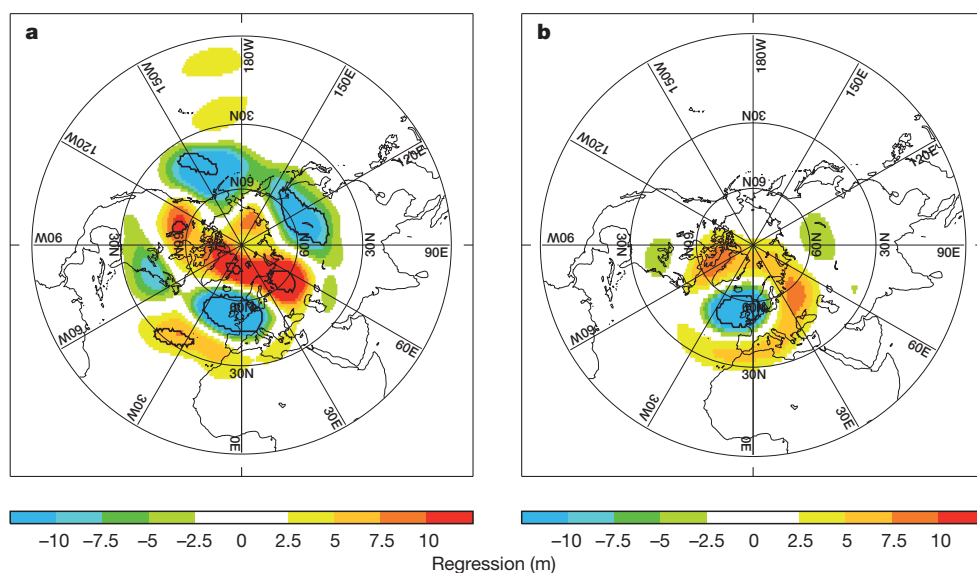


Figure 1 | Synoptic structure of Northern Hemisphere autumns. Regression pattern (m) of mean autumn 500-hPa geopotential height against total autumn England and Wales precipitation normalized by one standard deviation. **a**, For all autumns before autumn 2000 in ERA-40 (1957–99). **b**, For all simulations in the A2000 climate. Bold contours denote areas significant at 1%, assuming 43-member samples (number of ERA-40 autumns) and normally distributed regression variables. Hemispheric correlation of the two patterns is 0.69, falling within the 0.57–0.87 (5th–95th percentile) range of Monte Carlo bootstrap correlations between the A2000 pattern and patterns constructed using random 43-member sub-samples of A2000 simulations.

well-established ‘optimal fingerprinting’ analysis^{1,2}. Specifically, four spatial patterns of attributable warming were obtained from simulations with four coupled atmosphere–ocean climate models (HadCM3, GFDLR30, NCARPCM1 and MIROC3.2), and pattern amplitudes and associated uncertainties were constrained by historical observations (see Methods). Hence the full A2000N scenario actually comprises four scenarios with a range of SST patterns and sea ice, reflecting the uncertainty in large-scale anthropogenic greenhouse gas warming.

Numerous model simulations are required under both the A2000 and A2000N scenarios to capture what was considered a relatively unpredictable, rare event^{3,4,13,16,25}. Thus under each scenario we generate an ensemble of several thousand one-year weather simulations covering the autumn 2000 period, with perturbed initial conditions. This is beyond available conventional supercomputing resources, so we used a global, publicly volunteered distributed computing network, using architecture developed under the *climateprediction.net* project^{11,12}. The resulting large A2000 and A2000N ensembles of weather simulations respectively constitute our estimates of realistic and hypothetical autumn 2000 climates.

Autumn 2000 weather was characterized by a general eastwards displacement of the North Atlantic jet stream from its climatological position, bringing intense systems further into western Europe¹⁰. This displacement was associated with a commonplace but anomalously strong ‘Scandinavia’ atmospheric circulation pattern (a Rossby-wave-like train of tropospheric anomalies in geopotential height, extending from the subtropical Atlantic across Eurasia, with a cyclone over the UK and a strong anticyclone over Scandinavia). This Scandinavia pattern was itself catalysed by anomalous tropical Atlantic and South American upper-tropospheric convergence, and a possible weak secondary northern mid-Atlantic SST feedback¹⁰. A regression of mid-tropospheric geopotential height against England and Wales precipitation for all previous autumns (1957–99) in the observation-based ERA-40 reanalysis²⁷ certainly yields a structure (Fig. 1a) remarkably similar to the Scandinavia pattern.

We use a seasonal-forecast-resolution model that better represents the extra-tropical jets than lower-resolution counterparts typically used for climate simulations²⁴. Indeed, the ERA-40 pattern is consistent with the analogous synoptic pattern in our A2000 climate (Fig. 1b): it also displays a negative centre over the UK subsumed in a Rossby-wave-like train over the Atlantic–Eurasian region. Although a weak test, because ERA-40 autumns originate from different years with differing conditions whereas A2000 autumns originate from simulations with autumn 2000 conditions alone, this comparison nevertheless provides some confidence in the model’s ability to represent the relevant synoptic conditions.

Autumn 2000 flood episodes involved sequences of intense weather systems bringing heavy multi-day precipitation pulses to catchments that became saturated⁴. Hence we examine daily river runoff, which is a better measure of flooding than total precipitation. We synthesize this runoff using a relatively simple precipitation–runoff model²⁸, derived from a coupled land-surface and river-routing scheme with empirically estimated and optimized hydrologic parameters for England and Wales catchments (see Methods). We feed England and Wales total daily precipitation time-series from all our climate model simulations into this model to produce ensembles of synthetic daily river runoff associated with our A2000 and A2000N climates. To test if this runoff adequately represents autumn variability, we compare it with ERA-40 runoff, similarly synthesized using precipitation from all available autumns (1958–2001). Figure 2 demonstrates that England and Wales runoff variability in our A2000 climate is representative of that in ERA-40 autumns over a range of timescales.

We compare the runoff ensembles for A2000 and A2000N climates via occurrence frequency (or equivalently, ‘return time’) curves in Fig. 3. A given magnitude of runoff event generally occurs more frequently in the A2000 climate (a decreased return time), and so is more probable in any given autumn, relative to all four estimates of A2000N climate.

We thus estimate the fraction of flood risk in England and Wales in autumn 2000 that is attributable to twentieth-century anthropogenic greenhouse gas emissions. This is represented via the change in probability of a severe daily river runoff event, assuming an unchanging relationship between that hazard and resulting damage (this

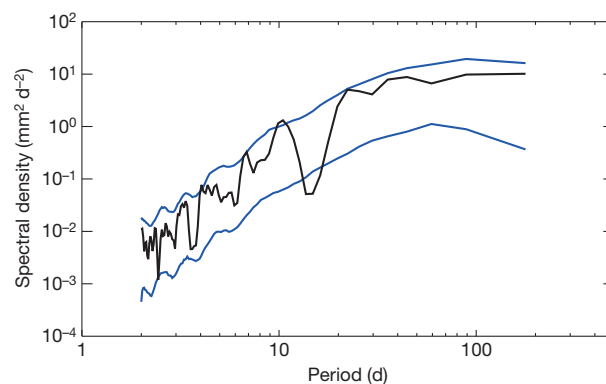


Figure 2 | Power spectra of daily river runoff for England and Wales autumns. Black line shows the spectrum for runoff synthesized from ERA-40 precipitation in all available autumns (1958–2001). Pair of blue lines marks the 5–95% confidence interval of the spectrum for runoff synthesized from all precipitation simulations in the A2000 climate.

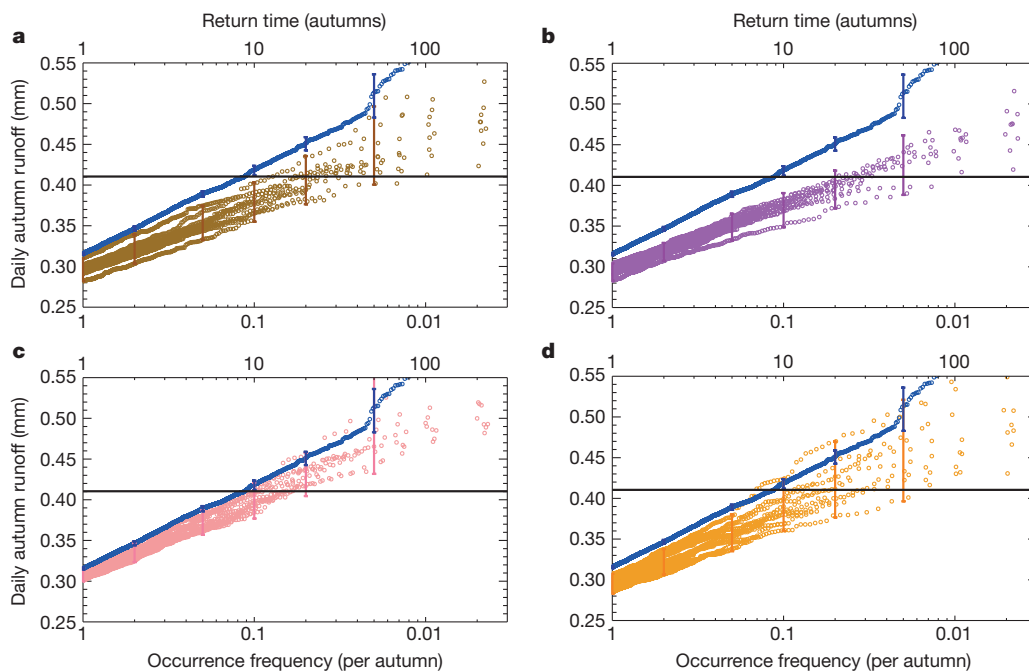


Figure 3 | Change in occurrence frequency of daily river runoff for England and Wales autumn 2000. **a–d**, Occurrence frequency curves of runoff (circles) synthesized from all precipitation simulations in A2000 and A2000N climates. Top axis of each panel is equivalent return time. Each panel shows identical A2000 runoff (blue). A2000N runoffs differ, being in climates generated using attributable SST warming estimates from HadCM3 (**a**; brown), GFDLR30 (**b**; purple), NCARPCM1 (**c**; pink) and MIROC3.2 (**d**; orange), with 10 curves corresponding to equiprobable amplitudes of warming. Bars represent 5–95% confidence intervals (see Methods). Horizontal line marks the highest autumn 2000 runoff synthesized from ERA-40 precipitation (0.41 mm).

focuses on hydrometeorological contributions to risk: other factors, such as the changing built environment, could also have contributed through changing vulnerability). As the observed floods involved a range of multi-day protracted flows rather than flash events⁴, these flows are also reflected in high daily values. Hence we define ‘severe’ to be anything exceeding the highest observation-based daily runoff for autumn 2000, as synthesized from ERA-40 precipitation (0.41 mm, denoted by the horizontal line in Fig. 3). R and R_N are then the fraction of runoff events in the A2000 and A2000N climates respectively that exceed this threshold. It follows that the fraction of attributable risk is $FAR = 1 - R_N/R$ (refs 13, 16). Uncertainty in this calculation is estimated using a Monte Carlo bootstrap sampling procedure on pairs of A2000 and A2000N runoff ensembles in Fig. 3 (see Methods).

The resulting distributions of FAR in Fig. 4 (coloured histograms) show significantly (at the 10% level) increased flood risk in the A2000 climate relative to all four estimates of A2000N climate. Assuming that these estimates effectively span uncertainty in the true A2000N climate, through the range of attributable SST warming estimates used in generating them, the full increase is given by the aggregate distribution (black histogram). It shows that the increase in risk of occurrence of floods in England and Wales in autumn 2000 that is attributable to twentieth-century anthropogenic greenhouse gas emissions is very likely (nine out of ten cases) to be more than 20%, and likely (two out of three cases) to be more than 90% (all to one significant figure).

This assessment assumes that attributable SST warming estimates can simply be subtracted from the SSTs observed in 2000, with seasonal to interannual modes of SST variability otherwise remaining unchanged. Although anthropogenic influence on such modes is indeed very uncertain¹, this assumption of additivity may be inappropriate for events highly dependent on them²⁹. However, the dependence of UK autumn 2000 precipitation on such modes appears minor^{10,25}, justifying our approach here.

The range of FAR estimated using our explicit-modelling framework (Fig. 4, black histogram) is approximately consistent with the FAR estimated using observations in the simple thermodynamic framework (Supplementary Fig. 2), and this consistency between approaches of vastly different complexity suggests our results are physically plausible. Allied to this, the range appears independent of any response to rising greenhouse gases of the key atmospheric mode of variability relevant to UK autumnal precipitation (Supplementary Fig. 3). Hence our results

should be relatively insensitive to the choice of modelling tools, but exploring sensitivity to choice of atmospheric and hydrologic model, and SST modes, remains a priority. So does further evaluation of our modelling set-up, although evaluation of extreme event statistics is hampered by limited historical records. We assume that any bias in England and Wales flooding between the A2000 climate and ERA-40 applies identically to the A2000N climate. This assumption is impossible to test explicitly, especially considering that absolute biases can be difficult to assess owing to variation between observation-based values themselves^{3,27}. Crucially, however, most runoff occurrence frequency curves in Fig. 3 remain approximately linear over a range of extreme values, so our FAR estimate would be consistent over a range of bias-corrected flood thresholds.

We have developed a ‘probabilistic event attribution’ framework that quantifies the anthropogenic contribution to flood risk. We stress that

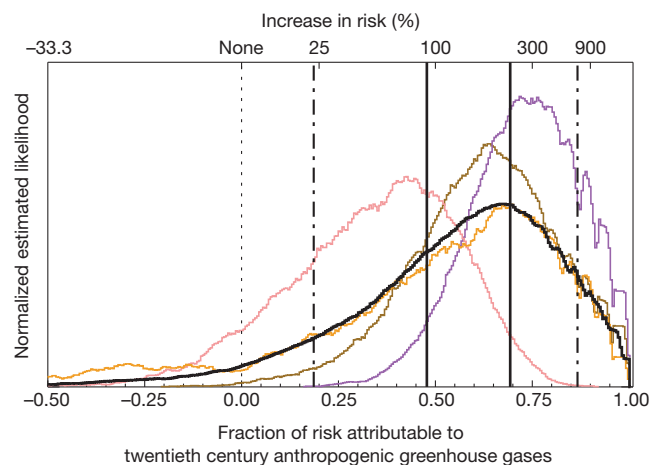


Figure 4 | Attributable risk of severe daily river runoff for England and Wales autumn 2000. Histograms (smoothed) of the fraction of risk of severe synthetic runoff in the A2000 climate that is attributable to twentieth-century anthropogenic greenhouse gas emissions. Each coloured histogram shows this fraction of attributable risk (FAR) with respect to one of four A2000N climate estimates in Fig. 3 (with corresponding colours). The aggregate histogram (black) represents the FAR relative to the full A2000N climate, with the dot-dashed (solid) pair of vertical lines marking 10th and 90th (33rd and 66th) percentiles. Top axis is equivalent increase in risk.

our results relate to autumn 2000-type floods. But other event-types, such as snow-melt floods, might have become less likely under anthropogenic climate change: our framework provides a method for also assessing those likelihoods. Furthermore, just because an event-type becomes more likely does not guarantee it will become even more likely in future—but it does highlight a potential impact of climate change.

With many purported climate change impacts being reported—many related to extreme weather—an objective method of distinguishing actual impacts is urgently needed. Our assessment is for the greenhouse gas contribution only: the total anthropogenic contribution would also require consideration of climate drivers such as sulphate aerosols and ozone. However, the recently launched Adaptation Fund, intended to finance climate change adaptation activities in developing nations, operates under the auspices of the United Nations Framework Convention on Climate Change that specifically defines ‘climate change’ as due to greenhouse gas emissions³⁰. By demonstrating the contribution of such emissions to the risk of a damaging event, our approach could prove a useful tool for evidence-based climate change adaptation policy.

METHODS SUMMARY

A2000 climate. HadAM3-N144 simulations run under the A2000 scenario were initially perturbed using a conventional next-day-difference technique, and started in April 2000 as wet spring conditions preceded autumn 2000⁴. The climate contains an ensemble of 2,268 one-year simulations.

A2000N climate. HadAM3-N144 simulations with similarly produced initial perturbations ran under four A2000N scenario estimates, constructed using attributable surface warming patterns from HadCM3, GFDLR30, NCARPCM1 and MIROC3.2. These spatial patterns each have an uncertainty distribution on their amplitude^{21,22}, estimated through optimal fingerprinting analysis^{1,2}. We scaled each pattern by deciles of this distribution, yielding 10 equiprobable estimates. Hence there are 10 curves per A2000N climate estimate in Fig. 3. These four climate estimates contain ensembles of 2,158, 2,159, 2,170 and 2,070 one-year simulations respectively.

Estimating runoff confidence intervals and FAR. We estimated runoff sampling uncertainty in Fig. 3 by Monte Carlo bootstrap sampling the A2000 ensemble, and each of the 10 scaling-ensembles per A2000N climate estimate. Corresponding confidence intervals are shown for the A2000 curve and the collective 10 curves in each A2000N climate estimate. For each sampled A2000–A2000N ensemble pair, we computed change in exceedance probability of our severe threshold, and hence FAR. The distributions of these FARs are coloured histograms in Fig. 4.

Precipitation-runoff model. Our runoff synthesis was derived from a coupled hydrologic–hydraulic scheme describing land-surface and river-routing processes, respectively. The hydrologic component was forced by precipitation constructed from ERA-40 using an analogue Monte Carlo method with statistical downscaling, and calibrated for 11 England and Wales catchments using observed runoff data. The hydraulic component was calibrated for these catchments using gauge flow statistics. We fitted a linear transfer function precipitation-runoff model²⁸ to long simulations with this scheme, with parameters accounting for different runoff timescales. This model was fed our climate model and ERA-40 precipitation, assuming it was uniformly falling rainfall.

Full Methods and any associated references are available in the online version of the paper at www.nature.com/nature.

Received 30 March; accepted 10 December 2010.

- Hegerl, G. C. *et al.* in *Climate Change 2007: The Physical Science Basis* (eds Solomon, S. *et al.*) Ch. 9, 663–746 (Cambridge Univ. Press, 2007).
- Stott, P. A. *et al.* Detection and attribution of climate change: a regional perspective. *Wiley Interdiscip. Rev. Clim. Change* **1**, 192–211 (2010).
- Alexander, L. V. & Jones, P. D. Updated precipitation series for the U.K. and discussion of recent extremes. *Atmos. Sci. Lett.* **1**, 142–150 (2000).
- Marsh, T. J. & Dale, M. The UK floods of 2000–2001: a hydrometeorological appraisal. *J. Chart. Inst. Wat. Environ. Mgmt* **16**, 180–188 (2002).
- Association of British Insurers. Flooding: a partnership approach to protecting people. (http://www.abi.org.uk/Publications/Flooding_A_partnership_Approach_to_Protecting_People1.aspx) (2001).
- Department for Environment, Food and Rural Affairs. *To What Degree Can the October/November 2000 Flood Events Be Attributed to Climate Change?* (Final Report FD2304, DEFRA, London, 2001).
- Environment Agency. *Lessons Learned: Autumn 2000 Floods* (Environment Agency, Bristol, 2001).
- Lenderink, G. & Van Meijgaard, E. Increase in hourly precipitation extremes beyond expectations from temperature changes. *Nature Geosci.* **1**, 511–514 (2008).
- O’Gorman, P. A. & Schneider, T. The physical basis for increases in precipitation extremes in simulations of 21st-century climate change. *Proc. Natl Acad. Sci. USA* **106**, 14773–14777 (2009).
- Blackburn, M. & Hoskins, B. J. Atmospheric variability and extreme autumn rainfall in the UK. (<http://www.met.rdg.ac.uk/~mike/autumn2000.html>) (2001).
- Allen, M. R. Do-it-yourself climate prediction. *Nature* **401**, 642 (1999).
- Massey, N. *et al.* Data access and analysis with distributed federated data servers in climateprediction.net. *Adv. Geosci.* **8**, 49–56 (2006).
- Allen, M. R. Liability for climate change. *Nature* **421**, 891–892 (2003).
- Pitt, M. *The Pitt Review: Lessons Learned from the 2007 Floods* (Cabinet Office, London, 2008).
- Wilby, R. L., Beven, K. J. & Reynard, N. S. Climate change and fluvial flood risk in the UK: more of the same? *Hydrol. Process.* **22**, 2511–2523 (2008).
- Stone, D. A. & Allen, M. R. The end-to-end attribution problem: from emissions to impacts. *Clim. Change* **71**, 303–318 (2005).
- Robson, A. J. Evidence for trends in UK flooding. *Phil. Trans. R. Soc. Lond.* **360**, 1327–1343 (2002).
- Hannaford, J. & Marsh, T. High-flow and flood trends in a network of undisturbed catchments in the UK. *Int. J. Climatol.* **28**, 1325–1338 (2008).
- Maraun, D., Osborn, T. J. & Gillett, N. P. United Kingdom daily precipitation intensity: improved early data, error estimates and an update from 2000 to 2006. *Int. J. Climatol.* **28**, 833–842 (2008).
- Fowler, H. J. & Kilsby, C. G. A regional frequency analysis of United Kingdom extreme rainfall from 1961 to 2000. *Int. J. Climatol.* **23**, 1313–1334 (2003).
- Stott, P. A. *et al.* Observational constraints on past attributable warming and predictions of future global warming. *J. Clim.* **19**, 3055–3069 (2006).
- Nozawa, T., Nagashima, T., Shiogama, H. & Crooks, S. A. Detecting natural influence on surface air temperature change in the early twentieth century. *Geophys. Res. Lett.* **32**, L20719 (2005).
- Stott, P. A., Stone, D. A. & Allen, M. R. Human contribution to the European heatwave of 2003. *Nature* **432**, 610–614 (2004).
- Pope, V. D. & Stratton, R. A. The processes governing horizontal resolution sensitivity in a climate model. *Clim. Dyn.* **19**, 211–236 (2002).
- Massacand, A. C. *Forecasting of Extreme Seasonal Precipitation: Insight into the ECMWF Potential* (Technical Memorandum No. 415, ECMWF, 2003).
- Reynolds, R. W., Rayner, N. A., Smith, T. M., Stokes, D. C. & Wang, W. Q. An improved in situ and satellite SST analysis for climate. *J. Clim.* **15**, 1609–1625 (2002).
- Uppala, S. M. *et al.* The ERA-40 re-analysis. *Q. J. R. Meteorol. Soc.* **131**, 2961–3012 (2005).
- Lohmann, D., Nolte-Holube, R. & Raschke, E. A large-scale horizontal routing model to be coupled to land surface parametrization schemes. *Tellus A* **48**, 708–721 (1996).
- Sexton, D. M. H., Rowell, D. P., Folland, C. K. & Karoly, D. J. Detection of anthropogenic climate change using an atmospheric GCM. *Clim. Dyn.* **17**, 669–685 (2001).
- United Nations Framework Convention on Climate Change (UNFCCC). *Report of the Conference of the Parties Serving as the Meeting of the Parties to the Kyoto Protocol on its Second Session, held at Nairobi from 6 to 17 November 2006* (FCCC/KP/CMP/2006/10, United Nations Office at Geneva, Geneva, 2007).

Supplementary Information is linked to the online version of the paper at www.nature.com/nature.

Acknowledgements We thank all members of the public who ran HadAM3-N144 climate model simulations using the BOINC open source computing platform, and the climateprediction.net team for their technical support; M. Collins, N. Rayner, A. Jones and C. Johnson for originally supplying the HadAM3-N144 model, observed SSTs and sea ice, sulphate fields, and ozone fields, respectively; G. Meehl and T. Knutson for permission to use NCARPCM1 and GFDLR30 temperature data, respectively; S. Hay and I. Tracey for assistance with beta tests; C. Lee for technical advice; and W. Ingram and D. Rowlands for scientific advice. P.P. was supported by a NERC CASE studentship with Risk Management Solutions Ltd, by WWF International, and by NCCR climate. D.A.S. and P.P. received partial support from the UK Department for Environment, Food, and Rural Affairs. P.A.S. was supported by the Joint DECC and Defra Integrated Climate Programme — DECC/Defra (GA01101). T.N. was supported by the Japanese Ministry of Education, Culture, Sports, Science and Technology. D.A.S. and M.R.A. received additional support from the Climate Change Detection and Attribution Project jointly funded by the US National Oceanic and Atmospheric Administration’s Office of Global Programs and the US Department of Energy. This research was also supported by the European Union (FP6) funded Integrated Project WATCH (contract number 036946) and the Smith School of Enterprise and the Environment.

Author Contributions M.R.A., D.A.S., P.P. and P.A.S. designed the probabilistic event attribution framework. P.P. and T.A. implemented the framework, generating HadAM3-N144 climate model simulations using climateprediction.net distributed computing architecture, and feeding them into the precipitation-runoff model for England and Wales catchments designed and developed by D.L. and A.G.J.H. P.A.S. and T.N. contributed estimates of attributable warming using coupled climate models. P.P., D.A.S., M.R.A., A.G.J.H. and P.A.S. wrote the paper.

Author Information Reprints and permissions information is available at www.nature.com/reprints. The authors declare no competing financial interests. Readers are welcome to comment on the online version of this article at www.nature.com/nature. Correspondence and requests for materials should be addressed to P.P. (pardeep.pall@env.ethz.ch).

METHODS

Generating the A2000 climate. All HadAM3-N144 simulations began with a climatological April base state obtained from running the model under average 1979–96 AMIP2 (Atmospheric Model Inter-comparison Project number 2) conditions²⁴. For each simulation, this state was initially perturbed via a unique adjustment to its atmospheric potential temperature (but not other variables, owing to distributed computing bandwidth constraints). These perturbations were derived from next-day surface differences in the AMIP2 simulation, and applied to model grid boxes with a vertical taper. Preliminary tests showed almost full divergence between perturbed simulations on all vertical levels within a model fortnight.

Each perturbed simulation then ran under the A2000 scenario that prescribed the following conditions in the model for the period April 2000 to March 2001: global-mean time-mean major greenhouse gas and halocarbon concentrations, obtained via the Carbon Dioxide Information Analysis Center^{31,32}; the approximate annual-mean effect of sulphate aerosols, via modification of cloud droplet effective radius using cloud albedo responses to sulphate emissions pre-estimated from versions of the Hadley Centre atmospheric model with an interactive sulphur cycle and predicted cloud droplet number concentration³³; zonal-mean monthly-mean ozone, extrapolated from 1990 estimates using a Hadley Centre chemical transport model and chlorine estimates for the troposphere and stratosphere respectively (C. Johnson, personal communication); weekly-mean observed²⁶ SSTs and sea ice, interpolated to suit the 360-day HadAM3-N144 year. All other conditions (for example, solar forcing, land surface properties) were kept at the base state or at model default settings.

All simulations ran under Windows and Linux operating systems, in a global network of publicly-volunteered computers using climateprediction.net^{11,12} client-server distributed computing architecture.

We fed each completed simulation's England and Wales total daily precipitation time-series from April 2000 onwards into our precipitation-runoff model²⁸, to synthesize September 2000 to November 2000 daily river runoff. Thereby we fed both the model's baseflow storage term accounting for preceding long-term processes and the model's convolution filter accounting for preceding short-term processes, in synthesizing the runoff for 1 September onwards. (We also note that for ERA-40, precipitation in non-30-day months is first scaled to accommodate for the 30-day HadAM3-N144 months.)

Generating the A2000N climate. All HadAM3-N144 simulations began with initially perturbed April base states similar to those for the A2000 climate. Each perturbed simulation then ran under the A2000N scenario constructed by altering A2000 scenario gases, SSTs, and sea ice, as described below (all other conditions left as in the A2000 scenario).

To construct A2000N gases, A2000 greenhouse gas and halocarbon concentrations were reduced to year 1900 annual-mean global-mean estimates taken from historical forcing data sets³⁴.

To construct corresponding A2000N SSTs, A2000 SSTs were altered by subtracting estimated twentieth-century warming attributable to greenhouse gas emissions (Supplementary Figs 4–6).

To construct corresponding A2000N sea ice, A2000 sea ice was altered using the A2000N SSTs, and a simple empirical SST–sea ice relationship determined from observed gridded weekly-mean SST and sea ice data²⁶. Aggregating these observed data over years 2000 to 2001 and all grid boxes, we constructed a scatter plot of sea ice fractional grid box coverage versus SST, for Northern and Southern Hemispheres separately. In each hemisphere we applied a linear fit to the scatter, with one end anchored at the freezing point of sea water corresponding to 100% sea ice coverage. This linear SST–sea ice relationship was then applied to the change from A2000 to A2000N SSTs at each HadAM3-N144 grid box, to determine corresponding change in sea ice fractional coverage there. Finally, this sea ice change was subtracted from the A2000 sea ice to produce corresponding A2000N sea ice, and in this way we preserved the scatter characteristics of sea ice coverage.

Similarly to the A2000 simulations, all A2000N simulations were generated using distributed computing, and fed into the precipitation-runoff model.

Calibrating the precipitation-runoff model. The coupled hydrologic–hydraulic scheme operates on a 10-m-resolution digital terrain model, with the hydrologic component strongly based on TOPMODEL³⁵ and the hydraulic component implementing a Muskingum–Cunge scheme. The hydrologic component runs in 3-h time steps (to capture the intra-day evaporation cycle) and was calibrated against observed³⁶ daily mean river runoff time-series available for 1986–95. The hydraulic component runs in 5-min time steps (mainly for stability) and was calibrated against return period statistics of the observed daily maxima at gauging stations available from as far back as 1883 to 2006. Parameters were optimized by minimizing the root-mean-squared error (RMSE) so that mismatches of high deviations (runoff peaks) were more heavily penalized; thus the scheme is expected to perform well for wet periods.

The scheme is evaluated in Supplementary Table 1, via RMSE and correlation against the observed 1986–95 daily mean river runoff for each of the 11 England and Wales catchments. RMSE varies between catchments, with higher values typically reflecting higher mean runoff. Importantly, correlation is good for all catchments and is perhaps a more insightful indicator of performance given the issues with assessing change in absolute biases and extremes noted in the main text.

For computational efficiency, we fitted a linear transfer function precipitation-runoff model²⁸ to 1,000 years of continuous daily river runoff time-series generated with the calibrated scheme, for the largest (area-wise) gauges in each catchment. This transfer function has a fast and slow component, accounting for direct surface runoff and baseflow processes respectively, with the latter incorporating a linear reservoir storage term active from the first day of input precipitation. Briefly, after computing each day's storage, fast and slow components are both passed through a convolution filter accounting for their lumped travel times to and within the catchment's river channel. Thus while this filter only has a 12-day memory, longer-term memory is accounted for via the storage term. This approach is reasonable, given that the ground saturated quickly at the beginning of autumn 2000 and remained that way⁴, so that while preceding wet spring conditions may have had some importance, shorter-term precipitation dominated flooding. Indeed, changes in 10-day and less rainfall events over recent decades have been implied³⁷ as being relevant to UK autumnal flooding.

The model is evaluated in Supplementary Table 2, in terms of England and Wales totals across catchments as considered in the main text. We only show correlations, both for the reasons above and because here we are more interested in how accurately precipitation is translated to runoff (that is, high/low runoff following high/low precipitation). The performance is reasonable and, though poorer for extremes reflecting the limitations of a relatively simple transfer function, is comparable to the coupled scheme's performance and is better for autumnal than annual runoff.

31. Keeling, C. D. & Whorf, T. P. in *Trends: A Compendium of Data on Global Change* (Carbon Dioxide Information Analysis Center, Oak Ridge National Laboratory, 2005).
32. Prinn, R. G. *et al.* A history of chemically and radiatively important gases in air deduced from ALE/GAGE/AGAGE. *J. Geophys. Res.* **105**, 17751–17792 (2000).
33. Johns, T. C. *et al.* Anthropogenic climate change for 1860 to 2100 simulated with the HadCM3 model under updated emissions scenarios. *Clim. Dyn.* **20**, 583–612 (2003).
34. Meehl, G. A. *et al.* Combinations of natural and anthropogenic forcings in twentieth-century climate. *J. Clim.* **17**, 3721–3727 (2004).
35. Beven, K. J. & Kirkby, M. J. A physically based, variable contributing area model of basin hydrology. *Hydrol. Sci. J.* **24**, 43–69 (1979).
36. Natural Environmental Research Council — Centre for Ecology & Hydrology. The National River Flow Archive. (<http://www.ceh.ac.uk/data/nrfa/>) (2010).
37. Fowler, H. J. & Kilsby, C. G. Implications of changes in seasonal and annual extreme rainfall. *Geophys. Res. Lett.* **30**, 1720 (2003).

Leadership, social capital and incentives promote successful fisheries

Nicolás L. Gutiérrez¹, Ray Hilborn¹ & Omar Defeo²

One billion people depend on seafood as their primary source of protein and 25% of the world's total animal protein comes from fisheries¹. Yet a third of fish stocks worldwide are overexploited or depleted^{1,2}. Using individual case studies, many have argued that community-based co-management³ should prevent the tragedy of the commons⁴ because cooperative management by fishers, managers and scientists often results in sustainable fisheries^{3,5,6}. However, general and multidisciplinary evaluations of co-management regimes and the conditions for social, economic and ecological success within such regimes are lacking. Here we examine 130 co-managed fisheries in a wide range of countries with different degrees of development, ecosystems, fishing sectors and type of resources. We identified strong leadership as the most important attribute contributing to success, followed by individual or community quotas, social cohesion and protected areas. Less important conditions included enforcement mechanisms, long-term management policies and life history of the resources. Fisheries were most successful when at least eight co-management attributes were present, showing a strong positive relationship between the number of these attributes and success, owing to redundancy in management regulations. Our results demonstrate the critical importance of prominent community leaders and robust social capital⁷, combined with clear incentives through catch shares and conservation benefits derived from protected areas, for successfully managing aquatic resources and securing the livelihoods of communities depending on them. Our study offers hope that co-management, the only realistic solution for the majority of the world's fisheries, can solve many of the problems facing global fisheries.

Fish are a critical natural resource, yet global catches have peaked while human populations and demand for seafood continue to rise¹. This increasing pressure has coincided with most fisheries worldwide being fully exploited or requiring rebuilding². In the past several decades, researchers have examined the circumstances under which common pool resources, and fisheries in particular, can be successfully managed^{3,5}. The dominant theme in fisheries management has been that privatization is necessary to avoid Hardin's tragedy of the commons⁴, whereas Ostrom and others^{6–9} have argued that community-based co-management can often achieve sustainability.

Community-based co-management (hereafter co-management) occurs when fishers and managers work together to improve the regulatory process. Advantages of co-management include: enhanced sense of ownership encouraging responsible fishing; greater sensitivity to local socioeconomic and ecological restraints; improved management through use of local knowledge; collective ownership by users in decision making; increased compliance with regulations through peer pressure; and better monitoring, control and surveillance by fishers^{9,10}.

Despite the increasingly widespread adoption of co-management for solving governance issues^{11,12}, few attempts have been made to synthesize individual case studies into a general fisheries co-management model. There are qualitative case studies, comparative analyses and a few localized quantitative reviews on the subject^{12,13}, but no comprehensive

evaluations to support the hypothesis that co-management improves fisheries' governance systems and performance indicators¹⁴. Here, we tested whether co-management improves fisheries' social, economic and ecological success, identified relevant attributes generated by isolated study cases in diverse disciplines (such as ecology and social sciences) and evaluated the relative merits of different co-management attributes across fisheries.

We assembled worldwide data from the peer-reviewed literature, government and non-governmental organization (NGO) reports and from interviews of experts on co-managed fisheries. We identified 130 co-managed fisheries in 44 countries (Fig. 1 and Supplementary Table 1) covering artisanal and industrial sectors, and a variety of ecosystem types, degrees of human development (Human Development Index (HDI)¹⁵), and social, economic and political settings (Supplementary Table 2). We extracted 19 variables relating co-management attributes under five categories suggested by Ostrom¹⁶ for analysing social-ecological systems (Table 1 and Supplementary Table 2). These were used to predict eight binary measures of success grouped into ecological (for example, increase in stock abundance), social (for example, increase in social welfare) and economic (for example, increase in unit price) indicators and summed them to obtain a single holistic success score that captures natural and human dimensions of fisheries¹⁷.

Statistically demonstrating a causal connection between co-management attributes and successful fisheries is challenging, because we are mostly dealing with non-experimental and observational studies in which random treatments and control groups are not present.

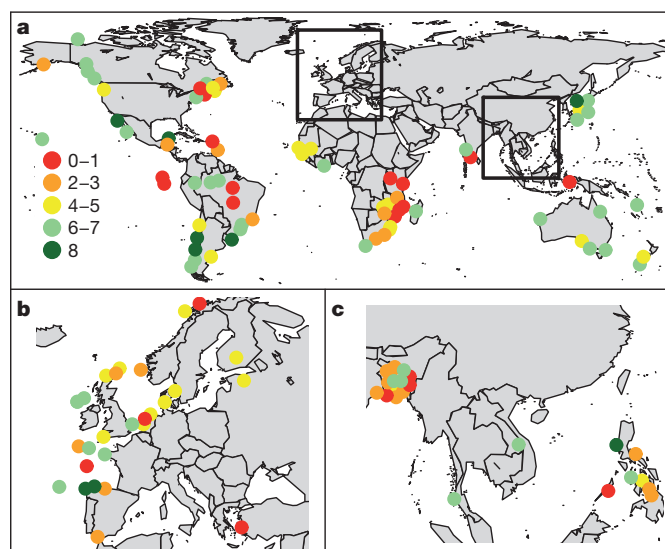


Figure 1 | Location and success score for all study cases of fisheries co-management. a–c, Success was grouped in five categories according to number of social, ecological and economic outcomes achieved. a, Global map. Insets are Europe (b) and Southeast Asia (c). $n = 130$.

¹School of Aquatic and Fishery Sciences, Box 355020, University of Washington, Seattle, Washington 98195-5020, USA. ²UNDECIMAR, Facultad de Ciencias, Iguá 4225, PO Box 10773, Montevideo 11400, Uruguay.

Table 1 | Fisheries co-management attributes and outcomes.

Group	Variable name	Frequency (%)
Co-management	Type (consultative, cooperative, delegated)	-
	Phase (pre-, implementation, post-)	-
	Time frame	-
Resource system	HDI (low, medium, high, very high)	-
	Governance Index	-
	Corruption Perceptions Index	-
	Resource type (single*, multi-species)	-
	Ecosystem (inland, coastal, offshore)	-
	Fishing sector (artisanal, industrial, sequential)	-
	Defined geographic boundaries	52
Resource unit	Sedentary/low mobility resources	38
Governance system	Central government support (local)	93
	Scientific advice	92
	Minimum size restrictions	76
	Long-term management policy	71
	Global catch quotas	52
	Monitoring, control and surveillance	47
	Protected areas	39
	Spatially explicit management	37
	Individual or community quotas	33
	Co-management in law (national)	32
	Seeding or restocking programs	19
	TURF	18
Users system	Social cohesion	78
	Self-enforcement mechanisms	71
	Leadership	62
	Tradition in self-organization	55
	Influence in local market	28
Outcomes	Community empowerment	85
	Fishery status (under or fully, over-exploited)	67
	Sustainable catches	62
	Increase in social welfare	61
	Increase in catch per unit of effort	54
	Add-on conservation benefits	45
	Increase in abundance	38
	Increase in unit prices	30

All attributes were grouped according to the classification of Ostrom¹⁶. Values in the frequency column denote percentage of co-management attributes reported as present within the co-management systems. For complete variable descriptions see Supplementary Table 2.

* Benthic, demersal, pelagic, mammal.

However, the large number of fisheries involved in our study, covering a wide spectrum of social, ecological and political settings, and the detailed information contained in the reviewed documents, provided the basis to assess causality through several criteria: (1) strength of association between co-management attributes and success measured by robust statistical methods; (2) consistency of association in various conditions across ecosystems, fishing sectors and degrees of human development; (3) plausibility of causal explanations; (4) coherence with co-management theories and knowledge of each fishery; and (5) temporality, where presence of attributes preceded success¹⁸. Furthermore, although comparison to top-down management would be of interest, the objective of this study was to identify and quantify the co-management attributes determining successful fisheries, and not explicitly to compare its performance with top-down centralized management.

We tested whether success scores differed among socio-economic conditions (HDI, fishing sector) and ecological settings (ecosystems, life history of exploited resources) and we identified specific attributes associated with their success (see Supplementary Information). Countries with high and very high HDIs were more successful than low and medium HDI countries, owing to higher redundancy in management tactics and stronger central governance structures. Industrial fisheries scored higher than artisanal fisheries mainly because of stronger enforcement mechanisms, whereas inland fisheries were less successful than coastal and offshore fisheries owing mostly to weaker social capital and short-term co-management arrangements. Co-management systems thrived in benthic and demersal fisheries, especially when accompanied by protected areas, territorial user rights for fishing (TURFs) and community or individual quotas allocated to well-defined groups of fishers. In contrast, less successful co-management observed in multi-species fisheries could be related to a mismatch between scales of distribution and mobility of stocks and the area of influence of the

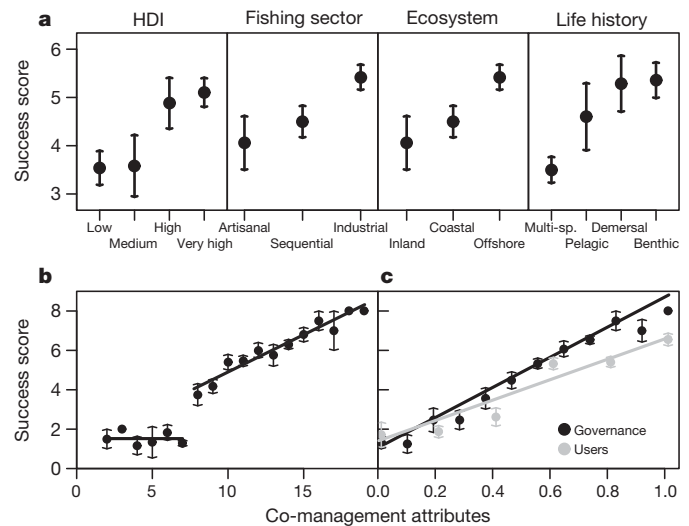


Figure 2 | Fisheries co-management performance. a, Success score discriminated by the HDI, fishing sector, ecosystem and life history. Multi-sp., multi-species. b, Success score correlated with the number of all co-management attributes present in the fishery. c, Success score correlated with proportion of governance and users' attributes separately (relative x-axis is shown for comparison purposes). Grouping variables are explained in Supplementary Table 2. All data are shown as mean \pm s.e.m.

fishing process and the management system (Fig. 2a, Supplementary Fig. 3 and Supplementary Table 4).

There was a distinctive two-step pattern between success scores and the total number of attributes in each fishery. If fewer than eight attributes were present, the success score was close to zero, whereas above this threshold there was a strong positive relationship, with increasing attributes leading to higher success scores (Fig. 2b). Success scores were also more strongly correlated with the number of governance attributes present than with the number of users/community attributes (Fig. 2c and Supplementary Table 4). This indicates that even though co-management is enhanced by strong central governance systems, local community attributes were also necessary for success. These results demonstrate that the likelihood of co-management success increases when more management tools are added, providing redundancy in management regulations^{19,20}. Further, no significant relationship ($P > 0.05$) was found between success and time frames of co-management regimes (omitting pre-implementation phase; mean \pm standard deviation = 15.9 ± 9.8 years), indicating that failure or success is independent of the number of years the regime has been in place.

Using regression trees and random forests²¹, we found that the most important co-management conditions necessary for successful management of fisheries are presence of community leaders, strong social cohesion, individual or community quotas, and community-based protected areas (Fig. 3a, b and Supplementary Table 2). Additional key attributes were enforcement mechanisms, long-term management policies and influence of fishers in local markets. Considering governance and users' attributes independently in the regression tree showed little differences in predictive accuracy compared to the joint tree ($<4\%$) and between governance and users' trees ($<5\%$). When analysed separately, community quotas were the most important management attribute followed by long-term management policies and protected areas, whereas leadership was by far the most significant users' attribute (Supplementary Fig. 4). These findings reinforce the notion that fisheries are complex social-ecological systems that need to be managed by addressing problems related not only to the resources themselves but to the people targeting them²².

Leadership was critical for successful co-management of fisheries. Presence of at least one singular individual with entrepreneurial skills, highly motivated, respected as a local leader and making a personal

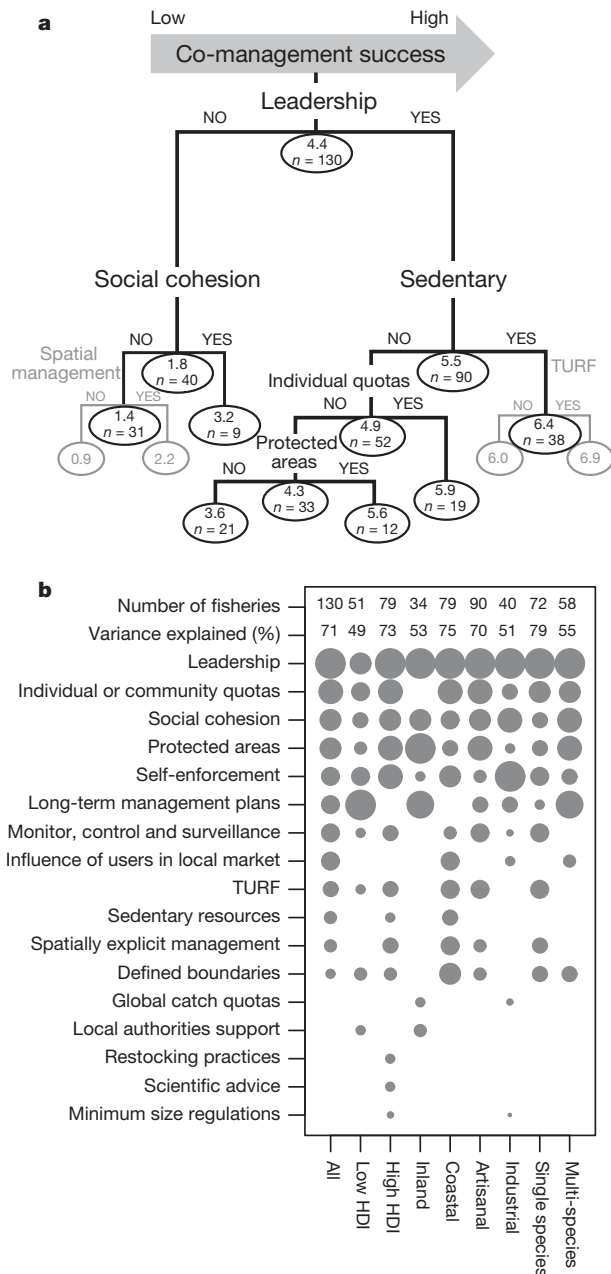


Figure 3 | Key co-management attributes for fisheries success. **a**, Regression tree showing the most important factors determining success. Higher branches offer greater explanatory power. Average success score and number of fisheries are listed at each node. The optimal tree explained 69% of the total deviance, and the vertical depth of each split is proportional to the variation explained by each attribute. **b**, Importance of individual attributes (rank proportional to circle size) for the full data set and for selected subsets of the data determined by random forests. The number of fisheries and variance explained are also indicated. Variables descriptions are given in Supplementary Table 2.

commitment to the co-management implementation process, was essential. Legitimate community leaders, when guided by collective interests and not self-benefits, give resilience to changes in governance, influence users' compliance to regulations and enhance conflict resolutions in quota allocations²³. Community cohesion founded on norms, trust, communication, and connectedness in networks and groups was also an important global attribute leading to successful fisheries co-management. This robust social capital^{7,24} serves as a buffer against changes in institutional arrangements, economic crises and resource overexploitation, and fosters sustainable co-management systems^{3,25}. Our results show that additional resources should be spent on efforts to identify

community leaders and build social capital rather than only imposing management tactics without users' involvement.

Catch shares, both by individual or community quotas and by TURFs, were a key management condition towards co-management success. Well-designed and implemented catch shares have helped to prevent overfishing²⁶, promote stability²⁷ and ecological stewardship²⁸. However, previous analyses of catch share programs have focused mainly on industrial fisheries in developed countries. We highlight the importance of users' security over catch or space in attaining social, economic and ecological success across all co-managed fisheries.

The effects of protected areas in achieving co-management success reaffirmed their strong link to social-ecological dynamics and the role of local communities in their successful implementation²⁹. Their potential value for improving fisheries management depends on proper incentives, decentralized institutional arrangements and cohesive social organizations, all of which are more likely to happen under well-established co-management regimes. Spatial considerations, through clearly defined geographic boundaries (such as lake or enclosed bay) and sedentary life history of the resources contributed to co-management success by confining the number of users, lowering associated costs of information gathering, monitoring and enforcement, and restricting the spatial dynamics of fishing effort to well-defined areas.

Self-enforcing mechanisms contributed significantly to co-management success when guided by self-interests²⁴ (for example, through systems of penalties imposed by strong operational rules designed, enforced and controlled by local fishers). Influence of fishers in local markets characterized most accomplished co-management regimes, by allowing for specific marketing tactics, improved product quality, shorter intermediaries' chains, market timing coordination and eco-labelling strategies. This influence of users in local markets may result in multiple benefits to local communities, minimizing the probability of overexploitation and enhancing economic revenues by higher income per unit of effort¹².

Our study is, to our knowledge, the first comprehensive global assessment of social, economic and ecological attributes contributing to fisheries co-management success. Our synthesis shows that co-management holds great promise for successful and sustainable fisheries worldwide. However, there is an urgent need to gather long-term ecological, economic and social data from a variety of fisheries in a multi-disciplinary context in order to compare empirically different degrees of users' involvement in management decisions and to better understand and improve fisheries co-management³⁰.

METHODS SUMMARY

We conducted a systematic search of the peer-reviewed and grey literature ($n = 1,168$ documents) to identify quantitative and qualitative evidences of the impacts of fisheries co-management practices around the world. We used the term community-based co-management to cover the whole spectrum of co-management arrangements (from formal consultation mechanisms between government and users to self-governance). The presence of well-established local co-management institutions with decision power in fisheries management was also used as compulsory criterion to classify a fishery as co-managed. Fisheries without sufficient or consistent information as well as co-management regimes in a pre-implementation phase were excluded from the analyses. For 130 fisheries (out of a total of 218 study cases; Supplementary Table 1) we compiled a database of 9 grouping or contextual variables including co-management type, co-management phase, duration of the management regime, HDI, Corruption Perception Index, Governance Index, ecosystem, fishing sector and resource type and 19 co-management attributes (Table 1 and Supplementary Table 2). We used aggregated social, economic and ecological binary outcomes to represent co-management success (success score; Supplementary Table 2). We built a regression tree model that graphically depicts quantitative relationships between predictor attributes and co-management success. Missing values were filled in using surrogate splits inside the regression model. A random forest model of 10,000 trees was used to estimate the relative importance of selected attributes in determining co-management success. The importance of contextual variables (for example, fishing sector) was also investigated by grouping them in the random forest models and by running independent models for each category (for example, artisanal, industrial). Model accuracy for trees and random forests were quantified using standard metrics,

and model selection was performed by backwards stepwise elimination of non-significant predictors (see Supplementary Information).

Received 7 September; accepted 18 November 2010.

Published online 5 January 2011.

1. Food and Agriculture Organization of the United Nations. *FAO Yearbook: Fishery and Aquaculture Statistics* 2007 (FAO, 2009).
2. Worm, B. *et al.* Rebuilding global fisheries. *Science* **325**, 578–585 (2009).
3. Ostrom, E. *Governing the Commons: The Evolution of Institutions for Collective Action* (Cambridge Univ. Press, 1990).
4. Hardin, G. The tragedy of the commons. *Science* **162**, 1243–1248 (1968).
5. Costanza, R. *et al.* Principles for sustainable governance of the oceans. *Science* **281**, 198–199 (1998).
6. Dietz, T., Ostrom, E. & Stern, P. The struggle to govern the commons. *Science* **302**, 1907–1912 (2003).
7. Pretty, J. Social capital and the collective management of resources. *Science* **302**, 1912–1914 (2003).
8. Beddington, J. R., Agnew, D. J. & Clark, C. W. Current problems in the management of marine fisheries. *Science* **316**, 1713–1716 (2007).
9. Berkes, F. Community-based conservation in a globalized world. *Proc. Natl Acad. Sci. USA* **104**, 15188–15193 (2007).
10. Pomeroy, R. S. & Williams, M. J. *Fisheries Co-Management and Small-Scale Fisheries: A Policy Brief* (ICLARM, 1994).
11. Borrini-Feyerabend, G., Pimbert, M., Farvar, M. T., Kothari, A. & Renard, Y. *Sharing Power: Learning by Doing in Co-Management of Natural Resources Throughout the World* (IIED and IUCN/CEESP/CMWG, 2004).
12. Defeo, O. & Castilla, J. C. More than one bag for the world fishery crisis and keys for co-management successes in selected artisanal Latin American shellfisheries. *Rev. Fish Biol. Fish.* **15**, 265–283 (2005).
13. Wilson, J., Yan, L. & Wilson, C. The precursors of governance in the Maine lobster fishery. *Proc. Natl Acad. Sci. USA* **104**, 15212–15217 (2007).
14. Basurto, X. & Ostrom, E. The core challenges of moving beyond Garrett Hardin. *J. Nat. Resour. Pol. Res.* **1**, 255–259 (2009).
15. United Nations Development Programme. *The Human Development Index* (UNDP, 2009).
16. Ostrom, E. A general framework for analyzing sustainability of social-ecological systems. *Science* **325**, 419–422 (2009).
17. Hilborn, R. Defining success in fisheries and conflicts in objectives. *Mar. Policy* **31**, 153–158 (2007).
18. Chetty, R. K. *et al.* A systematic approach to preclinical and clinical safety biomarker qualification incorporating Bradford Hill's principles of causality association. *Clin. Pharmacol. Ther.* **88**, 260–262 (2010).
19. Castilla, J. C. & Defeo, O. Paradigm shifts needed for world fisheries. *Science* **309**, 1324–1325 (2005).
20. Stefansson, G. & Rosenberg, A. A. Combining control measures for more effective management of fisheries under uncertainty: quotas, effort limitation and protected areas. *Phil. Trans. R. Soc. B* **360**, 133–146 (2005).
21. Breiman, L. Random forests. *Mach. Learn.* **45**, 5–32 (2001).
22. Hilborn, R. Managing fisheries is managing people: what has been learned? *Fish. Fish.* **8**, 285–296 (2007).
23. Olsson, P., Folke, C. & Hahn, T. Social-ecological transformation for ecosystem management: the development of adaptive co-management of a wetland landscape in southern Sweden. *Ecol. Soc.* **9**, 2 (2004).
24. Sigmund, K., De Silva, H., Traulsen, A. & Hauert, C. Social learning promotes institutions for governing the commons. *Nature* **466**, 861–863 (2010).
25. Olsson, P., Folke, C. & Berkes, F. Adaptive co-management for building resilience in social-ecological systems. *Environ. Manage.* **34**, 75–90 (2004).
26. Costello, C., Gaines, S. D. & Lynham, J. Can catch shares prevent fisheries collapse? *Science* **321**, 1678–1681 (2008).
27. Essington, T. E. Ecological indicators display reduced variation in North American catch share fisheries. *Proc. Natl Acad. Sci. USA* **107**, 754–759 (2010).
28. Branch, T. A. How do individual transferable quotas affect marine ecosystems? *Fish. Fish.* **10**, 39–57 (2009).
29. Pollnac, R. *et al.* Marine reserves as linked social-ecological systems. *Proc. Natl Acad. Sci. USA* (2010).
30. Levin, S. Crossing scales, crossing disciplines: collective motion and collective action in the Global Commons. *Phil. Trans. R. Soc. B* **365**, 13–18 (2010).

Supplementary Information is linked to the online version of the paper at www.nature.com/nature.

Acknowledgements N.L.G. was partially funded by the National Science Foundation (award 0308440) and a Fulbright-OAS Initiative in Ecology fellowship. O.D. acknowledges support by the Pew Charitable Trusts. We thank E. Ostrom, T. A. Branch, and X. Basurto for comments on the manuscript and A. E. Punt, W. N. Venables, R. Perera and S. Sethi for discussions on the methodological and statistical approach.

Author Contributions N.L.G. designed the study, compiled and analysed the data and performed the statistical analyses; O.D. compiled and analysed the data. All authors discussed the results and jointly wrote the manuscript.

Author Information Reprints and permissions information is available at www.nature.com/reprints. The authors declare no competing financial interests. Readers are welcome to comment on the online version of this article at www.nature.com/nature. Correspondence and requests for materials should be addressed to N.L.G. (nicolasg@uw.edu).

An early Ediacaran assemblage of macroscopic and morphologically differentiated eukaryotes

Xunlai Yuan¹, Zhe Chen¹, Shuhai Xiao², Chuanming Zhou¹ & Hong Hua³

The deep-water Avalon biota (about 579 to 565 million years old) is often regarded as the earliest-known fossil assemblage with macroscopic and morphologically complex life forms¹. It has been proposed that the rise of the Avalon biota was triggered by the oxygenation of mid-Ediacaran deep oceans². Here we report a diverse assemblage of morphologically differentiated benthic macrofossils that were preserved largely *in situ* as carbonaceous compressions in black shales of the Ediacaran Lantian Formation (southern Anhui Province, South China). The Lantian biota, probably older than and taxonomically distinct from the Avalon biota, suggests that morphological diversification of macroscopic eukaryotes may have occurred in the early Ediacaran Period, perhaps shortly after the Marinoan glaciation, and that the redox history of Ediacaran oceans was more complex than previously thought.

The Lantian fossils were collected from early Ediacaran slope-basinal black shales in southern Anhui Province, South China (Fig. 1). The Ediacaran System in southern Anhui consists of two formations—the Lantian Formation and the overlying Piyuancun Formation³, which are respectively correlated on the basis of regional lithostratigraphy with the Doushantuo (635–551 million years, Myr) and Dengying (551–542 Myr) formations in the Yangtze Gorges area^{4,5}. The Lantian Formation is divided into four members that are similar to and can be correlated with the four divisions of the Doushantuo Formation⁶. The lowest Member I is a 1.8-m-thick dolostone ('cap dolostone') conformably overlying a Marinoan-age glacial diamictite. The overlying Member II consists of 35 m of finely laminated fossiliferous black shales (Supplementary Figs 1 and 2). Member III is 34 m thick and characterized by dolostones interbedded with mudstones in

the lower part and ribbon rocks (limestone with dolostone intercalations; Supplementary Fig. 3) in the upper part. The uppermost Member IV consists of 20 m of black silty mudstones, which is overlain by siliceous rocks of the Piyuancun Formation and then the early Cambrian Hetang Formation⁷.

The correlation of the four lithostratigraphic members between the Lantian and Doushantuo formations is supported by chemostratigraphic data (Fig. 1, Supplementary Fig. 4 and Supplementary Tables 1, 2). The basal Lantian cap dolostone is characterized by sedimentary features and $\delta^{13}\text{C}_{\text{carb}}$ values^{8,9} similar to the 635-Myr-old basal Doushantuo cap dolostone¹⁰. Lantian Member III dolostones and ribbon rocks record a large negative $\delta^{13}\text{C}_{\text{carb}}$ excursion (Fig. 1 and Supplementary Fig. 4) that can be correlated with the negative excursion EN3 in Doushantuo Member III in the Yangtze Gorges area^{10,11}. In the Yangtze Gorges and neighbouring areas, ash beds within Doushantuo Member II gave a zircon U–Pb thermal ionization mass spectrometry (TIMS) age of 632.5 ± 0.5 Myr (ref. 12) and a zircon U–Pb sensitive high resolution ion microprobe (SHRIMP) age of 614 ± 7.6 Myr (ref. 13), and Doushantuo Member IV is constrained between 593 ± 17 Myr (Re–Os age)¹⁴ and 551.1 ± 0.7 Myr (zircon U–Pb TIMS age)¹². These dates indicate that the Lantian biota in Member II black shales is probably older than the 579–565 Myr Avalon biota¹.

Regional mapping and palaeogeographic reconstruction indicate that fossiliferous black shales of Lantian Member II belong to a widespread shale-dominated facies that extends along the marginal shelf to the deep basin of the Yangtze Block (Fig. 1)¹⁵. The fossiliferous black shales are finely laminated, lacking cross-stratification or other wave- or current-influenced sedimentary structures. No grading is found in the fine

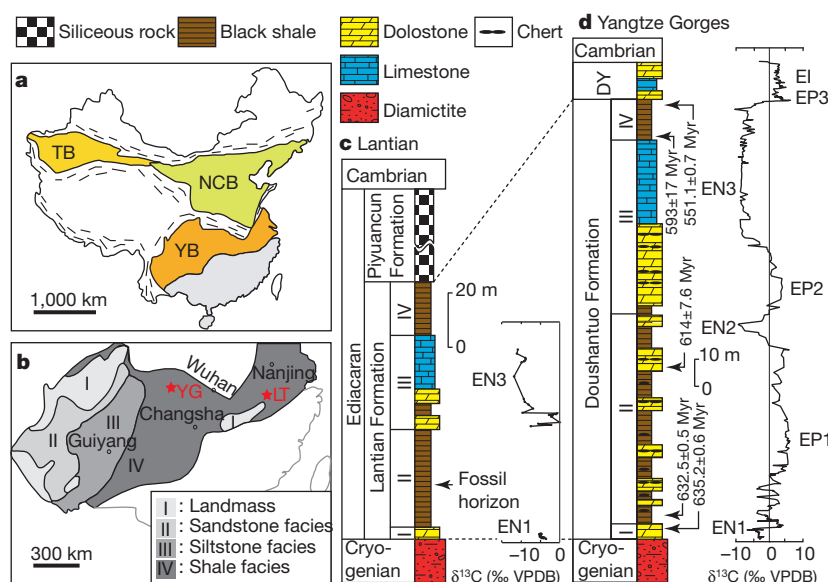


Figure 1 | Localities and stratigraphic columns. **a**, Yangtze Block (YB) in relation to North China Block (NCB) and Tarim Block (TB). **b**, Early Ediacaran facies distribution on Yangtze Block (simplified from ref. 15), with Yangtze Gorges (YG) and Lantian (LT) marked. **c**, **d**, Ediacaran stratigraphic columns of Lantian and Yangtze Gorges areas. Carbonate $\delta^{13}\text{C}$ data for basal Lantian cap dolostone (EN1) from ref. 8, and those for upper Lantian Formation from this study (Supplementary Table 1). Radiometric ages and $\delta^{13}\text{C}$ data in **d** from previously published data^{11–14,30}. Scale bars apply only to Lantian and Doushantuo formations. DY, Dengying Formation. Ediacaran positive, negative and inertial carbon isotope excursions EP1, EP2, EP3, EN1, EN2, EN3 and EI are based on ref. 10.

¹State Key Laboratory of Palaeobiology and Stratigraphy, Nanjing Institute of Geology and Palaeontology, Chinese Academy of Sciences, Nanjing 210008, China. ²Department of Geosciences, Virginia Polytechnic Institute and State University, Blacksburg, Virginia 24061, USA. ³State Key Laboratory of Continental Dynamics and Department of Geology, Northwest University, Xi'an 710069, China.

laminae (Supplementary Fig. 1b), indicating that they are not microturbidites but were deposited as suspensions settling below the storm wave base. The Lantian fossils are exceptionally preserved—with minimum fragmentation, random orientation (Supplementary Fig. 2), and lack of folded specimens—indicating that they were not transported by density currents and did not sink from surface water; instead, most of them were probably preserved *in situ*. The *in situ* preservation of epibenthic macroalgae⁴, some with intact holdfast, suggests deposition in a quiet environment below the storm wave base but within the photic zone.

Previous investigators have described numerous carbonaceous compressions from Lantian Member II (refs 3–5), including simple vesicles such as *Chuaria circularis*, dichotomously branching forms (Fig. 2a), loosely bundled filaments (Fig. 2b), conical structures with densely packed filaments (Fig. 2c), fan-shaped forms with fascicles of filaments and sometimes transverse bands (Fig. 2d–i), and chained rings (Fig. 2j). Our renewed excavation has recovered, from the same fossiliferous interval, more than 3,000 specimens of macroscopic carbonaceous compressions that show a considerable degree of taxonomic diversity and morphological differentiation.

The new fossils can be described under five morphological types. Type A fossils (five specimens; Fig. 3a–e) are 16–40 mm in length and characterized by a fan-shaped structure consisting of a globose holdfast at its base, a lower stalk, and an upper crown. The stalk was originally conical in shape, consisting of a splay of packed filaments and a truncated or slanted upper end. The crown consists of more than ten tentacle-like non-branching ribbons that are of unequal to sub-equal length (2–13 mm) and tend to have a rounded distal end. Type B (20 specimens; Fig. 3f) is similar to Type A but its crown consists of a

single broad ribbon, possibly representing a younger ontogenetic stage of Type A, although transitional forms are lacking. Type C (four specimens; Fig. 3g–i) is a centimetre-sized conical fossil, and has a fusiform inner body surrounded by diffuse organic stains. The inner body seems to be ornamented with longitudinal structures that converge distally to form a conical pyramid, which supports a cluster of filaments, each ~3 mm long and ~0.2 mm wide. Type D (one specimen; Fig. 3j) consists of a globose holdfast (0.5 mm in diameter), a thin stalk (1.3 mm long, 0.4 mm wide), and a cylindrical tube (18 mm long, 1.4 mm wide) with an axial dark trace (0.2–0.3 mm wide). Type E (one specimen; Fig. 3k) is similar to Type D in having a stalk and an axial structure, but it lacks or does not preserve a globose holdfast, its stalk is much longer, and its axial structure is encased in a much broader guitar-shaped structure.

The degree of morphological differentiation of the Lantian macrofossils suggests that they are multicellular eukaryotes, although their exact phylogenetic affinities are uncertain. Forms with dichotomously branching filaments are likely to be algae. Types A and B also resemble some morphologically differentiated modern algae¹⁶ such as the kelp *Postelsia palmaeformis*, which has a holdfast, a stalk, and a crown of splaying and unbranching blades. Indeed, the Lantian fossil *Flabellophyton lantianensis*, previously interpreted as a macroalga⁴, may be related to Types A and B; it consists of a splay of tightly packed filaments but lacks a crown of ribbons, and may represent only the stalk of Type A/B fossils.

The morphologies of Types C–E find no analogues among modern algae. Type C may be interpreted as a cnidarian-like organism, with the fusiform inner body representing a retracted polyp with a gastrovascular

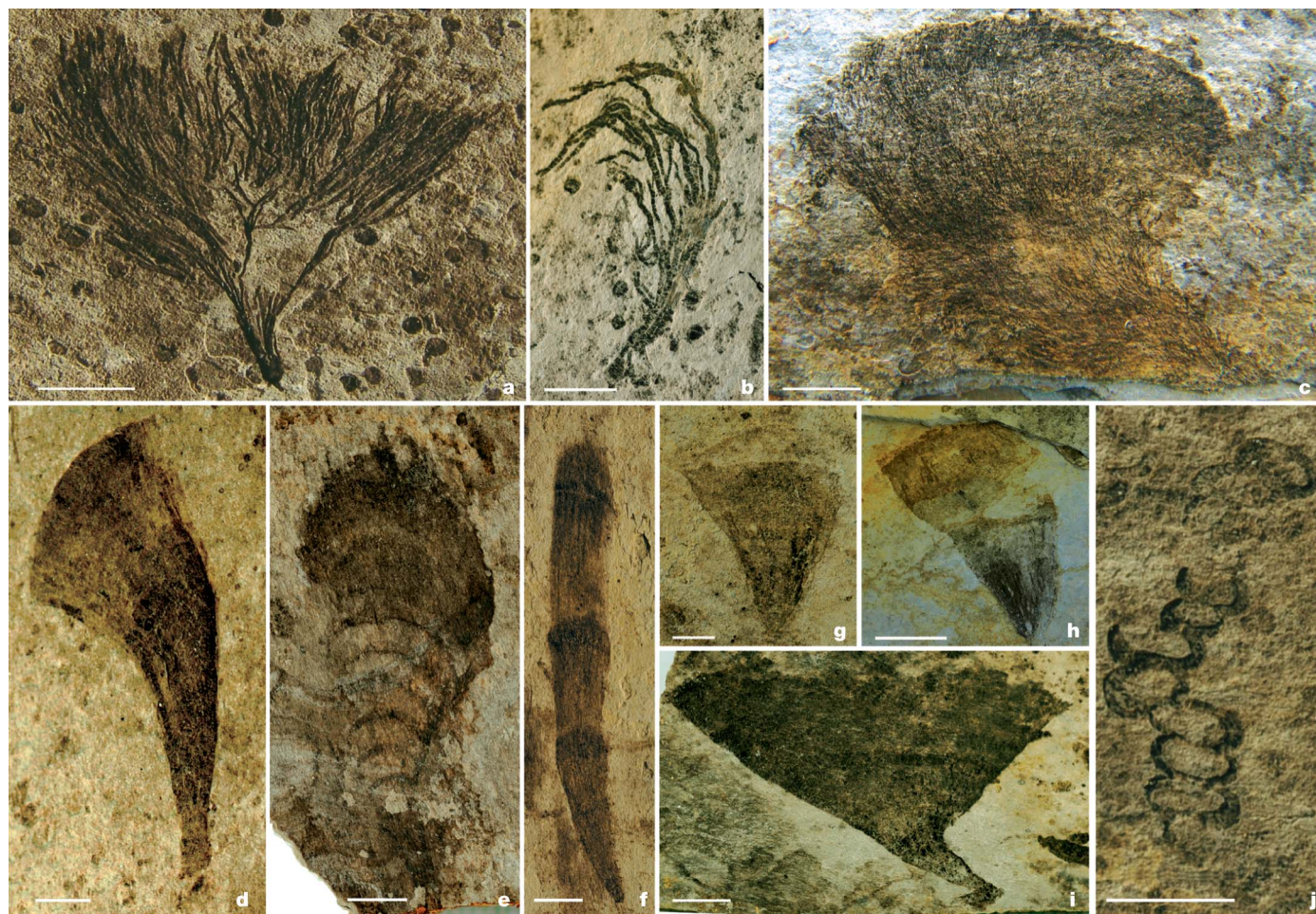


Figure 2 | Photomicrographs of Lantian macrofossils of probably algal affinities. a, *Doushantuophyton cometa*. b, *Huangshanophyton fluticulosum*. c, *Anhuiophyton lineatum*. d, *Flabellophyton lantianensis* with fan-shaped

thallus. e and f, *Flabellophyton strigata* with fan-shaped thallus and transverse bands. g–i, *Flabellophyton* sp. with fan-shaped or conical thallus. j, *Orbisiana* sp. Scale bars, 1 cm in b and h, 5 mm in all others.

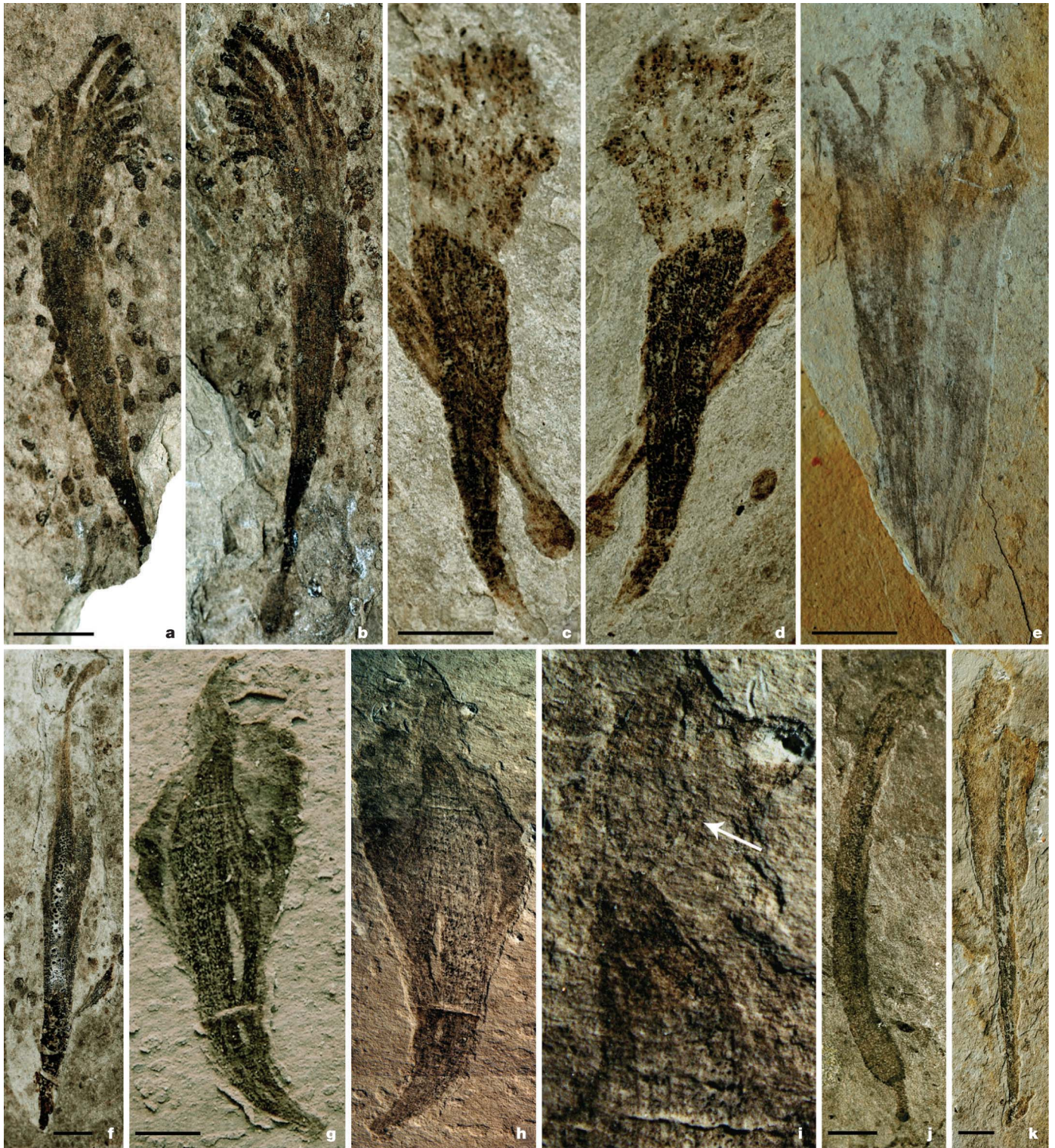


Figure 3 | Photomicrographs of new Lantian forms with uncertain phylogenetic affinities. a–e, f, g–i, j and k represent Type A, B, C, D and E, respectively. a, b, Part and counterpart. Note abundant *Chuarina circularis* fossils (circular carbonaceous impressions ~1 mm in diameter) in background. c, d, Part and counterpart. Scale bar, 3 mm. e, Incompletely preserved specimen. f, Specimen similar to a–e, but with a crown consisting of a single ribbon.

cavity surrounded by a hydrotheca-like integument; this interpretation implies the presence of retractor muscles. The longitudinal structures could represent ornamentation, retractor muscles, or mesentery-like structures. The axial structure in Types D and E is puzzling and it could represent the digestive structure of worm-like animals. In an animal

g–i, Part, counterpart and magnification of upper part showing a conical pyramid that supports a cluster of filaments (arrow in i). j, Specimen with a holdfast, a stalk, a cylindrical tube, and an axial trace. Scale bar, 2 mm. k, Specimen similar to j in having stalk and axial structure, but with a longer stalk and a broader structure surrounding axial trace. Scale bars, 5 mm unless otherwise noted.

model, the holdfast and stalk of Type D would be alternatively interpreted as the proboscis of an early worm-like organism. Intriguingly, a poorly preserved ribbon with an axial trace and a bulbous terminal structure from the Miaohu biota (Doushantuo Member IV) has been interpreted as a ‘putative bilaterian metazoan’¹⁷.

Regardless of the phylogenetic uncertainties, the taxonomic diversity and morphological complexity of the Lantian biota are notable. Even considering ontogenetic and preservational factors (see Supplementary Information), we estimate that the Lantian biota consists of ~15 morphospecies, many of which show complex morphological differentiation. This is in sharp contrast to pre-Ediacaran macrofossils, for which diversity is low, morphologies are simple, and eukaryotic affinity and multicellular nature are ambiguous¹⁸. Indeed, the Lantian biota nearly matches the Avalon biota¹⁹ in taxonomic diversity and morphological differentiation, although the phylogenetic compositions of the two biotas are drastically different, with the former dominated by macroalgae and the latter by modular rangeomorphs¹. Thus, the Lantian biota implies that some eukaryotic clades had achieved macroscopic and differentiated multicellularity before the Avalon biota, perhaps shortly after the Marinoan glaciation, thus raising the intriguing possibility that Neoproterozoic global glaciations drove the evolution of macroscopic multicellularity²⁰.

The Lantian macrofossils also place constraints on the redox history of Ediacaran oceans. Because a permissive amount of oxygen is required to maintain the metabolism of complex macroeukaryotes (particularly macrometazoans)²¹ and because modern anoxic environments are typically colonized only by microorganisms (including micrometazoans that are mostly derived from aerobic ancestors)²², the evolution of complex macroeukaryotes sets boundaries for the Ediacaran redox condition. Even the oxygen-producing macroalgae in the Lantian Formation would require free oxygen for respiration and would not have survived an oxygen-free environment, as suggested by the lack of macroalgae (and dominance of cyanobacteria and microalgae) in modern anoxic environments within the photic zone²³. Thus, the *in situ* preservation of complex macroeukaryotes in the lower Lantian Formation indicates that free oxygen was at least locally available below the storm wave base. If macrometazoans existed in the Lantian biota, their more active metabolism implies an even greater amount of free oxygen.

However, geochemical data indicate that many Ediacaran deep basins were anoxic²⁴, although some became oxygenated around 580 Myr ago along with the rise of the deep-water Avalon biota². In particular, geochemical studies of black shales in Lantian Member II in southern Anhui²⁵ and Doushantuo Member II in the Yangtze Gorges area²⁶ suggest deposition in largely anoxic (and sometimes euxinic) conditions, which would be hostile to benthic macroalgae and macrometazoans. To reconcile the conflicting geochemical and palaeontological indicators of palaeoredox conditions, we propose that the Lantian basin was largely anoxic but punctuated by brief oxic episodes. These oxic episodes were opportunistically capitalized on by benthic macroeukaryotes that were subsequently killed and preserved by frequent switch-backs to anoxic conditions. Brief oxic intervals also occurred in many Mesozoic anoxia events²⁷, and they are consistent with existing geochemical data from other Ediacaran basins suggesting significant temporal and spatial variations in redox conditions despite overall anoxia^{11,24,26,28,29}. This more complex picture of Ediacaran ocean redox history calls for integrated geochemical, palaeontological and sedimentological investigations at ultrahigh stratigraphic resolution.

Received 15 August 2010; accepted 7 January 2011.

- Narbonne, G. M. The Ediacara Biota: Neoproterozoic origin of animals and their ecosystems. *Annu. Rev. Earth Planet. Sci.* **33**, 421–442 (2005).
- Canfield, D. E., Poulton, S. W. & Narbonne, G. M. Late Neoproterozoic deep-ocean oxygenation and the rise of animal life. *Science* **315**, 92–95 (2007).
- Yan, Y., Jiang, C., Zhang, S., Du, S. & Bi, Z. Research of the Sinian System in the region of western Zhejiang, northern Jiangxi, and southern Anhui provinces. *Bull. Nanjing Inst. Geol. Mineral Resources (Chin. Acad. Geol. Sci.) Supp.* **12**, 1–105 (1992).
- Yuan, X., Li, J. & Cao, R. A diverse metapelite assemblage from the Neoproterozoic black shales of South China. *Lethaia* **32**, 143–155 (1999).

- Yuan, X., Xiao, S., Li, J., Yin, L. & Cao, R. Pyritized chuarids with excystment structures from the late Neoproterozoic Lantian Formation in Anhui, South China. *Precamb. Res.* **107**, 253–263 (2001).
- McFadden, K. A., Xiao, S., Zhou, C. & Kowalewski, M. Quantitative evaluation of the biostratigraphic distribution of acanthomorphic acritarchs in the Ediacaran Doushantuo Formation in the Yangtze Gorges area, South China. *Precamb. Res.* **173**, 170–190 (2009).
- Yuan, X. *et al.* Towering sponges in an Early Cambrian Lagerstätte: disparity between non-bilaterian and bilaterian epifaunal tiers during the Neoproterozoic–Cambrian transition. *Geology* **30**, 363–366 (2002).
- Zhou, C. *et al.* The Neoproterozoic tillites at Lantian, Xiuning County, Anhui Province. *J. Stratigr.* **25**, 247–252 (2001).
- Zhao, Y.-Y. & Zheng, Y.-F. Stable isotope evidence for involvement of deglacial meltwater in Ediacaran carbonates in South China. *Chem. Geol.* **271**, 86–100 (2010).
- Zhou, C. & Xiao, S. Ediacaran $\delta^{13}\text{C}$ chemostratigraphy of South China. *Chem. Geol.* **237**, 89–108 (2007).
- McFadden, K. A. *et al.* Pulsed oxygenation and biological evolution in the Ediacaran Doushantuo Formation. *Proc. Natl Acad. Sci. USA* **105**, 3197–3202 (2008).
- Condon, D. *et al.* U–Pb ages from the Neoproterozoic Doushantuo Formation, China. *Science* **308**, 95–98 (2005).
- Liu, P., Yin, C., Gao, L., Tang, F. & Chen, S. New material of microfossils from the Ediacaran Doushantuo Formation in the Zhangcunping area, Yichang, Hubei Province and its zircon SHRIMP U–Pb age. *Chin. Sci. Bull.* **54**, 1058–1064 (2009).
- Zhu, B., Becker, H., Jiang, S.-Y., Pi, D.-H. & Fischer-Gödde, M. Re-Os geochronology of black shales from the Doushantuo Formation, Yangtze Platform, South China. *Geol. Soc. Am. Programs Abstr.* **42** (5), 463 (2010).
- Zhu, M., Zhang, J. & Yang, A. Integrated Ediacaran (Sinian) chronostratigraphy of South China. *Palaeogeogr. Palaeoclimatol. Palaeoecol.* **254**, 7–61 (2007).
- Bold, H. C. & Wynne, M. J. *Introduction to the Algae* (Prentice-Hall, 1985).
- Xiao, S., Yuan, X., Steiner, M. & Knoll, A. H. Macroscopic carbonaceous compressions in a terminal Proterozoic shale: a systematic reassessment of the Miaohu biota, South China. *J. Paleontol.* **76**, 347–376 (2002).
- Sharma, M. & Shukla, Y. Taxonomy and affinity of Early Mesoproterozoic megascopic helically coiled and related fossils from the Rohtas Formation, the Vindhyan Supergroup, India. *Precamb. Res.* **173**, 105–122 (2009).
- Shen, B., Dong, L., Xiao, S. & Kowalewski, M. The Avalon explosion: evolution of Ediacara morphospace. *Science* **319**, 81–84 (2008).
- Boyle, R. A., Lenton, T. M. & Williams, H. T. P. Neoproterozoic ‘snowball Earth’ glaciations and the evolution of altruism. *Geobiology* **5**, 337–349 (2007).
- Catling, D. C., Glein, C. R., Zahnle, K. J. & McKay, C. P. Why O_2 is required by complex life on habitable planets and the concept of planetary ‘oxygenation time’. *Astrobiology* **5**, 415–438 (2005).
- Fenchel, T. & Finlay, B. J. *Ecology and Evolution in Anoxic Worlds* (Oxford University Press, 1995).
- Izaguirre, I. *et al.* Algal assemblages across a wetland, from a shallow lake to relictual oxbow lakes (Lower Paraná River, South America). *Hydrobiologia* **511**, 25–36 (2004).
- Canfield, D. E. *et al.* Ferruginous conditions dominated later Neoproterozoic deep-water chemistry. *Science* **321**, 949–952 (2008).
- Shen, Y., Zhang, T. & Hoffman, P. F. On the co-evolution of Ediacaran oceans and animals. *Proc. Natl Acad. Sci. USA* **105**, 7376–7381 (2008).
- Li, C. *et al.* A stratified redox model for the Ediacaran ocean. *Science* **328**, 80–83 (2010).
- Röhl, H.-J., Schmid-Röhl, A., Oschmann, W., Frimmel, A. & Schwark, L. The Posidonia Shale (Lower Toarcian) of SW-Germany: an oxygen-depleted ecosystem controlled by sea level and palaeoclimate. *Palaeogeogr. Palaeoclimatol. Palaeoecol.* **169**, 273–299 (2001).
- Fike, D. A., Grotzinger, J. P., Pratt, L. M. & Summons, R. E. Oxidation of the Ediacaran ocean. *Nature* **444**, 744–747 (2006).
- Ries, J. B., Fike, D. A., Pratt, L. M., Lyons, T. W. & Grotzinger, J. P. Superheavy pyrite ($\delta^{34}\text{S}_{\text{pyr}} > \delta^{34}\text{S}_{\text{SCAS}}$) in the terminal Proterozoic Nama Group, southern Namibia: a consequence of low seawater sulfate at the dawn of animal life. *Geology* **37**, 743–746 (2009).
- Jiang, G., Kaufman, A. J., Christie-Blick, N., Zhang, S. & Wu, H. Carbon isotope variability across the Ediacaran Yangtze platform in South China: implications for a large surface-to-deep ocean $\delta^{13}\text{C}$ gradient. *Earth Planet. Sci. Lett.* **261**, 303–320 (2007).

Supplementary Information is linked to the online version of the paper at www.nature.com/nature.

Acknowledgements This research was supported by the Chinese Academy of Sciences, the National Natural Science Foundation of China, the Chinese Ministry of Science and Technology, the National Science Foundation, the NASA Exobiology and Evolutionary Biology Program and the Guggenheim Foundation. We thank G. Jiang for useful discussions.

Author Contributions X.Y. and Z.C. led field excavation. X.Y., S.X., Z.C. and C.Z. conducted research and developed the interpretation. S.X. and X.Y. prepared the manuscript with input from Z.C., C.Z. and H.H.

Author Information Reprints and permissions information is available at www.nature.com/reprints. The authors declare no competing financial interests. Readers are welcome to comment on the online version of this article at www.nature.com/nature. Correspondence and requests for materials should be addressed to X.Y. (xlyuan@nigpas.ac.cn) or S.X. (xiao@vt.edu).

Tbx6-dependent Sox2 regulation determines neural or mesodermal fate in axial stem cells

Tatsuya Takemoto¹, Masanori Uchikawa¹, Megumi Yoshida¹, Donald M. Bell², Robin Lovell-Badge², Virginia E. Papaioannou³ & Hisato Kondoh¹

The classical view of neural plate development held that it arises from the ectoderm, after its separation from the mesodermal and endodermal lineages. However, recent cell-lineage-tracing experiments indicate that the caudal neural plate and paraxial mesoderm are generated from common bipotential axial stem cells originating from the caudal lateral epiblast^{1,2}. *Tbx6* null mutant mouse embryos which produce ectopic neural tubes at the expense of paraxial mesoderm³ must provide a clue to the regulatory mechanism underlying this neural versus mesodermal fate choice. Here we demonstrate that *Tbx6*-dependent regulation of *Sox2* determines the fate of axial stem cells. In wild-type embryos, enhancer N1 of the neural primordial gene *Sox2* is activated in the caudal lateral epiblast, and the cells staying in the superficial layer sustain N1 activity and activate *Sox2* expression in the neural plate^{4–6}. In contrast, the cells destined to become mesoderm activate *Tbx6* and turn off enhancer N1 before migrating into the paraxial mesoderm compartment. In *Tbx6* mutant embryos, however, enhancer N1 activity persists in the paraxial mesoderm compartment, eliciting ectopic *Sox2* activation and transforming the paraxial mesoderm into neural tubes. An enhancer-N1-specific deletion mutation introduced into *Tbx6* mutant embryos prevented this *Sox2* activation in the mesodermal compartment and subsequent development of ectopic neural tubes, indicating that *Tbx6* regulates *Sox2* via enhancer N1. *Tbx6*-dependent repression of *Wnt3a* in the paraxial mesodermal compartment is implicated in this regulatory process. Paraxial mesoderm-specific misexpression of a *Sox2* transgene in wild-type embryos resulted in ectopic neural tube development. Thus, *Tbx6* represses *Sox2* by inactivating enhancer N1 to inhibit neural development, and this is an essential step for the specification of paraxial mesoderm from the axial stem cells.

Evidence derived from cell marking and lineage tracing in mouse and chicken embryos indicates that the caudal lateral epiblast (CLE), the region of epiblast flanking the rostral primitive streak, serves as the common precursor pool for the paraxial mesoderm and caudal neural plate which later contributes to the caudal hindbrain and spinal cord^{1,2,7}. The bipotential precursors serve as the pool of ‘axial stem cells’ that contributes to the coordinated elongation of the neural tube—which develops from the cell population remaining in the superficial layer—and paraxial mesoderm derived from cells that ingress through the primitive streak^{8–10}. The most compelling evidence for this was provided by the single cell lineage analysis reported by a previous study⁸, which used intragenic recombination in a transgene to mark a clone, and demonstrated that a substantial fraction of individual axial stem cells do produce progenies of both cell fates. However, the regulatory mechanism underlying this neural versus mesodermal fate choice remained to be elucidated.

Expression of the transcription factor gene *Sox2* is regarded as the hallmark of the neural primordial cell state, and its activation is strongly correlated with the establishment of the embryonic neural plate (Fig. 1b

and Supplementary Fig. 1). Our earlier studies have indicated that among a number of enhancers regulating *Sox2*, enhancer N1 is responsible for *Sox2* activation in the caudally extending neural plate^{5,6} (Fig. 1a–c and Supplementary Fig. 1). The following three features of enhancer N1 indicate its involvement in the regulation of CLE-derived cells⁴. First, enhancer N1 is activated precisely in the region of the CLE and sustained in the zone at the caudal end of neural plate (ZCNP) (Fig. 1b, c). Its activation, however, does not immediately lead to *Sox2* expression in the CLE, owing to BMP signal-dependent repression of *Sox2* in the CLE. Only when the CLE cells become a part of ZCNP located immediately rostral are the cells relieved from the BMP signal and initiate *Sox2* expression. In fact, the inhibition of BMP signals results in precocious *Sox2* activation in the entire CLE⁴ (Supplementary Fig. 2). Second, enhancer N1 activity is normally shut off in the mesodermal precursors that have ingressed through the primitive streak, indicative of the release of this cell population from a neural fate⁴. Third, enhancer N1 is activated by the synergistic action of Wnt and Fgf signals⁴ (Fig. 1d, e), whereas the Fgf signal is required for the

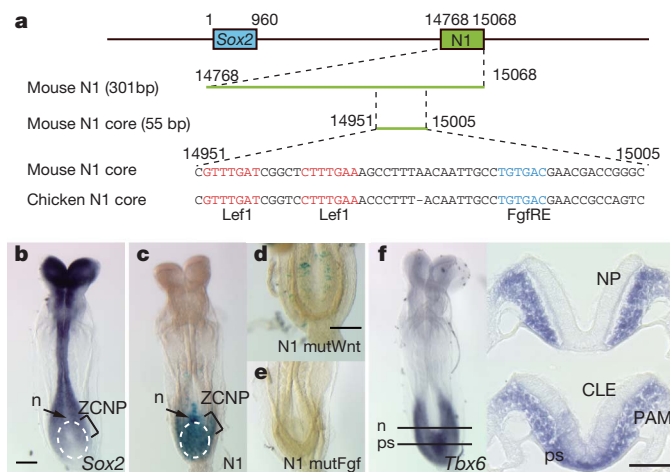


Figure 1 | Enhancer N1 of the mouse *Sox2* gene and its activity in comparison with *Sox2* and *Tbx6* expression. **a**, The position of enhancer N1 relative to the *Sox2* ORF and the N1 core sequence bearing the conserved Lef1-binding elements and Fgf-responsive element (FgfRE). **b**, Expression of *Sox2* in E8.5 normal embryo in dorsal view. **c**, Enhancer N1 activity at the same stage, indicated by the expression of enhancer N1-LacZ transgene in primary transgenic embryos. n, the position of node; ZCNP, zone at the caudal end of neural plate; dashed oval, the area of enhancer N1 activity. **d**, **e**, The loss of enhancer activity by the mutations in both Lef1 elements (**d**, mutWnt) or in FgfRE (**e**, mutFgf)⁴ in the transgenic embryos. **f**, *Tbx6* expression in E8.5 mouse embryo detected by *in situ* hybridization. The right panels show the cross-sections at the node (n; top panel) and primitive streak (ps; bottom panel) levels. CLE, caudal lateral epiblast; NP, neural plate; PAM, paraxial mesoderm. Scale bars: 200 μm (b–e); 50 μm (f, right panels).

¹Graduate School of Frontier Biosciences, Osaka University, 1-3 Yamadaoka, Suita, Osaka 565-0871, Japan. ²Division of Stem Cell Biology and Developmental Genetics, MRC National Institute for Medical Research, The Ridgeway, Mill Hill, London NW7 1AA, UK. ³Department of Genetics and Development, College of Physicians and Surgeons of Columbia University, 701 West 168th Street, New York, New York 10032, USA.

maintenance of the axial stem cells in the CLE^{1,11,12}. On the basis of these observations, we hypothesized that regulation of *Sox2* through enhancer N1 is an important mechanism to regulate cell fate in the CLE.

Given the CLE origin of paraxial mesoderm, the phenotype of *Tbx6* null mutant embryos is remarkable, where bilateral ectopic neural tubes develop at the expense of the paraxial mesoderm caudal to somite 6 level³. *Tbx6*, encoding a T-box transcription factor, is expressed in the primitive streak and presomitic paraxial mesoderm during gastrulation¹³ (Fig. 1f), and is presumed to have two major regulatory functions: (1) antineural fate regulation in the presomitic mesoderm, as indicated by the mutant phenotype; and (2) regulation of later somite segmentation involving *Mesp2* and *Dll1* genes^{14–17}.

We investigated the process of ectopic neural tube development from the presumptive paraxial mesoderm in homozygous *Tbx6* mutant embryos. In *Tbx6* mutant embryos at embryonic day (E)8.5, mesoderm development is already defective, as indicated by the absence of the normal pattern of *Uncx4.1* (also called *Uncx*) expression in the caudal part of segmented somites (Supplementary Fig. 3a). The expression of *Sox2* in normal embryos at E8.5 (5–6 somites) was confined to the neural plate and neural tube (Fig. 2a), whereas in *Tbx6* mutant embryos, the cells in the paraxial mesodermal compartment underlying the neural plate fully expressed *Sox2*, at levels comparable to those in the neural plate (Fig. 2b). The ectopic *Sox2* expression was followed by the ectopic development of neural tubes in the same compartment at E9.5 (Fig. 2c, d), where genes such as *Pax6* and *Pax3* were expressed, indicating the development of the dorso-ventral patterning of the ectopic neural tubes³ (see also Fig. 3).

In contrast to *Sox2*, other group B1 *Sox* genes—that is, *Sox1* and *Sox3*, which are normally expressed in the neural tube—were not activated in the paraxial mesodermal compartment (Fig. 2e–h). This observation strongly suggests that the activation of *Sox2* in the paraxial mesodermal compartment is causative of ectopic neural tube development in *Tbx6* mutant embryos.

By analogy to the process of caudal neural plate development, we speculated involvement of enhancer N1 activation, leading to *Sox2* expression, in ectopic neural tube development in *Tbx6* mutant embryos. To test this model, we compared enhancer N1 activity in *Tbx6* mutant and wild-type embryos (Fig. 2i, j and Supplementary Fig. 3b) using enhancer-N1-driven transgenes for *Egfp* (for *in situ* hybridization detection of transcripts) or *lacZ* (for histochemical enzyme staining). In wild-type embryos, enhancer-N1-dependent *Egfp* expression was clearly detected in the CLE and primitive streak, but not in the paraxial mesodermal compartment (Fig. 2i). Analysis of serial sections indicated that enhancer N1 loses its activity after the cells ingress through the primitive streak and when the cells migrate laterally into the mesodermal compartment (Fig. 2i, right panels). In contrast to the primitive-streak-restricted *Egfp* transcript in the mesodermal layer, more stable *LacZ* enzyme activity was detected in more laterally positioned cells. This observation is consistent with the model that the cells turn off enhancer N1 before migrating laterally (Supplementary Fig. 3b). An analogous sequence of events occurs in chicken embryos⁴.

Remarkably, in the *Tbx6* mutant embryos, enhancer N1 activation persisted in the paraxial mesodermal compartment, as indicated by strong *Egfp* and *LacZ* expression (Fig. 2j and Supplementary Fig. 3b). Even in *Tbx6* mutants, the trans-layer cell ingress pathway seems to be confined to the primitive streak, as the laminin-positive basal lamina separating the epiblastic and mesodermal cells was interrupted only in the primitive streak region (Supplementary Fig. 3c). These observations indicate that the persistent activity of enhancer N1 in the paraxial mesodermal compartment caused ectopic *Sox2* expression, which in turn leads to the development of ectopic neural tubes. Conversely, this indicates that in normal embryos the activity of *Tbx6* expressed in the paraxial mesoderm suppresses enhancer N1 activation, thereby preventing the development of neural tubes from the mesodermal precursors.

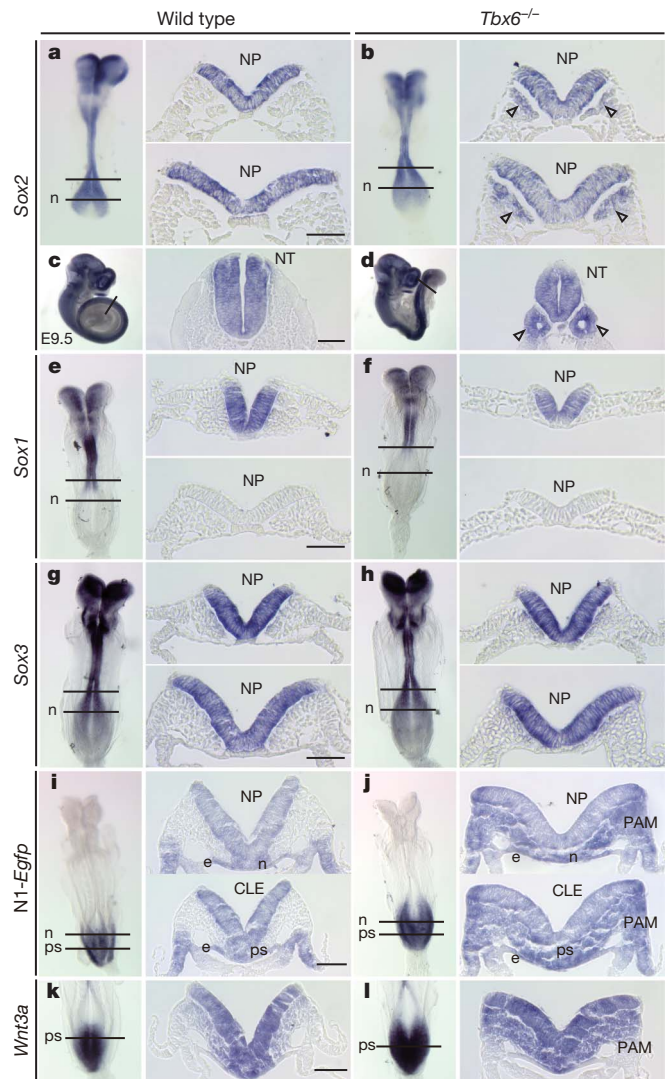


Figure 2 | Ectopic activation of enhancer N1, *Sox2* expression and neural development in the paraxial mesoderm compartment of *Tbx6*^{−/−} embryos.

a, b, *Sox2* expression in wild-type and *Tbx6*^{−/−} embryos at E8.5, shown by whole-mount *in situ* hybridization. Right panels (top and bottom) show transverse sections at the axial levels anterior to and through the node (n). NP, neural plate. Arrowheads indicate *Sox2* expression in the paraxial mesodermal compartment in *Tbx6*^{−/−} embryos. **c, d**, *Sox2* expression in wild-type and *Tbx6*^{−/−} embryos at E9.5. NT, neural tube. Arrowheads indicate development of *Sox2*-positive ectopic neural tubes. **e–h**, *Sox1* (**e, f**) and *Sox3* (**g, h**) expression in wild-type and *Tbx6*^{−/−} embryos at E8.5. **i, j**, Activity of enhancer N1 at E8.5 in wild-type embryos (**i**) or in *Tbx6*^{−/−} embryos (**j**) detected by *in situ* hybridization of *Egfp* transcripts. Right panels show transverse sections at the node (n) and primitive streak (ps) levels. In wild-type embryos, enhancer N1 activity was absent in the paraxial mesoderm compartments (PAM; **i**, right panels), whereas strong N1 activity was demonstrated in the PAM in *Tbx6*^{−/−} embryos (**j**, right panels). Enhancer activity was detected in the node and endoderm (e) in either genotype. **k, l**, Expression of *Wnt3a* at E8.5 in wild-type embryos (**k**) or *Tbx6*^{−/−} embryos (**l**) detected by *in situ* hybridization, and in transverse sections (right panel) at a primitive streak level. All scale bars, 50 μ m.

To confirm that the *Sox2* misexpression in the paraxial mesoderm compartment in *Tbx6* mutant embryos—leading to supernumerary neural tube development—is due to the ectopic activation of enhancer N1, we produced an enhancer N1 mutant allele in the mouse, in which only the enhancer N1 sequence was deleted from the *Sox2* locus (Supplementary Fig. 4). Homozygosity for the enhancer N1 mutation (Δ N1/ Δ N1) caused the loss of *Sox2* expression in the ZCNP, which is the nascent neural plate positioned immediately rostral to the CLE^{1,2,12}.

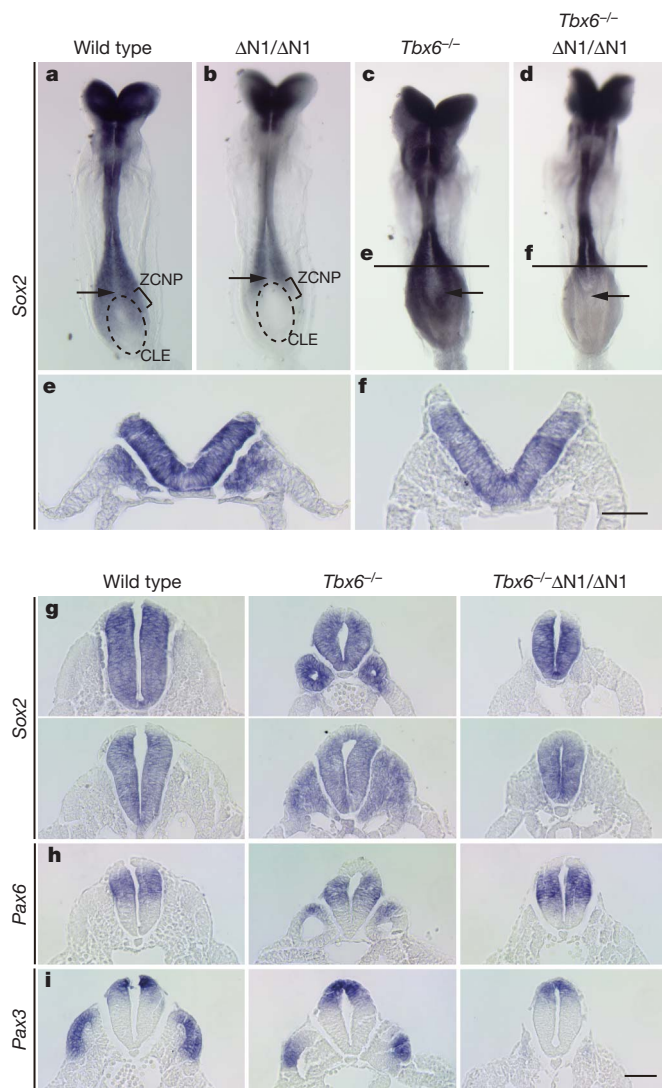


Figure 3 | Enhancer-N1-dependent paraxial *Sox2* expression and ectopic neural tube development in *Tbx6*^{-/-} embryos, and their suppression in *Tbx6*^{-/-} $\Delta N1/\Delta N1$ double mutants. **a–d**, Effects of the enhancer N1 mutation ($\Delta N1/\Delta N1$) on *Sox2* expression in the neural plate and paraxial tissues in wild-type and *Tbx6*^{-/-} embryos at E8.5. Arrows indicate the position of node. The CLE (dashed oval) and ZCNP are indicated. *Sox2* expression in the ZCNP is lost in the enhancer N1 mutant embryos. **c–f**, The loss of *Sox2* expression in the paraxial mesoderm compartment in *Tbx6*^{-/-} embryos (**e**) by the enhancer N1 mutation (**f**), demonstrated by sections of embryos of the relevant genotypes (**c**, **d**) at the axial levels indicated. Embryo specimens in **c** and **d** are overstained to confirm the absence of *Sox2* in the paraxial mesoderm compartment. **g–i**, Expression of *Sox2* (**g**, neural), *Pax6* (**h**, neural) and *Pax3* (**i**, both neural and mesodermal) was examined in embryos of respective genotypes at E9.5. All scale bars, 50 μm .

This loss of *Sox2* expression in the ZCNP in the $\Delta N1/\Delta N1$ embryos was noticeable after the 5-somite stages (E8.5) (Fig. 3b), consistent with the timing of enhancer N1 activation (Fig. 1c), and continued to E9.5. Despite this, *Sox2* was activated in the closing neural tube, and the development of the spinal cord proceeded without significant morphological defects (Fig. 3b). We presume this to be ascribable to the presence of another enhancer to back-up *Sox2* expression in the neural tube, and/or other group B1 *Sox* genes expressed in the neural plate to compensate for the role of *Sox2*.

By crossing *Tbx6*^{+/-} + $\Delta N1$ double heterozygotes, *Tbx6*^{-/-} $\Delta N1/\Delta N1$ double homozygous mutant embryos were successfully obtained. In *Tbx6*^{-/-} $\Delta N1/\Delta N1$ embryos at E8.5, the ectopic *Sox2* expression in the paraxial mesodermal compartment was totally absent (Fig. 3d, f),

in contrast to the case of *Tbx6*^{-/-} embryos (Fig. 3c, e), providing strong evidence that enhancer N1 determines the ectopic expression of *Sox2* in *Tbx6* mutants.

In the ectopic neural tubes that develop in *Tbx6*^{-/-} embryos at E9.5, *Sox2* expression continues, while expression of other genes that are associated with neural tube development is also initiated, namely *Sox1*, *Pax6* and *Pax3*, the latter two reflecting the dorso-ventral identity of the neural tube³ (Fig. 3 and Supplementary Fig. 5). In the *Tbx6*^{-/-} $\Delta N1/\Delta N1$ embryos at E9.5, however, the expression of all these neural genes in the paraxial compartment was extinct, concomitant with the absence of the tubular structure (Fig. 3). The paraxial tissue in the *Tbx6*^{-/-} $\Delta N1/\Delta N1$ embryos failed to express any of the mesoderm or endoderm marker genes examined, namely *Pax3* (Fig. 3i) and *Mox1* (also called *Meox1*) for paraxial mesoderm, *Pax2* for intermediate mesoderm, *Foxf1* (also called *Foxf1a*) for visceral lateral plate mesoderm, and *Foxa1* for endoderm (Supplementary Fig. 5). These observations indicate that *Tbx6* has two distinct functions in the mesodermal precursors: the inhibition of neural development by preventing enhancer N1 activation, and the promotion of mesodermal development.

To confirm that the *Sox2* misexpression in the paraxial mesoderm is causative of the ectopic neural tube development, haemagglutinin (HA)-tagged *Sox2* was ectopically expressed in the primitive paraxial mesoderm of wild-type embryos using the msd enhancer of the *Dll1* gene¹⁸ (Fig. 4a). Exogenous *Sox2*-HA was successfully expressed in the caudal-most mesodermal compartment (Fig. 4b), as indicated by HA tag immunostaining and mesodermal *Sox2* immunostaining (Fig. 4c–e). At a more rostral level of the paraxial mesoderm, where the msd enhancer activity was lost and exogenous *Sox2*-HA expression had ceased, endogenous *Sox2* expression persisted, indicating a positive feedback loop, where the former activated the latter. Notably, the clusters of cells with relatively high *Sox2* also expressed *Pax6* (Fig. 4d, open arrowheads), coincident with *Pax6* expression in the closing neural tube at the same axial level. At more rostral levels, the cells in the mesodermal compartment with an intensity of *Sox2* expression comparable to that in the neural tube formed *Pax6*-positive miniature neural tubes (Fig. 4e, white arrowheads). This result demonstrates that *Sox2* expression is sufficient for the initiation of neural tube development from the primitive paraxial mesoderm, even in wild-type embryos.

Finally, we asked whether the suppression of *Sox2* enhancer N1 activation by *Tbx6* involves direct interaction of the *Tbx6* protein with the enhancer N1 DNA sequence. Various overlapping fragments of the N1 sequence were tested for *Tbx6* binding using electrophoretic mobility shift assays (EMSA). None of the N1 subfragments exhibited T-box-factor-binding capacity, under conditions where all known T-box-binding sequences strongly bound *Tbx6* (Supplementary Fig. 6), indicating that the suppression of the enhancer N1 activity by *Tbx6* is probably not a direct regulation.

As enhancer N1 is activated by synergistic action of Wnt and Fgf signals⁴ (Fig. 1), we investigated the expression patterns of the genes encoding these protein ligands in the CLE and paraxial mesoderm^{19–22}. A remarkable change was observed in the expression pattern of *Wnt3a* (Fig. 2k, l). In normal embryos, *Wnt3a* expression is strongly expressed in the primitive streak, CLE and caudal neural plate, whereas its level is very low in the paraxial mesoderm (Fig. 2k). In *Tbx6* mutant embryos, however, the strong *Wnt3a* expression extends to the paraxial mesoderm compartment (Fig. 2l). On the other hand, the expression patterns of *Wnt8a* (absent in the mesoderm), *Fgf8* and *Fgf4* in the CLE and paraxial mesoderm compartment were not significantly altered in the *Tbx6* mutant embryos (Supplementary Fig. 7). We hypothesize that *Wnt3a* expression, normally repressed in the paraxial mesoderm, is de-repressed in the *Tbx6* mutant embryos, and the strong *Wnt3a* expression in the paraxial mesoderm is causative of the ectopic activation of enhancer N1, as shown in Fig. 4f. The strong spatial correlation between *Wnt3a* expression and enhancer N1 activity observed at various axial levels in both wild-type and *Tbx6* mutant embryos lends support for this model (Fig. 2i–l).

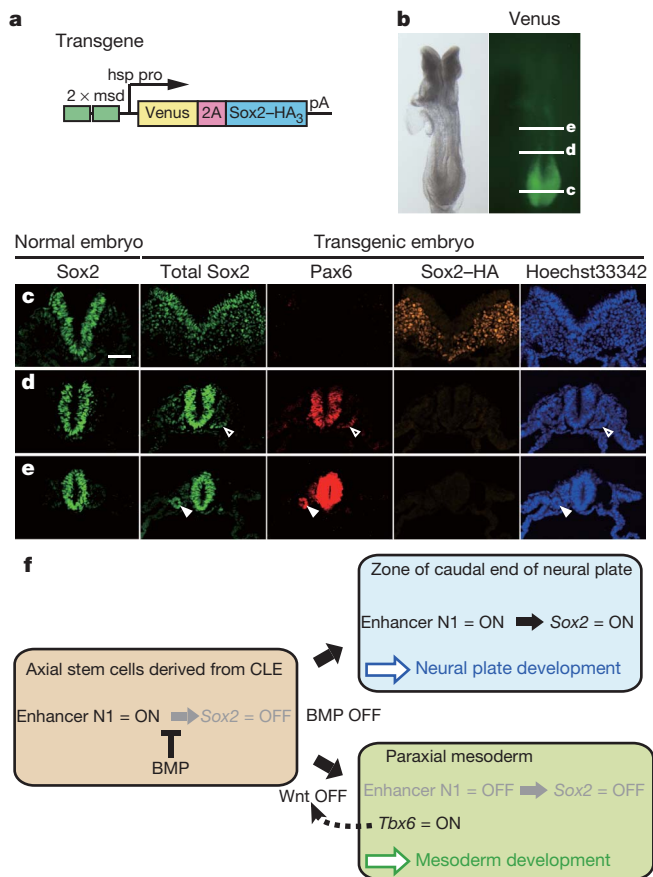


Figure 4 | Development of ectopic neural tubes from the wild-type paraxial mesoderm by misexpression of exogenous Sox2. **a**, Structure of the transgene. The msd enhancer of the gene *Dll1* (ref. 18) in a dimeric form was used for paraxial mesoderm-specific activation of the transgene coding for Venus and HA₃-tagged Sox2 joined with a 2A peptide sequence²³. **b**, Mesodermal precursor-specific activation of Venus in transgenic embryos at E8.5. **c–e**, Cross-sections at axial levels shown in **b**. Immunofluorescence for Sox2, Pax6 and HA tag, and Hoechst 33342 staining, and a comparison with Sox2 immunofluorescence of normal embryos. Scale bar, 50 μm. **f**, Model of enhancer N1 regulation and enhancer-N1-dependent Sox2 activation in normal and *Tbx6*^{-/-} embryos. In the CLE (left), where Wnt signal is above threshold, enhancer N1 is activated; however, despite this Sox2 expression itself is repressed by the inhibitory effect of BMP signals. In the ZCNP (right, top), where the Wnt signal stays ON, relief from the BMP-mediated inhibition effectuates enhancer-N1-dependent activation of Sox2 expression in the caudal neural plate. In the paraxial mesoderm (right, bottom), although the BMP signal is downregulated^{24,25}, Wnt signal drops below the threshold required for the activation of enhancer N1 when *Tbx6* activity is present, and Sox2 expression is not activated.

As discussed above, a significant fraction of the cells in the CLE domain have been shown to serve as the common precursors for the neural plate and paraxial mesoderm⁸. The present study clarifies the core regulatory circuit underlying the neural versus mesodermal dichotomous fate choice in the axial precursors, where Sox2 expression is regulated by *Tbx6* activity. As shown in Fig. 4f, the mechanism to activate Sox2 transcription operates first in CLE, namely enhancer N1 activation, and while this mechanism is still idle under the BMP-dependent Sox2 repression, a fraction of the cells migrate into the mesodermal compartment, where the activity of enhancer N1 is lost, probably due to the very low Wnt activity. *Tbx6*-dependent mesodermal development is then promoted. *Tbx6* seems to have two major functions: inhibition of Sox2 activation via enhancer N1, and activation of the mesoderm specification program. The former function is important for the latter, as Sox2 misexpression in wild-type embryos transforms

paraxial mesoderm into neural tissue (Fig. 4c–e). In the *Tbx6* mutant embryos, persistent enhancer N1 activity owing to a high Wnt3a level in the mesodermal compartment causes ectopic Sox2 expression, which is followed by expression of other neural specification genes, indicating that the Sox2 expression provides the ground state for further neural development.

The long-held view that segregation of three germ layers determines cell lineages is challenged by cell lineage analyses^{1,2,7,8} and this study, which indicate that a pool of bipotential precursor cells in the CLE serves as axial stem cells that concordantly produce neural tube and paraxial mesoderm. This characteristic of CLE is continuous with the chordo-neural hinge at later stages^{8,10}. Thus, the three germ layers describe spatial organization of tissues, but do not indicate the process of tissue derivation. Our evidence reinforces the axial stem cell model by providing the mechanistic basis for the fate choice, namely that *Tbx6*-dependent regulation of Sox2 determines the neural versus mesodermal fates in the axial stem cells derived from the CLE.

METHODS SUMMARY

In situ hybridization and immunostaining were performed to analyse the expression of relevant gene transcripts and protein products, respectively. Targeted knockout mice were used to analyse the consequence of loss in embryos of *Tbx6* and/or Sox2 enhancer N1, and transgenic mice were used to monitor enhancer N1 activity or to ectopically express Sox2. EMSA analysis was used to examine a possible interaction of *Tbx6* with enhancer N1 sequence.

Full Methods and any associated references are available in the online version of the paper at www.nature.com/nature.

Received 18 March; accepted 27 November 2010.

- Diez del Corral, R. & Storey, K. Opposing FGF and retinoid pathways: a signalling switch that controls differentiation and patterning onset in the extending vertebrate body axis. *Bioessays* **26**, 857–869 (2004).
- Wilson, V., Olivera-Martinez, I. & Storey, K. Stem cells, signals and vertebrate body axis extension. *Development* **136**, 1591–1604 (2009).
- Chapman, D. & Papaioannou, V. Three neural tubes in mouse embryos with mutations in the T-box gene *Tbx6*. *Nature* **391**, 695–697 (1998).
- Takemoto, T., Uchikawa, M., Kamachi, Y. & Kondoh, H. Convergence of Wnt and FGF signals in the genesis of posterior neural plate through activation of the Sox2 enhancer N-1. *Development* **133**, 297–306 (2006).
- Uchikawa, M., Ishida, Y., Takemoto, T., Kamachi, Y. & Kondoh, H. Functional analysis of chicken Sox2 enhancers highlights an array of diverse regulatory elements that are conserved in mammals. *Dev. Cell* **4**, 509–519 (2003).
- Kamachi, Y. *et al.* Evolution of non-coding regulatory sequences involved in the developmental process: reflection of differential employment of paralogous genes as highlighted by Sox2 and group B1 Sox genes. *Proc. Jpn. Acad. Ser. B* **85**, 55–68 (2009).
- Selleck, M. & Stern, C. Fate mapping and cell lineage analysis of Hensen's node in the chick embryo. *Development* **112**, 615–626 (1991).
- Tzouanacou, E., Wegener, A., Wymeersch, F., Wilson, V. & Nicolas, J. Redefining the progression of lineage segregations during mammalian embryogenesis by clonal analysis. *Dev. Cell* **17**, 365–376 (2009).
- Brown, J. & Storey, K. A region of the vertebrate neural plate in which neighbouring cells can adopt neural or epidermal fates. *Curr. Biol.* **10**, 869–872 (2000).
- Cambray, N. & Wilson, V. Two distinct sources for a population of maturing axial progenitors. *Development* **134**, 2829–2840 (2007).
- Mathis, L., Kulesa, P. & Fraser, S. FGF receptor signalling is required to maintain neural progenitors during Hensen's node progression. *Nature Cell Biol.* **3**, 559–566 (2001).
- Delfino-Machin, M., Lunn, J., Breitkreuz, D., Akai, J. & Storey, K. Specification and maintenance of the spinal cord stem zone. *Development* **132**, 4273–4283 (2005).
- Chapman, D., Agulnik, I., Hancok, S., Silver, L. & Papaioannou, V. *Tbx6*, a mouse T-Box gene implicated in paraxial mesoderm formation at gastrulation. *Dev. Biol.* **180**, 534–542 (1996).
- Yasuhiko, Y. *et al.* Functional importance of evolutionally conserved *Tbx6* binding sites in the presomitic mesoderm-specific enhancer of *Mesp2*. *Development* **135**, 3511–3519 (2008).
- Yasuhiko, Y. *et al.* *Tbx6*-mediated Notch signaling controls somite-specific *Mesp2* expression. *Proc. Natl Acad. Sci. USA* **103**, 3651–3656 (2006).
- Hofmann, M. *et al.* WNT signaling, in synergy with T/TBX6, controls Notch signaling by regulating *Dll1* expression in the presomitic mesoderm of mouse embryos. *Genes Dev.* **18**, 2712–2717 (2004).
- White, P. & Chapman, D. *Dll1* is a downstream target of *Tbx6* in the paraxial mesoderm. *Genesis* **42**, 193–202 (2005).
- Beckers, J. *et al.* Distinct regulatory elements direct *delta1* expression in the nervous system and paraxial mesoderm of transgenic mice. *Mech. Dev.* **95**, 23–34 (2000).

19. Bouillet, P. *et al.* A new mouse member of the *Wnt* gene family, *mWnt-8*, is expressed during early embryogenesis and is ectopically induced by retinoic acid. *Mech. Dev.* **58**, 141–152 (1996).
20. Yamaguchi, T. Genetics of Wnt signaling during early mammalian development. *Methods Mol. Biol.* **468**, 287–305 (2008).
21. Sun, X., Meyers, E., Lewandoski, M. & Martin, G. Targeted disruption of *Fgf8* causes failure of cell migration in the gastrulating mouse embryo. *Genes Dev.* **13**, 1834–1846 (1999).
22. Takada, S. *et al.* Wnt-3a regulates somite and tailbud formation in the mouse embryo. *Genes Dev.* **8**, 174–189 (1994).
23. Trichas, G., Begbie, J. & Srinivas, S. Use of the viral 2A peptide for bicistronic expression in transgenic mice. *BMC Biol.* **6**, 40 (2008).
24. Tonegawa, A. & Takahashi, Y. Somitogenesis controlled by Noggin. *Dev. Biol.* **202**, 172–182 (1998).
25. Dosch, R., Gawantka, V., Delius, H., Blumenstock, C. & Niehrs, C. Bmp-4 acts as a morphogen in dorsoventral mesoderm patterning in *Xenopus*. *Development* **124**, 2325–2334 (1997).

Supplementary Information is linked to the online version of the paper at www.nature.com/nature.

Acknowledgements We thank the members of Kondoh laboratory for discussions. This study was supported by Grants-in-Aid for Scientific Research from MEXT Japan to T.T. and H.K., an NIH grant to V.E.P., and MRC funding to R.L.-B.

Author Contributions T.T. and H.K. conceived the project; T.T. carried out major experiments; T.T. and H.K. analysed data; M.U. and M.Y. aided production and analysis of enhancer N1 mutant mice; V.E.P. provided *Tbx6* mutant mice; D.M.B., R.L.-B. and V.E.P. first indicated *Sox2* dysregulation in the *Tbx6* mutant mice; and T.T. and H.K. wrote the manuscript.

Author Information Reprints and permissions information is available at www.nature.com/reprints. The authors declare no competing financial interests. Readers are welcome to comment on the online version of this article at www.nature.com/nature. Correspondence and requests for materials should be addressed to H.K. (kondohh@fbs.osaka-u.ac.jp).

METHODS

In situ hybridization. Whole-mount *in situ* hybridization was done as previously described²⁶ with the following modifications: proteinase K treatment was done at 5 µg ml⁻¹ (E8 embryos) or 10 µg ml⁻¹ (E9 embryos) for 5 min; incubation with glycine after proteinase K treatment was omitted; digoxigenin-labelled probes were used at 0.5 µg ml⁻¹; and anti-digoxigenin antibody was reacted in 1.5% Blocking Reagent (Roche). The stained embryos were photographed in 80% Glycerol/PBT, then embedded in paraffin and sectioned. The probes used were: *Tbx6* (ref. 13), *Pax6* (ref. 27), *Uncx4.1* (ref. 28), *Foxf1* (ref. 29), *Pax2* (ref. 30), *Foxa1* (ref. 31), *Wnt8a* (ref. 32), *Fgf8* (ref. 33), *Fgf4* (ref. 34), *Sox1* 3' UTR (StuI-XhoI fragment), *Sox2* (SacII-AccI coding sequence fragment), *Sox3* (627–1,128 bp, GenBank NM_009237), *Pax3* (HindIII-PstI coding sequence fragment), *Mox1* (1,688–2,235 bp, GenBank NM_010791), *Egfp* (full coding sequence) and *Wnt3a* (a combination of probes for *Wnt3a* 3' UTR³⁵ and the *Wnt3a* coding sequence).

Immunostaining. Embryos were fixed overnight with 4% PFA in PBS, immersed in 15% and 25% sucrose in PBS in sequence for 2–3 h each step, and embedded in OCT compound. Cryosections with thickness of 10 µm were prepared, and treated at 105 °C for 15 min in antigen unmasking solution (Vector Laboratories) using an autoclave, which also quenched Venus fluorescence. The sections were reacted with 10% normal donkey serum for 30 min, then with the primary antibodies overnight at 4 °C. The primary antibodies, used at 1:200 dilutions, were: rabbit anti-laminin (L9393 Sigma), goat anti-Sox2 (AF2018 R&D Systems), rabbit anti-Pax6 (PRB-278 Covance), and rat anti-HA (1867423 Roche). After several washes, the samples were incubated with fluorescent-dye-coupled secondary antibodies for 1 h at ambient temperature. The following donkey antibodies were used at 1:200 dilutions: Alexa Fluor 488-labelled anti-goat IgG (A-11055 Molecular Probes), Alexa Fluor 555-labelled anti-rabbit IgG (A-31572 Molecular Probes), and CF 633-labelled anti-rat IgG (20137 Biotium). After several washes the samples were stained with 0.5 µg ml⁻¹ Hoechst 33342, and mounted in Permafluor (Thermo Scientific).

Transgenic mouse production, LacZ staining and embryo transfection. Transgene DNA constructs were linearized by digestion with restriction enzyme, freed from vector sequences. Injection of DNA (4 ng µl⁻¹) into the male pronucleus of fertilized eggs and LacZ enzyme staining were done using the standard procedures³⁶. Mice had genetic backgrounds derived from C57BL/6 × DBA crosses. N1-*tklacZ*⁶ and N1-*tkEgfp* were used to establish transgenic lines, whereas other transgenes were used in primary transgenic embryos. The integration of transgenes into embryo genomes was determined by PCR amplification of the *lacZ* or *Egfp/Venus* sequences from yolk sac DNA. Embryo culture and mesodermal transfection with pCAGGS-cNoggin⁴ were done as described previously³⁷.

Production of enhancer N1 mutant mice. The targeting vector used to create the enhancer N1 mutation was constructed by using a 15-kb mouse DNA fragment, which including enhancer N1, derived from the BAC clone RP23-274P9 (BACPAC Resource Center, Children's Hospital Oakland Research Institute). The STneoB cassette³⁸ was inserted 3' of enhancer N1, *loxP* sequences were inserted to flank these sequences, and a DT-A cassette³⁹ was inserted at the 3' terminus of the vector. The linearized vector was electroporated into R1 ES cells,

which had been engineered to have IRES-EGFP immediately downstream of the Sox2 ORF. Recombinants were characterized by Southern hybridization. After germline transmission from chimaeras, heterozygous mice were crossed with CAGGS-Cre mice⁴⁰ to obtain the N1-deleted allele of Sox2. A schematic of the procedure is shown in Supplementary Fig. 4.

Electrophoretic mobility shift assay. Full-length Tbx6 (436 amino acids) was synthesized using a TNT system (Promega), and EMSA analysis was performed as described previously⁴¹ using 0.1 µg µl⁻¹ poly(dI-dC) as a nonspecific competitor. The probe sequences used^{15,42,43} are indicated in Supplementary Fig. 6.

26. Wilkinson, D. G. *In situ hybridization: a practical approach* (IRL at Oxford Univ. Press, 1992).
27. Xu, P. *et al.* Regulation of Pax6 expression is conserved between mice and flies. *Development* **126**, 383–395 (1999).
28. Mansouri, A. *et al.* Paired-related murine homeobox gene expressed in the developing sclerotome, kidney, and nervous system. *Dev. Dyn.* **210**, 53–65 (1997).
29. Sawada, A. *et al.* Redundant roles of *Tead1* and *Tead2* in notochord development and the regulation of cell proliferation and survival. *Mol. Cell. Biol.* **28**, 3177–3189 (2008).
30. Dressler, G., Deutsch, U., Chowdhury, K., Nornes, H. & Gruss, P. Pax2, a new murine paired-box-containing gene and its expression in the developing excretory system. *Development* **109**, 787–795 (1990).
31. Sasaki, H. & Hogan, B. Differential expression of multiple fork head related genes during gastrulation and axial pattern formation in the mouse embryo. *Development* **118**, 47–59 (1993).
32. Kimura-Yoshida, C. *et al.* Canonical Wnt signaling and its antagonist regulate anterior-posterior axis polarization by guiding cell migration in mouse visceral endoderm. *Dev. Cell* **9**, 639–650 (2005).
33. Crossley, P. & Martin, G. The mouse *Fgf8* gene encodes a family of polypeptides and is expressed in regions that direct outgrowth and patterning in the developing embryo. *Development* **121**, 439–451 (1995).
34. Niswander, L. & Martin, G. Fgf-4 expression during gastrulation, myogenesis, limb and tooth development in the mouse. *Development* **114**, 755–768 (1992).
35. Roelink, H. & Nusse, R. Expression of two members of the Wnt family during mouse development—restricted temporal and spatial patterns in the developing neural tube. *Genes Dev.* **5**, 381–388 (1991).
36. Nagy, A., Gertsenstein, M., Vintersten, K. & Behringer, R. *Manipulating the Mouse Embryo: a Laboratory Manual* 3rd edn (Cold Spring Harbor Laboratory Press, 2003).
37. Yamamoto, M. *et al.* Nodal antagonists regulate formation of the anteroposterior axis of the mouse embryo. *Nature* **428**, 387–392 (2004).
38. Katoh, K., Takahashi, Y., Hayashi, S. & Kondoh, H. Improved mammalian vectors for high expression of G418 resistance. *Cell Struct. Funct.* **12**, 575–580 (1987).
39. Yagi, T. *et al.* A novel negative selection for homologous recombinants using diphtheria toxin A fragment gene. *Anal. Biochem.* **214**, 77–86 (1993).
40. Sakai, K. & Miyazaki, J. A transgenic mouse line that retains Cre recombinase activity in mature oocytes irrespective of the cre transgene transmission. *Biochem. Biophys. Res. Commun.* **237**, 318–324 (1997).
41. Kamachi, Y. & Kondoh, H. Overlapping positive and negative regulatory elements determine lens-specific activity of the delta 1-crystallin enhancer. *Mol. Cell. Biol.* **13**, 5206–5215 (1993).
42. Kispert, A. & Hermann, B. The Brachyury gene encodes a novel DNA binding protein. *EMBO J.* **12**, 4898–4899 (1993).
43. Conlon, F., Fairclough, L., Price, B., Casey, E. & Smith, J. Determinants of T box protein specificity. *Development* **128**, 3749–3758 (2001).

The novel gene *twenty-four* defines a critical translational step in the *Drosophila* clock

Chunghun Lim^{1*}, Jongbin Lee^{2*}, Changtaek Choi², Valerie L. Kilman¹, Juwon Kim², Sung Mi Park³, Sung Key Jang³, Ravi Allada¹ & Joonho Choe²

Daily oscillations of gene expression underlie circadian behaviours in multicellular organisms¹. While attention has been focused on transcriptional and post-translational mechanisms^{1–3}, other post-transcriptional modes have been less clearly delineated. Here we report mutants of a novel *Drosophila* gene *twenty-four* (*tyf*) that show weak behavioural rhythms. Weak rhythms are accompanied by marked reductions in the levels of the clock protein Period (PER) as well as more modest effects on Timeless (TIM). Nonetheless, PER induction in pacemaker neurons can rescue *tyf* mutant rhythms. TYF associates with a 5'-cap-binding complex, poly(A)-binding protein (PABP), as well as *per* and *tim* transcripts. Furthermore, TYF activates reporter expression when tethered to reporter messenger RNA even *in vitro*. Taken together, these data indicate that TYF potentially activates PER translation in pacemaker neurons to sustain robust rhythms, revealing a new and important role for translational control in the *Drosophila* circadian clock.

Transcriptional feedback loops are critical for setting the time of eukaryotic circadian clocks. In *Drosophila*, the Clock (Clk)/cycle (cyc) dimer activates the transcription of *period* (*per*), *timeless* (*tim*), *vri* (*vri*), *PAR domain protein 1* (*Pdp1*) and *clockwork orange* (*cwo*) genes, which in turn feedback to inhibit CLK-activated transcription or regulate Clk transcription². These components are also modified post-translationally to alter core clock timing^{2,3}. Regulation at multiple levels is thought to impose temporal delays in feedback, allowing sustained oscillations on a circadian time scale.

To discover novel clock components, we performed a genome-wide behavioural screen. Using the Korea Advanced Institute of Science and Technology (KAIST) GenExel *Drosophila* library, we identified ~4,000 EP lines containing P elements bearing the upstream activating sequence (UAS) for the yeast Gal4 transcription factor inserted near transcription start sites. These flies were crossed with transgenic flies expressing *GAL4* under the control of the *tim* promoter (*tim-GAL4*) to drive downstream gene expression in clock cells⁴. One EP line identified by a long-period rhythm was the G10872 line that contains an insertion 893 bp upstream of the CG4857 transcription start site (Supplementary Fig. 1a). Sequence analyses of the predicted amino acid sequence for CG4857 did not reveal any apparent functional domains or obvious vertebrate homologues but did reveal conservation with genes from different *Drosophila* species and other insects (Supplementary Fig. 2). We termed this novel gene *twenty-four* (*tyf*).

To characterize the phenotype in flies bearing *tyf* loss-of-function mutations, we generated a ~2.5 kb deletion by imprecise P-element excision (Supplementary Fig. 1a; *tyf*^{ΔG14151}; *tyf*^Δ), deleting amino acids 79–449 of *tyf* and resulting in a frame-shift and premature termination. In addition, we identified a *piggyBac* insertion line that shows markedly reduced levels of *tyf* transcript (*tyf*⁰⁰⁶¹⁴; *tyf*^Δ) without affecting the transcript levels of adjacent genes (Supplementary Fig. 1b). Wild-type *Drosophila* show morning and evening peaks under 12 h light:12 h dark cycles, anticipate the transitions between light-on and

light-off by gradually increasing their activity, and maintain their locomotor rhythm in subsequent constant dark. In *tyf* mutants, morning anticipation of lights-on was reduced and their rhythm was immediately less robust, resulting in weak but long periods in constant dark (Fig. 1 and Supplementary Table 1). Precise *piggyBac* excision in *tyf* restored wild-type circadian behaviour (Supplementary Table 1), indicating that *tyf* gene disruption is responsible for its circadian phenotype. Analyses in trans-heterozygous females show that *tyf* alleles are recessive and not complemented by deletions of the CG4857 locus (Supplementary Fig. 3).

Although circadian clocks are evident in multiple tissues, brain clocks are largely responsible for circadian behaviours⁴. Neuroanatomical studies have established two oscillator models in which distinct groups of clock cells control morning and evening locomotor activity and behavioural rhythms^{5,6}. The neuropeptide gene *Pigment-dispersing factor* (*Pdf*), expressed in ventral lateral neurons (LNs), has been implicated in driving morning anticipation and resetting evening clocks in the dorsal LNs/dorsal neurons (DNs)^{7–9}. To map the neurons important for *tyf* effects, we generated *tyf-GAL4* lines containing the *tyf* promoter region (from –3.0 kb to +0.5 kb), and visualized its expression using a UAS–GFP reporter. *tyf-GAL4* expression was relatively restricted to a subset of neurons in the adult brain (Supplementary Fig. 4a–f). Anti-PER antibody staining revealed that it is strongly expressed in PDF⁺ ventral LNs and weakly in dorsal LNs assessed in independent lines (data not shown). In contrast, *tyf-GAL4* expression was not detectable in the DNs. Consistent with the idea that *tyf-GAL4* reflects endogenous *tyf* expression, *tyf-GAL4* along with a UAS-*tyf* transgene fully rescues the behavioural phenotypes in *tyf* mutants (data not shown).

To map the loci of *tyf* function, we restricted TYF overexpression to the PDF⁺ ventral LNs using *Pdf-GAL4* (ref. 7). This results in a long period, similar to with the *tim-GAL4* driver, whereas Gal4 inhibition in PDF⁺ cells by a *Pdf-GAL80* transgene⁷ suppressed the long period phenotype (Supplementary Table 2). Independent UAS-*tyf* insertions confirmed these results. TYF expression restricted to PDF⁺ cells was also sufficient to rescue free-running locomotor rhythms in mutants (Supplementary Table 3). In addition, RNA interference (RNAi)-mediated knockdown of *tyf* expression in PDF⁺ cells phenocopied circadian behaviours in *tyf* hypomorphic mutants (Supplementary Table 3). These data indicate that *tyf* expression in the PDF⁺ pacemaker neurons is necessary and sufficient for robust behavioural rhythms.

To determine *tyf* effects on the core clock, we analysed molecular rhythms from head extracts, which largely reflect eye clocks¹⁰. We found that cycling expression of PER, TIM and PDP1 proteins in *tyf* mutants is comparable to wild type (data not shown). *tyf* transcript levels were relatively constant in a light–dark cycle and not affected in clock mutants (Supplementary Fig. 4g, h). We then focused on the behaviourally relevant pacemaker neurons. Anti-PDF immunofluorescence revealed

¹Department of Neurobiology and Physiology, Northwestern University, Evanston, Illinois 60208, USA. ²Department of Biological Sciences, Korea Advanced Institute of Science and Technology, Daejeon 305-701, Korea. ³Department of Life Sciences, Pohang University of Science and Technology, Pohang 790-784, Korea.

*These authors contributed equally to this work

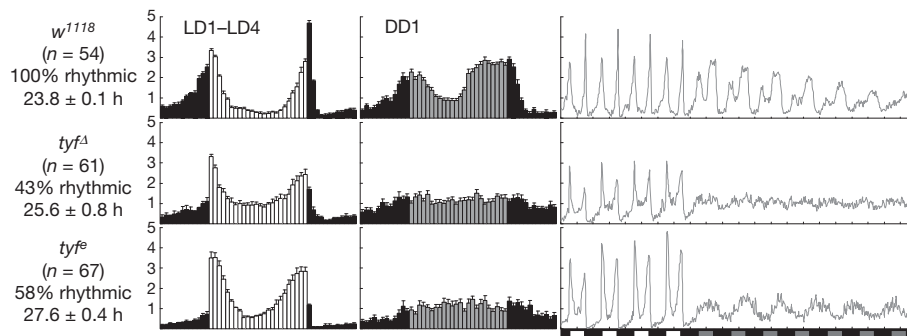


Figure 1 | Robust behavioural rhythms require *tyf*. Averaged activity profiles during 4 light–dark (LD1–LD4)/first constant dark (DD1) cycles (middle panel) and actograms throughout the behavioural analyses (right panel)

no overt defects in the neural projections from PDF⁺ ventral LNs of *tyf* mutants (Supplementary Fig. 5a). Adult-specific TYF expression using a drug-inducible Gal4 was sufficient for behavioural rescue in *tyf* mutants (Supplementary Table 4 and Supplementary Fig. 5c), further reducing the likelihood that *tyf* phenotypes are due to developmental defects.

Notably, we found that PER protein was barely detectable in LN clock cells of *tyf* mutants (Fig. 2a). PER cycling was dampened but not absent (Fig. 2b and Supplementary Fig. 6). *tyf* mutant effects were less severe in the DNs with PER at ~50% of wild-type peak levels. TYF expression in PDF⁺ neurons rescued PER cycling only in PDF⁺ clock cells of *tyf* mutants (Supplementary Fig. 7). Consistent with marked PER reductions, PDF levels increased in dorsal projections from the small ventral LNs of *tyf* mutants (Supplementary Fig. 5b), as observed

(n = 54–67). Percentage of rhythmic flies and period ± s.e.m. (n = 26–54) under constant dark cycles are given at the left. Error bars indicate s.e.m. White/black bars, light–dark cycle; grey/black bars, constant dark cycle.

in *per⁰¹* flies¹¹. TIM levels were also reduced in *tyf* mutants, but to a lesser extent than PER, with peak levels in *tyf* mutants reduced to ~50% of wild type (Supplementary Fig. 8a). Such effects may be indirect through PER, as we found that TIM reductions were also observed in *per⁰¹* flies and there was little effect of loss of *tyf* on TIM in *per⁰¹* mutants.

In contrast to strong effects on PER, *tyf* mutants normally expressed PDP1ε, CWO and CLK proteins (Fig. 2a and Supplementary Fig. 8b). The oscillating expression of PDP1ε protein as well as *tim* and *Pdp1ε* transcripts in *tyf* mutants was comparable to wild type (Supplementary Fig. 8c, d). We reason that light–dark cycles, the clock neural network and/or multiple feedback loops may buffer the molecular clock against loss of *tyf* function.

Given that the robust reductions in PER may be responsible for the arrhythmic behaviour, we proposed that PER expression via the *GAL4/UAS* system could rescue *tyf* locomotor rhythms¹². Indeed, we find that PER, but not TIM or CLK, overexpression specifically in PDF⁺ cells of *tyf* mutants restored wild-type levels of rhythmicity (Fig. 3, Supplementary Fig. 9 and Supplementary Table 5). These rescue data indicate that neither post-translational regulation of PER protein by TIM³ nor transcriptional activation of *per* gene expression by CLK² would be limiting for normal circadian behaviour in *tyf* mutants. Moreover, these behavioural data indicate that PER is a major target of TYF in PDF neurons.

We next examined at what regulatory step PER expression in *tyf* mutants is compromised. We observed that PER protein, but not *per* RNA levels were reduced in brain extracts (data not shown). Although consistent with post-transcriptional regulation, we cannot exclude the possibility that this result could arise from the masking effect of low-level non-cycling *per* RNA in non-circadian tissues. *tyf* effects were not evident on a CLK-activated *per* promoter-*GAL4* transgene (Supplementary Fig. 10) but were evident on a *per* transgene lacking its

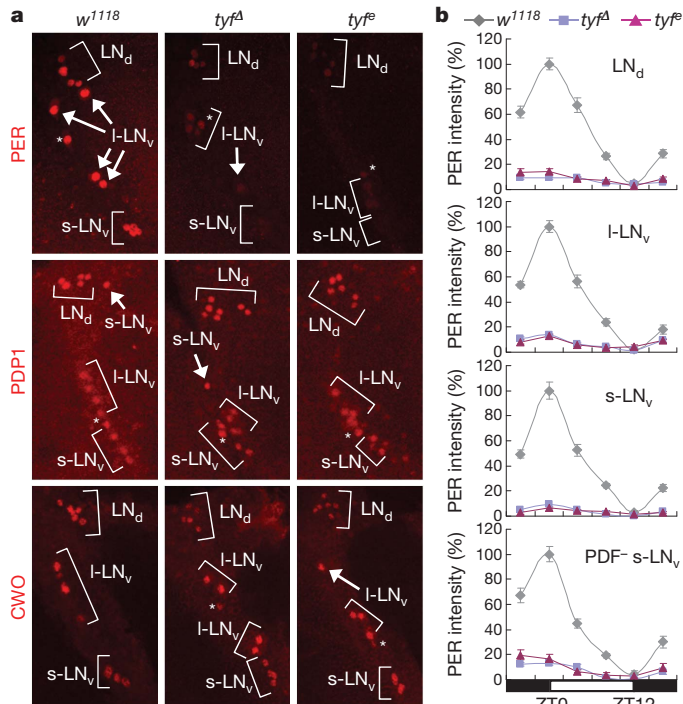


Figure 2 | *tyf* is crucial for PER expression in pacemaker neurons. a, Adult brains were immunostained with anti-PER (top, ZT0), anti-PDP1 (middle, ZT21) and anti-CWO (bottom, ZT3) antibodies. Clock cell groups were imaged with a ×60 oil objective lens and identified by co-staining with anti-PDF antibody (data not shown). LN_d, dorsal lateral neuron; I-LN_v, large ventral LN; s-LN_v, small ventral LN. Asterisk indicates PDF-negative small ventral LN. b, PER intensity in each clock cell group was quantified, averaged (n = 7–10), and normalized to the value of wild-type *Drosophila* at ZT0, which was set as 100%. Error bars indicate s.e.m.

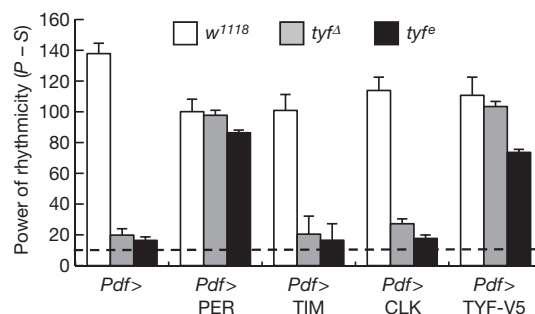


Figure 3 | PER induction rescues *tyf* mutant rhythms. Each clock gene was overexpressed in PDF⁺ cells of wild-type or *tyf* mutants and their rhythmicity under constant dark cycles was measured by power (P) – significance (S) values. x-axis shows *Pdf*-GAL4-driven overexpression of each clock transgene. Of note, each fly with P – S values greater than 10 (dotted line) is defined as rhythmic. Data represent average + s.e.m. (n = 18–48).

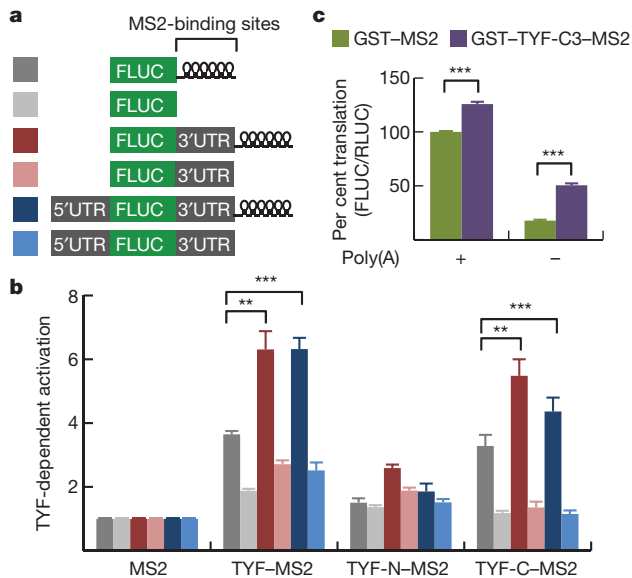


Figure 5 | TYF activates reporter expression when tethered to its RNA. **a**, S2 cells were transfected with MS2 reporter plasmid (depicted in **a**) and expression vector for MS2 fusion protein. Firefly luciferase activity (FLUC) was first normalized to *Renilla* luciferase activity (RLUC). Fold increase in activation was then calculated by normalizing to the value in the presence of MS2. Data represent average \pm s.d. ($n = 4-6$). 5' UTR and 3' UTR are in *per*. $**P < 0.01$ and $***P < 0.001$ as determined by Student's *t*-test. **c**, m⁷-G-capped MS2 reporter RNAs were synthesized using *in vitro* transcription, polyadenylated by bacterial poly(A) polymerase, and incubated with translation-competent S2 cell extracts and purified GST-MS2 fusion protein in *in vitro* translation reactions. Luciferase assays were performed as in **b**. Data represent average \pm s.e.m. ($n = 3-7$). $***P < 0.001$ as determined by one-way ANOVA, Tukey post-hoc test.

nuclear/cytoplasmic distribution were comparable between MS2- and TYF-MS2-transfected cells (Supplementary Fig. 14e, f). Moreover, analytical centrifugation through a sucrose cushion revealed that more reporter transcripts associate with high-density ribosomes in the presence of TYF-MS2 (Supplementary Fig. 14g; $P < 0.027$), further supporting a role in translational control.

To more directly test the translational activation function of TYF, we reconstituted this tethering system in *in vitro* translation assays. A C-terminal TYF region (TYF-C3, amino acids 1373–1911) fused to MS2, which robustly activated MS2 reporter expression in transfected cells (data not shown), was bacterially expressed, purified and incubated with *in vitro* transcribed MS2 reporter RNAs and translation-competent S2 cell extracts. TYF-C3-MS2 activated translation from a m⁷-G capped and poly(A)-tailed reporter RNA modestly (Fig. 5c; $P < 0.001$) and a non-polyadenylated RNA more strongly ($2.9\times$, $P < 0.001$). TYF-C3-MS2 effects are evident without affecting reporter RNA levels (data not shown). Moreover, this TYF region is not sufficient to bind PABP *in vitro* (Supplementary Fig. 12a), indicating that these effects are not mediated by PABP recruitment. These data clearly demonstrate a translation activation function of TYF *in vitro*, supporting a possible role in translation of poorly adenylated transcripts.

Relative to studies of transcriptional and post-transcriptional regulation, little is known about other post-transcriptional/translational mechanisms of core clock regulation in different organisms^{3,20}. Although a number of RNA-binding proteins are either rhythmically expressed¹ or important for behavioural rhythms²¹⁻²⁴, direct links between specific trans-acting factors, specific clock gene transcripts, and *in vivo* core clock function have yet to be clearly established, especially in metazoans. Indeed, a number of studies have indicated a role for post-transcriptional regulation in modulating *per* expression^{10,25-28}. Here we demonstrate with several lines of evidence that

TYF activates PER translation to sustain behavioural rhythms, revealing a new and important role for translational control in the *Drosophila* circadian clock. We observe robust *tyf* effects on PER and lesser effects on TIM yet no detectable reduction of the other core clock components we assayed. This observation indicates that impairing *tyf*-dependent translation is not critical for the expression of most clock components. Importantly, transgenic induction of PER, but not other clock components including TIM, can rescue *tyf* mutant phenotypes.

TYF function is especially important in pacemaker neurons. Both *tyf* and *per* expression in PDF⁺ ventral LNs is sufficient to strongly rescue behavioural rhythms in *tyf* mutants. Moreover, *tyf* effects on PER are, by far, most evident in these pacemaker neurons. The brain pacemaker neurons are also among the few clock cells that demonstrate robust free-running molecular rhythms in constant dark^{8,9}. Thus, TYF-mediated translational control may be a specialization of networked pacemakers in the brain crucial for sustaining free-running rhythmicity.

Our data also strongly support the model that TYF acts at the level of translational control. TYF associates with *per* and *tim* RNAs, as well as translational regulatory components such as the eIF4E-containing 5'-cap-binding complex and PABP, of which the latter is insensitive to RNase treatment. In addition, TYF tethered to a reporter RNA via MS2 can activate reporter expression without altering RNA levels in transfected cells and, importantly, in cell extracts providing exogenous RNA templates and purified TYF-MS2.

It remains unclear how TYF controls translation of its target RNAs. We observe specific effects on PER and TIM but not on other clock components, and we find that TYF interacts with translation components such as the eIF4E-containing cap-binding complex and PABP. We propose that RNA-binding translational repressors associate with newly transcribed *per* RNA, temporarily postpone translation and thus delay PER feedback repression on its own transcription (Supplementary Fig. 15). Such a delay could contribute to the observed lag between protein and RNA particularly in pacemaker neurons, although post-translational mechanisms may also contribute, at least in the eyes²⁹. TYF, which does not have a known RNA-recognition motif, could then be recruited to target transcripts by these translational repressors, releasing them to stimulate initiation of *per* translation. We have not been able to biochemically or genetically link TYF to RNA-binding proteins FMR, LARK, or the translation regulator Thor/4E-BP, which have been shown to contribute to circadian clock function^{21,22,24}. Nonetheless, TYF association with eIF4E and their similar polysome profiles implicate TYF as a novel translation initiation factor. In addition, the effects of TYF may be more evident on poorly adenylated transcripts on the basis of our *in vitro* data (Fig. 5c). Of note, the *Drosophila* homologue of the clock-regulated deadenylase *nocturnin*³⁰ has been shown to be important in DNs for circadian light responses but neither a LN function nor an RNA target has been described²⁴. Nevertheless, unique features of TYF-regulated transcripts may mediate the highly selective TYF effects on clock components *in vivo*.

Post-transcriptional regulation on *per* RNA has been considered to be modulatory to clock function. The identification of a critical role for TYF highlights an important role for PER translation in the *Drosophila* neural clockwork. It will be of interest to determine if proteins functionally analogous to TYF serve similarly important and specific functions in the mammalian clock.

METHODS SUMMARY

Plasmids. Total RNA from adult *Drosophila* heads was isolated using Trizol reagent and reverse-transcribed using Superscript III according to the manufacturer's instructions (Invitrogen). *tyf* complementary DNA (cDNA) was PCR-amplified by Platinum *Pfx* polymerase (Invitrogen) with the appropriate primer sets and inserted into pUAST vector for regular germline transformation and into its modified version with *attB* site and C-terminal V5 tag for site-specific germline transformation.

Drosophila stocks. All flies were reared with standard cornmeal-yeast-agar medium at 25 °C under light–dark (12 h light:12 h dark) cycles. EP lines G10872 and G14151 were obtained from the KAIST GenExel *Drosophila* library. To generate a *tyf* deletion line (*tyf*^d), P-element excision lines were established from the G14151 line and molecularly characterized by genomic DNA-PCR with the appropriate primer sets. *Df(1)HC244*, *Df(1)rb23* and UAS-mCD8-GFP lines were obtained from the Bloomington *Drosophila* stock centre. The UAS-*tyf*^{RNAi} line was obtained from the National Institute of Genetics (Japan). Several independent germline transformants were established from *w*¹¹¹⁸ embryos injected with UAS-*tyf* transgenic construct (BestGene).

Full Methods and any associated references are available in the online version of the paper at www.nature.com/nature.

Received 16 April 2009; accepted 1 December 2010.

- Doherty, C. J. & Kay, S. A. Circadian control of global gene expression patterns. *Annu. Rev. Genet.* **44**, 419–444 (2010).
- Zheng, X. & Sehgal, A. Probing the relative importance of molecular oscillations in the circadian clock. *Genetics* **178**, 1147–1155 (2008).
- Harms, E., Kivimäe, S., Young, M. W. & Saez, L. Posttranscriptional and posttranslational regulation of clock genes. *J. Biol. Rhythms* **19**, 361–373 (2004).
- Dubruille, R. & Emery, P. A plastic clock: how circadian rhythms respond to environmental cues in *Drosophila*. *Mol. Neurobiol.* **38**, 129–145 (2008).
- Stoleru, D., Peng, Y., Agosto, J. & Rosbash, M. Coupled oscillators control morning and evening locomotor behaviour of *Drosophila*. *Nature* **431**, 862–868 (2004).
- Grima, B., Chelot, E., Xia, R. & Rouyer, F. Morning and evening peaks of activity rely on different clock neurons of the *Drosophila* brain. *Nature* **431**, 869–873 (2004).
- Renn, S. C., Park, J. H., Rosbash, M., Hall, J. C. & Taghert, P. H. A *pdf* neuropeptide gene mutation and ablation of PDF neurons each cause severe abnormalities of behavioral circadian rhythms in *Drosophila*. *Cell* **99**, 791–802 (1999).
- Peng, Y., Stoleru, D., Levine, J. D., Hall, J. C. & Rosbash, M. *Drosophila* free-running rhythms require intercellular communication. *PLoS Biol.* **1**, e13 (2003).
- Lin, Y., Stormo, G. D. & Taghert, P. H. The neuropeptide pigment-dispersing factor coordinates pacemaker interactions in the *Drosophila* circadian system. *J. Neurosci.* **24**, 7951–7957 (2004).
- Zeng, H., Hardin, P. E. & Rosbash, M. Constitutive overexpression of the *Drosophila* period protein inhibits period mRNA cycling. *EMBO J.* **13**, 3590–3598 (1994).
- Park, J. H. *et al.* Differential regulation of circadian pacemaker output by separate clock genes in *Drosophila*. *Proc. Natl Acad. Sci. USA* **97**, 3608–3613 (2000).
- Yang, Z. & Sehgal, A. Role of molecular oscillations in generating behavioral rhythms in *Drosophila*. *Neuron* **29**, 453–467 (2001).
- Frisch, B., Hardin, P. E., Hamblen-Coyle, M. J., Rosbash, M. & Hall, J. C. A promoterless period gene mediates behavioral rhythmicity and cyclical per expression in a restricted subset of the *Drosophila* nervous system. *Neuron* **12**, 555–570 (1994).
- Kim, E. Y., Ko, H. W., Yu, W., Hardin, P. E. & Edery, I. A. DOUBLETIME kinase binding domain on the *Drosophila* PERIOD protein is essential for its hyperphosphorylation, transcriptional repression, and circadian clock function. *Mol. Cell. Biol.* **27**, 5014–5028 (2007).
- Blanchardon, E. *et al.* Defining the role of *Drosophila* lateral neurons in the control of circadian rhythms in motor activity and eclosion by targeted genetic ablation and PERIOD protein overexpression. *Eur. J. Neurosci.* **13**, 871–888 (2001).
- Sonenberg, N. & Hinnebusch, A. G. Regulation of translation initiation in eukaryotes: mechanisms and biological targets. *Cell* **136**, 731–745 (2009).
- Kula-Eversole, E. *et al.* Surprising gene expression patterns within and between PDF-containing circadian neurons in *Drosophila*. *Proc. Natl Acad. Sci. USA* **107**, 13497–13502 (2010).
- Keryer-Bibens, C., Barreau, C. & Osborne, H. B. Tethering of proteins to RNAs by bacteriophage proteins. *Biol. Cell* **100**, 125–138 (2008).
- Veleri, S., Brandes, C., Helfrich-Forster, C., Hall, J. C. & Stanewsky, R. A self-sustaining, light-entrainable circadian oscillator in the *Drosophila* brain. *Curr. Biol.* **13**, 1758–1767 (2003).
- Staiger, D. & Koster, T. Spotlight on post-transcriptional control in the circadian system. *Cell. Mol. Life Sci.* doi:10.1007/s00018-010-0513-5 (in the press).
- Dockendorff, T. C. *et al.* *Drosophila* lacking *dfmr1* activity show defects in circadian output and fail to maintain courtship interest. *Neuron* **34**, 973–984 (2002).
- Sofola, O. *et al.* The *Drosophila* FMRP and LARK RNA-binding proteins function together to regulate eye development and circadian behavior. *J. Neurosci.* **28**, 10200–10205 (2008).
- Kadener, S. *et al.* A role for microRNAs in the *Drosophila* circadian clock. *Genes Dev.* **23**, 2179–2191 (2009).
- Nagoshi, E. *et al.* Dissecting differential gene expression within the circadian neuronal circuit of *Drosophila*. *Nature Neurosci.* **13**, 60–68 (2010).
- So, W. V. & Rosbash, M. Post-transcriptional regulation contributes to *Drosophila* clock gene mRNA cycling. *EMBO J.* **16**, 7146–7155 (1997).
- Stanewsky, R., Jamison, C. F., Plautz, J. D., Kay, S. A. & Hall, J. C. Multiple circadian-regulated elements contribute to cycling period gene expression in *Drosophila*. *EMBO J.* **16**, 5006–5018 (1997).
- Majercak, J., Sidote, D., Hardin, P. E. & Edery, I. How a circadian clock adapts to seasonal decreases in temperature and day length. *Neuron* **24**, 219–230 (1999).
- Suri, V., Lanjuin, A. & Rosbash, M. TIMELESS-dependent positive and negative autoregulation in the *Drosophila* circadian clock. *EMBO J.* **18**, 675–686 (1999).
- Suri, V., Hall, J. C. & Rosbash, M. Two novel doubletime mutants alter circadian properties and eliminate the delay between RNA and protein in *Drosophila*. *J. Neurosci.* **20**, 7547–7555 (2000).
- Green, C. B. *et al.* Loss of Nocturnin, a circadian deadenylase, confers resistance to hepatic steatosis and diet-induced obesity. *Proc. Natl Acad. Sci. USA* **104**, 9888–9893 (2007).

Supplementary Information is linked to the online version of the paper at www.nature.com/nature.

Acknowledgements We thank I. Edery, J. Hall, H. Keshishian, M. Rosbash, F. Rouyer, A. Sehgal, the Bloomington *Drosophila* stock center, Harvard Exelixis *Drosophila* stock collection, KAIST GenExel *Drosophila* library and the National Institute of Genetics for *Drosophila* strains; P. Hardin, E. Izaurralde, A. Nakamura, M. Rosbash and N. Sonenberg for antibodies; J. Lykke-Andersen for plasmids; K. E. Duncan for suggestions on *in vitro* translation assays. This work was supported by grants from the Brain Research Center of the 21st Century Frontier Research Program through the National Research Foundation of Korea funded by the Ministry of Education, Science and Technology, the Republic of Korea (J.C.) and from the National Institutes of Health (R01NS059042, R01NS052903, R01MH067870; R.A.).

Author Contributions R.A. and J.C. conceived the study; R.A., C.L. and J.C. designed the experiments; C.L. (under the supervision of R.A.) and J.L. (under the supervision of J.C.) jointly completed Figs 1 and 2, Supplementary Figs 1, 4, 8, 14 and Supplementary Tables 2 and 3; J.L., S.M.P. and S.K.J. performed and analysed the experiments in Supplementary Fig. 13; J.L., C.C. and J.K. performed the genome-wide behavioural screen; C.C. performed GST pull-down studies in Supplementary Fig. 12a; V.L.K. performed PDF quantification analysis in Supplementary Fig. 5b; C.L. performed and analysed experiments in all remaining Figures, Supplementary Figures and Tables; C.L. and R.A. wrote the manuscript.

Author Information Reprints and permissions information is available at www.nature.com/reprints. The authors declare no competing financial interests. Readers are welcome to comment on the online version of this article at www.nature.com/nature. Correspondence and requests for materials should be addressed to R.A. (r-allada@northwestern.edu) or J.C. (jchoe@kaist.ac.kr).

METHODS

Plasmids. *Pabp* cDNA was amplified and inserted into pGEX-4T-1 (GE Healthcare) to purify GST–PABP protein from bacteria. To make a DNA construct for *tyf-GAL4* transgenic *Drosophila*, the *tyf* gene promoter region ranging from –3.0 kb to +0.5 kb relative to the transcription start site was PCR-amplified from wild-type genomic DNA and inserted into the pPTGAL4 vector³¹. cDNAs encoding an oligomerization-defective MS2 coat protein mutant and six tandem repeats of MS2 coat protein binding site (6×BS) were PCR-amplified from pcNMS2–Flag and pcB6bs³², respectively, and inserted into pAc5.1/V5 (Invitrogen). Firefly or *Renilla* luciferases cDNA with or without clock gene UTRs was inserted into pAc5.1/V5 or pAc/6×BS to generate MS2 reporter plasmids. cDNAs corresponding to wild type or deletion mutants of *tyf* were inserted into: (1) pAc5.1/V5 or pAc/MS2–V5 to express C-terminal V5 or MS2–V5 fusion proteins in transfected S2 cells; and (2) pcDNA3 (Invitrogen) for *in vitro* transcription and translation.

***Drosophila* stocks and behavioural assays.** *Pdf-GAL4*, *tim-GAL4*, *per-GAL4*, *Elav-Gene Switch-GAL4*, *Pdf-GAL80*, *cry-GAL80*, *UAS-per16*, *UAS-tim*, *UAS-Clk*, *perG*, *per(Δ)*–HA–His, *XLG-luc*, and 7.2:9 transgenic lines were described previously^{5,7,10,13–15,19,33–36}. For *phiC31* integrase-based transformation³⁷, the *UAS-tyf-V5* transgene was inserted into the *attP40* landing site³⁸ (Genetic Services). The locomotor activity of individual male or virgin female *Drosophila* was measured using *Drosophila* Activity Monitors (Trikinetics) and analysed using ClockLab analysis software (Actimetrics) as described previously³⁹. For adult-specific TYF overexpression, flies were fed with foods containing 0.5 mM RU486 (dissolved in 4% ethanol) or vesicle control (4% ethanol) from the first light–dark cycle of their behavioural assays to activate Gene Switch–*GAL4* (ref. 36) and induce TYF overexpression from *UAS-tyf* transgenes.

Quantitative RT–PCR. Semi-quantitative and real-time RT–PCR using total RNA from adult *Drosophila* heads and transfected S2 cells were performed as described previously^{39,40}. Primer sequences used in our transcript analyses are available on request.

Immunostaining. Whole-mount immunostaining in adult *Drosophila* brains was performed as described previously⁴⁰. For primary antibodies, we used rabbit anti-PER (a gift from M. Rosbash), rabbit anti-PDP1⁴⁰ and guinea pig anti-TIM⁴⁰, guinea pig anti-CWO⁴¹ and anti-CLK⁴², mouse anti-PDF (Developmental Studies Hybridoma Bank) and anti-V5 (Invitrogen) antibodies. Anti-mouse IgG Alexa 488, anti-mouse IgG Alexa 594, anti-rabbit IgG Alexa 594, anti-guinea pig IgG Alexa 594 and 633 antibodies (Invitrogen) were used for fluorescence-conjugated secondary antibodies. Images were obtained using confocal laser-scanning microscopes (Nikon C1 or Carl Zeiss Pascal). For the quantitative analysis, signal intensity from each group of clock cells was quantified using ImageJ software as described previously⁴³.

Immunoprecipitation. Immunoprecipitation from *Drosophila* head and S2 extracts were performed as described previously⁴⁰. For RNA analysis, ~200 *Drosophila* heads were homogenized in a lysis buffer (25 mM Tris–Cl pH 7.5, 300 mM NaCl, 10% glycerol, 1 mM EDTA, 1 mM dithiothreitol, 0.5% Nonidet P-40, 1 mM phenylmethylsulfonyl fluoride) containing 20 U ml^{–1} DNase I (Promega), 100 U ml^{–1} RNasin (Promega) and 8 mM vanadyl ribonucleoside complex (Sigma). After the immunoprecipitation with anti-V5 antibody, bound RNA was purified using Trizol reagent (Invitrogen) and subsequently used in transcript analyses by semiquantitative and real-time RT–PCR.

Antibodies. Mouse anti-V5 (Invitrogen), rat anti-HA (Roche), mouse anti-dFMR 6A15 (Abcam), human anti-P0 (Immunovision), rabbit anti-PER⁴⁰, guinea pig anti-TIM⁴⁰, rat anti-GE-1⁴⁴, rat anti-Tral⁴⁴, rabbit anti-dPABP⁴⁵ and rabbit anti-elf4E⁴⁶ antibodies were used in our protein analyses.

GST pull-down assay. *In vitro* binding assay was performed as described previously⁴⁰ with minor modifications. TYF and deletion mutant proteins were *in vitro* translated in the presence of ³⁵S-methionine using TNT T7 coupled reticulocyte lysate system (Promega).

GST fusion proteins were purified from bacterial cultures using glutathione–Sephadex 4B beads (GE Healthcare) and incubated with ³⁵S-labelled proteins in a binding buffer (20 mM HEPES pH 7.5, 100 mM KCl, 5% glycerol, 1 mM EDTA, 1 mM dithiothreitol, 0.1% Triton X-100, 1 mM phenylmethylsulfonyl fluoride). After the incubation for 1 h at 4 °C, the beads were washed three times in the same buffer. Bound proteins were eluted, resolved by SDS–PAGE, and detected by autoradiography.

Cap pull-down assay. S2 cells in 100-mm dishes were transfected with 1.2 μg of expression vector for TYF–V5 or deletion mutants. Cells were harvested at 48 h after transfection, washed in PBS, and resuspended in a lysis buffer (25 mM Tris–Cl pH 7.5, 150 mM NaCl, 10% glycerol, 1 mM EDTA, 1 mM dithiothreitol, 0.5% Nonidet P-40, 1 mM phenylmethylsulfonyl fluoride, protease inhibitors). Extracts were clarified by centrifugation and incubated with pre-equilibrated m⁷-GTP Sepharose 4B (GE Healthcare) for 1.5 h at 4 °C. Where indicated, 0.5 mM m⁷-GTP or GTP was added to the lysis buffer. The beads were washed

four times with the same buffer. Bound proteins were eluted by boiling in 1× SDS sample buffer, resolved by SDS–PAGE and immunoblotted with antibodies as shown.

Sucrose density gradient fractionation. Sucrose gradient sedimentations were performed as described previously^{47,48} with minor modifications. S2 cells were cultured in 100-mm dishes and transfected with 2 μg of Ac/TYF–3×HA using Effectene reagent (Qiagen). At 48 h after transfection, 200 μg ml^{–1} of cycloheximide was added to the media and incubated for a further 10 min. Cells were harvested, washed twice with PBS and lysed in 800 μl of polysome gradient buffer (15 mM Tris–Cl pH 7.5, 300 mM NaCl, 10 mM MgCl₂, 0.2 mg ml^{–1} cycloheximide, 50 U ml^{–1} RNasin, 0.1 mg ml^{–1} heparin, 1 mM dithiothreitol, 1 mM phenylmethylsulfonyl fluoride, complete protease inhibitor) containing 0.5% Nonidet P-40. For EDTA treatment, 10 mM MgCl₂ in the lysis buffer was replaced by 25 mM EDTA and cycloheximide was omitted. The lysates were incubated for 15 min at 4 °C and centrifuged twice. Clarified lysates were loaded on 10–50% linear sucrose gradient solution. Samples were spun in a SW 41Ti rotor (Beckman) at 36,000 r.p.m. for 2 h. Using tube piercer (Brandel) and FRAC-100, each fraction was collected from the bottom while UV absorbance at 254 nm was monitored continuously with UA-6 detector (ISCO). Proteins in each fraction were precipitated with chloroform/methanol⁴⁹ and used for western blotting analyses.

RNA tethering assay. S2 cells on 24-well plates were co-transfected with 5 ng of Ac/FLUC–6×BS (or its derivatives), 25 ng of Ac/RLUC, and 250 ng of Ac/MS2–V5 (or its derivatives). For competition experiments, S2 cells were co-transfected with 5 ng of Ac/5′-UTR-FLUC–3′-UTR–6×BS, 5 ng of Ac/RLUC, 125 ng of Ac/MS2–V5 or Ac/TYF–MS2–V5, and the increasing amount (125 or 375 ng) of Ac/TYF–V5 (or TYF deletion constructs). Cells were harvested at 48 h after transfection and dual luciferase assays were performed according to the manufacturer's instructions (Promega).

Subcellular fractionation. S2 cells were treated with 200 μg ml^{–1} of cycloheximide for 10 min before harvesting at 48 h after transfection. Cell pellets were resuspended in a hypotonic buffer (10 mM HEPES pH 7.9, 1.5 mM MgCl₂, 10 mM KCl, 0.5 mM dithiothreitol) on ice for 10 min. Nonidet P-40 were added to a final concentration of 0.5% and incubated for an additional 5 min on ice. Lysates were centrifuged at 5,000 r.p.m. for 5 min. RNA was isolated from supernatant (cytoplasmic fraction) and pellet (nuclear fraction), separately, using Trizol LS and Trizol reagents (Invitrogen), treated with DNase I and DpnI, reverse-transcribed by M-MLV reverse transcriptase (Promega), and quantified by real-time RT–PCR. *Fluc* RNA levels were first normalized to *cyc* RNA levels in each fraction and the ratio of normalized *Fluc* RNA levels in the cytoplasm fraction to the nuclear fraction was compared between MS2- and TYF–MS2-transfected cells.

Sucrose cushion centrifugation. Transfected cells were resuspended in 400 μl of the polysome gradient buffer containing 0.5% Nonidet P-40, homogenized by 20 strokes with a pestle homogenizer and further incubated for 15 min at 4 °C. Lysates were cleared by centrifugation at 12,000 r.p.m. for 5 min at 4 °C, and layered onto a 2 ml of 45% (wt/wt) sucrose cushion in the polysome gradient buffer. Samples were centrifuged in a SW55Ti (Beckman) for 2 h at 50,000 r.p.m. at 4 °C. After the centrifugation, RNA was isolated from sucrose cushion and pellet fractions, separately, using the RNeasy mini kit (Qiagen) and quantified as described earlier. On the basis of the quantification of 18S ribosomal RNA levels, 32 ± 5% of total ribosomes were pelleted by their higher density under these conditions. The ratio of normalized *Fluc* RNA levels in pellet fraction to sucrose cushion fraction was compared between MS2- and TYF–MS2-transfected cells.

***In vitro* translation assay.** *In vitro* translation assays using S2 cell extracts were performed as described previously^{50,51} with some modifications. S2 cells were harvested and washed three times in PBS. Cell pellets were resuspended and homogenized in 1 volume of hypotonic lysis buffer (10 mM HEPES–KOH pH 7.4, 10 mM KOAc, 0.5 mM Mg(OAc)₂, 5 mM dithiothreitol and protease inhibitors). After 10 min incubation on ice, the cell extracts were clarified by centrifugation at 13,000 r.p.m. for 10 min at 4 °C. Supernatants were immediately used in *in vitro* translation reaction or stored at –80 °C. For the template of MS2 reporter RNAs, firefly luciferase cDNA along with *per* 3′ UTR and MS2-binding sites was subcloned into pcDNA3. m⁷G-capped RNAs were *in vitro* transcribed using mMESSAGE mMACHINE kit (Ambion) and divided into two aliquots. Poly(A) tail (>150 nucleotides) was added to RNA transcripts in one aliquot using Poly(A) Tailing kit (Ambion) according to the manufacturer's instruction. For poly(A)[–] reporter RNA, poly(A) polymerase was omitted in a parallel reaction using the other aliquot. All RNAs were further purified using MEGAclear kit (Ambion), quantified, and stored in aliquots at –80 °C until use. m⁷G-capped and polyadenylated RNA for *Renilla* luciferase was similarly prepared and included as an internal control in *in vitro* translation reactions. Each *in vitro* translation reaction included 5 ng of firefly luciferase RNA containing *per* 3′ UTR and MS2-binding sites, 10 ng of *Renilla* luciferase RNA, 100 ng of bacterially purified GST–MS2 or GST–TYF–C3–MS2, 24 mM HEPES–KOH pH 7.4, 60 mM KOAc, 1.5 mM

Mg(OAc)₂, 0.1 mM spermidine, 1.2 mM dithiothreitol, 20 mM creatine phosphate, 60 μ M amino acids, 120 μ g ml⁻¹ creatine kinase, 0.1 mg ml⁻¹ yeast tRNA, 4 U RNasin (Promega), and 40% S2 extracts in 12.5 μ l reaction. The reaction was incubated for 90 min at 25 °C, stopped by adding 50 μ l of 1 \times Reporter lysis buffer (Promega), and kept on ice. Ten microlitres of the mixture was used for dual luciferase assay as described earlier. Total RNA was purified from the rest of the *in vitro* translation reaction using Trizol and quantified by realtime RT-PCR.

31. Sharma, Y., Cheung, U., Larsen, E. W. & Eberl, D. F. PPTGAL, a convenient GAL4 P-element vector for testing expression of enhancer fragments in *Drosophila*. *Genesis* **34**, 115–118 (2002).
32. Lykke-Andersen, J., Shu, M. D. & Steitz, J. A. Human Upf proteins target an mRNA for nonsense-mediated decay when bound downstream of a termination codon. *Cell* **103**, 1121–1131 (2000).
33. Kaneko, M. & Hall, J. C. Neuroanatomy of cells expressing clock genes in *Drosophila*: transgenic manipulation of the period and timeless genes to mark the perikarya of circadian pacemaker neurons and their projections. *J. Comp. Neurol.* **422**, 66–94 (2000).
34. Cheng, Y., Gvakharia, B. & Hardin, P. E. Two alternatively spliced transcripts from the *Drosophila* period gene rescue rhythms having different molecular and behavioral characteristics. *Mol. Cell. Biol.* **18**, 6505–6514 (1998).
35. Zhao, J. *et al.* *Drosophila* clock can generate ectopic circadian clocks. *Cell* **113**, 755–766 (2003).
36. Osterwalder, T., Yoon, K. S., White, B. H. & Keshishian, H. A conditional tissue-specific transgene expression system using inducible GAL4. *Proc. Natl Acad. Sci. USA* **98**, 12596–12601 (2001).
37. Groth, A. C., Fish, M., Nusse, R. & Calos, M. P. Construction of transgenic *Drosophila* by using the site-specific integrase from phage phiC31. *Genetics* **166**, 1775–1782 (2004).
38. Markstein, M., Pitsouli, C., Villalta, C., Celniker, S. E. & Perrimon, N. Exploiting position effects and the gypsy retrovirus insulator to engineer precisely expressed transgenes. *Nature Genet.* **40**, 476–483 (2008).
39. Lim, C. *et al.* Clockwork orange encodes a transcriptional repressor important for circadian-clock amplitude in *Drosophila*. *Curr. Biol.* **17**, 1082–1089 (2007).
40. Lim, C. *et al.* Functional role of CREB-binding protein in the circadian clock system of *Drosophila melanogaster*. *Mol. Cell. Biol.* **27**, 4876–4890 (2007).
41. Matsumoto, A. *et al.* A functional genomics strategy reveals clockwork orange as a transcriptional regulator in the *Drosophila* circadian clock. *Genes Dev.* **21**, 1687–1700 (2007).
42. Houl, J. H., Yu, W., Dudek, S. M. & Hardin, P. E. *Drosophila* CLOCK is constitutively expressed in circadian oscillator and non-oscillator cells. *J. Biol. Rhythms* **21**, 93–103 (2006).
43. Picot, M., Cusumano, P., Klarsfeld, A., Ueda, R. & Rouyer, F. Light activates output from evening neurons and inhibits output from morning neurons in the *Drosophila* circadian clock. *PLoS Biol.* **5**, e315 (2007).
44. Eulalio, A., Behm-Ansmant, I., Schweizer, D. & Izaurralde, E. P-body formation is a consequence, not the cause, of RNA-mediated gene silencing. *Mol. Cell. Biol.* **27**, 3970–3981 (2007).
45. Roy, G., Miron, M., Khaleghpour, K., Lasko, P. & Sonenberg, N. The *Drosophila* poly(A) binding protein-interacting protein, dPaip2, is a novel effector of cell growth. *Mol. Cell. Biol.* **24**, 1143–1154 (2004).
46. Nakamura, A., Sato, K. & Hanyu-Nakamura, K. *Drosophila* cup is an eIF4E binding protein that associates with Bruno and regulates oskar mRNA translation in oogenesis. *Dev. Cell* **6**, 69–78 (2004).
47. Monzo, K. *et al.* Fragile X mental retardation protein controls trailer hitch expression and cleavage furrow formation in *Drosophila* embryos. *Proc. Natl Acad. Sci. USA* **103**, 18160–18165 (2006).
48. Satterfield, T. F. & Pallanck, L. J. Ataxin-2 and its *Drosophila* homolog, ATX2, physically assemble with polyribosomes. *Hum. Mol. Genet.* **15**, 2523–2532 (2006).
49. Wessel, D. & Flugge, U. I. A method for the quantitative recovery of protein in dilute solution in the presence of detergents and lipids. *Anal. Biochem.* **138**, 141–143 (1984).
50. Thoma, C., Ostareck-Lederer, A. & Hentze, M. W. A poly(A) tail-responsive *in vitro* system for cap- or IRES-driven translation from HeLa cells. *Methods Mol. Biol.* **257**, 171–180 (2004).
51. Castagnetti, S., Hentze, M. W., Ephrussi, A. & Gebauer, F. Control of oskar mRNA translation by Bruno in a novel cell-free system from *Drosophila* ovaries. *Development* **127**, 1063–1068 (2000).

Lifespan extension induced by AMPK and calcineurin is mediated by CRTC-1 and CREB

William Mair^{1,2,3}, Ianessa Morantte^{1,2,3}, Ana P. C. Rodrigues^{1,4}, Gerard Manning^{1,4}, Marc Montminy^{1,3}, Reuben J. Shaw^{1,2,3} & Andrew Dillin^{1,2,3}

Activating AMPK or inactivating calcineurin slows ageing in *Caenorhabditis elegans*^{1,2} and both have been implicated as therapeutic targets for age-related pathology in mammals^{3–5}. However, the direct targets that mediate their effects on longevity remain unclear. In mammals, CREB-regulated transcriptional coactivators (CRTC)s⁶ are a family of cofactors involved in diverse physiological processes including energy homeostasis^{7–9}, cancer¹⁰ and endoplasmic reticulum stress¹¹. Here we show that both AMPK and calcineurin modulate longevity exclusively through post-translational modification of CRTC-1, the sole *C. elegans* CRTC. We demonstrate that CRTC-1 is a direct AMPK target, and interacts with the CREB homologue-1 (CRH-1) transcription factor *in vivo*. The pro-longevity effects of activating AMPK or deactivating calcineurin decrease CRTC-1 and CRH-1 activity and induce transcriptional responses similar to those of CRH-1 null worms. Downregulation of *crtc-1* increases lifespan in a *crh-1*-dependent manner and directly reducing *crh-1* expression increases longevity, substantiating a role for CRTCs and CREB in ageing. Together, these findings indicate a novel role for CRTCs and CREB in determining lifespan downstream of AMPK and calcineurin, and illustrate the molecular mechanisms by which an evolutionarily conserved pathway responds to low energy to increase longevity.

AMPK and calcineurin antagonistically regulate CRTCs in mammals⁸ to modulate energy homeostasis and endoplasmic reticulum (ER) stress^{9,11}. We therefore hypothesized that CRTCs may be critical longevity targets of AMPK and calcineurin, promoting their effects on lifespan through transcriptional regulation. We found a single *C. elegans* CRTC by homology search (Y20F4.2, now re-named CRTC-1) (Fig. 1a and Supplementary Fig. 1). *crtc-1* was expressed throughout the intestine of the worm, as well as in head and tail neurons (Fig. 1b), overlapping the expression pattern of the calcineurin catalytic subunit, *tax-6* (ref. 2) and the AMPK catalytic subunit, *aak-2* (Supplementary Fig. 2a). Strikingly, inhibition of *crtc-1* via RNA interference (RNAi) (Supplementary Fig. 2b) extended wild-type median lifespan by up to 53% (Fig. 1c), comparable to the effects of *tax-6* RNAi or AAK-2 activation (Fig. 1c, d). Given the significant role of CRTC-1 in longevity, we investigated whether AMPK and calcineurin modulate ageing through CRTC-1.

In mammals, activated AMPK blocks the transcriptional function of CRTC2 by restricting it to the cytosol⁹. We therefore tested the effect of starvation and heat stress, two conditions known to activate AMPK in *C. elegans*¹, on CRTC-1 cellular localization. A transgenic strain expressing CRTC-1::RFP revealed that CRTC-1 was present throughout the nucleus and cytosol under basal conditions (Fig. 1e and Supplementary Fig. 2b). Starvation and heat stress both induced CRTC-1::RFP translocation to the cytosol and nuclear exclusion in intestinal cells (Fig. 1f–h and Supplementary Fig. 3), illustrating that environmental stimuli that activate AMPK inactivate CRTC-1.

Next we investigated whether direct activation of AMPK rendered CRTC-1 cytosolic. Mammalian AMPK α catalytic subunits are activated by phosphorylation of threonine 172 in their activation loop. Mutation of this residue to aspartic acid or alanine results in a constitutively active or kinase-dead AMPK, respectively¹². Expression of CRTC-1::RFP with the equivalent activated AAK-2 mutation (amino acids (aa) 1–321, T181D)::GFP, caused nuclear exclusion of CRTC-1 under fed conditions at 20 °C (Fig. 2a). In contrast, coexpression of kinase-dead AAK-2 (aa 1–321, T181A)::GFP and CRTC-1::RFP did not induce nuclear exclusion (Fig. 2a), demonstrating that catalytic activation of AAK-2 by threonine 181 phosphorylation is required for AAK-2-dependent CRTC-1 nuclear exclusion.

Treatment with *tax-6* RNAi caused similar nuclear exclusion of CRTC-1::RFP under fed conditions (Fig. 2b). In addition, tricaine, a class of anaesthetic known to increase calcium flux¹³, induced *tax-6*-dependent nuclear localization of CRTC-1::RFP (Supplementary Fig. 4a). Suggesting CRTC-1 is a direct calcineurin target, CRTC-1::RFP containing site-specific mutations in the calcineurin binding site did not translocate to the nucleus in response to tricaine and was retained in the cytosol (Supplementary Fig. 4b).

Similar to mammalian CRTCs⁸, cytosolic retention of CRTC-1 required 14-3-3 proteins, as simultaneous RNAi knockdown of the two *C. elegans* 14-3-3 proteins *ftt-1* (also known as *par-5*) and *ftt-2* (ref. 14) via RNAi resulted in CRTC-1::RFP accumulation within the nucleus (Fig. 2c) and blocked CRTC-1::RFP cytosolic sequestering after heat stress (Supplementary Fig. 5). In addition, we determined that AMPK directly phosphorylates CRTC-1 at conserved 14-3-3-binding sites. Incubation of CRTC-1 with purified AMPK and AMP in an *in vitro* kinase assay resulted in phosphorylation of CRTC-1, as detected by anti-phospho-Ser 14-3-3 binding motif antibody (Fig. 2d).

Collectively, these data illustrate that in response to pro-longevity perturbations to AMPK and calcineurin, CRTC-1 becomes phosphorylated, cytosolically sequestered and inactivated.

To determine if the lifespan effects of AMPK and calcineurin are due to the inactivation of CRTC-1, we first examined if *crtc-1* RNAi-mediated longevity was epistatic to *tax-6*. Although *crtc-1* RNAi increased the lifespan of wild-type worms, it had no additive effect on the extended lifespan of *tax-6* mutants (Fig. 3a), in which CRTC-1 is already rendered cytosolic and inactive (Supplementary Fig. 4a), suggesting that these lifespan mediators function in a linear pathway.

To examine if CRTC-1 was a direct longevity target of AMPK and calcineurin, we inhibited phosphorylation of CRTC-1 at two conserved AMPK/calcineurin sites, S76 and S179, both of which reside within 14-3-3-binding motifs (Supplementary Fig. 1). Previous studies show that 14-3-3 proteins commonly bind tandem phosphorylated sites within a protein, resulting in significantly increased affinity over solitary sites due to cooperative binding^{15,16}. Compound mutation of serines 76 and 179 to alanines in CRTC-1 rendered it constitutively

¹The Salk Institute for Biological Studies, La Jolla, California 92037, USA. ²Howard Hughes Medical Institute, The Salk Institute for Biological Studies, La Jolla, California 92037, USA. ³The Glenn Foundation for Medical Research, The Salk Institute for Biological Studies, La Jolla, California 92037, USA. ⁴Razavi Newman Center for Bioinformatics, The Salk Institute for Biological Studies, La Jolla, California 92037, USA.

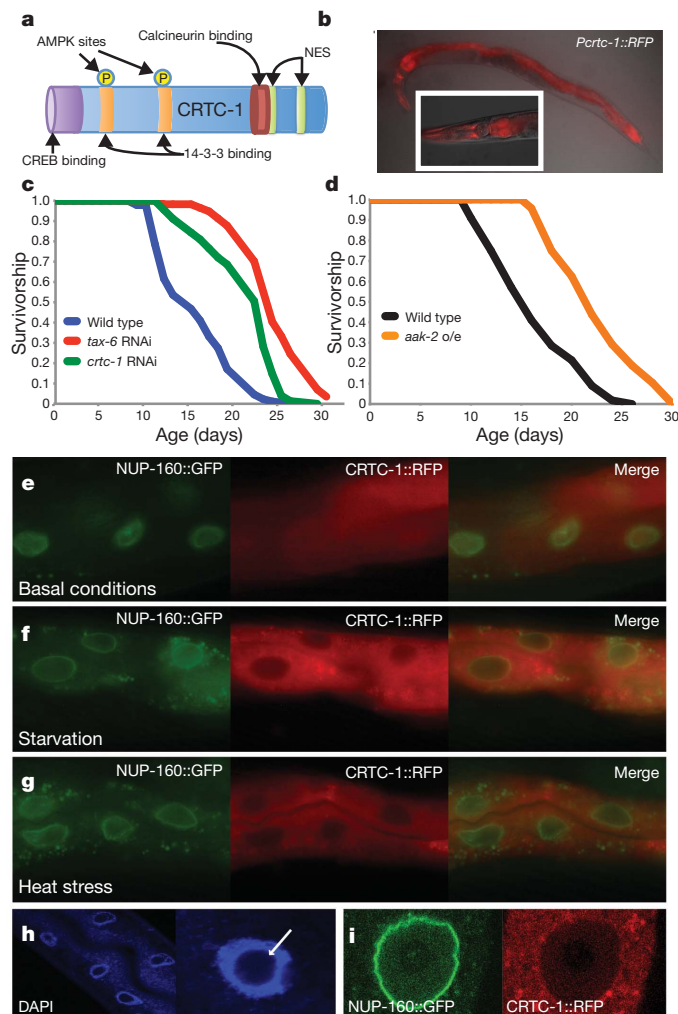


Figure 1 | CRTC-1 regulates longevity. **a**, CRTC-1 is the sole *C. elegans* CRTC family member, with conserved CREB-, calcineurin- and 14-3-3-binding domains and nuclear export signals (NES). Conserved AMPK phosphorylation sites are found at serines 76 and 179. **b**, *Pcrct-1::RFP* is expressed throughout the intestine of the worm and in neurons in the head (inset) and tail. **c**, RNAi inhibition of *crtc-1* and *tax-6* increases *C. elegans* wild-type median lifespan by 53% and 60% respectively (log rank, $P < 0.0001$ in each case). **d**, Overexpressing *aak-2* (aa 1–321) increases lifespan by 37.5% (log rank, $P < 0.0001$). **e–g**, Coexpression of the NUP-160::GFP nuclear pore complex subunit to mark the nuclear envelope (green), CRTC-1::RFP (red) and merge ($\times 20$ magnification). **e**, Under well-fed conditions CRTC-1::RFP is found throughout intestinal cells. **f**, **g**, Overnight starvation (**f**) or 33 °C overnight (**g**) induce cytosolic translocation of CRTC-1::RFP. **h**, 4',6-diamidino-2-phenylindole (DAPI) staining of *C. elegans* intestinal nuclei ($\times 20$). White arrow indicates nucleolus. **i**, Confocal image of NUP-160::GFP (green) marking nuclear membrane and CRTC-1::RFP (Red) after 33 °C overnight showing nuclear exclusion of CRTC-1::RFP after heat stress ($\times 100$).

nuclear and refractory to *tax-6* deactivation or *aak-2* activation (Fig. 3b, c and Supplementary Fig. 6).

Notably, although *tax-6* RNAi robustly extended the lifespan of *C. elegans* expressing wild-type CRTC-1::RFP, which translocated to the cytoplasm freely when calcineurin was not present (Fig. 3d), it had no effect on worms expressing constitutively nuclear CRTC-1 (S76A, S179A) (Fig. 3d). Post-translational modification of CRTC-1 is therefore critical for the effects of calcineurin on longevity. This longevity suppression was not due to general sickness as there was no significant difference between the lifespan of wild-type worms and those expressing CRTC-1 (S76A, S179A) (Supplementary Fig. 7a). Knocking down *tax-6* specifically during adulthood again increased wild-type lifespan but had no effect on the CRTC-1 (S76A, S179A) mutant (Supplementary Fig. 7 b–d), indicating that the CRTC-1-dependent effects of *tax-6* on lifespan are not solely acting during development.

We used the CRTC-1 (S76A, S179A) mutant to ask whether the extended lifespan of activated AMPK was also mediated by CRTC-1. Expression of CRTC-1 (S76A, S179A) fully suppressed the lifespan extension seen in AAK-2-overexpressing worms (Fig. 3e). This demonstrates that CRTC-1 is both a critical and direct target of

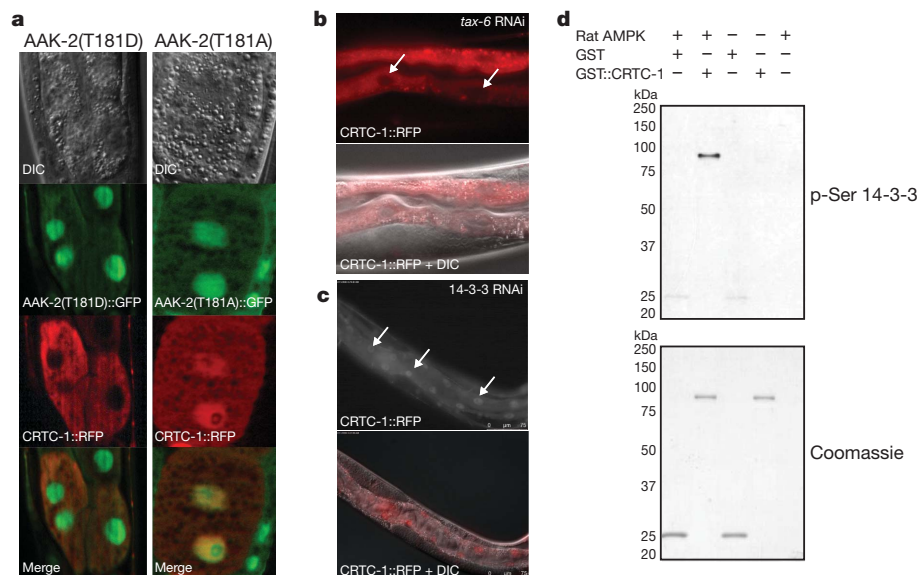


Figure 2 | CRTC-1 is a target of AAK-2 and TAX-6. **a**, CRTC-1::RFP (red) is excluded from the nucleus of intestinal cells when coexpressed with a constitutively active AMPK catalytic subunit AAK-2 (aa 1–321, T181D)::GFP but localized throughout the cell in the presence of kinase-dead AAK-2 (aa 1–321, T181A)::GFP ($\times 63$ magnification). **b**, *tax-6* RNAi results in nuclear exclusion of CRTC-1::RFP (red). White arrows represent intestinal nuclei ($\times 20$). DIC, differential interference contrast microscopy. **c**, Combined RNAi

for the two *C. elegans* 14-3-3 proteins results in nuclear localization of CRTC-1::RFP under basal conditions. White arrows represent intestinal nuclei ($\times 20$). **d**, *In vitro* kinase assay showing that AMPK directly phosphorylates CRTC-1. Purified rat AMPK holoenzyme was incubated with GST or GST::CRTC-1 in the presence of AMP. Phosphorylation was detected with phospho-Ser (p-Ser) 14-3-3 binding motif antibody. Coomassie stained gel shows protein loaded.

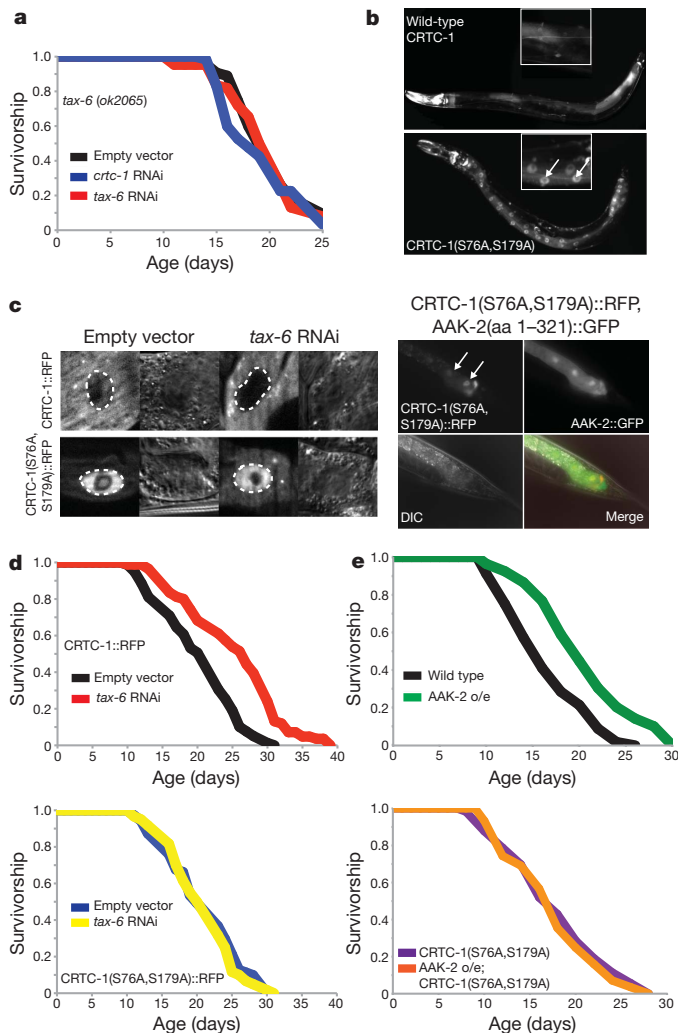


Figure 3 | Calcineurin and AMPK regulate lifespan through phosphorylation of CRTC-1. **a**, RNAi for *crtc-1* or *tax-6* has no effect in a *tax-6(ok2065)* mutant background (log rank, $P = 0.28$ and $P = 0.73$, respectively). **b**, Mutations to the conserved AMPK target sites serines 76 and 179 together are sufficient to retain CRTC-1::RFP in the nucleus ($\times 10$). Insets are magnification of intestinal region. **c**, CRTC-1(S76A,S179A) is refractory to both *tax-6* RNAi and AAK-2 overexpression (o/e) in *C. elegans* intestinal cells ($\times 40$). White dashed lines and arrows indicate nuclei. **d**, RNAi of *tax-6* extends the lifespan of *C. elegans* expressing wild-type CRTC-1::RFP (log rank, $P < 0.0001$), but has no effect on the S76A, S179A double mutant (log rank, $P = 0.57$). There is no significant difference between the lifespans of CRTC-1::RFP and CRTC-1(S76A,S179A) fed empty vector (log rank, $P = 0.48$). **e**, AAK-2 (aa 1–321) overexpression increases wild-type lifespan (log rank, $P < 0.0001$) but has no effect on worms expressing CRTC-1 (S76A, S179A) (log rank, $P = 0.65$).

aak-2-mediated longevity, and indicates that AMPK and calcineurin function upstream of a shared longevity pathway that signals through CRTC-1.

To understand the downstream effectors of CRTC-1, we examined CRH-1, the single *C. elegans* orthologue of the cyclic AMP response element binding (CREB) transcription factor family¹⁷. Mammalian CREBs (CREB, CREM and ATF1) associate with CRTCs to activate transcription and are involved in diverse processes including memory, immunity, DNA repair, energy homeostasis, fat storage and ER stress^{18,19}. *crh-1* is expressed throughout the worm, in overlapping tissues to *crtc-1* (Supplementary Fig. 8a). Co-immunoprecipitation of Flag::CRTC-1 and HA::CRH-1 demonstrated that these proteins interact *in vivo* (Fig. 4a and Supplementary Fig. 8b). The role of CRTC-1 in CRH-1 transcriptional activation was assessed by the

CREB reporter construct pCRE::GFP, which was significantly repressed by RNAi against *crh-1*, *crtc-1* and *tax-6* (Fig. 4b, c).

If the lifespan extension seen by activating AMPK or deactivating calcineurin functions through CRTC-1 to inactivate CREB, inactivating *crh-1* directly should increase longevity. Indeed, RNAi of *crh-1* increased the lifespan of both wild-type and RNAi-sensitive *rff-3(pk1426)* mutants (Fig. 4d and Supplementary Fig. 9). Furthermore, lifespan extension by *crtc-1* RNAi was not seen in *crh-1(nn3315)* null mutants (Fig. 4e), indicating that the longevity effects of inactivating *crtc-1* are mediated by *crh-1*.

We examined the effects of AMPK and calcineurin on CREB-regulated genes by comparing whole-genome gene expression of activated *aak-2*, *tax-6* null and *crh-1* null mutant animals to wild-type worms (Supplementary Table 1). Despite the many distinct roles of AMPK and calcineurin, we found that long-lived worms with activated *aak-2* or deactivated *tax-6* had transcriptional profiles significantly similar to *crh-1* null animals (Fig. 4f, g and Supplementary Fig. 10). The directionality of the transcriptional changes induced by activated *aak-2* and inactivated *tax-6* was also remarkably similar to *crh-1* nulls, with the majority of genes (150 or 67.5%) affected by all mutants exhibiting shared patterns of expression (Fig. 4f and Supplementary Fig. 11). Further, differentially expressed genes across all groups were highly enriched for cAMP regulatory elements (CRE) and the presence of a TATA box in their upstream promoter region (Fig. 4h and Supplementary Fig. 12a), two signatures of highly inducible CREB targets. Interestingly, and in contrast to CREB function in mammals, gene expression analysis revealed that CRH-1 may function as a bifunctional transcriptional regulator, as both upregulated and down-regulated genes in *crh-1* null animals were enriched for CREs (Supplementary Fig. 12b).

In mammals, AMPK and CREB are involved in energy homeostasis, particularly in response to starvation. Surprisingly, differentially expressed genes in *aak-2*-overexpressing, *tax-6* null mutant and *crh-1* null mutant animals were not markedly enriched for genes related to metabolism. Rather, there was strong upregulation of genes involved in ER stress, with 55% of known activated in blocked unfolded protein response family members (ABU)²⁰, upregulated by all mutants ($P = 1.7 \times 10^{-8}$, Fisher's exact test; Fig. 4f, Supplementary Fig. 10 and Supplementary Table 2). *abu* genes are induced in response to ER stress when the unfolded protein response pathway (UPR) is blocked and are therefore thought to act in parallel to the UPR to maintain protein homeostasis²⁰. *abu* genes are required for innate immunity²¹ and, notably, are activated by resveratrol and critical for its effects on longevity in *C. elegans*²². Furthermore, overexpression of *abu* family members increases lifespan in the worm²². It will be interesting to determine the potential role of ER stress in lifespan extension via AMPK–calcineurin–CRTC-1 signalling and whether CRTC-1 has a role in resveratrol-mediated lifespan extension.

Our data indicate that CRTC-1 is the critical direct longevity target of both AMPK and calcineurin in *C. elegans* and identify a new role for CRTCs and CREB in modulating longevity. They also represent the first analysis of the transcriptional profiles of long-lived activated AMPK and deactivated calcineurin organisms and suggest the primary longevity-associated role of these perturbations is the modulation of CRTC-1 and CRH-1 transcriptional activity. Notably, both the FOXO transcription factor *daf-16* (ref. 23) and genes involved in autophagy²⁴ have also been implicated in AMPK and calcineurin longevity, respectively. Further work to determine precisely where the AMPK–calcineurin–CRTC-1 pathway converges with FOXO and autophagy will be enlightening. It will also be interesting to determine if CRTC-1 mediates downstream effects of kinases other than AMPK. In mammals, CRTCs are regulated by multiple CAMKL kinase family members^{8,9,25} (Supplementary Table 3), and we saw additive effects of AMPK and related kinases on the localization of CRTC-1, in particular the MAP/microtubule affinity-regulating kinase (MARK) *par-1*, indicating that this kinase may also regulate CRTC-1 *in vivo* (Supplementary Fig. 13c, d). At present,

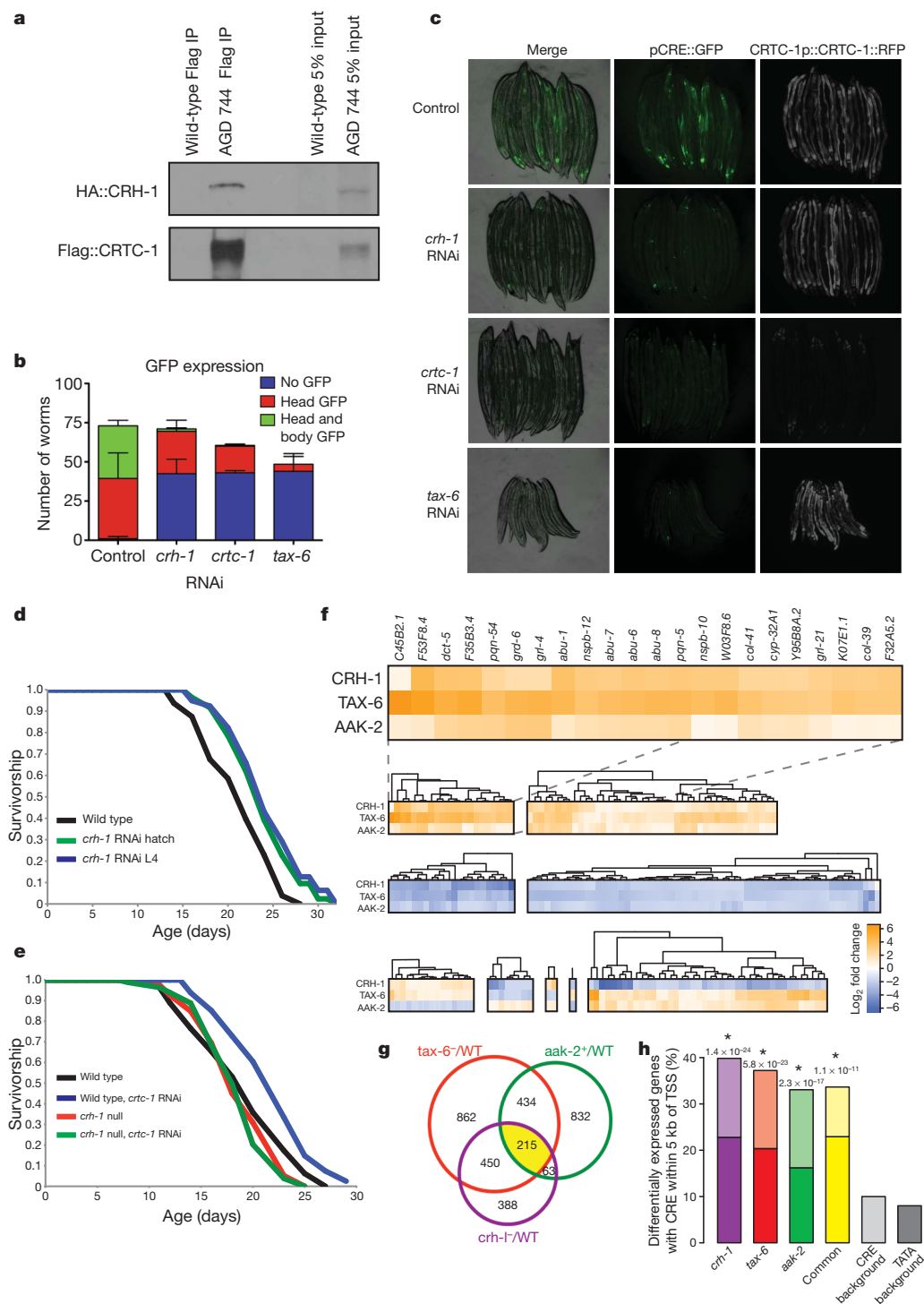


Figure 4 | CREB activity regulates lifespan. **a**, Co-immunoprecipitation using lysate from a *C. elegans* transgenic strain (AGD744) coexpressing 3×Flag::CRTC-1 and HA::CRH-1 showing CRTC-1 and CRH-1 interact *in vivo*. **b**, **c**, CREB transcriptional reporter (pCRE::GFP) is significantly affected by RNAi of *crh-1*, *crt-1* or *tax-6* (two-way ANOVA, $F = 18.54$, $P < 0.0001$). Error bars represent data \pm s.e.m. Control worms express GFP in head neurons and in some body tissues including muscle, hypodermis and intestine. **d**, RNAi of *crh-1* from larvae or adulthood extends wild-type lifespan (log rank, $P < 0.001$). **e**, RNAi of *crt-1* extends wild-type lifespan (log rank, $P < 0.001$) but has no effect on *crh-1* (*nn3315*) nulls (log rank, $P = 0.53$). **f**, Heat maps (clustered display of expression relative to wild-type) for genes differentially expressed in *crh-1* (*nn3315*) nulls, *tax-6* (*ok2065*) nulls, and *aak-2*

overexpressors (adjusted P value < 0.05 and fold change larger than twofold). The 22 most upregulated genes in all mutants are expanded (full gene list available in Supplementary Material). **g**, Venn diagram of all differentially expressed genes compared to wild-type in *tax-6* (*ok2065*) nulls, *aak-2* overexpressors and *crh-1* (*nn3315*) nulls. Transcriptional profiles of *aak-2* overexpressors and *tax-6* nulls are more similar to *crh-1* nulls than expected by chance (one-tailed Fisher's exact test, $P = 2.3 \times 10^{-19}$ and $P = 1.1 \times 10^{-225}$, respectively). WT, wild type. **h**, Promoters of differentially expressed genes are significantly enriched for CRE motifs (full bar) and TATA boxes (darker bar) (P values for binomial proportion test compared to CRE background shown above each mutant, asterisks indicate significant P -values). 'Common' denotes genes differentially expressed in all 3 strains. TSS, transcription start site.

however, AMPK is the only CAMKL kinase shown to be a positive regulator of longevity.

Collectively, these data identify CRTC-1 as a central node linking the upstream lifespan modifiers AMPK and calcineurin to CREB activity via a shared signal-transduction pathway, and demonstrate that post-translational modification of CRTC-1 is required for their effects on longevity (Supplementary Fig. 14). Complementing the pro-longevity effects of inhibiting CRTC function in *C. elegans*, reducing components of the CRTC/CREB pathway has recently been shown to confer health benefits to mice^{9,19,26–28}. Given the evolutionary conservation of this pathway from *C. elegans* to mammals²⁹ it will be fascinating to determine the role of CRTCs both as mammalian ageing modulators and as potential drug targets for patients with metabolic disorders and cancer.

METHODS SUMMARY

A detailed description of all experimental methods including *C. elegans* strains (Supplementary Table 4), growth, imaging, lifespan analysis and RNAi application is provided in Methods. None of the RNAi treatments used affected feeding rates (Supplementary Fig. 15). Transgenic strains were generated via microinjection into the gonad of adult hermaphrodites using standard techniques. Integrated transgenic lines were generated using gamma irradiation and outcrossed to wild-type at least four times. All lifespans were conducted at 20 °C with deaths scored and live worms transferred to new plates every 1–2 days, see Supplementary Table 5 for statistical analysis and replicate data. JMP 8/Graphpad Prism 5 and R/Bioconductor software were used for all statistical analyses.

Full Methods and any associated references are available in the online version of the paper at www.nature.com/nature.

Received 29 January; accepted 26 November 2010.

1. Apfeld, J., O'Connor, G., McDonagh, T., DiStefano, P. S. & Curtis, R. The AMP-activated protein kinase AAK-2 links energy levels and insulin-like signals to lifespan in *C. elegans*. *Genes Dev.* **18**, 3004–3009 (2004).
2. Dong, M. Q. *et al.* Quantitative mass spectrometry identifies insulin signaling targets in *C. elegans*. *Science* **317**, 660–663 (2007).
3. Steinberg, G. R. & Kemp, B. E. AMPK in health and disease. *Physiol. Rev.* **89**, 1025–1078 (2009).
4. Supnet, C. & Bezprozvanny, I. Neuronal calcium signaling, mitochondrial dysfunction, and Alzheimer's disease. *J. Alzheimers Dis.* **20** (suppl. 2), 487–498 (2010).
5. Shackelford, D. B. & Shaw, R. J. The LKB1–AMPK pathway: metabolism and growth control in tumour suppression. *Nature Rev. Cancer* **9**, 563–575 (2009).
6. Conkright, M. D. *et al.* TORCs: transducers of regulated CREB activity. *Mol. Cell* **12**, 413–423 (2003).
7. Liu, Y. *et al.* A fasting inducible switch modulates gluconeogenesis via activator/coactivator exchange. *Nature* **456**, 269–273 (2008).
8. Srean, R. A. *et al.* The CREB coactivator TORC2 functions as a calcium- and cAMP-sensitive coincidence detector. *Cell* **119**, 61–74 (2004).
9. Koo, S. H. *et al.* The CREB coactivator TORC2 is a key regulator of fasting glucose metabolism. *Nature* **437**, 1109–1111 (2005).
10. Komiya, T. *et al.* Enhanced activity of the CREB co-activator Crtc1 in LKB1 null lung cancer. *Oncogene* **29**, 1672–1680 (2010).
11. Wang, Y., Vera, L., Fischer, W. H. & Montminy, M. The CREB coactivator CRTC2 links hepatic ER stress and fasting gluconeogenesis. *Nature* **460**, 534–537 (2009).
12. Crute, B. E., Seefeld, K., Gamble, J., Kemp, B. E. & Witters, L. A. Functional domains of the $\alpha 1$ catalytic subunit of the AMP-activated protein kinase. *J. Biol. Chem.* **273**, 35347–35354 (1998).
13. Leffler, A. *et al.* The vanilloid receptor TRPV1 is activated and sensitized by local anesthetics in rodent sensory neurons. *J. Clin. Invest.* **118**, 763–776 (2008).
14. Wang, W. & Shakes, D. C. Expression patterns and transcript processing of *ftt-1* and *ftt-2*, two *C. elegans* 14-3-3 homologues. *J. Mol. Biol.* **268**, 619–630 (1997).
15. Kostecky, B., Saurin, A. T., Purkiss, A., Parker, P. J. & McDonald, N. Q. Recognition of an intra-chain tandem 14-3-3 binding site within PKC ϵ . *EMBO Rep.* **10**, 983–989 (2009).
16. Johnson, C. *et al.* Bioinformatic and experimental survey of 14-3-3-binding sites. *Biochem. J.* **427**, 69–78 (2010).
17. Kimura, Y. *et al.* A CaMK cascade activates CRE-mediated transcription in neurons of *Caenorhabditis elegans*. *EMBO Rep.* **3**, 962–966 (2002).
18. Mayr, B. & Montminy, M. Transcriptional regulation by the phosphorylation-dependent factor CREB. *Nature Rev. Mol. Cell Biol.* **2**, 599–609 (2001).
19. Xiao, X., Li, B. X., Mitton, B., Ikeda, A. & Sakamoto, K. M. Targeting CREB for cancer therapy: friend or foe. *Curr. Cancer Drug Targets* **10**, 384–391 (2010).
20. Urano, F. *et al.* A survival pathway for *Caenorhabditis elegans* with a blocked unfolded protein response. *J. Cell Biol.* **158**, 639–646 (2002).
21. Haskins, K. A., Russell, J. F., Gaddis, N., Dressman, H. K. & Aballay, A. Unfolded protein response genes regulated by CED-1 are required for *Caenorhabditis elegans* innate immunity. *Dev. Cell* **15**, 87–97 (2008).
22. Viswanathan, M., Kim, S. K., Berdichevsky, A. & Guarente, L. A role for SIR-2.1 regulation of ER stress response genes in determining *C. elegans* life span. *Dev. Cell* **9**, 605–615 (2005).
23. Greer, E. L. *et al.* An AMPK-FOXO pathway mediates longevity induced by a novel method of dietary restriction in *C. elegans*. *Curr. Biol.* **17**, 1646–1656 (2007).
24. Dwivedi, M., Song, H. O. & Ahnn, J. Autophagy genes mediate the effect of calcineurin on life span in *C. elegans*. *Autophagy* **5**, 604–607 (2009).
25. Jansson, D. *et al.* Glucose controls CREB activity in islet cells via regulated phosphorylation of TORC2. *Proc. Natl Acad. Sci. USA* **105**, 10161–10166 (2008).
26. Erion, D. M. *et al.* Prevention of hepatic steatosis and hepatic insulin resistance by knockdown of cAMP response element-binding protein. *Cell Metab.* **10**, 499–506 (2009).
27. Shaw, R. J. *et al.* The kinase LKB1 mediates glucose homeostasis in liver and therapeutic effects of metformin. *Science* **310**, 1642–1646 (2005).
28. Qi, L. *et al.* Adipocyte CREB promotes insulin resistance in obesity. *Cell Metab.* **9**, 277–286 (2009).
29. Lerner, R. G., Depatie, C., Rutter, G. A., Srean, R. A. & Balthasar, N. A role for the CREB co-activator CRTC2 in the hypothalamic mechanisms linking glucose sensing with gene regulation. *EMBO Rep.* **10**, 1175–1181 (2009).

Supplementary Information is linked to the online version of the paper at www.nature.com/nature.

Acknowledgements W.M. is funded by the George E. Hewitt Foundation for Medical Research, the American Federation for Aging Research and the Glenn Foundation for Medical Research. R.J.S. is funded by National Institutes of Health (NIH) R01 DK080425 and P01 CA120964. A.P.C.R. and G.M. are funded by NIH R01 HG004164, AG031097 and CA14195. A.D. is supported by NIH R01 DK070696 and AG027463. We thank the *Caenorhabditis* Genetics Center, the National Bioresearch Project for the Nematode and Mark Alkema for providing worm strains. We are grateful to M. Raices and M. D'Angelo for critical analysis of the manuscript, DAPI images and the NUP-160::GFP construct. We also thank members of the A.D. laboratory and M. Hansen for comments on the manuscript and discussion and K. Butler for technical assistance in the early stages of this project.

Author Contributions W.M., I.M., M.M., R.J.S. and A.D. designed the experiments. W.M. and I.M. performed the experiments. A.P.C.R. analysed the microarray data and performed the promoter analysis and W.M. analysed and performed statistical analysis on all other data. The manuscript was written by W.M. and edited by I.M., A.P.C.R., G.M., R.J.S. and A.D. All authors discussed the results and commented on the manuscript.

Author Information Data have been deposited at GEO under accession number GSE25513. Reprints and permissions information is available at www.nature.com/reprints. The authors declare no competing financial interests. Readers are welcome to comment on the online version of this article at www.nature.com/nature. Correspondence and requests for materials should be addressed to A.D. (dillin@salk.edu) or R.J.S. (shaw@salk.edu).

METHODS

Lifespan studies. All lifespan experiments were performed on standard 6-cm nematode growth media plates³⁰ supplemented with 100 µg ml⁻¹ carbenicillin at 20 °C. Plates were removed from 4 °C storage 2 days before seeding with 100 µl of *Escherichia coli* HT115 containing either empty vector or RNAi inducing plasmids. RNAi for a particular gene can be readily achieved in the worm by feeding *C. elegans E. coli* (HT115) that express double-stranded RNA of the gene of interest³¹. Bacterial cultures were grown overnight at 37 °C in the presence of both carbenicillin (100 µg ml⁻¹) and tetracycline (10 µg ml⁻¹) before seeding onto NGM plates. Once seeded, bacterial lawns were grown at room temperature (25 °C) for 48 h. RNAi was induced with 100 µl IPTG (100 mM) 2 h before worms were added to plates. To age-synchronize worms, five gravid adults (24 h post larval stage four, L4) were placed on plates with the appropriate control or RNAi bacteria and allowed to lay eggs for 5 h before being removed. These eggs were then cultured to adulthood (72 h post egg lay at 20 °C) before being moved to fresh plates at a density of 10 worms per plate, 10 plates per treatment. Age = 0 was defined as the day adults were moved to 10 worms a plate. Worms were moved to fresh plates every 1–2 days until day 14, after which only those on mould-contaminated plates were transferred. Worms were censored at the first sign of any bacterial contamination. Death was scored by gentle agitation with a worm pick and confirmed with no response after three attempts at both the head and tail. Death was scored every 1–2 days throughout.

RNAi constructs. RNAi *tax-6* and *crh-1* (1) (Supplementary Fig. 9) constructs used were taken from the Vidal RNAi library. The *crtc-1* (1) (Supplementary Fig. 9) RNAi plasmid was made by cloning full-length *crtc-1* cDNA between the two inverted T7 promoters in the pAD12 RNAi plasmid and transformed into HT115 cells. Remaining RNAi constructs used in Supplementary Fig. 9 are in the L4440 plasmid. Primers against cDNA were as follows. CRTC-1 (2): 5'-GG ATCACC GGTT CAGATGCAT, 3'-AGGTGCACCTTCAGCATTTGT. CRTC-1 (3): 5'-GAGCTCCAAGGACATCGAAGTCG, 3'-CTCGATGGATGCATTGG AACCATACC. CRH-1 (2): 5'-GAGCTCATGGCCACAATGGCGAG, 3'-CTCG AGCTTATCCGCCGTTTCTA.

DAPI staining. Worms were washed in 1 ml M9 (ref. 30) in a watch glass (1–3 times, until bacteria is removed). M9 was almost completely removed before 100–200 µl DAPI (200 ng ml⁻¹ in ethanol) was added. DAPI treatment was incubated in darkness for 20 min or until the ethanol had evaporated. One millilitre of M9 was then added to rehydrate for 1 h (up to 5 h at room temperature or overnight at 4 °C). One drop (~3 µl) of ProLong mounting medium was placed on a slide before transferring the stained worm. A cover slip was added and sealed with nail polish. Fluorescence was examined at 358 nm.

Heat stress and starvation assays. Effect of heat and starvation on CRTC-1::RFP was measured by placing *C. elegans* expressing *crtc-1::RFP* onto either OP50-seeded NGM plates at 33 °C overnight or into 9-well plates containing M9 media at 20 °C. Controls were *C. elegans* fed OP50 at 20 °C.

Microscopy. All microscopy was performed using 0.1 mg ml⁻¹ tetramisole hydrochloride in M9 as an anaesthetic, which pilot experiments revealed had no effect on CRTC-1 localization. Except for tricaine time-course experiments, worms were in 5 µl anaesthetic mounted on 2% agarose pads on glass slides under glass cover slips. All photographs were taken using a Zeiss Axiovert microscope and AxioCam. Pictures in Figs 2a and 3b used ApoTome optical sectioning. For the tricaine experiments (Supplementary Fig. 4a, b), L4 worms were placed in wells of a 96-well plate in 100 µl of tetramisole/M9 with or without tricaine (2 mg ml⁻¹). Pictures were taken during the time-course through the 96-well plate.

Kinase redundancy assays. Worms were subjected to RNAi for CAMKL kinases from hatch. Twenty-four hours post-L4 worms were then picked into M9 with tricaine (2 mg ml⁻¹) in wells of a 9-well plate. Worms were left on a rotational shaker at 20 °C for 2 h. Using a glass pipette³² worms were then placed onto NG plates seeded with *E. coli* (OP50). When tricaine solution had evaporated (approx 20 min), worms were picked onto fresh OP50 plates, 5 worms per plate. Localization of CRTC-1::RFP was then scored as 'all nuclear' (all intestinal cells showed only punctate nuclear CRTC-1), 'some cells nuclear' (intestinal cells showed mix of punctate nuclear CRTC-1 and cytosolic CRTC-1) and 'cytosolic' (CRTC-1 was dispersed evenly throughout nucleus and cytosol in all intestinal cells). Time = 0 was defined as when worms were moved to fresh OP50 plates.

Transgenic strain construction. Expression constructs were based on pPD95.77 from the Fire laboratory *C. elegans* vector kit. RFP in the manuscript refers to tdTOMATO, which replaced the GFP in pPD95.77. Transgenic strains were generated via microinjection into the gonad of adult hermaphrodites using standard techniques. Integrated transgenic lines were generated using gamma irradiation and out-crossed to wild-type at least four times.

Calcineurin-binding mutant. QuikChange mutagenesis was used to mutate residues within the conserved calcineurin-binding site in CRTC-1. This resulted

in changing the amino acid sequence (aa 423–428) as follows. Wild type: EALDIPKLITITNAEGA; calcineurin-binding mutant: EALDIKATAANAEGA. **Single-worm PCR for genotyping.** Single-worm lysis buffer (SWLB): 30 mM Tris pH 8.0, 8 mM EDTA, 100 mM NaCl, 0.7% NP-40, 0.7% Tween-20. Proteinase K was added to a final concentration of 100 µg ml⁻¹ just before use. To prepare the DNA template, one worm was added to a PCR tube containing 5 µl SWLB supplemented with Proteinase K and incubated for 60 min at 60 °C. Proteinase K was then heat-inactivated at 95 °C for 15 min before the reaction was cooled to 4 °C. To setup the PCR reaction, 5 µl of the worm lysate was used as template.

Expression of *C. elegans* proteins in 293T cells. Full-length *C. elegans crtc-1* and *crh-1* cDNA was cloned using gateway recombination into mammalian expression plasmid pcDNA3 containing in-frame 5' Flag or HA tag respectively. 293T cells were transfected using lipofectamine 2000 (Invitrogen) following manufacture's guidelines. Primer information is available on request.

293T cells immunoprecipitation. 293T cells were washed 1× with PBS and resuspended in 500 µl PLB supplemented with protease inhibitor cocktail (Roche). Cells were incubated for 10 min at 4 °C then sonicated to disrupt nuclei. Lysate was centrifuged at 10,000g for 30 min at 4 °C then precleared with Protein A/G PLUS-Agarose (Santa Cruz). Cleared lysate was incubated with anti-Flag M2 affinity gel (Sigma) overnight at 4 °C. For control anti-Flag M2 affinity gel was blocked with 50 µg Flag peptide for 1 h at 4 °C then lysate was added and incubation continued overnight at 4 °C. Immune complexes were collected by centrifugation and washed extensively. Complexes were eluted with Flag peptide then resolved by SDS-PAGE and transferred to nitrocellulose membrane. Western blot analysis was performed with anti-Flag M2-Peroxidase (Sigma) and anti-HA-Peroxidase (Roche).

***C. elegans* immunoprecipitation.** Approximately 25,000 N2 and AGD 744 animals were treated with 2 mg ml⁻¹ Tricaine for 2 hours, flash-frozen, then ground to fine powder using a mortar and pestle on dry ice. Powder was collected in 400 µl cell lysis buffer (Cell Signaling) supplemented with protease inhibitor cocktail (Roche) and sonicated to disrupt nuclei. Lysate was centrifuged at 16,000g for 30 min at 4 °C then precleared with Protein A/G PLUS-Agarose (Santa Cruz). Cleared lysate was incubated with EZview Red anti-Flag M2 affinity gel (Sigma) for 2 h at 4 °C. Immune complexes were collected by centrifugation and washed extensively. Complexes were eluted with 3× Flag peptide then resolved by SDS-PAGE and transferred to nitrocellulose membrane. Western blot analysis was performed with anti-Flag M2-Peroxidase (Sigma) and anti-HA (Abcam).

In vitro kinase assay. Recombinant GST::CRTC-1 and GST proteins (2 µg) were incubated with 100 mU purified AMPK (Millipore) in kinase reaction buffer (2.5 mM Tris, pH 7.5, 5 mM β-glycerophosphate, 2 mM DTT, 0.1 mM Na₃VO₄, 10 mM MgCl₂, 150 µM AMP, 125 µM ATP) for 30 min at 30 °C. Samples were resolved by SDS-PAGE then transferred to nitrocellulose membrane. Phosphorylation was determined by immunoblotting with phospho-Ser 14-3-3-binding motif antibody (Cell Signaling).

Microarray procedure. Egg preparations were made using standard bleaching techniques and larval stage one (L1) worms were synchronized by hatching eggs overnight in M9 buffer. Seven hundred and fifty L1 larvae were seeded per 10 cm NG plate seeded with OP50. Worms were harvested for RNA extraction when they reached L4 larval stage by snap-freezing in liquid nitrogen in TRIzol. All L1 larvae were seeded at the same time and samples frozen at different times to account for variation in development time between groups. Three thousand worms were used for each sample and three biological replicates done for each experimental group: N2, AGD383, RB1667 and *crh-1* (*nn3315*). Biological samples were prepared on separate days, RNA preparations were carried out at the same time (12 h before array) using TRIzol/chloroform extraction and then run through an RNeasy cleanup column. Arrays were done on Affymetrix *C. elegans* Genome Array from the same batch.

Microarray data analysis. Raw expression data files were obtained for three replicates each of L4 *crh-1* (*nn3315*), *tax-6* (*ok2065*) and *aak-2* (aa 1–321) mutants and three N2 control replicates with the Affymetrix *C. elegans* Genome Array. All microarray analysis was performed with Bioconductor³³. Standard data quality validation as suggested by Affymetrix³⁴ was carried out with the 'simpleaffy' package, followed by 'affyPLM', which identified no problematic chips. The raw data were preprocessed according to the GC-RMA method³⁵ (implemented in 'gcrma'), which performs probe-sequence-based background adjustment, quantile normalization, and utilizes a robust multi-chip average to summarize information into single expression measurements for each probeset (Supplementary Table 1). Before statistical testing, the data were submitted to a non-specific filter (via the package 'genefilter') that removed probesets with an expression interquartile range smaller than 0.5. To identify genes that were significantly differentially expressed between each mutant and the control, linear modelling and empirical Bayes analysis was performed using the 'limma' package³⁶. Limma computes an empirical Bayes adjustment for the *t*-test (moderated *t*-statistic), which is more robust than

the standard two-sample *t*-test comparisons. To correct for multiple testing, Benjamin and Hochberg's method to control for false discovery rate was used³⁷. Genes with an adjusted *P* value of 0.05 or smaller and a fold-change in expression larger than twofold were considered differentially expressed (Supplementary Table 2).

cAMP response element (CRE) identification. We gathered intergenic upstream sequences (up to 5 kb, from WS198) for differentially expressed genes and used MATCH³⁸ to search against the TRANSFAC³⁹ CRE matrix (M00039), an experimentally derived matrix based on 29 human CREB1-binding sequences⁴⁰. In the MATCH search we used the 'minFP' score cutoff, which aims to minimize false positives. In addition, we estimated the number of such sites that can be found by chance (background) by using the same procedure to search the upstream sequences of ten similarly sized samples of *C. elegans* genes that were not affected by any of the mutants. We used the same procedure to search against the TRANSFAC TATA matrix (M00252)⁴¹.

30. Hope, I. A. *C. elegans: A Practical Approach* (ed. Hames, B. D.) (Oxford Univ. Press, 1999).
31. Fire, A. *et al.* Potent and specific genetic interference by double-stranded RNA in *Caenorhabditis elegans*. *Nature* **391**, 806–811 (1998).
32. Mair, W. A simple yet effective method to manipulate *C. elegans* in liquid. *Worm Breed. Gaz.* **18**, 33 (2009).
33. Gentleman, R. C. *et al.* Bioconductor: open software development for computational biology and bioinformatics. *Genome Biol.* **5**, R80 (2004).
34. Affymetrix. *GeneChip Expression Analysis* (http://www.coriell.org/images/pdf/expression_manual.pdf) (Affymetrix, 2004).
35. Wu, Z., Irizarry, R. A., Gentleman, R., Martinez-Murillo, F. & Spencer, F. A model-based background adjustment for oligonucleotide expression arrays. *J. Am. Stat. Assoc.* **99**, 909–917 (2004).
36. Smyth, G. K. Linear models and empirical Bayes methods for assessing differential expression in microarray experiments. *Stat. Appl. Gen. Mol. Biol.* **3**, article 3 (2004).
37. Benjamini, Y. & Hochberg, Y. Controlling the false discovery rate: a practical and powerful approach to multiple testing. *J. R. Stat. Soc. B* **57**, 289–300 (1995).
38. Kel, A. E. *et al.* MATCH: a tool for searching transcription factor binding sites in DNA sequences. *Nucleic Acids Res.* **31**, 3576–3579 (2003).
39. Matys, V. *et al.* TRANSFAC and its module TRANSCOMP: transcriptional gene regulation in eukaryotes. *Nucleic Acids Res.* **34**, D108–D110 (2006).
40. Benbrook, D. M. & Jones, N. C. Different binding specificities and transactivation of variant CRE's by CREB complexes. *Nucleic Acids Res.* **22**, 1463–1469 (1994).
41. Bucher, P. Weight matrix descriptions of four eukaryotic RNA polymerase II promoter elements derived from 502 unrelated promoter sequences. *J. Mol. Biol.* **212**, 563–578 (1990).

CKI α ablation highlights a critical role for p53 in invasiveness control

Ela Elyada^{1*}, Ariel Pribluda^{1*}, Robert E. Goldstein¹, Yael Morgenstern¹, Guy Brachya¹, Gady Cojocaru¹, Irit Snir-Alkalay¹, Ido Burstain¹, Rebecca Haffner-Krausz², Steffen Jung³, Zoltan Wiener⁴, Kari Alitalo⁴, Moshe Oren⁵, Eli Pikarsky^{1,6} & Yinon Ben-Neriah¹

The mature gut renews continuously and rapidly throughout adult life, often in a damage-inflicting micro-environment. The major driving force for self-renewal of the intestinal epithelium is the Wnt-mediated signalling pathway, and Wnt signalling is frequently hyperactivated in colorectal cancer¹. Here we show that casein kinase Ia (CKI α), a component of the β -catenin-destruction complex¹, is a critical regulator of the Wnt signalling pathway. Inducing the ablation of *Csnk1a1* (the gene encoding CKI α) in the gut triggers massive Wnt activation, surprisingly without causing tumorigenesis. CKI α -deficient epithelium shows many of the features of human colorectal tumours in addition to Wnt activation, in particular the induction of the DNA damage response and cellular senescence, both of which are thought to provide a barrier against malignant transformation². The epithelial DNA damage response in mice is accompanied by substantial activation of p53, suggesting that the p53 pathway may counteract the pro-tumorigenic effects of Wnt hyperactivation. Notably, the transition from benign adenomas to invasive colorectal cancer in humans is typically linked to p53 inactivation, underscoring the importance of p53 as a safeguard against malignant progression³; however, the mechanism of p53-mediated tumour suppression is unknown. We show that the maintenance of intestinal homeostasis in CKI α -deficient gut requires p53-mediated growth control, because the combined ablation of *Csnk1a1* and either p53 or its target gene *p21* (also known as *Waf1*, *Cip1*, *Sdi1* and *Cdkn1a*) triggered high-grade dysplasia with extensive proliferation. Unexpectedly, these ablations also induced non-proliferating cells to invade the villous lamina propria rapidly, producing invasive carcinomas throughout the small bowel. Furthermore, in p53-deficient gut, loss of heterozygosity of the gene encoding CKI α caused a highly invasive carcinoma, indicating that CKI α functions as a tumour suppressor when p53 is inactivated. We identified a set of genes (the p53-suppressed invasiveness signature, PSIS) that is activated by the loss of both p53 and CKI α and which probably accounts for the brisk induction of invasiveness. PSIS transcription and tumour invasion were suppressed by p21, independently of cell cycle control. Restraining tissue invasion through suppressing PSIS expression is thus a novel tumour-suppressor function of wild-type p53.

To investigate the physiological roles of CKI α , we generated mice in which *Csnk1a1* was either deleted from the germline or *loxP* flanked (floxed) and therefore able to be conditionally deleted (Supplementary Fig. 1a). Whereas mice that were heterozygous for *Csnk1a1* (*Csnk1a1*^{+/-}) seemed to be normal, homozygous deficiency was embryonic lethal before embryonic day 6.5 (Supplementary Fig. 1b and Supplementary Table 1), suggesting a fundamental role for CKI α in embryogenesis.

To study the role of CKI α in gut physiology, we crossed mice in which *Csnk1a1* was floxed with mice expressing *Vil1*-Cre-ER^{T2}, generating

animals in which injection with tamoxifen causes deletion of the gene encoding CKI α exclusively in the intestinal epithelium (hereafter termed *Csnk1a1*^{Δgut} mice). Within 5 days of treatment with tamoxifen, CKI α expression was largely abolished throughout the epithelia of the small bowel (Fig. 1a, b and Supplementary Fig. 2a) and colon (data not shown), and was absent for at least 2 weeks, indicating that intestinal progenitor cells had been targeted by the recombinase Cre. CKI α loss was accompanied by a mild increase in CKI δ expression (Supplementary Fig. 2b), while the priming phosphorylation of β -catenin on the serine residue at position 45 (S45) was abolished, eliminating the rest of the phosphorylation cascade (T41, S37 and S33) (Fig. 1b). Consequently, β -catenin was stabilized in the cytoplasm and nucleus, including in differentiated cells of the villus (Fig. 1a, b and Supplementary Fig. 2d). Using RKO cells (a human colorectal cancer cell line), we confirmed this non-redundant function of the α -isoform of CKI *in vitro* (Supplementary Fig. 2c). These findings indicate that CKI α is indispensable for initiating the β -catenin phosphorylation-degradation cascade in the gut epithelium.

As expected, β -catenin accumulation in the gut of *Csnk1a1*^{Δgut} mice was accompanied by robust activation of many Wnt target genes, including *Myc*, *Axin2*, *Sox9*, *Cd44* and the genes encoding cyclin D1 and cyclin D2 (<http://www.stanford.edu/~rnusse/pathways/targets.html>) (Fig. 1c, d). Particularly striking was the distinct nuclear expression of cyclin D1, which spread into all villi throughout the small intestine. By contrast, in wild-type small bowel, cyclin D1 was restricted to the crypts. Likewise, CD44 and *Myc* were overexpressed in *Csnk1a1*^{Δgut} (Fig. 1d). In other mouse models of Wnt hyperactivation, ectopic Paneth cells are common⁴, and these are clearly observed in small-bowel villi of *Csnk1a1*^{Δgut} mice (Supplementary Fig. 2e). Thus, knockout of the gene encoding CKI α induced β -catenin stabilization and a massive Wnt response, comparable to other mouse models of Wnt activation and to colorectal cancers.

Surprisingly, despite the robust activation of mitogenic Wnt target genes, gut homeostasis was preserved, and tumorigenesis was not observed. This is in stark contrast to Wnt activation in the mouse gut after deletion of the adenomatous polyposis coli (*Apc*) gene, which resulted in immediate dysplastic transformation of the entire bowel and rapid death⁴. Instead, we found only mild atypia and minimal small-bowel crypt elongation, owing to an approximately twofold increase in the proliferating cell population (Supplementary Fig. 2e and data not shown). We therefore postulated that *Csnk1a1* ablation elicits a simultaneous reaction that restrains the hyperproliferation and tumorigenesis that is expected on Wnt hyperactivation.

Phenotypic changes in *Csnk1a1*^{Δgut} mice might resemble the oncogene-induced senescence⁵ associated with DNA-replication stress, persistent DNA damage⁶ and apoptosis⁷. Accordingly, p19^{ARF}, a hallmark of oncogene-induced senescence⁸, was found to be upregulated

¹The Lautenberg Center for Immunology, IMRIC, Hebrew University—Hadassah Medical School, Jerusalem 91120, Israel. ²Department of Veterinary Resources, The Weizmann Institute of Science, Rehovot 76100, Israel. ³Department of Immunology, The Weizmann Institute of Science, Rehovot 76100, Israel. ⁴Molecular Cancer Biology Program and the Institute for Molecular Medicine Finland, Biomedicum Helsinki, University of Helsinki, Helsinki 00014, Finland. ⁵Department of Molecular Cell Biology, The Weizmann Institute of Science, Rehovot 76100, Israel. ⁶Department of Pathology, IMRIC, Hebrew University—Hadassah Medical School, Jerusalem 91120, Israel.

*These authors contributed equally to this work.

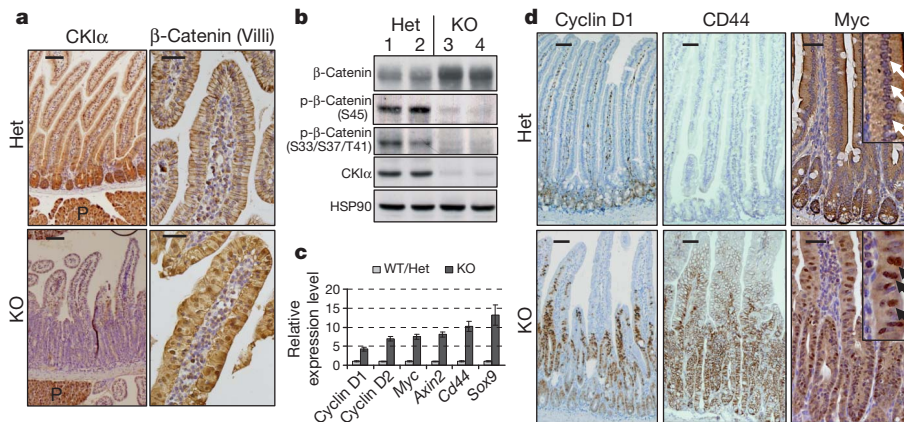


Figure 1 | *Csnk1a1* ablation induces Wnt hyperinduction.

a, Immunohistochemistry analysis of CKIα and β-catenin in heterozygous (*Csnk1a1*^{+/-Δgut}; Het) and homozygous (*Csnk1a1*^{Δgut}; KO) *Csnk1a1*-deleted mouse gut. For all immunohistochemistry analyses, brown indicates specific immunostaining, and purple indicates nuclear haematoxylin staining. Scale bars, 100 μm (left), 50 μm (right). P, pancreas. **b**, Western blotting analysis of intestinal epithelial cells (IECs) from Het (lanes 1 and 2) and KO (lanes 3 and 4) mice. Numbered lanes represent individual mice. HSP90 is a loading control. p-β-catenin, phospho-β-catenin. **c**, Quantitative real-time PCR (quantitative

in *Csnk1a1*^{Δgut} enterocytes (Fig. 2c). To assess the potential contribution of cellular senescence in protecting against proliferation and tumorigenesis, we sought signs of persistent DNA damage response (DDR), senescence and apoptosis on *Csnk1a1* ablation in mouse gut, mouse embryonic fibroblasts (MEFs) and primary human fibroblasts. *Csnk1a1* ablation triggered apoptosis, which was evident by TdT-mediated dUTP nick end labelling (TUNEL) assay and cleaved caspase-3 immunostaining (Fig. 2a and Supplementary Fig. 3a), as well as generated widespread signs of DDR (Fig. 2a, 53BP1) and senescence (Fig. 2b). Likewise, ablation of *Csnk1a1* in MEFs and mRNA depletion of the corresponding gene, *CSNK1A1*, in human primary fibroblasts (IMR-90 cells) resulted in a persistent DDR and a senescence phenotype (Supplementary Fig. 3b–f).

The ARF tumour suppressor (p19^{ARF} in mice) and DDR are two major activation arms of the tumour-suppressor protein p53, targeting the two p53 antagonists MDM2 and MDMX (also known as MDM4), respectively^{9,10}. Furthermore, *Mdmx* ablation in the gut induced p53 activation and apoptosis, albeit with no tissue abnormalities¹¹. *Csnk1a1* ablation in the gut caused marked reduction of MDMX expression (Fig. 2d and Supplementary Fig. 4a). We therefore postulated that

rtPCR) analysis of Wnt and β-catenin target gene expression in IECs of wild-type (WT) (*n* = 3), Het (*n* = 3) and KO (*n* = 6) mice. Data are presented as mean ± s.e.m. Data for expression by the WT and Het groups were combined and normalized to 1 (denoted WT/Het), and expression by other groups is calculated relative to WT/Het. **d**, Immunohistochemistry analysis of Wnt target gene expression. In the Myc panel, the insets show Myc-negative nuclei in Het cells (white arrows) and Myc-positive nuclei in KO cells (black arrows). Scale bars, 100 μm (left and centre), 50 μm (right).

the combined effect of p19^{ARF} induction and MDMX degradation might trigger p53 activation in *Csnk1a1*^{Δgut} mice. In non-perturbed wild-type gut, p53 is normally inactive¹². Indeed, p53 expression was undetectable in *Csnk1a1*^{+/-Δgut} (heterozygous) small or large bowel (Fig. 2d, e and data not shown). By contrast, *Csnk1a1*^{Δgut} mice showed marked p53 expression (Fig. 2d, e). Transcriptome analysis revealed that, not only the Wnt cascade, but also the p53 pathway is strongly induced by *Csnk1a1* ablation (Supplementary Table 2; *P* = 3.9 × 10⁻⁸). This was confirmed by monitoring the induction of several specific p53 target genes, including the anti-proliferative gene *p21* (ref. 13) (Fig. 2d, e and Supplementary Fig. 4b). The elevated p53 expression in *Csnk1a1*^{Δgut} enterocytes was apparently due to both transcriptional and post-transcriptional control mechanisms; although *p53* (also known as *Trp53*) mRNA was elevated, the fold increase in p53 protein levels exceeded mRNA upregulation (Fig. 2d, e and Supplementary Fig. 7a). Thus, p53 protein stabilization occurred concurrently with β-catenin stabilization in CKIα-depleted RKO (colorectal) cells (Supplementary Fig. 4c). These data point to robust p53 activation in *Csnk1a1*^{Δgut} epithelium as a possible means of counteracting the pro-tumorigenic effects of the Wnt pathway.

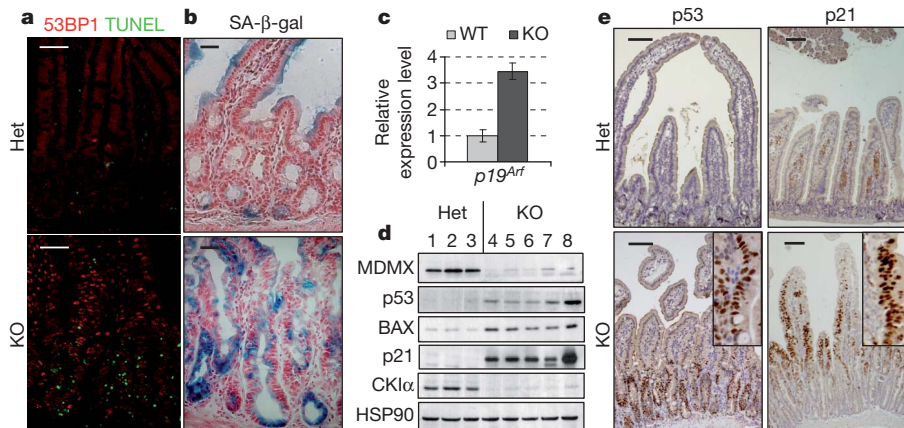


Figure 2 | Persistent DDR and cellular senescence in *Csnk1a1*^{Δgut} mice.

a, Double immunofluorescence staining of intestinal sections: TUNEL (an apoptotic marker, green); 53BP1 (a DDR marker, red). Scale bars, 50 μm. **b**, Senescence-associated β-galactosidase (SA-β-gal) staining (blue) and nuclear fast red as a counterstain (pink). Scale bars, 20 μm. **c**, Quantitative

rtPCR analysis of IECs of WT (*n* = 2) and KO (*n* = 2) mice. Data are presented as mean ± s.e.m. **d**, Western blotting analysis of IECs from Het (lanes 1–3) and KO (lanes 4–8) mice. HSP90 is a loading control. **e**, Immunohistochemistry analysis of p53 and p21 expression in Het and KO gut. Insets show a threefold magnification of positively stained areas. Scale bars, 100 μm.

As with *Csnk1a1*^{Δgut}, intestinal *Apc* ablation results in Wnt hyper-induction and widespread cyclin D1 expression^{4,14} (Supplementary Fig. 5a). However, the consequences of its ablation—with respect to both homeostasis and tumorigenesis—are profoundly different. One reason for this difference could be p53 activation. We observed only limited, sporadic activation of p53 and its target p21 in intestinal *Apc*^{Δgut} epithelium compared with the substantial p53 expression in *Csnk1a1*^{Δgut} epithelium (Supplementary Fig. 5a). Supporting these differences were our comparative transcriptome analysis of three enterocyte sources—*Csnk1a1*^{Δgut} (Supplementary Table 2), *Apc*^{Δgut} (ref. 4) and *Apc*^{1638N} (ref. 15)—showing far greater enrichment of p53 target genes in *Csnk1a1*^{Δgut} ($P = 3.9 \times 10^{-8}$) than in the APC-based mouse models ($P = 9.4 \times 10^{-3}$). Differential p53 activation by CK1α depletion was also observed in RKO cells harbouring wild-type p53 and *Apc* genes. Whereas β-catenin was strongly stabilized when either APC or CK1α was depleted using short hairpin RNAs (shRNAs), H2AX phosphorylation and p53 stabilization were observed only when CK1α was depleted (Supplementary Fig. 5b), indicating that DDR and p53 activation require more than just Wnt activation. Moreover, β-catenin depletion in CK1α-depleted RKO cells did not suppress DDR induction or p53 activation (Supplementary Fig. 5c), demonstrating that CK1α loss induces p53 independently of Wnt hyperinduction. Thus, the absence of intestinal tumours despite Wnt hyperactivation could be due to distinctive activation of p53 when *Csnk1a1* is ablated.

To assess the contribution of p53 to counteracting Wnt-driven tumorigenesis, we crossed *Csnk1a1*^{Δgut} mice with *p53*^{Δgut} mice. Remarkably, within 2 weeks of initiating the tamoxifen-induced co-ablation, the *Csnk1a1*^{Δgut}*p53*^{Δgut} (double-knockout) mice developed widespread high-grade dysplasia and numerous intramucosal carcinomas invading the lamina propria in most of the small-bowel crypts and villi (Fig. 3a (H&E) and Supplementary Fig. 6a), and they died shortly thereafter. Unlike *Csnk1a1*^{Δgut} (knockout) mice, double-knockout mice showed massive proliferation throughout the crypt–villus axis, up to the tips of the villi (Fig. 3a (BrdU) and Supplementary Fig. 6b). This, however, was not attributable to further hyperactivation of Wnt signalling in the double-knockout mice: β-catenin stabilization and Wnt gene induction in double-knockout mice were comparable to those in *Csnk1a1*^{Δgut} mice (Supplementary Fig. 6c–f). These data indicate that the tumour-suppressor function of p53 in *Csnk1a1*^{Δgut} mice is not exerted through the suppression of Wnt signalling. Whereas the *Bax* induction and activation-associated cleavage of BAX protein seen in *Csnk1a1*^{Δgut} mice were absent in double-knockout mice (Supplementary Fig. 7a, b), the extent of apoptosis in double-knockout mice was similar to that in *Csnk1a1*^{Δgut} mice (Supplementary Fig. 7c, cleaved caspase 3), indicating that apoptosis by itself, whether p53-dependent or p53-independent, is ineffective at suppressing intestinal carcinogenesis. By contrast, almost no expression of p21 was observed in double-knockout mice (Supplementary Fig. 7b, c), suggesting that p21 might be a key factor in offsetting excessive proliferation and tumorigenesis in *Csnk1a1*^{Δgut} mice.

Human colorectal carcinogenesis is a protracted process. It entails multiple genetic mutations and epigenetic events, which propel tumour progression from an aberrant crypt focus through adenoma to invasive carcinoma³. In various mouse models, this process, which probably spans 10–15 years in humans, commonly occurs over many months and by a similar sequence of molecular and histological events¹⁶. The exceptionally rapid development of invasive intramucosal carcinomas in *Csnk1a1*^{Δgut}*p53*^{Δgut} (double-knockout) mice, bypassing the adenomatous phase, prompted us to validate the cancerous nature of the observed lesions. Intestinal villi of double-knockout mice were removed and transplanted under the kidney capsule of immunodeficient (NOD SCID) mice. Invasive adenocarcinomas of intestinal origin permeating the kidney tissue were observed in two of five NOD SCID recipients of double-knockout villi (Fig. 3b), whereas no viable intestinal tissue was detectable in recipients of either CK1α-deficient

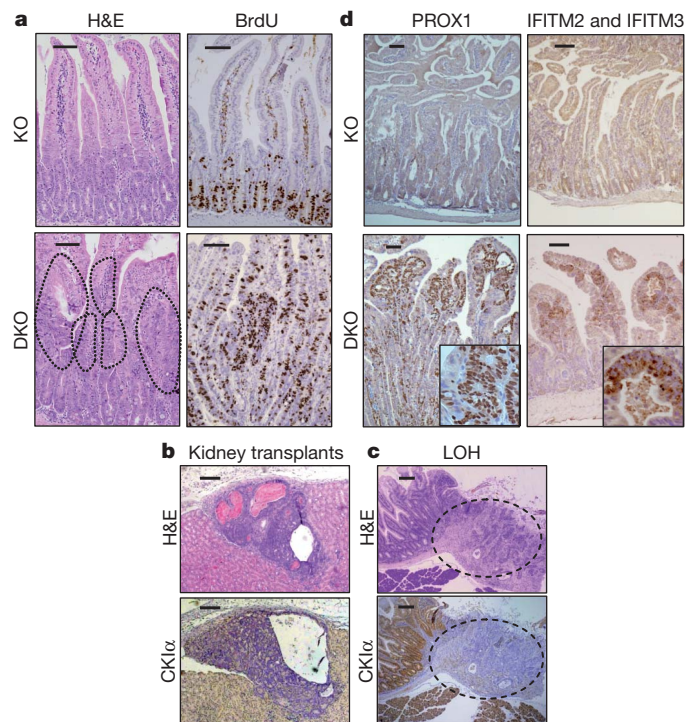


Figure 3 | Widespread invasive carcinomas in the *Csnk1a1*^{Δgut}*p53*^{Δgut} (double-knockout) bowel. **a**, Haematoxylin (nuclear, purple) and eosin (cytoplasmic, pink) (H&E) staining and immunohistochemistry analysis of BrdU (proliferation) in intestinal sections of double-knockout (*Csnk1a1*^{Δgut}*p53*^{Δgut}; DKO) mice compared with *Csnk1a1*^{Δgut} (KO) mice. Dashed lines in the H&E DKO panel demarcate intramucosal carcinomas. Scale bars, 100 μm. **b**, H&E staining and CK1α immunohistochemistry analysis after transplantation of DKO villi to NOD SCID mice ($n = 2$). CK1α-negative intestinal adenocarcinoma is shown permeating the kidney. Scale bars, 100 μm. **c**, H&E staining and CK1α immunohistochemistry analysis in serial intestinal sections of *Csnk1a1*^{+/Δgut}*p53*^{Δgut} mice (Het mice crossed with *p53* KO mice). Dashed lines demarcate a stage T4 carcinoma. Loss of CK1α protein expression is restricted to the tumour cells. Scale bars, 200 μm. **d**, Immunohistochemistry analysis of PROX1, IFITM2 and IFITM3 expression in KO and DKO gut, as in **a**. Insets show fourfold magnification of intramucosal carcinoma areas. Scale bars, 100 μm.

villi with one functional p53 allele ($n = 3$) or p53-deficient villi with one functional *Csnk1a1* allele ($n = 2$) (data not shown). This confirmed the occurrence of bona fide carcinogenesis in double-knockout mice.

Further evidence of the potent effect of combined loss of p53 and CK1α came from mice that were heterozygous for the gene encoding CK1α and lacked p53. *Csnk1a1*^{+/−} and *Csnk1a1*^{−/fl} (heterozygous) mice (where fl is a floxed allele) have a full lifespan without evidence of tumorigenesis (data not shown). Likewise, *p53* knockout mice do not develop intestinal tumours, at least until the age of 6 months, by which time they succumb mostly to lymphomas and sarcomas¹⁷. By contrast, seven of nine mice homozygous for gut-ablated *p53* and harbouring one active *Csnk1a1* allele in the gut (*Csnk1a1*^{+/Δgut}*p53*^{Δgut}) developed invasive carcinomas that permeated the bowel muscular wall into the subserosal fat and some of which involved the serosal surface (stage T4) within 6 months of gene ablation. Remarkably, by immunohistochemistry analysis, all of these malignant lesions are CK1α-negative (Fig. 3c). DNA analysis of carcinoma tissue implicated loss of heterozygosity (LOH) at the *Csnk1a1* locus as the source of carcinoma growth (Supplementary Fig. 8). Overall, our data point to a dual role for CK1α: it acts as a tumour suppressor by blocking Wnt-driven proliferation, and its absence activates p53 to counter carcinogenesis.

Whereas p53 inactivation often coincides with the transition of benign colorectal tumour to invasive carcinoma in humans, existing mouse models for colorectal cancer do not clearly show how wild-type p53 suppresses carcinogenesis^{18,19}. An advantage of the *Csnk1a1* ablation

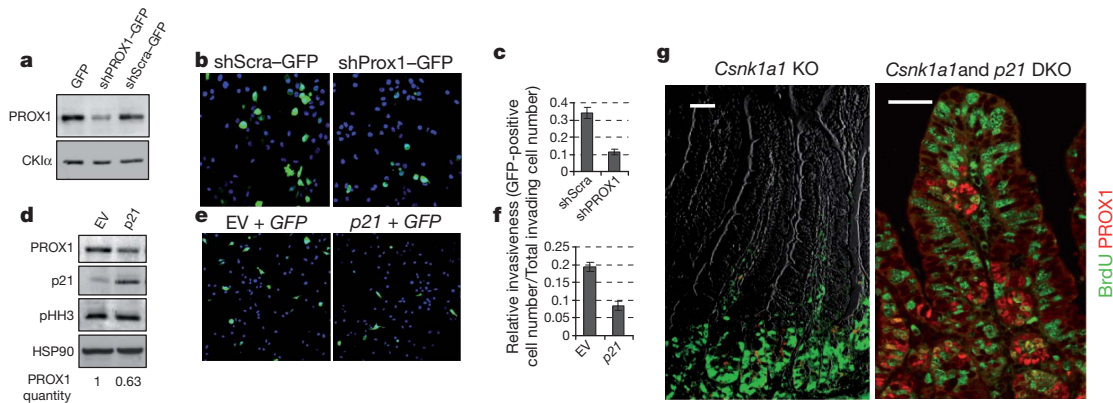


Figure 4 | Invasiveness suppression by p53, through p21. **a**, Western blotting analysis of COLO 205 cells transfected with lentiviral vectors expressing GFP and shRNA specific for PROX1 and GFP (shPROX1-GFP), scrambled sequence shRNAs and GFP (shScra-GFP) or GFP empty vector. CK1α is a loading control. **b**, Matrigel invasion assay of shPROX1-GFP-expressing cells compared with shScra-GFP-expressing cells (GFP, green). Relative transfection efficiencies were 1.07/1. Hoechst stain (blue) was used as a nuclear counterstain, to determine the total number of invading cells. **c**, Quantification (normalized to transfection efficiencies) of Matrigel invasion assay shown in **b**. Data are presented as mean \pm s.e.m. **d**, Western blotting analysis of COLO 205 cells transfected with a combination of p21 and GFP expression vectors (p21 + GFP) versus empty vector

and GFP (EV + GFP) (transfection efficiency, 50%). Phospho-histone H3 (pHH3) is a cell cycle marker. HSP90 is a loading control. PROX1 levels were quantified relative to HSP90 and normalized to EV. **e**, Matrigel invasion assay of p21 and GFP co-transfected COLO 205 cells compared with EV and GFP co-transfected cells. Relative transfection efficiencies for p21 and GFP versus EV and GFP were 1.14/1. Hoechst stain (blue) was used as a nuclear counterstain. **f**, Quantification of data in panel **e**. Data are presented as mean \pm s.e.m. **g**, Double immunofluorescence of BrdU (green) and PROX1 (red) in intestinal sections from *Csnk1a1* Δ gut (KO) and *Csnk1a1* Δ gutp21 $^{-/-}$ (DKO) mice. BrdU staining was negative in 83% of cells in invading clusters ($n = 186$) compared with 51% in non-invading epithelia ($n = 354$). Scale bars, 100 μ m (left); 50 μ m (right).

model is the robust, instantaneous emergence of intramucosal carcinoma, making it easier to track the origin of invasion. To elucidate the molecular basis of invasiveness in *Csnk1a1* Δ gutp53 Δ gut mice, we compared the transcriptome of the doubly ablated enterocytes with that of singly ablated (p53 Δ gut or *Csnk1a1* Δ gut) enterocytes. Among the upregulated genes, there is a subset, which we denote PSIS (p53-suppressed invasiveness signature), associated with diverse invasiveness functions, including loss of enterocyte polarity and adhesion (for example, *Prox1*), tissue remodelling (for example, the *Ifitm* gene family, *Plat* and *Mmp7*) and facilitation of motility (for example, *Pls3*) (Supplementary Table 3 and Supplementary Fig. 9a). *Ifitm* gene family members are new biomarkers for colorectal cancer²⁰ and are associated with invasion at early stages of human head and neck cancer²¹. PROX1 overexpression characterizes highly dysplastic colorectal adenoma and carcinoma, and it promotes colonic tumorigenesis by modulating polarity and adhesion²².

We found that *Prox1* and several *Ifitm* gene family members are strongly induced in *Csnk1a1* Δ gutp53 Δ gut enterocytes (Supplementary Fig. 9a). These genes harbour TCF-binding sites²³, indicating that they are transcriptionally induced by Wnt signals only if p53-mediated repression is abolished. Immunohistochemistry analysis indicates that PROX1, IFITM2 and IFITM3 proteins are abundantly expressed at foci of *Csnk1a1* Δ gutp53 Δ gut intramucosal carcinomas (Fig. 3d), whereas there is little or no expression of these genes in the gut of *Csnk1a1* $^{+/ \Delta$ gut or *Csnk1a1* Δ gut mice. Likewise, expression of PROX1, IFITM2 and IFITM3 is plentiful in the invasive carcinoma that develops following LOH at the *Csnk1a1* locus on a p53-null background and after transplantation of double-knockout villi to NOD SCID mice (Supplementary Fig. 9b). Consistent with these findings, the highest expression of PROX1 in human colorectal adenomas is observed in areas of severe dysplasia²², which are often enriched in p53 mutations²⁴. Together, these data point to cells that express PSIS being more capable of invading the lamina propria than neighbouring epithelial cells that do not express PSIS genes.

To confirm direct participation of a PSIS gene in invasiveness control, we depleted PROX1 in COLO 205 cells, a human colorectal cancer cell line in which APC and p53 are mutated. COLO 205 cells show Matrigel invasion on stimulation with phorbol myristate acetate (PMA). Depletion of PROX1 mediated by shRNA (Fig. 4a) resulted in a threefold reduction of Matrigel invasion (Fig. 4b, c). In addition,

depletion of p53 in MCF 10A (mammary) cells (which harbour wild-type p53) resulted in substantial PROX1 elevation and Matrigel invasion, which was suppressed by co-depletion of p53 and PROX1 (Supplementary Fig. 9c–e). These results indicate that PROX1 expression is a key component of the p53-controlled invasive phenotype.

In addition to its well-known tumour-suppressive role through transcriptional activation of cell cycle inhibitors and pro-apoptotic genes¹³, p53 can also mediate transcriptional repression, either through direct association with other transcription factors (for example, NFY²⁵) or through the activation of its target gene p21 (ref. 26). The p21 protein can repress transcription by various mechanisms, including indirect inactivation of E2F transcription factors through the Rb protein pathway, as well as direct binding to E2F1 and Myc²⁶. NFY-, E2F- and Myc-binding motifs are abundant among the promoters of genes upregulated in double-knockout mice, and nearly all of the PSIS genes harbour at least one of these binding sites (Supplementary Fig. 10a, b). To examine whether p21 can suppress PSIS and invasiveness, we overexpressed p21 concomitantly with green fluorescent protein (GFP) in COLO 205 cells. The resultant downregulation of PROX1 protein expression (Fig. 4d) and decrease in number of GFP-positive invading cells in a Matrigel assay (Fig. 4e, f) implied PSIS suppression by p21. PROX1 repression by p21 was not due to cell cycle arrest, as p21-overexpressing COLO 205 cells continued to proliferate (Fig. 4d, pHH3). These *in vitro* findings indicated that the p53–p21 pathway may control tissue invasion of epithelial cells through suppression of PSIS-gene expression. Of note, PROX1 expression is insufficient for inducing the invasion phenotype *in vivo*²²; rather, concerted action of several PSIS genes may be required to promote tissue invasion.

To elucidate the role of p21 in *Csnk1a1* Δ gut mice *in vivo*, we generated *Csnk1a1* Δ gutp21 $^{-/-}$ mice and examined the consequences of dual gene ablation. Much like *Csnk1a1* Δ gutp53 Δ gut mice, *Csnk1a1* Δ gutp21 $^{-/-}$ mice showed Wnt hyperinduction and massive proliferation, as evident from cyclin D1 and 5-bromodeoxyuridine (BrdU) staining spreading into the villi compartment (Supplementary Fig. 11a), indicating that p21 indeed mediates the p53-dependent growth arrest. *Csnk1a1* Δ gutp21 $^{-/-}$ mice expressed p53 and its typical target genes at *Csnk1a1* Δ gut-comparable levels (Supplementary Fig. 11b, c); however, like *Csnk1a1* Δ gutp53 Δ gut mice, *Csnk1a1* Δ gutp21 $^{-/-}$ mice developed severe dysplasia and intramucosal carcinomas throughout the small bowel (Supplementary Fig. 11a, H&E), providing direct genetic evidence that p21 is a mediator of

p53-dependent invasiveness control. This was also emphasized by gene expression array analysis showing repression of PSIS genes by p21 (Supplementary Fig. 11d and Supplementary Table 3).

Interestingly, the proliferation rate of the intramucosal carcinoma cells is significantly reduced compared with cells of the adjacent non-invasive epithelium: intramucosal carcinomas upregulate the PSIS marker PROX1 (Fig. 4g and Supplementary Fig. 11a (PROX1)) yet are mostly BrdU-negative (Fig. 4g). Therefore, p21 is a key factor in the suppression of p53-mediated invasiveness, independently of its role in cell cycle control.

Our studies implicate p53 as the guardian of invasiveness. In contrast to a recent report on cell lines²⁷, we detected no epithelial-to-mesenchymal transition in the *Csnk1a1*^{Δgut}p53^{Δgut} bowel (data not shown), distinguishing the invasiveness control function of p53 in intestinal carcinogenesis from other tumour-suppressor mechanisms. Furthermore, there is probably little in common between the invasiveness promotion of a gain-of-function p53 mutant, which functions like an oncogene²⁸, and the tumour-suppressive property of wild-type p53 described here. For instance, whereas epidermal growth factor receptor signalling is augmented in cells harbouring p53 gain-of-function mutants²⁸, it does not differ between *Csnk1a1*^{Δgut} and *Csnk1a1*^{Δgut}p53^{Δgut} enterocytes (data not shown).

Our *Csnk1a1*^{Δgut} and *Csnk1a1*^{Δgut}p53^{Δgut} knockout models recapitulate critical aspects of human colorectal carcinogenesis: Wnt hyperactivation, DDR and senescence, and p53 loss. Whereas Wnt activation, DDR and senescence are early molecular events in human colorectal tumorigenesis, p53 inactivation is typically a late event, concurrent with the transition of benign tumours to invasive colorectal cancer³. At this transition point, the control of tissue invasion—rather than the well-established cell-autonomous functions of p53 (apoptosis induction, cell cycle arrest and senescence⁷)—is probably the critical tumour-suppressive function of p53. Notably, in the alternative colorectal carcinogenesis model—the ‘*de novo*’ colorectal carcinogenesis model²⁹, in which, unlike the traditional adenoma–carcinoma sequence³, invasiveness precedes other aspects of neoplastic growth—p53 loss is an early carcinogenesis event. This alternative model is most common in human colorectal cancer associated with inflammatory bowel diseases²⁴, possibly indicating that environmental cues, such as inflammatory mediators, may synergize with p53 loss in upregulating PSIS genes, inducing rapid invasiveness. An inflammatory reaction sustaining cellular senescence³⁰ could fulfil a similar function in the *Csnk1a1* knockout model. We propose that invasion control, which could be triggered early or late in carcinogenesis, is a cardinal tumour-suppressive function of p53 in Wnt-driven tumours.

METHODS SUMMARY

Mice with a genetically modified *Csnk1a1* locus were generated by floxing exons 1 and 2 of the mouse *Csnk1a1* gene. *Pgk1*-Cre mice were used as a full deleter strain, and *Vill1*-Cre-ER^{T2} transgenic mouse as a gut-specific deleter strain. To generate double-knockout mice, p53^{Δfl} and p21^{−/−} mice were used. Conditional knockouts were induced by subcutaneous or intraperitoneal injection of tamoxifen (Sigma).

Full Methods and any associated references are available in the online version of the paper at www.nature.com/nature.

Received 11 March; accepted 17 November 2010.

1. Clevers, H. Wnt/β-catenin signaling in development and disease. *Cell* **127**, 469–480 (2006).
2. Bartkova, J. et al. Oncogene-induced senescence is part of the tumorigenesis barrier imposed by DNA damage checkpoints. *Nature* **444**, 633–637 (2006).
3. Fearon, E. R. & Vogelstein, B. A genetic model for colorectal tumorigenesis. *Cell* **61**, 759–767 (1990).
4. Sansom, O. J. et al. Loss of *Apc* in vivo immediately perturbs Wnt signaling, differentiation, and migration. *Genes Dev.* **18**, 1385–1390 (2004).
5. Collado, M. et al. Senescence in premalignant tumours. *Nature* **436**, 642 (2005).
6. Di Micco, R. et al. Oncogene-induced senescence is a DNA damage response triggered by DNA hyper-replication. *Nature* **444**, 638–642 (2006).

7. Junttila, M. R. & Evan, G. I. p53—a Jack of all trades but master of none. *Nature Rev. Cancer* **9**, 821–829 (2009).
8. Kamijo, T. et al. Tumor suppression at the mouse *INK4a* locus mediated by the alternative reading frame product p19^{ARF}. *Cell* **91**, 649–659 (1997).
9. Damalas, A., Kahan, S., Shutman, M., Ben-Ze'ev, A. & Oren, M. Deregulated β-catenin induces a p53- and ARF-dependent growth arrest and cooperates with Ras in transformation. *EMBO J.* **20**, 4912–4922 (2001).
10. Sherr, C. J. Divorcing ARF and p53: an unsettled case. *Nature Rev. Cancer* **6**, 663–673 (2006).
11. Valentin-Vega, Y. A., Box, N., Terzian, T. & Lozano, G. *Mdm4* loss in the intestinal epithelium leads to compartmentalized cell death but no tissue abnormalities. *Differentiation* **77**, 442–449 (2009).
12. Wilson, J. W., Pritchard, D. M., Hickman, J. A. & Potten, C. S. Radiation-induced p53 and p21^{WAF-1/CIP1} expression in the murine intestinal epithelium: apoptosis and cell cycle arrest. *Am. J. Pathol.* **153**, 899–909 (1998).
13. Riley, T., Sontag, E., Chen, P. & Levine, A. Transcriptional control of human p53-regulated genes. *Nature Rev. Mol. Cell Biol.* **9**, 402–412 (2008).
14. Andreu, P. et al. Crypt-restricted proliferation and commitment to the Paneth cell lineage following *Apc* loss in the mouse intestine. *Development* **132**, 1443–1451 (2005).
15. Fodde, R. et al. A targeted chain-termination mutation in the mouse *Apc* gene results in multiple intestinal tumors. *Proc. Natl Acad. Sci. USA* **91**, 8969–8973 (1994).
16. Taketo, M. M. & Edelman, W. Mouse models of colon cancer. *Gastroenterology* **136**, 780–798 (2009).
17. Donehower, L. A. et al. Mice deficient for p53 are developmentally normal but susceptible to spontaneous tumours. *Nature* **356**, 215–221 (1992).
18. Fazeli, A. et al. Effects of p53 mutations on apoptosis in mouse intestinal and human colonic adenomas. *Proc. Natl Acad. Sci. USA* **94**, 10199–10204 (1997).
19. Reed, K. R. et al. A limited role for p53 in modulating the immediate phenotype of *Apc* loss in the intestine. *BMC Cancer* **8**, 162 (2008).
20. Andreu, P. et al. Identification of the IFITM family as a new molecular marker in human colorectal tumors. *Cancer Res.* **66**, 1949–1955 (2006).
21. Hatano, H. et al. IFN-induced transmembrane protein 1 promotes invasion at early stage of head and neck cancer progression. *Clin. Cancer Res.* **14**, 6097–6105 (2008).
22. Petrova, T. V. et al. Transcription factor PROX1 induces colon cancer progression by promoting the transition from benign to highly dysplastic phenotype. *Cancer Cell* **13**, 407–419 (2008).
23. Cole, M. F., Johnstone, S. E., Newman, J. J., Kagey, M. H. & Young, R. A. Tcf3 is an integral component of the core regulatory circuitry of embryonic stem cells. *Genes Dev.* **22**, 746–755 (2008).
24. Yin, J. et al. p53 point mutations in dysplastic and cancerous ulcerative colitis lesions. *Gastroenterology* **104**, 1633–1639 (1993).
25. Tabach, Y. et al. The promoters of human cell cycle genes integrate signals from two tumor suppressive pathways during cellular transformation. *Mol. Syst. Biol.* **1**, 2005.0022 (2005).
26. Abbas, T. & Dutta, A. p21 in cancer: intricate networks and multiple activities. *Nature Rev. Cancer* **9**, 400–414 (2009).
27. Wang, S. P. et al. p53 controls cancer cell invasion by inducing the MDM2-mediated degradation of Slug. *Nature Cell Biol.* **11**, 694–704 (2009).
28. Muller, P. A. et al. Mutant p53 drives invasion by promoting integrin recycling. *Cell* **139**, 1327–1341 (2009).
29. Bedenne, L. et al. Adenoma–carcinoma sequence or ‘*de novo*’ carcinogenesis? A study of adenomatous remnants in a population-based series of large bowel cancers. *Cancer* **69**, 883–888 (1992).
30. Coppe, J. P., Desprez, P. Y., Krtolica, A. & Campisi, J. The senescence-associated secretory phenotype: the dark side of tumor suppression. *Annu. Rev. Pathol.* **5**, 99–118 (2010).

Supplementary Information is linked to the online version of the paper at www.nature.com/nature.

Acknowledgements We thank S. Robine for the *Vill1*-Cre-ER^{T2} mice, O. Sansom and B. Romagnolo for intestinal sections of *Apc*^{Δgut} mice, K. Rajewsky for the pGEM-loxP-Neo-loxP and pCA-NLS-Cre vectors; and E. Horwitz, M. Farago, D. Naor, N. Asherie and D. Knigin for providing expertise and reagents. We are grateful to A. Yaron for critical reading of the manuscript. This work was supported by the Dr. Miriam and Sheldon G. Adelson Medical Research Foundation (AMRF), the Israel Science Foundation, the RUBICON EC Network of Excellence, the Israel Cancer Research Fund and Deutsches Krebsforschungszentrum—Ministry of Science and Technology (DKFZ-MOST). Z.W. is supported by a Marie-Curie Intra-European Fellowship.

Author Contributions Most experiments were performed by E.E., A.P. and R.E.G. Additional experimental work was carried out by Y.M., G.B., G.C., I.S.-A., I.B., R.H.-K. and Z.W. Experimental design and interpretation of data were conducted by all authors. S.J. supervised the gene targeting. The project was supervised by E.P. and Y.B.-N., and the paper was written by E.E., A.P., R.E.G., K.A., M.O., E.P. and Y.B.-N.

Author Information Reprints and permissions information is available at www.nature.com/reprints. The authors declare no competing financial interests. Readers are welcome to comment on the online version of this article at www.nature.com/nature. Correspondence and requests for materials should be addressed to Y. B.-N. (ybinon@cc.huji.ac.il) and E.P. (epeli@hadassah.org.il).

METHODS

Plasmids and embryonic stem cell culture. A CK1 α expression vector was constructed on the basis of pGEM-11Zf(+), to which an XbaI- and SalI-digested fragment of a neomycin cassette flanked by two *loxP* sites was inserted from a pL2-neo expression vector. Exons 1 and 2 of the mouse *Csnk1a1* gene were cloned into the vector, flanked by *loxP* sites using a third *loxP* site. Short (1-kilobase) and long (5-kilobase) homology sequences were cloned upstream and downstream of the targeted exons, respectively. All genomic fragments were amplified by PCR from 129/SvJ mouse DNA. The vector was linearized with SalI and purified using phenol–chloroform extraction and ethanol precipitation methods. R1 embryonic stem (ES) cells (129/SvJ-mouse derived) were electroporated and cultured on a feeder layer of MEFs using DMEM supplemented with 15% ES-cell-tested FBS and 1,000 U ml⁻¹ ESGRO (Chemicon). Neomycin selection was done in 0.2 mg ml⁻¹ G418 (Sigma). pCA-NLS-Cre was used as a Cre expression vector for transient transfection of Cre into ES cells. Selection was done in 2 μ g ml⁻¹ puromycin.

Aggregation, mouse breeding and genotyping. R1 ES cells were aggregated to CD-1 mouse morulae. Chimaeric mice were bred with CD-1 mice to check for germline transmission. *Pgk1*-Cre transgenic mice³¹ were used as a deleter strain for the generation of germline *Csnk1a1* deletion. For generation of conditional *Csnk1a1* knockout mice, Cre was transiently expressed in ES cells to produce specific deletion of the neomycin cassette and an intact floxed *Csnk1a1* allele. A second aggregation was done, and *Vil1*-Cre-ER^{T2} (ref. 32) transgenic mice were used as a gut-specific deleter to generate a conditional *Csnk1a1* knockout mouse. Inducible double-knockout mice (*p53* and *Csnk1a1*) were generated by crossing mice in which *Csnk1a1* was floxed with mice in which *p53* was floxed³³. *p21*^{-/-} mice³⁴ were purchased from the Jackson Laboratory (stock #003263). Double-knockout mice (*p21* and *Csnk1a1*) were generated by crossing mice in which *Csnk1a1* was floxed with *p21*^{-/-} mice. Mice were kept under specific pathogen-free conditions at The Weizmann Institute of Science and at the Hadassah Medical School of the Hebrew University. All mouse experiments were performed in accordance with guidelines of the relevant institution's ethics committee.

For mouse genotyping, DNA from the tail or ear of 4-week-old pups was extracted by means of standard protocols. For embryo genotyping, a small section of the embryo was taken for DNA preparation. The following primers were used for simultaneous detection of wild-type and null *Csnk1a1* alleles: 5'-AACAGATGG CGGCCTCG (forward primer for wild-type and null *Csnk1a1*); 5'-CGCACCA GTTTGTATTTTCC (reverse primer for wild-type *Csnk1a1*); and 5'-GGGCGA ATTCTGCAGATATC (reverse primer for null *Csnk1a1*). The following primers were used for simultaneous detection of wild-type and floxed *Csnk1a1* alleles: 5'-CGTGACGCCGACAGAG (forward primer for wild-type *Csnk1a1*); 5'-ATAA GTGGGGAGGCTGCTA (reverse primer for wild-type *Csnk1a1*); 5'-GCAGG AAGTGGCAGTGAAAC (forward primer for floxed *Csnk1a1*); and 5'-GGGCGA ATTCTGCAGATATC (reverse primer for floxed *Csnk1a1*). Other primers that were used for genotyping: 5'-CACAAAAACAGGTTAAACCCAG (forward primer for wild-type and floxed *p53*); 5'-AGCACATAGGAGGCAGAGAC (reverse primer for wild-type and floxed *p53*); 5'-AGCAATTCACAGTATTT GG (forward primer for wild-type *p21*); 5'-TGACGAAGTCAAAGTTCCACC (reverse primer for wild-type *p21*); 5'-AAGCCTTGATTCTGATGTGGGC (forward primer for null *p21*); 5'-GCTATCAGGACATAGCGTTGGC (reverse primer for null *p21*); 5'-ATGTCCAATTTACTGACCGTACACC (forward primer for *cre*); and 5'-CGCCTGAAGATATAGAAGATAATCG (reverse primer for *cre*).

Tamoxifen administration, BrdU labelling and tissue preparation. Tamoxifen (Sigma) was dissolved in corn oil (Sigma), and mice were injected either subcutaneously (100 mg kg⁻¹ per injection), five to seven injections every other day for 10–14 days, or intraperitoneally (120 mg kg⁻¹) on two consecutive days. At 3–5 days after the last injection, each mouse was injected intraperitoneally with 10 μ l g⁻¹ BrdU (GE Healthcare) and killed 2 h later. The jejunum, ileum and the entire large intestine were flushed with ice-cold PBS, cut open longitudinally and subjected to fixation in 4% formaldehyde and paraffin embedding (FFPE). Small pieces of jejunum were embedded in Tissue-Tek O.C.T. Compound (Sakura) and frozen at -80 °C. Intestinal epithelial cells (IECs) were isolated from the middle part of the small intestine, as described previously³⁵ but with slight modifications: intestinal cells were separated into single cells in Hank's balanced salt solution containing 10 mM HEPES, 5 mM EDTA and 0.5 mM dithiothreitol, at 37 °C for 30 min.

Histology, immunohistochemistry, immunofluorescence, *in situ* hybridization and senescence-associated β -galactosidase analysis. Sections (5 μ m) were cut for haematoxylin and eosin (H&E) staining and immunohistochemistry analysis. For immunohistochemistry, sections were incubated with antibodies detecting CK1 α (C-19; 1/1,000; Santa Cruz Biotechnology), p21 (F-5; 1/50; Santa Cruz Biotechnology), c-Myc (N-262; 1/100; Santa Cruz Biotechnology), PROX1 (1/200; R&D Systems), EPHB2 (1/200; R&D Systems), β -catenin (1/200; BD Transduction), BrdU (Ab3; 1/100; NeoMarkers), cyclin D1 (SP4; 1/125; Lab Vision), CD44 (IM781; 1/200; eBioscience), p53 (CM5; 1/200; Novocastra), cleaved caspase 3 (1/100; Cell

Signaling Technology), IFITM2/3-Fragilis (1/400; Abcam) and lysozyme (1/5,000; Dako). Secondary antibodies were horseradish peroxidase (HRP)-polymer anti-mouse, anti-rabbit, anti-goat and anti-rat antibodies (Nichirei, Dako and Biocare). 3,3'-Diaminobenzidine (DAB) chromogen (Lab Vision) was used for detection. For dual detection of apoptosis and DDR, TUNEL (Roche) was performed according to the manufacturer's instructions, followed by overnight incubation with anti-53BP1 anti-serum (1/200; Bethyl) and detection with goat anti-rabbit antibodies conjugated to Alexa Fluor 647 (1/1,000; Molecular Probes). For double immunofluorescence of BrdU and PROX1, FFPE slides were blocked with 3% bovine serum albumin (BSA), 5% donkey serum and 0.1% Triton X-100 in Tris-buffered saline with Tween 20 (TBST) for 1 h, incubated for 16 h at 4 °C with primary antibodies as described, and then exposed to donkey anti-mouse antibodies conjugated to Alexa Fluor 488 and donkey anti-goat antibodies conjugated to Alexa Fluor 647 (1/1,000; Molecular Probes). Hoechst stain (1 μ g ml⁻¹; Molecular Probes) was used for nuclear counterstaining. For MDMX immunofluorescence, 5 μ m sections were cut from O.C.T.-embedded frozen tissues and fixed in cold acetone for 10 min. Sections were blocked and incubated overnight at 4 °C with anti-MDMX antibody (clone 82; 1/500; Sigma) and subjected to goat anti-mouse antibody conjugated to Alexa Fluor 647 (1/1,000; Molecular Probes). *In situ* hybridization with digoxigenin (DIG; Roche)-labelled cryptdin probe¹⁴ was carried out on FFPE sections. Following deparaffinization and rehydration, slides were immersed in 2 M HCl for 15 min, digested with proteinase K (Roche) for 15 min at 37 °C, fixed for 10 min in 4% paraformaldehyde, acetylated with acetic anhydride in 0.1 M triethanolamine solution, pH 8, pre-incubated at 70 °C for 1 h in hybridization buffer (saline sodium citrate (SSC; pH 4.5), 50% formamide, 2% blocking powder (Roche), 5 mmol l⁻¹ EDTA, 50 μ g ml⁻¹ yeast transfer RNA, 0.1% Tween 20, 0.05% 3[3-cholaminopropyl diethylammonio]-1-propane sulphonate and 50 μ g ml⁻¹ heparin), and incubated with the probe in a humidity chamber for 24–48 h at 70 °C. Following three washes in 2 \times SSC with 50% formamide, five washes in TBST and blocking for 1 h at 4 °C in TBST containing 0.5% blocking powder (Roche), slides were incubated for 16 h at 4 °C with anti-DIG Fab-alkaline phosphatase (1/2,000; Roche) in blocking solution (Roche). Following five washes in TBST and two rinses in 0.1 M Tris, pH 8.8, containing 0.1 M NaCl, slides were stained with nitroblue tetrazolium/5-bromo-4-chloro-3-indolyl-phosphate (NBT/BCIP) solution (BM purple; Roche) at 25 °C for 1–2 h, dehydrated and mounted. For senescence-associated β -galactosidase (SA- β -gal) staining, 10 μ m sections were cut from O.C.T.-embedded frozen tissue and allowed to adhere to coated slides at 25 °C for 1 min before fixation for 15 min in PBS containing 0.5% glutaraldehyde (Sigma). Sections were rinsed with PBS, pH 5.5, containing 1 mM MgCl₂ and incubated at 37 °C for 16 h in pre-warmed and filtered 5-bromo-4-chloro-3-indolyl- β -D-galactoside (X-gal) solution (0.1% X-gal (Ornat) dissolved in PBS, pH 5.5, containing 1 mM MgCl₂, 5 mM potassium ferrocyanide and 5 mM potassium ferricyanide). Sections were rinsed with PBS, post-fixed in 95% ethanol, rehydrated, counterstained with nuclear fast red, dehydrated and mounted.

Western blotting and RNA analysis. Protein was extracted by whole-cell-extract protocols from cell pellets in protein lysis buffer containing protease and phosphatase inhibitors (*p*-nitrophenyl phosphate (PNPP), sodium orthovanadate (Na₃VO₄), leupeptin, aprotinin, β -glycerophosphate and okadaic acid). Western blotting analysis was performed by means of standard techniques. Blots were incubated with antibodies detecting β -catenin (1/2,500; BD Transduction), phospho- β -catenin (S45; 1/750; Cell Signaling Technology), phospho- β -catenin (S33/S37/T41; 1/750; Cell Signaling Technology), phospho- β -catenin (T41/S45; 1/750; Cell Signaling Technology), CK1 α (C-19; 1/1,000; Santa Cruz Biotechnology), CK1 ϵ (1/250; Santa Cruz Biotechnology), CK1 δ (1/400; Icos), HSP90 α (1/5,000; Calbiochem), tubulin (1/5,000; Sigma), MDMX (clone 82; 1/1,000; Sigma), mouse p53 (CM5; 1/1,000; Novocastra), BAX (1/200; Santa Cruz Biotechnology), p21 (F-5; 1/200; Santa Cruz Biotechnology), MKP1 (1/750; Santa Cruz), p19^{ARF} (1/100; Upstate), human p53 (DO-1/1801 hybridoma mix; 1/10), phospho-Jun (S63; 1/1,000; Cell Signaling Technology), phospho-histone H2A.X (S139; 1/1,000; Millipore), PP2A-C (1/1,000; rabbit serum provided by D. Virshup), cyclin D1 (SP4; 1/500; Lab Vision) and PROX1 (1/1,000; R&D Systems). Secondary antibodies were HRP-linked goat anti-mouse, goat anti-rabbit, goat anti-rat and rabbit anti-goat antibodies (all 1/10,000; Jackson). Blots were developed using ECL (GE Healthcare). Total RNA was extracted from cell pellets using TRI Reagent (Sigma) and phenol–chloroform methods. RNA (2 μ g) was subjected to reverse transcription using M-MLV RT (Invitrogen), and mRNA expression levels were measured by quantitative real-time PCR using SYBR Green (Invitrogen) in a 7900HT Fast Real-Time PCR system (ABI). Relative quantities of gene transcripts were analysed in qBase 1.3.5 software and normalized to the *Ubc* and *Hprt* transcripts. Sequences of PCR primers are as follows: 5'-TAGGCGGAATGAAGATGG

AC (forward primer for *Axin2*); 5'-CTGGTCACCAACAAGGAGT (reverse primer for *Axin2*); 5'-ATGCGTCCACCAAGAAGCTGA (forward primer for *Bax*); 5'-AGCAATCATCTCTGCAGCTCC (reverse primer for *Bax*); 5'-CAGTATC TCCGGACTGAGG (forward primer for *Cd44*); 5'-GCCAACTTCATTGTGTC

CAT (reverse primer for *Cd44*); 5'-GGTGGCGAAGATCGGATCT (forward primer for *Csnk1a1*); 5'-TTCACCTGCCATCTCCTCGC (reverse primer for *Csnk1a1*); 5'-TGAGCCCCCTAGTGCTGCAT (forward primer for *Myc*); 5'-AGCCCGAC TCCGACCTCTT (reverse primer for *Myc*); 5'-TTGACTGCCGAGAAGTTGTG (forward primer for cyclin D1); 5'-CCACTTGAGCTTGTTACCA (reverse primer for cyclin D1); 5'-CACCGACAACCTCTGTGAAGC (forward primer for cyclin D2); 5'-TGCTCAATGAAGTCGTGAGG (reverse primer for cyclin D2); 5'-GCT GGCGCTATCTATCCCTTG (forward primer for cyclin G1); 5'-GGTCAAACTCTC GGCCACTTA (reverse primer for cyclin G1); 5'-GTAAAGCAGTACAGCC CAAA (forward primer for *Hprt*); 5'-AGGGCATATCCAACAACAACTT (reverse primer for *Hprt*); 5'-ATCTCCACGCTGACCATGT (forward primer for *Ifitm1*); 5'-CACCCACCATCTTCTGTCC (reverse primer for *Ifitm1*); 5'-CTG CTGCTGGGCTTCATAG (forward primer for *Ifitm3*); 5'-GGATGCTGAGG ACCAAGGTG (reverse primer for *Ifitm3*); 5'-TACCTGCCCTACCTGATG (forward primer for *Ly6a*); 5'-AGGAGGGCAGATGGGTAAAGC (reverse primer for *Ly6a*); 5'-TGTTGTAGCTGAGGGAGATG (forward primer for *Mdm2*); 5'-CA CTTACGCCATCGTCAAGA (reverse primer for *Mdm2*); 5'-TCATAATGCCA AACAGTCCAA (forward primer for *Mmp7*); 5'-AAGGCATGACCTAGAGTG TTCC (reverse primer for *Mmp7*); 5'-GTCACACGACTGGGCGATT (forward primer for *p19^{Arf}*); 5'-GACTCCATGCTGCTCCAGAT (reverse primer for *p19^{Arf}*); 5'-TCCACAGCGATATCCAGACA (forward primer for *p21*); 5'-AGACAACGGC ACATTGCT (reverse primer for *p21*); 5'-TGAAACGCGCAGCTATCCTTA (forward primer for *p53*); 5'-GGCACAAACACGAACCTCAA (reverse primer for *p53*); 5'-TGGAGAGGGTCAGAAAGCAAA (forward primer for *Pls3*); 5'-AA TCCACAACCGCAAACCTG (reverse primer for *Pls3*); 5'-AGTTCTGCTGG GTGCTGTC (forward primer for *Plat*); 5'-CGGGGACCACCCTGTATGTT (reverse primer for *Plat*); 5'-ATACCGAGCCCTCAACATGC (forward primer for *Prox1*); 5'-CGTAACGTGATCTGCGCAAC (reverse primer for *Prox1*); 5'-CAAG AAGAGCAGCATCGACA (forward primer for *Puma*); 5'-TAGTTGGGCTCCA TTCTGG (reverse primer for *Puma*); 5'-GGAGCTCAGCAAGACTCTGG (forward primer for *Sox9*); 5'-TGTAATCGGGTGGTCTTTCT (reverse primer for *Sox9*); 5'-CAGCCGTATATCTCCAGACT (forward primer for *Ubc*); 5'-CTC AGAGGGATGCCAGTAATCTA (reverse primer for *Ubc*).

Villi transplantation and LOH analyses. *Csnk1a1*^{Δ^{gut}}*p53*^{Δ^{gut}} (double-knockout) male mice ($n = 2$) were used as donors of intestinal villi, with *Csnk1a1*^{Δ^{gut}}*p53*^{+/Δ^{gut}} ($n = 2$) and *Csnk1a1*^{+/Δ^{gut}}*p53*^{Δ^{gut}} ($n = 2$) mice as controls. After knockout induction for 12 days and concomitant treatment for 1 week with an antibiotic mix of imipenem, vancomycin and metronidazole (each 0.25 mg ml⁻¹) in the drinking water, the mice were killed, their small intestines flushed twice with PBS and inverted, and their villi scraped from the upper mucosal layer. Villi were centrifuged and resuspended in 1 ml PBS. NOD SCID male mice aged 8 weeks were used as recipients for intestinal villi. The recipient mice were anaesthetized with ketamine/ xylazine, the left kidney was exposed, and 200 μl resuspended villi from donors were transplanted under the kidney capsule³⁶. Five mice received double-knockout villi, three received *Csnk1a1*^{Δ^{gut}}*p53*^{+/Δ^{gut}} villi and two received *Csnk1a1*^{+/Δ^{gut}}*p53*^{Δ^{gut}} villi. Transplanted recipient mice were kept in specific-pathogen-free conditions and given the above antibiotic mix in their drinking water. Six weeks after transplantation, the recipients were killed and FFPE sections of the kidneys were analysed. For LOH analysis, laser capture microdissection was carried out to obtain DNA from normal and cancerous tissues, extracted by means of standard protocols. PCR was performed with the following primers: 5'-GTAATTGGACCCGATGAATCG (forward primer), 5'-AAACGCAGCAGTGCAACAAAC (reverse primer), detecting 126 base pairs (bp) and 187 bp wild-type and floxed *Csnk1a1* alleles, respectively; 5'-CTAGCTTGCTGGACGTAAC (forward primer), 5'-AAACGCAGCAGT GCAACAAAC (reverse primer), detecting 150 bp of *Csnk1a1* null allele.

Cell cultures and shRNA depletions. Human fibroblasts (IMR-90) at early passage were grown with MEM supplemented with 10% serum. Cells were split after 2 days and left in culture for a total of 8 days, then split again and analysed at sub-confluence for SA-β-gal and γ-H2AX nuclear foci, after a total of 10 days in culture. *Csnk1a1*^{+/+}, *Csnk1a1*^{+/Δ^{gut}} and *Csnk1a1*^{Δ^{gut}} MEFs were collected from embryonic day 13.5 mice and prepared according to standard procedures. Early-passage MEFs were seeded at 1 × 10⁶ cells per 10-cm dish and grown with DMEM supplemented with 10% serum. The floxed *Csnk1a1* allele was subjected to Cre-mediated excision by transduction of the cells with 5 × 10⁷ plaque-forming units (PFU) ml⁻¹ of Cre-expressing adenovirus (Ad-Cre) (Gene Transfer Vector Core, University of Iowa). Cells were collected 6 days after transduction with Ad-Cre. Cells ($n \geq 100$) were counted by a cytometer, and their duplication rates were calculated. RKO cells were grown in DMEM supplemented with 10% serum. MG132 (20 μM; Calbiochem) was added for 3 h before cell collection. For cycloheximide treatment, RKO cells were transduced with shRNA vector for 7 days, then treated with 2 μg ml⁻¹ doxorubicin for 3 h or left untreated. Cells were then washed, incubated with 40 μg ml⁻¹ cycloheximide for the indicated times, and collected. COLO 205 human colorectal cells were grown in RPMI

supplemented with 10% serum. Transfection into COLO 205 cells was done using Amaya Cell Line Nucleofector Kit T (Lonza), and cells were collected 48 h after transfection. MCF 10A breast epithelial cells were grown in F12/DMEM. SA-β-gal staining for human and mouse fibroblasts was carried out as described previously³⁷. Cells were then washed with PBS, fixed in 4% paraformaldehyde for 15 min, washed with TBS, incubated for 10 min in 0.25% Triton X-100-containing TBS, washed with TBS, blocked in 3% BSA with 0.1% Triton X-100/TBS for 1 h and incubated for 16 h with anti-phospho-histone H2A.X (S139) antibody (1/1,000; Upstate). Staining was detected as described above. As a positive control for senescence and DDR, cells were treated with 30 Gy ionizing irradiation. pLKO-based (Open Biosystems) and pLL3.7-based lentiviral vectors were used to transduce cells with shRNA-encoding sequences. The lentiviral packaging system was provided by I. Verma^{38,39}. Human shRNA-encoding sequences that were used are as follows: *CSNK1A1* 5'-GCAGAAAT TTGCGATGTAATTA; *CSNK1D* and *CSNK1E* 5'-GGGCTTCTCCTATGACTAC; *APC* 5'-GCAGAGGAAGGTGATATTC; β-catenin 5'-GTGGGTGGTATAGAGG CTC; *p19^{Arf}* 5'-GTGATGATGATGGGCAACGTT; scrambled control 5'-TCCTA AGTTAAGTCGCCCTCG; *p53* 5'-CGGCGCACAGAGGAAGAGAAAT; *PROX1* 5'-TGAGCCAGTTTGATATGGATTTCAAGAGAATCCATATCAAACCTGGCT CTTTTTTC; scrambled control 5'-TGGTCAACGCTCTACTGGAATTCAAGAG ATTCCAGTAGACGTTTCGACCTTTTTTC. Mouse shRNA-encoding sequence that was used: mSAF (encoded by *Hnnp1u*) 5'-CTGATGAAGTTGAACCTCTC. A combination of CMV-p21 and CMV-GFP expression vectors was used for over-expression of p21, at a ratio of 10/1, respectively. CMV empty vector was used as a control.

Matrigel invasion assay. The *in vitro* Matrigel invasion assay was carried out in 8 μm Transwell dishes. Matrigel (BD Biosciences) was added to each well (20 μg per well) and was left to gel for at least 1 h. MCF 10A cells were seeded at low and high densities on top of the Matrigel and incubated for 20 h at 37 °C. For visualization, invasive cells were fixed in 4% paraformaldehyde and stained with 0.3% crystal violet. COLO 205 cells were seeded on top of the Matrigel and incubated for 48 h at 37 °C. To induce invasion of COLO 205 cells, 12.5 ng ml⁻¹ PMA⁴⁰ was added to the lower chambers. For visualization, invasive cells were fixed in 4% paraformaldehyde and stained with Hoechst stain.

cDNA array and transcription factor analyses. Gene expression was compared between *Csnk1a1*^{+/+} (WT), *Csnk1a1*^{+/Δ^{gut}} (Het) and *Csnk1a1*^{Δ^{gut}} (KO) using Mouse Genome 430 2.0 Arrays (Affymetrix). Gene expression was compared between *Csnk1a1*^{+/Δ^{gut}} (Het), *Csnk1a1*^{Δ^{gut}} (KO), *Csnk1a1*^{+/Δ^{gut}}*p53*^{Δ^{gut}} (p53 KO) and *Csnk1a1*^{Δ^{gut}}*p53*^{Δ^{gut}} (*Csnk1a1* and p53 DKO) using Mouse Gene 1.0 ST Arrays (Affymetrix). Gene Expression Omnibus accession number for microarray data is GSE24760. RNA was purified from two biological replicates in each group using the TRIzol extraction method (Invitrogen). Labelled cRNA was produced and hybridized according to manufacturer's instructions at the Center for Genomic Technologies, Hebrew University. Gene intensities were extracted from CEL files with Expression Console 1.1 (Affymetrix), using the RMA-Sketch method. Raw data were normalized using median intensities⁴¹. For each pair of biological replicates, the geometric mean and the ratio were calculated. Transcription factor occurrence was calculated using the DiRE program⁴². Cutoff was defined as the 20 genes with the highest importance score.

- Lallemand, Y., Luria, V., Haffner-Krausz, R. & Loni, P. Maternally expressed PGK-Cre transgene as a tool for early and uniform activation of the Cre site-specific recombinase. *Transgenic Res.* **7**, 105–112 (1998).
- el Marjou, F. *et al.* Tissue-specific and inducible Cre-mediated recombination in the gut epithelium. *Genesis* **39**, 186–193 (2004).
- Jonkers, J. *et al.* Synergistic tumor suppressor activity of BRCA2 and p53 in a conditional mouse model for breast cancer. *Nature Genet.* **29**, 418–425 (2001).
- Brugarolas, J. *et al.* Radiation-induced cell cycle arrest compromised by p21 deficiency. *Nature* **377**, 552–557 (1995).
- Greten, F. R. *et al.* IKKβ links inflammation and tumorigenesis in a mouse model of colitis-associated cancer. *Cell* **118**, 285–296 (2004).
- Davalli, A. M. *et al.* A selective decrease in the β cell mass of human islets transplanted into diabetic nude mice. *Transplantation* **59**, 817–820 (1995).
- Dimri, G. P. & Campisi, J. Molecular and cell biology of replicative senescence. *Cold Spring Harb. Symp. Quant. Biol.* **59**, 67–73 (1994).
- Naldini, L., Blomer, U., Gage, F. H., Trono, D. & Verma, I. M. Efficient transfer, integration, and sustained long-term expression of the transgene in adult rat brains injected with a lentiviral vector. *Proc. Natl Acad. Sci. USA* **93**, 11382–11388 (1996).
- Naldini, L. *et al.* *In vivo* gene delivery and stable transduction of nondividing cells by a lentiviral vector. *Science* **272**, 263–267 (1996).
- Ko, C. H., Shen, S. C., Lee, T. J. & Chen, Y. C. Myricetin inhibits matrix metalloproteinase 2 protein expression and enzyme activity in colorectal carcinoma cells. *Mol. Cancer Ther.* **4**, 281–290 (2005).
- Irizarry, R. A. *et al.* Exploration, normalization, and summaries of high density oligonucleotide array probe level data. *Biostatistics* **4**, 249–264 (2003).
- Gotea, V. & Ovcharenko, I. DiRE: identifying distant regulatory elements of co-expressed genes. *Nucleic Acids Res.* **36**, W133–W139 (2008).

Coronin 2A mediates actin-dependent de-repression of inflammatory response genes

Wendy Huang^{1,2}, Serena Ghisletti^{1,†}, Kaoru Saijo¹, Meghal Gandhi³, Myriam Aouadi⁴, Greg J. Tesz⁴, Dawn X. Zhang^{1,2}, Joyee Yao¹, Michael P. Czech⁴, Bruce L. Goode³, Michael G. Rosenfeld^{5,6} & Christopher K. Glass^{1,5}

Toll-like receptors (TLRs) function as initiators of inflammation through their ability to sense pathogen-associated molecular patterns and products of tissue damage^{1,2}. Transcriptional activation of many TLR-responsive genes requires an initial de-repression step in which nuclear receptor co-repressor (NCoR) complexes are actively removed from the promoters of target genes to relieve basal repression^{3,4}. Ligand-dependent SUMOylation of liver X receptors (LXRs) has been found to suppress TLR4-induced transcription potentially by preventing the NCoR clearance step^{5–7}, but the underlying mechanisms remain enigmatic. Here we provide evidence that coronin 2A (CORO2A), a component of the NCoR complex of previously unknown function^{8,9}, mediates TLR-induced NCoR turnover by a mechanism involving interaction with oligomeric nuclear actin. SUMOylated LXRs block NCoR turnover by binding to a conserved SUMO2/SUMO3-interaction motif in CORO2A and preventing actin recruitment. Intriguingly, the LXR transrepression pathway can itself be inactivated by inflammatory signals that induce calcium/calmodulin-dependent protein kinase II γ (CaMKII γ)-dependent phosphorylation of LXRs, leading to their deSUMOylation by the SUMO protease SENP3 and release from CORO2A. These findings uncover a CORO2A-actin-dependent mechanism for the de-repression of inflammatory response genes that can be differentially regulated by phosphorylation and by nuclear receptor signalling pathways that control immunity and homeostasis.

To delineate mechanisms by which SUMOylated LXRs block signal-dependent clearance of NCoR complexes from TLR4-inducible promoters, we searched for potential SUMO-interaction motifs (SIMs) in proteins that are associated with the NCoR complex and might mediate interactions with SUMOylated LXRs. This search identified a conserved motif in the carboxy terminus of CORO2A (Fig. 1a) that matches a recently identified SIM that is specific for SUMO2/SUMO3 (ref. 10).

CORO2A is a member of the coronin family of actin-binding proteins and was identified as a component of the NCoR complex in nuclear extracts of HeLa cells^{8,9}. It is highly expressed in cells of the haematopoietic lineage^{11,12}. All other members of the coronin family have been found to have roles in regulation of the actin cytoskeleton through interactions with F-actin^{13,14}, but the functional roles of CORO2A in the NCoR complex have not been established. We confirmed that CORO2A and the NCoR complex interact in primary macrophages by co-immunoprecipitation assay and found that, in contrast to other coronin family members, CORO2A is primarily localized to the nucleus in primary bone-marrow-derived macrophages (BMDMs) (Supplementary Fig. 2a, b).

In addition, immunofluorescence microscopy demonstrated that CORO2A co-localizes to NCoR-rich regions of the nucleus (Fig. 1b). Chromatin immunoprecipitation (ChIP) studies further demonstrated that CORO2A is localized to NCoR target promoters such as

the nitric oxide synthase 2 (*Nos2*) and CC-chemokine ligand 2 (*Ccl2*) gene promoters in resting macrophages, and the occupancy of these promoters by CORO2A was reduced by treatment with the TLR4 ligand lipopolysaccharide (LPS) (Fig. 1c). Sequential ChIP experiments indicated that CORO2A and the NCoR complex reside together on the *Nos2* promoter (Supplementary Fig. 2c). Reduction of NCoR expression in primary macrophages using specific short interfering RNAs (siRNAs) resulted in a corresponding reduction in CORO2A occupancy of the *Nos2* and *Ccl2* promoters without affecting total CORO2A protein expression (Supplementary 2d, e). By contrast, CORO2A was not found on the colony-stimulating factor 3 (*Csf3*) gene promoter (Supplementary Fig. 2d), which is not a target of NCoR repression¹⁵.

To investigate the potential role of CORO2A as a molecular 'beacon' for SUMOylated LXRs, co-immunoprecipitation studies were performed. HeLa cells were transfected with Flag-tagged wild-type LXR- β or a mutant of LXR- β (K410/448R) that cannot be SUMOylated⁵ and then treated with the synthetic LXR agonist GW3965. The mutant form of LXR- β did not co-precipitate with CORO2A, whereas wild-type LXR- β was co-precipitated with CORO2A and migrated at the expected molecular mass for SUMO-LXR- β in immunoblotting experiments (Fig. 1d). This interaction was largely dependent on treatment with GW3965 (Supplementary Fig. 3a). In addition, *in vitro* transcribed and translated CORO2A preferentially interacted with a recombinant glutathione S-transferase (GST)-LXR- β fusion protein conjugated to SUMO3 *in vitro*, compared with unconjugated GST-LXR- β or deSUMOylated LXR- β (Supplementary Fig. 3b).

Next, ChIP experiments were performed in primary macrophages that had been transfected with control or *Coro2a*-specific siRNAs. Knockdown of *Coro2a* expression resulted in an almost complete loss of recruitment of LXR to the *Nos2* and *Ccl2* promoters in response to GW3965 (Fig. 1e). Although a recent study reported that G-protein pathway suppressor 2 (GPS2) is required for the recruitment of SUMOylated LXR- β to the C-reactive protein (*Crp*) and haptoglobin (*Hp*) gene promoters in the liver⁷, GPS2 is not present above background levels on the *Nos2* or interleukin-1 β (*Il1b*) gene promoters, as determined by ChIP assay. In addition, *Gps2* knockdown had no effect on LXR-mediated transrepression of *Nos2* or *Il1b* in primary macrophages (Supplementary Fig. 4a).

Point mutations were therefore introduced into the SIM of CORO2A to evaluate its potential importance in recruiting SUMO-LXRs. HeLa cells were transfected with Flag-tagged wild-type CORO2A or SIM-mutant versions of CORO2A and treated with vehicle or GW3965. Both wild-type and SIM-mutant CORO2A were immunoprecipitated by anti-NCoR antibody; however, only wild-type CORO2A interacted with LXR, and this interaction was enhanced by treatment with GW3965 (Fig. 1f). In addition, a mammalian two-hybrid assay indicated that LXR interacts with CORO2A in a ligand- and SIM-dependent

¹Department of Cellular and Molecular Medicine, University of California, San Diego, 9500 Gilman Drive, La Jolla, California 92093-0651, USA. ²Biomedical Sciences Graduate Program, University of California, San Diego, 9500 Gilman Drive, La Jolla, California 92093-0651, USA. ³Department of Biology, Rosenstiel Basic Medical Science Research Center, Brandeis University, Waltham, Massachusetts 02454, USA. ⁴Program in Molecular Medicine, University of Massachusetts Medical School, 373 Plantation Street, Worcester, Massachusetts 01605, USA. ⁵Department of Medicine, University of California, San Diego, 9500 Gilman Drive, La Jolla, California 92093-0651, USA. ⁶Howard Hughes Medical Institute, University of California, San Diego, 9500 Gilman Drive, La Jolla, California 92093-0651, USA.

[†]Present address: Department of Experimental Oncology, European Institute of Oncology, Via Adamello 16, 20139 Milan, Italy.

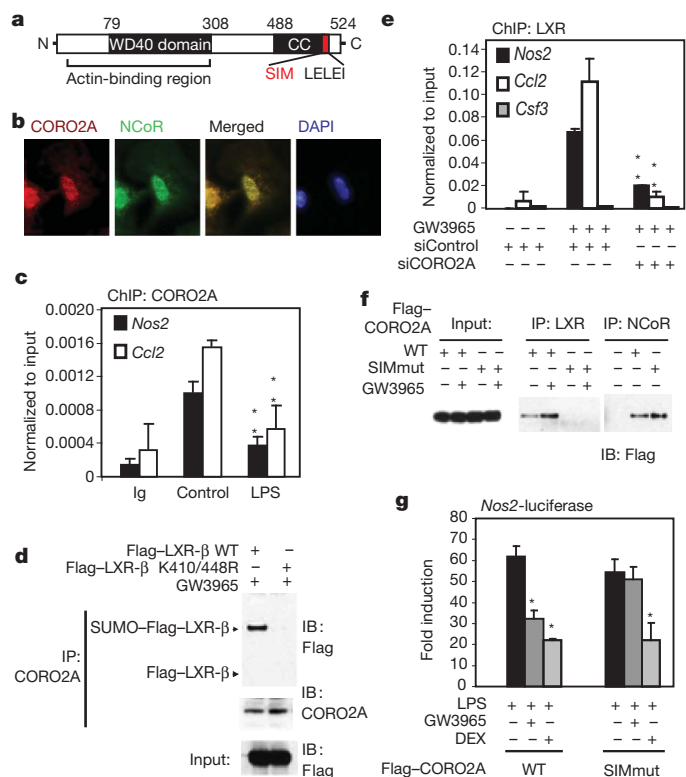


Figure 1 | The SIM of CORO2A is required for recruiting SUMOylated LXR to NCoR-occupied pro-inflammatory gene promoters. **a**, Known and predicted domain structure of mouse CORO2A. C, coiled-coil domain; N, amino terminus; SIM, SUMO2/SUMO3-interaction motif (with sequence LELEI). **b**, BMDMs were analysed for CORO2A (red) and NCoR (green) protein expression and localization using fluorescence microscopy (original magnification $\times 60$). A merged image shows where CORO2A and the NCoR complex co-localize (yellow), and the position of cell nuclei (blue) is shown after staining with 4',6-diamidino-2-phenylindole (DAPI). **c**, ChIP for CORO2A binding to the *Nos2* and *Ccl2* promoters in BMDMs. Ig, immunoglobulin. **d**, Lysates from HeLa cells transfected with the stated LXR- β expression vectors (top) and treated with GW3965 were subjected to immunoprecipitation (IP) with CORO2A-specific antibody and analysed by immunoblotting (IB) against Flag. SUMO-Flag-LXR, expected migration position for SUMO-LXR; WT, wild type. **e**, ChIP for LXR binding to the *Nos2*, *Ccl2* and *Csf3* promoters in BMDMs after transfection with siRNA and treatment with or without GW3965. The *Csf3* promoter is a negative control. Knockdown efficiencies are provided in Supplementary Fig. 10. siControl, control siRNA; siCORO2A, *Coro2a*-specific siRNA. **f**, Lysates from HeLa cells transfected with the stated vectors (left) and treated with or without GW3965 were subjected to IP with LXR- or NCoR-specific antibody and analysed by IB against Flag. SIMmut, SIM-mutant CORO2A. **g**, Luciferase assays were performed in RAW 264.7 macrophages transfected with *Nos2*-luciferase reporter plasmids and the stated CORO2A expression vectors (bottom) and then stimulated with LPS in the presence of GW3965 or dexamethasone (DEX). **c**, **e**, **g**, Histograms show means. Error bars, s.e.m. *, $P < 0.02$ versus LPS; **, $P < 0.04$ versus control.

manner (Supplementary Fig. 3c). When overexpressed in RAW 264.7 macrophages, the SIM-mutant CORO2A binds to the NCoR complex residing on the *Nos2* promoter (Supplementary Fig. 4b). However, ligand-mediated recruitment of LXR and its repression function was significantly reduced by overexpression of this mutant, which is consistent with the mutant having a dominant-negative function (Fig. 1g and Supplementary Fig. 4c). By contrast, dexamethasone-induced repression, which is mediated by the glucocorticoid receptor via an NCoR- and SUMOylation-independent mechanism¹⁶, remained unaffected (Fig. 1g).

Unexpectedly, knockdown of *Coro2a* expression resulted in impaired responsiveness of a subset of TLR-inducible NCoR target genes, including *Nos2*, *Il10*, *Il1b* and *Ccl2*, but not of non-NCoR-regulated promoters,

such as that of the interferon-regulatory factor 1 (*Irf1*) gene (Fig. 2a). ChIP experiments further showed that knockdown of *Coro2a* resulted in a failure of LPS to promote clearance of NCoR from the *Nos2* and *Il1b* promoter (Fig. 2b and Supplementary Fig. 5a). As there is increasing evidence that oligomeric nuclear actin has diverse transcriptional roles¹⁷, we considered the possible role of nuclear actin in NCoR clearance. We confirmed that CORO2A interacts with actin and, on the basis of conserved sequence features that are required for the interaction of mouse CORO1 with actin^{14,18,19}, introduced point mutations in CORO2A (K11A/R13A) that severely compromised actin binding (Supplementary Fig. 5b).

Overexpression of either an amino-terminal deletion mutant of CORO2A lacking the actin-binding domain or the CORO2A K11A/R13A mutant blocked LPS-induced NCoR clearance and impaired

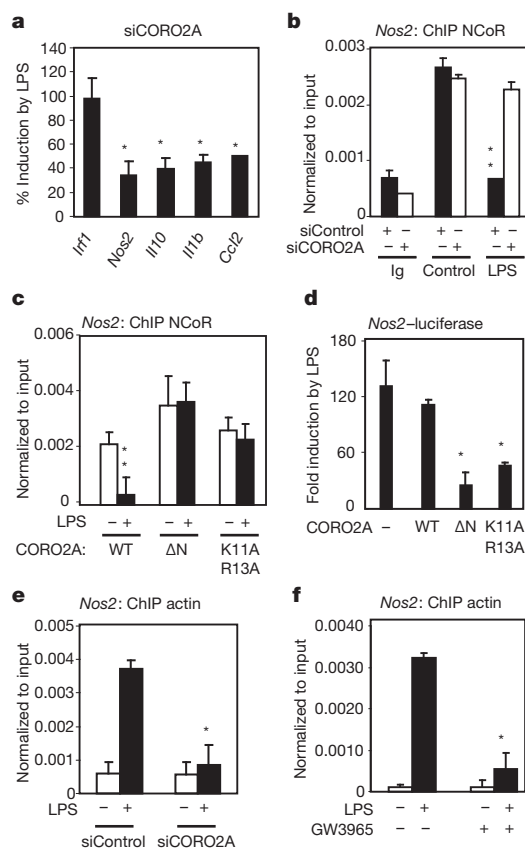


Figure 2 | The actin-binding domain of CORO2A is required for LPS de-repression of inflammatory gene promoters. **a**, BMDMs were transfected with *Coro2a*-specific siRNA or control siRNA and treated with or without LPS. Total RNA was then used to assay the levels of the indicated transcripts by quantitative PCR. Results are plotted as per cent induction of gene expression mediated by LPS in cells treated with *Coro2a*-specific siRNA. Induction of gene expression mediated by LPS in cells treated with control siRNA is set to be 100%. **b**, ChIP for IgG or NCoR binding to the *Nos2* promoter in BMDMs after transfection with the indicated siRNA (bottom) followed by 1 h stimulation with or without LPS. **c**, ChIP for NCoR binding to the *Nos2* promoter in RAW 264.7 macrophages transfected with *Nos2*-luciferase reporter plasmids and the indicated CORO2A expression vectors (bottom) and treated with or without LPS. Δ N, N-terminal deletion mutant of CORO2A lacking the actin-binding domain. **d**, Luciferase assays were performed in RAW 264.7 cells transfected with *Nos2*-luciferase reporter plasmids and the indicated expression vectors and treated with or without LPS. Luciferase activities in cells that were not treated with LPS were normalized to a value of 1.0. **e**, ChIP for actin binding to the *Nos2* promoter in BMDMs after transfection with the indicated siRNA (bottom) followed by 5 min stimulation with or without LPS. **f**, ChIP for actin binding to the *Nos2* promoter in BMDMs after treatment with or without LPS for 5 min, following pretreatment with or without GW3965. **a**–**f**, Data are presented as means \pm s.e.m. *, $P < 0.05$ versus LPS; **, $P < 0.05$ versus control.

activation of the *Nos2* promoter in RAW 264.7 macrophages (Fig. 2c, d). ChIP assays using an antibody (2G2) that specifically recognizes nuclear actin²⁰ showed transient recruitment of actin to the *Nos2* (Fig. 2e) and *Il1b* (Supplementary Fig. 5c) promoters coincident with the timing of LPS-induced NCoR clearance. Actin was not recruited to the TLR4-inducible, NCoR-independent *Csf3* promoter or to the ATP-binding cassette A1 (*Abca1*) gene promoter, which is a positive transcriptional target of LXRs that is occupied by NCoR in the absence of LXR agonists^{4,21} (Supplementary Fig. 5c). Actin recruitment was dependent on both NCoR and phosphorylation of Jun, as it was abolished in primary macrophages by *Ncor1* knockdown and in RAW 264.7 macrophages by overexpression of a mutant form of Jun that cannot be phosphorylated (Supplementary Fig. 5d, e). LPS-induced actin recruitment to the *Nos2* promoter in macrophages was also abolished by siRNA-mediated knockdown of *Coro2a* (Fig. 2e). Short-term treatment of primary macrophages with latrunculin A, which inhibits actin polymerization²², similarly blocked LPS-dependent NCoR clearance and induction of *Nos2* messenger RNA (Supplementary Fig. 6a, b). By contrast, latrunculin A did not affect TLR4 activation of the

NCoR-independent gene *Irf1*, LXR activation of the *Abca1* gene (Supplementary Fig. 6c–e) or TLR4-dependent phosphorylation of Jun (Supplementary Fig. 6f, g). Notably, treatment of primary macrophages with the LXR ligand GW3965 blocked LPS-induced actin recruitment (Fig. 2f) but not Jun phosphorylation (Supplementary Fig. 6h), suggesting that SUMOylated LXRs may exert anti-inflammatory effects by blocking the actin-dependent step required for NCoR clearance.

LXRs are unable to suppress the transcriptional responses of NCoR target genes to pro-inflammatory signals that induce CaMKII activation, including the TLR1 and TLR2 agonist Pam₃CSK₄ (Pam3) (ref. 21), the TLR2 and TLR6 agonist FSL-1 and *Salmonella enterica* serovar Typhimurium²³ (Supplementary Fig. 7a, b). Co-immunoprecipitation studies in RAW 264.7 macrophages showed that Pam3-mediated signalling significantly reduced the interaction of SUMO–LXR-β with CORO2A in a CaMKIIγ-dependent manner (Fig. 3a). Because the interaction of LXR with CORO2A requires SUMOylation, we considered the possible involvement of deSUMOylating enzymes in negatively regulating LXR repression functions. Using siRNAs to knock down SUMO proteases expressed in primary macrophages, we found

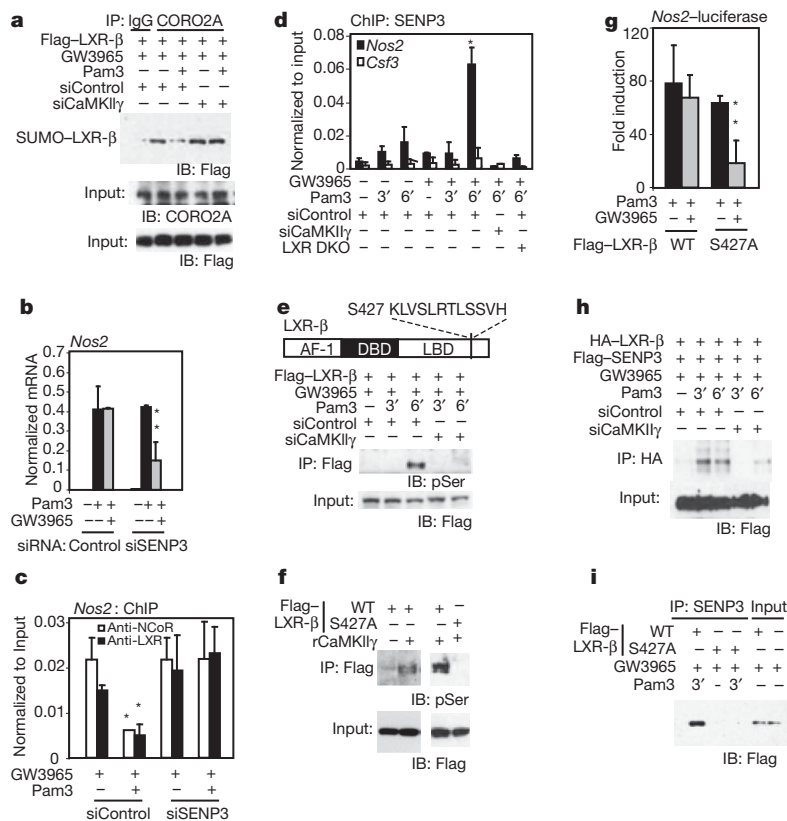


Figure 3 | The LXR-CORO2A axis is disrupted by CaMKIIγ phosphorylation and SENP3 deSUMOylation of LXR. **a**, RAW 264.7 macrophages were transfected with Flag-LXR-β expression vector and siRNAs as indicated. Cells were pretreated with GW3965 and challenged with Pam3. Lysates were subjected to IP with anti-CORO2A antibodies and analysed by IB against Flag. Knockdown efficiencies for CamKIIγ are provided in Supplementary Fig. 10c. siCaMKIIγ, *Camk2g*-specific siRNA. **b**, BMDMs were transfected with control siRNA or *Senp3*-specific siRNA (siSENP3) and pretreated with or without GW3965 followed by Pam3. *Nos2* transcript levels were assayed by quantitative PCR. Knockdown efficiencies for SENP3 are provided in Supplementary Fig. 10d. **c**, ChIP for LXR and NCoR binding to the *Nos2* promoter in BMDMs after transfection with the indicated siRNAs. **d**, ChIP for SENP3 occupancy of the *Nos2* or *Csf3* promoter in siRNA-transfected WT or *Lxra*^{-/-} *Lxrb*^{-/-} (LXR DKO) BMDMs. Cells were pretreated with GW3965 and then stimulated with Pam3. **e**, Domain structure of LXR. A predicted CaMKII phosphorylation site at S427 in the ligand-binding domain (LBD) is highlighted. RAW 264.7 cells were transfected with Flag-LXR-β expression vector and control or *Camk2g*-specific siRNAs. Cells were

treated with GW3965 and challenged with Pam3 for 0, 3 and 6 min. Lysates were subjected to IP with anti-Flag antibody and IB for phosphoserine (pSer, top) or Flag (bottom). AF-1, activation function-1 domain; DBD, DNA-binding domain. **f**, Flag-WT LXR-β or S427A mutant LXR-β expression vector was expressed in HeLa cells, captured on anti-Flag agarose and incubated with 0.5 μg activated recombinant CaMKIIγ (rCaMKIIγ). Anti-phosphoserine antibody was used to detect phosphorylated proteins by IB. **g**, RAW 264.7 cells were transfected with *Nos2*-luciferase reporter plasmids and the indicated expression vectors and treated with GW3965 followed by Pam3. Luciferase activity is represented as fold induction over the responses of untreated cells. **h**, RAW 264.7 cells were transfected with Flag-SENP3 and HA-LXR-β expression vectors, as well as control or *Camk2g*-specific siRNAs as indicated. Lysates were subjected to IP with anti-HA antibody, and the presence of SENP3 was detected by anti-Flag antibody. **i**, RAW 264.7 cells were transfected with the indicated Flag-LXR-β expression vectors, treated with GW3965 and challenged with Pam3. Lysates were used in IP assays with anti-SENP3 antibody and were analysed by IB against Flag. **b**, **c**, **d**, **g**, Data are presented as means ± s.e.m. *, *P* < 0.04 versus control; **, *P* < 0.04 versus Pam3.

that knockdown of *Senp3* restored the ability of LXRs to suppress TLR1/TLR2-dependent *Nos2* expression (Fig. 3b), interact with the *Nos2* promoter and prevent NCoR clearance (Fig. 3c). ChIP experiments further demonstrated that SENP3 was rapidly recruited to the *Nos2* promoter, but not the *Csf3* promoter, after stimulation with Pam3, and this recruitment was dependent on CaMKII γ (Fig. 3d). Knockdown of *Camk2g* also restored LXR-mediated transrepression of *Il1b* and *Bic* (the precursor of miR-155), as well as abolished SENP3 recruitment to these gene promoters (Supplementary Fig. 7c–f).

Co-immunoprecipitation experiments suggested a sequence in which Pam3 induced first the interaction between CaMKII and LXR, followed shortly thereafter by the SENP3–LXR interaction (Supplementary Fig. 8a). As both LXR- α and LXR- β contain a conserved motif that conforms to a CaMKII phosphorylation site (S427 in LXR- β) (Fig. 3e), we considered the possibility that LXRs were themselves the targets of CaMKII γ kinase activity and that phosphorylation of LXR might promote its interaction with SENP3. Consistent with this possibility, TLR1/TLR2 activation was found to result in robust serine phosphorylation of LXR- β in a CaMKII γ -dependent manner (Fig. 3e). Wild-type, Flag-tagged LXR- β was a substrate for recombinant CaMKII γ *in vitro*, but Flag-tagged LXR- β with a serine-to-alanine point mutation at residue 427 was not (Fig. 3f and Supplementary Fig. 8b). In addition, the phospho-null mutant of LXR continued to associate with the CORO2A–NCoR-bound *Nos2* promoter and retained transrepression activities on TLR1/TLR2 signalling (Fig. 3g and Supplementary Fig. 8c), recapitulating the effect of knocking down *Camk2g*²¹. This finding suggests that S427 of LXR- β is probably the major or only substrate of CaMKII that is relevant to inactivating the LXR-mediated transrepression pathway. By contrast, a phosphomimic mutant of LXR- β (S427D) was not able to interact with CORO2A to promote transrepression of the *Nos2*–luciferase reporter construct in RAW 264.7 macrophages (Supplementary Fig. 8d, e).

To investigate whether CaMKII phosphorylation of LXR- β created a docking site for SENP3, RAW 264.7 macrophages were transfected with expression vectors encoding HA–LXR- β , Flag–SENP3, and control or *Camk2g*-specific siRNAs. Cells were then treated with GW3965 in the absence or presence of Pam3. Immunoprecipitation assays demonstrated that TLR1/TLR2 activation induced a rapid interaction between SENP3 and LXR- β that was dependent on CaMKII γ (Fig. 3h). This interaction was not observed when the LXR- β S427A mutant was used (Fig. 3i).

We next used a thioglycollate-induced sterile peritonitis model²⁴ to investigate potential roles of the CORO2A–NCoR clearance pathway *in vivo*. Injection of thioglycollate into the peritoneal cavity leads to a massive infiltration of activated macrophages, which by 3 days after injection account for more than 90% of the total peritoneal cavity cell population. *In vivo* knockdown of *Coro2a* expression in this macrophage population, using two independent methods, significantly reduced expression of *Ccl2*, *Il1b* and the CXCL-chemokine ligand 10 gene (*Cxcl10*) but not *Abca1* (Fig. 4a and Supplementary Fig. 9a) and resulted in significantly increased occupancy of the *Ccl2*, *Il1b* and *Cxcl10* promoters by the NCoR complex (Fig. 4b). The presence of phosphorylated (active) CaMKII in the elicited macrophage population (Supplementary Fig. 9b) suggested that an endogenous LXR-mediated repression pathway in these cells might be inactivated. Consistent with this possibility, co-immunoprecipitation studies demonstrated that LXR- α and LXR- β were not associated with CORO2A in elicited macrophages in control animals but became associated with CORO2A in animals that were treated with the CaMKII inhibitor KN-93 (Supplementary Fig. 9b). In addition, treatment with KN-93 increased occupancy by the NCoR complex of the *Ccl2*, *Cxcl10* and *Il1b* promoters in macrophages in wild-type mice but not in mice lacking both LXR- α and LXR- β (*Lxra*^{−/−}*Lxrb*^{−/−} mice) (Fig. 4c). Finally, treatment with KN-93 reduced the expression of *Ccl2*, *Cxcl10* and *Il1b* in wild-type mice but not in *Lxra*^{−/−}*Lxrb*^{−/−} mice (Fig. 4d), suggesting that pharmacological inhibition of CaMKII

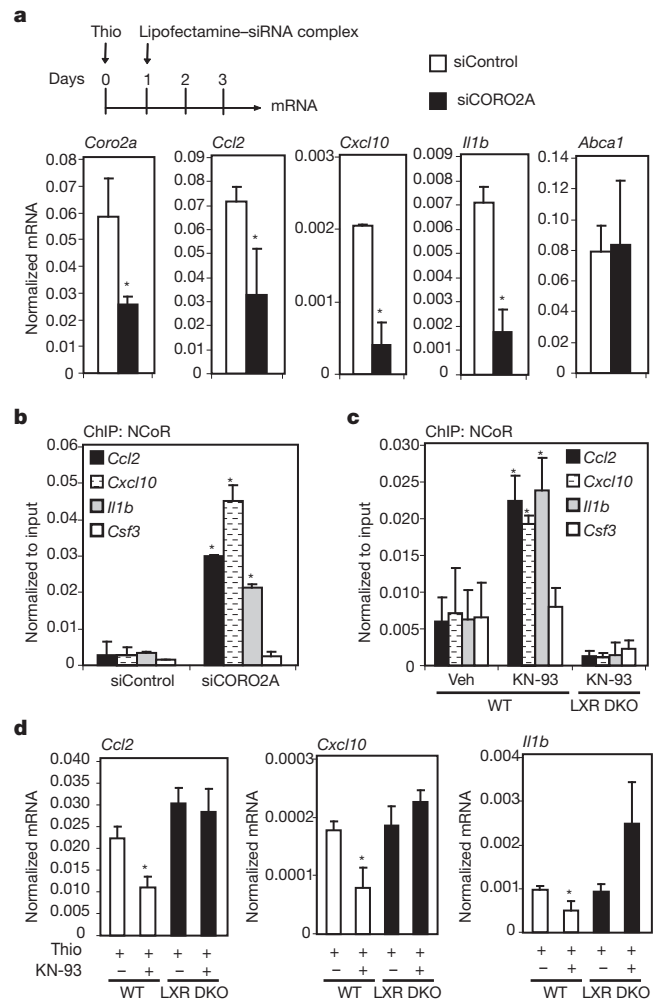


Figure 4 | Function of the CORO2A–LXR–CaMKII pathway in thioglycollate-elicited peritonitis. **a**, Sterile peritonitis was initiated by intraperitoneal injection of thioglycollate (Thio) on day 0. Mice were injected with lipofectamine–siRNA complexes on day 1, and peritoneal exudate cells were recovered for analysis of *Coro2a*, *Ccl2*, *Cxcl10*, *Il1b* and *Abca1* mRNA on day 3 ($n = 4$ per condition). Values are normalized to glyceraldehyde-3-phosphate dehydrogenase (*Gapdh*) mRNA. Data are presented as means \pm s.e.m. *, $P < 0.05$ versus siControl. **b**, ChIP for NCoR binding to the *Ccl2*, *Cxcl10*, *Il1b* and *Csf3* promoters in peritoneal exudate cells described in **a** ($n = 3$ per condition). Data are presented as means \pm s.e.m. *, $P < 0.05$ versus siControl. **c**, ChIP for NCoR binding to the *Ccl2*, *Cxcl10*, *Il1b* and *Csf3* promoters in peritoneal exudate cells derived from WT or LXR DKO mice treated with KN-93 or vehicle (Veh) as a control as indicated ($n = 3$ per condition). Data are presented as means \pm s.e.m. *, $P < 0.05$ versus non-KN-93 treated WT animals. **d**, *Ccl2*, *Cxcl10* and *Il1b* expression in peritoneal exudate cells derived from WT ($n = 5$ per condition) or LXR DKO ($n = 3$ per condition) mice treated with KN-93 as indicated. Data are presented as means \pm s.e.m. *, $P < 0.01$ versus non-KN-93 treated WT animals. **a–d**, Statistical significance was determined by a two-tailed Student's *t*-test.

‘rescues’ endogenous LXR-mediated transrepression activity in this inflammatory context.

Collectively, these findings provide evidence that CORO2A functions as an NCoR exchange factor that is required for de-repression of TLR target genes in macrophages (Supplementary Fig. 1). Recent findings provide evidence that nuclear actin has roles in the movement of specific chromosomal loci to transcriptional ‘hubs’^{25,26}, raising several interesting possibilities for how the localization of repression machinery is dynamically regulated. The ability of other members of the coronin family to mediate disassembly of actin polymers in the cytoplasm^{14,27} suggests that CORO2A may function to release inflammatory response genes from localized actin networks that are dedicated to repression

functions. The integrated functions of CORO2A as both a docking site for SUMOylated LXRs and as an actin-dependent NCoR exchange factor suggest a parsimonious transrepression model in which SUMOylated LXRs prevent NCoR turnover and repress responses to LPS by blocking actin recruitment. The ability of CaMKII γ to inactivate the LXR-mediated transrepression pathway by creating a docking site for SENP3 further identifies a new transcriptional role for SUMO proteases. This finding also uncovers an entry point for negative regulation of the LXR-mediated repression pathway that could be engaged by numerous other signalling pathways that mobilize intracellular calcium, such as those involving purinergic receptors²¹. It is notable that the SUMO2/SUMO3-specific SIM in CORO2A and the CaMKII γ phosphorylation sites in LXRs are highly conserved across vertebrate species, suggesting that there has been evolutionary pressure to maintain these regulatory pathways. Although such pressures presumably relate to key functions of the innate immune system in responding to infection and injury, signal-induced inactivation of the LXR-mediated transrepression pathway may also contribute to pathological forms of inflammation.

METHODS SUMMARY

BMDMs were generated from 6-week-old, wild-type C57BL/6 (Harlan) and *Lxra*^{-/-} *Lxrb*^{-/-} mice as described previously¹⁵. RAW 264.7 macrophages were cultured as described previously⁵. LPS, Pam3 and GW3965 were used at a concentration of 100 ng ml⁻¹, 300 ng ml⁻¹ and 1 μ M, respectively. GW3965 was used to pretreat macrophages for 1 h. LPS and Pam3 treatment was 1 h for ChIP assays and 6 h for luciferase assays and mRNA expression analysis, unless otherwise noted in the figure. ChIP assays were performed as described in detail previously¹⁵. Proximal promoter regions of *Nos2*, *Ccl2*, *Il1b*, *Csf3*, *Abca1* and *Bic* were amplified by real-time PCR. Values determined for mRNA, using real-time PCR, are normalized to glyceraldehyde-3-phosphate dehydrogenase (*Gapdh*) mRNA content. Data are represented as mean \pm s.e.m. of three independent experiments in duplicates. RAW 264.7 macrophages or HeLa cells were transfected with wild-type or mutant expression vectors for LXR and CORO2A as described previously²¹. For RNA interference (RNAi) experiments in cultured primary macrophages, scrambled control or SMARTpool siRNAs (Dharmacon) directed against *Coro2a*, *Senp3*, *Camk2g* and *Ncor1* were transfected into primary macrophages using lipofectamine 2000 (Invitrogen) as described previously¹⁵. For *in vitro* CaMKII kinase assays, 0.5 μ g recombinant CaMKII γ (Upstate Biotechnology) was incubated with bacterially purified GST-LXR- β (full-length) fusion proteins bound to glutathione beads. Thioglycollate-elicited sterile peritonitis was induced as described previously²⁸. Briefly, 2 ml thioglycollate medium was delivered to each animal by intraperitoneal injection, and elicited macrophages in the peritoneal cavities were collected with 10 ml of PBS after 3 days. For *in vivo* RNAi experiments, 100 μ g scrambled control siRNAs or *Coro2a*-specific siRNA was complexed in lipofectamine 2000 and serum-depleted medium (in 1 ml final volume) and delivered to animals by intraperitoneal injection as described previously²⁹. Alternatively, scrambled control siRNAs and *Coro2a*-specific siRNA were prepared in glucan-encapsulated RNAi particles (GeRPs) and delivered to animals by intraperitoneal injection for 5 consecutive days as described previously³⁰. Statistical significance was determined by two-tailed Student's *t*-test.

Full Methods and any associated references are available in the online version of the paper at www.nature.com/nature.

Received 12 April; accepted 22 November 2010.

- Medzhitov, R. & Horng, T. Transcriptional control of the inflammatory response. *Nature Rev. Immunol.* **9**, 692–703 (2009).
- Beutler, B. A. TLRs and innate immunity. *Blood* **113**, 1399–1407 (2009).
- Ogawa, S. *et al.* A nuclear receptor corepressor transcriptional checkpoint controlling activator protein 1-dependent gene networks required for macrophage activation. *Proc. Natl Acad. Sci. USA* **101**, 14461–14466 (2004).
- Pascual, G. *et al.* A SUMOylation-dependent pathway mediates transrepression of inflammatory response genes by PPAR- γ . *Nature* **437**, 759–763 (2005).
- Ghisletti, S. *et al.* Parallel SUMOylation-dependent pathways mediate gene- and signal-specific transrepression by LXRs and PPAR γ . *Mol. Cell* **25**, 57–70 (2007).
- Blaschke, F. *et al.* A nuclear-receptor corepressor-dependent pathway mediates suppression of cytokine-induced C-reactive protein gene expression by liver X receptor. *Circ. Res.* **99**, e88–e99 (2006).

- Venteclef, N. *et al.* GPS2-dependent corepressor/SUMO pathways govern anti-inflammatory actions of LXR-1 and LXR β in the hepatic acute phase response. *Genes Dev.* **24**, 381–395 (2010).
- Yoon, H. G. *et al.* Purification and functional characterization of the human N-CoR complex: the roles of HDAC3, TBL1 and TBLR1. *EMBO J.* **22**, 1336–1346 (2003).
- Yoon, H. G. *et al.* N-CoR mediates DNA methylation-dependent repression through a methyl CpG binding protein Kaiso. *Mol. Cell* **12**, 723–734 (2003).
- Qiyang, J. *et al.* Direct binding of CoREST1 to SUMO-2/3 contributes to gene-specific repression by the LSD1/CoREST1/HDAC complex. *Mol. Cell* **34**, 145–154 (2009).
- Wu, C. *et al.* BioGPS: an extensible and customizable portal for querying and organizing gene annotation resources. *Genome Biol.* **10**, R130 (2009).
- Lattin, J. E. *et al.* Expression analysis of G protein-coupled receptors in mouse macrophages. *Immunome Res.* **4**, 5 (2008).
- Uetrecht, A. C. & Bear, J. E. Coronins: the return of the crown. *Trends Cell Biol.* **16**, 421–426 (2006).
- Gandhi, M., Achard, V., Blanchoin, L. & Goode, B. L. Coronin switches roles in actin disassembly depending on the nucleotide state of actin. *Mol. Cell* **34**, 364–374 (2009).
- Ghisletti, S. *et al.* Cooperative NCoR/SMRT interactions establish a corepressor-based strategy for integration of inflammatory and anti-inflammatory signaling pathways. *Genes Dev.* **23**, 681–693 (2009).
- Ogawa, S. *et al.* Molecular determinants of crosstalk between nuclear receptors and Toll-like receptors. *Cell* **122**, 707–721 (2005).
- Bettinger, B. T., Gilbert, D. M. & Amberg, D. C. Actin up in the nucleus. *Nature Rev. Mol. Cell Biol.* **5**, 410–415 (2004).
- Appleton, B. A., Wu, P. & Wiesmann, C. The crystal structure of murine coronin-1: a regulator of actin cytoskeletal dynamics in lymphocytes. *Structure* **14**, 87–96 (2006).
- Gandhi, M., Jangi, M. & Goode, B. L. Functional surfaces on the actin-binding protein coronin revealed by systematic mutagenesis. *J. Biol. Chem.* **285**, 34899–34908 (2010).
- Gonsior, S. M. *et al.* Conformational difference between nuclear and cytoplasmic actin as detected by a monoclonal antibody. *J. Cell Sci.* **112**, 797–809 (1999).
- Huang, W. *et al.* Transcriptional integration of TLR2 and TLR4 signaling at the NCoR derepression checkpoint. *Mol. Cell* **35**, 48–57 (2009).
- Yarmola, E. G. *et al.* Actin-latrunculin A structure and function. Differential modulation of actin-binding protein function by latrunculin A. *J. Biol. Chem.* **275**, 28120–28127 (2000).
- Gewirtz, A. T. *et al.* *Salmonella typhimurium* induces epithelial IL-8 expression via Ca²⁺-mediated activation of the NF- κ B pathway. *J. Clin. Invest.* **105**, 79–92 (2000).
- Henderson, R. B., Hobbs, J. A., Mathies, M. & Hogg, N. Rapid recruitment of inflammatory monocytes is independent of neutrophil migration. *Blood* **102**, 328–335 (2003).
- Hu, Q. *et al.* Enhancing nuclear receptor-induced transcription requires nuclear motor and LSD1-dependent gene networking in interchromatin granules. *Proc. Natl Acad. Sci. USA* **105**, 19199–19204 (2008).
- Fullwood, M. J. *et al.* An oestrogen-receptor- α -bound human chromatin interactome. *Nature* **462**, 58–64 (2009).
- Brieher, W. M., Kueh, H. Y., Ballif, B. A. & Mitchison, T. J. Rapid actin monomer-insensitive depolymerization of *Listeria* actin comet tails by cofilin, coronin, and Aip1. *J. Cell Biol.* **175**, 315–324 (2006).
- Segal, B. H. *et al.* Thioglycollate peritonitis in mice lacking C5, 5-lipoxygenase, or p47^{phox}, complement, leukotrienes, and reactive oxidants in acute inflammation. *J. Leukoc. Biol.* **71**, 410–416 (2002).
- Amarzguioui, M. *et al.* *Ex vivo* and *in vivo* delivery of anti-tissue factor short interfering RNA inhibits mouse pulmonary metastasis of B16 melanoma cells. *Clin. Cancer Res.* **12**, 4055–4061 (2006).
- Aouadi, M. *et al.* Orally delivered siRNA targeting macrophage Map4k4 suppresses systemic inflammation. *Nature* **458**, 1180–1184 (2009).

Supplementary Information is linked to the online version of the paper at www.nature.com/nature.

Acknowledgements We thank S. Amano for preparation of GeRP delivery spheres. We thank L. Bautista for assistance with preparation of the manuscript. W.H. was supported by NRSA 1F31DK083913. These studies were supported by National Institutes of Health grants CA52599, DK074868, HC088093 and DK085853 and a Leducq Foundation Transatlantic Network Grant. M.G.R. is an investigator of the Howard Hughes Medical Institute.

Author Contributions W.H., S.G., K.S., M.C., B.L.G., M.G.R. and C.K.G. conceived the project and planned experiments and analysis, which were performed by W.H., S.G., K.S., M.G., M.A., G.T., D.Z. and J.Y. The entire project was supervised by C.K.G., who wrote the manuscript with W.H.

Author Information Reprints and permissions information is available at www.nature.com/reprints. The authors declare competing financial interests: details accompany the full-text HTML version of the paper at www.nature.com/nature. Readers are welcome to comment on the online version of this article at www.nature.com/nature. Correspondence and requests for materials should be addressed to C.K.G. (ckg@ucsd.edu).

METHODS

Reagents and plasmids. LPS and anti-Flag M2 antibodies were obtained from Sigma. Pam3 was from InvivoGen. GW3965 was kindly provided by GlaxoSmithKline. KN-93 was purchased from Calbiochem. Goat anti-CORO2A, rabbit anti-CORO2A, CaMKII, SENP3, LXR- α /LXR- β , Myc, HDAC4, goat anti-NCoR and normal rabbit and goat antibodies were from Santa Cruz Biotechnology. Rabbit anti-NCoR antibodies were from ABR. Anti-phospho-CaMKII antibodies and anti-tubulin antibodies were from Cell Signaling Technology, and anti-phosphoserine antibodies were from Chemicon. The reporter plasmid *Nos2*-luciferase has been described previously⁴. The expression vector encoding VP16-LXR- β was obtained from Xceptor. The expression constructs encoding Myc-SUMO3, Flag-LXR- β and HA-LXR- β have been described previously⁵. Mutations in expression vectors were made using the QuikChange Site-Directed Mutagenesis Kit (Stratagene).

Plasmid and siRNA transfection. Transient transfections of RAW 264.7 macrophages were performed as described previously⁵, using SuperFect Transfection Reagent (Qiagen). For siRNA experiments in RAW 264.7 cells, transfections were carried out with SuperFect (100 nM) for 48 h before activation with TLR ligands. Transfection data are presented as mean \pm s.e.m. of three independent experiments in triplicates. For RNA interference (RNAi) experiments in cultured primary macrophages, scrambled control or SMARTpool siRNAs (Dharmacon) directed against *Coro2a*, *Senp3*, *Camk2g* and *Ncor1* (see below) were transfected into primary macrophages by using lipofectamine 2000 (Invitrogen) as described previously¹⁵.

The following pools of four siRNAs were used in *in vitro* studies, and the siRNAs that are underlined were used for *in vivo* experiments. siGENOME Non-Targeting siRNA pool for controls (Dharmacon, D-001206-13): AUGAACGUGAAUUG CUCAA, UAAGGCUAUGAAGAGAUAC, AUGUAUUGGCCUGUAUUG, UAGCGACUAAACACAUCAA. siGENOME SMARTpool for mouse *Coro2a* (Dharmacon, D-058157): GAAAGUUGGACCCUCACUA, GCAAGAUUCGG AUUGUUGA, GGAUCGGUAUCAUGCCAAA, GAGGGAACGUCUUGGAC AU. siGENOME SMARTpool for mouse *Senp3* (Dharmacon, D-057149): GGACCACAGUGCCAACUAG, CGACGUACCAUCACCUAUU, GCUCUCC GACCCUCUCAUA, CAAACUCCGUCGUCAGAUC. siGENOME SMARTpool for mouse *Camk2g* (Dharmacon, D-040009): GGAAAGAUCUUUAUGGAAA, GUAGAGUGCUUACGCAAAU, GGAGUUGUUGAAGACAUU, AAACAU CUACGCAGGAAUA. siGENOME SMARTpool for mouse *Ncor1* (Dharmacon, D-058556): GAAAUCCACGGCAAGAU, CCAGGUCGAUGACAAGUGA, GCAGUGGAAGGAAGUAUA, GAUCAUCACCCGGCAAAU.

Preparation of GeRPs containing *Coro2a*-specific siRNA. Particles of β 1,3-D-glucan were purified from baker's yeast by a series of alkaline and solvent extractions, hydrolysing the outer cell wall and intracellular components and yielding purified, porous 2–4 μ m β 1,3-D-glucan particles, as described previously³⁰. To load siRNA into glucan shells for injection into mice, 5 nmol *Coro2a*-specific siRNA was incubated with 50 nmol Endo-Porter peptide (Gene Tools) in acetate buffer, pH 4.8, for 15 min at 21 °C. The siRNA–Endo-Porter solution was added to

1 mg glucan shells and then vortexed and incubated for 1 h. Tris-EDTA buffer, pH 8.4, was added to the particles, which were incubated for 15 min at room temperature to adjust the pH. The resultant glucan-encapsulated siRNA particles (GeRPs) were resuspended in PBS for intraperitoneal injections.

RNA isolation and real-time PCR. Total RNA (isolated by RNeasy Kit, Qiagen) was prepared from MEFs or macrophages treated as indicated in each figure legend. Total RNA (1 μ g) was used for complementary DNA synthesis, and 1 μ l cDNA was used for real-time PCR analysis, which was performed on a 7300 Real-time PCR System (Applied Biosystems). Values are normalized to *Gapdh* mRNA content. Data are presented as mean \pm s.e.m. of at least three independent experiments in duplicates.

Primers for quantitative PCR analysis of mRNA are as follows: *Gapdh* (AA TGTGTCCGTCTGGATCT, CATCGAAGGTGGAAGAGTGG); *Nos2* (AGCCT TGCATCCTCATTGG, CACTCTCTTGGCGGACCATCT); *Irf1* (AGGCCGATAC AAAGCAGGAGA, GCTGCCCTTGTCTCTACTCTG); *Il1b* (GCAACTGTTCC TGAACCAACT, ATCTTTTGGGGTCCGTCAACT); *Ccl2* (CCCAATGAGTAG GCTGGAGA, TCTGGACCCATTCTCTCTTG); *Senp3* (TTTGACTCCAGCGA ACTCT, AAAGAGACTATACAGGGGACCG); *Coro2a* (AGGGGATCGGTATC ATGCCAA, CATGGACACTGGCTCGATGAG); *Ncor1* (CTGTGCATGAGAAG CAGGAC, TGGTGAAGAATGAAGGCAAG); *Abca1* (AAAACCGCAGACATC CTTCAG, CATACCGAAACTCGTTCACCC); *Bic* (AAACCAGGAAGGGGAA GTGT, GTCAGTCAGAGGCCAAAACC); *Camk2g* (AACAAAAACAGTCTCG TAAGCCC, GCCCTTGATCCCATCTGTAGC); *Gps2* (AGGCGAAAGGAACA GAGTGA, GAGTACCTGGGCGATTGTGT).

Primers for promoter ChIP and quantitative PCR analysis are as follows: *Nos2* (GGAGTGTCCATCATGAATGAG, CAACTCCCTGTAAAGTTGTGACC); *Il1b* (GGACAATTGTGCAGATGGTG, CCTACCTTTGTTCCGCACAT); *Bic* (GCTG GAGACAAGTCCCTTGA, TCCTCCAGTGATTCCTTTGG); *Ccl2* (TCCAGGGT GATGCTACTCCT, AGTGAGAGTTGGCTGGTGCT); *Hp* (CACTAAGGCAG CATGGTTGA, TGGGAGAGGGTGTGGTTAG); *Csf3* (CCTACCTAGGGTGC TGTGGA, GGACAAACATCCCAGAGAGAA); *Abca1* (GGGGCTGAGCAAAC TAACAA, TTGTGGGTGTTGCTTTTTGA).

Co-immunoprecipitation assay. RAW 264.7 macrophages or HeLa cells were transfected with wild-type or mutant expression vectors for LXR and CORO2A. Cells were lysed in 10 mM Tris-HCl, pH 7.5, 450 mM NaCl, 0.5% NP-40, 1 mM EDTA with protease inhibitors and 10 μ M NEM. Co-immunoprecipitations were carried out with anti-SENP3, anti-LXR, anti-CaMKII, anti-NCoR or anti-Flag antibodies and detected by western blotting.

Kinase assays. For *in vitro* CaMKII kinase assays, 0.5 μ g recombinant CaMKII γ (Upstate Biotechnology) was incubated with bacterially purified GST-LXR- β (full-length) fusion proteins attached to glutathione beads. The beads were washed, boiled and then subjected to SDS-PAGE. Serine phosphorylation was detected by anti-phosphoserine antibody (Chemicon).

Statistics. Statistical significance was determined by two-tailed Student's *t*-test.

Embryonic lethal phenotype reveals a function of TDG in maintaining epigenetic stability

Daniel Cortázar^{1*}, Christophe Kunz^{1*}, Jim Selfridge², Teresa Lettieri^{3†}, Yusuke Saito¹, Eilidh MacDougall², Annika Wirz¹, David Schuermann¹, Angelika L. Jacobs¹, Fredy Siegrist⁴, Roland Steinacher^{1†}, Josef Jiricny³, Adrian Bird² & Primo Schär¹

Thymine DNA glycosylase (TDG) is a member of the uracil DNA glycosylase (UDG) superfamily of DNA repair enzymes. Owing to its ability to excise thymine when mispaired with guanine, it was proposed to act against the mutability of 5-methylcytosine (5-mC) deamination in mammalian DNA¹. However, TDG was also found to interact with transcription factors^{2,3}, histone acetyltransferases⁴ and *de novo* DNA methyltransferases^{5,6}, and it has been associated with DNA demethylation in gene promoters following activation of transcription^{7–9}, altogether implicating an engagement in gene regulation rather than DNA repair. Here we use a mouse genetic approach to determine the biological function of this multifaceted DNA repair enzyme. We find that, unlike other DNA glycosylases, TDG is essential for embryonic development, and that this phenotype is associated with epigenetic aberrations affecting the expression of developmental genes. Fibroblasts derived from *Tdg* null embryos (mouse embryonic fibroblasts, MEFs) show impaired gene regulation, coincident with imbalanced histone modification and CpG methylation at promoters of affected genes. TDG associates with the promoters of such genes both in fibroblasts and in embryonic stem cells (ESCs), but epigenetic aberrations only appear upon cell lineage commitment. We show that TDG contributes to the maintenance of active and bivalent chromatin throughout cell differentiation, facilitating a proper assembly of chromatin-modifying complexes and initiating base excision repair to counter aberrant *de novo* methylation. We thus conclude that TDG-dependent DNA repair has evolved to provide epigenetic stability in lineage committed cells.

TDG is one of four enzymes with UDG activity in mammalian cells, but its biological function has remained enigmatic¹⁰. We thus set out to generate and phenotypically investigate a *Tdg* knockout mouse (Supplementary Fig. 1a–c). ESC clones carrying the targeted allele gave rise to healthy heterozygous *Tdg* knockout mice but attempts to generate homozygous null mutants failed, indicating that TDG-deficiency may cause embryonic lethality. This was unexpected, given the generally mild phenotype of other DNA glycosylase knockouts¹¹. In timed matings, *Tdg* null embryos isolated up to embryonic day (E) 10.5 appeared alive and normal, whereas those isolated at E12.5 were dead, and none were detectable at E16.5 (Fig. 1a and Supplementary Fig. 1d). *Tdg* null embryos at E10.5 produced viable fibroblasts (MEFs) but only a third of E11.5 embryos did so, suggesting that by this stage most of them were dead. We thus concluded that lethality in *Tdg* null embryos occurs around E11.5. For the actual cause of lethality, closer examination of the *Tdg* null embryos at E10.5 indicated internal haemorrhage, and evidence for haemorrhagic necrosis (data not shown), but otherwise did not reveal an informative pathology.

We then explored the essential function of TDG in MEFs and ESCs, first addressing a potential DNA repair defect by classical genotoxicity and mutator analyses. The TDG status did not affect cell survival

following ionizing radiation or H₂O₂ exposure, both of which induce DNA base lesions processed by TDG *in vitro*¹⁰, nor did it affect mutation frequencies in a Big Blue transgenic mutation assay (Supplementary Fig. 2). We therefore concluded that the role of TDG in the repair of canonical base damage is minor and therefore unlikely to account for its essential function in mouse embryogenesis.

We next investigated a possible involvement of TDG in gene regulation by expression profiling of TDG-proficient and -deficient MEFs. To limit potential clonal biases, we compared the transcriptomes of early passages of litter-matched populations of SV40 immortalized MEFs. This identified 461 differentially transcribed genes ($P \leq 0.05$, fold change (FC) ≥ 1.5 , Fig. 1b), comprising many transcription factors and, thus, likely reflecting both direct and indirect consequences of TDG loss. Global pathway analyses revealed gene networks associated with embryogenesis and development as being most significantly misregulated in the absence of TDG (Supplementary Fig. 3a). Four out of six target genes analysed showed TDG-dependent differential expression also in independently isolated primary MEFs (Supplementary Fig. 3b).

Considering its putative involvement in DNA demethylation^{7–9}, we next investigated a possible occurrence of aberrant promoter methylation in TDG-deficient cells. We examined the CpG islands in the promoters of *Hoxa10*, *Hoxd13*, *Sfrp2*, *Twist2* and *Rarb*, all of which were downregulated in TDG-deficient MEFs (Fig. 1b and Supplementary Fig. 3a). These genes are developmentally regulated by the polycomb repressive system¹² and their promoter CpG islands are unmethylated in most normal tissues but subject to aberrant *de novo* methylation in human cancers^{13,14}. Na-bisulphite sequencing of the respective CpG islands revealed an increased occurrence of *de novo* methylation in the TDG-deficient MEFs (Fig. 1c and Supplementary Figs 4 and 5a). The patterns and frequency of these methylation events indicated that the loss of TDG generates hotspots of *de novo* methylation in certain gene promoters. We then used chromatin immunoprecipitation (ChIP) to examine a possible association of TDG with the promoters of these and additional differentially expressed genes. Compared with a randomly chosen intergenic sequence or the silent promoters of *Oct4* and *Tuba3*, DNA fragments surrounding the promoters of all genes examined were significantly enriched in the TDG precipitates (Fig. 1d). This indicated that TDG is targeted to specific gene promoters, possibly to protect them from acquiring aberrant CpG methylation and eventual epigenetic silencing. Consistently, further examination of the chromatin status revealed a general loss of activating (H3K4me2) and a concomitant increase of repressive histone marks (H3K27me3, H3K9me3) in TDG-deficient cells with promoter-specific patterns (Fig. 1e): a complete loss of H3K4 dimethylation was accompanied by a strong increase of H3K27 and/or H3K9 trimethylation at the *Hoxd13* and *Hoxa10* promoters; a partial reduction of H3K4me2 coincided with an enrichment of H3K27me3 but not H3K9me3 at

¹Institute of Biochemistry and Genetics, Department of Biomedicine, University of Basel, 4048 Basel, Switzerland. ²The Wellcome Trust Centre for Cell Biology, University of Edinburgh, Edinburgh EH9 3JR, UK. ³Institute of Molecular Cancer Research, University of Zürich, 8057 Zürich, Switzerland. ⁴Pharmaceutical Research, Global Preclinical Safety, F. Hoffmann-La Roche Ltd., 4058 Basel, Switzerland. [†]Present addresses: European Commission, Joint Research Centre, Institute for Environment and Sustainability, 21027 Ispra, Italy (T.L.); Department of Biochemistry, University of Oxford, Oxford OX1 3QU, UK (R.S.).

*These authors contributed equally to this work.

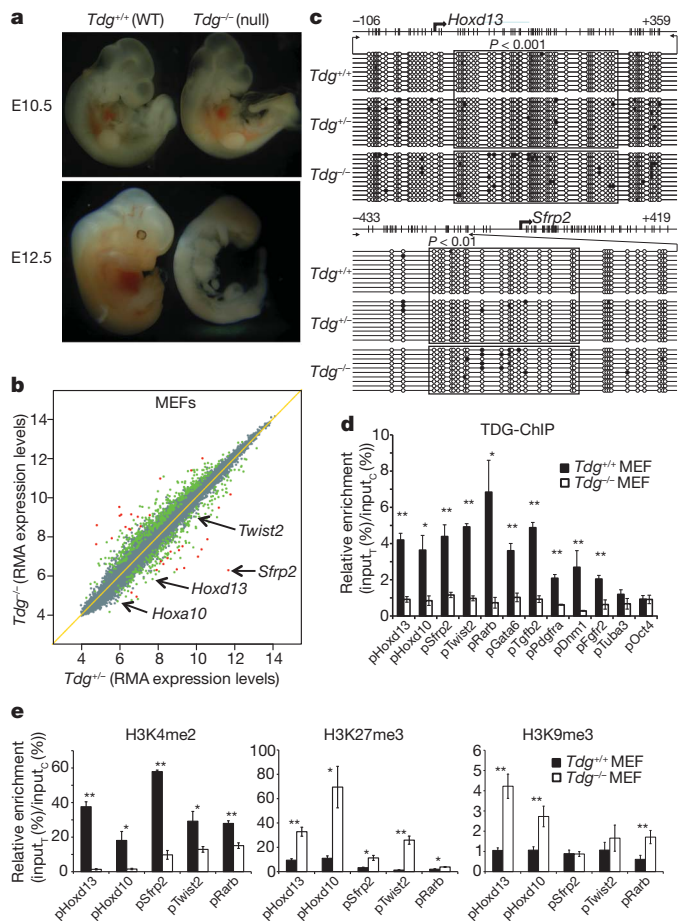


Figure 1 | Embryonic essential function of *Tdg* in epigenetic gene regulation. **a**, Whole mount images of typical examples of *Tdg*^{+/+} and *Tdg*^{-/-} littermate embryos taken at E10.5 and E12.5. **b**, Scatter plot comparing gene expression levels of matched *Tdg*^{+/+} and *Tdg*^{-/-} MEFs. Differentially expressed genes at $P < 0.05$ and $P < 0.01$ are indicated by green and red dots, respectively, and examples of developmental genes affected are denoted. **c**, Na-bisulphite sequencing of the *Hoxd13* and *Sfrp2* promoters in *Tdg*^{+/+}, *Tdg*^{+/-} and *Tdg*^{-/-} MEFs. White and black circles indicate unmethylated and methylated CpGs, respectively. P values indicate statistical difference of methylation frequencies as determined by contingency tables and χ^2 test. **d**, ChIP-quantitative PCR (qPCR) analysis of TDG association with the promoters of the genes indicated in chromatin from *Tdg*^{+/+} and *Tdg*^{-/-} MEFs. Shown are relative enrichments of TDG at these promoters normalized to a randomly chosen intergenic control region (means \pm s.e.m.; $n \geq 3$; $*P < 0.05$; $**P < 0.01$, unpaired Student's t -test). **e**, ChIP-qPCR analyses in *Tdg*^{+/+} and *Tdg*^{-/-} MEFs to assess the presence of activating (H3K4me2) and repressive (H3K9me3, H3K27me3) histone modifications at the promoter regions indicated. Shown are enrichments relative to appropriate negative controls: intracisternal A-particle (*Iap*) transposon for active chromatin marks and the *Hprt* promoter for silencing marks (means \pm s.e.m.; $n \geq 3$; $*P < 0.05$; $**P < 0.01$; unpaired Student's t -test). Subscript T, target region; subscript C, control region.

the *Sfrp2* and *Twist2* promoters; and reduction of H3K4me2 was coupled with an increase in H3K9me3 but not H3K27me3 at the *Rarb* promoter. Thus, promoter *de novo* methylation in TDG-deficient cells is associated with a loss of H3K4 methylation and a concomitant increase in trimethylation of H3K27 more than H3K9.

Stable expression of a TDG encoding complementary DNA (cDNA) in *Tdg*^{-/-} MEFs (Supplementary Fig. 1f) restored activity to the *Sfrp2* and *Twist2* genes (Fig. 2a). This correlated with a loss of H3K27 trimethylation in their promoters and an increase in H3K4 dimethylation in the case of *Twist2* (Fig. 2b). Expression of *Hoxd13* and *Hoxa10*, however, was not restored although a partial reduction of H3K27 trimethylation also occurred. This indicated that, once H3K4 methylation is lost (*Hoxd13*, *Hoxa10*), the repressive chromatin maintained by

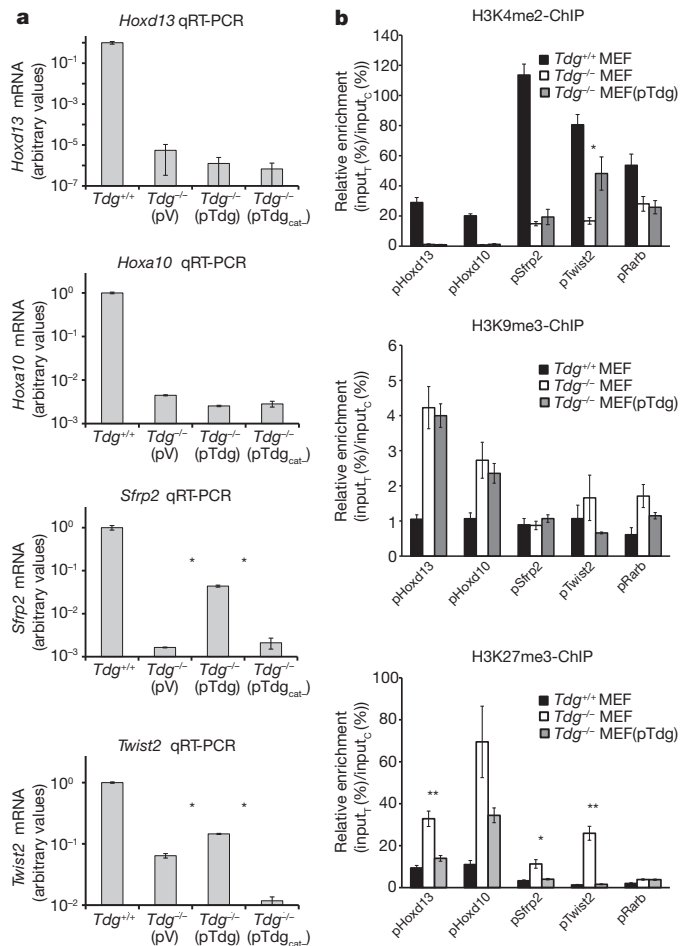


Figure 2 | Complementation of the loss of gene expression depends on the chromatin state of the promoter. **a**, *Hoxd13*, *Hoxa10*, *Sfrp2* and *Twist2* expression in *Tdg*^{+/+} and *Tdg*^{-/-} MEFs complemented with vectors expressing either a wild-type (pTdg) or a catalytically deficient *Tdg* (pTdg_{cat}, N151A), or a vector control (pV). Target-specific messenger RNA (mRNA) levels were assessed by qRT-PCR and normalized to *Gapdh* mRNA; values represent arbitrary units (means \pm s.d.; $n \geq 3$; $*P < 0.05$; unpaired Student's t -test). **b**, ChIP-qPCR analyses to detect H3K27me3 and H3K4me2 marks at the gene promoters indicated in chromatin of *Tdg*^{+/+}, *Tdg*^{-/-} and *Tdg*^{-/-} MEFs complemented with a wild-type *Tdg* cDNA. *IAP* and the *Hprt* promoter were used as normalizers for active and repressive chromatin marks, respectively (means \pm s.e.m.; $n = 3$; $*P < 0.05$; $**P < 0.01$; unpaired Student's t -test).

H3K9 and H3K27 methylation and aberrant CpG methylation cannot be reversed to an active state by re-expression of *Tdg*. If residual H3K4 methylation is present, however, promoter reactivation is possible, and this requires the catalytic function of TDG¹⁵ as shown for *Sfrp2* and *Twist2* (Fig. 2a).

To address the origin of the epigenetic aberrations in *Tdg* null MEFs, we investigated gene expression and chromatin states in TDG-proficient and -deficient ESCs before and after retinoic-acid-induced *in vitro* differentiation to neuronal progenitor cells¹⁶ (Supplementary Fig. 6a). Strikingly, gene expression differences were minor in ESCs (16 genes, $P \leq 0.05$, FC ≥ 1.5) but increased significantly upon differentiation to neuronal progenitor cells (297 genes, $P \leq 0.05$, FC ≥ 1.5) (Fig. 3a). This was not due to an inability of TDG-deficient ESCs to respond transcriptionally to retinoic acid (Supplementary Fig. 6b), although they showed somewhat faster kinetics of silencing pluripotency genes (*Oct4*, *Nanog*) and activating developmental genes (for example, *Gata6*, *Pax6*) (Supplementary Fig. 6c). Similar to the situation in MEFs, the genes most significantly misregulated in TDG-deficient neuronal progenitor cells control developmental functions, most of

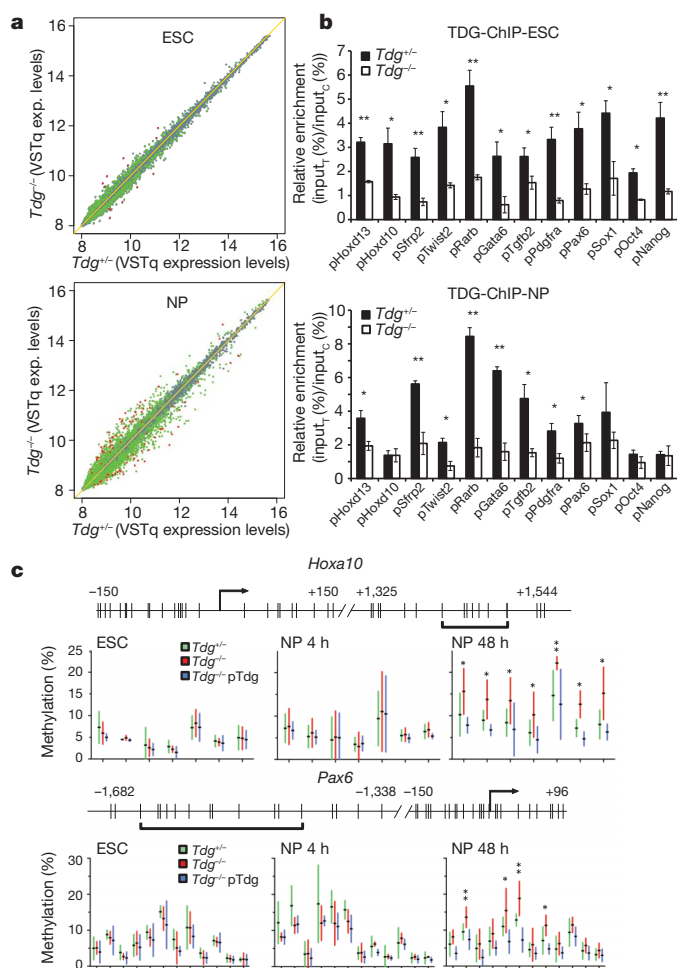


Figure 3 | TDG-dependent differences in gene expression and chromatin status arise during cell differentiation. **a**, Scatter plots comparing gene expression profiles of *Tdg*^{+/−} and *Tdg*^{−/−} ESCs or *in vitro* differentiated neuronal progenitors. Green and red dots indicate differentially expressed genes at $P < 0.05$ and $P < 0.01$, respectively. **b**, ChIP-qPCR analysis of TDG association with the gene promoters indicated in chromatin from *Tdg*^{+/−} and *Tdg*^{−/−} ESCs and neuronal progenitor (NP) cells. Shown is the relative enrichment of TDG at these promoters normalized to a randomly chosen intergenic control region (means \pm s.e.m.; ESCs, $n = 3$; neuronal progenitor cells, $n = 3$; $*P < 0.05$, $**P < 0.01$; unpaired Student's t -test). **c**, DNA methylation states at the *Hoxa10* and *Pax6* promoters in TDG-deficient ESCs and neuronal progenitor cells analysed by bisulphite pyrosequencing. Promoter regions are depicted schematically at the top. Vertical tick marks indicate CpG sites, bent arrows transcription start sites, and horizontal brackets the CpGs for which methylation data are presented in the graphs. Methylation levels are given as the percentage of methylated cytosines at each CpG analysed. Shown are means with the 95% confidence intervals (bars) obtained from three differentiation experiments. $*P < 0.05$; $**P < 0.01$; unpaired Student's t -test.

them having CpG islands in their promoters and being targets of the polycomb repressive system (Supplementary Fig. 7a). Using ChIP, we confirmed an enrichment of TDG at the promoters of differentially expressed genes both in ESCs and in neuronal progenitor cells (Fig. 3b). This also revealed that TDG associates with the promoters of *Oct4* and *Nanog* in ESCs but not in neuronal progenitor cells and MEFs (Fig. 3b and Supplementary Fig. 6d), suggesting that its interaction is lost upon heterochromatinization of these promoters. Notably, the inability to associate with heterochromatinized promoters may explain why re-expression of TDG in *Tdg* null MEFs failed to restore *Hoxd13* and *Hoxa10* transcription (Fig. 2).

Next, we examined the status of CpG methylation in gene promoters downregulated in TDG-deficient neuronal progenitor cells, making use of Na-bisulphite (pyro)sequencing and methylated

DNA-immunoprecipitation (MeDIP). Although MeDIP only detected trends for methylation differences at specific promoters (Supplementary Fig. 7b and unpublished observations), pyrosequencing revealed significantly increased DNA methylation in *Tdg* null neuronal progenitor cells at three out of five gene promoters tested (*Hoxa10*, *Pax6*, *Tgfb2*). Notably, these methylation differences were not present in ESCs nor in freshly dissociated embryonic bodies, they arose within 48 h of cultivation of the neuronal progenitor cells in progenitor medium (Fig. 3c and Supplementary Fig. 7c), and the phenotype was complemented by ectopic expression of *Tdg* during cell differentiation. Similarly, histone methylation marks were not different between TDG-proficient and -deficient ESCs but arose in neuronal progenitor cells with an enrichment of H3K27me3 at the promoters of *Hoxd13*, *Hoxa10* (Supplementary Fig. 8) and *Pdgfra* (unpublished observations). Thus, differences in DNA methylation and histone modifications became apparent at the neuronal progenitor cell stage but were not as pronounced as in MEFs, indicating an epigenetic phenotype that may progress upon further differentiation and/or cultivation. Consistently, attempts to differentiate TDG-deficient neuronal progenitor cells to terminal neurons failed because of a rapid loss of cell viability in neuronal-rich medium.

We then wondered whether this epigenetic function of TDG involves active DNA repair, as implicated by the inability of a catalytic-dead TDG (N151A) to complement the loss of *Sfrp2* and *Twist2* expression in *Tdg* null MEFs (Fig. 2). To monitor a possible engagement of downstream base excision repair, we first performed ChIP for XRCC1¹⁷. This revealed a specific, TDG-dependent enrichment of this critical base excision repair protein at the *Hoxd13*, *Hoxa10*, *Sfrp2* and *Twist2* promoters in MEFs but not in ESCs (Fig. 4a and Supplementary Fig. 5b). Hence, in MEFs, where TDG helps maintain these promoters in an active state, its presence correlates with an enrichment of XRCC1. In ESCs, however, where TDG also associates with these promoters but does not affect their chromatin status, XRCC1 enrichment is not observed. Besides XRCC1, we also found APE1, another component of base excision repair, to associate with these promoters in a TDG dependent manner in MEFs (Fig. 4a). Moreover, retinoic acid treatment of ESCs for 8 h increased the number of chromatin-associated XRCC1 foci in the presence but not in the absence of TDG (Supplementary Fig. 9), and TDG-proficient cells were significantly more sensitive to poly(ADP-ribose) polymerase (PARP) inhibition than TDG-deficient cells upon retinoic-acid-induced differentiation (Supplementary Fig. 10). These observations strongly suggest that cell differentiation-induced TDG activity feeds into PARP and XRCC1-dependent DNA single-strand break repair¹⁸.

Addressing the phenotype on histone modifications, we then found by ChIP that the absence of TDG also compromises the association of the H3K4-specific methyltransferase MLL1 with the promoters of *Hoxd13*, *Hoxa10*, *Sfrp2* and *Twist2* (Fig. 4b). This was apparent in TDG-deficient MEFs but not in ESCs, with the former indeed showing a loss of H3K4 methylation and an occurrence of aberrant CpG methylation at gene promoters reminiscent of the phenotype of MLL defects^{19–21}. Similar to MLL, the binding of CBP/p300 to these promoters was significantly reduced in the *Tdg* null MEFs (Fig. 4b). CBP/p300 is a transcription-activating histone acetyltransferase known to interact with TDG⁴ and, notably, its association with gene promoters has been reported to protect from polycomb-mediated H3K27 trimethylation²².

Taken together, our data suggest structural and catalytic functions of TDG in epigenetic maintenance (Fig. 4c). As a structural component, TDG complexes with activating histone modifiers (for example, MLL, CBP/p300) to maintain states of active (H3K4me2) and bivalent (H3K4me2, H3K27me3) chromatin during cell differentiation. In the absence of TDG, the assembly and function of such complexes is distorted and, consequently, chromatin modifications imbalanced towards repressive states. TDG also provides DNA repair capacity to erase CpG methylation locally. Aberrant methylation arises at GC-rich promoters in TDG-deficient cells following lineage commitment, and the frequencies and patterns of these events indicate an underlying

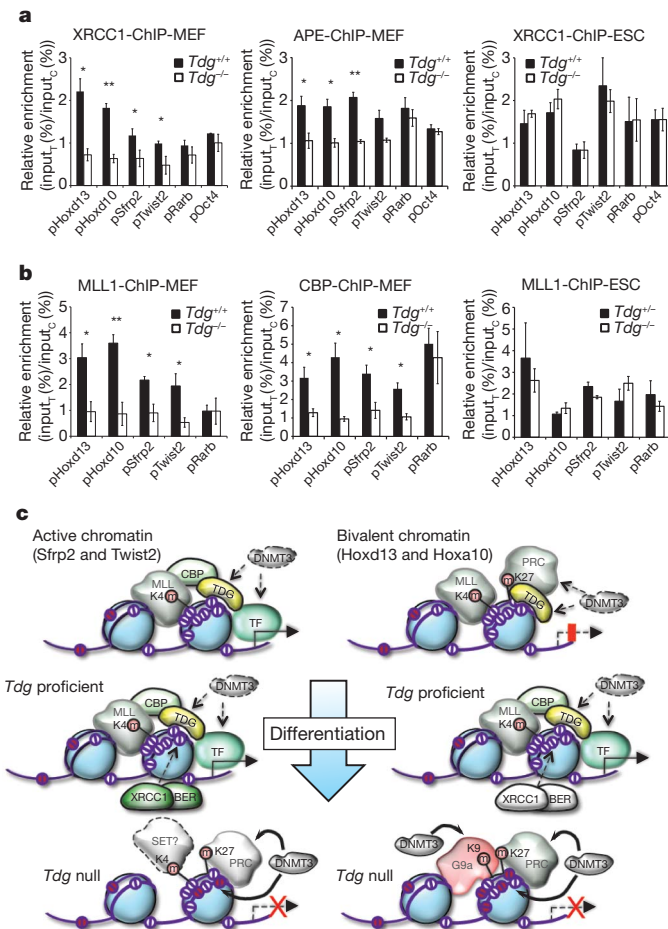


Figure 4 | Structural and catalytic functions of TDG in epigenetic maintenance. **a**, ChIP-qPCR analysis of XRCC1 and APE1 association with the gene promoters indicated in chromatin of TDG-proficient and -deficient MEFs and ESCs. Shown are relative enrichments of XRCC1 and APE1 at these promoters normalized to a randomly chosen intergenic control region (means \pm s.e.m.; $n \geq 3$; * $P < 0.05$; ** $P < 0.01$; unpaired Student's *t*-test). **b**, ChIP-qPCR analysis of MLL1 and CBP/p300 association with the gene promoters indicated in chromatin of TDG-proficient and -deficient MEFs and ESCs. Shown are relative enrichments of MLL1 and CBP/p300 at these promoters normalized to a randomly chosen intergenic control region (means \pm s.e.m.; $n \geq 3$; * $P < 0.05$; ** $P < 0.01$; unpaired Student's *t*-test). **c**, Model summarizing epigenetic aberrations and implicated functions observed in the absence of TDG. In ESCs TDG associates with gene promoters in an active 'open' (H3K4me2, for example; *Sfrp2* and *Twist2*, left side) or transiently silent 'bivalent' chromatin conformation (H3K4me2 and H3K27me3, for example; *Hoxd13* and *Hoxa10*, right side). In active chromatin, the lack of TDG results in a partial loss of H3K4 dimethylation and a gain of H3K27 trimethylation as well as in sporadic DNA hypermethylation (red balls) upon cell differentiation. Differentiation-associated activation of promoters in 'bivalent' chromatin involves the demethylation of H3K27me3 and transcription factor binding. The absence of TDG results in an aberrant loss of H3K4 dimethylation accompanied by a gain in repressive H3K9 and H3K27 trimethylation and in DNA methylation, eventually directing irreversible transcriptional silencing. In both cases, the loss of active and the gain in repressive histone marks can be accounted for by a failure of TDG-deficient cells to target MLL and CBP to these promoters. We propose that TDG, as part of transcription regulatory complexes, assures the establishment and the maintenance of proper epigenetic states at developmentally regulated gene promoters. As a DNA glycosylase, it protects these regions from aberrant CpG methylation in a process that engages XRCC1 and APE1, factors essential for downstream base excision repair.

stochastic process of *de novo* methylation. Hence, TDG keeps *de novo* DNMT activities in check to avoid erroneous methylation, and the engagement of XRCC1 and APE1 suggests that it operates through

base excision repair. Several previous studies have implicated TDG in active DNA demethylation^{8,9,23}. Mechanistically, it may do so on its own, acting as a 5-mC DNA glycosylase²³, or it may cooperate with a 5-mC deaminase (for example, AID/Apobec^{24,25} or DNMTs⁸), or a 5-mC hydroxylase (for example, TET1^{26,27}) that would convert 5-mC into a favourable substrate for TDG. Numerous efforts to reproduce 5-mC glycosylase activity for mouse and human TDG have failed (Supplementary Fig. 11 and unpublished observations). We therefore consider a deamination or hydroxylation-mediated, TDG-dependent repair process a preferable model for active cytosine demethylation. The mouse *Tdg* knockout phenotype shows that such an epigenetic control system has evolved to protect critical DNA sequences from *de novo* methylation and heterochromatinization during development.

METHODS SUMMARY

Tdg knockout mouse and cell lines. The *Tdg*-targeting construct (Supplementary Fig. 1) was generated by replacement of a *NarI*-*PacI* fragment enclosing exons 6 and 7 by a neomycin resistance cassette in a cloned fragment spanning exons 5–10 of the *Tdg* locus. This construct was used to target the *Tdg* allele in 129 mouse ESCs, which were then used to generate chimaeras and, ultimately, *Tdg*^{+/-} heterozygotes by backcrossing to C57BL/6. The generation and establishment of MEFs and *Tdg*^{-/-} ESCs was previously described²⁸.

In vitro differentiation. *In vitro* differentiation of ESCs was performed essentially according to the protocol published in ref. 16. RNA isolation for transcriptome analysis of MEFs or ESCs and neuronal progenitor cells was performed using the RNeasy Mini Kit (Qiagen) or the Trizol reagent (Invitrogen), respectively. Antibodies and sequences of oligonucleotides used for PCR with reverse transcription (RT-PCR), bisulphite sequencing and ChIP are listed in Supplementary Tables 1–4.

Full Methods and any associated references are available in the online version of the paper at www.nature.com/nature.

Received 22 February; accepted 17 November 2010.

Published online 30 January 2011.

- Gallinari, P. & Jiricny, J. A new class of uracil-DNA glycosylases related to human thymine-DNA glycosylase. *Nature* **383**, 735–738 (1996).
- Um, S. *et al.* Retinoic acid receptors interact physically and functionally with the T:G mismatch-specific thymine-DNA glycosylase. *J. Biol. Chem.* **273**, 20728–20736 (1998).
- Chen, D. *et al.* T:G mismatch-specific thymine-DNA glycosylase potentiates transcription of estrogen-regulated genes through direct interaction with estrogen receptor alpha. *J. Biol. Chem.* **278**, 38586–38592 (2003).
- Tini, M. *et al.* Association of CBP/p300 acetylase and thymine DNA glycosylase links DNA repair and transcription. *Mol. Cell* **9**, 265–277 (2002).
- Li, Y. Q., Zhou, P. Z., Zheng, X. D., Walsh, C. P. & Xu, G. L. Association of Dnmt3a and thymine DNA glycosylase links DNA methylation with base-excision repair. *Nucleic Acids Res.* **35**, 390–400 (2007).
- Gallais, R. *et al.* Deoxyribonucleic acid methyl transferases 3a and 3b associate with the nuclear orphan receptor COUP-TFI during gene activation. *Mol. Endocrinol.* **21**, 2085–2098 (2007).
- Zhu, B. *et al.* Overexpression of 5-methylcytosine DNA glycosylase in human embryonic kidney cells EcR293 demethylates the promoter of a hormone-regulated reporter gene. *Proc. Natl Acad. Sci. USA* **98**, 5031–5036 (2001).
- Metivier, R. *et al.* Cyclical DNA methylation of a transcriptionally active promoter. *Nature* **452**, 45–50 (2008).
- Kangaspeska, S. *et al.* Transient cyclical methylation of promoter DNA. *Nature* **452**, 112–115 (2008).
- Cortazar, D., Kunz, C., Saito, Y., Steinacher, R. & Schär, P. The enigmatic thymine DNA glycosylase. *DNA Repair (Amst.)* **6**, 489–504 (2007).
- Robertson, A. B., Klungland, A., Rognes, T. & Leiros, I. DNA repair in mammalian cells: Base excision repair: the long and short of it. *Cell. Mol. Life Sci.* **66**, 981–993 (2009).
- Boyer, L. A. *et al.* Polycomb complexes repress developmental regulators in murine embryonic stem cells. *Nature* **441**, 349–353 (2006).
- Furuta, J. *et al.* Silencing of Peroxiredoxin 2 and aberrant methylation of 33 CpG islands in putative promoter regions in human malignant melanomas. *Cancer Res.* **66**, 6080–6086 (2006).
- Cheng, Y. Y. *et al.* Frequent epigenetic inactivation of secreted frizzled-related protein 2 (SFRP2) by promoter methylation in human gastric cancer. *Br. J. Cancer* **97**, 895–901 (2007).
- Hardeland, U., Bentele, M., Jiricny, J. & Schär, P. Separating substrate recognition from base hydrolysis in human thymine DNA glycosylase by mutational analysis. *J. Biol. Chem.* **275**, 33449–33456 (2000).
- Bibel, M., Richter, J., Lacroix, E. & Barde, Y. A. Generation of a defined and uniform population of CNS progenitors and neurons from mouse embryonic stem cells. *Nature Protocols* **2**, 1034–1043 (2007).

17. Caldecott, K. W. XRCC1 and DNA strand break repair. *DNA Repair (Amst.)* **2**, 955–969 (2003).
18. Bryant, H. E. *et al.* Specific killing of BRCA2-deficient tumours with inhibitors of poly(ADP-ribose) polymerase. *Nature* **434**, 913–917 (2005).
19. Yu, B. D., Hanson, R. D., Hess, J. L., Horning, S. E. & Korsmeyer, S. J. MLL, a mammalian trithorax-group gene, functions as a transcriptional maintenance factor in morphogenesis. *Proc. Natl Acad. Sci. USA* **95**, 10632–10636 (1998).
20. Erfurth, F. E. *et al.* MLL protects CpG clusters from methylation within the Hoxa9 gene, maintaining transcript expression. *Proc. Natl Acad. Sci. USA* **105**, 7517–7522 (2008).
21. Wang, P. *et al.* Global analysis of H3K4 methylation defines MLL family member targets and points to a role for MLL1-mediated H3K4 methylation in the regulation of transcriptional initiation by RNA polymerase II. *Mol. Cell. Biol.* **29**, 6074–6085 (2009).
22. Pasini, D. *et al.* Characterization of an antagonistic switch between histone H3 lysine 27 methylation and acetylation in the transcriptional regulation of Polycomb group target genes. *Nucleic Acids Res.* **38**, 4958–4969 (2010).
23. Zhu, B. *et al.* 5-methylcytosine-DNA glycosylase activity is present in a cloned G/T mismatch DNA glycosylase associated with the chicken embryo DNA demethylation complex. *Proc. Natl Acad. Sci. USA* **97**, 5135–5139 (2000).
24. Morgan, H. D., Dean, W., Coker, H. A., Reik, W. & Petersen-Mahrt, S. K. Activation-induced cytidine deaminase deaminates 5-methylcytosine in DNA and is expressed in pluripotent tissues: implications for epigenetic reprogramming. *J. Biol. Chem.* **279**, 52353–52360 (2004).
25. Rai, K. *et al.* DNA demethylation in zebrafish involves the coupling of a deaminase, a glycosylase, and gadd45. *Cell* **135**, 1201–1212 (2008).
26. Tahiliani, M. *et al.* Conversion of 5-methylcytosine to 5-hydroxymethylcytosine in mammalian DNA by MLL partner TET1. *Science* **324**, 930–935 (2009).
27. Ito, S. *et al.* Role of Tet proteins in 5mC to 5hmC conversion, ES-cell self-renewal and inner cell mass specification. *Nature* **466**, 1129–1133 (2010).
28. Kunz, C. *et al.* Base excision by thymine DNA glycosylase mediates DNA-directed cytotoxicity of 5-fluorouracil. *PLoS Biol.* **7**, e91 (2009).

Supplementary Information is linked to the online version of the paper at www.nature.com/nature.

Acknowledgements We thank D. Klewe-Nebenius for preparations of mouse primary fibroblast, and F. Mohn and D. Schübeler for discussions and assistance in the setup and evaluation of the ChIP experiments. The work was supported by project grants from the Swiss National Science Foundation (3100A0-108436; 3100A0-122574/) and the Association For International Cancer Research (01-330).

Author Contributions D.C. established and performed the ChIP and MeDIP analyses and the *in vitro* differentiation experiments, and contributed to writing the paper; C.K. established and characterized MEF lines, designed and performed gene expression and DNA methylation analyses, and contributed to writing the paper; J.S. did blastocyst injections, established the first heterozygous *Tdg* knockout mice, characterized the lethal phenotype of the *Tdg* null embryos and provided SV40-immortalized MEFs; T.L. and Y.S. generated *Tdg*-targeting constructs and established heterozygous and homozygous *Tdg* knockout ES cell lines; Y.S. established *in vitro* differentiation protocols; E.MacD. performed the Big Blue mutation assays; A.W. performed ChIP experiments; D.S. isolated primary MEFs and performed RT-PCR validations of gene expression differences and the PARP inhibitor experiments; A.L.J. established and performed immunofluorescence experiments including XRCC1 foci analyses; F.S. performed bioinformatic analyses of gene expression array data; R.S. affinity-purified anti-TDG antibodies for ChIP; J.J. contributed genomic *Tdg* clones and supervised initial work of T.L.; A.B. was involved in study design (mutation analyses) and supervised the work of J.S. and E.MacD.; P.S. designed, coordinated and supervised the study, analysed the data and wrote the paper. All authors discussed the results and commented on the paper.

Author Information Gene expression array data have been deposited in the NCBI Gene Expression Omnibus under accession number GSE20693. Reprints and permissions information is available at www.nature.com/reprints. The authors declare no competing financial interests. Readers are welcome to comment on the online version of this article at www.nature.com/nature. Correspondence and requests for materials should be addressed to P.S. (primo.schaer@unibas.ch).

METHODS

Tdg knockout strategy. The *Tdg*-targeting construct (Supplementary Fig. 1) was generated by replacement of a *NarI*-*PacI* fragment enclosing exons 6 and 7 by a neomycin resistance cassette in a cloned fragment spanning exons 5–10 of the *Tdg* locus. This construct was used to target the *Tdg* allele in 129 mouse ESCs, which were then used to generate chimaeras and, ultimately, *Tdg*^{+/-} heterozygotes by backcrossing to C57BL/6. The generation and establishment of MEFs and *Tdg*^{-/-} ESCs was previously described²⁸.

Cell culture and ESC differentiation. SV40-immortalized MEF cell lines were previously described²⁹ and cultivated in growth medium (DMEM, 10% FCS, 2 mM L-glutamine) at 37 °C in a humidified atmosphere containing 5% CO₂. For growth of cell lines complemented with *Tdg*-expressing vectors, the growth medium was additionally supplemented with 1 µg ml⁻¹ puromycin.

For isolation of primary MEFs, 10.5 days post-coitum embryos were dissected, homogenized and cells dissociated in 0.05% trypsin-EDTA for 5 min before plating in modified ES cell medium without LIF (DMEM, 10% FCS serum, 1× non-essential amino acids, 1 mM sodium pyruvate, 2 mM L-glutamine and 50 µM β-mercaptoethanol, 1× penicillin/streptomycin) and cultivation for 10 days.

ESCs were grown in the presence of feeder cells at 37 °C in ES cell medium (ECM: DMEM, 15% heat-inactivated FCS, LIF (1,000 U ml⁻¹), 1× non-essential amino acids, 1 mM Na-pyruvate, 2 mM L-glutamine and 90 µM β-mercaptoethanol) in a humidified atmosphere containing 5% CO₂.

Before starting retinoic-acid-induced differentiation, ESCs were grown in the absence of feeder cells for two passages. For embryoid body formation during neuronal differentiation, 4 × 10⁶ *Tdg*^{+/-} or *Tdg*^{-/-} ESCs were plated into non-adherent bacterial dishes (Greiner Bio-one) in differentiation medium (ECM without LIF and with 10% FCS) and grown at 37 °C with a medium exchange after 2 days. After 4 days, 5 µM all-*trans* retinoic acid was added and cells were further incubated for 4 days with a medium exchange after 2 days. Embryoid bodies were washed twice with 1× PBS and dissociated with freshly prepared trypsin solution (0.05% TPCK-treated trypsin in 0.05% EDTA/1× PBS) at 37 °C for 3 min. Dissociated embryoid bodies were re-suspended in 10 ml differentiation medium and collected by centrifugation at 700g for 5 min at room temperature. The pellet was re-suspended in N2 medium (DMEM-F12 nutrient mixture 1:1, 1× N2 supplement) and the cell suspension filtered through a 40-µm nylon cell strainer (BD). Filtered cells were immediately plated onto poly-L-lysine and laminin-coated dishes at a density of 5 × 10⁶ cells per 60-mm dish or 1.5 × 10⁷ cells per 100-mm dish. The N2 medium was exchanged 2 and 24 h after plating, and cells were collected after 4 and 48 h for further analysis.

Retinoic-acid-induced differentiation of ESCs for time course, PARP inhibitor and immunofluorescence experiments was induced in ECM without LIF in the presence of 1 or 5 µM retinoic acid. The retinoic-acid-containing medium was exchanged every 24 h, and cells were collected at the indicated time points. For immunofluorescence experiments, 10⁵ ESCs were seeded onto gelatin-coated cover slips 1 day before differentiation. For the analysis of PARP inhibition on cell survival during differentiation, 10⁵ ESCs were seeded into gelatin-coated 12-well dishes, 1 day before the addition of 5 µM retinoic acid or further cultivation in ECM. After 24 h, increasing concentrations of the PARP inhibitor AG-014699 (a gift of SelleckChem) were added and cell numbers determined 24 h later with the CASY cell counter. The 50% lethal dose of the inhibitor and statistical differences between *Tdg*-proficient and -deficient cells were calculated on triplicate experiments by linear regression with 95% confidence intervals using GraphPad Prism software.

Microarray gene expression analysis. For the analysis of differential gene expression between *Tdg*^{+/-} and *Tdg*^{-/-} MEFs, total RNA was isolated from three independent cultures of each cell line using the RNeasy Mini Kit (Qiagen), cDNA synthesized from 13 µg RNA with the SuperScript double-Stranded cDNA Synthesis Kit (Invitrogen) followed by *in vitro* transcription reactions using the MEGA Script T7 Kit (Ambion) supplemented with 1.5 mM Bio-11-CTP and Bio-16-UTP (Enzo Life Sciences). cDNAs and cRNAs were purified using the GeneChip Sample Cleanup Module (Qiagen). cRNA (15 µg) was fragmented and hybridized to GeneChip Mouse Expression Arrays 430A (Affymetrix). Hybridized arrays were stained and washed according to the manufacturer's protocol and scanned with an Affymetrix Scanner 3000 7G. Scanned images were processed with Microarray Suite software and obtained 'cel' files used for further data analysis.

For gene expression analysis of ESCs and *in vitro* differentiated neuronal progenitor cells, total RNA was extracted from independent triplicates using the Trizol reagent (Invitrogen). RNA was quantified using the Quant-iT RiboGreen RNA Assay (Invitrogen) and 500 ng of total RNA subjected to cDNA synthesis and subsequent *in vitro* transcription to biotinylated cRNA using the Illumina TotalPrep RNA Amplification Kit (Ambion, USA). cRNA (1.5 µg) was hybridized to MouseWG-6v2 slides (Illumina) according to the manufacturer's protocol. Bead arrays were washed and stained using FluoroLink Cy3 Streptavidin (GE

Healthcare). Fluorescent signals were imaged using the iScan system (Illumina). Scanner images files were processed to probe intensity files by the manufacturer's software and further processed with the genome studio software (Illumina) without normalization and background correction.

Affymetrix data and Illumina probe intensity data were either processed by robust multi-array average or variance stabilization transformation, respectively, using R/Bioconductor software and 'affy' or 'lumi' libraries, followed by quantile normalization. Significance of effects for probes (Illumina) or probe-sets (Affymetrix) was tested in R/Bioconductor ('limma' library) using a moderated *t*-test and the false discovery rate (=5%) method of Benjamini and Hochberg for multiple testing correction. No unspecific filter was applied and multiple probe-sets per gene or probe-sets with ambiguous genomic targets were retained.

Methylation analyses. Genomic DNA from MEFs, ESCs and neuronal progenitor cells was isolated with the QIAamp DNA Mini Kit (Qiagen). DNA (2 µg) was subjected to bisulphite conversion using the EZ DNA Methylation Kit (Zymo Research). Respective target regions were amplified from bisulphite-treated DNA with TrueStart Taq polymerase (New England Biolabs). For conventional bisulphite sequencing, *Hoxd13* or *Sfrp2* promoter regions were amplified from converted DNA and cloned into the *XhoI* and *BamHI* restriction sites of pBluescript SK- before sequencing of individual clones. For pyrosequencing, potential regions of hypermethylation were first identified by COBRA. Pyrosequencing primers (Supplementary Table 1) were designed using the PyroMark Assays Design software (version 2.0.1.15, Qiagen). Primer pairs included either one biotinylated primer or one primer containing a universal region. In the latter case, products were subjected to a second amplification using a biotinylated universal primer and Phusion Hot Start High-Fidelity DNA Polymerase (Finnzymes). PCR products were purified using the QIAquick PCR Purification Kit (Qiagen), quantified and 300–500 ng were used for pyrosequencing in a PyroMark Q24 (Qiagen). Reactions were analysed using PyroMark Q24 software (version 2.0.6, Qiagen). Significance of methylation differences between different *Tdg*-proficient and -deficient cell lines at individual CpG sites was evaluated by unpaired, two-tailed *t*-tests.

ChIP. To crosslink protein-bound DNA, MEFs, ESCs and neuronal progenitor cells were incubated in freshly prepared crosslinking solution (PBS pH 7.4, 1% formaldehyde) at room temperature. The reaction was quenched after 10 min by addition of glycine to a final concentration of 125 mM. After washing twice with cold PBS, cells were collected using a cell scraper and subsequent centrifugation at 600g and 4 °C. Nuclei were isolated by incubation in 200 µl of cold CHIP Buffer I (10 mM HEPES pH 6.5, 10 mM EDTA, 0.5 mM EGTA, 0.25% Triton X-100) for 5 min on ice followed by two incubations of 5 min on ice in 200 µl cold CHIP buffer II (10 mM HEPES pH 6.5, 1 mM EDTA, 0.5 mM EGTA, 200 mM NaCl). Pelleted nuclei were lysed in 400 µl ChIP buffer III (50 mM Tris-HCl pH 8.0, 1 mM EDTA, 0.5% Triton X-100, 1% SDS, 1 mM PMSF) for 10 min on ice followed by sonication for 15 min (15 s on, 30 s off, power high) using a Bioruptor sonicator (Diagenode) to produce random chromatin fragments ranging from 300 to 1,000 base pairs. The solution was cleared by centrifugation at 14,000g and 4 °C for 10 min and the concentration of chromatin was estimated by absorbance at 260 nm. For ChIP of TDG, MLL and APE1 100–150 µg of chromatin were diluted ten times in ChIP dilution buffer I (50 mM Tris-HCl pH 8.0, 1 mM EDTA, 150 mM NaCl, 0.1% Triton X-100, 1 mM PMSF). For histone ChIPs, 25–75 µg of chromatin were diluted in ChIP dilution Buffer II (16.7 mM Tris-HCl pH 8.0, 1.2 mM EDTA, 167 mM NaCl, 1.1% Triton X-100, 0.01% SDS, 1 mM PMSF). Diluted chromatin was pre-cleared at 4 °C for 1 h with 40 µl of a 50% slurry of magnetic Protein G beads (Invitrogen) preblocked with 1 mg ml⁻¹ BSA and 1 mg ml⁻¹ tRNA (TDG, XRCC1, APE1 and MLL-ChIPs) or salmon sperm single-stranded DNA (histone ChIPs). Pre-cleared chromatin was incubated with 2–5 µg of the respective antibody (Supplementary Table 2) overnight at 4 °C under slow rotation. Immuno-complexes were precipitated with 40 µl of a 50% slurry of blocked Protein G beads and further incubated at 4 °C for 2 h. Beads were then serially washed with 500 µl ChIP wash buffer I (20 mM Tris-HCl pH 8.0, 2 mM EDTA, 150 mM NaCl, 0.1% SDS, 1% Triton X-100), 500 µl ChIP wash buffer II (20 mM Tris-HCl pH 8.0, 2 mM EDTA, 500 mM NaCl, 0.1% SDS, 1% Triton X-100) and 500 µl ChIP wash buffer III (10 mM Tris-HCl pH 8.0, 1 mM EDTA, 250 mM LiCl, 1% sodium deoxycholate, 1% NP-40). For TDG, APE1 and MLL ChIPs, beads were washed once with 500 µl ChIP wash buffer I and twice with 500 µl ChIP wash buffer II. After two additional washes with 500 µl TE buffer (10 mM Tris-HCl pH 8.0, 1 mM EDTA), bound complexes were eluted by two sequential incubations with 150 µl elution buffer (1% SDS, 0.1 M NaHCO₃) at 65 °C for 10 min. Crosslink reversal of eluates and respective input samples (1% of chromatin used for ChIP) was done in the presence of 200 mM NaCl at 65 °C for 4 h followed by proteinase K digestion (50 µg ml⁻¹) in the presence of 10 mM EDTA at 45 °C for 1 h. DNA was purified by phenol/chloroform extraction and Na-acetate/ethanol precipitation, and re-suspended in 10 mM Tris-HCl pH 8.0. qPCR analysis with target specific primers (Supplementary Table 3) was performed using Quantitect SYBR Green (Qiagen) with

a Rotor-Gene 3000 thermocycler (Qiagen). The significance of different ChIP efficiencies among Tdg-proficient and -deficient cell lines was evaluated from triplicate experiments by non-paired, two-tailed *t*-tests.

MeDIP. MeDIP assays were performed as described in ref. 30. Briefly, genomic DNA was prepared from 5×10^6 cells by incubation in lysis buffer (20 mM Tris-HCl pH 8.0, 4 mM EDTA, 20 mM NaCl, 1% SDS and 1 mg ml⁻¹ proteinase K) at 55 °C for 5 h and subsequent phenol/chloroform extraction and Na-acetate/ethanol precipitation. DNA pellets were re-suspended in TE containing 20 µg ml⁻¹ RNase. DNA was sonicated as described for ChIP followed by NaCl (400 mM)/EtOH precipitation in the presence of glycogen-carrier. Fragmented DNA (4 µg) in 450 µl TE was denatured at 95 °C for 10 min and immediately chilled on ice. After addition of 10× immunoprecipitation buffer (100 mM sodium phosphate pH 7.0, 1.4 M NaCl, 0.5% Triton X-100), the DNA was incubated with 10 µg of a monoclonal anti 5-methylcytidine antibody (clone 33D2, Eurogentec) at 4 °C for 2 h. Immuno-complexes were precipitated by the addition of 40 µl M-280 sheep anti mouse IgG antibody coupled Dynabeads (Invitrogen) and incubation at 4 °C for 2 h followed by three washes in 700 µl IP buffer. Bound material was treated with 250 µl proteinase K digestion buffer (50 mM Tris-HCl pH 8.0, 10 mM EDTA, 0.5% SDS and 0.25 mg ml⁻¹ proteinase K) at 50 °C for 3 h. Immunoprecipitated methylated DNA was purified by phenol/chloroform extraction followed by Na-acetate/ethanol precipitation and re-suspended in TE. qPCR analysis of sonicated genomic input DNA and MeDIP DNA with target specific primers (Supplementary Table 3) was performed as described for ChIP, and significance of MeDIP efficiencies tested by non-paired, two-tailed *t*-tests.

Quantitative RT-PCR analyses. Total RNA (2–4 µg) extracted by RNeasy Mini Kit or by Trizol methods was reverse transcribed with the RevertAid H Minus M-MuLV Kit (Fermetas) according to the manufacturer's protocol. qPCR with target specific primers (Supplementary Table 4) was performed using Power SYBR Green Master Mix (Applied Biosystems) with a Rotor-Gene 3000 thermocycler. Conditions for each target were validated by standard and melting curve analyses. Target-specific amplifications were normalized to a GAPDH control and data of at least three independent experiments were analysed by unpaired, two-tailed *t*-tests. Tdg genotype-specific target gene expression in primary MEFs was analysed by the non-parametric Kruskal–Wallis test and *post hoc* Dunn's multiple comparison.

Western blot analyses. Whole-cell extracts were prepared by cell lysis in lysis buffer (50 mM Na-phosphate pH 8.0, 125 mM NaCl, 1% NP-40, 0.5 mM EDTA, 1 mM PMSF, 1 mM DTT, 1× complete protease inhibitor, 2× phosphatase inhibitor cocktail 1 and 2) on ice for 30 min and clarification by centrifugation (15 min, 20,000g, 4 °C). Chromatin extracts were isolated as described for ChIP assays. Soluble proteins (50 µg) were separated on 7% or 10% SDS-polyacrylamide gels and transferred to a nitrocellulose membrane (Millipore). Membranes were washed once with TBS-T (100 mM Tris-HCl pH 8.0, 150 mM NaCl, 0.1% Tween-20), blocked with blocking buffer (TBS-T, 5% dry milk) at room temperature for 1 h and incubated with the primary antibody at 33 °C (anti-mTDG) or room temperature (anti-DNMT1, anti-DNMT3a, anti-XRCC1, anti-APE1, anti-MLL, anti-β-actin) for 1 h in blocking buffer. Dilutions were 1:10,000 for the rabbit anti-mTDG, the mouse anti-β-actin and the anti-DNMT1 antibodies; 1:1,000 for the anti-DNMT3a and anti-XRCC1 antibodies; 1:500 for the anti-APE1 and anti-MLL antibodies. Washing steps after hybridization were once at 33 °C and twice at room temperature for 15 min for anti-mTDG, or three times at room temperature for 10 min for all other antibodies. Membranes were incubated with secondary HRP-conjugated antibodies diluted 1:5,000 in blocking buffer and at room temperature for 1 h. After three washing steps of 10 min at room temperature, detection of the signals was performed using the Immobilon Western Chemiluminescent HRP Substrate (Millipore).

Cytotoxicity assays. For measurement of γ-ray sensitivity, MEF single-cell suspensions at a cell density of 2×10^5 cells ml⁻¹ in PBS were irradiated with the

indicated doses in a Gammacell 40 irradiator using ¹³⁷Cs as a radioactive source. Irradiated cells were plated in 96-well microtitre plates at a density of 1000 cells per well in growth medium, and survival was measured after 3 days using the Cell Counting Kit-8 (Dojindo). Alternatively, survival was determined by clonogenic growth by plating 500–2000 cells in triplicate in 10-cm dishes containing growth medium and counting of Giemsa-stained colonies after 10 days. To measure sensitivity to H₂O₂, cells were plated at 2,500 cells per well in 96-well plates. After 24 h cells were treated for 15 min with the indicated concentrations of H₂O₂, washed with PBS and incubated in fresh growth medium for a further 24 h before measurement of survival with the Cell Counting Kit-8. Survival was determined as the percentage of mock-treated cells.

Base release assay. For base release assays, 25–50 µg of ESC whole-cell extracts were incubated with 0.5 pmol of a fluorescein-labelled GC/TG, GCm/CG or GCm/mCG DNA substrate in reaction buffer (50 mM Tris-HCl pH 8.0, 1 mM EDTA, 1 mM DTT, 1 mg ml⁻¹ BSA) at 37 °C for 1 h (GC/TG) or overnight (methylated substrates). Resulting AP-sites were cleaved by the addition of NaOH to a final concentration of 100 mM and heating to 95 °C for 10 min. Subsequently, DNA was ethanol-precipitated overnight at –20 °C in the presence of 0.3 M Na-acetate pH 5.2 and 0.4 mg ml⁻¹ carrier t-RNA. DNA was collected by centrifugation (20 min, 20,000g, 4 °C) and washed with 80% ethanol. Air-dried pellets were re-suspended in loading buffer (1× TBE, 90% formamide), heated at 95 °C for 5 min and immediately chilled on ice. Reaction products were separated on denaturing 8 M urea/15% polyacrylamide gels in 1× TBE. The fluorescein-labelled DNA was visualized with a Typhoon 9400 and quantified using ImageQuant TL software (GE Healthcare).

Immunofluorescence. For detection of XRCC1 foci during retinoic acid stimulation, cells were fixed in ice-cold methanol for 5 min, then permeated in 0.2% Triton X-100/PBS pH 7.4 and 0.2% Triton X-100/0.2% NaBH₄/PBS pH 7.4 on ice for 5 min each. The inducibility of XRCC1 foci formation in ESCs was tested by incubation with H₂O₂ (50 µM in PBS) or PBS for 15 min at 37 °C and an additional 5 min in ECM with LIF before further processing. Coverslips were blocked in blocking buffer (1% BSA/0.05% Tween20/PBS pH 7.4), stained with rabbit anti-XRCC1 antibody (1:100 in blocking buffer) at room temperature for 1 h and washed three times for 10 min with blocking buffer before labelling with goat anti-rabbit Alexa Fluor 594 (1:200 in blocking buffer) for 30–60 min. After two washes of 10 min with blocking buffer, cells were again fixed in –20 °C cold methanol, incubated in blocking buffer for 1 h and stained with a mouse monoclonal anti-PCNA antibody (1:100 dilution) in blocking buffer overnight at 4 °C. Slides were counterstained for DNA with 50 ng ml⁻¹ DAPI and mounted in VectaShield mounting medium (Vector Lab). Slides were randomized and blinded before z-stacks were acquired on a Leica SP5 with the 405-nm diode, argon 488 nm and He-Ne 594-nm laser lines. XRCC1 foci numbers for individual cells were determined by visual inspection of the three-dimensional stacks. One hundred and fifty (retinoic acid stimulation) or 50 (H₂O₂) cells per sample were analysed. For co-staining of PAR and XRCC1 during retinoic acid differentiation, cells were fixed with 2% formaldehyde/PBS at room temperature for 30 min and permeabilized with PBS/0.2% Triton-X100 for 30 min. Antigen detection was done with a 1:250 diluted monoclonal α-PAR antibody 10H (Enzo Life Sciences) and a polyclonal α-XRCC1 as described above, but using 1:250 diluted anti-rabbit Alexa Fluor 594 and anti-mouse Alexa Fluor 488 secondary antibodies (Invitrogen). Pictures were acquired with a Nikon Diaphot 300 epifluorescence microscope using identical settings for all slides.

29. Kunz, C. *et al.* Base excision by thymine DNA glycosylase mediates DNA-directed cytotoxicity of 5-fluorouracil. *PLoS Biol.* **7**, e91 (2009).

30. Weber, M. *et al.* Chromosome-wide and promoter-specific analyses identify sites of differential DNA methylation in normal and transformed human cells. *Nature Genet.* **37**, 853–862 (2005).

CORRIGENDUM

doi:10.1038/nature09759

Human melanoma-initiating cells express neural crest nerve growth factor receptor CD271

Alexander D. Boiko, Olga V. Razorenova, Matt van de Rijn, Susan M. Swetter, Denise L. Johnson, Daphne P. Ly, Paris D. Butler, George P. Yang, Benzion Joshua, Michael J. Kaplan, Michael T. Longaker & Irving L. Weissman

Nature 466, 133–137 (2010)

In this Letter, Fig. 1b and Table 2 (summarizing experiments presented in Supplementary Figs 2–4 and 7–9) contained an error reflecting the total number of tumours formed, and the total number of injections with CD271⁺ cells isolated directly from patients (26 out of 37). The correct number is 25 out of 38. The total number of injections with CD271⁺ cells from xenografted tumours was incorrectly listed as 54 instead of 55, and the total number of injections with CD271[–] should have been 44 rather than 43. In Table 1 (summarizing experiments with xenografted tumours P0, Pi) the total number of injections with CD271⁺ cells was incorrectly listed as 36 instead of 37, and the total number of injections with CD271[–] cells should have been 26 rather than 25. In addition, in Fig. 3d the stacked bar column that shows the proportion of patients with different ranges of TYR positivity should indicate 19 instead of 17 for the 0%–positivity group, and 1 instead of 2 for the 90–98%–positivity group. Supplementary Table 3 also contained some errors. None of these alterations affect the significant differences or change the *P* value between CD271⁺ and CD271[–] cells in their ability to initiate melanomas in RG mice, as discussed in the original report. The corrected Figs 1b, 3d and Tables 1 and 2 are shown below.

Table 1 | Summary of engraftments from xenografted tumours

Cell surface phenotype (Xenografted samples P0, Pi)	Frequency of tumour formation
CD271 ⁺	70% (26 of 37)*
CD271 [–]	19% (5 of 26)*

Table 2 | Comparative analysis of melanoma initiation

Tumour cell source	Frequency of tumour formation	
	CD271 ⁺	CD271 [–]
Patient samples	66% (25 of 38)	7% (3 of 41)*
Xenografted samples (P0, Pi, Ps)	71% (39 of 55)	23% (10 of 44)*

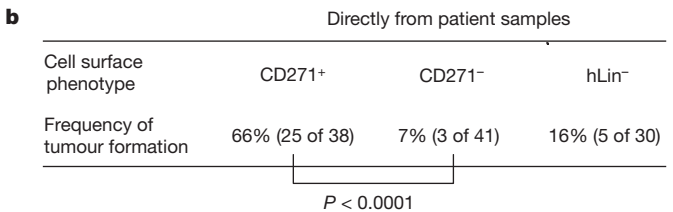


Figure 1

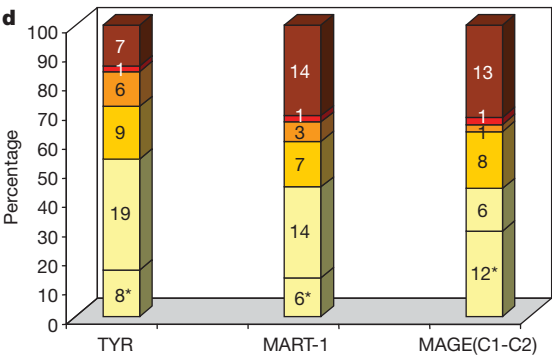


Figure 3

CORRECTIONS & AMENDMENTS

CORRIGENDUM

doi:10.1038/nature09808

A population-specific *HTR2B* stop codon predisposes to severe impulsivity

Laura Bevilacqua, Stéphane Doly, Jaakko Kaprio, Qiaoping Yuan, Roope Tikkanen, Tiina Paunio, Zhifeng Zhou, Juho Wedenoja, Luc Maroteaux, Silvina Diaz, Arnaud Belmer, Colin A. Hodgkinson, Liliana Dell'Oso, Jaana Suvisaari, Emil Coccaro, Richard J. Rose, Leena Peltonen, Matti Virkkunen & David Goldman

Nature **468**, 1061–1066 (2010)

In this Article, the key in Fig. 3d is incorrect as the red line and squares should correspond to the wild-type (WT) mice, and the blue line and squares to the *Htr2b*^{-/-} mice. Furthermore, the Acknowledgements section should state that we thank E. Moore for her contribution to information technology.

CORRIGENDUM

doi:10.1038/nature09813

A cryptic sensor for HIV-1 activates antiviral innate immunity in dendritic cells

Nicolas Manel, Brandon Hogstad, Yaming Wang, David E. Levy,
Derya Unutmaz & Dan R. Littman

Nature **467**, 214–217 (2010)

In the Acknowledgements of this Letter, the National Institutes of Health (NIH) grants supporting author D.E.L. should be listed as AI28900 and Northeast Biodefense Center U54-AI057158.

CAREERS

TURNING POINT Award helps in fight against paediatric malaria in Kenya **p.425**

POSTDOC JOURNAL Scientists should beware of academic survival tactics **go.nature.com/3fttcj**

NATUREJOBS For the latest career listings and advice **www.naturejobs.com**



INTERNATIONAL OPPORTUNITIES

The science of diplomacy

The US government employs researchers to delve into matters of state. But a special set of soft skills is essential.

BY KAREN KAPLAN

In January, Sharon Hrynkow was preparing for a meeting of health ministers from the eight nations with territory in the Arctic. A lot was at stake and Hrynkow, a neuroscientist with a long-standing interest in global health, had a key part to play. As senior adviser to the assistant secretary of the Bureau of Oceans and International Environmental and Scientific Affairs (OES) in the US Department of State,

she was to help the United States decide on priorities for the meeting's agenda and inform the health-science topics covered, such as climate change and global health. As sea ice shrinks, the region is facing escalating pollution from oil and gas exploration as well as a rise in commercial shipping. Navigating such tricky terrain can be further complicated by territorial disputes between nations. But Hrynkow was undaunted by the prospect — it is just part of her job.

Hrynkow is not the only scientist who has found her way into international relations and diplomacy. Although US science diplomacy and international policy do not have a well-defined career path, researchers with the right combination of tact, finesse and negotiating skills may find niches in government agencies, science societies, non-governmental organizations or industry. Scientific acumen is not enough: to make their mark, scientists need a passion for international issues with science import, a knack for and interest in building relationships, and a curiosity about and fascination for other nations and cultures. “From the scientific perspective, the diplomatic community is an important ally, as it can pave the way for exchanges of scientists, help foster international research partnerships and build relationships to spur innovation,” says Hrynkow. At stake are global issues such as climate change, food security, pandemic disease and trans-boundary pollution.

LEAVING THE LAB

Hrynkow started on the diplomatic path early in her career. She has worked with officials from other nations on international and global-health issues for nearly 20 years, since finishing her postdoc at the University of Oslo. Hrynkow had travelled to Norway to conduct research using retroviruses to study the developing brain, but after completing the project, she realized that she preferred to leave the lab. Hrynkow decided to apply for a Science & Technology Policy Fellowship from the American Association for the Advancement of Science (AAAS) in Washington DC to explore her long-standing interest in international issues. She was posted to the OES, where she helped to develop US policy on AIDS.

After Hrynkow's fellowship ended, the bureau hired her. “I was the first full-time health scientist within the OES and the state department as a civil servant,” says Hrynkow. Since then, she has held executive positions at the John E. Fogarty International Center of the US National Institutes of Health (NIH) in Bethesda, Maryland; the United Nations Foundation in Washington DC; and the NIH's National Institute of Environmental Health Sciences in Research Triangle Park, North Carolina. Now she's back at the OES, working to advance the American global health mission. Although she does not work as a neuroscientist, Hrynkow notes that she has applied many facets of her degree to her work. At Fogarty, she helped launch a programme ▶

► on brain disorders in developing nations; and throughout her career, she has relied daily on her scientific values, including transparency, the importance of peer review and open competition. “Having a solid understanding of how science is conducted in this country is helpful as we reach out to partners abroad,” says Hrynkow.

FEDERAL CASE

Although the US government has long recognized the importance of science in international relations, diplomacy and policy-making, there aren't a huge number of federal positions available. But the situation may improve. The state department — which manages US relations with the governments and people of other countries — hopes to boost its science-and-technology-based diplomatic corps, says Andrew Reynolds, deputy science and technology adviser to the secretary of state. An important gap, says Reynolds, has emerged in the number of foreign-service officers with science backgrounds. In the 1990s the department's ranks thinned; as people left, they weren't replaced. In addition to foreign-service officers, the state department employs foreign-affairs officers in the civil service who are based in the United States but are sometimes called on to travel.

Reynolds notes that the department's first Quadrennial Diplomacy and Development Review (QDDR), released in late 2010, calls for science and technology to be incorporated into current and future international-development policy. “Science, engineering, technology and innovation are the engines of modern society,” the state department said in the QDDR, “and [are] a dominant force in globalization and international economic development.” The report, a review of the department's objectives and planned strategies, is closely tied to the first Presidential Policy Directive on Global Development, signed last September, which includes initiatives on health and climate-change research. The department has not yet determined how many people with science and technology backgrounds will be hired, or for which bureaux or divisions. It currently employs some 13,000 foreign-service officers and 8,000 members of the civil service. “We want to create a career path here for people in science, technology, engineering and maths,” says Reynolds. “We need to restore our

capacity.”

The United States Agency for International Development (USAID) also has a foreign service, but its hiring outlook may not be good. The agency had been planning to expand as a result of a congressional initiative launched in 2008, which called for USAID to improve its ability to provide overseas support — a remit that includes anything from helping farmers develop stronger crops to creating maternal-health programmes. Under this scheme, the agency had been aiming to double the size of its foreign-service workforce, including scientists. But the plan could be in jeopardy as a result of possible federal budget cuts in future years.

Still, the state department and USAID aren't the only federal options for entering international policy. Depending on a scientist's field, he or she might investigate the Fogarty International Center, where positions could involve establishing a training programme in a developing country to help address health crises, or the National Institute of Allergy and Infectious Diseases in Bethesda, where one might build partnerships in infectious-disease research overseas. The US Centers for Disease Control and Prevention in Atlanta, Georgia, often has international opportunities in areas such as working with health ministries to build public-health surveillance systems in developing countries, or building global-health policies and programmes. And all US federal agencies with a science-oriented or technical mission have a foreign-service workforce.

FINDING A NICHE

Not all scientific diplomacy positions are government-based. Vaughan Turekian, chief international officer at the AAAS and director of the association's Center for Science Diplomacy in Washington DC, knew early on that he wanted to work in international relations, but he has largely avoided the civil-servant role, apart from an assignment as special assistant to the under secretary of state for global affairs at the start of his career. Once he had earned his doctorate in atmospheric geochemistry, Turekian knew that he wanted to widen his scientific scope. So he did a two-month stint as a visiting professor at the American University of Armenia in Yerevan, and worked at the US National Academy of Sciences in Washington DC, where he was the study director for a report on climate-change science that had been commissioned by the White House. Turekian believes that his international-relations efforts are as effective as those of the government. “The types of diplomacy that are outside the realm of government-to-government are focused on a problem, and you engage different parts of communities to help address that problem,” he says. “You're involved in building a relationship. You're not there as a perceived threat.”

Regardless of the sector, many scientists who work in diplomacy and international policy say that the most promising career path is through

a fellowship. The most frequently cited programmes include: the AAAS Science & Technology Policy Fellowship; the Scholars and Fellows scheme offered by the Fogarty centre; the state department's Professional Science and Engineering Society Fellows Program; and the Embassy Science Fellows programme, co-run by the state department and the National Science Foundation, for those already working at

“Scientists are treated with a certain level of trust that other government officials don't receive.”

a federal agency. Fellows in each of these programmes often work as science advisers. A doctoral degree is usually required, along with exceptional competence in one's speciality and an

awareness of global issues.

The AAAS programme in particular has a solid track record in funnelling former fellows — there have been about 2,000 since the programme began in 1973 — into positions. Fellows placed at the state department and USAID often find it an excellent stepping stone to a career in foreign policy, says Cynthia Robinson, the programme's director. The NIH has hired nearly half of the AAAS fellows that it has hosted in the past ten years. Robinson says that 43 former fellows now work overseas for the state department, in positions including consular officer in Mumbai, India, and foreign-affairs officer in Kabul. A further 43 work abroad for USAID in positions such as climate-change adviser for the Africa Bureau or health-development officer for the Office of Technical Support at the Asia and the Near East Bureau.

SKILL SET

All of these positions require soft skills that don't come easily to every scientist. Working in any tense international negotiation requires a knack for putting people at ease to comfortably discuss sensitive issues.

Alex Kahl, an AAAS fellow at the state department, credits his parents, who have spent their lives in sales, for his ability to win people over and gain support. His interest in policy began in graduate school and blossomed while he was working as a postdoc at Rutgers University in New Brunswick, New Jersey. He was studying polar ecosystems in Antarctica, where he lectured about the region to thousands of cruise-ship passengers. He quickly learned that he was good at engaging people and building relationships, and decided that foreign policy and international relations was a better career choice for him than research. He hopes to join the foreign service because, he says, science can open doors that may be barred to other bureaucrats. “Scientists are treated with a certain level of trust that other government officials don't receive,” adds Kahl.

Turekian recommends that prospective diplomats build their communication skills



“A solid understanding of how science is conducted is helpful as we reach out to partners abroad.”

Sharon Hrynkow

E. BRANSON/NIH

by presenting at conferences, participating in science workshops and writing mock grant proposals for practice. The ability to write clearly and concisely, he says, is key. "Science diplomacy has implications for the way policy-makers look at something," he says. "You have to write coherent and understandable statements." He suggests that scientists write up as many abstracts as they can, both real and mock, to hone the skill of writing tightly and clearly.

Learning how to listen effectively and to treat one's counterparts from other cultures with respect is critical, says Peter Jackson, chief of the AIDS research review branch at the National Institute of Allergy and Infectious Diseases. Jackson, who has been doing international outreach work since the 1990s and has served as a fellow in a National Academies programme and at the state department as an Embassy Science fellow — for which he travelled to Croatia to work with the University of Zagreb on establishing best practices for its research office — says that it helps to immerse oneself in the target area before arriving. "Get some information about the culture, read up about the people in terms of the science involved in the mission, and understand what they're doing before you show up," he says. Once there, the visiting scientist should be respectful and courteous, says Jackson: "You've got to listen to what people are saying. You can't come in as the big Western scientist and say, 'I'm going to tell you what we're going to do.'"

Branching out from one's area of expertise is also imperative. Turekian advises scientists intending to work abroad to seek out journal articles, conferences and workshops outside their specialities, to help them view issues through a different lens. "You can't compromise the science," he says, "but you have to understand that some of the ways in which things are communicated and the assumptions that one goes in with are not the same everywhere." Cultivating patience is also crucial, adds Turekian.

A scientist entering the diplomatic realm must become familiar with the concerns and priorities of the diplomatic community, says Hrynkow. They can do this by reading diplomacy journals and publications, joining diplomacy associations and organizations, and becoming active in related online communities.

Trans-boundary issues such as polar ice, the atmosphere and climate "offer perfect opportunities to get scientists from many countries working together," says Kahl. "If you have shared objectives and are working toward a common solution, you can build bridges." ■

Karen Kaplan is Nature's assistant editor for Careers.

TURNING POINT

Collins Ouma

Collins Ouma became a molecular biologist to help thwart malaria's high mortality rate in his native Kenya. Last November, he won the Royal Society Pfizer award for his work on identifying genes that may confer protection to children suffering from severe malarial anaemia in western Kenya.

Why did you decide to study malaria?

I had a revelation between 1994 and 1998 while working on my science degree at Kenyatta University in Nairobi. I got sick twice and insisted on tests, which found I had malaria parasites. My symptoms were akin to what I saw when growing up, and I realized that my relatives probably died of malaria. This heightened my curiosity about factors that predispose people to severe malarial disease and even death. Little is known about the genetic and immunological basis of severe malarial anaemia, yet current estimates suggest that the disease causes between 190,000 and 974,000 deaths every year among children under five years old.

How did you get started in this field?

After my undergraduate degree, I worked for a short time as a molecular biologist at the US Centers for Disease Control and Prevention (CDC) malaria lab at the Kenya Medical Research Institute (KEMRI) in Kisumu. It was the perfect impetus to guide my research career towards the molecular biology of malaria. The CDC had the structure and equipment for the training I needed, but couldn't offer a permanent job. So I went on to do a master's degree at Kenyatta University.

What brought you to the University of New Mexico for your PhD work?

I met Douglas Perkins, a tropical-disease specialist at the University of New Mexico (UNM), while finishing my master's. He was in Kenya with funding from the US National Institutes of Health (NIH) and the NIH's Fogarty International Center to support and train local scientists conducting research on endemic diseases. He was directed to me at the exact time I needed to do a PhD. His grants funded me throughout my PhD and partially through my postdoc at UNM. As a postdoc, I spent three months training in the United States every year for three years, and the other nine months in Kenya conducting vaccine and genetics-susceptibility research.

Have you formed any collaborations between Kenya and New Mexico?

Yes. I'm an associate professor of genetics at Maseno University (MU) near Kisumu, and a



postdoctoral fellow at UNM. I still do research both in the United States and in their collaborative labs at KEMRI. The three research institutions [UNM, MU and KEMRI] have established a collaborative relationship, but I'm interested in working with any group that is eager to help eliminate this disease.

Why did you apply for this award?

When Wilson Odero, a public-health researcher at MU, encouraged me to apply and offered a letter of recommendation, I got to work and wrote a proposal to set up a state-of-the-art molecular-biology laboratory at MU and to identify individuals to train.

How will you use the £60,000 (US\$96,700) award?

Part of my work takes place at Siaya District Hospital in western Kenya. As children suffer the most from this disease, we intend to first identify molecules that can be used to design a malaria vaccine for children under five. Second, we will continue to identify children who are at risk of severe malarial disease. Over the past 8 years we have enrolled about 1,400 children. We have followed-up on about 800 children quarterly to see how they progress with drugs and in handling disease outcomes. We then associate their improvement with their genetic make-up to see if certain genes protect them against disease or increase their susceptibility.

What impact has your research had so far?

So far, we have reduced mortality rates from 22% to 7% among 1,400 children under five at this hospital in rural western Kenya. But my ultimate goal is to develop an effective long-lasting malaria vaccine through active research. ■

INTERVIEW BY VIRGINIA GEWIN

by presenting at conferences, participating in science workshops and writing mock grant proposals for practice. The ability to write clearly and concisely, he says, is key. "Science diplomacy has implications for the way policy-makers look at something," he says. "You have to write coherent and understandable statements." He suggests that scientists write up as many abstracts as they can, both real and mock, to hone the skill of writing tightly and clearly.

Learning how to listen effectively and to treat one's counterparts from other cultures with respect is critical, says Peter Jackson, chief of the AIDS research review branch at the National Institute of Allergy and Infectious Diseases. Jackson, who has been doing international outreach work since the 1990s and has served as a fellow in a National Academies programme and at the state department as an Embassy Science fellow — for which he travelled to Croatia to work with the University of Zagreb on establishing best practices for its research office — says that it helps to immerse oneself in the target area before arriving. "Get some information about the culture, read up about the people in terms of the science involved in the mission, and understand what they're doing before you show up," he says. Once there, the visiting scientist should be respectful and courteous, says Jackson: "You've got to listen to what people are saying. You can't come in as the big Western scientist and say, 'I'm going to tell you what we're going to do.'"

Branching out from one's area of expertise is also imperative. Turekian advises scientists intending to work abroad to seek out journal articles, conferences and workshops outside their specialities, to help them view issues through a different lens. "You can't compromise the science," he says, "but you have to understand that some of the ways in which things are communicated and the assumptions that one goes in with are not the same everywhere." Cultivating patience is also crucial, adds Turekian.

A scientist entering the diplomatic realm must become familiar with the concerns and priorities of the diplomatic community, says Hrynkow. They can do this by reading diplomacy journals and publications, joining diplomacy associations and organizations, and becoming active in related online communities.

Trans-boundary issues such as polar ice, the atmosphere and climate "offer perfect opportunities to get scientists from many countries working together," says Kahl. "If you have shared objectives and are working toward a common solution, you can build bridges." ■

Karen Kaplan is Nature's assistant editor for Careers.

TURNING POINT

Collins Ouma

Collins Ouma became a molecular biologist to help thwart malaria's high mortality rate in his native Kenya. Last November, he won the Royal Society Pfizer award for his work on identifying genes that may confer protection to children suffering from severe malarial anaemia in western Kenya.

Why did you decide to study malaria?

I had a revelation between 1994 and 1998 while working on my science degree at Kenyatta University in Nairobi. I got sick twice and insisted on tests, which found I had malaria parasites. My symptoms were akin to what I saw when growing up, and I realized that my relatives probably died of malaria. This heightened my curiosity about factors that predispose people to severe malarial disease and even death. Little is known about the genetic and immunological basis of severe malarial anaemia, yet current estimates suggest that the disease causes between 190,000 and 974,000 deaths every year among children under five years old.

How did you get started in this field?

After my undergraduate degree, I worked for a short time as a molecular biologist at the US Centers for Disease Control and Prevention (CDC) malaria lab at the Kenya Medical Research Institute (KEMRI) in Kisumu. It was the perfect impetus to guide my research career towards the molecular biology of malaria. The CDC had the structure and equipment for the training I needed, but couldn't offer a permanent job. So I went on to do a master's degree at Kenyatta University.

What brought you to the University of New Mexico for your PhD work?

I met Douglas Perkins, a tropical-disease specialist at the University of New Mexico (UNM), while finishing my master's. He was in Kenya with funding from the US National Institutes of Health (NIH) and the NIH's Fogarty International Center to support and train local scientists conducting research on endemic diseases. He was directed to me at the exact time I needed to do a PhD. His grants funded me throughout my PhD and partially through my postdoc at UNM. As a postdoc, I spent three months training in the United States every year for three years, and the other nine months in Kenya conducting vaccine and genetics-susceptibility research.

Have you formed any collaborations between Kenya and New Mexico?

Yes. I'm an associate professor of genetics at Maseno University (MU) near Kisumu, and a



postdoctoral fellow at UNM. I still do research both in the United States and in their collaborative labs at KEMRI. The three research institutions [UNM, MU and KEMRI] have established a collaborative relationship, but I'm interested in working with any group that is eager to help eliminate this disease.

Why did you apply for this award?

When Wilson Odero, a public-health researcher at MU, encouraged me to apply and offered a letter of recommendation, I got to work and wrote a proposal to set up a state-of-the-art molecular-biology laboratory at MU and to identify individuals to train.

How will you use the £60,000 (US\$96,700) award?

Part of my work takes place at Siaya District Hospital in western Kenya. As children suffer the most from this disease, we intend to first identify molecules that can be used to design a malaria vaccine for children under five. Second, we will continue to identify children who are at risk of severe malarial disease. Over the past 8 years we have enrolled about 1,400 children. We have followed-up on about 800 children quarterly to see how they progress with drugs and in handling disease outcomes. We then associate their improvement with their genetic make-up to see if certain genes protect them against disease or increase their susceptibility.

What impact has your research had so far?

So far, we have reduced mortality rates from 22% to 7% among 1,400 children under five at this hospital in rural western Kenya. But my ultimate goal is to develop an effective long-lasting malaria vaccine through active research. ■

INTERVIEW BY VIRGINIA GEWIN

DREAM GIRL

Mind games.

BY SWAPNA KISHORE

Alia's dream, splashed on the monitor, was obviously going to fail the audit. Rita, a spunky 20-year-old in a scarlet skinsuit, raced down an alley alongside innocent-eyed Bambi. Hanu-Man, a trapeze artist on gossamer threads, scooped her up; she whizzed through the air with him when Bhayankar Asura grabbed her away, blood dripping from its claws. Rita squirted Jaipur pepper into its eyes.

Although Alia knew she'd have to pay a hefty penalty, she couldn't help grinning; she was thrilled to see the screen displaying the perfectly imagined Rita, her alter-ego, a character she had created herself. Pity the other characters were copyrighted.

"Watch this." The auditor twisted a knob; purple splotches filled the screen. "Your neural patterns match copyrighted neurotags at 60%, well above permissible limits for residual thoughts. Your second offence, so that'll be 20,000 rupees."

This was not the time to rant about India's signing the World Copyright Act six months ago, a betrayal of the basic human right to think and dream: a law was a law. No one could think or dream of copyrighted characters without paying royalty. Even so, 20 thou! That meant skipping dinners, card payments and phone top-ups. No new shoes. Waking at 4 to take the Mumbai Metro to the office, no auto-rickshaw, and definitely no taxi.

"Can I have a copy of that recording?" Alia asked, as she signed the charge slip.

The officer frowned. "It's permitted, but viewing it will worsen your problem. I'd suggest image-guided surgical microscraping. Or pay perpetuity royalty for fan-think and fan-dreams. Because the next time you default, the penalty will be 40."

"I know." Alia kept her expression bashful. "The recording will remind me of what I shouldn't do."

An hour later, Alia, though poorer by 20 thou, smiled as she sipped steaming coffee at a roadside stall. Her Rita was now available in flesh — well, pixels — in her handbag. And Alia had an idea.

Mumbai Book Bazaar's window abounded with the latest graphic novels — a tease, given Alia's depleted financial state. She would have treated herself nevertheless, but today she had an idea to chase, so she passed the shop and entered the shanty-town Dharavi II.

Shakespearewallah was a dingy, musty



godown that stocked second-hand books that carried no neurotags. You broke no laws if you thought or dreamed about them. Creative companies, keen on collecting perpetuity royalty, had bought and destroyed most such books, but some shops like Shakespearewallah had survived. Alia indulged herself here when her budget was low.

She selected books on drawing, animation and lucid dreaming. The shopkeeper totted up the amount. "I see you here often. Are you an artist?"

"Hoping to be one."

The shopkeeper hesitated, then said: "If you want inspiration, we carry dreamsules."

A million butterflies fluttered in Alia's stomach. Dreamsules were bottled dreams. Illegal.

"You make them?" Alia asked.

"We purchase dreams and edit out any neurotags so that viewers don't get caught in dream-audits."

Alia shuddered. "I know about audits; I failed one today."

"We also offer cheap purge pills."

No way! Purge pills destroyed all neural connections that had copyright neurotags. If taken immediately after reading a copyrighted book, the pill's damage was limited, but Alia, greedy gobbler of books, incorrigible brooder and day-dreamer, had mulled over too many tagged characters for too many days. Her tags must have spread all over her brain. Purging now would be like bulldozing a building to kill a swarm of mosquitoes.

No, Alia had to choose between paying in perpetuity for every book she read; or the inevitable penalties when summoned for 'random' dream-audits.

➔ **NATURE.COM**
Follow Futures on
Facebook at:
go.nature.com/mtoodm

She couldn't afford either. But hey, she could sell her dreams.

JACEY

All three of her graphic novels featured Rita Razor, a common girl with uncommon spunk. Anyone would snap this up, thought Alia, as she sat across from Mr Vandrewala, Universal Creations. He flipped through her sketches, face expressionless. Alia squirmed. She had expected more enthusiasm. "Would you like to buy them?"

"Where's the creative history?"

"Sorry?" Alia blinked.

He toyed with a crystal paperweight, his face like the scheming Sher Khan in Mowgli comics. "Rita, an orphan with magical ability, could be a female Harry Potter."

"She's not," Alia snapped, indignant.

"Did you get a certified all-clear brain audit before you started creating her? While working on this, did you refrain from copyrighted reading? Did you get official purges done after every recorded read? Can you prove your work isn't based on any copyrighted knowledge?"

"No one can prove —"

"Royalty must be paid for characters used. Without a documented, foolproof derivation, anyone can sue." Contempt laced Vandrewala's voice. "Amateurs underestimate the rigour involved."

Rigour? For two years, Alia had struggled to create Rita while also doing her day job. She'd sold her dreams for extra money and scrimped to pay perpetuity royalty to avoid dream-audit fines. Trained herself on lucid dreaming. Drawing. Pixellating. All wasted.

She noticed light glinting off the paperweight when she got up: a micro-camera? How naive of her — she should have anticipated such tricks.

"Rita is my creation and has figured in my dreams for years," Alia said, anger scaffolding her voice. "My early dream-audits, archived at the Copyright Directorate, prove that."

Portfolio gripped in her hand, she walked into Mumbai Book Bazaar. "An up-to-date book on copyright law and creative works," she demanded. She'd figure out how to publish her novels; she had to, because she was already planning another one with Vandrewala as villain: *Rita Razor beats Andre the Plagiarist*.

You dream, girl, she told herself. ■

Swapna Kishore is a software consultant in Bangalore, India. She has published technical books and a business novel. She also writes speculative fiction.

ABOUT THE JOURNAL SCOPE

Clinical Pharmacology & Therapeutics is the authoritative, cross-disciplinary journal in experimental and clinical medicine devoted to publishing advances in the nature, action, efficacy and evaluation of therapeutics in humans. *CPT* welcomes original reports and articles in the emerging areas of translational, predictive and personalized medicine; new therapeutic modalities including gene and cell therapies; pharmacogenomics, proteomics and metabolomics; bioinformation and applied systems biology complementing areas of pharmacokinetics and pharmacodynamics, human investigation and clinical trials, pharmacovigilance, pharmacoepidemiology, pharmacometrics, and population pharmacology. The journal also publishes articles by invitation. Commentary and Point-Counterpoint provide a forum for perspectives in clinical pharmacology and therapeutics in the context of contemporary scientific, political, economic and social issues. State of the Art contributions summarize the latest advances in the science underpinning drug discovery, development, regulation and utilization. *CPT* highlights issues transforming the practice of clinical pharmacology, including ethics, education and public policy. Bench-to-bedside translation in therapeutics is presented in the context of clinical applications of basic pharmacology, discovery and translational medicine and drug development. *CPT* will not consider case reports or animal studies.

ABSTRACTING

This journal is covered by: Biological Abstracts, BIOSIS Previews, Chemical Abstracts, Current Contents, Derwent Biotechnology Abstracts, EMBASE, Index to Scientific Reviews, Inpharma Weekly, International Pharmaceutical Abstracts, Medline, Nutrition Abstracts, Nutrition Research Newsletter, Personal Alert, Pharmacoeconomics and Outcomes News, Protozoological Abstracts, Reactions of Aromatic and Medicinal Plants, Review of Medical and Veterinary Mycology, Science Citation, Scopus and Tropical Diseases Bulletin.

IMPACT FACTOR

With an impact factor of 6.961, *CPT* is the top-ranked journal publishing primary research in the field of pharmacology and pharmacy.

URL <http://www.nature.com/cpt>

ISSN 0009-9236

EISSN 1532-6535

FREQUENCY Printed monthly. Advance Online Publication once weekly.

PREPARATION OF MANUSCRIPTS CONTENT TYPES

Author Submissions (1) Article, (2) Clinical Trial, (3) Letter to the Editor, (4) Report

Invited Submissions (5) Book Review, (6) Commentary, (7) Conference Proceedings, (8) Development, (9) Discovery, (10) Macroscopy, (11) Opinions, (12) Point-Counterpoint, (13) Practice, (14) Review, (15) State of the Art, (16) Translation. Submissions that do not adhere to the guidelines provided in this document will be returned to the author prior to consideration. Material that cannot fit within the allowed limit may be submitted as supplementary information.

ORIGINAL RESEARCH

(1) Article

Word Limit: 4,000 words excluding abstract, references, tables, and figures

Abstract: 150 words maximum

References: 50 maximum

Figures/Tables: 7 maximum

Substantial novel research

(2) Clinical Trial

Word Limit: 5,000 words excluding abstract, references, tables, and figures

Abstract: 150 words maximum

References: 60 maximum

Figures/Tables: 8 maximum

Manuscripts developed from well-conducted, well reported, and relevant clinical trials. See Clinical Trials: Guide to Authors for additional information.

(3) Letter to the Editor

Word Limit: 400 words excluding references, tables, and figures

Abstract: no abstract for this article type

References: 5 maximum

Figures/Tables: 1 maximum

Typically should address issues concerning recently published information in Clinical Pharmacology & Therapeutics. A Letter to the Editor must reference the original source, and a Response to Letter must reference the Letter to the Editor in the first few paragraphs. Letters to the Editor can use an arbitrary title, but a Response must cite the title of the Letter: e.g., Response to [title of Letter]

(4) Report

Word Limit: 2,000 words excluding abstract, references, tables, and figures

Abstract: 75 words maximum

References: 30 maximum

Figures/Tables: 3 maximum

Substantial novel research

OTHER CONTRIBUTIONS

(5) Book Review [only by invitation of Editors]

Word Limit: 700 words

Abstract: no abstract for this article type

References: no references for this article type

Figures/Tables: Cover image will be secured prior to publication by the Editorial Office

(6) Commentary [only by invitation of Editors]

Word Limit: 1,600 words excluding abstract, references, tables, and figures

Abstract: no abstract for this article type; should include a 75-word introduction

References: 10 maximum

Figures/Tables: 2 maximum

Typically highlights findings of a paper in the same issue, presented in a wider scientific and clinical context

(7) Conference Proceedings [only by invitation of Editors]

Word Limit: 1,600 words excluding abstract, references, tables, and figures

Abstract: no abstract for this article type; should include a 75-word introduction

References: 10 maximum

Figures/Tables: 2 maximum

Typically highlights topics from recent conferences that impact clinical pharmacology

(8) Development [only by invitation of Editors]

Word Limit: 3,000 words excluding references, tables, and figures

Abstract: no abstract for this article type; should include a 75-word introduction

References: 40 maximum

Figures/Tables: 3 maximum

Illustrations: 1 required

Emerging innovations in tools, platforms, and applications transforming diagnostic and therapeutic development; new algorithms optimizing the clinical utility of patient- and

population-based interventions; evolution of regulatory and economic policies centered on optimizing disease management

(9) Discovery [only by invitation of Editors]

Word Limit: 3,000 words excluding references, tables, and figures

Abstract: no abstract for this article type; should include a 75-word introduction

References: 40 maximum

Figures/Tables: 3 maximum

Illustrations: 1 required

Cellular or molecular mechanisms emerging from enabling platform technologies providing insight into pathophysiology, opening new avenues for diagnostic and therapeutic intervention; novel integration of fundamental principles across communities of practice and disciplines producing unexpected paradigms with transformative clinical potential

(10) Macroscopy [only by invitation of Editors]

Word Limit: 1,600 words

Abstract: no abstract for this article type

References: 5 maximum

Figures/Tables: 1 maximum

Should offer a broad view on critical issues facing clinical pharmacology and therapeutics in science, healthcare, policy, and society

(11) Opinions

Word Limit: 1,500 words excluding references, tables, and figures

Abstract: no abstract for this article type; should include a 75-word introduction

References: 5 maximum

Figures/Tables: 2 maximum

These short pieces are designed to give the author's perspective on current topics of relevance to the readership in areas of education, ethics, and public policy

(12) Point-Counterpoint [only by invitation of Editors]

Word Limit: 1,600 words excluding abstract, references, tables, and figures

Abstract: no abstract for this article type; should include a 75-word introduction

References: 10 maximum

Figures/Tables: 2 maximum

Balanced discussion of controversies in clinical pharmacology

(13) Practice [only by invitation of Editors]

Word Limit: 2,000 words excluding references, tables, and figures.

Abstract: no abstract for this article type; should include a 75-word introduction

References: 30 maximum

Figures/Tables: 3 maximum

Illustrations: 1 required

Cases of exceptional novelty that hold teaching points applicable to clinical pharmacology and established therapeutic approaches in clinical care

(14) Review [only by invitation of Editors]

Word Limit: 8,000 words excluding references, tables, and figures

Abstract: no abstract for this article type; should include a 75-word introduction

References: 75 maximum

Figures/Tables: 8 maximum

Illustrations: 2 required

High-quality, timely reviews and perspectives covering important topics in the entire field of clinical pharmacology and therapeutics

(15) State of the Art [only by invitation of Editors]

Word Limit: 8,000 words excluding references, tables, and figures

Abstract: 150 words maximum

References: 75 maximum

Figures/Tables: 8 maximum

Illustrations: 2 required

Typically topical reviews, award lectures, keynote addresses, and State of the Art Lectures

(16) Translation [only by invitation of Editors]

Word Limit: 3,000 words excluding references, tables, and figures

Abstract: no abstract for this article type; should include a 75-word introduction

References: 40 maximum

Figures/Tables: 3 maximum

Illustrations: 1 required

Emerging innovations in tools, platforms, and applications transforming diagnostic and therapeutic development; new algorithms optimizing the clinical utility of patient- and population-based interventions; evolution of regulatory and economic policies centered on optimizing disease management

FORMAT OF MANUSCRIPTS

General format Manuscripts must be typed in English and be in a single column, double-spaced format. All manuscript pages must be numbered.

Title page This should include (a) the complete manuscript title; (b) all authors' names (listed as first and middle initials followed by last name) and affiliations; and (c) the name and address for correspondence, fax number, telephone number, and e-mail address. The title page should also include word counts for the abstract, introduction, and the manuscript as a whole; the number of references, figures, and tables; and key words.

Text For contributions requiring abstracts, the lengths are defined in the respective sections of *Preparation of Manuscripts*. For contributions that do not require an abstract, introductory paragraphs may contain references to cited work. Articles and Reports should consist of the following ordered sections:

Title Page
Abstract
Introduction
Results
Discussion
Methods (must contain IRB or IACUC approval: see **Informed Consent and Ethics** below)
Acknowledgements
Conflict of Interest/Disclosure
References
Figure Legends
Tables

Originality A submitted manuscript must be an original contribution not previously published (except as an abstract), must not be under consideration for publication elsewhere, and, if accepted, must not be reproduced elsewhere without the consent of the American Society for Clinical Pharmacology and Therapeutics (ASCP). Although the editors, editorial board, and referees make every effort to ensure the validity of published manuscripts, the final responsibility rests with the authors, not with *Clinical Pharmacology & Therapeutics*, its editors, the ASCPT, or Nature Publishing Group.

Informed Consent and Ethics CPT adheres to the *Uniform Requirements for Manuscripts Submitted to Biomedical Journals* established by the International Committee of Medical Journal Editors. A full description of recommendations can be found at <http://www.icmje.org>. Research projects involving human subjects require review and approval by an Institutional Review Board (IRB). When reporting experiments on human subjects, indicate whether the procedures were in accordance with the ethical standards of the responsible committee on human experimentation or with the Helsinki Declaration of 1975 (as revised in 1983). IRB or IACUC approval must be cited in the Methods section of the text. If there has been no IRB review of the study, please so indicate in the cover letter. In such situations, the manuscript

will be reviewed to determine if IRB review should have been conducted. The result of this review may determine whether or not the manuscript will be considered for publication.

Clinical Trials Registry Registration in a public trials registry is required for publication in CPT. A clinical trial is defined as any research project that prospectively assigns human subjects to intervention or comparison groups to study the cause-and-effect relationship between a medical intervention and a health outcome. Studies designed for other purposes, including exploring pharmacokinetics or safety and tolerability (e.g., phase 1 trials) are exempt. Registration must be with a registry that meets the following criteria: (1) accessible to the public at no charge; (2) searchable by electronic methods; (3) open to all prospective registrants free of charge or at minimal cost; (4) validates registered information; (5) identifies trials with a unique number; and (6) includes information on the investigator(s), research question or hypothesis, methodology, intervention and comparisons, eligibility criteria, primary and secondary outcomes measured, date of registration, anticipated or actual start date, anticipated or actual date of last follow-up, target number of subjects, status (anticipated, ongoing or closed), and funding source(s). Examples of registries that meet these criteria include (1) The registry sponsored by the United States National Library of Medicine (<http://www.clinicaltrials.gov>); (2) The International Standard Randomised Controlled Trial Number Registry (<http://www.controlled-trials.com>); (3) The Cochrane Renal Group Registry (<http://www.cochrane-renal.org/trials/submitform.php>); (4) The National (United Kingdom) Research Register (<http://www.update-software.com/national/>); and (5) European Clinical Trials Database (<http://eudract.emea.eu.int/>).

Abbreviations Abbreviations should be defined at the first mention in the text and in each table and figure. For a list of standard abbreviations, please consult the CSE Manual for Authors, Editors, and Publishers (available from the Council of Science Editors, 12100 Sunset Hills Road, Suite 130, Reston, VA 20190) or other standard sources. Write out the full term for each abbreviation at its first use unless it is a standard unit of measure.

Style *The American Medical Association Manual of Style* (9th edition), *Stedman's Medical Dictionary* (27th edition) and *Merriam-Webster's Collegiate Dictionary* (10th edition) should be used as standard references. Refer to drugs and therapeutic agents by their accepted generic or chemical name, and do not abbreviate them (a proprietary name may be given only with the first use of the generic name). Code names should be used only when a generic name is not yet available (the chemical name and a figure giving the chemical structure of the drug is required). Copyright or trade names of drugs should be capitalized and placed in parentheses after the name of the drug. Names and locations (city and state in United States; city and country outside United States) of manufacturers of drugs, supplies, or equipment cited in a manuscript are required to comply with trademark law and should be provided in parentheses.

Language Editing Authors who require editing for language are encouraged to consult language editing services prior to submission. Contact the Editorial Office for recommendations.

AUTHOR RESPONSIBILITY

Upon submission, the corresponding author must confirm full access to all data in the study and final responsibility.

ACKNOWLEDGMENTS

This should include sources of support, including federal and industry support. All authors who have

contributed to the manuscript must be acknowledged. Medical writers, proofreaders, and editors should not be listed as authors, but acknowledged at the beginning or end of the text.

DISCLOSURE

At the time of submission, each author must disclose and describe any involvement, financial or otherwise, that might potentially bias his or her work. Disclosure must be included in the text of the manuscript.

REFERENCES

Should be listed in order of appearance (Vancouver style). In the text, number references in order of appearance using Arabic numerals (e.g., 1, 2, 3) in parentheses for citations. The publisher will convert parenthetical citations to superscript at the proofing stage. The reference list (starting on a separate page) should contain the references in the order in which they are cited in the text. Citations included in tables/figures count toward the maximum references allowed for the article type and must be included in the reference list. Tables created solely of references are not permitted. Only published works, as well as manuscripts in press, should be included in the reference list; articles that are submitted or in preparation should be referred to as "unpublished data" in the text (for which all authors up to 6 total should be listed, then et al.). For publications in the reference list, all authors should be included unless there are more than six, in which case only the first author should be given, followed by 'et al.' Authors should be listed last name first, followed by a comma and initials of given names. Titles of cited articles are required for all article types. Titles of articles should be in Roman text and titles of books in italics. The titles should be written exactly as they appear in the work cited except that article titles should have only the first word capitalized, and they should end with a period. Journal names are italicized and abbreviated (with periods after each abbreviated word) according to common usage; refer to Index Medicus (PubMed) for details. Volume numbers appear in bold. For book citations, the publisher and city of publication are required; include the country (and state for US) for lesser-known cities or where any ambiguity is possible (e.g., John Wiley & Sons, Hoboken, New Jersey, USA, 2003; MIT Press, Cambridge, Massachusetts, USA). Please note the following examples:

Journal articles:

Kashuba, A.D. et al. Effect of fluvoxamine therapy on the activities of CYP1A2, CYP2D6, and CYP3A as determined by phenotyping. *Clin. Pharmacol. Ther.* **64**, 257–268 (1998).

Books:

Eisen, H.N. *Immunology: An Introduction to Molecular and Cellular Principles of the Immune Response* 5th edn. (Harper & Row, New York, 1974).

Articles in books:

Weinstein, L. & Schwartz, M.N. Pathogenic properties of invading microorganisms. In *Pathologic Physiology: Mechanisms of Disease* (eds. Sodeman, W.A., Jr. & Sodeman, W.A.) 457–473 (W.B. Saunders, Philadelphia, 1974).

CPT is supported by EndNote Styles. To download the CPT style file, visit <http://www.endnote.com/support/enstyles.asp> and search for "Clinical Pharmacology & Therapeutics."

FIGURES

Should be labeled sequentially, numbered, and cited in the text. If a table, figure or any other previously published material is included, the authors must obtain written permission to reproduce the material in both print and electronic formats from the copyright owner and submit it with the manuscript. The original

source should be cited. Figures and tables must be uploaded separately from the manuscript text.

FIGURE LEGENDS

Legends should be brief and specific and should appear on a separate manuscript page after the Reference section.

GUIDELINES FOR FIGURES AND ARTWORK

Detailed guidelines for submitting figures and artwork can be found at: <http://www.nature.com/aj/artworkguidelines.pdf>. Using the guidelines, please submit production quality artwork with your initial online submission. If you have followed the guidelines, we will not require unchanged artwork to be resubmitted following the peer-review process.

FIGURES IN PRINT

Accepted figure files include JPEG, TIFF, EPS, AI, and PSD.

[color charges may apply]

Minimum resolutions:

Halftone images, 300 dpi (dots per inch)

Color images, 300 dpi saved as CMYK

Images containing text, 400 dpi

Line art, 1,000 dpi

Sizes:

Figure width – single image 86 mm (should be able to fit into a single column of the printed journal)

Figure width – multi-part image 178 mm (should be able to fit into a double column of the printed journal)

Text size

8 point (should be readable after reduction – avoid large type or thick lines) line width between 0.5 and 1 point

COLOR ON THE WEB

For FREE color figures on the web (only available in the HTML (full text) version of manuscripts), authors should supply separate JPEG or GIF files. These files should be submitted as supplementary information and indicated as such in the submission letter.

For single images:

Width 500 pixels (authors should select “constrain proportions,” or equivalent instructions, to allow the application to set the correct proportions automatically)

Resolution 125 dpi (dots per inch)

Format JPEG for photographs, GIF for line drawings or charts

File naming Please save image with .jpg or .gif extension to ensure it can be read by all platforms and graphics packages

For multi-part images:

Width 900 pixels (authors should select “constrain proportions,” or equivalent instructions, to allow the application to set the correct proportions automatically)

Resolution 125 dpi (dots per inch)

Format JPEG for photographs, GIF for line drawings or charts

File naming Please save image with .jpg or .gif extension to ensure it can be read by all platforms and graphics packages

TABLES

Accepted file types include MS Word (tables should be editable, not embedded images) and Excel. Each table should be double-spaced on a separate sheet and numbered consecutively in the order of first citation in the text. Minimize empty space and restrict the number of characters per row to 130. Supply a brief title for each, but place explanatory matter in the footnotes (not in the heading). Do not use internal horizontal and vertical lines.

JOURNAL STYLE

Papers should be prepared as follows:

1. See the artwork guidelines above
2. Do not make rules thinner than 1 pt (0.36mm)
3. Use a coarse hatching pattern rather than shading for tints in graphs
4. Color should be distinct when used as an identifying tool
5. Commas should be used to separate thousands
6. Abbreviations should be preceded by the words for which they stand in the first instance of use
7. Text should be double-spaced with a 1 inch margin
8. At first mention of a manufacturer, the town (state if USA) and country should be provided

FILE FORMATS & REQUIREMENTS

File formats are provided in the online forms. Use a common word-processing package (MS Word is preferred) for the text. Please note: A Word 2007 document must be saved as a copy fully compatible with Word 97-2003 prior to submission. Tables should be provided at the end of the Word document.

Authors are required to submit final, publication-ready files at the revision stage, along with a version tracking all changes to the paper. Use the Track Changes mode in MS Word or indicate the revised text with bold, highlighted, or colored type.

SUPPLEMENTARY INFORMATION

Supplementary information is peer-reviewed material directly relevant to the conclusion of an article that cannot be included in the printed version owing to space or format constraints. It is posted on the journal's web site and linked to the article when the article is published; it may include data files, graphics, movies, or extensive tables. The printed article must be complete and self-explanatory without the supplementary information. Supplementary information must be supplied to the editorial office in its final form for peer review. On acceptance, the final version of the peer-reviewed supplementary information should be submitted with the accepted paper. To ensure that the contents of the supplementary information files can be viewed by the editor(s), referees, and readers, please also submit a ‘read-me’ file containing brief instructions on how to use the file.

Supplementary Information Charges Supplementary information may be included online at a rate of \$125 per file.

Supplying Supplementary Information Files Authors should ensure that supplementary information is supplied in its FINAL format, as it is not copy edited and will appear online exactly as submitted. It cannot be altered, nor new supplementary information added, after the paper has been accepted for publication. Please supply the supplementary information via the electronic manuscript submission and tracking system in an acceptable file format (see below). Authors should include a text summary (no more than 50 words) to describe the contents of each file, identify the types of files (file formats) submitted and include the text ‘Supplementary information is available at <http://www.nature.com/cpt>’ at the end of the body of text and before the references.

Accepted File Formats Quick Time files (.mov), graphical image files (.gif), HTML files (.html), MPEG movie files (.mpg), JPEG image files (.jpg), sound files (.wav), plain ASCII text (.txt), Acrobat files (.pdf), MS Word documents (.doc), Postscript files (.ps), MS Excel spreadsheet documents (.xls), and Powerpoint (.ppt). We cannot accept TeX or LaTeX. File sizes must be as small as possible to expedite downloading. Images should not exceed 640 x 480 pixels. For movies, we recommend 480 x 360 pixels as the maximum frame size and a frame rate of 15 frames per second. If applicable to the presentation of the information, use a 256-color palette. Please consider the use

of lower specification for all of these points if the supplementary information can still be represented clearly. Our recommended maximum data rate is 150 KB/s. The number of files should be limited to eight, and the total file size should not exceed 8 MB. Individual files should not exceed 1 MB. Seek advice from the editorial office before sending files larger than our maximum size to avoid delays in publication. Questions about the submission or preparation of supplementary information should be directed to the editorial office.

EDITORIAL POLICIES

PLAGIARISM

Plagiarism is when an author attempts to represent someone else's work as his or her own. Duplicate publication, sometimes called self-plagiarism, occurs when an author reuses substantial parts of his or her own published work without providing the appropriate references. This can range from getting an identical paper published in multiple journals, to ‘salami-slicing’, where authors add small amounts of new data to a previous paper. Plagiarism can be said to have clearly occurred when large chunks of text have been cut-and-pasted. Such manuscripts would not be considered for publication in a Nature journal. But minor plagiarism without dishonest intent is relatively frequent, for example, when an author reuses parts of an introduction from an earlier paper. The journal editors judge any case of which they become aware (either by their own knowledge of and reading about the literature, or when alerted by referees) on its own merits. If a case of plagiarism comes to light after a paper is published, the journal will conduct a preliminary investigation. If plagiarism is found, the journal will contact the author's institute and funding agencies. A determination of misconduct will lead the journal to run a statement, bidirectionally linked online to and from the original paper, to note the plagiarism and to provide a reference to the plagiarized material. The paper containing the plagiarism will also be obviously marked on each page of the PDF. Depending on the extent of the plagiarism, the paper may also be formally retracted.

IMAGE INTEGRITY AND STANDARDS

Images submitted with a manuscript for review should be minimally processed (for instance, to add arrows to a micrograph). Authors should retain their unprocessed data and metadata files, as editors may request them to aid in manuscript evaluation. If unprocessed data are unavailable, manuscript evaluation may be stalled until the issue is resolved. A certain degree of image processing is acceptable for publication (and for some experiments, fields and techniques is unavoidable), but the final image must correctly represent the original data and conform to community standards. The guidelines below will aid in accurate data presentation at the image processing level; authors must also take care to exercise prudence during data acquisition, where misrepresentation must equally be avoided. Authors should list all image acquisition tools and image processing software packages used. Authors should document key image gathering settings and processing manipulations in the Methods. Images gathered at different times or from different locations should not be combined into a single image, unless it is stated that the resultant image is a product of time-averaged data or a time-lapse sequence. If juxtaposing images is essential, the borders should be clearly demarcated in the figure and described in the legend. The use of touch-up tools, such as cloning and healing tools in Photoshop, or any feature that deliberately obscures manipulations, is to be avoided. Processing (such as changing brightness and contrast) is appropriate only when it is applied equally across the entire image and is applied equally to controls. Contrast should not be adjusted so that data disappear. Excessive manipulations, such as processing to emphasize one region in the image at

the expense of others (for example, through the use of a biased choice of threshold settings), is inappropriate, as is emphasizing experimental data relative to the control. When submitting revised final figures upon conditional acceptance, authors may be asked to submit original, unprocessed images.

CONFIDENTIALITY

CPT editors and editorial staff keep confidential all details about a submitted manuscript and do not comment to any outside organization about manuscripts under consideration by the journal while they are under consideration or if they are rejected. The journal editors may comment publicly on published material, but their comments are restricted to the content itself and their evaluation of it. After a manuscript is submitted, correspondence with the journal, referees' reports and other confidential material, whether or not the submission is eventually published, must not be posted on any website or otherwise publicized without prior permission from the editors. The editors themselves are not allowed to discuss manuscripts with third parties or to reveal information about correspondence and other interactions with authors and referees. Referees of manuscripts submitted to CPT undertake in advance to maintain confidentiality of manuscripts and any associated supplementary data.

PRE-PUBLICITY

Authors must not discuss contributions with the media (including other scientific journals) until the publication date; advertising the contents of any contribution to the media may lead to rejection. The only exception is in the week before publication, during which contributions may be discussed with the media if authors and their representatives (institutions, funders) clearly indicate to journalists that their contents must not be publicized until the journal's press embargo has elapsed. Authors will be informed of embargo dates and timings after acceptance for publication of their articles.

COMMUNICATION WITH THE MEDIA

Material submitted to CPT must not be discussed with the media, except in the case of accepted contributions, which can be discussed with the media no more than a week before the publication date under our embargo conditions. We reserve the right to halt the consideration or publication of a paper if this condition is broken. From time to time CPT will distribute to a registered list a press release summarizing selected content of the next issue's publication. Journalists are encouraged to read the full version of any papers they wish to cover, and are given the names of corresponding authors, together with phone and fax numbers and email addresses. They receive access to the full text of papers about a week before publication on a password-protected website, together with other relevant material (for example, an accompanying News and Views article, and any extra illustrations provided by the authors). The content of the press release and papers is embargoed until the time and date clearly stated on the press release. Authors may therefore receive calls or emails from the media during this time; we encourage them to cooperate with journalists so that media coverage of their work is accurate and balanced. Authors whose papers are scheduled for publication may also arrange their own publicity (for instance through their institutional press offices), but they must strictly adhere to our press embargo.

COMMUNICATION BETWEEN SCIENTISTS

CPT does not wish to hinder communication between scientists. For that reason, different embargo guidelines apply to work that has been discussed at a conference or displayed on a preprint server and picked up by the media as a result. (Neither conference presentations nor posting on recognized preprint servers constitute prior publication.)

CORRECTION AND RETRACTION POLICY

We recognize our responsibility to correct errors that we have previously published. Our policy is to consider refutations (readers' criticisms) of primary research papers, and to publish them (in concise form) if and only if the author provides compelling evidence that a major claim of the original paper was incorrect. Corrections are published for significant errors in non-peer-reviewed content of the Nature journals at the discretion of the editors. Readers who have identified such an error should send an email to the editorial office of the journal, clearly stating the publication reference, title, author and section of the article, and briefly explaining the error.

CORRECTIONS TO THE PRINT AND ONLINE VERSIONS OF PEER-REVIEWED CONTENT

Publishable amendments requested by the authors of the publication are represented by a formal printed and online notice in the journal because they affect the publication record and/or the scientific accuracy of published information. Where these amendments concern peer-reviewed material, they fall into one of four categories: erratum, corrigendum, retraction, or addendum, described here.

Erratum Notification of an important error made by the journal that affects the publication record or the scientific integrity of the paper, or the reputation of the authors, or of the journal.

Corrigendum Notification of an important error made by the author(s) that affects the publication record or the scientific integrity of the paper, or the reputation of the authors or the journal. All authors must sign corrigenda submitted for publication. In cases where coauthors disagree, the editors will take advice from independent peer-reviewers and impose the appropriate amendment, noting the dissenting author(s) in the text of the published version.

Retraction Notification of invalid results. All coauthors must sign a retraction specifying the error and stating briefly how the conclusions are affected, and submit it for publication. In cases where coauthors disagree, the editors will seek advice from independent peer reviewers and impose the type of amendment that seems most appropriate, noting the dissenting author(s) in the text of the published version.

Addendum Notification of a peer-reviewed addition of information to a paper, usually in response to readers' request for clarification. Addenda are published only rarely and only when the editors decide that the addendum is crucial to the reader's understanding of a significant part of the published contribution.

SUBMISSION AND PUBLICATION

SUBMISSION OF PAPERS

Manuscripts must be submitted online at <http://mts-cpt.nature.com>. Manuscripts are assessed by an editor upon submission. Only manuscripts that meet our editorial criteria are sent out for formal review. One compelling, negative review may be sufficient for a decision to reject.

Submission Fee (Does not apply to invited authors) Manuscripts submitted for consideration will incur a submission fee of \$75 to cover, in part, the time and resources required to manage submissions. Members of ASCPT will receive a discounted submission rate. Fees must be paid prior to final submission of a paper and will not be waived or refunded.

COPYRIGHT

Ownership is to be transferred to the American Society for Clinical Pharmacology and Therapeutics. The Copyright Statement form must be signed and returned to the editorial office prior to publication. Failure to do so will result in delays to the publication of your paper. A single designated author may sign the

Copyright Statement form on behalf of all authors. The enclosure of a copyright transfer form in a request for a revised manuscript does not imply that the revised manuscript will be accepted. The Copyright Statement is also available under "Instructions & Forms" on the online submission page: <http://mts-cpt.nature.com>.

NIH Open Access Policy In compliance with the National Institutes of Health Open Access Policy, ASCPT grants limited copyright release to authors who have received funding for research on which the article is based from the National Institutes of Health to deposit the accepted paper into PubMed Central. It remains the legal responsibility of the author(s) to deposit the final, peer-reviewed paper upon acceptance for publication, to be made publicly available no sooner than 12 months after the official date of publication.

PAGE AND COLOR CHARGES

(Do not apply to invited authors)

Page charges Manuscripts accepted for publication in Clinical Pharmacology & Therapeutics will incur page charges to cover, in part, the cost of publication. A charge of \$50 will be issued for each journal page.

Color charges Authors will be expected to contribute towards the cost of publication of color figures. A quote will be supplied upon acceptance of the paper.

Charges are:

- 1 figure: \$846
- 2 figures: \$1,260
- 3 figures: \$1,674
- 4 figures: \$1,926
- 5 figures: \$2,178
- 6 figures: \$2,394
- 7+ figures: \$216 per additional figure

Upon acceptance authors must fill in the color artwork form available at <http://mts-cpt.nature.com>.

Offprints May be ordered using the order form available for download with the proofs.

PROOFS

An email will be sent to the corresponding author with a URL link from where proofs can be collected. Proofs must be returned by fax within 48 hours of receipt. Failure to do so may result in a delay to publication. Extensive corrections cannot be made at this stage.

ADVANCE ONLINE PUBLICATION

All original articles and reviews are published ahead of print on Advance Online Publication. This will be the final version of the manuscript and will subsequently appear, unchanged, in print.

CONTACT INFORMATION

EDITORIAL

All business regarding manuscripts and peer review should be addressed to:

Clinical Pharmacology & Therapeutics
528 North Washington Street
Alexandria, VA 22314

USA

Tel: +1.703.836.6981

Fax: +1.703.836.6996

Attn: cpt@ascpt.org, Managing Editor & Director of Publications

cpt2@ascpt.org, Senior Editorial Coordinator

BUSINESS MATTERS

All business correspondence and inquiries should be addressed to:

Clinical Pharmacology & Therapeutics
Nature Publishing Group
75 Varick Street, 9th Floor
New York, NY 10013
USA

Tel: +1.212.726.9301

Consequences of climate change on the tree of life in Europe

Wilfried Thuiller¹, Sébastien Lavergne¹, Cristina Roquet¹, Isabelle Boulangeat¹, Bruno Lafourcade¹ & Miguel B. Araujo^{2,3}

Many species are projected to become vulnerable to twenty-first-century climate changes^{1,2}, with consequent effects on the tree of life. If losses were not randomly distributed across the tree of life, climate change could lead to a disproportionate loss of evolutionary history^{3–5}. Here we estimate the consequences of climate change on the phylogenetic diversities of plant, bird and mammal assemblages across Europe. Using a consensus across ensembles of forecasts for 2020, 2050 and 2080 and high-resolution phylogenetic trees, we show that species vulnerability to climate change clusters weakly across phylogenies. Such phylogenetic signal in species vulnerabilities does not lead to higher loss of evolutionary history than expected with a model of random extinctions. This is because vulnerable species have neither fewer nor closer relatives than the remaining clades. Reductions in phylogenetic diversity will be greater in southern Europe, and gains are expected in regions of high latitude or altitude. However, losses will not be offset by gains and the tree of life faces a trend towards homogenization across the continent.

Evidence is accumulating that ongoing climate changes already affect living organisms⁶. Although species have been continuously exposed to climate changes throughout their evolutionary histories⁷, there is concern that the pace of current changes poses unprecedented challenges for many species⁸. Evidence exists that certain clades are more vulnerable to anthropogenic pressures than others⁹, causing portions of Earth's evolutionary history to be disproportionately altered. Here we investigate whether climate change could have a similar effect.

Climatic tolerances vary across species, causing some species to be more vulnerable to climate change than others¹⁰. Because climate tolerances are not randomly distributed across phylogenies¹¹, species sensitivities to climate change are expected to be clustered along the phylogeny. It follows that if vulnerable species are closely related, shared internal branches of the tree of life have higher risks of collapsing¹² (Supplementary Fig. 1). In contrast, overdispersed extinctions in the phylogeny would mitigate the loss of internal edges⁹. However, phylogenetically clumped extinctions should cause disproportionate loss of phylogenetic diversity only when extinctions are in clades with long edges overall⁵ (Supplementary Fig. 1, scenario A). In contrast,

extinctions clumped in recent—often widespread and fast-evolving—clades, with short branches (Supplementary Fig. 1, scenario B), should have impacts no different, or even smaller, than under a model of random extinctions⁹ (Supplementary Fig. 1, scenario C).

We report a comprehensive analysis of the impacts of climate change on the European tree of life (see Supplementary Fig. 2 for a workflow of the analysis). First, we test whether changes in suitable climate (consensus projections extracted from several species distribution models and high-resolution climate model projections) among 1,280 plant, 340 bird and 140 mammal European species show a significant phylogenetic signal. Second, using contractions of suitable climate as proxies for extinction risk, we test whether losses would cause greater decline in phylogenetic diversity than expected under a null model of extinction. Third, we ask whether expected changes in phylogenetic diversity are spatially structured. To this end, we map the current and future phylogenetic diversity of each study group and investigate changes in regional phylogenetic diversity and its spatial turnover¹³ across Europe.

Changes in suitable climate among European species were generally more similar between closely related species, but the strength of the phylogenetic signal was weak (Fig. 1, Supplementary Table 1 and Supplementary Figs 3 and 4). This pattern of clustering appeared consistently across the high-resolution phylogenies, emission scenarios and periods studied (Supplementary Table 1 and Supplementary Figs 3 and 4). For example, among plants, most suitable climate for *Draba* (whitlow grasses) and *Arabis* (rockcress) species contracted (72% of *Draba* species contracted by >30% and 50% of *Arabis* species contracted by >50%). Among birds, most *Tringa* (shanks and tattlers) and *Numenius* (curlew) species had suitable climate contractions of >30%, whereas most *Ardeidae* (herons and egrets) expanded their ranges. Mammals were generally less vulnerable to climate change, although more than half of the *Sorex* (long-tailed shrews) species could lose more than 30% of their suitable climate (Fig. 1 and Supplementary Fig. 5).

Reductions in phylogenetic diversity arising from climate change were not greater than expected under a model of random extinctions

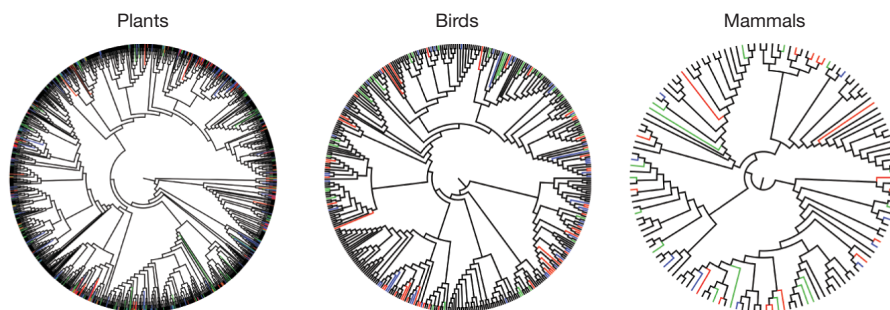


Figure 1 | Changes in suitable climate (A1FI scenario for 2080) mapped onto the phylogeny of European plants, birds and mammals. Black edges indicate positive changes in suitable climate (CSC), that is, range expansion.

Other colours indicate negative changes in suitable climate (range contraction): green for CSC > -15%, blue for CSC > -30% and red for CSC > -50%.

¹Laboratoire d'Ecologie Alpine, UMR CNRS 5553, Université Joseph Fourier, BP 53, FR-38041 Grenoble Cedex 9, France. ²Department of Biodiversity and Evolutionary Biology, National Museum of Natural Sciences, CSIC, Calle Gutierrez Abascal, 2, 28006, Madrid, Spain. ³Rui Nabeiro Biodiversity Chair, CIBIO, University of Évora, Largo dos Colegiaes, 7000 Évora, Portugal.

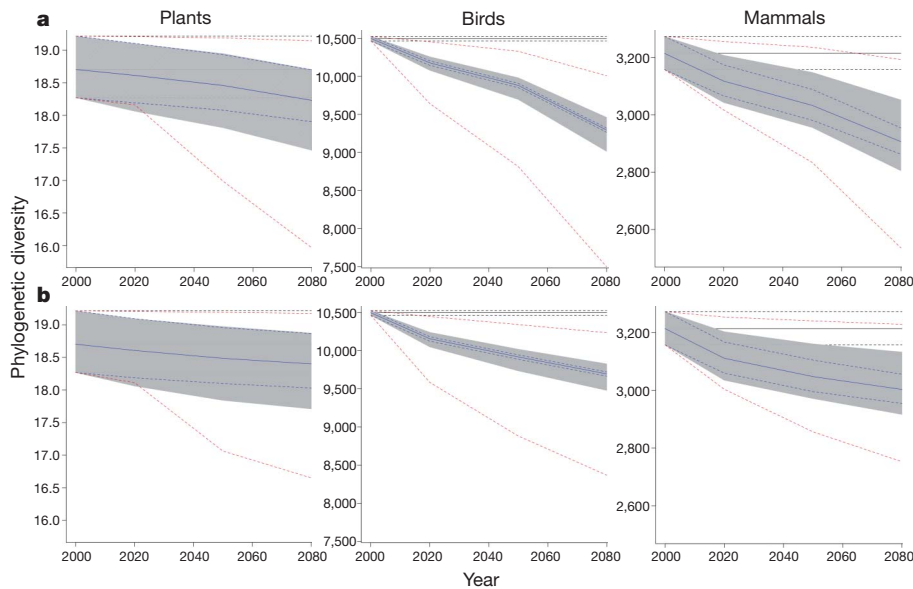


Figure 2 | Changes in phylogenetic diversity versus scenarios of random extinction for plants, birds and mammals. a, Emission scenario A1FI; **b,** emission scenario B1. Black solid and dashed lines depict the median, maximum and minimum current phylogenetic diversities across the sample of trees. Blue solid and dashed lines represent the median, maximum and minimum projected phylogenetic diversities due to range change across the

sample of trees. The grey area is the quantile range of projected phylogenetic diversity due to range contraction (from 2020 onward), randomly scattered across the sample of trees. The red lines are the remaining phylogenetic diversity when the risk of extinction is positively (lower line) or negatively (upper line) related to the evolutionary distinctiveness of the taxa.

across the phylogeny (Fig. 2 and Supplementary Fig. 6). That is, species whose suitable climates contract are not clustered in species-poor clades with long branches (where projected future phylogenetic diversity should be lower than under random species losses), nor are they clustered on the shortest branches (where projected future phylogenetic diversity should be higher than under random species losses). Instead they are clustered across both long and short edges of the tree. Again, these results were consistent across the three clades studied, the sampled trees, the four emission scenarios and the time slices 2050 and 2080. Sensitivity analysis across climate model projections and species distribution models revealed that results were also not affected by variability across models (Supplementary Fig. 7). For plants at risk, reductions in phylogenetic diversity were relatively low: approximately 2.7% in the worst-case scenario (A1FI) and for the time slice with greater impacts, that is, 2080 (current phylogenetic diversity, 18.7; future phylogenetic diversity, 18.2). Reductions of the same order of magnitude were recorded for phylogenetic diversity in birds (11.5% reduction) and mammals (9.6% reduction).

Spatial analyses of projected phylogenetic diversity revealed a marked homogenization of phylogenetic diversity across Europe, with strong reductions of spatial turnover (approximately –34%, –32% and –30% for plants, birds and mammals, respectively) following climate change. However, regions are not all equally affected by climate changes (Fig. 3). At present, the spatial distribution of plant phylogenetic diversity separates the northern Iberian Peninsula, Italy and France, with high total phylogenetic diversity, from northern European countries and the Alps, with low total phylogenetic diversity (Fig. 3). Similar patterns are found for birds, with higher phylogenetic diversity in the Mediterranean basin than in the rest of Europe, and mammals, with higher phylogenetic diversity in the southeast of Europe than in the northeast. Increases in phylogenetic diversity in northern Europe and in the Alps are accompanied by consistent decreases in phylogenetic diversity in southern Europe, causing a general reduction in the spatial variation of phylogenetic diversity (Fig. 3). These predicted spatial changes in phylogenetic diversity are not entirely due to changes in species richness (Supplementary Fig. 8). Indeed, regions such as Scandinavia (for plants), Germany (for birds) and Sweden (for mammals) are projected

to have more phylogenetic diversity in the future than is expected on the basis of their future projected species richness (Supplementary Fig. 8). This can be explained by northern biotas being more likely to sample species that are less phylogenetically redundant in the future. The projected reduction of phylogenetic diversity in southern Europe could, however, be alleviated by species immigration from Northern Africa, especially if immigrant species belong to phylogenetic clades that are not present in the northern Mediterranean basin.

Linking phylogenetic and biogeographic information can help identify regions of past production and present maintenance of biodiversity (so-called cradles and graves)¹⁴, but projecting them into the future is challenging. Our study addresses this challenge and presents a unique large-scale assessment of the potential impacts of climate change on the evolutionary history of plants, birds and mammals. Although our assessment integrates uncertainty in phylogenetic reconstructions, it should be noted that projected changes in evolutionary history are also inevitably sensitive to the species distribution and climate models used. To address this problem, we have used cutting-edge bioclimatic ensemble forecasting methodologies. Because high-resolution climate projections have large uncertainties (owing to the difficulty of simulating local climates and the inaccuracy of interpolation techniques¹⁵), we have included three well-known global change models encompassing a large variation in future climate and shown that our results were robust to this variation. Accordingly, we show that although different metrics of species vulnerability to climate change tend not to be randomly distributed with regards to the tree of life, the loss of European phylogenetic diversity is not greater than expected under a model of random extinctions⁴. The International Union for Conservation of Nature Red List of Threatened Species provides clear evidence that extinction risk is selective among particular groups such as the amphibians, birds and mammals¹⁶. The prevalence of threatened species differs significantly among these groups and among the families and orders within each group^{9,16}. The fossil record also provides evidence of phylogenetically clustered extinctions, although the previous five mass extinctions provide examples of less extreme selectivity^{17,18}. Our projections do not predict a large drop in total phylogenetic diversity, but they do suggest a future restructuring of the spatial distribution of

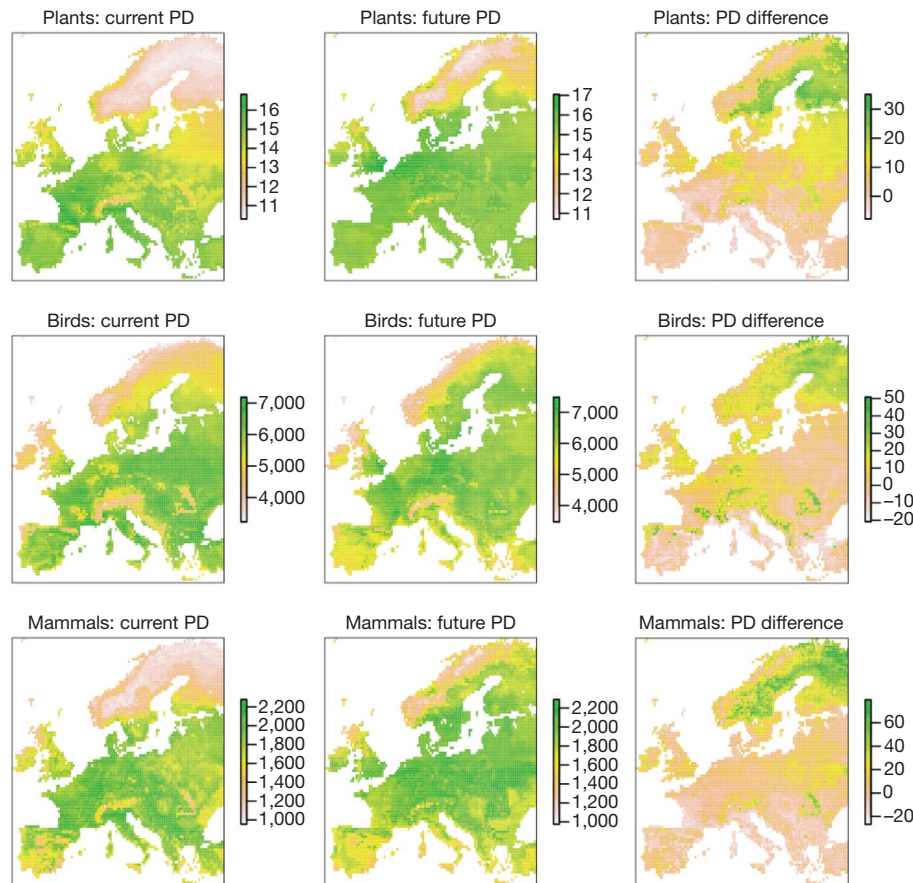


Figure 3 | Map of current and future phylogenetic diversities (A1FI scenario for 2080) and their relative differences for the three species groups. Maps represent average phylogenetic diversity (PD; colour scale) across the sample of 100 phylogenetic trees used for each study group.

the tree of life. Phylogenetic diversity over Europe will be homogenized owing to the reshuffling of species assemblages and the migration of the tree of life into higher latitudes and elevations.

METHODS SUMMARY

We modelled changes in suitable climate for 1,280 European plants, 140 mammals and 340 birds, using six species distribution models¹⁹, three 10' high-resolution global climate models (HadCM3, CSIRO2, CGCM2¹⁵ from CRU-TYN-SC-1.0) and four emission scenarios (A1FI, A2, B1 and B2²⁰), over the periods 1961–1990, 1991–2020, 2021–2050 and 2051–2080. Given the low variability across species distribution models and global climate models (Supplementary Information and Supplementary Fig. 7), we kept the median consensus projection for each scenario and time slice²¹.

Species vulnerability was estimated as the change in the total area of suitable climate assuming unlimited dispersal (CSC, ranging from -100 to >100). Another measure ('loss' of suitable climate (LSC), ranging from -100 to 0) gave similar results (Supplementary Figs 4 and 5).

We developed mega-phylogenies by mixing supertree and supermatrix approaches²² with sequences from GenBank. Optimal alignment for each region was obtained with four algorithms, and by choosing and deparating the best alignment with TRIMAL. Phylogenetic analyses were conducted using maximum-likelihood estimation by constraining heuristic searches with a family-level supertree. We retained 100 maximum-likelihood trees for plants and birds. For mammals, we used 100 phylogenetic trees based on ref. 23 with polytomies randomly resolved.

Estimation and test of phylogenetic signal in species vulnerability was performed using Abouheif's test²⁴, Blomberg's K (ref. 25) and Pagel's λ (ref. 26).

To estimate the potential impacts of climate change on the tree of life, we used CSC as a surrogate for probability of extinction, $p(\text{ext})$, and calculated future phylogenetic diversity by weighting the probability of an edge persisting as $1 - p(\text{ext})$ of all its descendent species²⁷. The null model expectation was extracted by randomizing $p(\text{ext})$ across the tips and recalculating phylogenetic diversity.

Spatial distribution of phylogenetic diversity was estimated on the pixel basis with species projected to be present. Spatial turnover was measured as the total projected phylogenetic diversity minus the mean local phylogenetic diversity over Europe¹³.

Received 7 June; accepted 29 November 2010.

Published online 16 February 2011.

1. Thomas, C. D. *et al.* Extinction risk from climate change. *Nature* **427**, 145–148 (2004).
2. Thuiller, W., Lavorel, S., Araújo, M. B., Sykes, M. T. & Prentice, I. C. Climate change threats to plant diversity in Europe. *Proc. Natl Acad. Sci. USA* **102**, 8245–8250 (2005).
3. Mace, G. M., Gittleman, J. L. & Purvis, A. Preserving the tree of life. *Science* **300**, 1707–1709 (2003).
4. Nee, S. & May, R. M. Extinction and the loss of evolutionary history. *Science* **288**, 328–330 (1997).
5. Heard, S. B. & Mooers, A. O. Phylogenetically patterned speciation rates and extinction risks change the loss of evolutionary history during extinctions. *Proc. R. Soc. Lond. B* **267**, 613–620 (2000).
6. Parmesan, C. Ecological and evolutionary responses to recent climate change. *Annu. Rev. Ecol. Syst.* **37**, 637–669 (2006).
7. Meyers, L. A. & Bull, J. J. Fighting change with change: adaptive variation in an uncertain world. *Trends Ecol. Evol.* **17**, 551–557 (2002).
8. Thuiller, W. Climate change and the ecologist. *Nature* **448**, 550–552 (2007).
9. Purvis, A. Phylogenetic approaches to the study of extinction. *Annu. Rev. Ecol. Syst.* **39**, 301–319 (2008).
10. Thuiller, W., Lavorel, S. & Araújo, M. B. Niche properties and geographical extent as predictors of species sensitivity to climate change. *Glob. Ecol. Biogeogr.* **14**, 347–357 (2005).
11. Prinzing, A., Durka, W., Klotz, S. & Brandl, R. The niche of higher plants: evidence for phylogenetic conservatism. *Proc. R. Soc. Lond. B* **268**, 2383–2389 (2001).
12. McKinney, M. L. Extinction vulnerability and selectivity: combining ecological and paleontological views. *Annu. Rev. Ecol. Syst.* **28**, 495–516 (1997).
13. Lande, R. Statistics and partitioning of species diversity, and similarity among multiple communities. *Oikos* **76**, 5–13 (1996).
14. Chown, S. L. & Gaston, K. J. Areas, cradles and museums: the latitudinal gradient in species richness. *Trends Ecol. Evol.* **15**, 311–315 (2000).

15. Mitchell, T. D. & Jones, P. D. An improved method of constructing a database of monthly climate observations and associated high-resolution grids. *Int. J. Climatol.* **25**, 693–712 (2005).
16. Baillie, J. E. M., Hilton-Taylor, C. & Stuart, S. N. (eds) *2004 IUCN Red List of Threatened Species. A Global Species Assessment* (International Union for Conservation of Nature, 2004).
17. Bambach, R. K. Phanerozoic biodiversity mass extinctions. *Annu. Rev. Earth Planet. Sci.* **34**, 127–155 (2006).
18. Koch, P. L. & Barnosky, A. D. Late Quaternary extinctions: state of the debate. *Annu. Rev. Ecol. Syst.* **37**, 215–250 (2006).
19. Thuiller, W., Lafourcade, B., Engler, R. & Araujo, M. B. BIOMOD – a platform for ensemble forecasting of species distributions. *Ecography* **32**, 369–373 (2009).
20. Nakicenovic, N. & Swart, R. *Emissions Scenarios: A Special Report of Working Group III of the Intergovernmental Panel on Climate Change* 570 (Cambridge Univ. Press, 2000).
21. Marmion, M., Parviainen, M., Luoto, M., Heikkinen, R. K. & Thuiller, W. Evaluation of consensus methods in predictive species distribution modelling. *Divers. Distrib.* **15**, 59–69 (2009).
22. Smith, S. A., Beaulieu, J. M. & Donoghue, M. J. Mega-phylogeny approach for comparative biology: an alternative to supertree and supermatrix approaches. *BMC Evol. Biol.* **9**, 37–48 (2009).
23. Fritz, S. A., Bininda-Emonds, O. R. P. & Purvis, A. Geographical variation in predictors of mammalian extinction risk: big is bad, but only in the tropics. *Ecol. Lett.* **12**, 538–549 (2009).
24. Pavoine, S., Ollier, S., Pontier, D. & Chessel, D. Testing for phylogenetic signal in phenotypic traits: new matrices of phylogenetic proximities. *Theor. Popul. Biol.* **73**, 79–91 (2008).
25. Blomberg, S. P., Garland, T. & Ives, A. R. Testing for phylogenetic signal in comparative data: behavioral traits are more labile. *Evolution* **57**, 717–745 (2003).
26. Pagel, M. Inferring the historical patterns of biological evolution. *Nature* **401**, 877–884 (1999).
27. Witting, L. & Loeschke, V. The optimization of biodiversity conservation. *Biol. Conserv.* **71**, 205–207 (1995).

Supplementary Information is linked to the online version of the paper at www.nature.com/nature.

Acknowledgements This research was funded by the EU ECOCHANGE (GOCE-CT-2007-036866) and DIVERSITALP (ANR-2007-BDIV-014) projects. C.R. was supported by a grant from Fundación Ramón Areces. We thank P. Pearman and A. Mooers for comments on earlier drafts. Computations were performed using the CIMENT infrastructure (<https://ciment.ujf-grenoble.fr>), supported by the Rhône-Alpes region (GRANT CPER07-13 CIRA).

Author Contributions W.T. and S.L. designed the study, C.R. built the plant and bird phylogenies, I.B. and B.L. helped with R code writing, and W.T. performed all the analyses. W.T., S.L. and M.B.A. wrote the manuscript with substantial contributions from all authors.

Author Information Reprints and permissions information is available at www.nature.com/reprints. The authors declare no competing financial interests. Readers are welcome to comment on the online version of this article at www.nature.com/nature. Correspondence and requests for materials should be addressed to W.T. (wilfried.thuiller@ujf-grenoble.fr).

Tumour-infiltrating regulatory T cells stimulate mammary cancer metastasis through RANKL–RANK signalling

Wei Tan^{1†*}, Weizhou Zhang^{1*}, Amy Strasner¹, Sergei Grivennikov¹, Jin Q. Cheng², Robert M. Hoffman^{3,4} & Michael Karin¹

Inflammatory mechanisms influence tumorigenesis and metastatic progression even in cancers whose aetiology does not involve pre-existing inflammation or infection, such as breast and prostate cancers¹. For instance, prostate cancer metastasis is associated with the infiltration of lymphocytes into advanced tumours and the upregulation of two tumour-necrosis-factor family members: receptor activator of nuclear factor- κ B (RANK) ligand (RANKL) and lymphotoxin². But the source of RANKL and its role in metastasis have not been established. RANKL and its receptor RANK control the proliferation of mammary lobuloalveolar cells during pregnancy³ through inhibitor of nuclear factor- κ B (I κ B) kinase- α (IKK- α)⁴, a protein kinase that is needed for the self-renewal of mammary cancer progenitors⁵ and for prostate cancer metastasis². We therefore examined whether RANKL, RANK and IKK- α are also involved in mammary/breast cancer metastasis. Indeed, RANK signalling in mammary carcinoma cells that overexpress the proto-oncogene *ErbB2* (also known as *Neu*)⁶, which is frequently amplified in metastatic human breast cancers^{7,8}, was important for pulmonary metastasis. Metastatic spread of *ErbB2*-transformed carcinoma cells also required CD4⁺CD25⁺ T cells, whose major pro-metastatic function was RANKL production. Most RANKL-producing T cells expressed forkhead box P3 (FOXP3), a transcription factor produced by regulatory T cells, and were located next to smooth muscle actin (SMA)⁺ stromal cells in mouse and human breast cancers. The dependence of pulmonary metastasis on T cells was replaceable by exogenous RANKL, which also stimulated pulmonary metastasis of RANK⁺ human breast cancer cells. These results are consistent with the adverse impact of tumour-infiltrating CD4⁺ or FOXP3⁺ T cells on human breast cancer prognosis^{9,10} and suggest that the targeting of RANKL–RANK can be used in conjunction with the therapeutic elimination of primary breast tumours to prevent recurrent metastatic disease.

RANK signalling controls osteoclastogenesis and bone resorption and has been targeted to prevent bone metastasis in breast and prostate cancers^{11–13}. A humanized anti-RANKL antibody seems to be a more effective inhibitor of bone metastasis than other osteoclast-targeting drugs^{12,13}. To examine whether RANK signalling controls additional aspects of breast cancer metastasis, we used mice on the FVB/N background in which *ErbB2* was expressed under the control of the mouse mammary tumour virus promoter (*MMTV-ErbB2*-transgenic mice)⁶. In these mice, mammary carcinomas are induced by a gene that is overexpressed in 30% of human breast cancers⁷. Because *Rank*-null mice are osteopetrotic and have retarded growth¹¹, we used *MMTV-ErbB2*-transgenic *Rank*^{+/-} heterozygotes on the FVB/N background (*MMTV-ErbB2/Rank*^{+/-}), which were indistinguishable from *MMTV-ErbB2/Rank*^{+/+} mice (on the same background) in appearance, weight

and general health. Although reduced *Rank* gene dosage did not affect primary tumour development, tumoral RANK expression was reduced, and *MMTV-ErbB2/Rank*^{+/-} mice gave rise to 50% fewer lung metastases than did *MMTV-ErbB2/Rank*^{+/+} mice (Fig. 1a). The role of RANK signalling was further examined using an orthotopic tumour model in which primary mammary carcinoma cells from an *MMTV-ErbB2* tumour (PCaM cells) were injected into the number 2 mammary gland of FVB/N mice. Injection of recombinant RANKL, after inoculation with tumour cells, significantly increased the incidence and multiplicity of pulmonary metastases (Fig. 1b).

We also generated an immortalized *ErbB2*-induced mammary carcinoma cell line, MT2, which doubled every 24 h, showed epithelial morphology, and formed colonies in soft agar and mammospheres when grown in suspension without serum (Supplementary Fig. 1a–c). MT2 cells expressed as much RANK as did PCaM cells. However, RANK expression was very low in non-transformed mammary epithelial cells from tumour-free virgins, and neither PCaM nor MT2 cells expressed RANKL (Supplementary Fig. 1d, e). After transplantation to the number 2 mammary gland, MT2 cells underwent pulmonary metastasis that was further enhanced by RANKL injection (Fig. 1c). To ascertain that the results were not affected by a putative ERBB2-elicited immune response, we transplanted MT2 cells to *MMTV-ErbB2* mice on the FVB/N background that had been tolerized to the *ErbB2* oncogene¹⁴. The results were almost identical to those obtained in normal FVB/N mice (Fig. 1c). Silencing of RANK expression (Supplementary Fig. 1f) reduced the pulmonary metastasis of MT2 cells (Fig. 1d) and blocked the response of MT2 cells to RANKL (Supplementary Fig. 2a). Neither administration of RANKL nor silencing of RANK expression significantly influenced the primary tumorigenic growth of MT2 cells, which was identical in FVB/N mice and *MMTV-ErbB2* mice on the FVB/N background (Supplementary Fig. 2b, c). Similar results were obtained by administration of a RANK–Fc fusion protein, which blocks RANK signalling¹⁵, to mice bearing MT2 mammary tumours. Whereas RANK–Fc marginally inhibited tumour growth at the primary site, it greatly reduced pulmonary metastasis (Supplementary Fig. 3).

RANK engagement induced nuclear translocation and phosphorylation of IKK- α molecules that were not associated with IKK- β and IKK- γ (also known as NEMO), the two other subunits of the IKK complex (Supplementary Fig. 4a–c). This finding indicates that free IKK- α or IKK- α that belongs to a complex of a different composition is targeted by RANK. Such RANK-induced IKK- α activation repressed expression of the metastasis inhibitor maspin (also known as SERPINB5) (Supplementary Fig. 5a–c). MT2 cells that overexpressed ectopic maspin (maspin–MT2 cells) showed marginally reduced tumorigenic growth but much less pulmonary metastasis (Supplementary Fig. 5d–g). Treatment with exogenous RANKL stimulated the metastasis of enhanced green fluorescent protein (eGFP)-expressing

¹Laboratory of Gene Regulation and Signal Transduction, Departments of Pharmacology and Pathology, University of California San Diego School of Medicine, 9500 Gilman Drive, Mail Code 0723, La Jolla, California 92093, USA. ²Department of Molecular Oncology, H. Lee Moffitt Cancer Center, Tampa, Florida 33612, USA. ³Department of Surgery, University of California San Diego, San Diego, California 92103-8220, USA. ⁴AntiCancer Inc., San Diego, California 92111, USA. [†]Present address: Pfizer Oncology Research Unit West, San Diego, California 92121, USA.

*These authors contributed equally to this work.

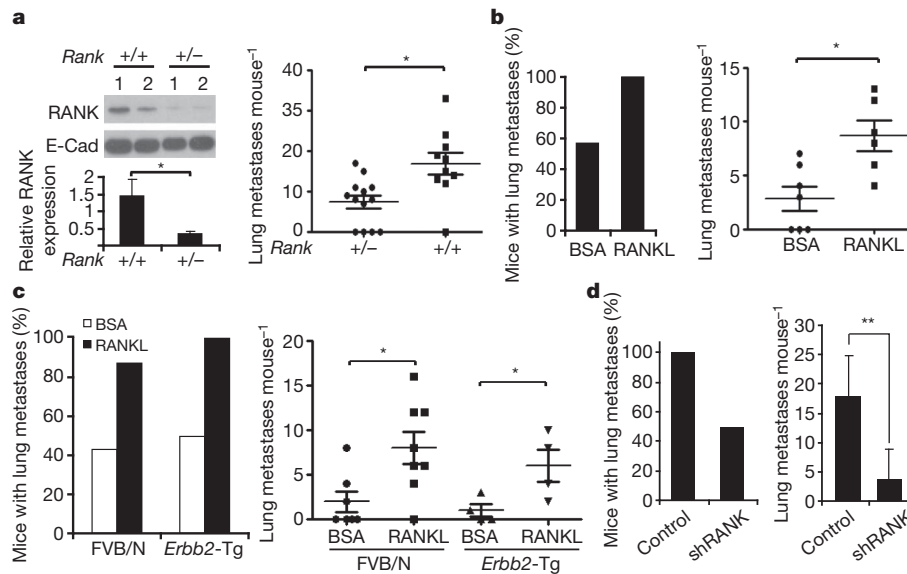


Figure 1 | RANK signalling in mammary carcinoma cells enhances metastasis. **a**, *MMTV-ErbB2/Rank*^{+/+} and *MMTV-ErbB2/Rank*^{+/-} mice were killed 8 weeks after tumour onset. Tumour RANK expression was analysed by immunoblotting (each lane represents a different mouse tumour, top left), quantified by densitometry and normalized to E-cadherin (E-Cad) expression (bottom left; data presented as mean \pm s.e.m.; $n = 6$). Metastasis multiplicity was determined by haematoxylin and eosin (H&E) staining of *MMTV-ErbB2/Rank*^{+/+} ($n = 10$) and *MMTV-ErbB2/Rank*^{+/-} ($n = 13$) mouse lungs. Individual mouse data are shown (right; mean, horizontal line; error bars, s.e.m.). **b**, *MMTV-ErbB2*-transgenic PCaM cells were grafted (1×10^6 cells) into the number 2 mammary glands of FVB/N mice, which were then subjected to twice weekly intratumoural injections of bovine serum albumin (BSA) or recombinant RANKL ($80 \mu\text{g kg}^{-1}$), starting 1 week after inoculation with tumour cells. On day 35, the lungs were isolated, sectioned, stained with H&E

and the metastatic lesions counted. Data are presented as the proportion of mice in each group that developed metastases (left) and as the number of metastases developed by each mouse (right; mean, horizontal line; error bars, s.e.m.; BSA: $n = 7$; RANKL: $n = 6$). **c**, MT2 cells (1×10^6 cells) were grafted as in **b** into FVB/N mice or *MMTV-ErbB2*-transgenic (*ErbB2*-Tg) mice on the FVB/N background, which were then treated with BSA or RANKL, and analysed for pulmonary metastases. Data are presented as incidence of metastases (left) and multiplicity of metastases (right; individual mouse data; mean, horizontal line; error bars, s.e.m.; $n = 7-8$). **d**, Mice were inoculated with MT2 cells (1×10^6 cells) that had been transduced with short hairpin RNA specific for *RANK* (shRANK) or control MT2 cells (1×10^6 cells), and lung metastases were counted 56 days later. Data are presented as in **b** and **c** except that multiplicity is shown as mean \pm s.e.m. ($n = 6$). **a-d**, *, $P < 0.05$; **, $P < 0.01$ (non-parametric Mann-Whitney *U* test).

MT2 cells but did not affect the growth of primary tumours from either maspin-MT2 or eGFP-expressing MT2 cells; moreover, it did not enhance the weak metastatic activity of maspin-MT2 cells (Supplementary Fig. 5h). As expected⁵, the silencing of IKK- α expression in MT2 cells slowed tumorigenic growth (Supplementary Fig. 6a, b), blocked pulmonary metastasis, even in mice given exogenous RANKL (Supplementary Fig. 6c), and upregulated maspin expression (Supplementary Fig. 6d).

Treatment of primary tumour cells or cells that had reduced *Rank* gene dosage with RANKL did not affect the formation of primary mammospheres (Supplementary Fig. 7a, b). Although RANKL was reported to stimulate metastasis by enhancing cancer cell motility¹⁶, no significant effect of RANKL on motility or invasiveness of MT2 cells was observed (Supplementary Fig. 7c). *In vivo*, treatment with RANKL led to fewer apoptotic cells in late-stage tumours (Supplementary Fig. 7d). Conversely, silencing of IKK- α expression increased the number of apoptotic cells in late-stage tumours by 2.2 fold, and this increase was not reversed by treatment with RANKL (Supplementary Fig. 7e, f). Pre-incubation of tail-vein-injected MT2 cells in RANKL and subsequent *in vivo* treatment with RANKL enhanced the extravasation of MT2 cells into the lungs in a RANK-dependent manner (Supplementary Fig. 7g). *In vitro*, RANKL strongly inhibited the apoptosis of suspended MT2 cells (Supplementary Fig. 7h). Hence, the pro-metastatic effect of RANKL and IKK- α may be due to the increased survival of circulating metastasis-initiating cells.

For *ErbB2*-induced mammary tumours, RANKL expression was detected in the surrounding stroma but not in the carcinoma portion (Fig. 2a and Supplementary Fig. 8a, b) or in metastatic lung nodules, which were surrounded by a few CD5⁺ lymphocytes (Supplementary Fig. 8a). Activated lymphocytes produce RANKL during inflammation¹⁷ and are present in breast tumours¹⁸. We therefore examined

their role in tumour RANKL expression. The staining of sequential tumour sections showed an almost identical distribution of RANKL⁺ cells and CD5⁺ lymphocytes (Fig. 2a). Correspondingly, tumours grown in recombination activating gene 1 (*Rag1*)^{-/-} mice, which lack mature T and B cells (Supplementary Fig. 9), contained less *Rankl* messenger RNA than did tumours in wild-type mice (Fig. 2b) and were devoid of RANKL⁺ cells (Fig. 2a). Decreased *Rankl* mRNA was also seen in tumours grown in *Cd4*^{-/-} mice (Fig. 2c), which lack only CD4⁺ T cells (Supplementary Fig. 9). Tumours in *Cd4*^{-/-} mice were almost completely devoid of RANKL⁺ cells, although they contained a few CD5⁺ cells (Fig. 2a).

To identify further the major RANKL-expressing cell type during metastatic spread, we grew MT2 cells in *Rag1*^{-/-} mammary glands that had been reconstituted with splenic B cells, CD4⁺ T cells or CD8⁺ T cells from FVB/N mice. Reconstitution efficiency was confirmed by flow cytometry (Supplementary Fig. 10). Only CD4⁺ T cells substantially increased tumour *Rankl* mRNA above the low basal level in mock-reconstituted *Rag1*^{-/-} mice (Supplementary Fig. 11a). We analysed B cells, CD4⁺ T cells and CD8⁺ T cells from spontaneous *MMTV-ErbB2* tumours for *Rankl* mRNA and found this to be at the highest level in CD4⁺ T cells (Supplementary Fig. 11b). Likewise, CD4⁺ T cells from MT2 tumours contained much more *Rankl* mRNA than B cells from MT2 tumours (Supplementary Fig. 11c). Despite their lower contribution to *Rankl* mRNA, tumoral CD8⁺ T cells were more numerous than CD4⁺ T cells, and both T-cell subsets were far more abundant than tumoral B cells (Supplementary Fig. 12a). The absence of lymphocytes in *Rag1*^{-/-} mice did not affect the number of tumour-associated macrophages (Supplementary Fig. 12b), and no differences in stromal constituents were found between tumours grown in FVB/N mice and those in *MMTV-ErbB2* mice on the FVB/N background (Supplementary Fig. 2d, e).

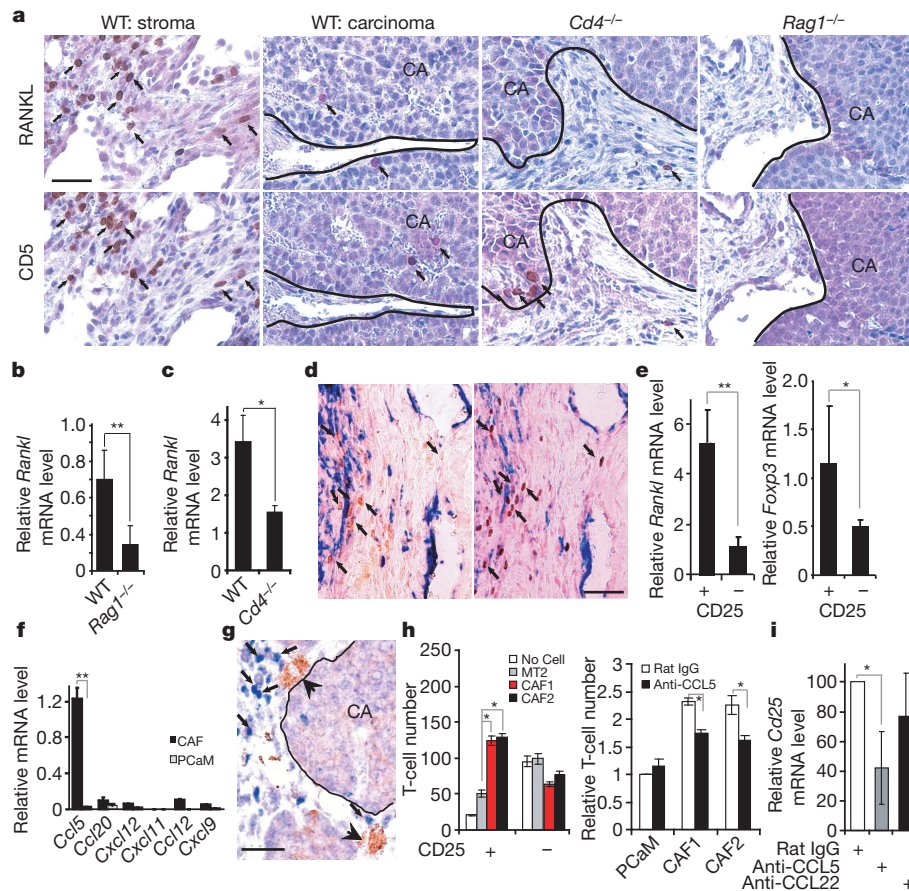


Figure 2 | Expression of RANKL in mammary tumours depends on CD4⁺ T cells. **a**, Mammary glands of indicated mouse strains were inoculated with *MMTV-ErbB2*-transgenic PCaM cells (1×10^6 cells). After 56 days, tumours were paraffin embedded. Sequential sections were stained with anti-RANKL and anti-CD5 antibodies and counterstained with haematoxylin. Panels show stroma- and carcinoma-containing (CA) regions separated by a line, when relevant. Arrows indicate CD5⁺ and RANKL⁺ cells. Scale bar, 20 μ m (all images). WT, wild type. **b**, MT2 cells were transplanted to the indicated mouse strains as in **a**. After 56 days, tumours were excised, and *Rankl* mRNA was quantified by quantitative PCR with reverse transcription (RT-PCR) and normalized to cyclophilin mRNA levels. Data are presented as mean \pm s.e.m. ($n = 3$). **c**, *MMTV-ErbB2*-transgenic PCaM cells were transplanted to the indicated mouse strains as in **a**. After 56 days, tumours were excised, and *Rankl* mRNA was quantified as in **b**. Data are presented as mean \pm s.e.m. ($n = 3$). **d**, Tumours raised in WT mice as in **a** were excised, and sequential sections were stained with anti-FOXP3 (brown), anti-RANKL (brown) and anti-SMA (blue) antibodies. Arrows indicate RANKL⁺ cells (left) and FOXP3⁺ cells (right). **e**, Tumour-infiltrating CD4⁺CD25⁺ and CD4⁺CD25⁻ T cells were purified and analysed for *Rankl* and *Foxp3* mRNA expression as in **b**. Data are

presented as mean \pm s.e.m. ($n = 3$). **f**, CAFs and PCaM cells were purified from *MMTV-ErbB2*-transgenic tumours. Chemokine mRNAs were quantified as in **b**. Data are presented as mean \pm s.e.m. *Cxcl*, CXC-chemokine ligand. **g**, *MMTV-ErbB2*-transgenic tumours were sectioned and stained with anti-CCL5 (brown, large arrowheads) and anti-FOXP3 (blue, small arrowheads) antibodies. Scale bar, 20 μ m. **h**, The indicated cell types were plated onto multiwell plates at 2×10^5 cells per well with no addition (left) 3 μ g ml⁻¹ rat IgG (right) or anti-CCL5 antibody (right). Splenocytes from tumour-bearing *MMTV-ErbB2*-transgenic mice were added to the upper compartments of the Boyden chambers. After 24 h, the CD4⁺CD25⁺ and CD4⁺CD25⁻ T cells in the bottom compartments were quantified by flow cytometry. CAF1 and CAF2 are two independent preparations. Relative T-cell number is relative to that for PCaM cells treated with IgG. Data are presented as mean \pm s.e.m. ($n = 3$). **i**, Rat IgG, anti-CCL5 or anti-CCL22 antibodies (2 mg kg⁻¹) were injected intraperitoneally into FVB/N female mice bearing MT2 tumours twice weekly. After 1 week, tumours were excised, and *Cd25* mRNA was quantified by quantitative RT-PCR. Data are presented relative to the *Cd25* mRNA levels in rat IgG-treated mice; mean \pm s.e.m. ($n = 4$). **b**, **c**, **e**, **f**, **h**, **i**, *, $P < 0.05$; **, $P < 0.01$ (non-parametric Mann-Whitney *U* test).

Among CD4⁺ T-cell types, FOXP3⁺ regulatory T (T_{reg}) cells showed the most similar distribution to RANKL⁺ cells in mammary tumours (Fig. 2d). Notably, T_{reg} cells in breast tumours are associated with an invasive phenotype and poor prognosis^{9,10}. Most FOXP3⁺ and RANKL⁺ cells were in contact with stromal SMA⁺ cells (Fig. 2d). Congruently, CD4⁺CD25⁺ tumoral T cells, which are FOXP3 enriched⁹, expressed fourfold more *Rankl* mRNA than CD4⁺CD25⁻ T cells (Fig. 2e). Furthermore, FOXP3 and RANKL were co-localized in tumours (Supplementary Fig. 13a). These results suggest that tumour-infiltrating CD4⁺FOXP3⁺ T_{reg} cells are the most critical cells for maintaining RANKL expression in the micro-environment of metastatic mammary tumours.

The proximity of RANKL⁺ T cells to SMA⁺ cells, which expressed fibroblast markers (Supplementary Fig. 14), prompted us to examine whether SMA⁺ cells express T-cell-attracting chemokines. CC-chemokine ligand 5 (CCL5; also known as RANTES), a T-cell-attracting

chemokine involved in breast cancer metastasis^{20,21}, was expressed by cancer-associated myofibroblasts (CAFs) but not by PCaM cells (Fig. 2f). Expression of CC-chemokine receptor 1 (CCR1), one of the cognate receptors for CCL5 (ref. 22), was increased in tumour CD4⁺ T cells relative to splenic CD4⁺ T cells (Supplementary Fig. 13b, left). Notably, tumoral CD4⁺CD25⁺ T cells expressed more *Ccr1* mRNA than their CD4⁺CD25⁻ T-cell counterparts (Supplementary Fig. 13b, right). Furthermore, tumoral FOXP3⁺ T cells were in close proximity to CCL5⁺ stromal cells (Fig. 2g). Similarly, in *in vitro* experiments, CAFs attracted more CD4⁺CD25⁺ T cells than CD4⁺CD25⁻ T cells from spleens of tumour-bearing mice, although the latter were sixfold more abundant (Fig. 2h, left). Recruitment was partly dependent on CCL5 (Fig. 2h, right). Neutralization of CCL5 also inhibited the recruitment of tumoral CD25⁺ T cells *in vivo* (Fig. 2i).

To examine the requirement for T cells for pulmonary metastasis, we transplanted freshly isolated PCaM cells to the mammary glands of

wild-type, *Rag1*^{-/-}, *Cd4*^{-/-} and *Cd8*^{-/-} mice, all on the FVB/N background. Although the primary tumour volume was a little larger in *Cd4*^{-/-} mice and *Rag1*^{-/-} mice than in wild-type mice or *Cd8*^{-/-} mice (Supplementary Fig. 15a), pulmonary metastasis was greatly diminished in *Cd4*^{-/-} mice and *Rag1*^{-/-} mice but unaltered in *Cd8*^{-/-} mice compared with wild-type mice (Fig. 3a and Supplementary Fig. 15b). *ErbB2* mRNA quantification confirmed a threefold decrease in pulmonary metastasis in *Cd4*^{-/-} mice (Fig. 3b). MT2-cell-inoculated *Rag1*^{-/-} mice showed substantially reduced metastasis compared with MT2-cell-inoculated wild-type mice (Fig. 3c), but this was restored by transplanting CD4⁺ T cells, which were much more effective at restoring metastasis than CD8⁺ T cells or B cells (Fig. 3d). Treatment with exogenous RANKL restored pulmonary metastasis in the absence of T cells (Fig. 3e). CD4⁺CD25⁺ T cells were far more effective at restoring pulmonary metastasis in MT2-cell-inoculated *Rag1*^{-/-} mice than were CD4⁺CD25⁻ T cells (Fig. 3f), and this effect was almost completely blocked by administering RANK-Fc (Fig. 3g).

We examined whether RANKL stimulates the metastasis of human breast carcinoma cells. Of 19 carcinoma cell lines, the lines AU565, SK-BR-3, ZR-75-1 and SUM1315 expressed the most RANK protein or mRNA (Fig. 4a and Supplementary Fig. 16a). None of the cell lines expressed more *Rankl* mRNA than did untreated human mammary epithelial cells, which expressed RANKL only after treatment with progesterone (Supplementary Fig. 16b). ZR-75-1 and AU565 cells were inoculated into the number 2 mammary glands of nude mice (which lack mature T cells), and only ZR-75-1 cells formed slow growing primary tumours (data not shown), which gave rise to pulmonary metastases in 20% of mice, with an average multiplicity lower than 1 (Fig. 4b).

Administration of human RANKL increased metastasis incidence and multiplicity (Fig. 4b) and decreased maspin mRNA expression by ZR-75-1 cells (Fig. 4c). The carcinoma cell line T-47D, which is RANK⁻, did not respond to RANKL (Supplementary Fig. 17). In the stroma of human breast cancers, RANKL⁺ and FOXP3⁺ cells were present in close proximity to SMA⁺ cells (Fig. 4d). RANKL expression was higher in invasive ductal carcinomas than in ductal carcinomas *in situ* or lymph-node-positive tumours (Fig. 4e).

Our results provide a new mechanistic explanation for the association of CD4⁺ T-cell and T_{reg}-cell markers with a more aggressive behaviour in advanced breast cancers^{9,10,18,23}, by demonstrating that tumour-infiltrating CD4⁺CD25⁺FOXP3⁺ T_{reg} cells are a major source of RANKL, which stimulates the metastatic progression of RANK-expressing breast/mammary carcinoma cells (Supplementary Fig. 18). These findings and the demonstration that the pro-metastatic function of T cells can be replaced by exogenous RANKL differ from those obtained using the *MMTV-PyMT* mouse model of mammary carcinogenesis, in which CD4⁺ T helper 2 cells stimulate tumour progression through production of interleukin-4 and polarization of tumour-associated macrophages towards M2 macrophages¹⁸. Our mouse results correlate well with human breast cancer studies. In both cases, RANKL⁺ and FOXP3⁺ T_{reg} cells are concentrated in the tumour stroma and do not come into contact with carcinoma cells. Furthermore, in both cases, the presence of tumoral T_{reg} cells correlates with invasion, metastasis and poor prognosis^{9,10,23,24}. The recruitment of T_{reg} cells to CAFs is partly dependent on CCL5, a chemokine whose presence is associated with higher grades of human breast cancer and metastasis^{20,21}. Our suggestion that CAFs and CCL5 act through T cells,

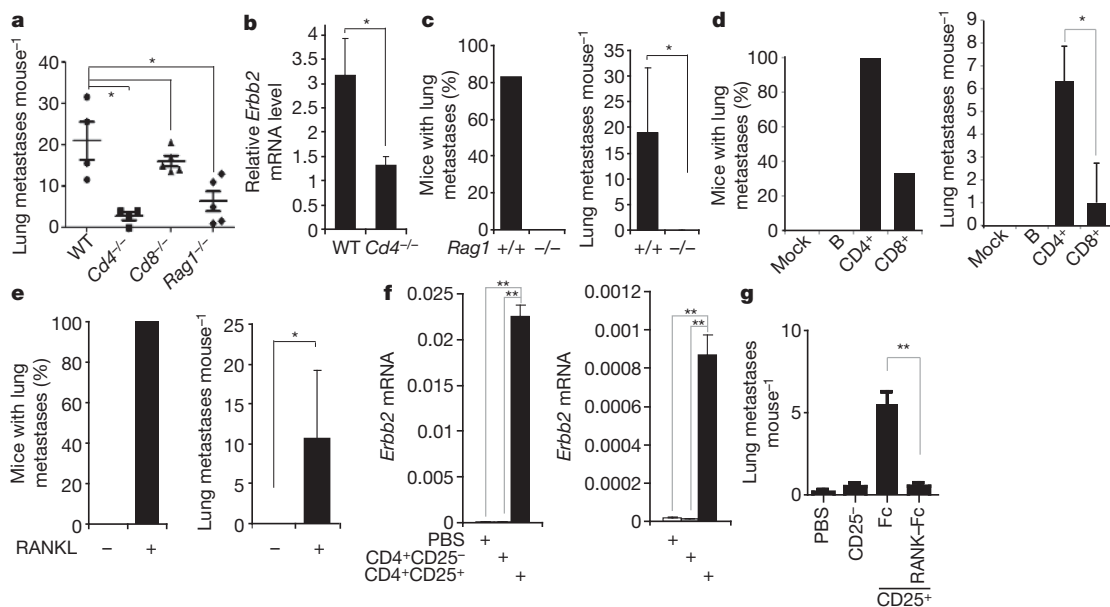


Figure 3 | Tumour-infiltrating CD4⁺ cells stimulate pulmonary metastasis. **a**, **b**, *MMTV-ErbB2*-transgenic PCaM cells (1×10^6 cells) were transplanted as in Fig. 1b to the indicated mouse strains. **a**, Lung metastasis multiplicity was calculated 56 days later. Individual mouse data are presented (mean, horizontal line; error bars, s.e.m.; $n = 4-6$). **b**, *ErbB2* expression in pulmonary metastases in the indicated mice was quantified by quantitative RT-PCR analyses of lung RNA with *MMTV-ErbB2*-specific primers. Data are presented as mean \pm s.e.m. ($n = 4$). **c**, MT2 cells were transplanted as in Fig. 1c to the indicated mouse strains. After 56 days, pulmonary metastasis incidence (left) and multiplicity (right) were quantified. Data are presented as mean \pm s.e.m. ($n = 6$). **d**, *Rag1*^{-/-} mice were reconstituted with the indicated cell types and then inoculated with MT2 cells 3 days after reconstitution. After 35 days, pulmonary metastasis incidence (left) and multiplicity (right) were quantified. Data are presented as mean \pm s.e.m. ($n = 3$). **e**, MT2-cell-inoculated *Rag1*^{-/-} mice were treated with BSA or RANKL ($80 \mu\text{g kg}^{-1}$) twice weekly, starting 1 week after

inoculation with tumour cells. After 35 days, pulmonary metastasis incidence (left) and multiplicity (right) were quantified. Data are presented as mean \pm s.e.m. ($n = 6-7$). **f**, MT2 cells were transplanted to *Rag1*^{-/-} mice, which were reconstituted 3 days before tumour cell injection with the indicated cell types or PBS as in **d**. After 56 days, *ErbB2* mRNA in lung metastases was measured by quantitative RT-PCR and normalized to cyclophilin mRNA levels. Each histogram represents an independent littermate group. Data are presented as mean \pm s.e.m. ($n = 3$). **g**, MT2 cells were transplanted to *Rag1*^{-/-} female littermates, which were reconstituted 3 days before tumour cell injection with PBS or T cells as in **f**. After 1 week, mice that had been reconstituted with CD4⁺CD25⁺ T cells received Fc protein (as a control) or RANK-Fc (2.5 mg kg^{-1}) twice weekly. Pulmonary metastasis multiplicity was measured on day 35 after inoculation with tumour cells. Data are presented as mean \pm s.e.m. ($n = 4-5$). *, $P < 0.05$; **, $P < 0.01$ (non-parametric Mann-Whitney U test).

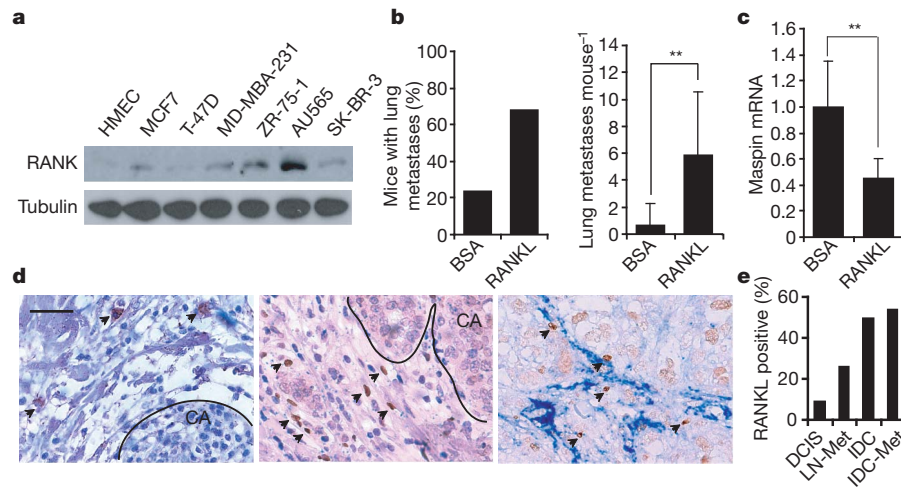


Figure 4 | RANKL in human breast cancer. **a**, RANK expression in the indicated human breast cancer cell lines was analysed by immunoblotting, with tubulin expression as a control. **b**, ZR-75-1 cells were transplanted to the number 2 mammary glands of nude mice, which were then treated with BSA or RANKL ($80 \mu\text{g kg}^{-1}$) twice weekly, starting 1 week after inoculation with tumour cells. After 84 days, pulmonary metastasis incidence (left) and multiplicity (right) were quantified. Data are presented as mean \pm s.e.m. ($n = 6$). **c**, Maspin mRNA in ZR-75-1 tumours from the mice in **b** was analysed by quantitative RT-PCR and normalized to cyclophilin mRNA levels. Data are presented as mean \pm s.e.m. ($n = 6$). **d**, Human breast cancer sections were

stained with anti-RANKL (left, brown), anti-FOXP3 (centre and right, brown), and anti-SMA (right, blue) antibodies. Arrows indicate RANKL⁺ cells (left) and FOXP3⁺ cells (centre and right). Scale bar, 20 μm (all images). **e**, Tissue arrays containing 50 samples each of ductal carcinoma *in situ* (DCIS), lymph-node macro-metastasis (LN-Met), invasive ductal carcinoma without metastasis (IDC) and IDC with metastasis (IDC-Met) were analysed for RANKL-expressing cells. Samples were considered to be positive when at least two cells per field ($\times 200$ magnification) were RANKL⁺. **b, c**, **, $P < 0.01$ (non-parametric Mann-Whitney U test).

in addition to having direct effects on carcinoma cells²⁰, fits the observation that the depletion of CAFs from mammary tumours decreased T_{reg}-cell infiltration and pulmonary metastasis²⁵. We postulate that the potent pro-metastatic effect of tumour-infiltrating T_{reg} cells can be dismantled by RANKL-RANK antagonists, which should leave the potential antitumorigenic activity of T helper 1 cells and CD8⁺ T cells intact. Such inhibitors of RANK signalling need to be used together with the surgical resection of primary breast tumours and the administration of antitumour immunotherapy to prevent the recurrence of metastatic disease, but may be an ineffective treatment after metastasis recurs. RANKL has also been reported to act at an early stage of tumour development, at which it mediates the tumour-promoting effect of progesterins^{26,27}. Thus, RANKL antagonists may also have a preventive ability.

METHODS SUMMARY

C57BL/6 *Rank*^{+/-} mice¹¹ were backcrossed to FVB/N *MMTV-ErbB2*-transgenic mice for at least six generations. FVB/N *MMTV-ErbB2/Rank*^{+/-} mice were intercrossed to generate FVB/N *MMTV-ErbB2/Rank*^{+/+} and FVB/N *MMTV-ErbB2/Rank*^{+/-} mice. *Cd4*^{-/-}, *Cd8*^{-/-} and *Rag1*^{-/-} mice were maintained on the FVB/N background. PCaM or MT2 single-cell suspensions were injected into the number 2 mammary gland. Tumour size was measured weekly with a caliper. At the study's end, mice were killed, and primary tumours and lungs were analysed.

Received 12 October; accepted 25 November 2010.

Published online 16 February 2011.

- Grivennikov, S. I., Greten, F. R. & Karin, M. Immunity, inflammation, and cancer. *Cell* **140**, 883–899 (2010).
- Luo, J. L. *et al.* Nuclear cytokine-activated IKK α controls prostate cancer metastasis by repressing Maspin. *Nature* **446**, 690–694 (2007).
- Fata, J. E. *et al.* The osteoclast differentiation factor osteoprotegerin-ligand is essential for mammary gland development. *Cell* **103**, 41–50 (2000).
- Cao, Y. *et al.* IKK α provides an essential link between RANK signaling and cyclin D1 expression during mammary gland development. *Cell* **107**, 763–775 (2001).
- Cao, Y., Luo, J. L. & Karin, M. I κ B kinase α kinase activity is required for self-renewal of ErbB2/Her2-transformed mammary tumor-initiating cells. *Proc. Natl Acad. Sci. USA* **104**, 15852–15857 (2007).
- Guy, C. T. *et al.* Expression of the *neu* protooncogene in the mammary epithelium of transgenic mice induces metastatic disease. *Proc. Natl Acad. Sci. USA* **89**, 10578–10582 (1992).

- Slamon, D. J. *et al.* Studies of the HER-2/neu proto-oncogene in human breast and ovarian cancer. *Science* **244**, 707–712 (1989).
- Tiwari, R. K., Borgen, P. I., Wong, G. Y., Cordon-Cardo, C. & Osborne, M. P. HER-2/neu amplification and overexpression in primary human breast cancer is associated with early metastasis. *Anticancer Res.* **12**, 419–425 (1992).
- Bohling, S. D. & Allison, K. H. Immunosuppressive regulatory T cells are associated with aggressive breast cancer phenotypes: a potential therapeutic target. *Mod. Pathol.* **21**, 1527–1532 (2008).
- Ohara, M. *et al.* Possible involvement of regulatory T cells in tumor onset and progression in primary breast cancer. *Cancer Immunol. Immunother.* **58**, 441–447 (2009).
- Dougall, W. C. *et al.* RANK is essential for osteoclast and lymph node development. *Genes Dev.* **13**, 2412–2424 (1999).
- Body, J. J. *et al.* Effects of denosumab in patients with bone metastases, with and without previous bisphosphonate exposure. *J. Bone Miner. Res.* **25**, 440–446 (2010).
- Fizazi, K. *et al.* Randomized phase II trial of denosumab in patients with bone metastases from prostate cancer, breast cancer, or other neoplasms after intravenous bisphosphonates. *J. Clin. Oncol.* **27**, 1564–1571 (2009).
- Ercolini, A. M. *et al.* Recruitment of latent pools of high-avidity CD8⁺ T cells to the antitumor immune response. *J. Exp. Med.* **201**, 1591–1602 (2005).
- Hsu, H. *et al.* Tumor necrosis factor receptor family member RANK mediates osteoclast differentiation and activation induced by osteoprotegerin ligand. *Proc. Natl Acad. Sci. USA* **96**, 3540–3545 (1999).
- Jones, D. H. *et al.* Regulation of cancer cell migration and bone metastasis by RANKL. *Nature* **440**, 692–696 (2006).
- Kawai, T. *et al.* B and T lymphocytes are the primary sources of RANKL in the bone resorptive lesion of periodontal disease. *Am. J. Pathol.* **169**, 987–998 (2006).
- DeNardo, D. G. *et al.* CD4⁺ T cells regulate pulmonary metastasis of mammary carcinomas by enhancing protumor properties of macrophages. *Cancer Cell* **16**, 91–102 (2009).
- Fontenot, J. D., Gavin, M. A. & Rudensky, A. Y. Foxp3 programs the development and function of CD4⁺CD25⁺ regulatory T cells. *Nature Immunol.* **4**, 330–336 (2003).
- Karnoub, A. E. *et al.* Mesenchymal stem cells within tumour stroma promote breast cancer metastasis. *Nature* **449**, 557–563 (2007).
- Luboshits, G. *et al.* Elevated expression of the CC chemokine regulated on activation, normal T cell expressed and secreted (RANTES) in advanced breast carcinoma. *Cancer Res.* **59**, 4681–4687 (1999).
- Gao, J. L. *et al.* Structure and functional expression of the human macrophage inflammatory protein 1 α /RANTES receptor. *J. Exp. Med.* **177**, 1421–1427 (1993).
- Gobert, M. *et al.* Regulatory T cells recruited through CCL22/CCR4 are selectively activated in lymphoid infiltrates surrounding primary breast tumors and lead to an adverse clinical outcome. *Cancer Res.* **69**, 2000–2009 (2009).
- Bates, G. J. *et al.* Quantification of regulatory T cells enables the identification of high-risk breast cancer patients and those at risk of late relapse. *J. Clin. Oncol.* **24**, 5373–5380 (2006).

25. Liao, D., Luo, Y., Markowitz, D., Xiang, R. & Reisfeld, R. A. Cancer associated fibroblasts promote tumor growth and metastasis by modulating the tumor immune microenvironment in a 4T1 murine breast cancer model. *PLoS ONE* **4**, e7965 (2009).
26. Gonzalez-Suarez, E. *et al.* RANK ligand mediates progestin-induced mammary epithelial proliferation and carcinogenesis. *Nature* **468**, 103–107 (2010).
27. Schramek, D. *et al.* Osteoclast differentiation factor RANKL controls development of progestin-driven mammary cancer. *Nature* **468**, 98–102 (2010).

Supplementary Information is linked to the online version of the paper at www.nature.com/nature.

Acknowledgements We thank L. Coussens for discussions and suggestions, V. Temkin and G. He for advice, and H. Herschman for critical reading. Work was supported by the National Institutes of Health (NIH). W.T. and W.Z. were supported by postdoctoral fellowships from the Susan G. Komen Breast Cancer Foundation. A.S. was supported by

NIH Asthma Research and Cancer Therapeutic training grants, and S.G. was supported by a research fellowship from the Crohn's and Colitis Foundation of America. M.K. is an American Cancer Society research professor.

Author Contributions W.T., W.Z., A.S. and M.K. designed the research. W.T., W. Z. and A.S. performed most of the experiments and analysed the data. W.T., W.Z., A.S. and M. K. wrote the manuscript. S.G. performed some of the experiments and analysed their data. J.Q.C. and R.M.H. provided essential reagents, *in vivo* imaging and technical discussions.

Author Information Reprints and permissions information is available at www.nature.com/reprints. The authors declare no competing financial interests. Readers are welcome to comment on the online version of this article at www.nature.com/nature. Correspondence and requests for materials should be addressed to M.K. (karinoffice@ucsd.edu).

Intrinsic transition of embryonic stem-cell differentiation into neural progenitors

Daisuke Kamiya^{1,2}, Satoe Banno¹, Noriaki Sasai¹, Masatoshi Ohgushi¹, Hidehiko Inomata¹, Kiichi Watanabe¹, Masako Kawada¹, Rieko Yakura¹, Hiroshi Kiyonari³, Kazuki Nakao³, Lars Martin Jakt⁴, Shin-ichi Nishikawa⁴ & Yoshiki Sasai^{1,2}

The neural fate is generally considered to be the intrinsic direction of embryonic stem (ES) cell differentiation. However, little is known about the intracellular mechanism that leads undifferentiated cells to adopt the neural fate in the absence of extrinsic inductive signals. Here we show that the zinc-finger nuclear protein Zfp521 is essential and sufficient for driving the intrinsic neural differentiation of mouse ES cells. In the absence of the neural differentiation inhibitor BMP4, strong Zfp521 expression is intrinsically induced in differentiating ES cells. Forced expression of Zfp521 enables the neural conversion of ES cells even in the presence of BMP4. Conversely, in differentiation culture, Zfp521-depleted ES cells do not undergo neural conversion but tend to halt at the epiblast state. Zfp521 directly activates early neural genes by working with the co-activator p300. Thus, the transition of ES cell differentiation from the epiblast state into neuroectodermal progenitors specifically depends on the cell-intrinsic expression and activator function of Zfp521.

Previous studies, particularly in amphibians, have demonstrated that the initial step of vertebrate neural differentiation from uncommitted embryonic ectodermal cells occurs via a cell-intrinsic mechanism and requires only that inhibitory signals for neural differentiation such as BMP4 are absent (so-called default model)^{1–5}. However, the intrinsic mechanism of the initial neural differentiation step, especially in mammals, is still poorly understood.

Besides medical applications⁶, the *in vitro* differentiation of ES cells also provides a versatile experimental system for analysing the elementary regulatory steps in mammalian development. Mammalian pluripotent cells adopt a neural fate when exogenous signals are minimized in differentiation culture^{7–9} and can mimic the step-wise differentiation into pluripotent epiblast, definitive ectoderm (late epiblast cells) and neuroectoderm^{10,11}. In our previous studies, we established an efficient system for the *in vitro* neural differentiation of mouse and human ES cells involving floating aggregate culture in growth-factor-minimized medium^{8,12} (serum-free culture of embryoid-body-like aggregates; hereafter referred to as SFEB). In SFEB culture, ES cells spontaneously undergo selective neural differentiation without the induction of meso- or endodermal differentiation, and their differentiation highly recapitulates the ontogenetic process of brain development, including the formation of polarized telencephalic neuroectodermal structures⁸. In the present study, using this culture system, we searched for molecules that initiate the neural conversion of ES cells.

Zfp521 induces neural conversion

First, we performed a GeneChip-based screen for genes induced in the initial phase of neural differentiation. We used mouse ES (mES) cells with GFP knocked-in at the locus of *Sox1*, a neural-progenitor-specific gene (*Sox1*-GFP cells)¹³, and isolated the neural (GFP⁺/E-cadherin[−]) and non-neural (GFP[−]/E-cadherin⁺; including pluripotent cells) populations from differentiating ES cells by fluorescence-activated cell

sorting (FACS) on day 3 of SFEB culture when *Sox1*-GFP expression first appeared (Fig. 1a). Using the multiple-sample comparison algorithm of expression patterns that we previously reported¹⁴, we identified 104 genes whose expression was high in the GFP⁺/E-cadherin[−] cells (day 3) but low in the GFP[−]/E-cadherin⁺ cells (day 3) and in undifferentiated mES cells. Among these candidates, 29 genes showed little expression in mesodermal cells and encoded proteins relevant to cell differentiation such as nuclear proteins and signal transducers (Supplementary Table 1). The cDNAs of the candidate genes were then subcloned into a mammalian expression vector and overexpressed by lipofection in mES cells cultured in differentiation medium containing 10% fetal calf serum (FCS), which is inhibitory for neural differentiation.

Among the 29 candidates, one clone exhibited a potent neural-differentiation-promoting effect on neural differentiation in mES cells under the inhibitory culture conditions. This clone, *Zfp521* (refs 15, 16), encoded a multiple-zinc-finger nuclear protein of the Krüppel class (C2H2) (Fig. 1b, c) that is structurally related to Zfp423 (also called OAZ)¹⁶. Its expression was strongly detected in the *Sox1*-GFP⁺ population but not in the *Sox1*-GFP[−]/E-cad⁺ population or in ES cells (Fig. 1d; see Fig. 1e for relative expression levels compared to other cells/tissues). Upon neural differentiation, expression of *Zfp521* increased by 60-fold during the first 5 days of SFEB culture (Fig. 1f, black column), whereas its expression was markedly reduced by the addition of FCS (grey column) or BMP4 (open column), a potent inhibitor of neural differentiation^{1–4,7}. Notably, the forced expression of *Zfp521* induced substantial expression of early neural markers such as *Sox1*, *Sox3* and N-cadherin (*Ncad*; also called *Cdh2*) in the non-permissive culture containing FCS (Fig. 1g–m).

The forced expression of *Zfp521* also enhanced *Ncad* expression in SFEB culture under the permissive conditions (Fig. 1n, lane 2). Furthermore, whereas the addition of BMP4 to the culture suppressed *Ncad* expression (Fig. 1n, lane 3, filled column), this suppression was markedly reversed by *Zfp521* overexpression (Fig. 1n, lane 3, open

¹Organogenesis and Neurogenesis Group, RIKEN Center for Developmental Biology, Kobe 650-0047, Japan. ²Department of Medical Embryology, Kyoto University Graduate School of Medicine, Kyoto 606-8501, Japan. ³Laboratory of Animal Resource and Genetic Engineering, RIKEN Center for Developmental Biology, Kobe 650-0047, Japan. ⁴Laboratory of Stem Cell Research, RIKEN Center for Developmental Biology, Kobe 650-0047, Japan.

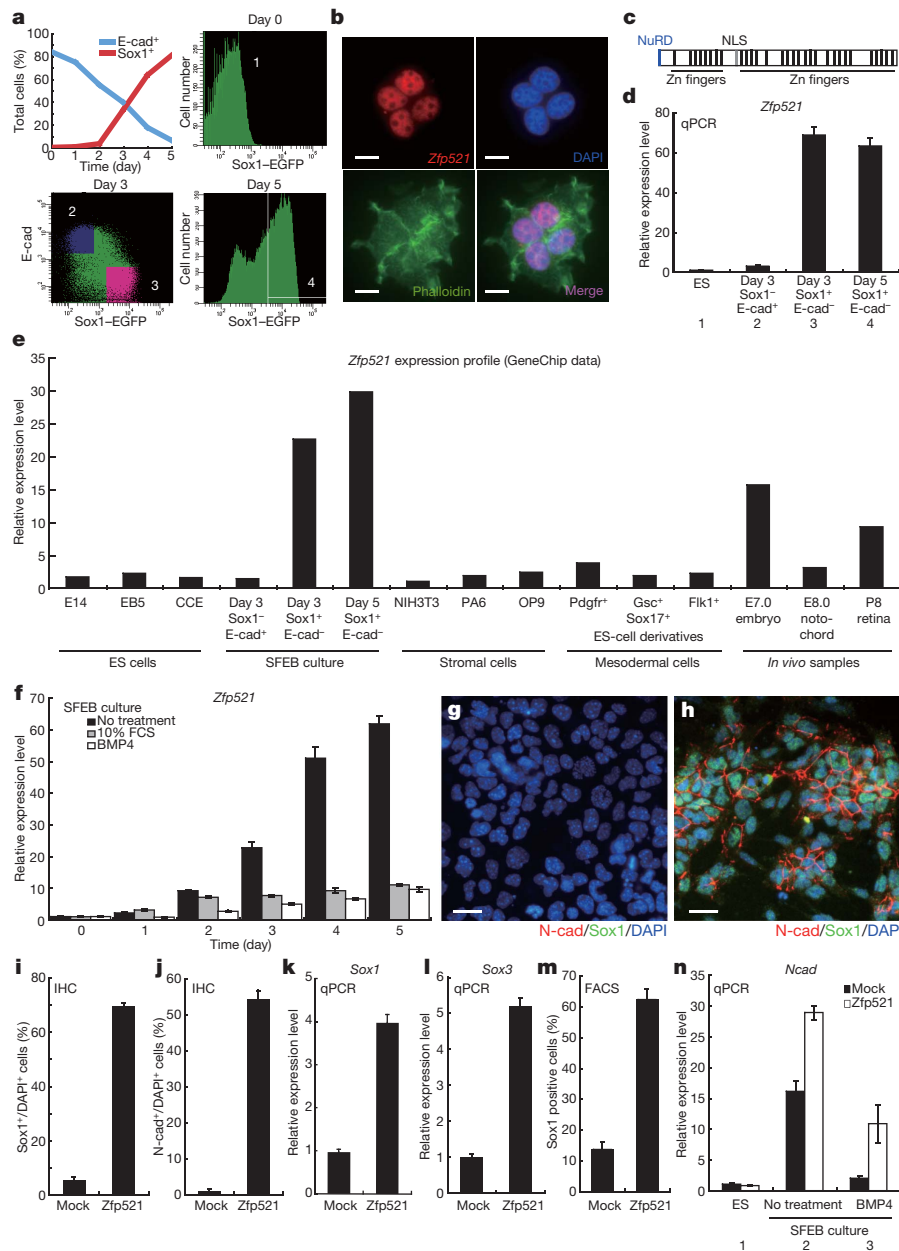


Figure 1 | The early neuroectodermal gene *Zfp521* strongly promotes neural differentiation in ES cell culture. **a**, Expression profile of the early neuroectodermal marker Sox1 and the undifferentiated-state marker E-cadherin in SFEB-cultured differentiating mES cells. For screening, ES cells (1) and differentiated cells (2–4) were sorted and subjected to microarray analysis. **b**, Localization of Zfp521 protein to the nucleus. HEK293T cells transfected with the Zfp521-expression vector were stained with an anti-Zfp521 antibody, DAPI or phalloidin. Scale bars, 10 μ m. **c**, Protein structure of Zfp521. Zfp521 contains 30 Zn-finger motifs. **d**, Relative expression level of Zfp521 mRNA analysed by qPCR. Lanes 1–4 correspond to samples 1–4 in **a**. **e**, Expression profile of Zfp521 in various cell types. **f**, Temporal expression profile of Zfp521 by qPCR. ES cells were cultured in differentiation medium

alone, or with 10% FCS, or 1 nM BMP4. **g–j**, Immunocytochemistry of mES cells that were transfected with the control (**g**) or Zfp521-expression (**h**) vector and cultured in differentiation medium containing 10% FCS for 5 days. Scale bars in **g** and **h**, 20 μ m. Sox1-GFP mES cells were used. Cells were stained with anti-N-cadherin (red) and anti-GFP (green) antibodies. Nucleus staining, DAPI (blue). **i, j**, Percentage of Sox1⁺ (**i**) and N-cadherin⁺ cells (**j**). IHC, immunohistochemistry. **k, l**, qPCR analysis of Sox1 (**k**) and Sox3 (**l**) expression on day 5. **m**, Percentage of Sox1⁺ cells analysed by FACS. **n**, qPCR analysis of N-cadherin expression. Mock and Zfp521-transfected mES cells were cultured in differentiation medium alone (lane 2), or with 0.5 nM BMP4 (lane 3) for 5 days. **d, f, i–n**, Error bars indicate \pm s.d. ($n = 4$).

column), indicating that the neuralizing activity of Zfp521 could override the inhibitory effect of BMP4. However, this activity of Zfp521 was not due to its direct interference with BMP signalling per se, as BRE (ref. 17) (BMP-response element)-luciferase assays showed that Zfp521 overexpression did not suppress the cells' response to BMP4 in SFEB culture (Supplementary Fig. 1a, lanes 3, 4). This idea was also supported by the observation that Zfp521 overexpression did not substantially affect the expression of *Smad7*, a

direct target gene of BMP signalling¹⁸, in SFEB-cultured ES cells (Supplementary Fig. 1b).

In an *in situ* hybridization analysis of the early mouse embryo, no substantial expression of Zfp521 was detected in the inner cell mass (ICM) of the blastocyst (Fig. 2a), and a weak Zfp521 expression diffusely appeared between embryonic day (E)6.5–7.0 (not shown; see Supplementary Fig. 1c for qPCR data). As gastrulation proceeded (E7.0–E8.0), strong Zfp521 expression was seen in the epiblast, particularly in

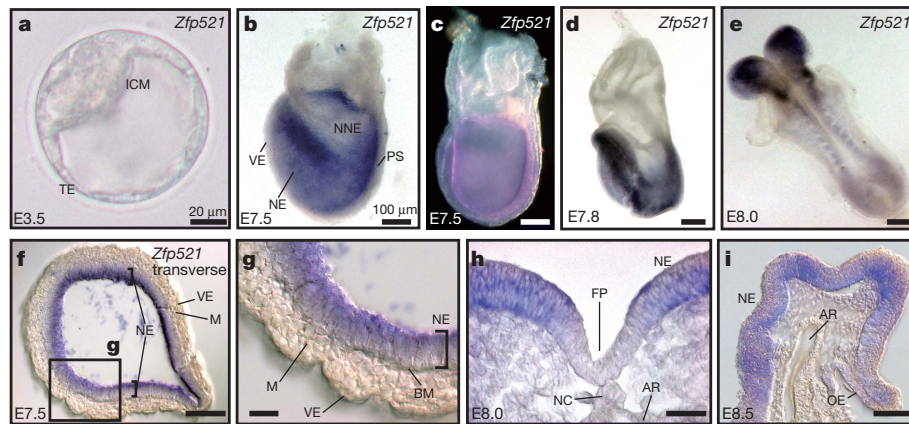


Figure 2 | *Zfp521* expression pattern in early mouse embryos. **a–e**, Whole-mount *in situ* hybridization of *Zfp521* in the embryo at the indicated stage. The rostral side is on the left in **b–e**. **f–h**, Transverse section of the E7.5 mouse embryo (**f**, **g**) or E8.0 head neural plate (**h**). **i**, Sagittal section at the head region of the E8.5 embryo. AR, archenteron; BM, basement membrane; FP, floor plate;

ICM, inner cell mass; M, mesoderm; NC, notochord; NE, neuroectoderm; NNE, non-neural ectoderm; OE, oral ectoderm; PS, primitive streak; TE, trophectoderm; VE, visceral endoderm. Scale bars: **a**, 20 μ m; **b–f**, **h**, 100 μ m; **g**, 50 μ m; **i**, 200 μ m.

the neuroectodermal region, but not in the endoderm, involuting mesoderm or non-neural ectoderm (Fig. 2b–h, Supplementary Fig. 1d–g and not shown; its weak expression was also detected in the N-cad⁺ head mesenchyme, Supplementary Fig. 1g). These findings show that *Zfp521* is an early neural nuclear protein with a potent neural differentiation-promoting activity. After gastrulation, strong *Zfp521* expression was detected more preferentially in the neuroectoderm of the rostral neural tube (except in the floor plate region; Fig. 2e, h, i), whereas its caudal neural expression became weak (Fig. 2e and Supplementary Fig. 1h).

Requirement for intrinsic differentiation

We next examined whether *Zfp521* is required for the neural differentiation of mES cells. The introduction of short hairpin RNA (shRNA) targeting *Zfp521* into mES cells strongly suppressed the expression not only of *Zfp521* (Fig. 3a) but also of other early neural markers such as *Sox3* and *Ncad* in SFEB-cultured mES cells (Fig. 3b, c; see Supplementary Fig. 2a–c for the specific and reproducible suppression in multiple independent subclones carrying *Zfp521* shRNA and controls). Immunostaining also showed that *Zfp521* shRNA markedly decreased the percentages of the Sox1⁺ and N-cad⁺ populations in SFEB-cultured mES cells (Fig. 3d–h). The expression of these neural markers in *Zfp521*-depleted ES cells was rescued by the forced expression of codon-swapped *Zfp521* (*Zfp521mt*; Fig. 3i, j; further confirmed by qPCR and by Sox1–EGFP flow cytometry in Fig. 3k–m), which is insensitive to *Zfp521* shRNA (Supplementary Fig. 3a, b). In the co-aggregation culture of control and *Zfp521* shRNA ES cells, the neural differentiation of *Zfp521* shRNA ES cells was not substantially rescued by the presence of the control cells, indicating that the inhibitory effect of the *Zfp521* knockdown on neural differentiation was cell autonomous (Supplementary Fig. 4a–c). The *Zfp521* knockdown also attenuated neural and neuronal differentiation of mES cells in two other neural differentiation cultures (SDIA culture⁷ and the EB-RA method¹⁹; Supplementary Fig. 5a–d and e–h).

Taken together with the overexpression data, these observations showed that *Zfp521* expression is both essential and sufficient for mES cells to undergo neural conversion. In addition, *Zfp521* expression was induced during the early phase of neural differentiation of human ES cells in SFEB culture (Fig. 3n and Supplementary Fig. 6a, b), and *Zfp521* knockdown attenuated *Sox3* expression (Fig. 3o and Supplementary Fig. 6c, d), indicative of its conserved role in both species.

Next, we performed a blastocyst injection study using control and *Zfp521*-knockdown ES cells (Supplementary Fig. 7; RFP-labelled).

When analysed at E9.5, the progeny of the injected control ES cells were found in a wide range of embryonic tissues including rostral and caudal neural tissues (Supplementary Fig. 7a). In contrast, the injected *Zfp521*-knockdown ES cells failed to contribute substantially to the rostral neural tube tissues (forebrain to rostral spinal cord), although the progeny of both control and knockdown cells were equally seen in the peripheral tissues and in the caudal spinal cord, where *Zfp521* expression is weak (Supplementary Fig. 7b–j). Thus, the requirement of *Zfp521* function is more obvious in the rostral neural tube where *Zfp521* is strongly and persistently expressed (Fig. 2). The difference between the rostral and caudal neural tissues may reflect the fact that the caudal neural tube tissue develops via the intricate secondary neurulation²⁰, unlike the rostral neural plate tissue, the development of which depends on the BMP-inhibitor-driven primary neural induction.

Transition from epiblast to neuroectoderm

Zfp521 overexpression did not induce neural differentiation in ES cells cultured in the presence of LIF (not shown) or the FGFR inhibitor SU5402 (Supplementary Fig. 8a), which blocks the initial step of differentiation from ES cells towards epiblast status²¹ (the role of FGF signalling in SFEB culture seems to be permissive, as the addition of exogenous FGF signals did not promote neural differentiation; Supplementary Fig. 8b).

We then asked which step in the process of ES cell differentiation was dependent on *Zfp521*. To this end, we analysed the effects of *Zfp521* depletion on the expression of stage- and lineage-specific markers (Fig. 4). In the differentiation (SFEB) culture of mES cells, the depletion of *Zfp521* did not strongly affect the downregulation of the ES cell/ICM-specific markers *Rex1* (also called *Zfp42*) and *Nanog* during days 3–7 of culture (Fig. 4a, b). In contrast, the epiblast-marker gene *Fgf5* was downregulated in controls by day 7 but not in the *Zfp521*-depleted mES cells (Fig. 4c). A similar persistent expression was seen for *Oct3/4* (also called *Pou5f1*), a marker expressed in ES cells, the ICM and the epiblast²² (Fig. 4d). Immunostaining showed that a large portion of the *Zfp521*-depleted mES cells were still Oct3/4⁺, Cripto⁺ (another epiblast marker)²³ and Sox1[–] on day 5 of SFEB culture, when the majority of the control mES cells had already undergone neural differentiation and shut off the immature markers (Fig. 4e, f; see panel g for percentages). These findings indicate that mES cells lacking *Zfp521* can differentiate into epiblast-like cells but fail to proceed to neuroectodermal differentiation.

The persistent expression of the epiblast markers in *Zfp521*-depleted mES cells prompted us to test whether ES cells lacking this

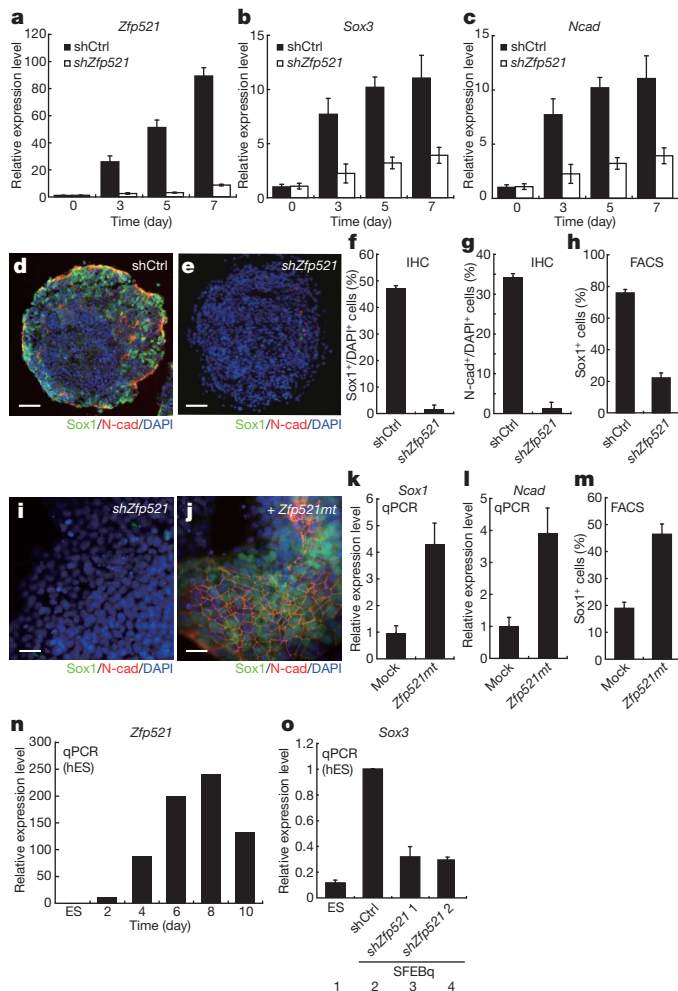


Figure 3 | Zfp521 is required for early neural differentiation of ES cells. **a–c**, Temporal expression profile of *Zfp521* (**a**), *Sox3* (**b**) and *N-cadherin* (**c**) mRNA. mES cells carrying control shRNA or *Zfp521* shRNA were cultured in differentiation medium by the SFEB method for 7 days. **d, e**, Immunocytochemistry of control shRNA (**d**) or *Zfp521* shRNA (**e**). mES cell aggregates cultured in differentiation medium by SFEB for 5 days. Scale bars, 80 μ m. **f, g**, Percentage of Sox1⁺ (**f**) and N-cadherin⁺ (**g**) cells. **h**, Percentage of Sox1⁺ cells analysed by FACS. **i, j**, Immunocytochemistry of *Zfp521* shRNA mES cell aggregate cultured in differentiation medium for 5 days. Cells were transfected with the mock (**i**) or *Zfp521mt* expression (**j**) plasmid. Scale bars, 20 μ m. **k, l**, Relative expression levels of *Sox1* (**k**) or *N-cadherin* (**l**) by qPCR. **m**, Percentage of Sox1⁺ cells analysed by FACS. **n**, Temporal expression of *Zfp521* during neural differentiation of human ES cells in SFEB culture. **o**, Expression levels of *Sox3* analysed by qPCR. Human ES cells (lane 1) were transfected with control (lane 2) or *Zfp521* shRNA (lane 3 and 4; two independent shRNAs (*shZfp521* 1 and *shZfp521* 2))-expressing plasmids and subjected to SFEB culture for 3 days. **a–c, f–h, k–m, o**, Error bars indicate \pm s.d. ($n = 4$).

factor could differentiate into non-neural lineages *in vitro* under growth-factor-driven inductive conditions (see Methods). A qPCR analysis demonstrated that both the control and the *Zfp521*-depleted ES cells were similarly induced to express marker genes for the early mesodermal (*brachyury* (*T*)), endodermal (*Sox17*), visceral endodermal (*Gata4* and *Gata6*) and non-neural ectodermal (keratin 14 (*Krt14*)) lineages (Supplementary Fig. 9a–e). In addition, immunostaining showed that the *Zfp521*-depleted ES cells could efficiently differentiate into SMA⁺ smooth muscle cells (Fig. 4h, i), HNF3- β ⁺/E-cad⁺ endodermal epithelia (Fig. 4j, k) and keratin 14⁺ epidermal precursors (Fig. 4l, m). Thus, the *Zfp521*-depleted ES cells differentiated beyond the epiblast state without halting when cultured in the presence of inductive signals for non-neural differentiation. Collectively, these

findings demonstrate that *Zfp521* is selectively required for advancing the differentiation step into the early neuroectodermal fate. Given that the epidermal differentiation was not impaired in *Zfp521*-depleted ES cells, *Zfp521* should have an active role specifically in driving the transition from the common ectodermal-progenitor state into the neuroectodermal fate (Fig. 4n).

Zfp521 transactivates early neural genes

Finally, we sought to understand the molecular mode of *Zfp521*'s function. To examine whether the nuclear protein *Zfp521* associated preferentially with neural or non-neural gene loci, we performed a chromatin immunoprecipitation (ChIP) assay using SFEB-cultured mES cells expressing Flag-tagged *Zfp521*. The *Zfp521* protein clearly associated with neuroectoderm-specific gene loci including *Sox1*, *Sox3* and *Pax6*, but not with the ES cell marker genes *Klf4* or *Rex1*, the epiblast-specific marker gene *Fgf5* or the mesodermal marker gene *Brachyury* (*T*) (Fig. 5a). No clear enhancement in ChIP was observed for *Oct6* (also called *Pou3f1*) (Fig. 5a), a marker for the epiblast and early neuroectoderm, the expression of which (Supplementary Fig. 10a) starts before the onset of strong *Zfp521* expression in SFEB-cultured mES cells (Supplementary Fig. 10c). Thus, *Zfp521* protein is located preferentially at early neuroectoderm-specific genes and not at non-neural genes or early genes relevant to ES/epiblast cells. This finding is in accordance with the observation that *Zfp521* overexpression substantially increased the expression of *Sox1*, *Sox3* and *Pax6*, but not of *Oct6* or *Fgf5*, in mES cells cultured under the non-permissive conditions (Fig. 5b and not shown). These findings indicate that *Zfp521* promotes neural differentiation by activating early neuroectodermal genes rather than by inhibiting the expression of non-neural genes. Consistent with this idea, although *Zfp521* contains a NuRD (co-repressor complex)-binding motif at its amino terminus^{16,24}, the deletion of this motif did not substantially affect *Zfp521*'s neuralizing activity (Δ NuRD in Supplementary Fig. 11a, row 2).

Thus, unlike in other contexts^{24,25}, *Zfp521* seems to have a transactivator role in neural specification. The following observations indicated that, among the early neuroectodermal genes, at least *Sox3* is a target gene directly regulated by *Zfp521*. First, the *Sox3* locus was strongly associated with *Zfp521* in the ChIP assay (Fig. 5a). Second, the overexpression of *Sox3* in *Zfp521*-depleted ES cells significantly rescued *Ncad* expression (>twofold; Fig. 5c, lane 2) in SFEB culture, whereas the overexpression of *Oct6* (lane 3), *Pax6* or *Zic2* did not (not shown). Third, in the ChIP assay for the binding of the co-activator p300²⁶, which has been shown to reflect the activation state of specific gene loci in a genome-wide fashion²⁷, the association of p300 with the *Sox3* locus was substantially enhanced by the forced expression of *Zfp521* (Fig. 5d) and reduced by *Zfp521* shRNA (Fig. 5e). Furthermore, in a co-transfection luciferase assay using the *Sox3* promoter²⁸ (7.2-kilobase fragment driving its neural-specific expression), the forced expression of *Zfp521* induced a substantial elevation of luciferase activity even in 293T cells (Fig. 5f, lane 2; *Zfp521*-VP16 induced an even greater elevation, lane 3).

Interestingly, during these analyses, we noticed that the forced expression of p300 alone promoted neural differentiation in ES cells cultured in serum-containing medium (Fig. 5g, lane 1, open column). This promoting effect of p300 presumably involved its histone acetylase activity, at least in part, because co-expression of the histone deacetylases²⁹ HDAC1 and HDAC3 (Supplementary Fig. 11b, lanes 2, 5, 6) suppressed the activity of p300 and the HDAC inhibitor TSA mimicked its promoting activity (lane 7). Importantly, the promotion of neuralization by p300 was not observed in *Zfp521*-depleted ES cells (Fig. 5g, lane 2), indicating that *Zfp521* is required for p300 to facilitate neural differentiation. Moreover, an immunoprecipitation analysis showed that *Zfp521* physically associated with p300 even in the absence of the target DNA (Fig. 5h, lane 4), indicating that the co-localization of *Zfp521* and p300 at the neuroectodermal gene loci (for example, *Sox3*) was not just a coincidence. The first eight zinc-finger motifs of *Zfp521*,

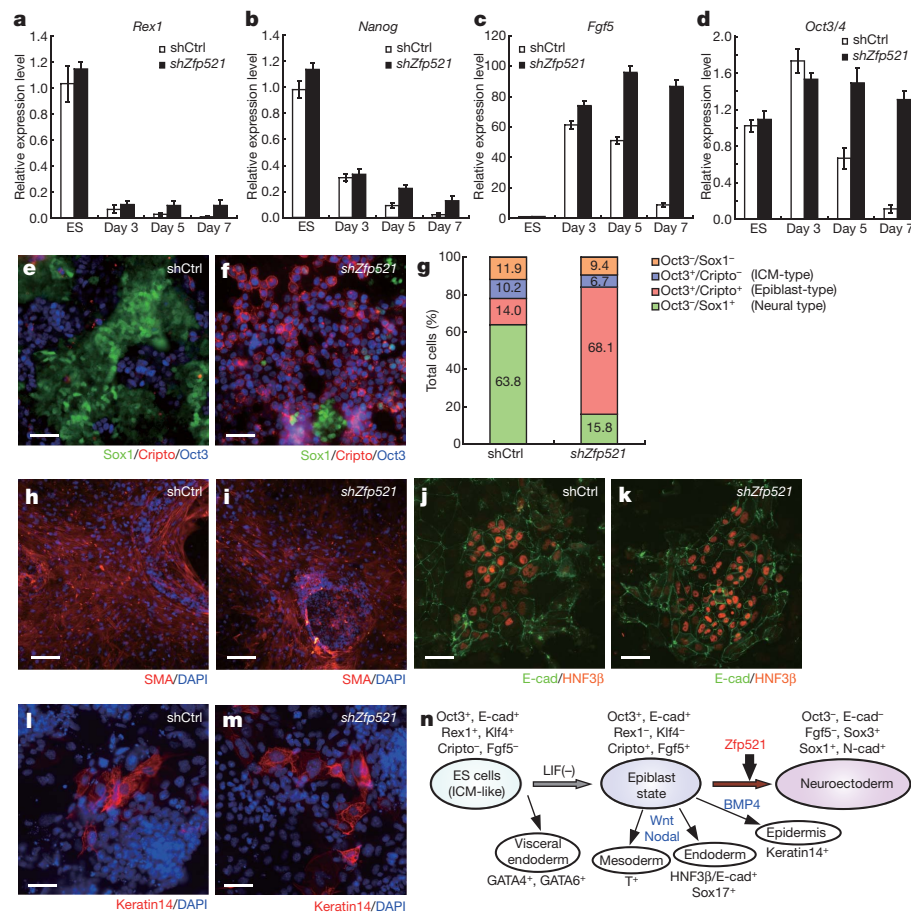


Figure 4 | Zfp521 is required to advance the differentiation step from the epiblast-like state into the early neuroectodermal state. **a–d**, Temporal expression profile of *Rex1* (**a**), *Nanog* (**b**), *Fgf5* (**c**) and *Oct3/4* (**d**) in SFEB-cultured mES cells. Control and Zfp521-depleted ES cells were compared. Error bars indicate \pm s.d. ($n = 4$). **e–g**, Control (**e**) or Zfp521-depleted (**f**) ES cells on day 5 of SFEB culture were immunostained for *Sox1*-GFP (green), *Cripto* (red) and *Oct3* (blue). Scale bars, 20 μ m. Quantification as percentages is shown in

g. **h–m**, Immunostaining of mesendodermal and epidermal marker expression in control or Zfp521-depleted mES cells under inductive conditions. DAPI, blue. **h**, **i**, Smooth muscle (red). Scale bars, 40 μ m. **j**, **k**, E-cadherin (green) and HNF3- β (orange). Scale bars, 20 μ m. **l**, **m**, Epidermal keratin 14 (red). Scale bars, 20 μ m. **n**, Schematic of Zfp521's role in the neuroectodermal differentiation from ES cells.

which have structural characteristics known for DNA binding³⁰, were essential and sufficient for its physical association with p300 (Supplementary Fig. 11c, lane 6; Δ ZF9–30), and were essential for Zfp521's neuralizing activity (Supplementary Fig. 11a, row 3; Δ ZF1–8; but not sufficient, as shown in row 4). Conversely, the first 13 motifs are sufficient for promoting neuralization (Supplementary Fig. 11a, row 5; Δ ZF14–30). Thus, the zinc-finger motifs at the amino-terminal region are important for both the neuralizing activity and the p300 interaction of Zfp521. Collectively, Zfp521 is an essential and sufficient factor for the neural differentiation of ES cells that activates at least some key neuroectoderm-specific genes by working together with the co-activator p300 (and presumably with another co-activator, CBP, because its knockdown also substantially reduced *Ncad* induction in SFEB culture; data not shown).

Model for intrinsic neural differentiation

Figure 6 summarizes our working model for Zfp521, an essential promoting regulator of neural differentiation of ES cells. When ES cell differentiation reaches the definitive ectodermal (or late-epiblast-equivalent) state, the expression of Zfp521 is cell-intrinsically induced unless the cells are cultured with neural differentiation inhibitors such as BMP4 (Fig. 1f). Importantly, once expressed, Zfp521 can cause the neural conversion of ES cells even in the presence of BMP4 (Fig. 1n), showing that the suppression of Zfp521 expression is a major downstream event of the inhibitory BMP signalling in the neuroectodermal specification of ES cells. Together with the co-activator p300, Zfp521

directly activates early neuroectodermal genes such as *Sox3*, and at least to some extent, *Sox1* and *Pax6*. The direct activation of the *Sox* genes by Zfp521 is intriguing, because previous studies have shown that the class-B *Sox* family factors promote neural gene activation³¹, at least in part by cooperating with class III Pou-domain factors^{32,33} such as *Oct6* and *Brn2* (also called *Pou3f2*). *Oct6*, which is expressed in both the embryonic epiblast and the early neuroectoderm³⁴, may also be involved in the cell-intrinsic expression of Zfp521. In SFEB culture, *Oct6* expression was neither substantially increased by Zfp521 overexpression (Fig. 5b) nor suppressed by Zfp521 depletion (Fig. 5i). Notably, the forced expression of *Oct6* (but not that of *Zic2*; not shown) increased the expression of Zfp521 and early neuroectodermal marker genes in differentiating ES cells (Fig. 5j lanes 1–4), but not in the presence of BMP4 (Fig. 5j, lanes 5–8) nor in Zfp521-depleted ES cells (Fig. 5c), demonstrating that the neuralizing activity of *Oct6* largely depends on Zfp521.

The simplest interpretation of the neural default model is that the neural fate is a 'left-over' choice passively determined by the elimination of other pathways of differentiation. However, the present study demonstrates that Zfp521 has an active role in the procession to neural commitment of the ES-cell-derived definitive ectodermal progenitors. This neural conversion involves the p300-dependent activation of neuroectodermal genes, and Zfp521 has no obvious negative effects on the expression of non-neural genes (Fig. 4) or of *Rest* (also called *NRSF*) (data not shown), which has been suggested to have a role in the suppression of neuronal genes³⁵. In summary, the cell-intrinsic activation

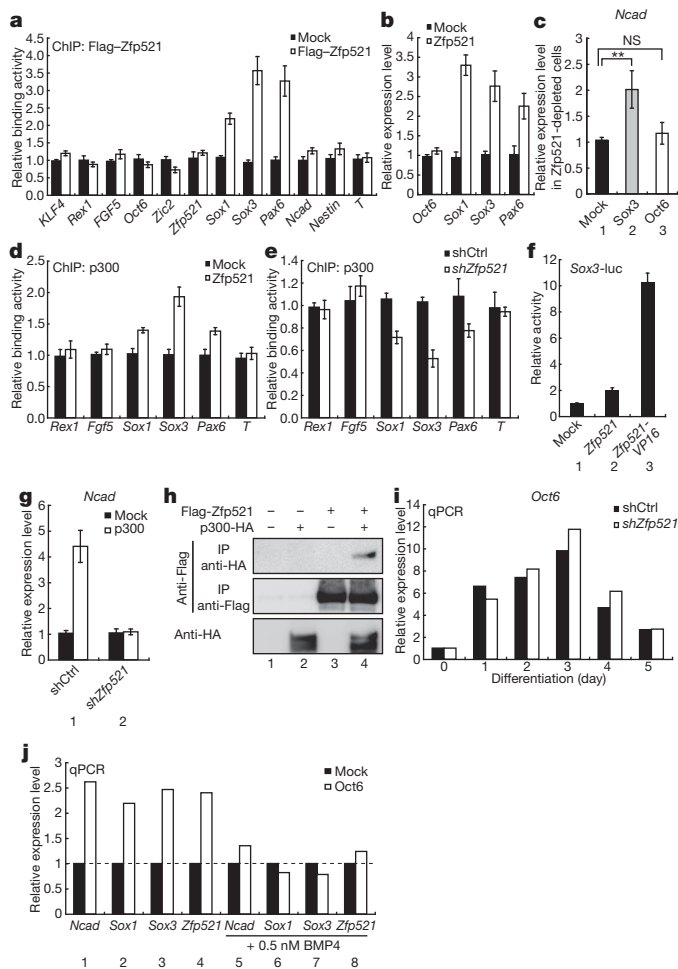


Figure 5 | Zfp521 is directly involved in the activation of early neuroectodermal genes and functions together with the co-activator p300.

a, Flag-Zfp521 ChIP analysis. ES cells were cultured in FCS-containing differentiation medium for 3 days. **b**, qPCR for Oct6, Sox1, Sox3 and Pax6 expression in ES cells transfected with the mock or Zfp521 vector. **c**, qPCR for N-cadherin expression in Zfp521-depleted mES cells transfected with mock, Sox3- or Oct6-expressing vector and cultured in differentiation medium for 5 days. Statistical significance was analysed by ANOVA with a post-hoc Dunnett's test (NS, not significant; $^{**}P < 0.01$, $n = 4$). **d**, **e**, p300 ChIP analysis. Forced expression of Zfp521 (**d**) or Zfp521-depleted (**e**) mES cells cultured in differentiation medium for 3 days. **f**, Luciferase assay for Sox3 promoter activity. Error bars indicate \pm s.d. ($n = 3$). **g**, N-cadherin expression in control or Zfp521-depleted mES cells transfected with the mock or p300-expression vector. **h**, Co-immunoprecipitation of Zfp521 and p300. HEK293T cells were transfected with the Flag-Zfp521 and/or p300-HA plasmids and cultured for 24 h. **i**, qPCR analysis of the Oct6 expression profile in SFEB-cultured control or Zfp521-depleted mES cells. **j**, Relative levels by qPCR of Ncad, Sox1, Sox3 and Zfp521 expression in ES cells transfected with the mock or Oct6-expression vector and cultured in differentiation medium without (lanes 1–4) or with (lanes 5–8) 0.5 nM BMP4. **a–e**, **g**, Error bars indicate \pm s.d. ($n = 4$).

of Zfp521 and its negative regulation by BMP signals form the core regulatory intersection for the differentiation transition of ES cells into the neuroectodermal lineage.

The conservation of Zfp521's role in early neural differentiation across vertebrate species remains to be elucidated. In *Xenopus*, although a Zfp521 homologue is expressed in the neural plate, the onset of its expression is relatively late (stage 12), that is, after the early gastrula stage (stage 10.5) when neural induction is initiated by the Spemann organizer (Supplementary Fig. 12a–h). Overexpression of Zfp521 alone did not strongly induce Sox2 expression (Supplementary Fig. 12i, j), whereas Zfp521 promoted neuronal differentiation *in vivo* and in animal caps neuralized with chordin (Supplementary Fig. 12k–r).

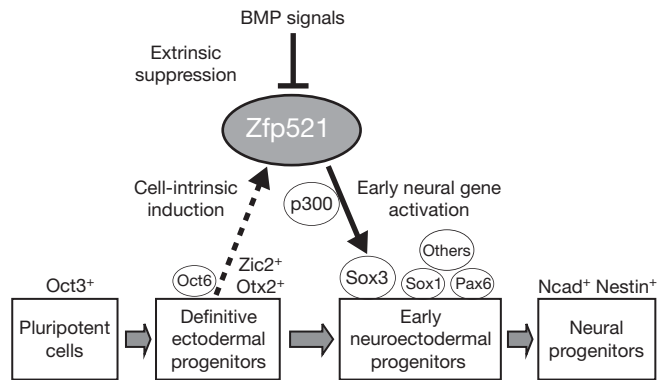


Figure 6 | Summary of Zfp521's role in the initiation of neural differentiation. Working model for the molecular regulation of and by Zfp521 in early neuroectodermal specification.

Therefore, it seems that *Xenopus* Zfp521 mainly has a role in the consolidation of neural specification and the promotion of neuronal differentiation, rather than in the initial neural induction. We speculate that, in *Xenopus*, the expression of multiple anti-neuralizing transcription factors directly downstream of BMP (for example, Gata1/2, Msx1/2, and Foxi1) can potentially counteract the neural-inducing activity of Zfp521; this possibility is an intriguing open question for future study.

METHODS SUMMARY

ES cell culture, differentiation and gene overexpression. Mouse ES cells (EB5 and Sox1-GFP cells) were maintained as described⁸. For their neural differentiation by SFEB culture, ES cells were quickly re-aggregated using low-cell-adhesion 96-well plates (Sumilon Spheroid Plates, Sumitomo Bakelite) in G-MEM-based differentiation medium (5,000 cells per 150 μ l per well) supplemented with 10% Knockout Serum Replacement. For non-permissive conditions for neural differentiation, 10% FCS or BMP4 was added to the medium in the SFEB culture. For functional screening, ES cells were cultured in FCS-containing differentiation medium on gelatin-coated plates. For transient gene overexpression, ES cells were transfected by lipofection with the pCAG-IRES-Puro expression vector and subjected to differentiation culture.

Full Methods and any associated references are available in the online version of the paper at www.nature.com/nature.

Received 1 February; accepted 30 November 2010.

Published online 16 February 2011.

- Muñoz-Sanjuán, I. & Hemmati-Brivanlou, A. Neural induction, the default model and embryonic stem cells. *Nature Rev. Neurosci.* **3**, 271–280 (2002).
- De Robertis, E. M. & Sasai, Y. A common plan for dorsoventral patterning in Bilateria. *Nature* **380**, 37–40 (1996).
- Sasai, Y., Lu, B., Steinbeisser, H. & De Robertis, E. M. Regulation of neural induction by the chd and BMP-4 antagonistic patterning signals in *Xenopus*. *Nature* **376**, 333–336 (1995).
- Lamb, T. M. *et al.* Neural induction by the secreted polypeptide noggin. *Science* **262**, 713–718 (1993).
- Reversade, B., Kuroda, H., Lee, H., Mays, A. & De Robertis, E. M. Depletion of Bmp2, Bmp4, Bmp7 and Spemann organizer signals induces massive brain formation in *Xenopus* embryos. *Development* **132**, 3381–3392 (2005).
- Di Giorgio, F. P., Carrasco, M. A., Siao, M. C., Maniatis, T. & Eggan, K. Non-cell autonomous effect of glia on motor neurons in an embryonic stem cell-based ALS model. *Nature Neurosci.* **10**, 608–614 (2007).
- Kawasaki, H. *et al.* Induction of midbrain dopaminergic neurons from ES cells by stromal cell-derived inducing activity. *Neuron* **28**, 31–40 (2000).
- Watanabe, K. *et al.* Directed differentiation of telencephalic precursors from embryonic stem cells. *Nature Neurosci.* **8**, 288–296 (2005).
- Smukler, S. R., Runciman, S. B., Xu, S. & van der Kooy, D. Embryonic stem cells assume a primitive neural stem cell fate in the absence of extrinsic influences. *J. Cell Biol.* **172**, 79–90 (2006).
- Wichterle, H., Lieberam, I., Porter, J. A. & Jessell, T. M. Directed differentiation of embryonic stem cells into motor neurons. *Cell* **110**, 385–397 (2002).
- Abranches, E. *et al.* Neural differentiation of embryonic stem cells *in vitro*: a road map to neurogenesis in the embryo. *PLoS ONE* **4**, e6286 (2009).
- Eiraku, M. *et al.* Self-organized formation of polarized cortical tissues from ESCs and its active manipulation by extrinsic signals. *Cell Stem Cell* **3**, 519–532 (2008).

13. Aubert, J. *et al.* Screening for mammalian neural genes via fluorescence-activated cell sorter purification of neural precursors from *Sox1-GFP* knock-in mice. *Proc. Natl Acad. Sci. USA* **100**, 11836–11841 (2003).
14. Jakt, L. M., Okada, M. & Nishikawa, S.-I. An open source client-server system for the analysis of Affymetrix microarray data. *Genome Informat.* **14**, 276–277 (2003).
15. Warming, S. *et al.* Evi3, a common retroviral integration site in murine B-cell lymphoma, encodes an EBFA-related Krüppel-like zinc finger protein. *Blood* **101**, 1934–1940 (2003).
16. Bond, H. M. *et al.* Early hematopoietic zinc finger protein-zinc finger protein 521: a candidate regulator of diverse immature cells. *Int. J. Biochem. Cell Biol.* **40**, 848–854 (2008).
17. von Bubnoff, A. *et al.* Phylogenetic footprinting and genome scanning identify vertebrate BMP response elements and new target genes. *Dev. Biol.* **281**, 210–226 (2005).
18. Benchabane, H. & Wrana, J. L. GATA- and Smad1-dependent enhancers in the *Smad7* gene differentially interpret bone morphogenetic protein concentrations. *Mol. Cell. Biol.* **23**, 6646–6661 (2003).
19. Gajović, S., St-Onge, L., Yokota, Y. & Gruss, P. Retinoic acid mediates Pax6 expression during *in vitro* differentiation of embryonic stem cells. *Differentiation* **62**, 187–192 (1997).
20. Takada, S. *et al.* Wnt-3a regulates somite and tailbud formation in the mouse embryo. *Genes Dev.* **8**, 174–189 (1994).
21. Kunath, T. *et al.* FGF stimulation of the Erk1/2 signalling cascade triggers transition of pluripotent embryonic stem cells from self-renewal to lineage commitment. *Development* **134**, 2895–2902 (2007).
22. Tesar, P. J. *et al.* New cell lines from mouse epiblast share defining features with human embryonic stem cells. *Nature* **448**, 196–199 (2007).
23. Ding, J. *et al.* Cripto is required for correct orientation of the anterior-posterior axis in the mouse embryo. *Nature* **395**, 702–707 (1998).
24. Lin, A. C., Roche, A. E., Wilk, J. & Svensson, E. C. The N termini of Friend of GATA (FOG) proteins define a novel transcriptional repression motif and a superfamily of transcriptional repressors. *J. Biol. Chem.* **279**, 55017–55023 (2004).
25. Wu, M. *et al.* Zfp521 antagonizes Runx2, delays osteoblast differentiation *in vitro*, and promotes bone formation *in vivo*. *Bone* **44**, 528–536 (2009).
26. Chan, H. M. & La Thangue, N. B. p300/CBP proteins: HATs for transcriptional bridges and scaffolds. *J. Cell Sci.* **114**, 2363–2373 (2001).
27. Visel, A. *et al.* ChIP-seq accurately predicts tissue-specific activity of enhancers. *Nature* **457**, 854–858 (2009).
28. Brunelli, S., Silva Casey, E., Bell, D., Harland, R. & Lovell-Badge, R. Expression of Sox3 throughout the developing central nervous system is dependent on the combined action of discrete, evolutionarily conserved regulatory elements. *Genesis* **36**, 12–24 (2003).
29. de Ruijter, A. J., van Gennip, A. H., Caron, H. N., Kemp, S. & van Kuilenburg, A. B. Histone deacetylases (HDACs): characterization of the classical HDAC family. *Biochem. J.* **370**, 737–749 (2003).
30. Tsai, R. Y. & Reed, R. R. Identification of DNA recognition sequences and protein interaction domains of the multiple-Zn-finger protein Roaz. *Mol. Cell. Biol.* **18**, 6447–6456 (1998).
31. Zhao, S., Nichols, J., Smith, A. G. & Li, M. SoxB transcription factors specify neuroectodermal lineage choice in ES cells. *Mol. Cell. Neurosci.* **27**, 332–342 (2004).
32. Kuhlbrodt, K. *et al.* Cooperative function of POU proteins and SOX proteins in glial cells. *J. Biol. Chem.* **273**, 16050–16057 (1998).
33. Tanaka, S. *et al.* Interplay of SOX and POU factors in regulation of the Nestin gene in neural primordial cells. *Mol. Cell. Biol.* **24**, 8834–8846 (2004).
34. Zwart, R., Broos, L., Grosveld, G. & Meijer, D. The restricted expression pattern of the POU factor Oct-6 during early development of the mouse nervous system. *Mech. Dev.* **54**, 185–194 (1996).
35. Jørgensen, H. F. *et al.* REST selectively represses a subset of RE1-containing neuronal genes in mouse embryonic stem cells. *Development* **136**, 715–721 (2009).

Supplementary Information is linked to the online version of the paper at www.nature.com/nature.

Acknowledgements We are grateful to H. Niwa for comments; M. Okada for advice on the GeneChip study; Y. Toyooka-Kamiya for constant encouragement and technical advice; H. Akimaru for advice on the shRNA knockdown study; and members of the Sasai laboratory for discussion and advice. This work was supported by grants-in-aid from MEXT, the Kobe Cluster Project and the Leading Project (Y.S.).

Author Contributions Y.S. designed the research and D.K. performed the majority of mES cell experiments with technical help from S.B., M.K. and R.Y. N.S., M.O., H.I. and K.W. collaborated with D.K. in the ChIP, hES cell, *Xenopus* and SFEB experiments. H.K. and K.N. performed the blastocyst injections and L.M.J. and S.-i.N. helped GeneChip screening.

Author Information Microarray data have been deposited in GEO under accession number GSE25593. Reprints and permissions information is available at www.nature.com/reprints. The authors declare no competing financial interests. Readers are welcome to comment on the online version of this article at www.nature.com/nature. Correspondence and requests for materials should be addressed to Y.S. (yoshikisasai@cdb.riken.jp).

METHODS

Mouse ES cell culture and differentiation. Mouse ES cells (EB5) and *Sox1-GFP* ES cells (46C; a gift from A. Smith) were maintained as described⁸. The differentiation medium was G-MEM supplemented with 10% Knockout Serum Replacement (KSR; Invitrogen), 2 mM glutamine, 1 mM pyruvate, 0.1 mM non-essential amino acids, and 0.1 mM 2-ME with or without 10% fetal calf serum (FCS; JRH). For the SFEBq culture, ES cells were dissociated to single cells in 0.25% trypsin-EDTA (Invitrogen) and quickly re-aggregated in the differentiation medium (5,000 cells per 150 µl per well) using low-cell-adhesion 96-well plates (Sumilon Spheroid Plates, Sumitomo Bakelite). For mesendodermal differentiation, ES cells were seeded onto 90-mm MPC-coated dishes (Nalge Nunc) and cultured in differentiation medium with 15% FCS and 50 ng ml⁻¹ Wnt3a (R&D) for 3 or 6 days. For epidermal differentiation, ES cells were cultured under adhesion conditions in differentiation medium for 14 days, during which 0.5 nM BMP4 and 10% FCS were added on days 3 and 8, respectively.

Neural differentiation and knockdown study with human ES cells. Human ES cells (KhES-1) cells were maintained as described³⁶. Differentiation medium was G-MEM supplemented with 20% KSR, 2 mM glutamine, 1 mM pyruvate, 0.1 mM nonessential amino acids, 10 µM SB431542 (Sigma), and 10 µM Y27632 (Tocris). For SFEB culture, ES cells were dissociated to single cells with TrypLE Select (Invitrogen) and quickly re-aggregated in the differentiation medium (9,000 cells per 150 µl per well) using low-cell-adhesion 96-well plates. For the knockdown study, human ES cells were co-transfected with the pSIREN-RetroQ (Clontech) and the pCAG-venus vectors using the FuGENE HD reagent (Roche). Cells were cultured with SFEB for 3 days. Venus⁺ transfected cells were sorted by FACS. The target sequences were GACTACACAAATCAGCGATTT (control: shRNA *lacZ*), GCGCATCTTGCCCTCAAAGAAT (*hZfp521* shRNA 1) and GCACGTCCC ACTGGAGAATAT (*hZfp521* shRNA 2).

Whole-mount *in situ* hybridization. Embryos were dissected at the indicate stages, fixed for overnight at 4 °C in 4% paraformaldehyde/PBS, dehydrated through a series of increasing methanol concentrations, and stored at -20 °C. Whole-mount *in situ* hybridization was performed as described³⁷. The specimens were then subjected to frozen sections (20 µm). The *Zfp521* probe (3' UTR of *Zfp521* mRNA) was prepared by *in vitro* transcription using T7 polymerase (Stratagene).

Immunohistochemistry. Immunohistochemistry was performed as described previously⁸ with the primary antibodies described below. For statistical analysis, 100–200 cells were examined for each experiment, which was repeated four times. Antibodies against the following proteins were used at the indicated dilutions: N-cadherin (mouse/1:1,000/BD Pharmingen), Sox1 (rabbit/1:200/custom-made), GFP (rat/1:200/Nakalai-Tesque), Cripto (rat/1:1000/R&D), Oct3 (mouse/1:200/BD Pharmingen), SMA (mouse/1:50/ Dako), E-cadherin (rat/1:200/Takara), HNF3-β (goat/1:150/R&D), keratin 14 (mouse/1:20/Biomedica) and *Zfp521* (guinea-pig/1:1,000/custom made).

FACS analysis and sorting. Cells were counted with a FACSAria (BD) and the data were analysed with the FACSDiva software (BD). The cells were dissociated to single cells by 0.25% trypsin-EDTA treatment and analysed at 4 °C. For isolation, *Sox1-GFP* cells were stained with the anti-E-cadherin antibody (ECCD2-APC) for 45 min at 37 °C before sorting. The quality of sorting was confirmed by re-analysing the sorted cells by FACS.

DNA microarray analysis. DNA microarray analysis was performed as reported¹⁴. Briefly, the total RNA was extracted using RNeasy (Invitrogen) from ES cells, and from the Sox1-GFP⁺/E-cadherin⁻ and Sox1-GFP⁺/E-cadherin⁻ populations on days 3 and 5 of SFEB culture. Double-stranded cDNA was synthesized using the Superscript Choice System (Invitrogen). Biotin-labelled cRNA

was synthesized using the BioArray RNA Transcript Labelling Kit (Affymetrix). The biotin-labelled cRNA was fragmented and subjected to hybridization with the murine genome U74 version 2 GeneChip array series (Affymetrix) according to the manufacturer's instructions. The expression data were analysed using an in-house-developed program (eXintegrator, <http://www.cdb.riken.jp/scb/documentation/index.html>).

Functional screening. The cDNAs of the candidate genes were amplified by PCR and subcloned into the pCAG-IRES-Puro expression vector, a gift of H. Niwa. *Sox1-GFP* ES cells were transfected with the expression vectors using Lipofectamine 2000 (Invitrogen), seeded onto 0.1% gelatin-coated 8-well culture slides that were coated with poly-D-lysine (BD) and cultured in GMEM containing 10% KSR and 10% FCS for 5 days. The cells were fixed with 4% PFA and subjected to immunohistochemistry using the anti-N-cadherin and anti-GFP antibodies.

Knockdown study with shRNA. The shRNA target sequence for *Zfp521* knockdown was designed using the software at the siRNA Target Designer (<http://www.promega.com/siRNA Designer/program/>). The *Zfp521*-shRNA target sequence was GCACGUGACCAUCCACUUUAAU (2043–2063bp) and the control shRNA had a scrambled sequence (control shRNA: GAUCAUCCCGACUCGUUUAA). The retroviral vector pQCXIX-U6-BamHI-EcoRI-HindIII-puro, which was based on the pQCXIX retroviral vector (Clontech), was used to express shRNA. The oligonucleotides encoding the short hairpins were inserted into the BamHI/HindIII site. The plasmids were co-transfected with the pGAG/Pol and pVSVG helper plasmids into HEK293T cells and the culture supernatant containing the produced virus was applied to *Sox1-GFP* ES cells. Colonies were picked after drug selection with 2 µg ml⁻¹ puromycin for 10 days.

Quantitative PCR. Quantitative PCR was performed using the 7500 Fast Real Time PCR System (Applied Biosystems) according to the manufacturer's instruction and the data were normalized for *GAPDH* expression. The primers used for qPCR are listed in Supplementary Table 2.

Immunoprecipitation and ChIP assay. Immunoprecipitation assays were performed with Protein-G Sepharose (GE Healthcare) and the proteins were subsequently analysed by western blot using the anti-Flag, anti-HA (Sigma), and anti-p300 (Cell Signaling Technology) antibodies. The ChIP assays were performed using the anti-Flag and anti-p300 antibodies. The primers used for the qPCR in the ChIP assay are listed in Supplementary Table 2.

Luciferase reporter assay. The luciferase reporter assay was performed using the Dual-Luciferase Reporter Assay System (Promega). The BRE-luciferase¹⁷ and Sox3-promoter luciferase vector³⁸ and/or *Zfp521* expression vector (pCAG-IRES-Puro-Zfp521) was co-transfected with the *Renilla* luciferase plasmid into HEK293T cells. Twenty-four hours later, the cells were lysed in Passive Lysis Buffer (PLB) and analysed by a Lumat LB 9507 (Berthold Technologies) according to the manufacturer's instruction.

Embryonic manipulation and microinjection in *Xenopus*. Eight-cell embryos were injected with synthetic mRNAs using a fine glass capillary and a pneumatic pressure injector (Narishige). Excised animal caps were cultured in 1× LCMR supplemented with 0.2% BSA until given stages. Whole-mount *in situ* hybridization analysis was performed with DIG-labelled antisense RNA probes.

36. Watanabe, K. *et al.* A ROCK inhibitor permits survival of dissociated human embryonic stem cells. *Nature Biotechnol.* **25**, 681–686 (2007).
37. Nagy, A., Gertsenstein, M. G., Vintersten, K. & Behringer, R. Manipulating the Mouse Embryo (Cold Spring Harbor Press, 2003).
38. Ikeya, M. *et al.* Gene disruption/knock-in analysis of mONT3: vector construction by employing both *in vivo* and *in vitro* recombinations. *Int. J. Dev. Biol.* **49**, 807–823 (2005).

Crystal structure of a potassium ion transporter, TrkH

Yu Cao^{1*}, Xiangshu Jin^{2*}, Hua Huang^{1*}, Mehabaw Getahun Derebe³, Elena J. Levin¹, Venkataraman Kabaleeswaran¹, Yaping Pan¹, Marco Punta^{4,5}, James Love⁴, Jun Weng¹, Matthias Quick^{6,7}, Sheng Ye³, Brian Kloss⁴, Renato Bruni⁴, Erik Martinez-Hackert⁸, Wayne A. Hendrickson⁸, Burkhard Rost^{4,5}, Jonathan A. Javitch^{6,7,9}, Kanagalaghatta R. Rajashankar¹⁰, Youxing Jiang³ & Ming Zhou¹

The TrkH/TrkG/KtrB proteins mediate K⁺ uptake in bacteria and probably evolved from simple K⁺ channels by multiple gene duplications or fusions. Here we present the crystal structure of a TrkH from *Vibrio parahaemolyticus*. TrkH is a homodimer, and each protomer contains an ion permeation pathway. A selectivity filter, similar in architecture to those of K⁺ channels but significantly shorter, is lined by backbone and side-chain oxygen atoms. Functional studies showed that TrkH is selective for permeation of K⁺ and Rb⁺ over smaller ions such as Na⁺ or Li⁺. Immediately intracellular to the selectivity filter are an intramembrane loop and an arginine residue, both highly conserved, which constrict the permeation pathway. Substituting the arginine with an alanine significantly increases the rate of K⁺ flux. These results reveal the molecular basis of K⁺ selectivity and suggest a novel gating mechanism for this large and important family of membrane transport proteins.

K⁺ is highly concentrated in all living cells and plays diverse physiological roles such as setting membrane potential¹, regulating turgor pressure² and maintaining intracellular pH^{3–5}. Because K⁺ is virtually impermeable to the cell membrane, specialized K⁺ transporters have evolved to mediate its uptake. In animal cells, K⁺ uptake is mainly achieved by the Na⁺/K⁺-ATPase⁶, whereas in non-animal cells, the task is shared by at least two different systems, one of which, the superfamily of K⁺ transporters (SKT proteins)⁷, is the focus of this research.

An SKT protein has four tandem domains with low homology to each other, each resembling a single protomer from a simple K⁺ channel with a predicted M1–P–M2 transmembrane topology^{8–10}. M1 and M2 are transmembrane helices that are connected by P, the re-entrant pore loop, which is composed of a half-membrane-spanning helix followed by an extended loop¹¹. In K⁺ channels, the half-membrane-spanning helix is called the pore helix, and the extended loop harbours the highly conserved signature sequence TVGYG, which forms the selectivity filter responsible for the coordination of K⁺. In SKT proteins, the equivalent sequences in the P-loops are less strictly conserved. It has been proposed that SKT proteins have a structure that resembles K⁺ channels^{9,10,12}. Results from functional studies have been consistent with this view: mutating a conserved glycine residue in the P-loops changes ion selectivity of SKT proteins in bacteria^{7,13} and plants¹⁴; whereas epitope tagging of a yeast SKT protein showed that its transmembrane topology is consistent with four M1–P–M2 repeats¹⁵.

Studies have shown that the selectivity of K⁺ channels is highly sensitive to changes to the structure of the selectivity filter. Introducing point mutations to the signature sequence of K⁺ channels compromises K⁺

selectivity¹⁶; and the NaK channel, which has a slightly modified signature sequence of TVGDG resulting in an altered selectivity filter conformation, is essentially non-selective between K⁺ and Na⁺ (ref. 17). How, then, can the selectivity of the SKT proteins be maintained, given that their signature sequences are so highly degraded (Supplementary Fig. 1)? Furthermore, if SKT proteins have the architecture of a K⁺ channel pore, how is transport of K⁺ controlled? To address these questions we targeted the bacterial TrkG/TrkH/KtrB proteins, the largest sub-family of SKT proteins, for structural and functional studies. The importance of these proteins in bacteria has been shown in *Escherichia coli*, which does not grow in less than 5 mM K⁺ when its *trkG* and *trkH* genes are deleted¹⁸, and in *Francisella tularensis*, which loses its ability to cause tularaemia when lacking TrkH¹⁹. We crystallized and solved the structure of a TrkH from *V. parahaemolyticus* (hereafter VpTrkH).

Function of VpTrkH

VpTrkH was expressed and purified to homogeneity. The purified VpTrkH eluted as a single symmetrical peak on a size-exclusion column (Supplementary Fig. 2a), and by combining the size-exclusion chromatography with light scattering and refractive index measurements, the molecular mass of the purified protein was estimated to be approximately 100 kDa. Because the molecular mass of each VpTrkH protomer is approximately 54 kDa, the detergent-solubilized VpTrkH is a homodimer. The homodimeric quaternary assembly was further verified by running the protein on an SDS–polyacrylamide gel electrophoresis (SDS–PAGE) gel after incubation with covalent cross-linkers, which produced a band roughly twice the molecular mass (Supplementary Fig. 2b). Dimeric assembly has also been reported

¹Department of Physiology & Cellular Biophysics, College of Physicians and Surgeons, Columbia University, 630 West 168th Street, New York, New York 10032, USA. ²Center for Computational Biology and Bioinformatics, Department of Biochemistry and Molecular Biophysics, Howard Hughes Medical Institute, Columbia University, 1130 St Nicholas Avenue, Room 815, New York, New York 10032, USA.

³Department of Physiology and Howard Hughes Medical Institute, University of Texas Southwestern Medical Center, Dallas, Texas 75390, USA. ⁴New York Consortium on Membrane Protein Structure, New York Structural Biology Center, 89 Convent Avenue, New York, New York 10027, USA. ⁵Department of Computer Science and Institute for Advanced Study, Technical University of Munich, D-85748 Munich, Germany. ⁶Center for Molecular Recognition and Department of Psychiatry, Columbia University, 630 West 168th Street, New York, New York 10032, USA. ⁷New York State Psychiatric Institute, Division of Molecular Therapeutics, 1051 Riverside Drive, New York, New York 10032, USA. ⁸Department of Biochemistry and Molecular Biophysics, Howard Hughes Medical Institute, Columbia University, 630 West 168th Street, New York, New York 10032, USA. ⁹Department of Pharmacology, Columbia University, 630 West 168th Street, New York, New York 10032, USA. ¹⁰Department of Chemistry and Chemical Biology, Cornell University, NE-CAT, Advanced Photon Source, Argonne, Illinois 60439, USA.

*These authors contributed equally to this work.

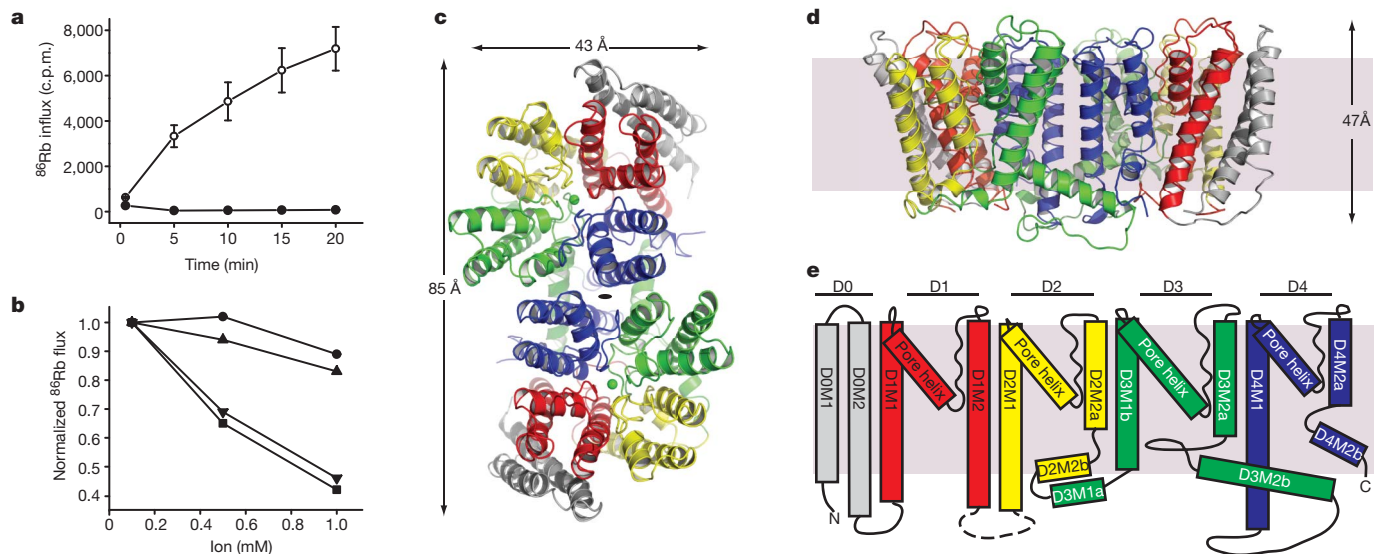


Figure 1 | Function and structure of VpTrkH. **a**, Time-dependent ^{86}Rb influx into liposomes reconstituted with VpTrkH (open circle) or empty vesicles (filled circle). **b**, ^{86}Rb influx at 20 min in the presence of three concentrations of K^+ (square), Rb^+ (inverted triangle), Na^+ (circle) and Li^+ (triangle). **c**, The VpTrkH dimer coloured by domain and viewed from the extracellular side. The twofold symmetry axis is marked as a black oval. The green spheres are K^+ atoms. **d**, VpTrkH viewed from within the membrane

with the extracellular side on top. The dimer is rotated by 90° about the x and y axes relative to **c**. Grey rectangle representing the membrane is shown with a thickness of 30 Å. **e**, VpTrkH topology shown with the extracellular side on top. The five domains are coloured according to the same scheme as in the previous panels. The grey rectangle indicates the thickness of the cell membrane, and the unresolved loop is shown as a dashed line.

for the KtrB protein from *Bacillus subtilis*^{20,21}, a protein closely related to VpTrkH.

Because VpTrkH had not been functionally characterized, we proceeded to measure its function in two experiments. First, the *VptrkH* gene was introduced into an *E. coli* strain, LB650 (ref. 18), that lacks both the *trkG* and *trkH* genes. LB650 cells have a slow growth phenotype in media with less than 5 mM K^+ , and expression of VpTrkH rescued the growth of these cells (Supplementary Fig. 2c), suggesting that VpTrkH mediates K^+ uptake. Second, purified and detergent-solubilized VpTrkH protein was reconstituted into liposomes, and K^+ permeation was measured indirectly by monitoring uptake of radioactive $^{86}\text{Rb}^+$ (refs 17, 22). In this experiment, the proteoliposomes contain a high internal concentration of K^+ and are diluted into an external solution with a low concentration of K^+ and a trace amount of radioactive $^{86}\text{Rb}^+$. Efflux of K^+ down its chemical gradient via VpTrkH creates an electrical potential across the bilayer that drives uptake of $^{86}\text{Rb}^+$, an ion that is known to permeate K^+ channels. Uptake of $^{86}\text{Rb}^+$ was observed only in vesicles reconstituted with VpTrkH (Fig. 1a), indicating that VpTrkH is permeable to both K^+ and Rb^+ . Further experiments showed that $^{86}\text{Rb}^+$ uptake is inhibited by external K^+ or Rb^+ but relatively unaffected by the presence of Na^+ or Li^+ in the external solution (Fig. 1b). These results indicate that, despite the weak conservation of its signature sequence, VpTrkH exhibits selectivity for K^+ and Rb^+ over Na^+ and Li^+ . In addition, they also suggest that VpTrkH is capable of mediating facilitated diffusion of K^+ driven by an electrochemical gradient.

Overall structure

Crystals of both native and selenomethionine-substituted VpTrkH were grown under oil by the microbatch method, and the best native protein crystals diffracted to 3.5 Å and belonged to the space group $P2_12_1$ (Supplementary Table 1). Initial phases were obtained by single-wavelength anomalous diffraction²³ using a selenomethionine substituted VpTrkH crystal. The building and refinement of the structural model were facilitated by the presence of a twofold non-crystallographic symmetry (NCS) axis and the positions of the selenium atoms. The final refined model contains residues 1–157, 174–484 and one K^+ per subunit. The region encompassing residues

158–173, which is a loop between two transmembrane helices, is disordered.

Each asymmetric unit contains a dimer of VpTrkH protomers related by a twofold symmetry axis perpendicular to the plane of the membrane. Their amino (N) and carboxy (C) termini both probably reside on the cytoplasmic side as inferred from the experimentally determined topology of a highly homologous TrkH protein from *E. coli*²⁴. Two views of the dimer are shown in Fig. 1c, d. Viewed along the twofold axis from the extracellular side, the dimer has a parallelogram shape with sides of approximately 85 and 43 Å. Along the twofold axis, VpTrkH is approximately 47 Å thick. Stereo views of the VpTrkH dimer in three orientations are shown in Supplementary Fig. 3a–c.

Each VpTrkH protomer is composed of five domains, defined sequentially from the N terminus to the C terminus as D0 to D4 (Fig. 1e and Supplementary Figs 1 and 3b, d). D0, which is found only in the TrkH/TrkG subfamily of SKT proteins, has two transmembrane segments. D1 to D4 each have a K^+ -channel-like M1–P–M2 topology, although the M2 helices of D2 to D4 are composed of two shorter ones (Fig. 2a). The secondary structure of each P-loop also resembles that of a K^+ channel, composed of a half membrane-spanning helix, the pore helix, followed by an extended loop that forms the selectivity filter. D1 to D4 assemble around a pseudo-fourfold symmetry axis to form an ion permeation pathway; when observed from the extracellular side along the pseudo-fourfold axis, they are arranged in an anticlockwise direction (Supplementary Fig. 3b). An extensive dimer interface is composed of helices from D3 and D4, with a buried surface of 2,225 Å² per protomer. There is a hydrophobic cavity in the middle of the interface, but it is sealed off from the aqueous medium by two layers of hydrophobic residues on both sides of the membrane (Supplementary Fig. 4). The ion permeation pathway, which is contained within each protomer, has an hourglass shape and two salient features: a selectivity filter and an intramembrane loop (Fig. 2b).

Selectivity filter

The selectivity filter is surrounded by the four pore helices, which are arranged with the negative ends of their helix-dipole moments pointing to the middle of the membrane (Supplementary Fig. 5). A similar arrangement of pore helices is present in K^+ channels, and its role in

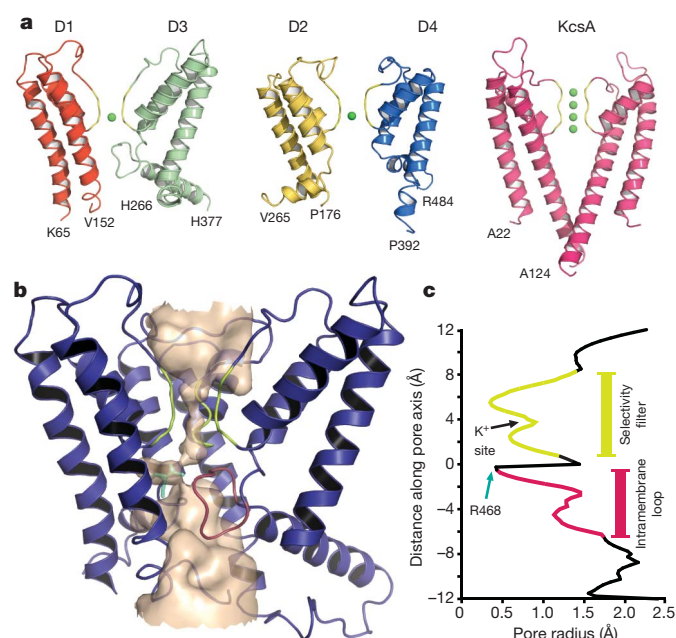


Figure 2 | The VpTrkH pore. **a**, Views of a VpTrkH protomer showing only the D1 and D3 domains (left) or the D2 and D4 domains (middle). Two domains of KcsA are shown on the right for comparison. K^+ atoms are shown as green spheres, and the N- and C-terminal residues are labelled. **b**, Surface representation of the pore of a TrkH subunit obtained with the program Hollow⁴³ using a 1.4-Å probe radius for the vestibules and a 0.75-Å probe radius for the constricted region. The protein is shown with domain 2 removed for clarity and the selectivity filter (yellow), the intramembrane loop (magenta) and residue R468 (teal) highlighted. **c**, Radius of the pore calculated with the program HOLE.

minimizing the free energy of a permeating cation has been discussed for the KcsA K^+ channel^{11,25}.

The four selectivity filter signature sequences are located on the P-loops (Fig. 3a), and these elements come together to form the selectivity filter (omit map in Fig. 3b and Supplementary Fig. 6a, $2F_o - F_c$ map in Supplementary Fig. 6b). Compared with those of K^+ channels, the selectivity filter has a wider opening on the extracellular side and a

much shorter constricted region where K^+ is coordinated (Fig. 3c, d and Supplementary Figs 6c and 7). In the constricted region, main-chain and side-chain oxygen atoms form stacks of oxygen rings that could coordinate and stabilize dehydrated K^+ , a feature that is preserved from the K^+ channels. In an $F_o - F_c$ map calculated with K^+ omitted, two peaks of positive electron density appear in the filter (Fig. 3d and Supplementary Fig. 7a), which we call the upper and lower site and interpret as potential positions where K^+ binds. Owing to the modest resolution of the diffraction data, we cannot unambiguously determine the contribution of K^+ to these densities, as opposed to partial contribution from water molecules or calcium ions that were included in the crystallization solution. Because Rb^+ and Ba^{2+} are known to occupy K^+ positions in the selectivity filter of the KcsA K^+ channel^{11,26}, we took advantage of this knowledge and grew crystals in the presence of Rb^+ or Ba^{2+} (Supplementary Table 1). Difference electron densities corresponding to Fourier coefficients $F_{Rb} - F_K$ or $F_{Ba} - F_K$ are shown in Fig. 3e. In both cases, a strong positive electron density peak is present in the upper site, consistent with substitution of a K^+ with a more electron dense Rb^+ or Ba^{2+} . The upper site lines up with site 3 (S3) in the KcsA K^+ channel, and is constructed entirely by backbone carbonyl oxygen atoms (Fig. 3c and Supplementary Fig. 6c). In the KcsA K^+ channels, Rb^+ does not occupy every K^+ binding site in the selectivity filter, and Rb^+ permeates with a much slower rate than K^+ (refs 27, 28). A slower rate of Rb^+ uptake was also observed by TrkH in *E. coli*²⁹. Therefore, we postulate that the lower peak in the K^+ difference map, which aligns with S4 in KcsA, could potentially be a K^+ binding site (Fig. 3d and Supplementary Fig. 7), although there was no density at this location in either the Rb^+ or Ba^{2+} difference maps.

Although only one binding site has been confirmed by heavy atoms and modelled into the structure, the limited resolution of the data probably reduced our ability to observe more. Comparison with the KcsA structure suggests that the selectivity filter could potentially accommodate a maximum of three K^+ binding sites without requiring a substantial structural change. In addition to the confirmed site and the possible site corresponding to S4 in KcsA, the backbone carbonyls from the highly conserved glycine residues form a ring of oxygen atoms above the confirmed ion-binding site, and could potentially form another K^+ binding site that would line up with S2 in KcsA (Fig. 3d and Supplementary Fig. 7). The S1 site is lost because of the widening of the selectivity filter in TrkH. This is not wholly unexpected owing to

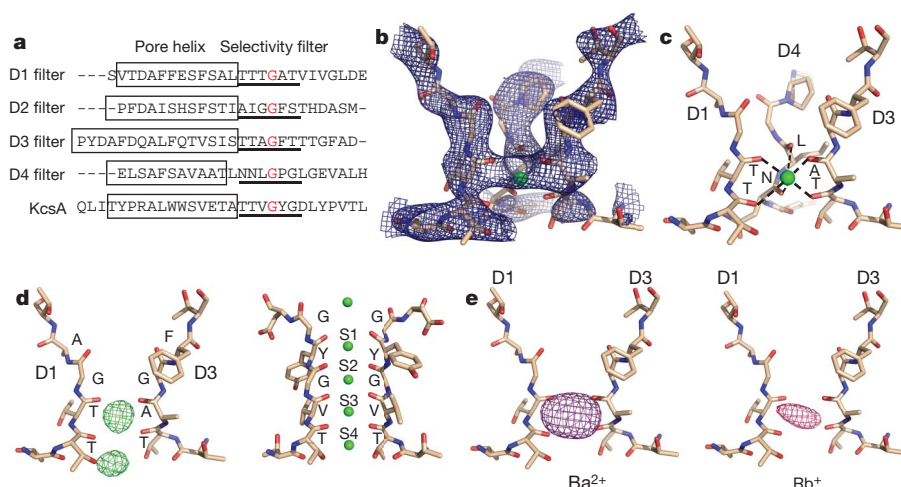


Figure 3 | Selectivity filter of VpTrkH. **a**, Amino-acid sequence alignment of the selectivity filter regions (underlined) and pore helices (box) in VpTrkH with the selectivity filter of the KcsA K^+ channel. The highly conserved glycine residue is marked in red. **b**, **c**, The selectivity filter with domain 2 removed, shown with **b** an NCS-averaged, simulated annealing omit map calculated with six residues from each selectivity filter omitted, contoured at 1σ , or **c** the coordination geometry of the K^+ (green sphere) highlighted. **d**, D1 and D3

from the K^+ structure are shown with $F_o - F_c$ electron density calculated without K^+ in the model and contoured at 3.5σ . The filter of KcsA is shown on the right for comparison. **e**, Ion-binding sites in the selectivity filter. Ba^{2+} (left) and Rb^+ (right) ($F_{o(ion)} - F_{o(K)}$) difference Fourier maps are shown contoured at 6.0 and 3.5σ levels, respectively, calculated using phases from the K^+ structure. The stick models are D1 and D3 from the K^+ structure.

the differences in the selectivity filter sequence between TrkH and KcsA: the second glycine residue in the signature sequence of K^+ channels is not conserved in TrkH (Fig. 3a), and in the high-resolution KcsA structure³⁰ the backbone torsion angles of this residue lie in an unfavourable region of the Ramachandran plot for non-glycine residues. Regardless of the number of sites, the structure shows that at least one dehydrated K^+ binds to VpTrkH through coordination by oxygen atoms in a manner similar to a K^+ channel. Further experiments are needed to measure more accurately the occupancy of K^+ and whether VpTrkH exhibits the high selectivity characteristic of K^+ channels. In addition, because the four-site configuration is crucial for a high K^+ throughput in K^+ channels^{27,31}, we conjecture that VpTrkH, if it operates by a channel-like mechanism, conducts K^+ with a lower throughput.

The ion permeation pathway

Although each protomer forms a continuous pore, a K^+ permeating from the extracellular side encounters a barrier shortly after it exits the selectivity filter (Fig. 2c). The barrier is composed of two elements: Arg 468 from the second transmembrane segment of domain 4 (D4M2), and an intramembrane circular loop between D3M2a and D3M2b (Figs 2b and 4a). This is a unique feature and is not observed in any known K^+ channel structures.

Arg 468 is conserved in almost all bacterial SKT proteins. The guanidinium group points towards the centre of the permeation pathway and is approximately 3.1 Å away from the backbone carbonyl oxygen atom of Gly 353, which is part of the intramembrane loop formed by Gly 346 to Lys 357 (Fig. 4a). This loop is present in all TrkH, TrkG and KtrB families, is rich in glycine and other small residues such as alanine and serine, and contains several highly conserved residues (Supplementary Figs 1 and 8). In addition, Glu 470,

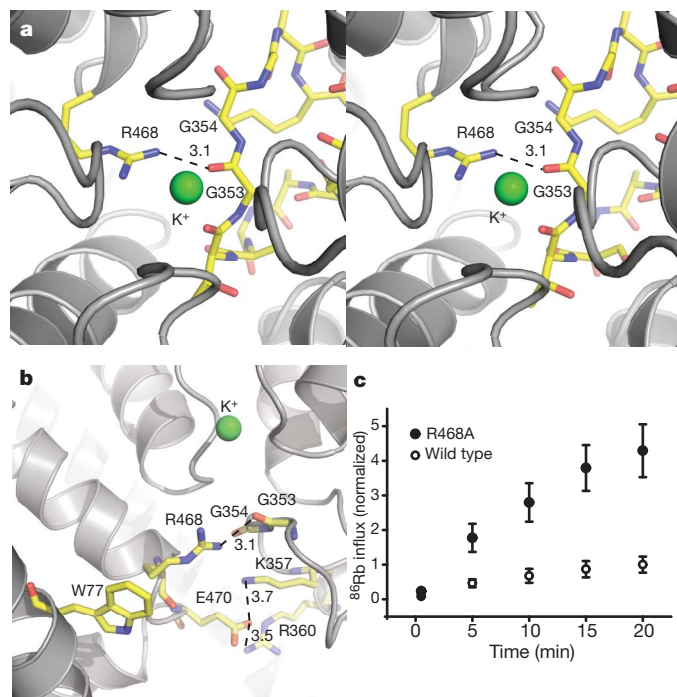


Figure 4 | Constriction formed by Arg 468 and the intramembrane loop. **a**, Stereo view of the interactions between the intramembrane loop and Arg 468 as viewed looking down the selectivity filter from the extracellular side. **b**, Interactions between the intramembrane loop and Arg 468 and Glu 470 as viewed from within the plane of the membrane. Residues Gly 353–354, Lys 357, Arg 360, Arg 468 and Glu 470 are shown as stick representations, and the dashed lines indicate distances between them. **c**, Time-dependent ^{86}Rb influx into proteoliposomes reconstituted with wild-type (open circle) or R468A (filled circle) VpTrkH. Error bars, s.e.m.

another highly conserved residue on D4M2, is close to Lys 357 in the loop and Arg 360 in D3M2b: a carboxylate oxygen on Glu 470 is 3.7 and 3.5 Å away from the terminal nitrogens of Lys 357 and Arg 360, respectively. These electrostatic interactions probably further stabilize the position of the intramembrane loop (Fig. 4b and Supplementary Fig. 9).

The narrow constriction formed by Arg 468 and the intramembrane loop has to widen for a K^+ to reach the intracellular side. To understand further the role of Arg 468 in K^+ permeation, we substituted it with an alanine and reconstituted the R468A mutant protein into liposomes. $^{86}\text{Rb}^+$ flux was then measured both for the wild type and for the R468A mutant in side-by-side experiments. Tracer uptake by the R468A mutant is significantly faster than that by the wild type (Fig. 4c), consistent with the observation that R468 occludes K^+ permeation. An earlier study showed that mutating the equivalent of Arg 468 in a KtrB reduces K^+ uptake in *E. coli*³², which seems to contradict our functional results and the role of Arg 468 inferred from the structure. However, because the KtrB mutant was assayed *in vivo*, additional factors such as expression levels or association with auxiliary proteins could have affected the measurement. As for the role of the intramembrane loop, a recent study showed that various deletions of the corresponding loop in a KtrB significantly increase K^+ transport activity³³, consistent with its position shown by the structure.

Discussion

The pseudo-symmetry arising from duplication of an ancestral channel that is observed in the SKT family is not unique among ion channel/transporter families. In the animal kingdom, gene fusion or duplication of a more complex potassium channel, the voltage-dependent K^+ channel (K_v), generated voltage-dependent Na^+ and Ca^{2+} channels (Na_v and Ca_v , respectively)^{34,35}. Similar to the SKT proteins, four pseudo-subunits of K_v channels are expressed as a single polypeptide chain in the Na_v and Ca_v channels, although the domains are assembled in a clockwise direction when viewed from the extracellular side^{36,37} in contrast to the anticlockwise orientation observed in VpTrkH. The pseudo-fourfold symmetry in VpTrkH is strongest at the ion-binding sites in the selectivity filter region, where each domain contributes similarly to coordination of a K^+ . However, the symmetry starts to break down outside the selectivity filter where the pore helices vary in length and form different angles with the membrane normal, and the symmetry becomes considerably weaker for the M1 and M2 helices from different homologous domains. Especially notable is D3, which contains the intramembrane loop and the tilted D3M2b helix, and therefore is expected to contribute to gating of the permeation pathway more than the other domains. It is probable that in Na_v and Ca_v channels, the fourfold symmetry is maintained at the selectivity region for coordination of permeating ions but gradually breaks down so that the voltage-sensing modules and the connected gating machinery of a particular pseudo-subunit may contribute more than the others.

TrkH/TrkG and KtrB assemble with the cytosolic adenine nucleotide-binding proteins TrkA^{38,39} and KtrA⁴⁰, respectively. KtrA forms a ring and can undergo significant conformational changes upon binding to, or changes in the oxidation state of, ligands such as NAD and ATP^{20,41,42}. The ring has a twofold symmetry that matches that of the homodimeric assembly of the transmembrane subunits, and could potentially allosterically control K^+ permeation. We speculate that the dimeric assembly is required for regulation of K^+ transport by TrkA, although each protomer contains an independent ion permeation pathway. Although the structure of VpTrkH alone does not answer the question of whether TrkH operates as a channel or a transporter, it provides a framework for further studies that will reveal the molecular mechanism of K^+ uptake and its regulation by the intracellular TrkA subunit.

METHODS SUMMARY

Both native and selenomethionine-substituted VpTrkH were expressed in *E. coli* with a C-terminal polyhistidine tag, extracted into decylmaltoside, and purified

by a metal-affinity column. The proteins were further purified by size-exclusion chromatography and concentrated to 8–10 mg ml⁻¹ for crystallization trials. Crystals were obtained by microbatch crystallization under paraffin oil. Co-crystallization with different ions was achieved by running the size-exclusion chromatography in buffers containing 150 mM of KCl or RbCl, or co-crystallization with BaCl₂. Initial phases were obtained by single-wavelength anomalous diffraction from a 3.9-Å data set collected on selenomethionine-derivatized VpTrkH, and a 3.5-Å native data set (with K⁺) was used for refinement of the final model. The final values of *R* and *R*_{free} were 24.9% and 29.9%, respectively. Purified VpTrkH was reconstituted into liposomes for ⁸⁶Rb⁺ flux assays as described previously^{17,22}.

Full Methods and any associated references are available in the online version of the paper at www.nature.com/nature.

Received 9 July; accepted 3 December 2010.

Published online 13 February 2011.

- Hille, B. *Ion Channels of Excitable Membranes* Ch. 1, 3rd edn (Sinauer, 2001).
- Schultz, S. G., Epstein, W. & Solomon, A. K. Cation transport in *Escherichia coli*. IV. Kinetics of net K uptake. *J. Gen. Physiol.* **47**, 329–346 (1963).
- Kroll, R. G. & Booth, I. R. The role of potassium transport in the generation of a pH gradient in *Escherichia coli*. *Biochem. J.* **198**, 691–698 (1981).
- Plack, R. H. Jr & Rosen, B. P. Cation/proton antiport systems in *Escherichia coli*. Absence of potassium/proton antiporter activity in a pH-sensitive mutant. *J. Biol. Chem.* **255**, 3824–3825 (1980).
- Bakker, E. P. & Mangerich, W. E. Interconversion of components of the bacterial proton motive force by electrogenic potassium transport. *J. Bacteriol.* **147**, 820–826 (1981).
- Skou, J. C. The influence of some cations on an adenosine triphosphatase from peripheral nerves. *Biochim. Biophys. Acta* **23**, 394–401 (1957).
- Tholema, N. *et al.* All four putative selectivity filter glycine residues in KtrB are essential for high affinity and selective K⁺ uptake by the KtrAB system from *Vibrio alginolyticus*. *J. Biol. Chem.* **280**, 41146–41154 (2005).
- Jan, L. Y. & Jan, Y. N. Cloned potassium channels from eukaryotes and prokaryotes. *Annu. Rev. Neurosci.* **20**, 91–123 (1997).
- Durell, S. R., Hao, Y., Nakamura, T., Bakker, E. P. & Guy, H. R. Evolutionary relationship between K⁺ channels and symporters. *Biophys. J.* **77**, 775–788 (1999).
- Durell, S. R. & Guy, H. R. Structural models of the KtrB, TrkH, and Trk1,2 symporters based on the structure of the KcsA K⁺ channel. *Biophys. J.* **77**, 789–807 (1999).
- Doyle, D. A. *et al.* The structure of the potassium channel: molecular basis of K⁺ conduction and selectivity. *Science* **280**, 69–77 (1998).
- Durell, S. R., Bakker, E. P. & Guy, H. R. Does the KdpA subunit from the high affinity K⁺-translocating P-type KDP-ATPase have a structure similar to that of K⁺ channels? *Biophys. J.* **78**, 188–199 (2000).
- Tholema, N., Bakker, E. P., Suzuki, A. & Nakamura, T. Change to alanine of one out of four selectivity filter glycines in KtrB causes a two orders of magnitude decrease in the affinities for both K⁺ and Na⁺ of the Na⁺ dependent K⁺ uptake system KtrAB from *Vibrio alginolyticus*. *FEBS Lett.* **450**, 217–220 (1999).
- Mäser, P. *et al.* Glycine residues in potassium channel-like selectivity filters determine potassium selectivity in four-loop-per-subunit HKT transporters from plants. *Proc. Natl Acad. Sci. USA* **99**, 6428–6433 (2002).
- Zeng, G. F., Pypaert, M. & Slayman, C. L. Epitope tagging of the yeast K⁺ carrier Trk2p demonstrates folding that is consistent with a channel-like structure. *J. Biol. Chem.* **279**, 3003–3013 (2004).
- Heginbotham, L., Lu, Z., Abramson, T. & MacKinnon, R. Mutations in the K⁺ channel signature sequence. *Biophys. J.* **66**, 1061–1067 (1994).
- Shi, N., Ye, S., Alam, A., Chen, L. & Jiang, Y. Atomic structure of a Na⁺- and K⁺-conducting channel. *Nature* **440**, 570–574 (2006).
- Stumpe, S. & Bakker, E. P. Requirement of a large K⁺-uptake capacity and of extracytoplasmic protease activity for protamine resistance of *Escherichia coli*. *Arch. Microbiol.* **167**, 126–136 (1997).
- Alkhuder, K., Meibom, K. L., Dubail, I., Dupuis, M. & Charbit, A. Identification of *trkH*, encoding a potassium uptake protein required for *Francisella tularensis* systemic dissemination in mice. *PLoS ONE* **5**, e8966 (2010).
- Albright, R. A., Ibar, J. L., Kim, C. U., Gruner, S. M. & Morais-Cabral, J. H. The RCK domain of the KtrAB K⁺ transporter: multiple conformations of an octameric ring. *Cell* **126**, 1147–1159 (2006).
- Albright, R. A., Joh, K. & Morais-Cabral, J. H. Probing the structure of the dimeric KtrB membrane protein. *J. Biol. Chem.* **282**, 35046–35055 (2007).
- Heginbotham, L., Kolmakova-Partensky, L. & Miller, C. Functional reconstitution of a prokaryotic K⁺ channel. *J. Gen. Physiol.* **111**, 741–749 (1998).
- Hendrickson, W. A. Determination of macromolecular structures from anomalous diffraction of synchrotron radiation. *Science* **254**, 51–58 (1991).
- Daley, D. O. *et al.* Global topology analysis of the *Escherichia coli* inner membrane proteome. *Science* **308**, 1321–1323 (2005).
- Roux, B. & MacKinnon, R. The cavity and pore helices in the KcsA K⁺ channel: electrostatic stabilization of monovalent cations. *Science* **285**, 100–102 (1999).
- Lockless, S. W., Zhou, M. & MacKinnon, R. Structural and thermodynamic properties of selective ion binding in a K⁺ channel. *PLoS Biol.* **5**, e121 (2007).
- Morais-Cabral, J. H., Zhou, Y. & MacKinnon, R. Energetic optimization of ion conduction rate by the K⁺ selectivity filter. *Nature* **414**, 37–42 (2001).
- LeMasurier, M., Heginbotham, L. & Miller, C. KcsA: it's a potassium channel. *J. Gen. Physiol.* **118**, 303–314 (2001).
- Schlösser, A., Meldorf, M., Stumpe, S., Bakker, E. P. & Epstein, W. TrkH and its homolog, TrkG, determine the specificity and kinetics of cation transport by the Trk system of *Escherichia coli*. *J. Bacteriol.* **177**, 1908–1910 (1995).
- Zhou, Y., Morais-Cabral, J. H., Kaufman, A. & MacKinnon, R. Chemistry of ion coordination and hydration revealed by a K⁺ channel-Fab complex at 2.0 Å resolution. *Nature* **414**, 43–48 (2001).
- Zhou, M. & MacKinnon, R. A mutant KcsA K⁺ channel with altered conduction properties and selectivity filter ion distribution. *J. Mol. Biol.* **338**, 839–846 (2004).
- Kato, N. *et al.* Role of positively charged amino acids in the M2_D transmembrane helix of Ktr/Trk/HKT type cation transporters. *Channels (Austin)* **1**, 161–171 (2007).
- Hänelt, I. *et al.* Gain of function mutations in membrane region M2_{C2} of KtrB open a gate controlling K⁺ transport by the KtrAB system from *Vibrio alginolyticus*. *J. Biol. Chem.* **285**, 10318–10327 (2010).
- Noda, M. *et al.* Primary structure of *Electrophorus electricus* sodium channel deduced from cDNA sequence. *Nature* **312**, 121–127 (1984).
- Mikami, A. *et al.* Primary structure and functional expression of the cardiac dihydropyridine-sensitive calcium channel. *Nature* **340**, 230–233 (1989).
- Li, R. A. *et al.* Clockwise domain arrangement of the sodium channel revealed by μ -conotoxin (GIIIA) docking orientation. *J. Biol. Chem.* **276**, 11072–11077 (2001).
- Stary, A., Shafir, Y., Hering, S., Wolschann, P. & Guy, H. R. Structural model of the Ca_v1.2 pore. *Channels (Austin)* **2**, 210–215 (2008).
- Bossemeyer, D. *et al.* K⁺-transport protein TrkA of *Escherichia coli* is a peripheral membrane protein that requires other *trk* gene products for attachment to the cytoplasmic membrane. *J. Biol. Chem.* **264**, 16403–16410 (1989).
- Schlösser, A., Hamann, A., Bossemeyer, D., Schneider, E. & Bakker, E. P. NAD⁺ binding to the *Escherichia coli* K⁺-uptake protein TrkA and sequence similarity between TrkA and domains of a family of dehydrogenases suggest a role for NAD⁺ in bacterial transport. *Mol. Microbiol.* **9**, 533–543 (1993).
- Nakamura, T., Yuda, R., Unemoto, T. & Bakker, E. P. KtrAB, a new type of bacterial K⁺-uptake system from *Vibrio alginolyticus*. *J. Bacteriol.* **180**, 3491–3494 (1998).
- Roosild, T. P., Miller, S., Booth, I. R. & Choe, S. A mechanism of regulating transmembrane potassium flux through a ligand-mediated conformational switch. *Cell* **109**, 781–791 (2002).
- Roosild, T. P. *et al.* KTN (RCK) domains regulate K⁺ channels and transporters by controlling the dimer-hinge conformation. *Structure* **17**, 893–903 (2009).
- Ho, B. K. & Gruswitz, F. HOLLOW: generating accurate representations of channel and interior surfaces in molecular structures. *BMC Struct. Biol.* **8**, 49 (2008).

Supplementary Information is linked to the online version of the paper at www.nature.com/nature.

Acknowledgements Data for this study were measured at beamlines X4A, X4C, X25 and X29 of the National Synchrotron Light Source and the NE-CAT 24ID-C and E at the Advanced Photon Source. This work was supported by the U.S. National Institutes of Health (grants HL086392, DK088057 and GM05026-sub0007 to M.Z.) and the American Heart Association (0630148N to M.Z.). M.Z. is a Pew Scholar in Biomedical Sciences. The New York Consortium on Membrane Protein Structure central facility is supported by grant GM05026 to W.A.H. as part of the Protein Structure Initiative (PSI-2) established by the National Institute of General Medical Sciences. We thank B. Honig for support, K. Jung for providing *E. coli* LB650, and J. Morais-Cabral, S.-Y. Lee, H. R. Guy, C. L. Slayman and E. P. Bakker for discussions and comments on the manuscript. M.Z. is grateful to R. MacKinnon for advice and support throughout the project.

Author Contributions M.P., J.L., B.R. and W.A.H. identified TrkH/TrkG/KtrB homologues in the database. R.B., B.K. and J.L. cloned and tested expression of the homologues. Y.C., H.H., J.W., E.J.L. and M.Z. scaled up production of proteins, produced and refined VpTrkH crystals, and collected and analysed X-ray diffraction data. X.J., E.J.L. and M.Z. solved and refined the structures. V.K., S.Y. and E.M.H. analysed diffraction data and obtained a partial model in early stages of the project. Y.C., M.G.D., M.Q., Y.P., Y.J., J.A.J. and M.Z. characterized VpTrkH function. K.R.R. and W.A.H. advised on data collection and crystallography. E.J.L. and M.Z. wrote the manuscript with inputs from all authors.

Author Information Atomic coordinates and structure factors are deposited in Protein Data Bank under accession number 3PJZ. Reprints and permissions information is available at www.nature.com/reprints. The authors declare no competing financial interests. Readers are welcome to comment on the online version of this article at www.nature.com/nature. Correspondence and requests for materials should be addressed to M.Z. (mz2140@columbia.edu).

METHODS

Homology screen, cloning and initial protein expression. TrkH was first established to be a valid target for structural studies by a bioinformatics analysis^{44,45}. A total of 91 *trkG/trkH/ptrB* genes from 58 prokaryotic genomes were identified, and the genes were amplified by PCR from the genomic DNAs, inserted into a modified pET plasmid (Novagen) with a C-terminal deca-histidine tag and a TEV protease recognition site, and expressed in a small-scale culture. Protein expression was then examined using western blots as a readout, and western-positive clones were pursued for further study. Identification and cloning of homologues, and the initial expression study, were performed by a high-throughput approach in the central facility of the New York Consortium on Membrane Protein Structure; a detailed description of the procedures can be found in ref. 44.

Large-scale protein expression, purification and crystallization. Western-positive clones received from the New York Consortium on Membrane Protein Structure were scaled up for mid- to large-scale expression studies. Five proteins (TrkHs from *V. parahaemolyticus*, *Vibrio fischeri*, *Idiomarina loihiensis*, *Campylobacter jejuni* and a KtrB from *V. fischeri*) had yields higher than 0.25 mg l⁻¹ cell culture and three of them (TrkHs from *V. parahaemolyticus*, *I. loihiensis* and *C. jejuni*) exhibited a mono-dispersed profile in size-exclusion chromatography. Among those proteins, only TrkH from *V. parahaemolyticus* (VpTrkH) produced diffracting crystals and thus became the focus of crystallization efforts.

For large-scale purification of native VpTrkH, BL21(DE3) cells were grown in Luria broth at 37 °C and induced with 0.5 mM isopropyl β-D-1-thiogalactopyranoside (IPTG) after absorbance ($A_{600\text{ nm}}$) reached 1.0; for expression of selenomethionine-incorporated proteins, the cells were grown in minimal medium containing 32.2 mM K₂HPO₄, 11.7 mM KH₂PO₄, 6 mM (NH₄)₂SO₄, 0.68 mM Na citrate, 0.17 mM Mg₂SO₄, 32 mM glucose, 0.008% (w/v) alanine, arginine, aspartic acid, asparagine, cysteine, glutamic acid, glycine, histidine, proline, serine, tryptophan, glutamine and tyrosine, 0.02% (w/v) isoleucine, leucine, lysine, phenylalanine, threonine and valine, 25 mg l⁻¹ L-selenium-methionine, 32 mg l⁻¹ thiamine, and 32 mg l⁻¹ thymine, and induced at an absorbance ($A_{600\text{ nm}}$) of 0.6. The cell membranes were solubilized with 40 mM *n*-decyl-β-D-maltoside (Anatrace) and the His-tagged protein was purified with TALON Metal Affinity Resin (Clontech). After removal of the tag with tobacco etch virus protease, the native protein was subjected to size-exclusion chromatography with a Superdex 200 10/300 GL column (GE Health Sciences) equilibrated in a buffer of 150 mM KCl, 20 mM HEPES, pH 7.5, 5 mM β-mercaptoethanol and 3.5 mM *n*-decyl-β-D-maltoside. The selenomethionine-incorporated VpTrkH protein was purified by the same procedure. The native protein was concentrated to 8 mg ml⁻¹ and the selenomethionine-substituted protein to 10 mg ml⁻¹ as approximated by ultraviolet absorbance.

Although both the native and selenomethionine-substituted VpTrkH yielded crystals readily, the crystals diffracted anisotropically and an overwhelming majority failed to reach 4.0 Å. More than 3,000 crystals were screened over a period of over 3 years. Native VpTrkH crystals were grown by microbatch crystallization under paraffin oil where 1.5 μl of the protein solution was mixed with an equal volume of crystallization solution containing 35% PEG400, 200 mM calcium acetate and 100 mM sodium acetate, pH 5.3. Rb⁺-derivatized crystals were obtained by the same method except that the size-exclusion chromatography during purification was conducted in a buffer using 150 mM RbCl to replace KCl. Ba²⁺-derivatized crystals were obtained by adding 10 mM BaCl₂ into the native protein before mixing with crystallization solution. Before flash-freezing in liquid nitrogen, the crystals were cryoprotected in mother liquor for 2–5 s. The mother liquor was obtained by vapour diffusion in sitting drops mixed from 3 μl of the protein solution and an equal volume of well solution containing 35% PEG400, 200 mM calcium acetate and 100 mM sodium acetate, pH 5.3.

Data collection and structure solution. Diffraction data were collected on beamlines X25 and X29 at the National Synchrotron Light Source and 24ID-C and 24ID-E at the Advanced Photon Source. A 3.9-Å data set was collected at a wavelength of 0.9791 Å on selenomethionine-derivatized VpTrkH. The data were indexed, integrated and scaled using HKL2000 (ref. 46). The data set showed anisotropy, but nonetheless exhibited a strong anomalous signal and was therefore used to obtain the initial phases to 3.9 Å by single-wavelength anomalous diffraction. The positions of 18 out of 24 available selenium sites in the asymmetric unit were located using the program phenix.hyss⁴⁷. Initial experimental phases were improved by twofold NCS averaging and solvent flattening using RESOLVE⁴⁷. The resultant density-modified experimental map was used to build manually a partial Cα trace with COOT⁴⁸. The phases were gradually extended to a higher-resolution native data set at 3.5 Å using twofold NCS averaging, solvent flattening and histogram matching in DM⁴⁹. Manual model building and sequence assignments were done iteratively using COOT, and the structure

refinement was done using PHENIX⁴⁷ with strong twofold NCS restraints. The final refined model contained residues 1–157, 174–484, and one K⁺ in each subunit in the asymmetric unit. The anomalous difference Fourier map calculated with phases from the refined model confirmed the correctness of the initial selenium sites, all of which overlay well with ordered methionine residues in the final model, and identified two additional sites corresponding to two N-terminal methionines in the asymmetric unit (Supplementary Fig. 10a–c). The region encompassing residues 158–173 is disordered, consistent with the absence of anomalous peaks expected from Met 158 and Met 174 within this region. At the model-building stage, diffraction data were corrected for anisotropy using the Anisotropy Server⁵⁰ and a second model was refined with anisotropy correction. Models with or without the correction essentially overlap; however, map quality is improved in several regions after the correction.

The final refined model devoid of K⁺ was used to calculate the $F_{\text{Rb}} - F_{\text{K}}$ and $F_{\text{Ba}} - F_{\text{K}}$ difference maps for structures containing Rb⁺ and Ba²⁺.

E. coli complementation assay. *E. coli* strain LB650 competent cells were transformed with pET31 vector carrying *V. parahaemolyticus trkH*. Two media, Hi-K and Lo-K, were prepared based on ref. 51, both containing 8 mM ammonium sulphate, 0.4 mM magnesium sulphate, 1 mM sodium citrate, 1 mg l⁻¹ thiamine and 2 g l⁻¹ glucose. For the Hi-K medium, 115 mM potassium phosphate (pH 7.0) was added; for the Lo-K medium, 115 mM sodium phosphate (pH 7.0) was added. The two solutions were mixed in different ratios to produce the desired K⁺ concentration. The transformation cell culture was spread onto agar plates prepared with solutions with different K⁺ concentrations and incubated at 37 °C overnight. As a blank control, pET31 vector without insertions was used to transform *E. coli* strain LB650 competent cells.

Reconstitution of TrkH into proteoliposomes. Purified VpTrkH was reconstituted into lipid vesicles composed of 1-palmitoyl-2-oleoyl-phosphatidylethanolamine and 1-palmitoyl-2-oleoyl-phosphatidylglycerol (Avanti Polar Lipids) in a ratio of 3:1 by mass, as previously described⁵¹. The protein to lipid ratio was 1:150 by mass. The solution was then subjected to several rounds of dialysis against reconstitution solution until the detergent was totally removed. At the end of each experiment, valinomycin was added to the reaction mixture to monitor the maximum uptake.

Determination of protein oligomeric state. The mass of the VpTrkH protein in solution was measured using a Wyatt miniDAWN TREOS 3 angle-static light-scattering detector, a Wyatt Optilab rEX refractive index detector and an Agilent Variable Wavelength Detector ultraviolet absorbance detector⁵². Purified protein sample (5 μl) was injected onto a TSKgel SuperSW3000 (4.6 mm internal diameter × 30 cm) silica-gel size-exclusion column in buffer containing 0.016% dodecyl-maltoside at a rate of 0.25 ml min⁻¹. The differential refractive index (dn/dc) value for dodecylmaltoside was calculated to be 0.128 ml g⁻¹ using the Wyatt Optilab rEX refractive index detector. Deconvolution of the protein–detergent conjugate was then achieved using a previously described method⁵³. The calculation did not account for refractive index contributions due to bound lipid.

⁸⁶Rb flux assay. The ⁸⁶Rb⁺ flux assay was performed as described previously²². In the competition assays, Li⁺, Na⁺, K⁺ or Rb⁺ were added directly into the flux buffer, and the readings were taken at the 20 min time point.

44. Love, J. *et al.* The New York Consortium on Membrane Protein Structure (NYCOMPS): a high-throughput platform for structural genomics of integral membrane proteins. *J. Struct. Funct. Genomics* **11**, 191–199 (2010).
45. Punta, M. *et al.* Structural genomics target selection for the New York consortium on membrane protein structure. *J. Struct. Funct. Genomics* **10**, 255–268 (2009).
46. Otwinowski, Z. & Minor, W. Processing of X-ray diffraction data collected in oscillation mode. *Methods Enzymol.* **276**, 307–326 (1997).
47. Adams, P. D. *et al.* PHENIX: a comprehensive Python-based system for macromolecular structure solution. *Acta Crystallogr. D* **66**, 213–221 (2010).
48. Emsley, P. & Cowtan, K. Coot: model-building tools for molecular graphics. *Acta Crystallogr. D* **60**, 2126–2132 (2004).
49. Cowtan, K. Error estimation and bias correction in phase-improvement calculations. *Acta Crystallogr. D* **55**, 1555–1567 (1999).
50. Strong, M. *et al.* Toward the structural genomics of complexes: crystal structure of a PE/PPE protein complex from *Mycobacterium tuberculosis*. *Proc. Natl Acad. Sci. USA* **103**, 8060–8065 (2006).
51. Epstein, W. & Kim, B. S. Potassium transport loci in *Escherichia coli* K-12. *J. Bacteriol.* **108**, 639–644 (1971).
52. Slotboom, D. J., Durkens, R. H., Olieman, K. & Erkens, G. B. Static light scattering to characterize membrane proteins in detergent solution. *Methods* **46**, 73–82 (2008).
53. Kendrick, B. S., Kerwin, B. A., Chang, B. S. & Philo, J. S. Online size-exclusion high-performance liquid chromatography light scattering and differential refractometry methods to determine degree of polymer conjugation to proteins and protein–protein or protein–ligand association states. *Anal. Biochem.* **299**, 136–146 (2001).

Submillimetre galaxies reside in dark matter haloes with masses greater than 3×10^{11} solar masses

Alexandre Amblard¹, Asantha Cooray^{1,2}, Paolo Serra¹, B. Altieri³, V. Arumugam⁴, H. Aussel⁵, A. Blain², J. Bock^{2,6}, A. Boselli⁷, V. Buat⁷, N. Castro-Rodríguez^{8,9}, A. Cava^{8,9}, P. Chanial¹⁰, E. Chapin¹¹, D. L. Clements¹⁰, A. Conley¹², L. Conversi³, C. D. Dowell^{2,6}, E. Dwek¹³, S. Eales¹⁴, D. Elbaz⁵, D. Farrah¹⁵, A. Franceschini¹⁶, W. Gear¹⁴, J. Glenn¹², M. Griffin¹⁴, M. Halpern¹¹, E. Hatziminaoglou¹⁷, E. Ibar¹⁸, K. Isaak¹⁴, R. J. Ivison^{18,4}, A. A. Khostovan¹, G. Lagache¹⁹, L. Levenson^{2,6}, N. Lu^{2,20}, S. Madden⁵, B. Maffei²¹, G. Mainetti¹⁶, L. Marchetti¹⁶, G. Marsden¹¹, K. Mitchell-Wynne¹, H. T. Nguyen^{6,2}, B. O'Halloran¹⁰, S. J. Oliver¹⁵, A. Omont²², M. J. Page²³, P. Panuzzo⁵, A. Papageorgiou¹⁴, C. P. Pearson^{23,24}, I. Pérez-Fournon^{8,9}, M. Pohlen¹⁴, N. Rangwala¹², I. G. Roseboom¹⁵, M. Rowan-Robinson¹⁰, M. Sánchez Portal³, B. Schulz^{2,20}, Douglas Scott¹¹, N. Seymour²³, D. L. Shupe^{2,20}, A. J. Smith¹⁵, J. A. Stevens²⁵, M. Symeonidis²³, M. Trichas¹⁰, K. Tugwell²⁶, M. Vaccari¹⁶, E. Valiante¹¹, I. Valtchanov³, J. D. Vieira², L. Vigroux²², L. Wang¹⁵, R. Ward¹⁵, G. Wright¹⁸, C. K. Xu^{2,20} & M. Zemcov^{2,6}

The extragalactic background light at far-infrared wavelengths^{1–3} comes from optically faint, dusty, star-forming galaxies in the Universe with star formation rates of a few hundred solar masses per year⁴. These faint, submillimetre galaxies are challenging to study individually because of the relatively poor spatial resolution of far-infrared telescopes^{5,6}. Instead, their average properties can be studied using statistics such as the angular power spectrum of the background intensity variations^{7–10}. A previous attempt¹¹ at measuring this power spectrum resulted in the suggestion that the clustering amplitude is below the level computed with a simple ansatz based on a halo model¹². Here we report excess clustering over the linear prediction at arcminute angular scales in the power spectrum of brightness fluctuations at 250, 350 and 500 μm . From this excess, we find that submillimetre galaxies are located in dark matter haloes with a minimum mass, M_{min} , such that $\log_{10}[M_{\text{min}}/M_{\odot}] = 11.5^{+0.7}_{-0.2}$ at 350 μm , where M_{\odot} is the solar mass. This minimum dark matter halo mass corresponds to the most efficient mass scale for star formation in the Universe¹³, and is lower than that predicted by semi-analytical models for galaxy formation¹⁴.

Despite recent successes in attributing most of the extragalactic background light at submillimetre wavelengths to known galaxy populations through stacking analyses^{15–17}, we have not individually detected the faint galaxies that are responsible for more than 85% of the total extragalactic intensity at these wavelengths¹⁸. The faint star-forming galaxies are expected to trace the large-scale structure of the Universe, especially in models where galaxy formation and evolution is closely connected to dark matter haloes. Although galaxies are not individually detected in low-resolution observations, their clustering is expected to leave a distinct signature in the total intensity variations at submillimetre wavelengths. The amplitude of the power spectrum of intensity variations as a function of the angular scale provides details on the redshift distribution and the dark-matter-halo mass scale of dusty, star-forming galaxies in the Universe⁷.

For this analysis, we use data from the Herschel Multi-tiered Extragalactic Survey¹⁸ (HerMES), recorded with the Spectral and Photometric Imaging Receiver (SPIRE¹⁹) on board the Herschel Space Observatory²⁰, during the Science Demonstration Phase of Herschel. The data come from a wide, 218'–by–218', area in the Lockman Hole overlapping with the Spitzer Wide-Area Infrared Extragalactic Survey (SWIRE), complemented by a narrow, but very deep (30 repeated scans), map of the Great Observatories Origins Deep Survey North (GOODS-N) field covering 30' by 30'. These fields have been very well studied at other wavelengths and they are known to have a low Galactic dust density, making it easier to distinguish the extragalactic component we wish to study. The observing time to complete each of the two fields was about 13.5 h, observing simultaneously at 250, 350 and 500 μm .

To limit the influence of a few bright galaxies on the measurement of the power spectrum, we remove galaxies brighter than 50 mJy in all three passbands by masking pixels in our maps with values larger than 50 mJy per beam, as well as the neighbouring pixels. We use the cross-power spectrum of two submaps as our estimate of the sky power spectrum to remove the contribution from the instrumental noise and alleviate potential systematic effects. We correct the raw cross-power spectra for the effects of the angular response function of the instrument and the transfer function of the map-making process. The angular response is established from a set of SPIRE observations targeting Neptune, which is a strong, point-like source for SPIRE, and involving a fine sampling of the beam with a total of 700 scans²¹. The effects of the filtering of the time-ordered data and of the map pixelization are captured with a large set of sky simulations. To estimate our uncertainties, we propagate the errors from the beam measurement, and the simulations provide us with the instrumental and sky variance. The quadratic sum of these errors constitutes our error estimate.

The measured angular power spectrum (Fig. 1a) contains contributions from spatial variations in the brightness of Galactic dust clouds (cirrus brightness) at large angular scales, the clustering of galaxies

¹Department of Physics & Astronomy, University of California, Irvine, California 92697, USA. ²California Institute of Technology, 1200 East California Boulevard, Pasadena, California 91125, USA. ³Herschel Science Centre, European Space Astronomy Centre, Villanueva de la Cañada, 28691 Madrid, Spain. ⁴Institute for Astronomy, University of Edinburgh, Royal Observatory, Blackford Hill, Edinburgh EH9 3HJ, UK. ⁵Laboratoire AIM-Paris-Saclay, CEA/DSM/Irfu - CNRS - Université Paris Diderot, CE-Saclay, pt courrier 131, F-91191 Gif-sur-Yvette, France. ⁶Jet Propulsion Laboratory, 4800 Oak Grove Drive, Pasadena, California 91109, USA. ⁷Laboratoire d'Astrophysique de Marseille, OAMP, Université Aix-Marseille, CNRS, 38 rue Frédéric Joliot-Curie, 13388 Marseille cedex 13, France. ⁸Instituto de Astrofísica de Canarias, E-38200 La Laguna, Tenerife, Spain. ⁹Departamento de Astrofísica, Universidad de La Laguna, E-38205 La Laguna, Tenerife, Spain. ¹⁰Astrophysics Group, Imperial College London, Blackett Laboratory, Prince Consort Road, London SW7 2AZ, UK. ¹¹Department of Physics & Astronomy, University of British Columbia, 6224 Agricultural Road, Vancouver, British Columbia V6T 1Z1, Canada. ¹²Department of Astrophysical and Planetary Sciences, CASA 389-UCB, University of Colorado, Boulder, Colorado 80309, USA. ¹³Observational Cosmology Lab, Code 665, NASA Goddard Space Flight Center, Greenbelt, Maryland 20771, USA. ¹⁴Cardiff School of Physics and Astronomy, Cardiff University, Queens Buildings, The Parade, Cardiff CF24 3AA, UK. ¹⁵Astronomy Centre, Department of Physics & Astronomy, University of Sussex, Brighton BN1 9QH, UK. ¹⁶Dipartimento di Astronomia, Università di Padova, Vicolo Osservatorio, 3, 35122 Padova, Italy. ¹⁷ESO, Karl-Schwarzschild-Strasse 2, 85748 Garching bei München, Germany. ¹⁸UK Astronomy Technology Centre, Royal Observatory, Blackford Hill, Edinburgh EH9 3HJ, UK. ¹⁹Institut d'Astrophysique Spatiale, Bâtiment 121, Université Paris-Sud 11 and CNRS (UMR 8617), 91405 Orsay, France. ²⁰Infrared Processing and Analysis Center, MS 100-22, California Institute of Technology, JPL, Pasadena, California 91125, USA. ²¹School of Physics and Astronomy, The University of Manchester, Alan Turing Building, Oxford Road, Manchester M13 9PL, UK. ²²Institut d'Astrophysique de Paris, UMR 7095, CNRS, UPMC Univ. Paris 06, 98bis Boulevard Arago, F-75014 Paris, France. ²³Space Science & Technology Department, Rutherford Appleton Laboratory, Chilton, Didcot OX11 0QX, UK. ²⁴Institute for Space Imaging Science, University of Lethbridge, Lethbridge, Alberta T1K 3M4, Canada. ²⁵Centre for Astrophysics Research, University of Hertfordshire, College Lane, Hatfield AL10 9AB, UK. ²⁶Mullard Space Science Laboratory, University College London, Holmbury St Mary, Dorking RH5 6NT, UK.

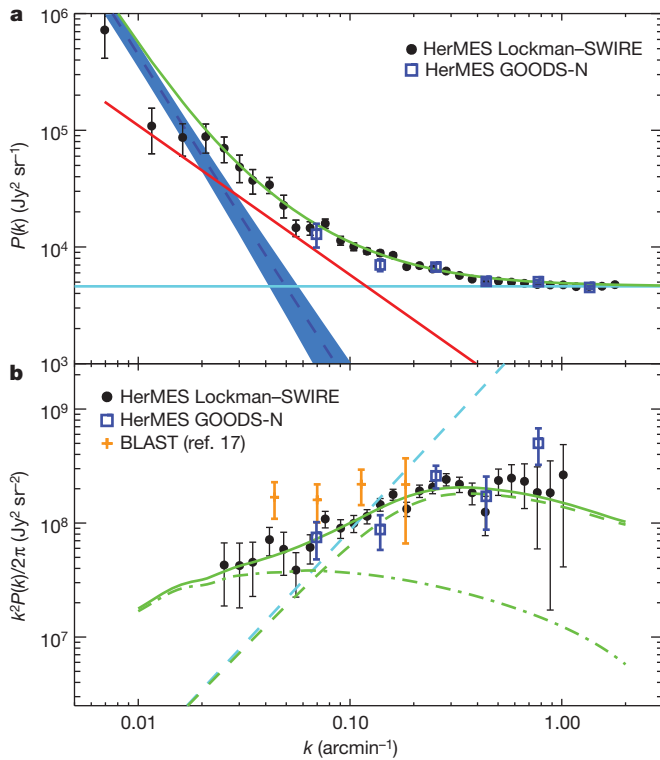


Figure 1 | The two-dimensional power spectrum of the Herschel map.

a, The total power spectrum, $P(k)$, at 350 μm as a function of the wavenumber, k , in inverse arcminutes. The error bars are uncertainties at the 68% confidence level. The shaded region is the cirrus signal in our Lockman-SWIRE field. To describe the total power spectrum, we take a power law with $P(k) = A(k/k_1)^n + P_{\text{SN}}$, where k_1 is fixed at 0.1 arcmin^{-1} and P_{SN} is the shot noise amplitude. At 350 μm , we find that $A = (5.79 \pm 0.26) \times 10^3 \text{ Jy}^2 \text{ sr}^{-1}$ and $n = -1.28 \pm 0.07$, shown by the red line. The light-blue line is the best-fit shot noise amplitude, which has a value of $4,600 \pm 70 \text{ Jy}^2 \text{ sr}^{-1}$, in agreement with the value of $4,500 \pm 220 \text{ Jy}^2 \text{ sr}^{-1}$ predicted by best-determined source counts²⁸. The shot noise errors include the 15% uncertainty in the SPIRE absolute flux calibration²¹. In green, we show the total power spectrum combined with the mean estimate of the cirrus signal. **b**, The angular clustering power spectrum at 350 μm as a function of wavenumber, with errors showing uncertainties at the 68% confidence level. The best-fit shot noise value (dashed blue line) has been removed from the data and its uncertainty added to the overall error in quadrature. The green lines show the best-fit halo model with a reduced χ^2 value of 1.02. The dot-dash line shows the two-halo term and the dashed line shows the one-halo term, which is responsible for the clustering at small angular scales. Data in the lowest-wavenumber bins contaminated by cirrus brightness have been omitted. For comparison, we also show a previous measurement of the power spectrum of brightness fluctuations at 350 μm , made with BLAST¹¹. The results related to 250 and 500 μm are summarized in Supplementary Information.

at intermediate angular scales and a white-noise component at small angular scales arising from the Poisson behaviour of the faint galaxies^{7,9}. The cirrus signal in our Lockman-SWIRE field is taken from existing measurements in the same field with the Infrared Astronomical Satellite, at 100 μm , and the Multiband Imaging Photometer for Spitzer²², and extends this spectrum from 100 μm to SPIRE wavelengths using the spectral dependence of a Galactic dust model²³. We remove this cirrus power spectrum from our measurements and account for the uncertainty in it by adding its error in quadrature to errors in our power spectrum points.

The Poisson behaviour of sources leads to an additional term in the angular power spectrum that is scale independent. The clustering component we measure is the excess of clustered background fluctuations above this shot noise level. As the confusion noise is at the level of 6 mJy at SPIRE wavelengths⁵, with fluctuations in the brightness of the background we are probing the clustering of faint galaxies with fluxes at the level of a few millijanskys at 350 μm . To extract astrophysical

information on faint galaxies from the clustering power spectrum, we make use of the halo model¹². This phenomenological approach connects the spatial distribution of galaxies in the Universe to that of dark matter. To model submillimetre galaxies in dark matter haloes, we use the following halo occupation distribution, which describes the number of galaxies as a function of the halo mass, M , when M is greater than a minimum mass scale, M_{min} : $N_{\text{gal}}(M) = 1 + (M/M_1)^\alpha$. Here M_1 is the mass scale at which more than one galaxy is present in a single dark matter halo, taken to be between 10 to 25 times M_{min} , and α is the power-law scaling of satellite galaxies with halo mass. The halo model involves two parts: the one-halo term, with clustering of galaxies within haloes, and the two-halo term, with clustering of galaxies between haloes. Whereas with the two-halo term alone, parameters related to the occupation number are degenerate with each other and the bias factor or the number density of galaxies, with clustering in the one-halo part of the power spectrum also included, the parameter degeneracies are broken and M_{min} can be determined more accurately¹².

At scales of a few arcminutes and above, we measure a clustering excess, arising from the one-halo term, over the two-halo term tracing the linear-density-field power spectrum scaled by galaxy bias (Fig. 1b). The one-halo term arises when more than one far-infrared galaxy occupies the same halo. A hint of the one-halo term was previously seen in the clustering of the bright (>30 -mJy) submillimetre galaxies²⁴, but evidence for such clustering was not found for bright galaxies in a different Herschel data set²⁵. To describe the power spectrum of the intensity fluctuations, we also need a prescription for the redshift evolution of the source intensity. Although models exist in the literature^{26,27}, our data are of sufficient quality that we can directly constrain the redshift evolution of the source intensity from our measurements: we constrain its value in four redshift bins in the range 0–4.0. The halo model parameters, the source intensity parameters and the shot noise amplitude are jointly estimated with Markov chain Monte Carlo fits to the power spectrum measurements. We impose the additional prior on our parameter estimates that the redshift-integrated source intensity from our model fits, including the fractional contribution from bright sources that we have masked, be within the 68% range of the known background light intensity in each of the three wavebands². We combine the estimates of the source intensity evolution in the three wavebands (250, 350 and 500 μm) and in the four redshift bins to measure the bolometric luminosity density between 8 and 1,100 μm as a function of the redshift (Fig. 2). We find that the far-infrared luminosity density continues to be significant out to a redshift of four and is at least a factor of ten larger than the luminosity density of individually detected submillimetre sources with flux densities above 30 mJy alone¹⁸.

Using the halo model fits, we estimate that the minimum dark matter mass scale for dusty, star-forming galaxies at the peak of the star formation history of the Universe is such that $\log_{10}[M_{\text{min}}/M_\odot] = 11.5^{+0.7}_{-0.2}$ at 350 μm , with a bias factor for the galaxies of $2.4^{+1.0}_{-0.2}$. For the minimum halo masses at 250 and 500 μm , $\log_{10}[M_{\text{min}}/M_\odot] = 11.1^{+1.0}_{-0.6}$ and $11.8^{+0.4}_{-0.3}$, respectively. The corresponding bias factors for the galaxies are $2.0^{+0.9}_{-0.1}$ and $2.8^{+0.4}_{-0.5}$. The differences in the minimum halo masses and the bias factors between the three wavelengths are probably due to a combination of effects including overall calibration uncertainties, the fact that at longer wavelengths we may be probing colder dust than at shorter wavelengths, and differences in the prior assumption on the total background intensity. In future, numerical models on the distribution of submillimetre galaxies will become useful in properly understanding some of these subtle differences. Averaged over the three wavelengths, the minimum halo mass for submillimetre galaxies is at the level of $3 \times 10^{11} M_\odot$, with an overall statistical uncertainty of roughly ± 0.4 in $\log_{10}[M_{\text{min}}/M_\odot]$.

On the basis of a variety of observed scaling relations such as that between stellar mass and circular velocity, the dark matter halo mass scale for efficient star formation has been indirectly inferred to be about $10^{11} M_\odot$ (ref. 13). As the submillimetre galaxies are the most active star-forming galaxies in the Universe, it is likely that the minimum halo

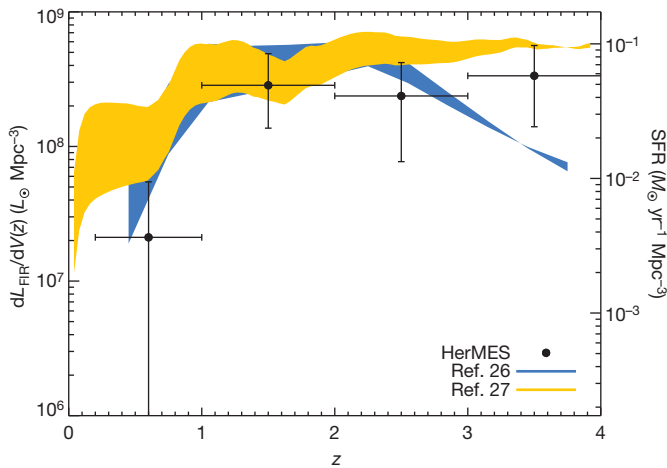


Figure 2 | Far-infrared bolometric luminosity density (8–1,110 μm) and star formation rate (SFR) as a function of redshift. The far-infrared bolometric luminosity density was estimated using the values of the source intensity in four redshift bins between redshifts $z = 0$ and 4 derived from model best fits to each of the power spectra from the three wavebands and with prior selection of models with $\alpha > 1$ for the power-law slope of the occupation number. We have assumed a modified black-body spectrum for the spectral energy distribution of the spatially unresolved sources, with an emissivity index of 1.5 and a dust temperature of 28 ± 8 K (ref. 29). We propagate the uncertainty in the dust temperature as an additional error when computing errors in the luminosity density in each of the redshift bins. The vertical bars show errors at the 68% confidence level propagated from errors in the source intensity evolution estimates and from the temperature prior, and the horizontal bars indicated the redshift range of each of the bins used for model fits. The yellow and blue shaded areas represent models^{26,27} with the same flux cut ($S > 50$ mJy) and the same temperature prior as our data. Our measurements are consistent with both these models. The redshift evolution of the far-infrared luminosity is a measure of the star formation history of the Universe³⁰, and by converting our estimate we find respective star formation rates of $< 0.01 M_{\odot}$, $(0.05 \pm 0.03) M_{\odot}$, $(0.04 \pm 0.03) M_{\odot}$ and $(0.06 \pm 0.04) M_{\odot} \text{ yr}^{-1} \text{ Mpc}^{-3}$ in the redshift bins with $z < 1$, $1 < z < 2$, $2 < z < 3$ and $3 < z < 4$. L_{\odot} , solar luminosity.

mass scale for such galaxies that we determine from brightness fluctuations corresponds to the preferred mass scale of active star formation in the Universe. In dark matter haloes below this mass, star formation is expected to be inefficient as a result of photoionization feedback¹³. The underlying astrophysics needed to explain the numerical value we find is still missing from galaxy formation theories: existing semi-analytical models predict a mass scale for faint, submillimetre galaxies that are roughly ten times larger¹⁴. We provide strong evidence for a minimum mass scale for active star-forming galaxies by studying the background intensity variations generated by those galaxies in our sky maps. Our direct estimate of the minimum dark matter halo mass provides a critical value needed to improve theoretical models of submillimetre galaxies and the overall picture of galaxy formation and evolution.

Received 11 August; accepted 20 December 2010.

Published online 16 February 2011.

1. Puget, J.-L. *et al.* Tentative detection of a cosmic far-infrared background with COBE. *Astron. Astrophys.* **308**, L5–L8 (1996).
2. Fixsen, D. J., Dwek, E., Mather, J. C., Bennett, C. L. & Shafer, R. A. The spectrum of the extragalactic far-infrared background from the COBE FIRAS observations. *Astrophys. J.* **508**, 123–128 (1998).
3. Dwek, E. *et al.* The COBE Diffuse Infrared Background Experiment Search for the cosmic infrared background. IV. Cosmological implications. *Astrophys. J.* **508**, 106–122 (1998).
4. Hughes, D. *et al.* High-redshift star formation in the Hubble Deep Field revealed by a submillimetre-wavelength survey. *Nature* **394**, 241–247 (1998).
5. Nguyen, H. T. *et al.* HerMES: the SPIRE confusion limit. *Astron. Astrophys.* **518**, L5 (2010).
6. Hauser, M. G. & Dwek, E. The cosmic infrared background: measurements and implications. *Annu. Rev. Astron. Astrophys.* **39**, 249–307 (2001).
7. Amblard, A. & Cooray, A. Anisotropy studies of the unresolved far-infrared background. *Astrophys. J.* **670**, 903–911 (2007).

8. Haiman, Z. & Knox, L. Correlations in the far-infrared background. *Astrophys. J.* **530**, 124–132 (2000).
9. Knox, L., Cooray, A., Eisenstein, D. & Haiman, Z. Probing early structure formation with far-infrared background correlations. *Astrophys. J.* **550**, 7–20 (2001).
10. Negrello, M. *et al.* Astrophysical and cosmological information from large-scale submillimetre surveys of extragalactic sources. *Mon. Not. R. Astron. Soc.* **377**, 1557–1568 (2007).
11. Viero, M. P. *et al.* BLAST: correlations in the cosmic far-infrared background at 250, 350, and 500 μm reveal clustering of star-forming galaxies. *Astrophys. J.* **707**, 1766–1778 (2009).
12. Cooray, A. & Sheth, R. Halo models of large scale structure. *Phys. Rep.* **372**, 1–129 (2002).
13. Bouché, N. *et al.* The impact of cold gas accretion above a mass floor on galaxy scaling relations. *Astrophys. J.* **718**, 1001–1018 (2010).
14. Gonzalez, J. E., Lacey, C. G., Baugh, C. M. & Frenk, C. S. The role of submillimetre galaxies in hierarchical galaxy formation. *Mon. Not. R. Astron. Soc.* (submitted); preprint at (<http://arxiv.org/abs/1006.0230>) (2010).
15. Devlin, J. M. *et al.* Over half of the far-infrared background light comes from galaxies at $z \geq 1.2$. *Nature* **458**, 737–739 (2009).
16. Dole, H. *et al.* The cosmic infrared background resolved by Spitzer. Contributions of mid-infrared galaxies to the far-infrared background. *Astron. Astrophys.* **451**, 417–429 (2006).
17. Marsden, G. *et al.* BLAST: resolving the cosmic submillimetre background. *Astrophys. J.* **707**, 1729–1739 (2009).
18. Oliver, S. *et al.* HerMES: SPIRE galaxy number counts at 250, 350 and 500 microns. *Astron. Astrophys.* **518**, L21 (2010).
19. Griffin, M. J. *et al.* The Herschel-SPIRE instrument and its in-flight performance. *Astron. Astrophys.* **518**, L3 (2010).
20. Pilbratt, G. *et al.* Herschel Space Observatory – an ESA facility for far-infrared and submillimetre astronomy. *Astron. Astrophys.* **518**, L1 (2010).
21. Swinyard, B. *et al.* In-flight calibration of the Herschel-SPIRE instrument. *Astron. Astrophys.* **518**, L4 (2010).
22. Lagache, G. *et al.* Correlated anisotropies in the cosmic far-infrared background detected by the multiband imaging photometer for Spitzer: constraint on the bias. *Astrophys. J.* **665**, L89–L92 (2007).
23. Schlegel, D. J., Finkbeiner, D. P. & Davis, M. Maps of dust infrared emission for use in estimation of reddening and cosmic microwave background radiation foregrounds. *Astrophys. J.* **500**, 525–534 (1998).
24. Cooray, A. HerMES: halo occupation number and bias properties of dusty galaxies from angular clustering measurements. *Astron. Astrophys.* **518**, L22 (2010).
25. Maddox, S. J. *et al.* Herschel ATLAS: the angular correlation function of submillimetre galaxies at high and low redshift. *Astron. Astrophys.* **518**, L11 (2010).
26. Lagache, G., Dole, H. & Puget, J.-L. Modelling the infrared galaxy evolution using a phenomenological approach. *Mon. Not. R. Astron. Soc.* **338**, 555–571 (2003).
27. Valiante, E. *et al.* A backward evolution model for infrared surveys: the role of AGN- and color- L_{TIR} distributions. *Astrophys. J.* **701**, 1814–1838 (2009).
28. Glenn, J. *et al.* HerMES: deep galaxy number counts from a $P(D)$ fluctuation analysis of SPIRE Science Demonstration Phase observations. *Mon. Not. R. Astron. Soc.* **409**, 109–121 (2010).
29. Amblard, A. *et al.* Herschel-ATLAS: dust temperature and redshift distribution of SPIRE and PACS detected sources using submillimetre colours. *Astron. Astrophys.* **518**, L9 (2010).
30. Kennicutt, R. C. Jr. Star formation in galaxies along the Hubble sequence. *Annu. Rev. Astron. Astrophys.* **36**, 189–232 (1998).

Supplementary Information is linked to the online version of the paper at www.nature.com/nature.

Acknowledgements SPIRE has been developed by a consortium of institutes led by Cardiff University (UK) and including the University of Lethbridge (Canada); NAOC (China); CEA and IAC (France); IFSI and the University of Padua (Italy); IAC (Spain); Stockholm Observatory (Sweden); Imperial College London, RAL, UCL-MSSL, UKATC and the University of Sussex (UK); and Caltech/JPL, IPAC and the University of Colorado (USA). This development has been supported by national funding agencies: CSA (Canada); NAOC (China); CEA, CNES and CNRS (France); ASI (Italy); MCINN (Spain); SNSB (Sweden); STFC (UK); and NASA (USA). We thank M. Viero for comments. A.A., A. Cooray, P.S., A.A.K., K.M.-W. and other US co-authors are supported by NASA funds for US participants in Herschel through an award from JPL.

Author Contributions This paper represents the combined work of the HerMES collaboration, the SPIRE Instrument Team's Extragalactic Survey, and has been extensively internally reviewed. A. Cooray planned the study, supervised the research work of A.A. and P.S., and wrote the draft version of this paper. A.A. performed the power spectrum measurements and P.S. interpreted those measurements with the halo model. All other co-authors of this paper contributed extensively and equally by their varied contributions to the SPIRE instrument, Herschel mission, analysis of SPIRE and HerMES data, planning of HerMES observations and scientific support of HerMES, and by commenting on this manuscript as part of an internal review process.

Author Information The data presented in this paper are publicly available from the ESA/Herschel Science Archive (<http://herchel.esac.esa.int>) under the observational identifications 1342186108, 1342186109 and 1342185536. Derived products by the HerMES collaboration, such as source catalogues, will be released through HeDaM (<http://hedam.oamp.fr/HerMES>). Reprints and permissions information is available at www.nature.com/reprints. The authors declare no competing financial interests. Readers are welcome to comment on the online version of this article at www.nature.com/nature. Correspondence and requests for materials should be addressed to A. Cooray (acooray@ucl.edu).

Co-adjuvant effects of retinoic acid and IL-15 induce inflammatory immunity to dietary antigens

R. W. DePaolo^{1*}, V. Abadie^{1*}, F. Tang¹, H. Fehlner-Peach¹, J. A. Hall^{2,3}, W. Wang¹, E. V. Marietta^{4,5}, D. D. Kasarda⁶, T. A. Waldmann⁷, J. A. Murray⁸, C. Semrad¹, S. S. Kupfer¹, Y. Belkaid², S. Guandalini⁹ & B. Jabri^{1,9,10}

Under physiological conditions the gut-associated lymphoid tissues not only prevent the induction of a local inflammatory immune response, but also induce systemic tolerance to fed antigens^{1,2}. A notable exception is coeliac disease, where genetically susceptible individuals expressing human leukocyte antigen (HLA) HLA-DQ2 or HLA-DQ8 molecules develop inflammatory T-cell and antibody responses against dietary gluten, a protein present in wheat³. The mechanisms underlying this dysregulated mucosal immune response to a soluble antigen have not been identified. Retinoic acid, a metabolite of vitamin A, has been shown to have a critical role in the induction of intestinal regulatory responses^{4–6}. Here we find in mice that in conjunction with IL-15, a cytokine greatly upregulated in the gut of coeliac disease patients^{3,7}, retinoic acid rapidly activates dendritic cells to induce JNK (also known as MAPK8) phosphorylation and release the proinflammatory cytokines IL-12p70 and IL-23. As a result, in a stressed intestinal environment, retinoic acid acted as an adjuvant that promoted rather than prevented inflammatory cellular and humoral responses to fed antigen. Altogether, these findings reveal an unexpected role for retinoic acid and IL-15 in the abrogation of tolerance to dietary antigens.

Induction of regulatory intestinal responses to oral antigens prevents the subsequent development of systemic T-helper type-1 (T_H1) responses to those antigens, a phenomenon referred to as oral tolerance². An exception to this is coeliac disease, where patients mount a T_H1 immune response to dietary gluten³. To determine whether the presence of IL-15 may affect intestinal homeostasis, we first examined its effects on the generation of inducible regulatory T cells (T_{reg}) expressing the transcription factor forkhead box P3 (Foxp3). Under physiological conditions, mesenteric lymph node (MLN) dendritic cells drive *de novo* differentiation of T_{reg} cells^{4–6}. In the presence of IL-15-stimulated MLN dendritic cells, T_{reg}-cell generation from unfractionated CD4⁺ T cells (Fig. 1a) or naive CD44^{lo} CD4⁺ T cells (Supplementary Fig. 1a) was impaired. Further, IL-15 had no effect on T_{reg}-cell differentiation in the presence of dendritic cells lacking the IL-2–IL-15-receptor- β/γ -chain (IL-2–IL-15-R β/γ c) heterodimeric signalling receptor complex⁸ (Supplementary Fig. 2a) and in dendritic-cell-free systems (Supplementary Figs 1b, 5), demonstrating that IL-15 was acting at the level of dendritic cells and not T cells to block T_{reg} generation. To assess the relevance of our *in vitro* findings, we tested the response to fed chicken ovalbumin (OVA), a model antigen used in oral tolerance experiments, in D^d-IL-15 transgenic mice⁹ that over-express IL-15 in the lamina propria and MLN but not in the intestinal epithelium (Supplementary Fig. 3). In agreement with our *in vitro* observations, the number of naive OT-II RAG1^{−/−} CD4⁺ T cells converted into T_{reg} cells was significantly reduced in OVA-fed D^d-IL-15 transgenic mice compared to wild-type mice (Fig. 1b). Retinoic acid

(RA), which is reported to have a critical role in T_{reg} differentiation^{4–6}, further decreased the conversion of T_{reg} cells *in vivo* in OVA-fed D^d-IL-15 transgenic mice (Fig. 1c).

To determine the mechanisms by which IL-15-stimulated dendritic cells prevent the conversion of T_{reg} cells and to assess further the role of RA, we used splenic dendritic cells (Supplementary Fig. 2b), which, unlike MLN dendritic cells, lack the ability to produce constitutively high levels of RA^{4,6}. Conditioned media obtained from IL-15-treated splenic dendritic cells contained high levels of IL-12p70 and IL-23, but no IL-6 (Supplementary Fig. 4a), and decreased T_{reg}-cell conversion (Supplementary Fig. 2c). The proinflammatory properties of IL-15 were enhanced further in the presence of RA (Supplementary Fig. 4a). As previously reported¹⁰, IL-12p70 significantly suppressed T_{reg} differentiation at concentrations found in IL-15-conditioned dendritic cell supernatant (Supplementary Fig. 4b), and this effect was enhanced by IL-23 in a dose-dependent manner (Supplementary Fig. 4b). The requirement for IL-12 in IL-15-mediated suppression of T_{reg} differentiation was demonstrated using IL-12p40-deficient dendritic cells (Fig. 1d and Supplementary Fig. 4c) and neutralizing anti-IL-12p40 antibody (Supplementary Fig. 4d).

Inhibition of T_{reg}-cell conversion in the presence of IL-15 was accompanied by the induction of T_H1 responses *in vitro* (Fig. 2a and Supplementary Fig. 6a) and *in vivo* in OVA-fed D^d-IL-15 transgenic mice (Fig. 2b and Supplementary Fig. 6c). As expected, the ability of IL-15 to induce T_H1 responses *in vitro* (Fig. 2c) and *in vivo* (Fig. 2f) was dependent on IL-12. RA further promoted (Fig. 2a, b and Supplementary Fig. 6a–c) and was central for T_H1 polarization in the presence of IL-15 (Fig. 2d, e). In addition, RA acted in concert with IL-12p70 at the level of T cells and with IL-6 to amplify T_H1-cell differentiation (Supplementary Figs 5, 6b) and T_H17-cell responses (Supplementary Fig. 7a–d), respectively. The critical role of IL-15 in the induction of inflammatory T-cell responses to dietary antigen was demonstrated by blocking IL-15 signalling *in vivo* using either a neutralizing anti-IL-15 or IL-15/IL-2R β antibody¹¹ (Fig. 2f, g and Supplementary Figs 6d, 7e, f). Altogether these observations indicate a sequential model whereby IL-15 first acts in concert with RA to induce IL-12 and IL-23 in MLN dendritic cells (Fig. 2d and data not shown). Along with RA, these inflammatory mediators then operate at the level of T cells to promote T_H1-cell differentiation and, when IL-6 is present¹², T_H17-cell differentiation. Although our finding of the adjuvant effect of RA is unexpected within the field of mucosal immunity, it is consistent with its usage as a beneficial proinflammatory adjuvant in anti-tumour immunity^{13,14}.

On the basis of our observations indicating that IL-15 and RA act primarily at the level of dendritic cells to disrupt intestinal immune homeostasis, we investigated which signalling pathway was critical for

¹Department of Medicine, University of Chicago, Chicago, Illinois 60637, USA. ²Mucosal Immunology Unit, Laboratory of Parasitic Diseases, National Institute of Allergy and Infectious Diseases, National Institutes of Health, Bethesda, Maryland 20892, USA. ³Immunology Graduate Group, University of Pennsylvania, Philadelphia, Pennsylvania 19104, USA. ⁴Department of Dermatology, Mayo Clinic College of Medicine, Rochester, Minnesota 55905, USA. ⁵Department of Immunology, Mayo Clinic College of Medicine, Rochester, Minnesota 55905, USA. ⁶US Department of Agriculture, Agricultural Research Service, Western Regional Research Center, 800 Buchanan Street, Albany, California 94710, USA. ⁷Metabolism Branch, National Cancer Institute, Bethesda, Maryland 20892-1374, USA. ⁸Department of Medicine, Division of Gastroenterology and Hepatology, Mayo Clinic College of Medicine, Rochester, Minnesota 55905, USA. ⁹Department of Pediatrics, University of Chicago, Chicago, Illinois 60637, USA. ¹⁰Department of Pathology, University of Chicago, Chicago, Illinois 60637, USA.

*These authors contributed equally to this work.

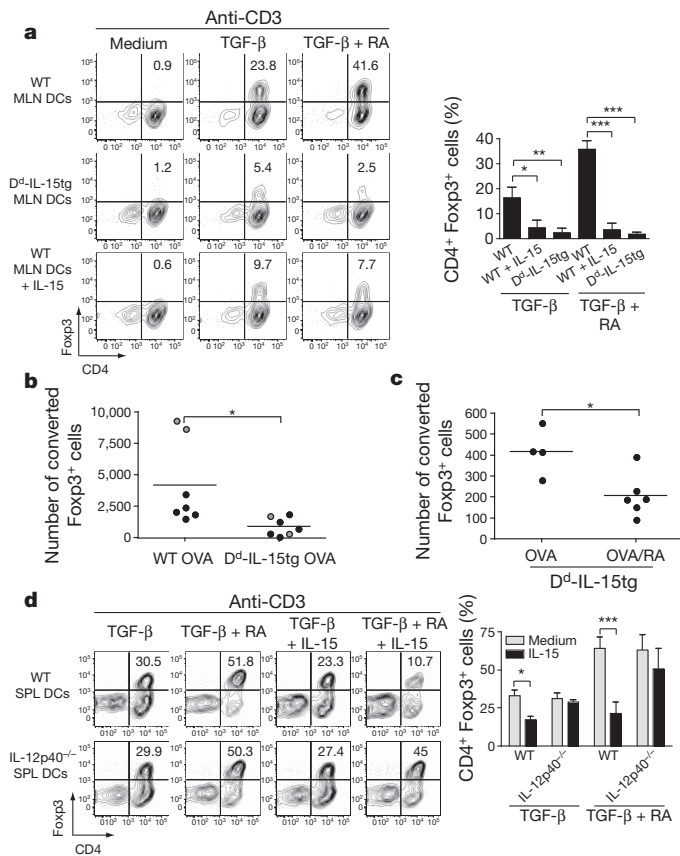


Figure 1 | IL-15-activated dendritic cells in the presence of retinoic acid prevent induction of Foxp3⁺ regulatory T cells. **a**, 10^5 CD4⁺ Foxp3⁻ T cells were cultured with 4×10^4 MLN dendritic cells (DCs) isolated from wild-type (WT) or D^d-IL-15 transgenic (D^d-IL-15tg) mice with anti-CD3 alone or combined with IL-15, TGF- β and RA. The percentages of Foxp3⁺ cells are shown. Graph depicts pooled data \pm s.e.m. ($n = 3$). **b**, RAG1^{-/-} OT-II CD45 congenic CD25⁻ CD4⁺ T cells were transferred into wild-type and D^d-IL-15 transgenic mice that were fed OVA in drinking water for five days (black dots) or by gavage every other day for 10 days (grey dots). T_{reg} cell conversion was assessed in the MLN by intracellular staining for Foxp3 and detected by flow cytometry. The absolute numbers of converted CD4⁺ Foxp3⁺ T cells are shown. Data are representative of two experiments performed independently. The decrease in the number of converted T_{reg} cells was associated with a significant decrease in the number of detectable transferred T cells in D^d-IL-15 transgenic mice (data not shown). This is probably due to the inability to detect inflammatory T cells that are more susceptible to cell death than Foxp3⁺ T_{reg} cells, which express anti-apoptotic factors. **c**, Ly5.2⁺ OT-II T cells were transferred into Ly5.1⁺ and D^d-IL-15tg-Ly5.1⁺ recipient mice that were fed OVA or OVA and RA five times during ten days. The absolute number of CD4⁺ Foxp3⁺ Ly5.2⁺ converted T cells in the MLN is shown as in **a**. **d**, As in **a**, CD4⁺ Foxp3⁻ T cells were cultured with splenic (SPL) dendritic cells isolated from wild-type and IL-12p40^{-/-} mice. The percentages of Foxp3⁺ cells are indicated. Graph depicts three pooled experiments \pm s.e.m. * $P < 0.05$, ** $P < 0.01$, *** $P < 0.001$ (unpaired Student's *t*-test).

their proinflammatory effects. IL-15 rapidly induced JNK phosphorylation in a dose-dependent manner in dendritic cells (Fig. 3a). The ability of RA to synergize with IL-15 to promote IL-12p70 (Fig. 3b) and IL-23 (Supplementary Fig. 8a) production by dendritic cells and significantly reduce T_{reg} differentiation (Fig. 3c) was paralleled by its ability to synergize with IL-15 to promote JNK phosphorylation (Fig. 3d). The co-adjuvant effects of RA were mediated via the RA receptor α (RAR α)/JNK signalling pathway (Fig. 3e–g and Supplementary Fig. 8b–d) and may involve previously reported¹⁵ non-genomic signalling effects of the RAR (Fig. 3h). We do not exclude the possibility that RA may signal *in vivo* via an alternative RAR such as RAR β , however. Of note, extracellular signal-regulated kinase

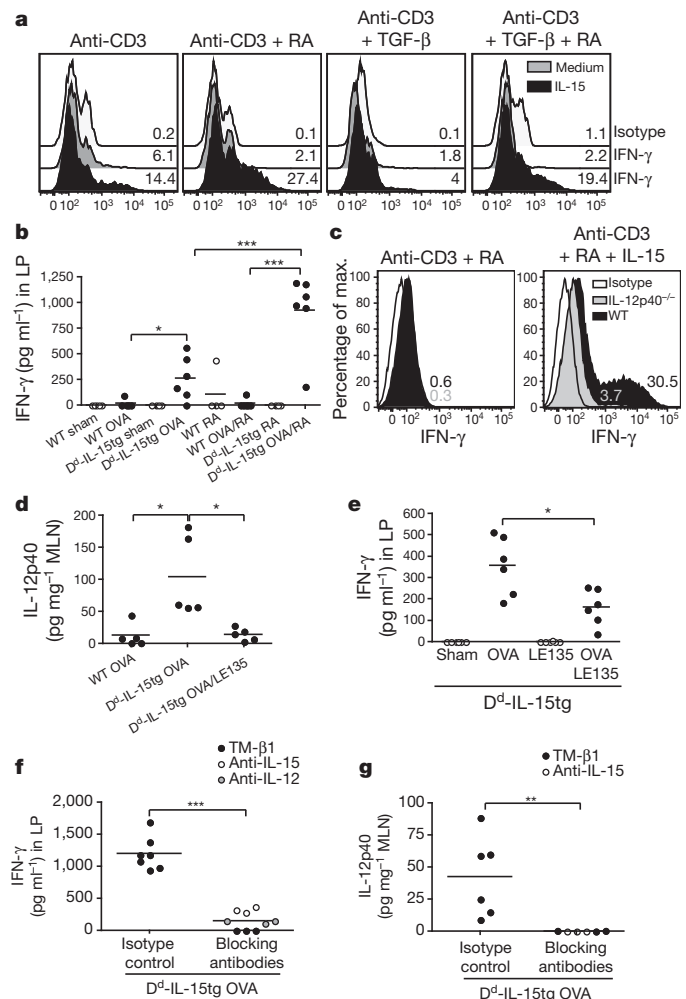


Figure 2 | Retinoic acid exerts an adjuvant effect on IL-15-mediated inflammatory T-cell responses. **a**, CD4⁺ T cells were cultured with wild-type splenic dendritic cells with the indicated cytokines. Representative histograms gated on CD4⁺ T cells show IFN- γ expression ($n = 5$). **b**, D^d-IL-15 transgenic and wild-type mice were fed PBS (sham), OVA, RA, or a mixture of OVA and RA. IFN- γ secretion by lamina propria (LP) cells re-stimulated for 24 h with OVA. The results are the means of triplicate samples obtained from two independent experiments. **c**, CD4⁺ T cells were cultured with splenic dendritic cells isolated from wild-type or IL-12p40^{-/-} mice as described in **a**. Intracellular staining for IFN- γ of gated CD4⁺ T cells is shown. Results are representative of two experiments. **d**, Levels of IL-12p40 in the MLN of wild-type and D^d-IL-15 transgenic mice fed OVA, or a mixture of OVA and the RAR antagonist LE135. The results are the means of triplicate samples obtained from two independent experiments. Similar results were obtained for IL-12p70 and IL-23 (data not shown). **e**, IFN- γ secretion by lamina propria cells isolated from D^d-IL-15 transgenic mice fed PBS (sham), OVA and LE135. The results are the means of triplicate samples obtained from two independent experiments. **f**, **g**, D^d-IL-15 transgenic mice were fed OVA and treated with blocking anti-IL-12p40, anti-IL-15 and TM β -1 (anti-IL-2R β) or isotype control monoclonal antibodies. The levels of IL-12p40 in the MLN (**f**) and IFN- γ in lamina propria cells re-stimulated overnight with OVA (**g**) were quantified. When anti-IL-15 and anti-IL-12 treatment experiments were performed in parallel, control mice received a mixture of corresponding isotype controls. Data represent two pooled experiments ($n = 6$ mice per group) except for the anti-IL-12 treatment ($n = 3$ individual mice). * $P < 0.05$, ** $P < 0.01$, *** $P < 0.001$ (unpaired Student's *t*-test).

(ERK; also known as MAPK1) and p38 MAPK (also known as MAPK14) were dispensable (Supplementary Fig. 8e).

An intriguing aspect of coeliac disease pathogenesis is how an inflammatory T_H1 response is induced against dietary gluten proteins. Owing to the large number of proline residues they contain, gluten

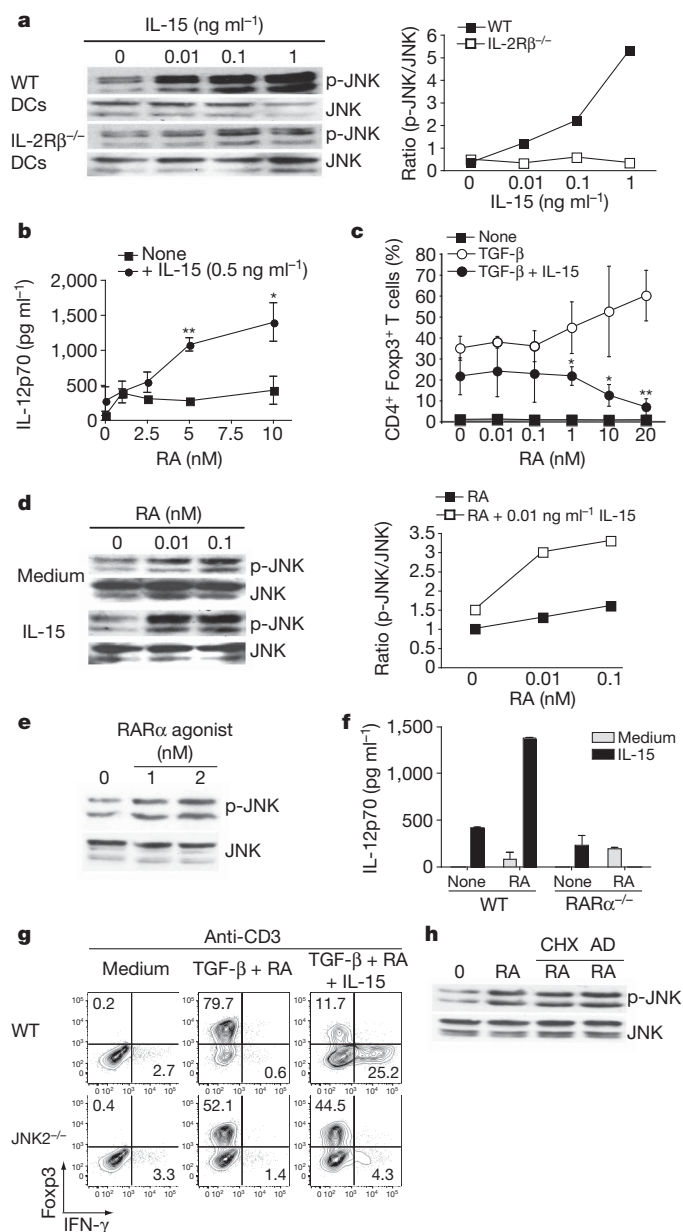


Figure 3 | Retinoic acid and IL-15 act in synergy to induce dendritic cells with proinflammatory properties in a JNK-dependent manner.

a, Concentration-dependent JNK phosphorylation in wild-type or IL-2Rβ^{-/-} bone-marrow-derived dendritic cells upon IL-15 stimulation analysed by western blot (left panel) and quantified (right panel). **b**, IL-12p70 secretion after overnight culture of wild-type splenic dendritic cells with increasing doses of RA, with and without IL-15. Results are mean values \pm s.e.m. ($n = 3$). **c**, CD4⁺ Foxp3⁺ T cells were cultured with wild-type splenic dendritic cells with anti-CD3 alone or combined with IL-15, TGF-β and increasing doses of RA. The percentages of Foxp3⁺ cells are shown. Graph depicts pooled data \pm s.e.m. ($n = 3$). **d**, Concentration-dependent JNK phosphorylation in wild-type bone-marrow-derived dendritic cells upon stimulation with IL-15 (0.01 ng ml⁻¹) and increasing doses of RA stimulation by western blot (left panel) and quantified (right panel). **e**, Concentration-dependent JNK phosphorylation in wild-type bone-marrow-derived dendritic cells upon stimulation with a RARα agonist (AM580). **f**, IL-12p70 secretion after overnight culture of wild-type and RARα^{-/-} bone-marrow-derived dendritic cells with IL-15 alone or combined with RA. Data are shown as means and s.e.m. ($n = 2$). **g**, CD4⁺ Foxp3⁺ T cells were cultured with splenic dendritic cells isolated from wild-type or JNK2^{-/-} mice with the indicated cytokines. The percentages of Foxp3⁺ and IFN-γ⁺ among CD4⁺ T cells are indicated. **h**, JNK phosphorylation in bone-marrow-derived dendritic cells pretreated with cyclohexamide (CHX) or actinomycin D (AD) before stimulation with 0.1 nM RA. Results are representative of two independent experiments. * $P < 0.05$, ** $P < 0.01$ (unpaired Student's t -test).

proteins are resistant to enzymatic degradation, leading to the generation of long peptides that are selectively presented in the gut by HLA-DQ2 or HLA-DQ8 molecules³. However, these observations alone fail to explain why 40% of the population expresses the coeliac-disease-associated HLA-DQ2 and HLA-DQ8 molecules, yet induction of gluten-specific inflammatory CD4⁺ and CD8⁺ T-cell responses^{16,17} occurs in less than 2% of these individuals³. In addition, patients with coeliac disease typically develop antibodies to gluten and to the enzyme tissue transglutaminase 2 (TG2; also known as TGM2)^{3,18}. To test the hypothesis that IL-15 overexpressed in the lamina propria may break tolerance to dietary gluten, D^d-IL-15 transgenic mice that have levels of IL-15 in the lamina propria comparable to those observed in the lamina propria of coeliac disease patients⁷ (compare Supplementary Fig. 3a and Fig. 4e) and lack IL-15 upregulation in intestinal epithelial cells (IECs) (Supplementary Fig. 3b), were crossed onto humanized HLA-DQ8 transgenic mice¹⁹ (DQ8-D^d-IL-15 transgenic mice). The presence of IFN-γ-producing anti-gliadin T cells (Fig. 4a and Supplementary Figs 9a, 10a, b, d, e) in conjunction with anti-gliadin (Fig. 4b) and anti-TG2 (Fig. 4c) antibodies and intraepithelial lymphocytosis (Fig. 4d) in DQ8-D^d-IL-15 transgenic mice fed gliadin, phenocopies an early stage of coeliac disease²⁰ where villous atrophy is absent. The normal intestinal morphology and intraepithelial lymphocytes (IELs) phenotype in D^d-IL-15 transgenic mice (data not shown) mirrors human observations indicating that IL-15 expression by IECs drives IELs to become fully licensed killer cells and induce villous atrophy^{3,21}. In accordance with human studies^{22,23}, anti-gliadin T_H17 cells were detected only at a very low frequency (Supplementary Figs 9b, c, 10c). Similar to the observations in OVA-fed D^d-IL-15 transgenic mice, the induction of inflammatory anti-gliadin T_H1 and T_H17 responses was dependent on (Supplementary Fig. 11) and promoted by RA (Fig. 4a and Supplementary Figs 9a–c, 10). Of note, gliadin-fed DQ8 transgenic mice had a slight induction in IFN-γ-producing T cells, which may be related to the reported innate effects of gliadin³. Supporting the hypothesis that IL-15 may disrupt tolerance to gluten in coeliac disease patients by inducing IL-12, the levels of IL-15 and IL-12p70 were correlated in the lamina propria of active coeliac disease patients (Fig. 4e). This discovery also gives a functional foundation to the identification of IL-12A as a genetic risk factor for coeliac disease by genome-wide association studies²⁴.

Our study reveals that in the presence of IL-15, RA has unforeseen co-adjuvant properties that induce T_H1 immunity to fed antigens (Fig. 4f). It indicates further that under infectious conditions associated with induction of IL-15 and IL-6 in the intestinal mucosa, RA will also promote T_H17 immunity. These observations caution against the use of vitamin A and RA for the treatment of autoimmunity and inflammatory intestinal disorders associated with high levels of IL-15. Indeed, a causal relationship between retinoids used for the treatment of acne and inflammatory bowel disease has been implicated in a subset of patients²⁵. Conversely, these findings provide an explanation as to why children suffering from vitamin A deficiency in developing countries²⁶ respond less efficiently to oral vaccines than children from developed countries^{26,27}, and also indicate that engineering mucosal vaccines that induce IL-15 may be beneficial owing to their ability to induce concomitantly protective IgA antibodies and T_H1 immunity.

More generally, our study supports the concept that there are no 'unconditional' suppressive factors, and that integration of tissue and exogenous signals determine the class of the immune response, which ultimately needs to be tailored to the tissue and the antigen. In line with the idea that the same proinflammatory factors trigger different immunological outcomes depending on the tissue in which they are induced, we found that the ability of IL-12 to inhibit T_{reg}-cell induction was blocked by butyrate, a metabolite produced by commensal bacteria present in the colon but not in the small bowel (data not shown).

One final aspect of our study is that we may have in hand a long-awaited physiopathologically relevant murine model mimicking the early stages of coeliac disease. This model is unique in that development

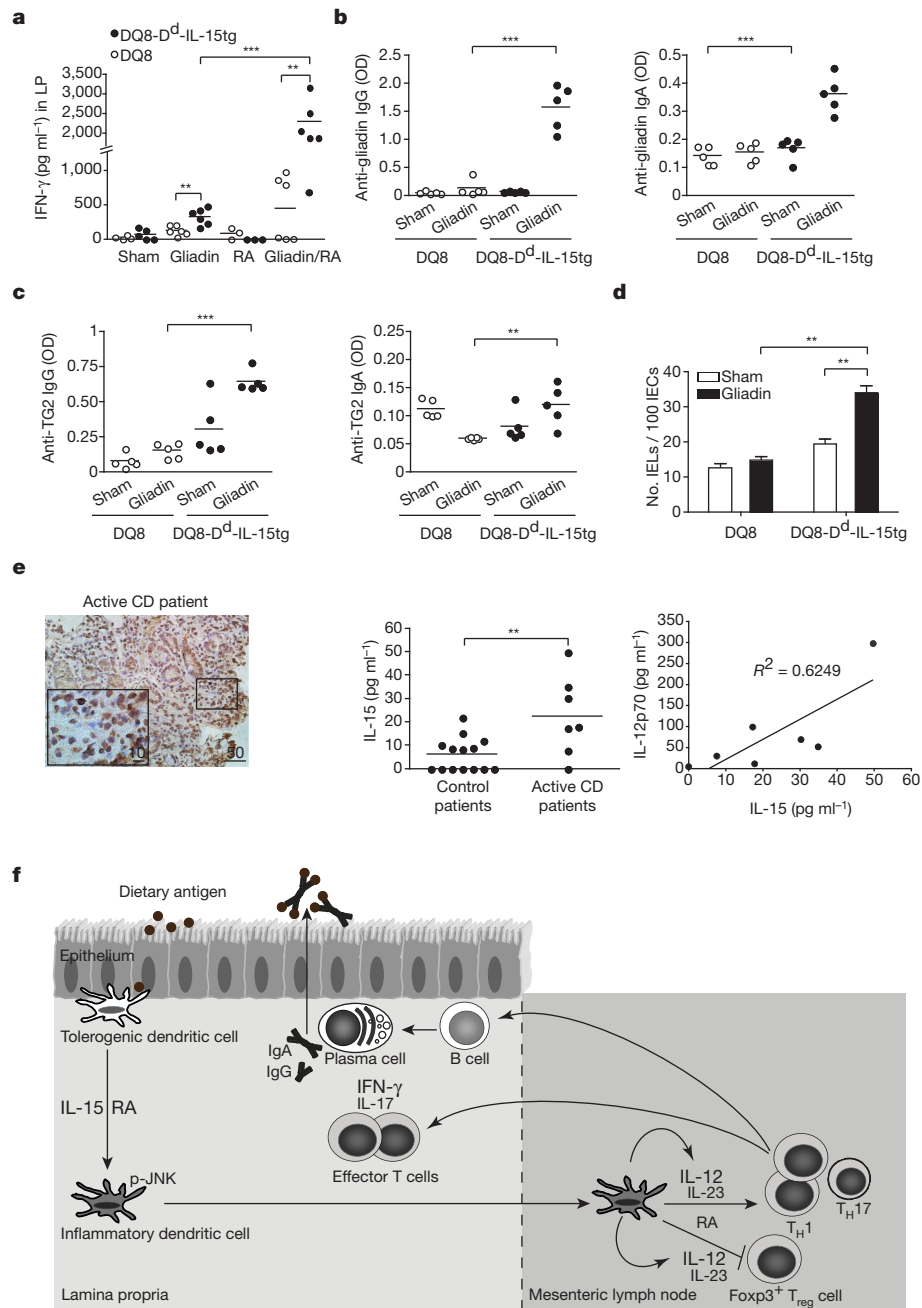


Figure 4 | DQ8-D^d-IL-15 transgenic mice fed gliadin mimic early stages of coeliac disease reflecting dysregulation in the adaptive immune response to gluten. **a–d**, DQ8 and DQ8-D^d-IL-15 transgenic mice were fed gliadin every other day for ten days. **a**, IFN- γ secretion by lamina propria cells after overnight culture with gliadin. **b**, **c**, Anti-gliadin IgG, anti-gliadin IgA, anti-TG2 IgG and anti-TG2 IgA titres from serum collected fifteen days after feeding. Antibody titres were detected by ELISA and calculated according to the formula: (OD_{450 nm} of sample – OD_{450 nm} of blank) \times serum dilution, where OD is optical density. **d**, Quantification of IELs among IECs in small intestines fifteen days after the last gliadin feeding. Two independent counts of IELs among 200 IECs were performed for each mouse. Data are shown as means and s.e.m. ($n = 3$ individual mice). Similar results were obtained in another set of experiments where mice were fed with α -gliadin. **e**, IL-15 and IL-12 expression in the lamina propria of coeliac disease patients. Immunohistochemical

stainings for IL-15 in gut tissue from an active coeliac disease (CD) patient (left panel). Lamina propria cells were harvested from biopsies obtained from control ($n = 14$) or active coeliac disease patients ($n = 7$) and assayed for levels of IL-15 and IL-12p70 by ELISA (middle and right panels). Equal concentration of total proteins was analysed for each sample. ** $P < 0.01$, *** $P < 0.001$ (unpaired Student's t -test). **f**, Proposed model for the co-adjuvant effects of RA and IL-15 in the intestinal mucosa. Under inflammatory conditions, the expression of the proinflammatory cytokine IL-15 is upregulated in the lamina propria of the small intestine. Through the synergistic action of IL-15 and RA, dendritic cells acquire the ability to release inflammatory cytokines, particularly IL-12 and IL-23. These inflammatory mediators then act in concert with RA to prevent the induction of Foxp3⁺ T_{reg} cells and drive T_H1 and potentially T_H17 polarization. In turn, inflammatory T cells may provide help to B cells to produce specific IgG and IgA antibodies.

of inflammatory anti-gluten immunity develops without microbial adjuvant or systemic immunization in immunologically competent mice with a polyclonal T-cell-receptor repertoire. However, further studies are warranted to establish whether the anti-TG2 antibodies are gluten dependent. Especially relevant to coeliac disease is the

identification of IL-15 in the lamina propria as a causative factor driving the differentiation of anti-gluten CD4⁺ and CD8⁺ T_H1 cells in the intestinal mucosa, resulting in the break of tolerance to gluten. Our observations may also explain why oral tolerance is disrupted in patients with inflammatory bowel disease²⁸ who also have dysregulated

IL-15 expression in the gut²⁹. Lastly, our results indicate that inhibiting IL-15 signalling may constitute a therapeutic intervention to restore mucosal tolerance to luminal antigens.

METHODS SUMMARY

All knockout and transgenic mice used in these studies are on the C57BL/6 background. D^d-IL-15 transgenic mice⁹ expressing IL-15 under the minimal MHC class I D^d promoter were used to perform the studies. To study the response to dietary gluten, D^d-IL-15 transgenic mice were crossed to humanized HLA-DQ8 mice¹⁹ that had been backcrossed for twelve generations to MHC class II^{-/-} C57BL/6 mice. To assess T_{reg} conversion *in vivo*, RAG^{-/-} OT-II CD25⁻ CD4⁺ T cells were adoptively transferred into congenic OVA-fed C57BL/6 and D^d-IL-15 transgenic mice. For *in vivo* experiments mice were fed OVA, α -gliadin, or crude gliadin. T_{reg} differentiation assays were performed using CD4⁺eGFP⁺ T cells isolated from Foxp3^{eGFP} reporter mice and MLN or splenic dendritic cells from IL-15 transgenic or wild-type mice stimulated with IL-15, TGF- β and RA. To assess the role of IL-2R β , JNK2 or IL-12p40 on T_{reg}- and T_H1-cell differentiation, dendritic cells deficient in these different factors were purified from the corresponding knockout mice. To assess the role of RA, experiments were performed either in the presence of the RAR antagonist (LE135), a RAR α agonist, or with RAR α ^{-/-} dendritic cells³⁰. JNK phosphorylation was analysed by western blot following dendritic-cell stimulation with IL-15 and RA. Lamina propria cells were isolated from intestinal biopsies of control and active coeliac disease patients to determine levels of IL-12 and IL-15 expression by ELISA.

Full Methods and any associated references are available in the online version of the paper at www.nature.com/nature.

Received 25 March 2010; accepted 19 January 2011.

Published online 9 February 2011.

1. Curotto de Lafaille, M. A. & Lafaille, J. J. Natural and adaptive Foxp3⁺ regulatory T cells: more of the same or a division of labor? *Immunity* **30**, 626–635 (2009).
2. Faria, A. M. & Weiner, H. L. Oral tolerance. *Immunol. Rev.* **206**, 232–259 (2005).
3. Jabri, B. & Sollid, L. M. Tissue-mediated control of immunopathology in coeliac disease. *Nature Rev. Immunol.* **9**, 858–870 (2009).
4. Coombes, J. L. *et al.* A functionally specialized population of mucosal CD103⁺ DCs induces Foxp3⁺ regulatory T cells via a TGF- β and retinoic acid-dependent mechanism. *J. Exp. Med.* **204**, 1757–1764 (2007).
5. Mora, J. R., Iwata, M. & von Andrian, U. H. Vitamin effects on the immune system: vitamins A and D take centre stage. *Nature Rev. Immunol.* **8**, 685–698 (2008).
6. Mucida, D. *et al.* Reciprocal TH17 and regulatory T cell differentiation mediated by retinoic acid. *Science* **317**, 256–260 (2007).
7. Mention, J. J. *et al.* Interleukin 15: a key to disrupted intraepithelial lymphocyte homeostasis and lymphomagenesis in coeliac disease. *Gastroenterology* **125**, 730–745 (2003).
8. Tagaya, Y., Bamford, R. N., DeFilippis, A. P. & Waldmann, T. A. IL-15: a pleiotropic cytokine with diverse receptor/signaling pathways whose expression is controlled at multiple levels. *Immunity* **4**, 329–336 (1996).
9. Fehniger, T. A. *et al.* Fatal leukemia in interleukin-15 transgenic mice follows early expansions in natural killer and memory phenotype CD8⁺ T cells. *J. Exp. Med.* **193**, 219–232 (2001).
10. Caretto, D. *et al.* Cutting edge: the Th1 response inhibits the generation of peripheral regulatory T cells. *J. Immunol.* **184**, 30–34 (2010).
11. Yokoyama, S. *et al.* Antibody-mediated blockade of IL-15 reverses the autoimmune intestinal damage in transgenic mice that overexpress IL-15 in enterocytes. *Proc. Natl Acad. Sci. USA* **106**, 15849–15854 (2009).
12. Bettelli, E. *et al.* Reciprocal developmental pathways for the generation of pathogenic effector TH17 and regulatory T cells. *Nature* **441**, 235–238 (2006).
13. Gao, Y., Camacho, L. H. & Mehta, K. Retinoic acid-induced CD38 antigen promotes leukemia cells attachment and interferon- γ /interleukin-1 β -dependent apoptosis of endothelial cells: implications in the etiology of retinoic acid syndrome. *Leuk. Res.* **31**, 455–463 (2007).
14. Mohy, M. *et al.* All-trans retinoic acid skews monocyte differentiation into interleukin-12-secreting dendritic-like cells. *Br. J. Haematol.* **122**, 829–836 (2003).

15. Rochette-Egly, C. & Germain, P. Dynamic and combinatorial control of gene expression by nuclear retinoic acid receptors (RARs). *Nucl. Recept. Signal.* **7**, e005 (2009).
16. Mazzarella, G. *et al.* Gliadin activates HLA class I-restricted CD8⁺ T cells in coeliac disease intestinal mucosa and induces the enterocyte apoptosis. *Gastroenterology* **134**, 1017–1027 (2008).
17. Nilsen, E. M. *et al.* Gluten specific, HLA-DQ restricted T cells from coeliac mucosa produce cytokines with Th1 or Th0 profile dominated by interferon gamma. *Gut* **37**, 766–776 (1995).
18. Dieterich, W. *et al.* Identification of tissue transglutaminase as the autoantigen of coeliac disease. *Nature Med.* **3**, 797–801 (1997).
19. Black, K. E., Murray, J. A. & David, C. S. HLA-DQ determines the response to exogenous wheat proteins: a model of gluten sensitivity in transgenic knockout mice. *J. Immunol.* **169**, 5595–5600 (2002).
20. Marsh, M. N. Gluten, major histocompatibility complex, and the small intestine. A molecular and immunobiologic approach to the spectrum of gluten sensitivity ('celiac sprue'). *Gastroenterology* **102**, 330–354 (1992).
21. Meresse, B. *et al.* Coordinated induction by IL15 of a TCR-independent NKG2D signaling pathway converts CTL into lymphokine-activated killer cells in coeliac disease. *Immunity* **21**, 357–366 (2004).
22. Monteleone, I. *et al.* Characterization of IL-17A-producing cells in coeliac disease mucosa. *J. Immunol.* **184**, 2211–2218 (2010).
23. Bodd, M. *et al.* HLA-DQ2-restricted gluten-reactive T cells produce IL-21 but not IL-17 or IL-22. *Mucosal Immunol.* **3**, 594–601 (2010).
24. Hunt, K. A. *et al.* Newly identified genetic risk variants for coeliac disease related to the immune response. *Nature Genet.* **40**, 395–402 (2008).
25. Reddy, D., Siegel, C. A., Sands, B. E. & Kane, S. Possible association between isotretinoin and inflammatory bowel disease. *Am. J. Gastroenterol.* **101**, 1569–1573 (2006).
26. Stephensen, C. B. & Livingston, K. A. Vitamin supplements and vaccines: maximize benefits, evaluate potential risks. *Am. J. Clin. Nutr.* **90**, 457–458 (2009).
27. Holmgren, J. & Czerkinsky, C. Mucosal immunity and vaccines. *Nature Med.* **11** (suppl.), S45–S53 (2005).
28. Kraus, T. A. *et al.* Failure to induce oral tolerance to a soluble protein in patients with inflammatory bowel disease. *Gastroenterology* **126**, 1771–1778 (2004).
29. Liu, Z. *et al.* IL-15 is highly expressed in inflammatory bowel disease and regulates local T cell-dependent cytokine production. *J. Immunol.* **164**, 3608–3615 (2000).
30. Hill, J. A. *et al.* Retinoic acid enhances Foxp3 induction indirectly by relieving inhibition from CD4⁺CD44^{hi} cells. *Immunity* **29**, 758–770 (2008).

Supplementary Information is linked to the online version of the paper at www.nature.com/nature.

Acknowledgements We thank coeliac disease patients and their family members as well as the University of Chicago Celiac Disease Center for supporting our research. We thank B. Sally, L. M. Sollid and M. Musch for critical reading of the manuscript. We thank C. Ciszewski, B. Uzunpamark, and N. Grandison for their help with the collection and analysis of human biopsies. We thank M. Constantinides for technical assistance with mice breeding. We also thank the University of Chicago flow cytometry facility for technical assistance. D^d-IL-15 transgenic mice were a gift from M. Caligiuri. RAR α -deficient mice were provided by P. Chambon and C. Benoist. This work was supported by the Digestive Disease Research Core Center at the University of Chicago (DK42086), R01 DK67180 (for B.J.), R01DK71003 (for J.A.M.), and the Crohn's and Colitis Foundation (for V.A.).

Author Contributions R.W.D. and V.A. provided input into the conceptual development and execution of the studies, as well as preparation of the manuscript. F.T., H.F.-P., J.A.H. and W.W. provided technical assistance and input into data analyses. J.A.M. and E.V.M. helped with the analysis of the humanized HLA-DQ8 transgenic mice. D.D.K. provided preparations of α -gliadin used in the feeding experiments. T.A.W. provided TM β -1 antibody, and Y.B. helped with the realization of T-cell transfer experiments and provided us with RAR α -deficient bone-marrow. C.S., S.K. and S.G. followed patients with coeliac disease and provided intestinal biopsies for cytokines analysis. Y.B., J.A.M., D.D.K. and T.A.W. participated in discussion and review of the manuscript. B.J. conceived the idea, wrote the manuscript and supervised all investigations.

Author Information Reprints and permissions information is available at www.nature.com/reprints. The authors declare no competing financial interests. Readers are welcome to comment on the online version of this article at www.nature.com/nature. Correspondence and requests for materials should be addressed to B.J. (bjabri@bsd.uchicago.edu).

METHODS

Mice. C57BL/6 wild-type, IL-12p40^{-/-} and IL-2Rβ^{-/-} mice were purchased from Jackson Laboratory. RAG^{-/-} OT-II mice were bred and housed in our animal facility. Foxp3^{eGFP} reporter mice were previously described³¹. JNK2^{-/-} mice were provided by A. Lin. D^d-IL-15 transgenic mice⁹ expressing IL-15 under the minimal MHC class I promoter were donated by M. Caligiuri and crossed onto Ly5.1⁺ C57BL/6 mice or crossed onto HLA-DQ8 mice¹⁹, which were previously bred on an MHC class II^{-/-} C57BL/6 background. All mice were kept under specific pathogen-free conditions at the animal facility of the University of Chicago. All mice were maintained on standard rodent chow; however, DQ8 and DQ8-D^d-IL-15 transgenic mice were maintained on gluten-free chow obtained from Research Diets (AIN-76A). All experiments were performed in accordance with the Institutional Biosafety Committee and the Institutional Care and Use Committee.

T-cell and dendritic-cell purification. For CD4⁺ eGFP⁻ T-cell isolation, spleens and peripheral lymph nodes were mechanically disrupted through a 70-μm cell strainer. CD4⁺ cells were isolated by positive immunoselection using CD4-(L3T4) microbeads (Miltenyi Biotec). Purified CD4 T cells were sorted for GFP expression using BD FACS Aria (BD Bioscience). In some experiments, purified CD4⁺ CD44^{lo} GFP⁻ T cells were sorted using the FACS Aria (BD Bioscience).

For dendritic-cell isolation, MLN and spleen were digested with 400 units ml⁻¹ collagenase type IV (Sigma-Aldrich). Cells were filtered, resuspended in 22.5% Optiprep (Sigma-Aldrich), overlaid with Hank's Buffered Saline (HBS) and centrifuged at 670g for 30 min. Dendritic cells were then enriched from the interface by positive immunomagnetic selection using anti-CD11c-coated beads according to the manufacturer's recommendations (Miltenyi Biotec). Purification yielded up to 90% CD11c⁺ cells.

In vitro T_{reg}-cell-differentiation assay. For dendritic-cell-free cultures, 2 × 10⁵ CD4⁺ eGFP⁻ T cells were cultured for three days with 1 μg ml⁻¹ plate-bound anti-CD3ε (eBioscience) and 2 μg ml⁻¹ anti-CD28 (eBioscience). For cultures containing dendritic cells, 1 × 10⁵ CD4⁺ eGFP⁻ T cells and 4 × 10⁴ purified splenic or MLN dendritic cells were cultured for three days with 1 μg ml⁻¹ plate-bound anti-CD3ε (eBioscience). Specified recombinant cytokines (listed below) or neutralizing antibodies were added to the cultures.

Recombinant cytokines used were: TGF-β (2 μg ml⁻¹); IL-15 (20 ng ml⁻¹); IL-12p70 (250 pg ml⁻¹ to 2 ng ml⁻¹); IL-23 (250 pg ml⁻¹ to 2 ng ml⁻¹) (R&D). Neutralizing IL-12p40 antibody (1 μg ml⁻¹) (R&D). RA (10 nM) (Sigma-Aldrich); RAR antagonist LE135 (1 μM) (Tocris Bioscience).

T_H17 polarization. T_H17 differentiation was performed as previously described³². Briefly, purified CD4⁺ T cells were stimulated with plate bound anti-CD3ε (1 μg ml⁻¹) and anti-CD28 (2 μg ml⁻¹) in the presence of 2 ng ml⁻¹ TGF-β, 20 ng ml⁻¹ IL-6 in the presence or absence of 10 nM RA and 20 ng ml⁻¹ IL-15.

Bone-marrow-derived dendritic-cell culture. Culture of bone-marrow-derived dendritic cells was performed as previously described³³. 10⁵ bone-marrow-derived dendritic cells from RARα^{-/-} (ref. 34) or wild-type mice were cultured overnight with IL-15 (20 ng ml⁻¹) and RA (10 nM) or IL-15 (20 ng ml⁻¹) and RARα agonist AM580 (10 nM) (Tocris).

Antibodies and flow cytometry. The following conjugated antibodies were purchased from eBioscience (San Diego): CD4 (GK1.5), CD11c (N418), CD8β (eBioH35-17.2), TCRβ (H57-597), CD45.1 (A20), CD45.2 (104), IFN-γ (XMG1.2), IL-17 (eBio17B7), Foxp3 (FJK-16a) and isotype controls. The following antibodies were purchased from BD Biosciences: CD44 (IM7), H-2D^b (KH95), H-2D^d (34-2-12), H-2K^b (AF6-88.5), CD45 (30-F11), CD13 (R3-242) and isotype controls. Cells were permeabilized with the CytoFix/CytoPerm kit (BD Biosciences) for intra-cytoplasmic detection of IFN-γ and IL-17 cytokines. Foxp3 fixation/permeabilization kit was used for intranuclear detection of Foxp3 (eBioscience). Flow cytometry analysis was performed with a FACSCanto (BD Biosciences).

Preparation of conditioned media and stimulation of T-cell cultures. 10⁵ splenic CD11c⁺ cells were stimulated with 10 nM RA, 1 μM LE135 and/or 20 ng ml⁻¹ rIL-15 and cultured for 24 h. One hundred and fifty microlitres of the supernatants were added to 2 × 10⁵ CD4⁺ Foxp3^{eGFP} T cells and differentiated on anti-CD3ε- and anti-CD28-coated plates for 72 h as described earlier.

IEL and lamina propria lymphocytes isolation. IELs³⁵ and lamina propria lymphocytes³⁶ were isolated as previously described using EDTA containing calcium-free media and collagenase VIII, respectively.

Cell signalling. Wild-type or IL-2Rβ^{-/-} dendritic cells were serum deprived overnight before stimulation with indicated doses of IL-15 or IL-15 and RA for 15 min. Preparation of cells and protein was performed as previously described³³. Before stimulation with IL-15, bone-marrow-derived dendritic cells were

pre-incubated for 30 min with various concentrations of MAP kinase inhibitors specific for MEK1/2 (PD98059), JNK (SP600125) and P38 (SB203580). In some experiments bone-marrow-derived dendritic cells were pre-incubated with cyclohexamide (10 μg ml⁻¹) (Sigma) or actinomycin D (10 μg ml⁻¹) (Sigma) for 15 min before stimulation with RA (0.1 ng ml⁻¹). Cells treated with DMSO were used as control for cells treated with MAP kinase inhibitors, cyclohexamide and actinomycin D.

T-cell transfers. CD4⁺ CD25⁻ T cells were purified from the spleen of RAG^{-/-} OT-II Ly5.1 or RAG^{-/-} OT-II Ly5.2 mice. 5 × 10⁵ cells were then transferred intravenously into naive Ly5.1 or Ly5.2 C57BL/6 and D^d-IL-15 transgenic mice. One day after transfer the mice received OVA dissolved in drinking water for five days or were administered 100 μg OVA every day for ten days by gavage as indicated in the figure legends. Mice were killed one day after the last feeding and intranuclear levels of Foxp3 were evaluated by flow cytometry in the transferred T cells.

Antigen feeding and immunization. Mice were fed by intragastric gavage using an 18-gauge round-tipped needle (Kent Scientific) with the following proteins: 100 μg ovalbumin (OVA) (Sigma-Aldrich), 100 μg recombinant α-gliadin³⁷ dissolved in water, or 20 mg crude gliadin (Sigma-Aldrich). In some experiments, mice were also fed with LE135 (1 μM) or RA (1 μM) resuspended in corn oil. Feeding occurred every other day for ten days. In some experiments, D^d-IL-15 transgenic mice were injected i.p. with 100 μg of anti-IL-12p40 (R&D systems, clone C17.8, rat IgG2a) at the time of feedings, or with 20 μg of anti-mouse IL-15 antibody (M96, Amgen, mouse IgG2a) once a week before and during feeding, or 200 μg of a purified anti-mouse CD122 antibody (clone TM-β1, rat IgG2b) twice a week before and during feeding.

One day following the last feeding, lamina propria and MLN cells were isolated and re-stimulated for 24 h or 48 h, respectively with 50 μg ml⁻¹ OVA or gliadin as noted in the figure legend. Supernatants were analysed for cytokines by ELISA.

Detection of cytokines by ELISA. Cell supernatants were evaluated for IL-23 (R&D), IL-12p70 (BD Biosciences), IL-6, (BD Biosciences), IFN-γ (BD Biosciences) and IL-17 (R&D). Tissue pellets from epithelium, lamina propria and MLN were quantified for IL-15 (eBioscience).

Anti-TG2 and anti-gluten ELISA. Serum was harvested 15 days after mice received last gluten feeding. ELISA assays were performed as previously described³⁸.

Patients and controls. Seven patients (age: 3–46 years) with active coeliac disease were investigated. Diagnosis of coeliac disease was based on the detection of anti-transglutaminase antibodies, the expression of HLA DQ2 or DQ8, villous atrophy, and clinical and histological response to a gluten-free diet. Fourteen individuals (age: 1–55 years) undergoing endoscopies and biopsies for functional intestinal disorders of non-coeliac origin were studied as controls. Lamina propria cells were isolated from biopsies or surgical specimens as previously described²³. All subjects gave written informed consent, and research was approved by the institutional review boards. Lamina propria cells were centrifuged and resuspended in 500 μl PBS. Protein concentration was determined and total protein was analysed for levels of IL-15 (eBioscience) and IL-12p70 (BD Biosciences).

Histology. Haematoxylin & eosin staining was performed on 5 μM 10% formalin-fixed paraffin-embedded intestinal sections. Slides were analysed under a Leica DM 2500 microscope with a HC PLAN APO ×20/0.7 NA and a HCX PL APO ×100/1.40–0.70 objectives.

- Fontenot, J. D. *et al.* Regulatory T cell lineage specification by the forkhead transcription factor Foxp3. *Immunity* **22**, 329–341 (2005).
- Veldhoen, M. *et al.* TGFβ in the context of an inflammatory cytokine milieu supports *de novo* differentiation of IL-17-producing T cells. *Immunity* **24**, 179–189 (2006).
- DePaolo, R. W. *et al.* Toll-like receptor 6 drives differentiation of tolerogenic dendritic cells and contributes to LcrV-mediated plague pathogenesis. *Cell Host Microbe* **4**, 350–361 (2008).
- Hill, J. A. *et al.* Retinoic acid enhances Foxp3 induction indirectly by relieving inhibition from CD4⁺ CD44^{hi} cells. *Immunity* **29**, 758–770 (2008).
- Park, S. H. *et al.* Selection and expansion of CD8α/α¹ T cell receptor α/β¹ intestinal intraepithelial lymphocytes in the absence of both classical major histocompatibility complex class I and nonclassical CD1 molecules. *J. Exp. Med.* **190**, 885–890 (1999).
- Lefrançois, L. & Lycke, N. Isolation of mouse small intestinal intraepithelial lymphocytes, Peyer's patch, and lamina propria cells. *Curr. Protoc. Immunol.* doi:10.1002/0471142735.im0319s17 (2001).
- Bernardin, J. E., Kasarda, D. D. & Mecham, D. K. Preparation and characterization of α-gliadin. *J. Biol. Chem.* **242**, 445–450 (1967).
- Marietta, E. *et al.* A new model for dermatitis herpetiformis that uses HLA-DQ8 transgenic NOD mice. *J. Clin. Invest.* **114**, 1090–1097 (2004).

Using induced pluripotent stem cells to investigate cardiac phenotypes in Timothy syndrome

Masayuki Yazawa¹, Brian Hsueh^{1†}, Xiaolin Jia^{1†}, Anca M. Pasca^{1†}, Jonathan A. Bernstein², Joachim Hallmayer³ & Ricardo E. Dolmetsch¹

Individuals with congenital or acquired prolongation of the QT interval, or long QT syndrome (LQTS), are at risk of life-threatening ventricular arrhythmia^{1,2}. LQTS is commonly genetic in origin but can also be caused or exacerbated by environmental factors^{1,3}. A missense mutation in the L-type calcium channel $\text{Ca}_v1.2$ leads to LQTS in patients with Timothy syndrome^{4,5}. To explore the effect of the Timothy syndrome mutation on the electrical activity and contraction of human cardiomyocytes, we reprogrammed human skin cells from Timothy syndrome patients to generate induced pluripotent stem cells, and differentiated these cells into cardiomyocytes. Electrophysiological recording and calcium (Ca^{2+}) imaging studies of these cells revealed irregular contraction, excess Ca^{2+} influx, prolonged action potentials, irregular electrical activity and abnormal calcium transients in ventricular-like cells. We found that roscovitine, a compound that increases the voltage-dependent inactivation of $\text{Ca}_v1.2$ (refs 6–8), restored the electrical and Ca^{2+} signalling properties of cardiomyocytes from Timothy syndrome patients. This study provides new opportunities for studying the molecular and cellular mechanisms of cardiac arrhythmias in humans, and provides a robust assay for developing new drugs to treat these diseases.

The risk of sudden death due to genetic and drug-induced LQTS is a major concern for patients, clinicians and pharmaceutical companies. Genetic LQTS has an estimated prevalence of 1 in 7,000 individuals and results from mutations in at least 10 genes^{1,4,5,9–12}. Drug-induced LQTS is a side effect of many approved drugs and is a common cause of drug failure in clinical trials. Despite our knowledge of many of the genes that cause LQTS, the mechanisms that underlie the disease in humans are incompletely understood. Mouse models of human LQTS have proved to be problematic because the mouse resting heart rate is approximately tenfold faster than that of humans and therefore mouse cardiomyocytes have different electrical properties than their human counterparts. Therefore it is essential to develop models of LQTS that use human cardiomyocytes.

$\text{Ca}_v1.2$ is the main L-type channel in the mammalian heart and is essential for generating the cardiac action potential and for excitation contraction coupling^{13–15}. Ca^{2+} influx through L-type channels in the plasma membrane causes Ca^{2+} release through ryanodine receptors in the sarcoplasmic reticulum, leading to muscle contraction^{14–17}. A single amino acid substitution in exon 8a of *CACNA1C*, the gene encoding $\text{Ca}_v1.2$ in humans, causes Timothy syndrome, a disorder characterized by LQTS, syndactyly (webbing of fingers and toes), immune deficiency and autism⁴. Exon 8a is an alternatively spliced exon of $\text{Ca}_v1.2$, and the Timothy syndrome mutation is a glycine to arginine (G to R) substitution that impairs inactivation of the channel^{4,5,18,19}. $\text{Ca}_v1.2$ channels undergo both voltage-dependent inactivation and Ca^{2+} -dependent inactivation, and the G406R mutation severely impairs voltage-dependent inactivation and subtly affects Ca^{2+} -dependent inactivation. Precisely how this leads to LQTS or arrhythmias in humans is not known.

To generate induced pluripotent stem cells (iPSCs) from Timothy syndrome patients, we first obtained dermal fibroblasts from two patients by punch biopsy. We confirmed the presence of the Timothy syndrome mutation in these cells by sequencing the genomic DNA using two primer sets that recognize exon 8a in *CACNA1C* (ref. 4). We next reprogrammed the fibroblasts to generate iPSCs using four retroviruses containing *SOX2*, *OCT3/4* (also known as *POU5F1*), *KLF4* and *MYC* (refs 20, 21). Three to four weeks after the infection, we picked human embryonic stem cell (hESC)-like colonies based on their morphology and expanded them for characterization and *in vitro* differentiation into cardiac cells (Fig. 1a). We generated a total 16 iPSC lines from two Timothy syndrome patients, and 10 control lines from two unrelated individuals without Timothy syndrome.

We selected five Timothy syndrome and five control iPSC lines for further characterization and generation of cardiomyocytes (Supplementary Table 1). We used genomic sequencing to confirm that the Timothy syndrome iPSCs preserved the Timothy syndrome mutation (Supplementary Fig. 1), and we mapped the integration sites of the retroviruses using nested polymerase chain reaction (PCR)²² (Supplementary Table 1). We found that all the lines had independent retroviral insertion sites and that the sites did not occur in the coding region of any gene. To examine whether the iPSC lines express human embryonic stem cell markers, we used immunocytochemistry to look for *NANOG* and *TRA2-49-6E* (alkaline phosphatase) expression, and found that all of the lines expressed these markers (Supplementary Fig. 2). We also used reverse transcriptase PCR (RT-PCR) to confirm that iPSCs expressed *NANOG* and *Rex-1* and that they had silenced the exogenous genes that were used for reprogramming (Supplementary Fig. 3). In addition, we performed genome-wide microarray analyses of the cells and found that the gene expression patterns of iPSCs closely resembled those of hESCs and not of fibroblasts or neurons (GEO database <http://www.ncbi.nlm.nih.gov/geo/query/acc.cgi?token=jncfcucugewaha&acc=GSE25542>). We also karyotyped the iPSC lines to ensure that they did not have large chromosomal abnormalities (Fig. 1b and Supplementary Table 1) and injected them into immunodeficient mice to verify that they could generate teratomas. Both control and Timothy syndrome iPSCs were able to form tissues derived from all three germ layers including neural tissues (ectoderm), cartilage (mesoderm) and gut-like epithelium (endoderm) (Supplementary Fig. 2 and Supplementary Table 1), indicating that the iPSCs that we have generated are pluripotent.

To generate human cardiomyocytes from iPSCs, we first prepared embryoid bodies (EBs) from five control and five Timothy syndrome iPSC lines. After one week in suspension culture (day 7), we placed ~80 EBs onto gelatin-coated 100-mm dishes to allow EBs to attach. Thirty days (day 37) after plating, we observed that ~0.5–20% of the EBs showed rhythmic contractions (Fig. 1c). There were no significant differences in the number of contracting EBs formed from control and Timothy syndrome iPSC lines (data not shown). RT-PCR

¹Department of Neurobiology, Stanford University School of Medicine, Stanford, California 94305, USA. ²Department of Pediatrics, Stanford University School of Medicine, Stanford, California 94305, USA.

³Department of Psychiatry & Behavioral Science, Stanford University School of Medicine, Stanford, California 94305, USA. †Present addresses: Department of Chemistry, Princeton University, Princeton, New Jersey 08544, USA (B.H.); Baylor College of Medicine, Houston, Texas 77030, USA (X.J.); Lucile Packard Children's Hospital, Stanford University, Palo Alto, California 94304, USA (A.M.P.).

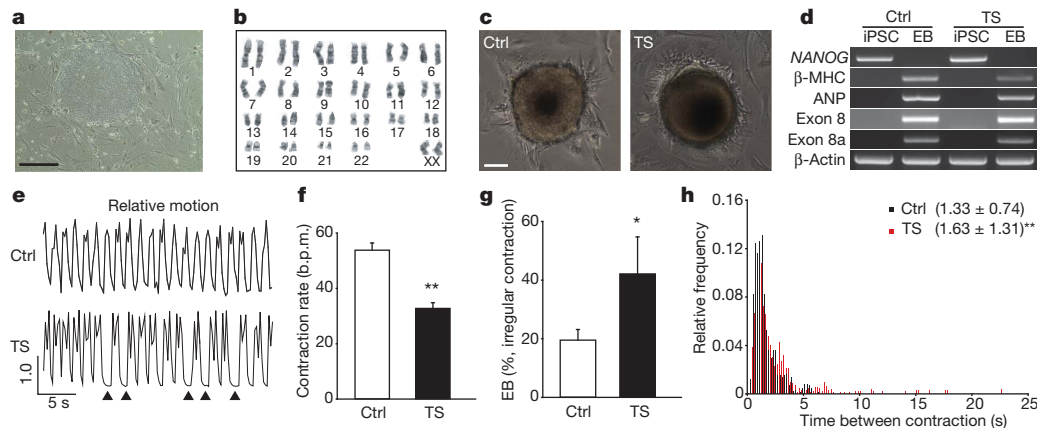


Figure 1 | Generation of cardiomyocytes from control and Timothy syndrome iPSCs. **a**, Phase contrast images of iPSC line (9862-61) derived from a Timothy syndrome patient. Scale bar, 400 μ m. **b**, Karyogram of Timothy syndrome iPSCs (7643-5). **c**, Images of spontaneously contracting embryoid bodies (EBs) generated from control (Ctrl, left) and Timothy syndrome iPSCs (TS, right). Scale bar, 100 μ m. **d**, Examination of pluripotent and cardiac gene expression using RT-PCR with primer sets for a pluripotent gene (*NANOG*), cardiac markers (β -MHC and ANP), $\text{Ca}_v1.2$ channels (exon 8 and 8a) and a housekeeping gene (β -actin). **e**, Relative motion of contracting control and Timothy syndrome EBs. Arrowheads show missing contractions.

analysis revealed that the spontaneously contracting EBs expressed cardiac markers (Fig. 1d) and both exons 8 and 8a of *CACNA1C* but not *NANOG*, indicating that these contain cardiomyocytes but not iPSCs.

To examine the contractile properties of cardiomyocytes we collected time-lapse images of spontaneously contracting EBs and analysed their movement using image analysis software (Supplementary Movies 1–4 and Fig. 1e, f). We collected movies of 113 EBs derived from five Timothy syndrome iPSC lines and compared them to EBs derived from the five control lines. Control EBs contracted at approximately 60 beats per minute (b.p.m.), similar to the resting heart rate in humans, whereas the Timothy syndrome cardiomyocytes contracted at only ~ 30 b.p.m. Contraction of the Timothy syndrome EBs was significantly more irregular than contraction of control cardiomyocytes (Fig. 1e, g). This was reflected in the broader distribution of inter-contraction intervals in Timothy syndrome EBs relative to those of controls (Fig. 1h). These results indicate that contracting EBs from multiple iPSC lines from two Timothy syndrome patients have disease-specific defects.

To characterize the underlying defects in cardiomyocytes from Timothy syndrome patients further, we dissociated contracting EBs into single cells. We stained these cells with antibodies that recognize the cardiac markers α -actinin, which is present at the Z-line of the sarcomere, and cardiac troponin I, which is a cardiac-specific myofilament protein (Fig. 2a and Supplementary Fig. 4). More than 65% of the cells from the beating EBs expressed both proteins and had well-organized sarcomeres. There were no differences in the staining pattern of Timothy syndrome and control cardiomyocytes. We next used whole-cell patch clamping to determine whether the Timothy syndrome mutation altered L-type channel voltage-dependent inactivation in human cardiomyocytes. We measured L-type-channel-generated currents using Ba^{2+} as the charge carrier and found that the L-type channel current in Timothy syndrome cardiomyocytes had significantly reduced voltage-dependent inactivation compared to control cells (Fig. 2b–e and Supplementary Fig. 4). This was apparent both from the increased amplitude of the residual current after a 350-ms depolarization and from increased current elicited by a 300-ms test pulse after a 2-s depolarizing pulse to different voltages. In contrast, there was no difference between control and Timothy syndrome

cardiomyocytes in the current–voltage relationship or the peak amplitudes of Ba^{2+} currents (Fig. 2d). These results are broadly consistent with the properties of the Timothy syndrome mutant channel observed in heterologous expression systems^{4,18,19}.

Ca^{2+} influx through L-type channels contributes to the plateau phase of the cardiac action potential, so we asked whether the shape or duration of the action potential in cardiomyocytes was altered by the Timothy syndrome mutation. Using current-clamp recording, we examined spontaneous action potentials in control and Timothy syndrome cardiomyocytes. Because human cardiomyocyte populations generated from iPSCs contain nodal-like, ventricular-like and atrial-like myocytes^{23,24}, we harvested the mRNA from each patch-clamped cardiomyocyte and used single-cell RT-PCR of cardiac ventricular myosin light chain 2v (*MLC2v*, Supplementary Fig. 5) to identify ventricular cells. We found that ventricular-like myocytes from Timothy syndrome patients had action potentials that were three times as long as those of control cells (Fig. 2f, g). In addition, the Timothy syndrome cardiomyocytes exhibited a large number of depolarizing events that failed to trigger a full action potential. These depolarizations were similar to the delayed afterdepolarizations (DADs) that arise after ectopic release of Ca^{2+} from the sarcoplasmic reticulum and which are associated with cardiac arrhythmias (Fig. 2f, h). In contrast we did not find significant differences in the action potential properties of nodal-like and atrial-like myocytes from control and Timothy syndrome patients (Supplementary Fig. 5). These findings indicate that ventricular cardiomyocytes derived from Timothy syndrome iPSCs are defective and provide a possible cellular basis for LQTS and arrhythmia in these patients.

$\text{Ca}_v1.2$ channels have a crucial role in activating Ca^{2+} -induced Ca^{2+} release from the sarcoplasmic reticulum but the effect of altering $\text{Ca}_v1.2$ inactivation on this process is not known. We therefore asked how the Timothy syndrome mutation affects Ca^{2+} signalling in Timothy syndrome cardiomyocytes. We used a confocal microscope to perform fast line-scan imaging of human cardiomyocytes loaded with the Ca^{2+} indicator Fluo-4. The Ca^{2+} elevations in spontaneously contracting Timothy syndrome cardiomyocytes were more irregular than those of control cardiomyocytes (Fig. 3 and Supplementary Fig. 6). In addition, the Timothy syndrome mutation led to significantly larger and more prolonged Ca^{2+} elevations, indicating that channel

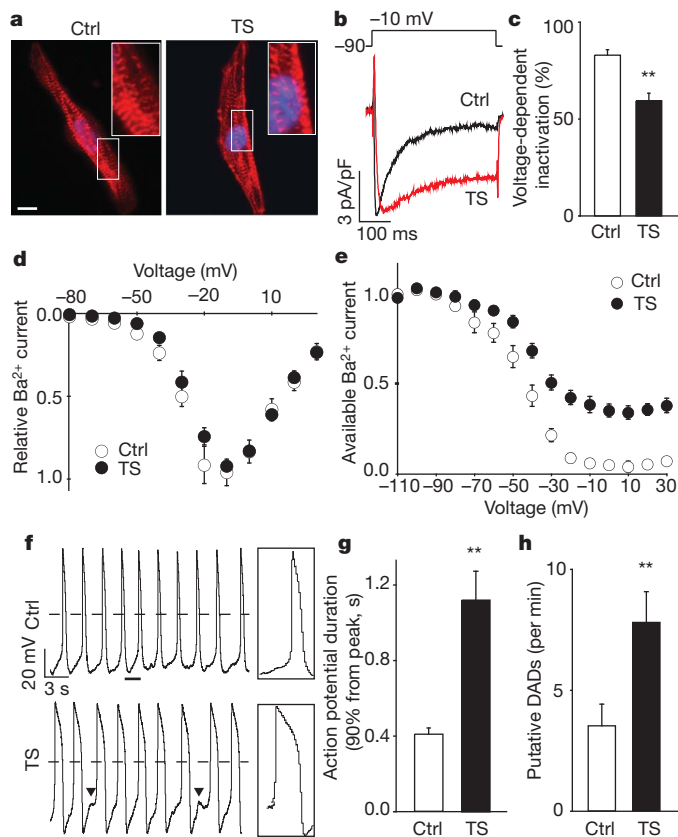


Figure 2 | Electrophysiological features of Timothy syndrome cardiomyocytes. **a**, Immunocytochemistry of human cardiomyocytes generated from control (left) and Timothy syndrome iPSCs (right) using anti- α -actinin antibodies (red). The nuclei (blue) are marked by Hoechst staining. Insets show high magnification images of the sarcomeres. Scale bar, 10 μm . **b**, Voltage-clamp recording of Ba^{2+} currents in control (black) and Timothy syndrome (red) cardiomyocytes show a defect in voltage-dependent channel inactivation after a voltage pulse from -90 to -10 mV. **c**, Voltage-dependent inactivation in control and Timothy syndrome cardiomyocytes 350 ms after the start of the pulse (** $P < 0.01$; Student's t -test). **d**, The I-V relationship of Timothy syndrome (filled circles) and control (open circles) Ca^{2+} currents (mean \pm s.e.m.) are statistically identical. There were no significant differences in the peak amplitude of Ba^{2+} currents between control and Timothy syndrome cardiomyocytes (data not shown). **e**, Ba^{2+} current in control and Timothy syndrome myocytes stimulated with a test pulse to $+10$ mV after a family of prepulses from -110 to $+30$ mV in 10-mV increments (raw traces in Supplementary Fig. 4c; control, $n = 23$ cells in 4 lines; Timothy syndrome, $n = 19$ in 4 lines, mean \pm s.e.m.). **f**, Spontaneous action potentials in control and Timothy syndrome ventricular-like myocytes measured in current-clamp mode. Boxes show the regions indicated by underlines at an expanded timescale. Arrowheads show putative delayed afterdepolarizations (DADs). Dashed lines show 0 mV. **g**, Action potential duration in Timothy syndrome and control ventricular cardiomyocytes. The expression of the ventricular marker, MLC2v , was confirmed with single-cell RT-PCR immediately after whole-cell patch recording (Supplementary Fig. 5). **h**, Putative DADs in Timothy syndrome and control ventricular-like cardiomyocytes (control, $n = 22$ cells in 4 lines; Timothy syndrome, $n = 14$ in 4 lines, mean \pm s.e.m.). Statistical analyses were performed with Student's t -test (** $P < 0.01$).

inactivation is important for maintaining the timing and the amplitude of the ventricular Ca^{2+} release.

The finding that cardiomyocytes from Timothy syndrome patients have disease-specific electrical defects indicates that they might be a useful system for testing possible therapeutic compounds. As a proof of principle, we investigated whether roscovitine, a cyclin-dependent kinase inhibitor that increases voltage-dependent inactivation in HEK 293 cells expressing $\text{Ca}_v1.2$ channels^{6–8}, could rescue the phenotypes of Timothy syndrome cardiomyocytes. We examined the effect of

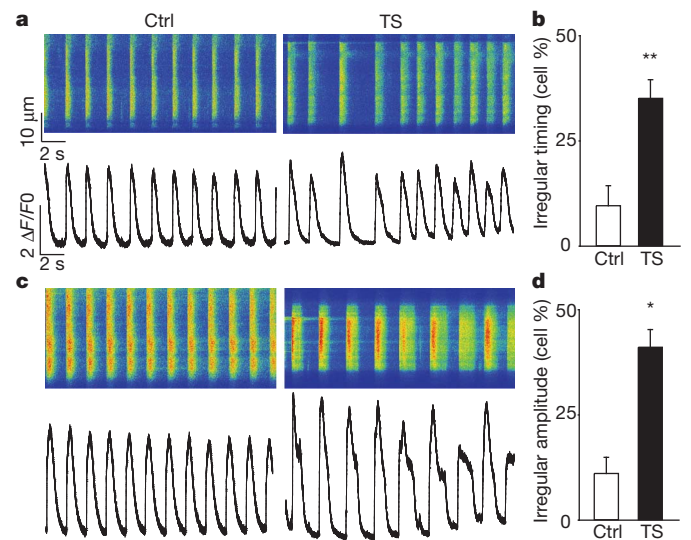


Figure 3 | Ca^{2+} signalling in Timothy syndrome and control cardiomyocytes. **a**, **c**, Representative line-scan images (top) and spontaneous Ca^{2+} transients (bottom) in control (left) and Timothy syndrome cardiomyocytes (right). **b**, **d**, Timothy syndrome cardiomyocytes showed more irregular timing (**b**) and amplitude (**d**) of spontaneous Ca^{2+} transients compared to control cells (see Supplementary Fig. 6 and Methods for details about the analysis; control, $n = 102$ cells in 4 lines; Timothy syndrome, $n = 149$ in 4 lines, mean \pm s.e.m.). Statistical analyses were performed with Student's t -test (* $P < 0.05$, ** $P < 0.01$).

three different concentrations of roscovitine (10, 33.3 and 100 μM) on the timing and amplitude of spontaneous Ca^{2+} transients in Timothy syndrome cardiomyocytes. Treatment with 100 μM roscovitine completely eliminated contractions but 33.3 μM roscovitine significantly reduced both the irregular timing and amplitude of Ca^{2+} transients (Fig. 4a, b and Supplementary Fig. 7). Washing out roscovitine partially restored the irregular Ca^{2+} transients in Timothy syndrome cardiomyocytes but this effect did not reach significance^{6–8}.

To determine if roscovitine rescues the electrophysiological properties of Timothy syndrome cardiomyocytes, we used whole-cell patch clamping to measure $\text{Ca}_v1.2$ currents and action potentials in Timothy syndrome cardiomyocytes in the presence and absence of roscovitine. Roscovitine significantly increased $\text{Ca}_v1.2$ voltage-dependent inactivation in Timothy syndrome cardiomyocytes (Fig. 4c, d) but had only a mild effect on control cardiomyocytes (Supplementary Fig. 8). Roscovitine also reduced the duration of action potentials in Timothy syndrome cardiomyocytes and decreased the frequency of abnormal depolarizing events (Fig. 4e, f). These results indicate that cardiomyocytes from patients with LQTS can be used to screen potential drugs, and suggest that drugs related to roscovitine might be valuable tools for treating Timothy syndrome and other cardiac arrhythmias.

We have developed a new *in vitro* model for studying cardiac arrhythmias that has important advantages relative to existing approaches²⁵. In contrast to mouse cardiomyocytes, iPSC-derived EBs spontaneously contract at a rate that is similar to that of the human heart, and single cells derived from these EBs have structural and electrical properties that are similar to those of cardiomyocytes from human patients. Importantly, cardiomyocytes derived from five different iPSC lines from two independent patients with LQTS had cellular defects that are consistent with the cardiac defects of the patients. The EBs from Timothy syndrome patients contracted slowly relative to control EBs, consistent with bradycardia in many Timothy syndrome patients. Ventricular cardiomyocytes from Timothy syndrome patients also had prolonged action potentials that probably delay the repolarization of the heart and lead to LQTS. Both the isolated cardiomyocytes and the EBs contracted arrhythmically and the cardiomyocytes had

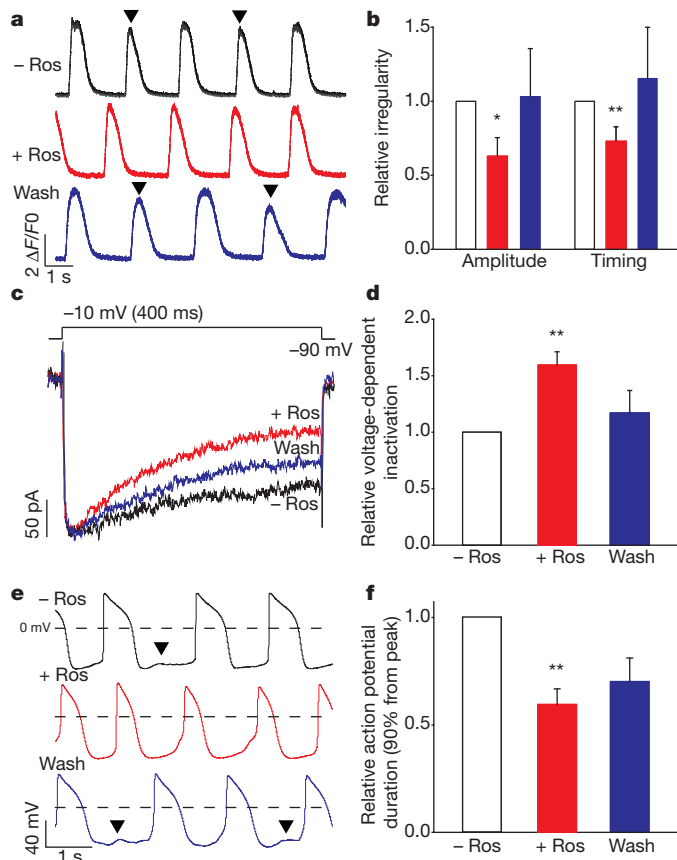


Figure 4 | Roscovitine rescues the cellular phenotypes of Timothy syndrome cardiomyocytes. **a**, Spontaneous Ca^{2+} transients in Timothy syndrome cardiomyocytes before (black) and during treatment with 33.3 μM roscovitine (red) as well as after wash-out (blue). Arrowheads show irregular Ca^{2+} elevations. **b**, Effects of roscovitine on the relative irregularity of the amplitude and timing of the spontaneous Ca^{2+} transients in Timothy syndrome cardiomyocytes ($n = 8$ cells in 2 lines, $*P < 0.05$, $**P < 0.01$, mean \pm s.e.m.). **c**, Ba^{2+} currents in Timothy syndrome cardiomyocytes recorded in voltage-clamp mode before (black) during (red) and after (blue) treatment with 33.3 μM roscovitine. Roscovitine promoted inactivation of currents in Timothy syndrome cardiomyocytes. **d**, Effects of roscovitine on $\text{Ca}_v1.2$ voltage-dependent inactivation in cardiomyocytes ($n = 5$ cells in 2 lines, $**P < 0.01$, mean \pm s.e.m.). **e**, Spontaneous action potentials recorded in current-clamp recording before, during and after treatment with roscovitine. Arrowheads show putative DADs. **f**, Roscovitine prevented action potential prolongation observed in Timothy syndrome cardiomyocytes ($n = 8$ cells in 2 lines, $**P < 0.01$, mean \pm s.e.m.).

frequent depolarizing events that failed to produce action potentials and were similar to DADs.

The phenotype of Timothy syndrome cardiomyocytes stands in contrast to the phenotype of cardiomyocytes from patients with LQTS1 (ref. 12). Only ventricular cardiomyocytes from Timothy syndrome patients had prolonged action potentials, whereas both ventricular- and atrial-like cardiomyocytes from LQTS1 had this phenotype. Furthermore, arrhythmias and delayed depolarizations were observed in spontaneously beating Timothy syndrome cardiomyocytes whereas they could only be elicited in LQTS1 cardiomyocytes by stimulation with isoproterenol. Although it is difficult to link these features to the torsade de points and to ventricular fibrillations in Timothy syndrome patients, these findings set the stage for the development of more sophisticated models of LQTS. Finally, this study demonstrates that iPSC-derived cardiomyocytes are a useful platform for identifying drug candidates. Roscovitine restored the action potential duration in Timothy syndrome cardiomyocytes and prevented the occurrence of arrhythmias. Even though roscovitine has

other targets²⁶ it could be a useful lead compound for the development of new types of antiarrhythmics.

METHODS SUMMARY

Control and Timothy syndrome iPSC lines were generated using retroviral infection with pMXs-SOX2, pMXs-OCT3/4, pMXs-MYC and pMXs-KLF4 expression plasmids (Addgene) generated by S. Yamanaka's group²⁰. The iPSCs were cultured on irradiated DR4 mouse embryonic fibroblast feeders using standard ES media with 10–15 ng ml⁻¹ bFGF (R & D Systems), and cells were passaged with dispase (3 unit ml⁻¹, Invitrogen). The G1216A substitution in exon 8a was detected by sequencing of PCR products from DNA harvested from fibroblasts and iPSC lines using primers for human $\text{Ca}_v1.2$ exon 8a. Immunocytochemistry, RT-PCR, microarray, karyotyping and teratoma formation assay were performed using standard protocols. For *in vitro* generation of cardiomyocytes, embryoid bodies were cultured with Wnt3a (100 ng ml⁻¹, R&D Systems)²⁷. Whole-cell patch clamp recordings in single cardiomyocytes were conducted using standard methods. Live-cell Ca^{2+} imaging was performed in single cardiomyocytes loaded with 5 μM Fluo-4 AM and 0.02% Pluronic F-127 (Molecular Probes) using fast line scanning (1.92 ms/line) on a confocal microscope (LSM 510 Meta, Carl Zeiss) with a $\times 63$ lens (NA = 1.4). R-roscovitine was obtained from Sigma-Aldrich.

Full Methods and any associated references are available in the online version of the paper at www.nature.com/nature.

Received 9 November 2010; accepted 21 January 2011.

Published online 9 February 2011.

- Keating, M. T. The long QT syndrome. A review of recent molecular genetic and physiologic discoveries. *Medicine* **75**, 1–5 (1996).
- Huikuri, H. V., Castellanos, A. & Myerburg, R. J. Sudden death due to cardiac arrhythmias. *N. Engl. J. Med.* **345**, 1473–1482 (2001).
- Paakkari, I. Cardiotoxicity of new antihistamines and cisapride. *Toxicol. Lett.* **127**, 279–284 (2002).
- Splawski, I. *et al.* $\text{Ca}_v1.2$ Ca^{2+} channel dysfunction causes a multisystem disorder including arrhythmia and autism. *Cell* **119**, 19–31 (2004).
- Splawski, I. *et al.* Severe arrhythmia disorder caused by cardiac L-type Ca^{2+} channel mutations. *Proc. Natl Acad. Sci. USA* **102**, 8089–8096 (2005).
- Yarotsky, V. & Elmslie, K. S. Roscovitine, a cyclin-dependent kinase inhibitor, affects several gating mechanisms to inhibit cardiac L-type ($\text{Ca}_v1.2$) Ca^{2+} channels. *Br. J. Pharmacol.* **152**, 386–395 (2007).
- Yarotsky, V., Gao, G., Peterson, B. Z. & Elmslie, K. S. The Timothy syndrome mutation of cardiac $\text{Ca}_v1.2$ (L-type) channels: multiple altered gating mechanisms and pharmacological restoration of inactivation. *J. Physiol. (Lond.)* **587**, 551–565 (2009).
- Yarotsky, V. *et al.* Roscovitine binds to novel L-channel ($\text{Ca}_v1.2$) sites that separately activate and inactivate. *J. Biol. Chem.* **285**, 43–53 (2010).
- Roden, D. M. & Viswanathan, P. C. Genetics of acquired long QT syndrome. *J. Clin. Invest.* **115**, 2025–2032 (2005).
- Chen, L. *et al.* Mutation of an A-kinase-anchoring protein causes long-QT syndrome. *Proc. Natl Acad. Sci. USA* **104**, 20990–20995 (2007).
- Roden, D. M. Clinical practice. Long-QT syndrome. *N. Engl. J. Med.* **358**, 169–176 (2008).
- Moretti, A. *et al.* Patient-specific induced pluripotent stem-cell models for long-QT syndrome. *N. Engl. J. Med.* **363**, 1397–1409 (2010).
- Reuter, H. Ion channels in cardiac cell membranes. *Annu. Rev. Physiol.* **46**, 473–484 (1984).
- Flucher, B. E. & Franzini-Armstrong, C. Formation of junctions involved in excitation-contraction coupling in skeletal and cardiac muscle. *Proc. Natl Acad. Sci. USA* **93**, 8101–8106 (1996).
- Seisenberger, C. *et al.* Functional embryonic cardiomyocytes after disruption of the L-type $\alpha_1\text{C}$ ($\text{Ca}_v1.2$) Ca^{2+} channel gene in the mouse. *J. Biol. Chem.* **275**, 39193–39199 (2000).
- Takeshima, H. *et al.* Embryonic lethality and abnormal cardiac myocytes in mice lacking ryanodine receptor type 2. *EMBO J.* **17**, 3309–3316 (1998).
- Yazawa, M. *et al.* TRIC channels are essential for Ca^{2+} handling in intracellular stores. *Nature* **448**, 78–82 (2007).
- Barrett, C. F. & Tsien, R. W. The Timothy syndrome mutation differentially affects voltage- and calcium-dependent inactivation of $\text{Ca}_v1.2$ L-type Ca^{2+} channels. *Proc. Natl Acad. Sci. USA* **105**, 2157–2162 (2008).
- Thiel, W. H. *et al.* Proarrhythmic defects in Timothy syndrome require calmodulin kinase II. *Circulation* **118**, 2225–2234 (2008).
- Takahashi, K. *et al.* Induction of pluripotent stem cells from adult human fibroblasts by defined factors. *Cell* **131**, 861–872 (2007).
- Yu, J. *et al.* Induced pluripotent stem cell lines derived from human somatic cells. *Science* **318**, 1917–1920 (2007).
- Aoi, T. *et al.* Generation of pluripotent stem cells from adult mouse liver and stomach cells. *Science* **321**, 699–702 (2008).
- He, J. Q., Ma, Y., Lee, Y., Thomson, J. A. & Kamp, T. J. Human embryonic stem cells develop into multiple types of cardiac myocytes: action potential characterization. *Circ. Res.* **93**, 32–39 (2003).
- Zhang, J. *et al.* Functional cardiomyocytes derived from human induced pluripotent stem cells. *Circ. Res.* **104**, e30–e41 (2009).

25. Brunner, M. *et al.* Mechanisms of cardiac arrhythmias and sudden death in transgenic rabbits with long QT syndrome. *J. Clin. Invest.* **118**, 2246–2259 (2008).
26. Meijer, L. *et al.* Biochemical and cellular effects of roscovitine, a potent and selective inhibitor of the cyclin-dependent kinases cdc2, cdk2 and cdk5. *Eur. J. Biochem.* **243**, 527–536 (1997).
27. Tran, T. H. *et al.* Wnt3a-induced mesoderm formation and cardiomyogenesis in human embryonic stem cells. *Stem Cells* **27**, 1869–1878 (2009).

Supplementary Information is linked to the online version of the paper at www.nature.com/nature.

Acknowledgements We thank K. Timothy and the Timothy syndrome patients who participated in this study; U. Francke for discussion and for providing karyotyping expertise; A. Cherry and D. Bangs for fibroblast isolation; K. C. Chan for iPSC cultures; O. Shcheglovitov for help with electrophysiological recordings; and A. Olson for help with the confocal microscope. Funding was provided by grants from the Japan Society

for the Promotion for Science and the American Heart Association Western States to M.Y., and a National Institutes of Health Director's Pioneer Award, a grant from the Simons Foundation to R.E.D and gifts from L. Miller, B. and F. Horowitz and M. McCaffery.

Author Contributions M.Y. and R.E.D. designed research and wrote the manuscript; J.A.B., J.H. and R.E.D. recruited the Timothy syndrome patients; M.Y. and X.J. generated and characterized control and Timothy syndrome iPSCs; A.M.P. conducted karyotyping; M.Y. performed generation and characterization of human cardiomyocytes, whole-cell patch clamp, and Ca^{2+} imaging; M.Y. and B.H. analysed cardiomyocytes contraction rates.

Author Information Reprints and permissions information is available at www.nature.com/reprints. The authors declare no competing financial interests. Readers are welcome to comment on the online version of this article at www.nature.com/nature. Correspondence and requests for materials should be addressed to R.E.D. (ricardo.dolmetsch@stanford.edu).

METHODS

Cell culture. HEK 293T cells were cultured in Dulbecco's Modified Eagle Media (DMEM) supplemented with 10% fetal bovine serum (FBS), 2 mM L-glutamine, 100 unit ml⁻¹ penicillin and 100 µg ml⁻¹ of streptomycin (all from Invitrogen). Human fibroblasts were maintained in Minimum Essential Medium, Eagle (MEME, ATCC) containing 10% FBS, 100 unit ml⁻¹ penicillin and 100 µg ml⁻¹ of streptomycin. The patient fibroblasts were obtained by punch biopsy following a protocol approved by the Stanford Institutional Review Board (IRB). Human iPSCs were cultured on irradiated DR4 mouse embryonic fibroblast feeders using DMEM/F12 (1:1) medium containing 20% knockout SR, 1 mM non-essential amino acids (all from Invitrogen), 3 mM L-glutamine, 0.1 mM β-mercaptoethanol (Sigma-Aldrich), 100 unit ml⁻¹ penicillin and 100 µg ml⁻¹ streptomycin and 10–15 ng ml⁻¹ bFGF (R & D Systems). Human cardiomyocytes generated from iPSCs were maintained in EB5 media: DMEM/F12 with GlutaMAX (Invitrogen) containing 5% FBS, 1 mM non-essential amino acids, 1 mM L-glutamine, 0.1 mM β-mercaptoethanol, 100 unit ml⁻¹ penicillin and 100 µg ml⁻¹ streptomycin.

Plasmids. pMXs-SOX2, pMXs-OCT3/4, pMXs-MYC and pMXs-KLF4 expression plasmids were generated by S. Yamanaka's group²⁰ and were obtained from Addgene. The pUMVC packaging plasmid and pCMV-VSV-G envelope plasmids were used to prepare the retroviruses. A retrovirus encoding yellow fluorescent protein (YFP) was generated to examine the infection efficiency of human fibroblasts. pMXs-YFP was amplified using Taq polymerase, subcloned into the vector fragment of pMXs-OCT3/4, digested with EcoRI and verified by sequencing.

iPSC generation with retroviral infection. To prepare the retroviruses, HEK 293T cells were plated at 6–8 × 10⁵ cells per well in 6-well plates coated with 20 µg ml⁻¹ of poly-ornithine. Twenty-four hours after plating, the cells were transfected with pMXs plasmids containing the coding sequences for YFP, SOX2, OCT3/4, MYC or KLF4, along with pUMVC and pCMV-VSV-G plasmids at the ratio of 2.125 µg of plasmid DNA to 5 µl of Lipofectamine2000 in 500 µl OpiMEM (both from Invitrogen). The ratio of pMXs:pUMVC:pCMV-VSV-G was 8:8:1. Twenty-four hours after transfection, the DMEM media was replaced with fibroblast (MEME) media. The next day the culture media containing the retroviruses was harvested and mixed 1:1 with 0.6 µg ml⁻¹ polybrene (Sigma-Aldrich). The cell debris in the mixtures was removed using 0.45 µm low-protein-binding filters (Nalgene).

The patient and human fibroblasts were plated at 1 × 10⁵ cells per well in 6-well plates one day before infection with the retroviruses. The retrovirus solution was added to the fibroblasts for 8 h per day for 4 days to reduce cell death. The viruses were prepared fresh for each infection. To prevent cell crowding which can inhibit cell growth, the infected fibroblasts were passaged every other day with a dilution ratio of 1:3. Six days after the first infection, infected fibroblasts were plated at 1–50 × 10³ cells per dish in gelatin-coated 100 mm dishes containing ~1.5 × 10⁶ irradiated DR4 feeder cells per dish. The density of infected cells on feeders was critical for successful reprogramming so cells were always seeded at three different densities. One day after plating on DR4 feeder cells, the media was changed to human iPSC media made as described above. Human ES-like colonies were observed 21–30 days after the initial infection. These colonies were treated with 3 unit ml⁻¹ dispase (Invitrogen) for 10 min at 37 °C and washed three times with iPSC media, before being mechanically isolated with 22G needles under a microscope for subcloning.

iPSC characterization. The Timothy syndrome mutation in patient-derived cells was confirmed using DNA sequencing. Genomic DNA was isolated using DNeasy Blood and Tissue Kit (Qiagen) and the region encoding CACNA1C exon 8a was amplified using PCR and the primer set: forward 5'-TACACTAATCATCATAGGGTCAT-3'; reverse 5'-TAGCGATTCCCAGTTTAGGTAC-3'. The PCR product (~1.2 kb) was purified using the QIAquick PCR purification kit (Qiagen) and directly sequenced using the original forward primer and a new reverse primer (Ori-R-MY): 5'-CTCAGAGATAGACTGCTCAGTCTATG-3'.

To investigate the number and site of viral integration in iPSC genome we used nested PCR to amplify iPSC genomic DNA treated with BamHI + BglII or PstI as has been previously described²². The primer sets used are shown in Supplementary Table 2. The PCR products were purified and direct-sequenced or subcloned into pCR4-TOPO vector (Invitrogen).

To examine the expression of pluripotent markers, we placed the iPSCs on 15-mm round coverslips (Warner Instruments, CS-15R) coated with Matrigel (BD Biosciences) in 24-well plates. The iPSCs were fixed using 4% paraformaldehyde (PFA, Electron Microscopy Sciences, EM grade), 2% sucrose in PBS for 20 min at room temperature and washed three times with PBS. The cells were then blocked overnight with a solution containing 5% donkey serum (Calbiochem), 1% bovine serum albumin (BSA, Sigma-Aldrich) and 0.1% Triton X-100 (Sigma-Aldrich) in PBS for anti-NANOG staining or with a solution containing 3% BSA and 0.25% Triton X-100 in PBS for anti-TRA-2-49/6E antibody staining. The samples were then washed six times using PBS and incubated with the anti-NANOG (1/20 dilution in the

NANOG blocking solution; R&D Systems) and TRA-2-49/6E antibodies (1/80 dilution in the blocking solution without any detergents; the antibody developed by P. W. Andrews was obtained from Development Studies Hybridoma Bank developed under the auspices of the NICHD and maintained in the University of Iowa, Department of Biological Sciences) for at least 24 h at 4 °C. After incubation with primary antibodies, samples were washed six times (5 min each), and incubated in secondary antibody, Alexa Fluor 594 (Molecular Probes, 2 µg ml⁻¹), for 30 min at room temperature, washed with PBS six times (5 min each), stained with Hoechst 33285 (Molecular Probes, 1/10,000 dilution in PBS) and mounted on slides (Becton, Dickinson) using Aqua Poly/Mount (Polysciences). Images were acquired using a ×10 (NA = 0.5) objective lens or ×40 (NA = 1.3) oil immersion objective lens (Nikon) on the stage of a Nikon Eclipse TE2000U inverted microscope.

Karyotyping of iPSCs was achieved using standard protocols. For RT-PCR, RNA from fibroblasts and iPSCs was prepared using the RNeasy Mini kit and RNase-Free DNase set (Qiagen). cDNA was synthesized from 1 µg RNA using the SuperScript III First-Strand Synthesis System for RT-PCR (Invitrogen). The cDNA (21 µl) was diluted with DNase-free water (Invitrogen) at 1:5 and 1 µl of the samples was used for conventional RT-PCR with AccuPower PCR PreMix (Bioneer, K-2016) using primer sets (Supplementary Table2). For quantitative RT-PCR, FastStart Universal SYBR Green Master (Rox, Roche) and Mastercycler ep realplex (Eppendorf) were used.

Teratoma formation assays. Teratoma formation experiments were performed by injecting subcutaneously ~1 × 10⁶ cells in 50% Matrigel and 10 µM Y-27632 (Calbiochem) in iPSC media (~1 × 10⁷ cell ml⁻¹) into 8-week-old severe combined immunodeficient (SCID) beige mice (Charles River Laboratories). The mice were killed ~8 weeks after injection, the tumours were dissected, fixed with PBS containing 4% PFA and 10–30% sucrose and embedded in Tissue-Tek OCT compound (Sakura Finetek). Sections were stained with Haematoxylin 7211 and Eosin-Y (Thermo Scientific). All animal protocols and handling for the teratoma formation assay were performed following the guidelines established by Stanford University Administrative Panel on Laboratory Animal Care (APLAC) Committee.

Differentiation of iPSCs into cardiomyocytes. iPSCs in 6-well plates (Falcon, 353046) were treated with 3 unit ml⁻¹ of dispase for ~20 min at 37 °C to detach the colonies completely. The colonies were collected by allowing the iPSC colonies settle to the bottom of the 50 ml tubes for ~6 min. The iPSC colonies were then washed and placed in Ultra-low 100-mm dishes (Corning Life Sciences) with iPSC media containing 10 µM Y-27632 without bFGF to form embryoid bodies. The next day the media was changed to EB20 with Wnt3a (DMEM/F12 with GlutaMAX containing 20% FBS, 1 mM non-essential amino acids, 1 mM L-glutamine, 0.1 mM β-mercaptoethanol, 100 unit ml⁻¹ penicillin, 100 µg ml⁻¹ streptomycin and 100 ng ml⁻¹ Wnt3a (R&D Systems²⁷)). Between days three and six, the media was changed to EB20 media without Wnt3a and media replaced every other day. At day 7, the EBs (~80 per dish) were plated into 100-mm dishes (BD Biosciences) coated with gelatin in EB5 media as described above. During days 7–37, the media was changed daily, and at around day 17 some of the EBs were observed to contract spontaneously. At day 37, EBs were isolated mechanically using a 22G needle, placed into 15-ml tubes, washed with PBS once, centrifuged (1,000 r.p.m., 2 min) and incubated in 0.25% trypsin and 0.03% EDTA (Invitrogen) for 4 min at room temperature with gentle shaking. EB5 media was then added to the tube, the cells were isolated by centrifugation and washed before using 1 ml of EB5 media and a P1000 filter tip (~30 times) to dissociate the EBs into single cells. The cells were plated on gelatin-coated 15-mm round coverslips in 24-well plates or 4-well LAB-TEK II chambers (Nalge Nunc International, chamber #1.5 German coverglass system). A single EB was sufficient for a few coverslips or wells of a chamber. For about 7 days after dissociation, cells were observed without conducting experiments, to ensure that the coverslips and chambers were not contaminated with fast-growing cell populations such as fibroblast-like cells and progenitors. The antibodies to cardiac Troponin I (clone 284, 1/200 dilution, Abcam) and α-actinin (clone EA-53, 1/200 dilution, Sigma-Aldrich) were used to characterize the dissociated cardiomyocytes.

Analysis of cardiomyocytes contraction. Images were collected at a rate of 5 frames per second using OpenLab software (Perkin Elmer) and converted to multiframe TIFF images for analysis using the Image Processing Toolbox in MATLAB R2009b (Mathworks). Relative motion between successive frames was quantified by subtracting each frame from the preceding frame and summing across all pixels. Movement was calculated by plotting the relative motion over time. Contractions were detected as a peak of relative motion and a second, typically smaller peak, corresponded to the relaxation of the EBs. Peaks were selected manually and the length of time between contractions was measured. Rhythmicity was measured by calculating the ratio of the standard deviation to the mean of the intervals between contractions. The threshold for classifying an EB

as contracting arrhythmically was two standard deviations from the average rhythmicity of control cells.

Patch-clamp electrophysiology. Whole-cell patch-clamp recordings of human cardiomyocytes generated from iPSCs were conducted using an EPC-10 patch-clamp amplifier (HEKA) and an inverted microscope equipped with differential interface optics (Nikon, TE2000-U). The glass pipettes were prepared using borosilicate glass (Sutter Instrument, BF150-110-10) using a micropipette puller (Sutter Instrument, Model P-87). Voltage-clamp measurements were conducted using an extracellular solution consisting of 5 mM BaCl₂, 160 mM TEA and 10 mM HEPES (pH 7.4 at 25 °C) and a pipette solution of 125 mM CsCl, 0.1 mM CaCl₂, 10 mM EGTA, 1 mM MgCl₂, 4 mM MgATP, 0.3 mM NaGTP and 10 mM HEPES (pH 7.4 with CsOH at 25 °C). The following pulse protocols were used: cells were held at -90 mV and depolarized to +30 mV for 400 ms at a rate of 0.1 Hz (Fig. 2b-d and Supplementary Fig. 4b); cells were held at -90, stimulated with a 2-s family of pulses from -110 to +30 which was followed by a 300-ms test pulse to -10 mV (Fig. 2e and Supplementary Fig. 4c). Current-clamp recording were conducted in normal Tyrode solution containing 140 mM NaCl, 5.4 mM KCl, 1 mM MgCl₂, 10 mM glucose, 1.8 mM CaCl₂ and 10 mM HEPES (pH 7.4 with NaOH at 25 °C) using the pipette solution: 120 mM K D-gluconate, 25 mM KCl, 4 mM MgATP, 2 mM NaGTP, 4 mM Na₂-phospho-creatin, 10 mM EGTA, 1 mM CaCl₂ and 10 mM HEPES (pH 7.4 with KCl at 25 °C). *R*-roscovitine (Sigma-Aldrich, R7772) was dissolved in DMSO and the same concentration of DMSO was used as a control.

Single-cell RT-PCR. Immediately after whole-cell patch-clamp recording, the glass recording pipette was changed to a larger glass pipette containing ~5 µl of lysis buffer (CellsDirect one-sep for qRT-PCR, Invitrogen) to harvest the intact cell for cDNA preparation. Harvesting pipettes were prepared using borosilicate glass with filament (Warner Instruments, G150T-4) with the following parameters: (heat, velocity, time) (1) 730, 20, 250; (2) 720, 20, 250; (3) 720, 20, 250; (4) 640,

36, 250, using a micropipette puller. The lysis solution containing the cell was transferred to a sterile PCR tube containing ~5 µl of the lysis buffer (total volume ~8 µl) using pressure from a syringe. The sample was incubated at 75 °C for 5 min and then chilled to 4 °C. Next, 10 µl of 2× RT Reaction Mix and 2 µl of RT Enzyme Mix (SuperScript III First-Strand Synthesis SuperMix for qRT-PCR, Invitrogen) were added. To synthesize cDNA from single cells the sample was incubated at 25 °C for 10 min; 50 °C for 30 min; 85 °C for 5 min; 4 °C for 5 min. To remove RNA, 1 µl of RNase H was added and the sample was incubated at 37 °C for 20 min. To perform RT-PCR, 1 µl of the samples were used as template for a 60–70 cycles.

Ca²⁺ imaging. Cardiomyocytes were placed in 4-well slide chambers and loaded with 5 µM Fluo-4 AM and 0.02% Pluronic F-127 (both reagents from Molecular Probes) in Tyrodes solution for 15 min at 37 °C. Ca²⁺ imaging was conducted with a confocal microscope (Carl Zeiss, LSM 510 Meta) with a ×63 lens (NA = 1.4) operated by Zen software (Carl Zeiss). Line scans were acquired at a sampling rate of 1.92 ms line⁻¹ (total 10,000 times for 19.2 s recoding) at room temperature. Fiji software, a derivative of ImageJ (National Institutes of Health), Excel (Microsoft) and programs developed by B.H. were used to analyse irregularity of spontaneous Ca²⁺ transients.

Analysis of calcium imaging traces. The time course of intracellular Ca²⁺ was determined by using Fiji software to average the intensity across each line. The Ca²⁺ traces were then analysed using MATLAB to calculate the irregularity of the timing and amplitude of the Ca²⁺ transients. The period of the transients (timing) was defined as the peak-to-peak interval for two successive Ca²⁺ elevations with peaks determined automatically from the smoothed second derivative of the Ca²⁺ signal using MATLAB's Signal Processing Toolbox. The amplitude of Ca²⁺ transients (amplitude) was determined by numerically integrating the area underneath each Ca²⁺ peak relative to the baseline. Irregularity in both timing and amplitude was defined in the same manner as described above for EB contraction rates.